Indirect Searches for Physics Beyond the Standard Model

by

Christopher Robert Dessert

A dissertation submitted in partial fulfillment
of the requirements for the degree of
Doctor of Philosophy
(Physics)
in the University of Michigan
2022

Doctoral Committee:

Professor Aaron Pierce, Co-Chair
Professor Benjamin R. Safdi, University of California Berkeley, Co-Chair
Professor Fred C. Adams
Professor Elena Gallo
Professor Joshua Miller Spitz

Christopher Robert Dessert
dessert@umich.edu
ORCID iD: 0000-0003-1994-088X

Acknowledgements

Since I was very young I have been interested in learning as much about how the universe works as I possibly can. Now that I have been able to contribute to some small slice of that knowledge, I am eternally grateful to the people who have helped make that possible over the course of my graduate career at Michigan.

I would first like to thank my advisor Ben Safdi. I started working with Ben in my first week of graduate school and since that day I have always felt that the projects I was working on were important both to our group and to the field as a whole. Over the last five years, Ben has been a supportive advisor both academically and personally, and has been genuinely committed to creating a working environment in which his students can succeed.

There are a number of postdocs who I have been especially fortunate to work with in graduate school. I would like to thank both Nick Rodd and Andrew Long, both of whom I collaborated with early on, for being amazingly patient as I made the transition from a student to a researcher, Malte Buschmann for saving me innumerable hours debugging `Fortran` code, and Raymond Co for always being willing to answer physics questions I should have already known the answer to. I also benefited greatly from the pedagogy of and career advice from faculty at Michigan, including Aaron Pierce, Finn Larsen, Henriette Elvang, Dragan Huterer, and Fred Adams.

I appreciate so much the UC Berkeley physics group who welcomed me when I moved to California for my last year of graduate school. In particular, I am so glad I was able to get to know Simon Knapen, Toby Opferkuch, Linda Xu, Nadav Outmezguine, Soubhik Kumar, and David Dunsky.

I also have to thank the number of closer friends who got me through not only graduate school but a pandemic. Firstly I want to thank Josh Foster, for making the sheer volume of Zoom calls bearable by "sharing memes," but also for being a great role model both in physics and as a graduate student. Secondly, Zach Johnson, for sharing the physics understanding he usually picked up quicker than I, and for keeping me motivated to continue learning. In addition, Ben Sheff, Marina David, Jon Wang, and Huy Ngyuen, for their friendship.

I would be remiss not to thank those who played the largest part in getting me where I

am today: my parents, Amy and David, and my brother Jack, for their unwavering support of my goals no matter what they are. Lastly, I am so grateful to my partner Julia, without whom I surely would not have been able to achieve anywhere near what I did. Meeting you was the most important part of my life at Michigan, and I am so delighted to move on to the next stage of our lives together.

Table of Contents

List of Tables

List of Figures

List of Appendices

Abstract

Despite the overwhelming success of the Standard Model of particle physics, there are several outstanding issues, perhaps most notably the lack of a dark matter candidate. In this thesis, we develop novel astrophysical probes to search for evidence of a few of these candidates.

In the first part of this thesis, we make use of the 20-year dataset of the XMM-Newton telescope to search for evidence of sterile neutrino dark matter decays. Sterile neutrino dark matter can decay to an active neutrino and a photon, the latter of which would appear in X-ray datasets if the sterile neutrino mass is on the keV-scale. We first show that the previously-observed 3.5 keV line does not originate from dark matter decay. We then constrain dark matter decays across the 5-16 keV mass range, setting the strongest limits to-date up to 12 keV in sterile neutrino mass.

In the second part of this thesis, we detail several searches for low-mass axion-like particles, although they do not have to be dark matter. We spend the majority of this section looking for evidence of excess hard X-ray emission in nearby magnetic neutron stars and white dwarfs. When an axion is produced inside the core of a compact object, it will free-stream out of the star and may convert into an X-ray photon in the magnetosphere of the star. This process will lead to an approximately thermal X-ray signature at the temperature of the star's core. Intriguingly, we find an excess roughly consistent with that expected from an axion in a set of nearby neutron stars known as the Magnificent Seven. However, the lack of such a signal in a nearby white dwarf somewhat disfavors the axion interpretation of that excess. We also search for axions at super star clusters, and through polarization signals at magnetic white dwarfs, and we use NS cooling observations to constrain the QCD axion mass.

Finally, we investigate macroscopic dark matter. We show that macroscopic dark matter can ignite fusion in the cores of red giant stars, leading to a distinct signal at globular clusters. We search for this signal at the globular cluster M15 to set a novel constraint on macroscopic dark matter.

Chapter 1

Introduction

The ordinary matter described by the Standard Model (SM) of particle physics accounts for approximately only one-sixth of the total matter in our universe. A plethora of diverse astrophysical and cosmological measurements indicate that the vast majority of the matter in the universe is dark, but the precise microscopic properties of this dark matter (DM) is unknown. Although DM experiences gravitational interactions—these interactions form the complete basis for our existing knowledge of its properties—we do not know what other interactions it may have or indeed even its mass. Discerning the particle nature of DM is one of the primary goals of the particle physics program, and success on this front would open up a slew of measurements of physics beyond the SM.

The first evidence for the existence of DM was provided in 1933 by Fritz Zwicky [72]. The classical technique to measure the mass M of an astrophysical body is relatively straightforward: one multiplies the luminosity L of the object by its mass-to-light ratio M/L, leading to the trivial equation

$$M = L \times M/L. \tag{1.1}$$

Clearly one needs an independent estimate of the mass-to-light ratio. Estimates of the mass-to-light ratio from nearby stars in our galaxy [73] indicate that this ratio in solar units is about 1-10 for the stellar populations in galaxies, depending on the exact stellar properties. On the other hand, Zwicky measured the velocity dispersion in the Coma galaxy cluster, and computed that the mass-to-light ratio of Coma is roughly 60 times that of the stellar matter under the assumption of the virial theorem. From this he deduced that there must be additional mass beyond stellar material that makes up the majority of the mass of the Coma cluster. In fact, there are additional baryonic contributions to the ordinary matter beyond stars, for example hot X-ray emitting gas, but even including these does not nearly

fully account for the discrepancy.

Much later, in the 1970s Rubin measured the rotation speed of the Andromeda galaxy [74] (among others), and found that the rotation speeds were constant as a function of distance from the center of the galaxy. From Newtonian mechanics, the circular velocity $v(r)$ of stars at a distance r from a galactic center, enclosing mass $M(r)$, is

$$v(r) = \sqrt{\frac{GM(r)}{r}}. \tag{1.2}$$

If the total enclosed mass has converged, *i.e.* for distances beyond the Galactic disk, $M(r)$ is constant so $v \propto 1/\sqrt{r}$. However, in many galaxies, v is constant even at radii much larger than the disk radius, such that the enclosed mass must be still increasing $M(r) \propto r$; this mass is attributed to DM.

The above evidence points to that the DM exists and is dark, but does not say much about its interactions with itself. One of the most famous pieces of evidence that DM is weakly interacting with itself is that of the Bullet Cluster, which is a set of two galaxy clusters that are immediately post-merger. The bulk of the luminous ordinary (and self-interacting) matter is traced by the hot X-ray gas, while weak gravitational lensing probes map the distribution of the total matter in the cluster. However, observations show that these two reservoirs of matter are spatially separated, and the luminous matter traveled slower than the total mass distribution post-merger. So, while the luminous matter experienced friction due to its self-interactions, the DM component appears not to have any such self-interaction (or at most a small one).

Perhaps the most robust evidence for the existence of DM comes from measurements of the two-point correlation function of the Cosmic Microwave Background (CMB). The *Planck* telescope has now measured the dark matter component to have energy density

$$\Omega_{\rm DM} h^2 = 0.120 \pm 0.001, \tag{1.3}$$

just over five times that of the baryonic component [75].

In the following two sections we turn to examining particular particle models for DM and more generically physics beyond the SM. DM particle candidates are particularly interesting when they can also address additional unsolved problems in particle physics. For example, the first candidate discussed in this thesis, sterile neutrino DM, can simultaneously solve the problem of the neutrino masses, which are set to zero in the SM. Similarly, the second candidate, the axion, solves the strong CP problem.

1.1 Sterile Neutrino Dark Matter

The existence of neutrino oscillations has firmly established that the SM neutrinos have mass [76], with a present-day upper bound on the sum of neutrino masses $\sim$0.15 eV [77]. If they get their mass from the Higgs mechanism, then the neutrino mass term (simplified to the one-generation case) is

$$\mathcal{L}_{\text{Dirac}} = -m(\overline{\nu_R}\nu_L + \overline{\nu_L}\nu_R) \tag{1.4}$$

where the R and L subscripts refer to the right- and left-handed neutrino states. In the SM the right-handed neutrinos do not appear in the Lagrangian as they are SM singlets, so it is not clear that they exist. However, if the neutrino mass is Dirac, then right-handed neutrinos do exist.

Another curiosity about this mass term is that the neutrino masses are much smaller than that of the other fermions which obtain mass via the Higgs mechanism. The massive states in the SM broadly speaking have Yukawa couplings of $\mathcal{O}(10^{-3})$, within a few orders of magnitude. On the other hand, to generate such a small Dirac mass for the neutrinos, the neutrino Yukawa couplings must be $\lesssim 10^{-12}$. The discrepancy between these sets of Yukawa couplings, while not explicitly disallowed, is strange and points to perhaps another mechanism of mass generation for the neutrinos.

There is another type of mass term allowed by gauge invariance, called the Majorana mass term, which is formed out of two SM singlets: the right-handed neutrino ν_R and the left-handed antineutrino ν_R^c, where here the c superscript indicates that the charge and parity operations have been applied to ν_R. This term looks like

$$\mathcal{L}_{\text{Majorana}} = -\frac{M}{2}(\overline{\nu_R^c}\nu_R + \overline{\nu_R}\nu_R^c). \tag{1.5}$$

In general one can have both types of mass terms, and in that case the Lagrangian can be rewritten as

$$\mathcal{L}_{\text{Seesaw}} = -\frac{1}{2}\begin{pmatrix}\overline{\nu_L} & \overline{\nu_R^c}\end{pmatrix}\begin{pmatrix}0 & m\\ m & M\end{pmatrix}\begin{pmatrix}\overline{\nu_L^c}\\ \overline{\nu_R}\end{pmatrix}. \tag{1.6}$$

Here the mass matrix is written in the chiral basis, but the physical states are given in the mass-diagonal basis. Of particular interest is that the eigenvalues of the mass matrix in the limit $m \ll M$ are approximately given by m^2/M and M. By adding this term to the SM, the light neutrino states (that are dominantly the left-handed neutrinos in the SM) acquire a mass m^2/M. Under this scenario, neutrinos may be given a Dirac mass by the

Higgs mechanism, but end up with a much smaller physical mass. On the other hand, the heavy neutrino states (that are dominantly the right-handed neutrinos) have a large mass M, and dubbed the "sterile neutrinos" as they only weakly interact with the SM through their mixing with the light states, suppressed by m/M. For $\mathcal{O}(1)$ Yukawa neutrino couplings and GUT-scale M, this scenario, known as the Seesaw mechanism, explains the existence of neutrino masses and why they are so small relative to that of the other SM fermions.

Intriguingly, if the mass of the sterile neutrino is instead at the keV scale, then it can be dark matter. In this case, one does not get much Seesaw effect, but in many sterile neutrino extensions of the Standard Model, such as the νMSM [78], one introduces three sterile neutrino states, two of which Seesaw to realize the atmospheric and solar neutrino mass scales, while the third state does not so that it can be the dark matter. The sterile neutrinos are dark and only weakly interact with the SM. For sterile neutrinos to be a DM candidate, they must also be able to take on the observed abundance in the universe today, and as a corollary they must be stable over cosmological timescales. Although a variety of production mechanisms exist for sterile neutrinos, we will provide a brief overview of the simplest mechanism, called the Dodelson-Widrow mechanism [79]. This mechanism is a freeze-in production of DM, so that the initial abundance of sterile neutrinos is null. However, when the active neutrinos interact with the SM bath in the early universe, there is a small probability of order the active-sterile neutrino mixing angle that a sterile neutrino is produced in the interaction. Because the active neutrino abundance is in equilibrium with the SM bath, it is not reduced by this process, and in principle the sterile neutrino production can happen continuously. In practice, it is cut off when the active neutrino interaction rate with the SM bath becomes too small for many interactions to occur, and the sterile neutrino abundance freezes out at that time. This mechanism is able to produce the observed DM abundance, although the required active-sterile neutrino mixing angles are now excluded by X-ray searches for sterile neutrino DM decay. Resonant production mechanisms, such as the Shi-Fuller mechanism [80], in which the sterile neutrino production is enhanced in the early universe because of an MSW-effect arising from lepton asymmetries, can produce the required DM abundance while still living in allowed parameter space. Even sterile neutrinos produced via resonant mechanisms are extremely constrained due to the BBN limit on the lepton chemical potential [81], and searches like those outlined in this thesis may soon probe the entire parameter space.

Once the sterile neutrino abundance is produced, it must not decay away before today. Sterile neutrino DM has two decay channels, $\nu_s \to \nu_a \gamma$ and $\nu_s \to \nu_a \nu_a \overline{\nu_a}$, where ν_s and ν_a refer to sterile and active neutrinos respectively. Of these two, the latter decay is much faster, and requiring that the decay time is larger than the age of the universe leads to the

bound $m_s < 40$ keV [82]. Although the former decay is slower, it produces a monochromatic X-ray signal, and searches for this signal, such as those described later in this thesis, provide the leading constraints on sterile neutrino DM parameter space.

1.2 Axions and Axion-Like Particles

The axion is a hypothetical pseudoscalar particle that was originally introduced to solved the Strong CP problem, *i.e.*, the problem of why the neutron has no electric dipole moment (EDM). Classically, one would generically expect that the neutron has an EDM of order the product of its charge of its constituents and their charge separation,

$$d_n \approx 10^{-13}\ e\ \times \text{cm}, \tag{1.7}$$

if the constituent quarks are arbitrarily distributed throughout the neutron. On the other hand, experiments designed to detect a neutron EDM have probed far beyond this naive expectation, with the current upper limit $d_n < 10^{-26}\ e \times$ cm [83] and no evidence for a neutron EDM.

Fundamentally, the neutron EDM arises from the term in the QCD Lagrangian

$$\mathcal{L}_{\text{QCD}} \supset -\frac{\theta g_s^2}{32\pi^2} G^a_{\mu\nu} \tilde{G}^{\mu\nu,a} \tag{1.8}$$

where g_s is the strong coupling constant, $G^a_{\mu\nu}$ is the gluon field strength tensor running over the gluon labeled by $a \in \{1, ..., 8\}$, and $\tilde{G}^{\mu\nu,a} = \frac{1}{2}\epsilon^{\mu\nu\lambda\sigma} G^a_{\lambda\sigma}$ is its Hodge dual. To satisfy the neutron EDM constraints, this parameter θ is required to be less than 10^{-10}. In principle this is possible, but this term can be generated through divergent loop corrections, so θ is needed to renormalize the divergence. Furthermore, there is an additional contribution from this term. Under a chiral rotation of the quark fields that diagonalizes their mass matrix M,

$$q \to \exp(i\theta' M\gamma^5) q,\ \ \bar{q} \to \bar{q} \exp(i\theta'\gamma^5), \tag{1.9}$$

because the path integral measure is not invariant under this rotation, we have $\theta \to \theta - \theta' \equiv \bar{\theta}$. In that case, we are left with a CP violating term

$$\mathcal{L}_{\text{QCD}} \supset -\frac{\bar{\theta} g_s^2}{32\pi^2} G^a_{\mu\nu} \tilde{G}^{\mu\nu,a} \tag{1.10}$$

that contains two phases, one from QCD and one from the weak sector. Either of these phases could take on values in $(-\pi, \pi]$, but their difference must be less than 10^{-10}, which

seems very unlikely. This is the essence of the Strong CP problem.

One can come to the axion solution by looking at the Chiral Lagrangian, which contains a term

$$\mathcal{L}_{\chi \mathrm{L}} \supset \Lambda_{\mathrm{QCD}}^3 \mathrm{tr}\left[MU + M^\dagger U^\dagger\right]. \tag{1.11}$$

If we use a chiral rotation to put all of the CP violation in the Yukawa couplings, we get complex quark masses, so that the vacuum energy from this term depends on $\bar{\theta}$ as $-\Lambda_{\mathrm{QCD}}^3 \cos\bar{\theta}$, which is minimized at $\bar{\theta} = 0$. $\bar{\theta}$ is not dynamical, but what if it was?

Peccei and Quinn suggested to solve the strong CP problem by making θ a dynamical parameter of the theory by introducing a new particle called the axion a, which couples to QCD in the same way as does $\bar{\theta}$ [84]:

$$\mathcal{L}_a \supset -\left(\bar{\theta} + \frac{a}{f_a}\right) \frac{g_s^2}{32\pi^2} G^a_{\mu\nu} \tilde{G}^{\mu\nu,a}. \tag{1.12}$$

Here f_a is the PQ scale of the the UV completion, taken to be much higher than the weak scale. Now the same term in the that originally only contributed to the vacuum energy contributes a potential to the axion that, when worked out in detail, gives [85]

$$V(a) = -m_\pi^2 f_\pi^2 \sqrt{1 - \frac{4 m_u m_d}{(m_u + m_d)^2} \sin^2\left(\frac{a}{2f_a} + \frac{\bar{\theta}}{2}\right)}. \tag{1.13}$$

When the axion minimizes its potential in the early universe, $a/f_a \to -\theta$, and the neutron EDM vanishes. The axion which has such a coupling to QCD is known as a QCD axion.

This potential also generates a mass for the QCD axion approximately given by

$$m_a \approx 10^{-6}\ \mathrm{eV} \left(\frac{10^{12}\ \mathrm{GeV}}{f_a}\right). \tag{1.14}$$

Furthermore, the QCD axion mixes with the neutral pion, which induces an axion coupling to electromagnetism analogously to the axion-gluon coupling. Finally, derivative couplings to fermions are induced by renormalization group evolution if they are zero at tree level.

Throughout most of this thesis we will not be probing the QCD axion, which is largely too weakly coupled to be probed through astrophysics unless its mass is larger than a few meV. We will study a broader class of axions, known as axion-like particles (ALPs), which do not couple to gluons and therefore do not solve the strong CP problem, but still have the other couplings. Such theories may be motivated by string theory constructions that predict many ALPs arising from the compactification. These ALPs have small masses, typically

much smaller than that of the QCD axion. Later in this thesis we will make use of the ALP couplings to electromagnetism and matter to devise searches for axions. Furthermore, both the QCD axion and ALPs can be the DM of the universe, although throughout this thesis I will not make any such assumption.

1.3 Thesis Overview

Chapter 2: *The dark matter interpretation of the 3.5-keV line is inconsistent with blank-sky observations* with Nicholas L. Rodd and Benjamin R. Safdi. *Science* 367 (2020) 6485, 1465-1467; 1812.06976 [astro-ph.CO]

In the first two chapters of this thesis, we discuss efforts to detect sterile neutrino DM. We use astrophysical X-ray observations of the inner Milky Way (MW) galaxy with the *XMM-Newton* telescope to search for evidence of a putative DM signal known as the 3.5 keV line. The 3.5 keV line is a narrow, emission line-like feature observed in some X-ray spectra of galaxies and galaxy clusters at 3.5 keV that has no obvious astrophysical explanation. Intriguingly, the line could be explained by decaying DM with a mass around 7 keV—in particular, sterile neutrino DM. Most previous detections of (and null searches for) this line had been at galaxies and galaxy clusters. In this chapter, we make the general argument that the MW halo is the most sensitive target at which to search for evidence of decaying DM, both because the expected signal size is similar to or larger than those at clusters, and because the astrophysical background is smaller. Furthermore, we use every existing *XMM-Newton* observation of the inner 45° of the MW halo, totaling about 30 Ms of exposure time, to search for evidence sterile neutrino DM decays into the 3.5 keV line. We find no evidence of the 3.5 keV line in that dataset and set an upper limit on the sterile neutrino-active neutrino mixing angle that precludes the explanation of the 3.5 keV line as a product of sterile neutrino DM decay.

Chapter 3: *Deep Search for Decaying Dark Matter with XMM-Newton Blank-Sky Observations* with Joshua W. Foster, Marius Kongsore, Yujin Park, Nicholas L. Rodd, Kyle Cranmer, and Benjamin R. Safdi. *Phys.Rev.Lett.* 127 (2021) 5, 051101

We use a similar dataset to that in Chapter 2 to search for signals of decaying sterile neutrino DM across a broad mass range of 5-16 keV. We use in sum 547 Ms of *XMM-Newton* exposure time to analyze background-subtracted spectra of the inner MW halo, where the background is determined by the data near the Galactic anti-Center. This work is the

first time that the non-parametric Gaussian process modeling technique has been applied to astrophysical data. Because the spectral analysis is non-parametric, the modeling of the astrophysical background has increased flexibility and improved robustness to mismodeling, which is particularly important due to the extreme amount of data incorporated into the analysis. We find no evidence for decaying sterile neutrino dark matter and set the strongest constraints on the sterile neutrino-active neutrino mixing angle in most of the search parameter space. This work also provides a confirmation of the non-observation of the 3.5 keV line with an alternate analysis strategy from that discussed in Chapter 2.

Chapter 4: X-ray Signatures of Axion Conversion in Magnetic White Dwarf Stars with Andrew J. Long and Benjamin R. Safdi. *Phys.Rev.Lett.* (2019) 6, 061104

Starting from chapter 4, we shift focus to indirect detection of axions. We propose for the first time that magnetic white dwarf (WD) stars may produce hard X-ray emission if there is an axion in the theory. WDs have been probes of axions for decades because they may cool excessively quickly due to axion emission from the hot stellar core. These axions are emitted by axion bremsstrahlung in electron-nucleon scattering. In this chapter, we show that these axions may convert into photons as they traverse the stellar magnetosphere, leading to an excess of hard X-rays originating from the magnetic WD. We use an archival *Suzaku* observation of a magnetic WD RE J0317-853 to set the strongest constraints on the product of the axion-electron and axion-photon couplings. We show that future *Chandra* observations of this WD could again increase the sensitivity to that coupling product by over an order of magnitude.

Chapter 5: *No Evidence for Axions from Chandra Observation of the Magnetic White Dwarf RE J0317-853* with Andrew J. Long and Benjamin R. Safdi. *Phys.Rev.Lett.* 128 (2022) 7, 071102

We observed the magnetic WD RE J0317-853 with the *Chandra* X-ray telescope for 40 ks to search for evidence of axion emission as described in Chapter 4. This observation detected no X-ray signal from RE J0317-853, from which we placed the strongest constraints on the product of the axion-electron and axion-photon couplings by two orders of magnitude in total. These constraints disfavor the axion-based explanation of several astrophysical anomalies, including some of the parameter space explaining the increased transparency of the universe to TeV-energy gamma-rays, and of that explaining the observation of increased stellar cooling in WDs and horizontal branch stars.

Chapter 6: *Hard X-ray Excess from the Magnificent Seven Neutron Stars* with Joshua W. Foster and Benjamin R. Safdi. *Astrophys.J.* 904 (2020) 1, 42

We analyze the hard X-ray spectra of seven nearby isolated neutron stars (NS), known as the Magnificent Seven, because they are the only known seven NSs that are pure thermal emitters. Although naively unrelated to axion detection, as we will show in Chapter 7, the search we perform here can be adapted to probe axions. We use all of the available X-ray data on each NS, from the telescopes *XMM-Newton* and *Chandra*, to search for evidence of any nontrivial hard X-ray emission. We find significant hard X-ray excesses from two of the seven NSs, RX J1856.6-3754 and RX J0420.0-5022. We show that these excesses are likely not due to the main possible systematics such as co-linear point sources or detector pileup, and that there are no known astrophysical mechanisms that can replicated the observations.

Chapter 7: *Axion Emission Can Explain a New Hard X-Ray Excess from Nearby Isolated Neutron Stars* with Malte Buschmann, Raymond T. Co, and Benjamin R. Safdi. *Phys.Rev.Lett.* 126 (2021) 2, 021102

Axions can be produced via axion bremsstrahlung in nucleon-nucleon scattering inside NS cores, free-stream out of the star, and convert into X-rays in the NS magnetosphere, in a process nearly identical to that operating in WDs as discussed in Chapters 4 and 5. In this work we interpret the data analyzed in Chapter 6 in the context of this scenario. We discuss our modeling of the NS star with the NS cooling code `NSCool` and the theoretical uncertainties, including those arising from the modeling of the NS, such as superfluidity, equation of state, and core temperature. We find that the hard X-ray excess observed from the Magnificent Seven NSs can be explained by an axion with couplings sufficiently small that it would not have been previously observed in any laboratory or astrophysical experiment.

Chapter 8: *X-ray Searches for Axions from Super Star Clusters* with Joshua W. Foster and Benjamin R. Safdi. *Phys.Rev.Lett.* 125 (2020) 26, 261102

We focus on a novel target for axion indirect detection: super star clusters. Super star clusters (SSCs) are thought to be the precursors of globular clusters, and are home to hundreds of young, hot, and massive stars. Axions can be produced in these stars via the Primakoff process. Although these stars have no or small magnetic fields, so that conver-

sion to photons in the stellar magnetosphere is small, the axions may be converted as they traverse the galactic magnetic field on the way to Earth. SSCs are optimal targets for axion searches because of the hot interiors of the stars and the fact that they host many of the stars, so that the expected axion luminosity can be approximately multiplied by the number of stars in the SSC as compared to searches at a single star. We use *NuSTAR* data of two SSCs, Quintuplet and Westerlund 1, to search for evidence of axions, and model the stars using the stellar modeling package `Modules for Experiments in Stellar Astrophysics`. We find no evidence in favor of the axion model and place the most stringent constraints on axions with masses less than 10^{-10} eV.

Chapter 9: *Upper Limit on the QCD Axion Mass from Isolated Neutron Star Cooling* with Malte Buschmann, Joshua W. Foster, Andrew J. Long, Benjamin R. Safdi. *Phys.Rev.Lett.* 128 (2022) 9, 091102

We focus on developing robust and statistically-grounded probes of the axion via NS cooling, focusing in particular on the QCD axion. In particular, we examine the cooling of five NSs with precise surface luminosity measurements and kinematically-derived ages under the QCD axion model. We model the cooling of these NSs with the NS cooling code *NSCool*, which we have modified to incorporate axion emission, and we profile over the equation of state, NS masses, surface composition, and superfluidity models. We additionally update *NSCool* to reflect the latest calculations of axion and neutrino emissivities. We develop an analysis framework to set frequentist limits on the axion mass, which has been somewhat neglected in previous literature. We find no evidence for the axion model, and constrain the KSVZ axion to have mass less than 16 meV at 95% confidence.

Chapter 10: *Upper limit on the axion-photon coupling from magnetic white dwarf polarization* with David Dunsky and Benjamin R. Safdi. *Phys.Rev.D* 105 (2022) 10, 103034

It has been previously realized that polarization measurements of magnetic WDs can probe axions. The thermal radiation of the WD leaves the surface nearly unpolarized, but the photons polarized parallel to the magnetic field may convert into axions so that the radiation at Earth has an effective linear polarization perpendicular to the magnetic field. In fact this process could operate at all types of stars, but in this chapter, we make a generic argument that magnetic WDs would have the largest polarization of all stellar types. We then analyze archival linear polarization data from many magnetic WDs to showcase possible future analysis frameworks. Of all the magnetic WDs with archival data, SDSS J135141.13+541947.4

provides the most stringent constraints on axions. Those limits disfavor the entire axion parameter space explaining the TeV transparency hints. We identify future magnetic WD targets that may have improved sensitivity to axions but have no existing linear polarization data, and suggest future improvements to the modeling of the astrophysically-induced linear polarization.

Chapter 11: *Red-Giant Branch Stellar Cores as Macroscopic Dark Matter Detectors* with Zachary Johnson. arXiv:2112.06949 [hep-ph]

In this final chapter we turn to indirect detection of macroscopic DM. Macroscopic DM is much less abundant (in number density) than either axions or sterile neutrinos, and to observe even one event requires enormous exposure. Here we use the stellar cores of red-giant branch (RGB) stars, with exposures of around 10^{33} kT yr, to search for macroscopic DM. In particular, we show that if macroscopic DM elastically scatters on the degenerate core of an RGB star with geometric cross-section, helium fusion can be prematurely ignited in the core. The ignition of the RGB core transitions the star to a horizontal branch star over an astrophysically-quick timescale. This process modifies the RGB luminosity function of globular clusters (GCs), and we analyze the luminosity function of the GC M15 in the context of this model. We use the stellar modeling package `Modules for Experiments in Stellar Astrophysics` to model the M15 RGB stars, and construct RGB luminosity functions in the presence of macroscopic DM. We find no evidence for macroscopic DM and constrain DM with masses around 10^{17-20} g and cross sections 10^{2-7} cm^2 assuming the dominant DM density in M15 is sourced by that in the MW halo.

Chapter 2

The Dark Matter Interpretation of the 3.5-keV Line is Inconsistent with Blank-Sky Observations

A plethora of cosmological and astrophysical measurements indicate that dark matter (DM) exists and makes up ∼80% of the matter in the Universe, but its microscopic nature is unknown. If DM consists of particles that can decay into ordinary matter, the decay process may produce photons that are detectable with X-ray telescopes. Some DM models, such as sterile neutrino DM, predict such X-ray emission lines [86]. If the sterile neutrinos exist with a mass-energy of a few kilo–electron volts, they may explain the observed abundance of DM [79, 80, 87]. The detection of an unidentified X-ray line (UXL) around 3.5 keV in a stacked sample of nearby galaxy clusters [88] and an independent detection in one of those clusters and a galaxy [89] have been interpreted as evidence for DM decay [25]. Other less-exotic explanations have also been proposed, such as emission lines of potassium or argon, from hot gas within the clusters [90], or charge-exchange lines from interactions of the hot intracluster plasmas and cold gas clouds [91, 92].

The 3.5-keV UXL (hereafter just UXL) has been confirmed by several groups using different astrophysical targets and telescopes. These include observations of the Perseus cluster using the Chandra [88] and Suzaku [93] telescopes, observations of the Galactic Center of the Milky Way with XMM-Newton (X-ray Multi-Mirror Mission) [94], and observations of the diffuse Milky Way halo with *Chandra* deep-field data [95]. Several non-detections of the UXL have also been reported [96–100]. It is possible for a decaying DM model to be consistent with both the positive detections and negative results. Fig. 2.1 shows the existing detections and upper limits for the UXL, in the plane of sterile neutrino DM mass m_s and sterile-active mixing parameter $\sin^2(2\theta)$, which characterizes (and linearly scales with) the

decay rate of the sterile neutrino DM state [101].

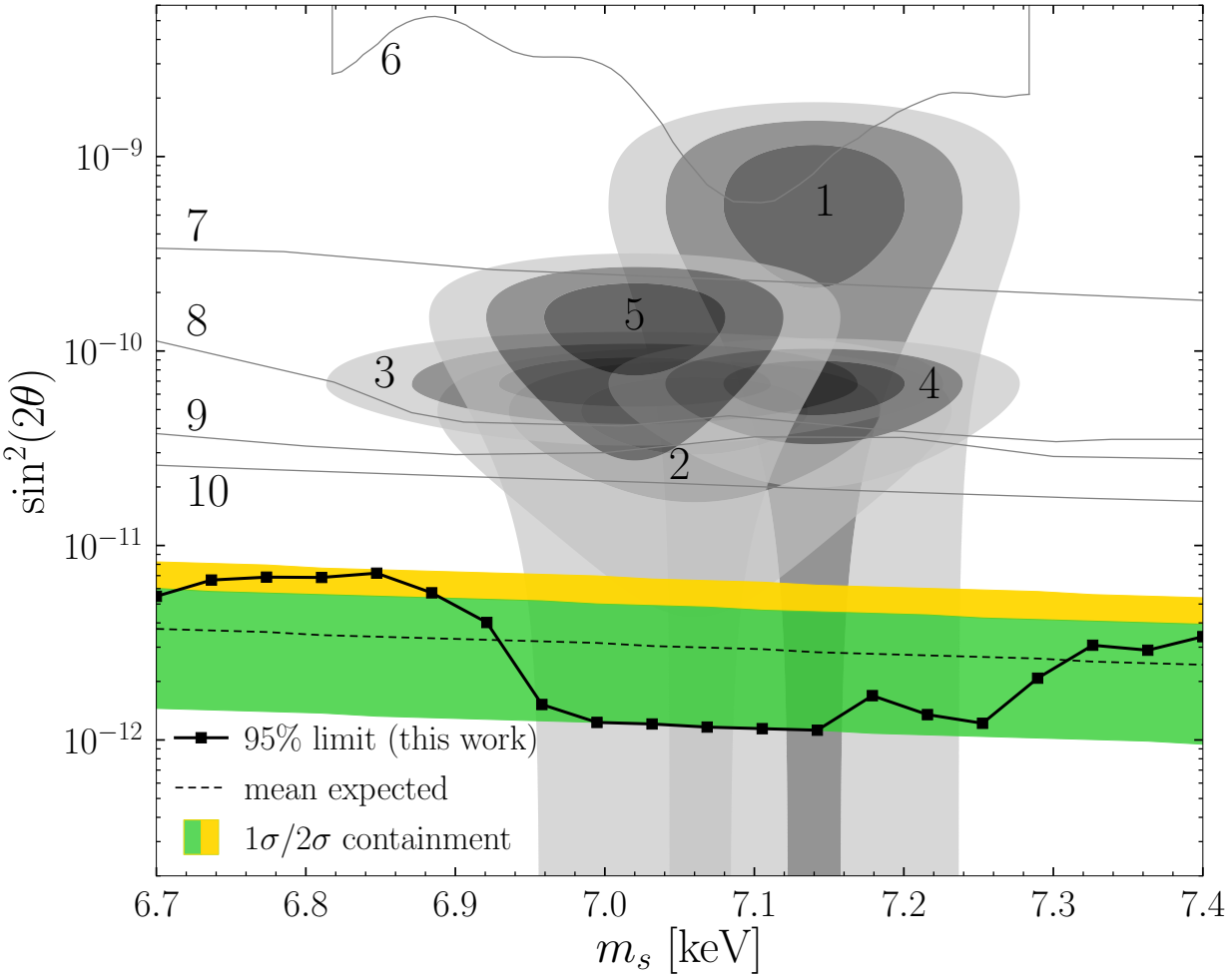

Figure 2.1: Our upper limits on sterile neutrino decay. The one-sided 95% upper limit on the sterile neutrino DM mixing parameter $\sin^2(2\theta)$ as a function of the DM mass m_s from our analysis of *XMM-Newton* BSOs (black squares). We compare with the expected sensitivity from the Asimov procedure (1σ shown in green and 2σ in yellow), and previous constraints (gray lines) and parameters required for DM decay explanations of previous UXL detections (3σ in dark gray, 2σ in gray, and 1σ in light gray). We also show several existing detections (labelled 1 to 5) and constraints (6 to 10) [25].

We seek to constrain the DM decay rate in the mass range relevant for the UXL by using *XMM-Newton* blank-sky observations (BSOs). Our analysis utilizes $\sim 10^3$ BSOs, which we define as observations away from large X-ray emitting regions, for a total of 30.6 Ms of exposure time. We focus on the line signal predicted from DM decay within the Milky Way, which should be present at every point in the sky. The sensitivity of this technique can be estimated in the limit of large counts, in other words, detected photons. Then the test statistic (TS) in favor of detection of DM decay (related to the significance $\sigma \sim \sqrt{\mathrm{TS}}$), scales

as TS $\sim S^2/B$, where S is the number of signal photons from DM decay and B is the number of background photons. The number of signal photons expected from a given location in the sky is proportional to the product of the decay rate of DM and the integrated column density of DM along the line of sight, which is quantified by the D factor, $D = \int ds\, \rho_{\rm DM}(s)$ where $\rho_{\rm DM}$ is the DM density and s is the line-of-sight distance.

We use these scalings to estimate the expected sensitivity of a BSO analysis, given the previous UXL observations. For example, the UXL has been detected with a 320-ks observation of the Perseus cluster using the *XMM-Newton* Metal Oxide Semiconductor (MOS) camera at roughly the 4σ level (TS ~ 16) [88]. The background X-ray flux from Perseus is much higher than that for the BSOs, typically by a factor of 50. Averaged over the field of view of *XMM-Newton*, the D factor of the Perseus cluster is $D_{\rm Pers} \sim 3 \times 10^{28}\,{\rm keVcm}^{-2}$, which is approximately the same as $D_{\rm BSO}$, the D factor within the Milky Way halo for observations $\sim$45° away from the Galactic Center. We calculated both D factors assuming a Navarro-Frenk-White (NFW) DM profile [102]. Although the signal power should therefore be the same between Perseus and the BSO, we expect the same sensitivity to the UXL with a 6 ks BSO observation—assuming a DM origin—because the BSO background is expected to be lower than that of Perseus. Our analysis below uses ~ 30 Ms of BSO exposure time, which implies that the UXL would be seen with a TS $\sim 10^5$, corresponding to a detection significance of $> 100\sigma$, if it is caused by decaying DM with the same properties as that in the Perseus cluster.

We analyzed all publicly-available archival *XMM-Newton* observations that pass a set of quality cuts. For our fiducial analysis, we first restrict to the observations used to those between 5° and 45° of the Galactic Center. Within this region there are 1492 observations, with 4303 total exposures, for $\sim$86 Ms of exposure time. These observations are distributed quite uniformly through our fiducial region, although there is a bias towards the Galactic plane. There are more exposures than observations because each of the *European Photon Imaging Cameras* charged coupled devices (CCDs) onboard XMM-Newton [two MOS and one positive-negative (PN)] [103, 104] records a separate exposure, and each camera may have multiple exposures in a single observation if the data taking was interrupted. For each observation we process and reduce the data using the standard tools for extended emission [101]. In addition to the photon-count data, we also extract the quiescent particle background (QPB). The QPB is an instrumental background caused by high-energy particles interacting with the detector, rather than true photon counts. The magnitude of the QPB contribution is estimated from parts of the instrument that are shielded from incident X-rays; we refer to this as the QPB data.

We then perform a background-only analysis of each of the exposures to determine prop-

erties that are used for further selection. We calculate the QPB contribution and the astrophysical flux over the energy range of 2.85 to 4.2 keV. The QPB rate is estimated from the QPB data, whereas the astrophysical flux is measured using the likelihood analysis described below. We rescale the astrophysical flux measured in the restricted energy range to a wider energy range of 2 to 10 keV by assuming a power-law spectrum of $dN/dE \sim E^{-1.5}$ where N is the photon flux and E is energy. The cosmic X-ray background has a 2 to 10 keV intensity of $I_{2-10} \approx 2 \times 10^{-11}$ erg cm^{-2} s^{-1} deg^{-2} [105, 106]. In our fiducial analysis we remove exposures with $I_{2-10} > 10^{-10}$ erg cm^{-2} s^{-1} deg^{-2} to avoid including exposures with either extended emission or flux from unresolved point sources. Approximately 58% of the exposures pass this cut, whereas ∼13% of the exposures have $I_{2-10} < 3 \times 10^{-11}$ erg cm^{-2} s^{-1} deg^{-2}. Because the individual exposures are in the background-dominated regime and the signal we are searching for is restricted to a narrow energy range, even a clearly detectable DM line would have no effect on this selection criterion. We further remove exposures with anomalously high QPB rates; for our fiducial analysis, we keep the 68% of exposures with the lowest QPB rates. We apply this criterion separately to the MOS and PN exposures. Lastly, we remove exposures with < 1 ks of exposure time, because these exposures do not substantially improve our sensitivity and the associated low photon counts reduce the reliability of the background estimates. After these cuts, we are left with ∼30.6 Ms of exposure time distributed between 1397 exposures and 752 distinct observations.

We analyze the ensemble of exposures for evidence of the UXL by using a joint likelihood procedure. Individual exposures are not stacked. To evaluate the UXL hypothesis for a given m_s, we first construct profile likelihoods for the individual exposures as functions of the DM-induced line flux F. The X-ray counts are analyzed with a Poisson likelihood, from the number of counts in each energy channel. The associated model is a combination of the DM-induced flux represented by an X-ray line broadened by the detector response and two independent power laws for the background astrophysical emission and the instrumental QPB, where the normalization and spectral indices of each power law are free parameters. This same QPB power-law contribution is also fitted to the estimated QPB data using a Gaussian likelihood. Both datasets are restricted to the energy range $m_s/2 \pm 0.25\,\mathrm{keV}$, which was chosen to be wider than the energy resolution of the detector (∼0.1 keV) but small enough that our power-law background models are valid over the whole energy range.

The two likelihoods for the X-ray counts and the QPB estimate are then combined, providing a likelihood that, for a given m_s, is a function of five parameters: the DM-induced line flux F and the normalization factors and spectral indices of the astrophysical and QPB power laws. The last four of these are treated as nuisance parameters; that is, we maximize the individual likelihoods over the valid ranges of these parameters. Each dataset was

therefore reduced to a profile likelihood as a function of F. This flux can be converted to a lifetime and, hence, $\sin^2(2\theta)$ [86, 101], once the D factor for this region of the sky is known. In our fiducial analysis we compute the D factors by assuming that the DM density profile of the Milky Way is an NFW profile with a 20 kpc scale radius. We normalize the density profile, assuming a local DM density of 0.4 GeVcm^{-3} [107], and take the distance between the Sun and the Galactic Center to be 8.13 kpc [108].

Joining the resulting likelihoods associated with each exposure yields the final joint likelihood that is a function of only $\sin^2(2\theta)$ for a given m_s. This likelihood is then used to calculate the one-sided 95% confidence limit on the mixing angle and to search for evidence for the UXL using the discovery TS, which is defined as twice the log-likelihood difference between the maximum likelihood and the likelihood at the null hypothesis [assuming the likelihood is maximized at a positive value of $\sin^2(2\theta)$]. For statistical consistency, we must include negative values of $\sin^2(2\theta)$ in the profile likelihood, which correspond to under-fluctuations of the data.

To calibrate our expectation for the sensitivity under the null hypothesis, we construct the 68 and 95% expectations for the limit using the Asimov procedure [109]. The Asimov procedure requires a model for the data under the null hypothesis; we compute this model by performing the likelihood fits described above under the null hypothesis [$\sin^2(2\theta) = 0$]. We use this to set one-sided power-constrained limits [110]. The measured limit is not allowed to go below the 68% containment region for the expected limit, so as to prevent setting tighter limits than expected because of downward statistical fluctuations.

In Fig. 2.2, we show the summed spectra over all exposures included in the analysis for the MOS and PN data separately. We emphasize that we do not use the summed spectra for our fiducial data analysis; instead we use the joint likelihood procedure described above. However, the summed spectra are shown for illustrative purposes. We also show the summed best-fitting background models. Because our full model has independent astrophysical and QPB power-law models for each exposure, these curves are not single power laws but sums over 2794 independent power-laws. The summed data closely match the summed background models. Fig. 2.2 also shows the expected signal for $m_s = 7.105$ keV and $\sin^2(2\theta) = 10^{-10}$, which are values we chose to be in the middle of the parameter space for explaining the observed UXL (Fig. 2.1). Fig. 2.2 shows that this model is inconsistent with the data.

Our fiducial one-sided power-constrained 95% upper limit is shown in Fig. 2.1 along with mean, 1σ, and 2σ expectations under the null hypothesis. The upper limit is consistent with the expectation values and strongly disfavors the decaying DM explanation of the UXL. Our results disagree with the parameters required to explain the previous UXL observations as decaying DM by over an order of magnitude in $\sin^2(2\theta)$. In Fig. 2.3, we show the TS for

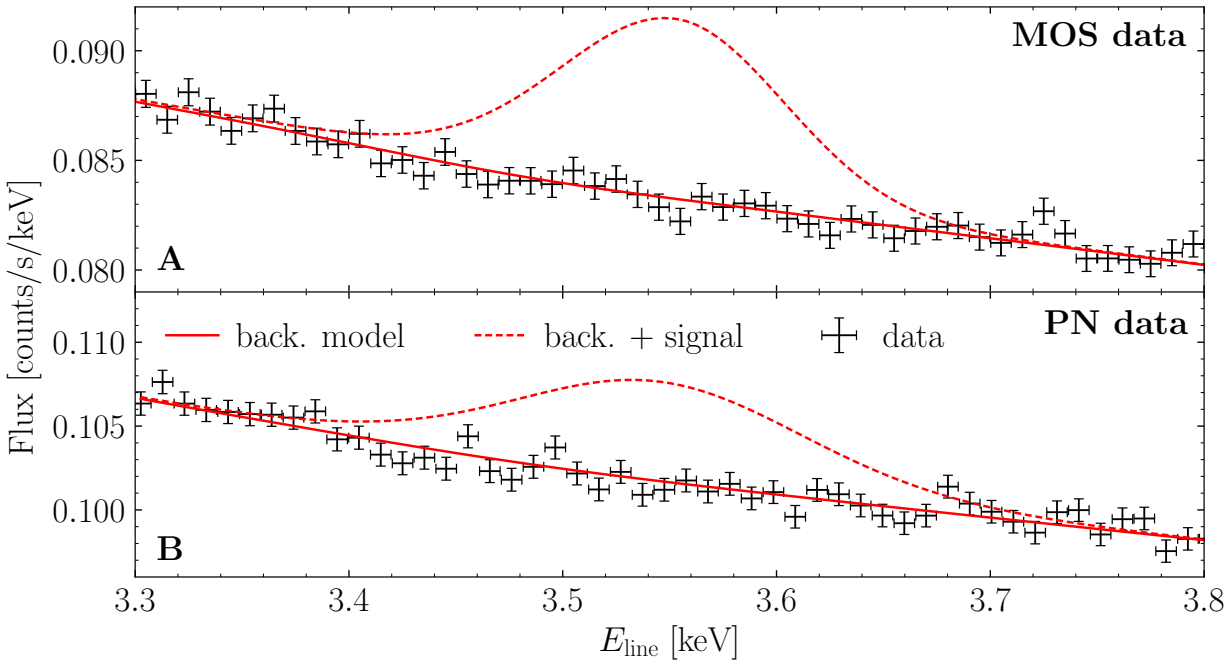

Figure 2.2: The summed spectra. The summed MOS (A) and PN (B) spectra (black data points) for the exposures used in our fiducial analysis. We also show the summed best-fitting background (back.) models (red solid line) and an example signal contribution with $m_s = 7.105$ keV and $\sin^2(2\theta) = 10^{-10}$ (red dashed line).

decaying DM as a function of DM mass, with the 1 and 2σ expectations under the null hypothesis; we find no evidence for decaying DM.

Fig. 2.3 shows the TS for the joint-likelihood analysis over the ensemble of exposures. However, we can also calculate a TS for decaying DM from each individual exposure. Under the null hypothesis, Wilks' theorem states that the distribution of TSs from the individual exposures should asymptotically follow a χ^2 distribution. In the inset of Fig. 2.3, we show the histogram of the number of exposures that are found for a given TS, for our reference mass of $m_s = 7.105$ keV. The distribution matches the expectation under the null hypothesis. We also performed a Kolmogorov-Smirnov test comparing the observed TSs with the expected one-sided χ^2 distribution, and found a P value of 0.77, which indicates that the TS data is consistent with the null hypothesis.

Although Fig. 2.3 shows that our results appear to be consistent with the expected statistical variability, there remains the possibility that systematic effects such as un-modeled instrumental lines could conspire to hide a real line. We test for such systematics in A.9 by analyzing the data from the individual cameras separately [101], in Fig. A.14 by explicitly allowing for extra possible instrumental lines in the background model [101], and in Figs. A.16 and A.17 by looking at the data in sub-regions increasingly far away from the Galactic

Center [101]. Accounting for these possible systematics in a data-driven way may weaken our limits to as much as $\sin^2(2\theta) < 2 \times 10^{-11}$ (Fig. A.17, Reg. 4), which still strongly rules out the decaying DM interpretation of the UXL. We also analyze the summed X-ray count data shown in Fig. 2.2 directly [101], and found, again, that the decaying DM interpretation of the UXL was excluded (see Fig. A.18).

We have analyzed ∼30 Ms of *XMM-Newton* BSOs for evidence of DM decay in the energy range of 3.35 to 3.7 keV. We found no evidence for DM decay. Our analysis rules out the decaying DM interpretation of the previously observed 3.5 keV UXL because our results exclude the required decay rate by more than an order of magnitude.

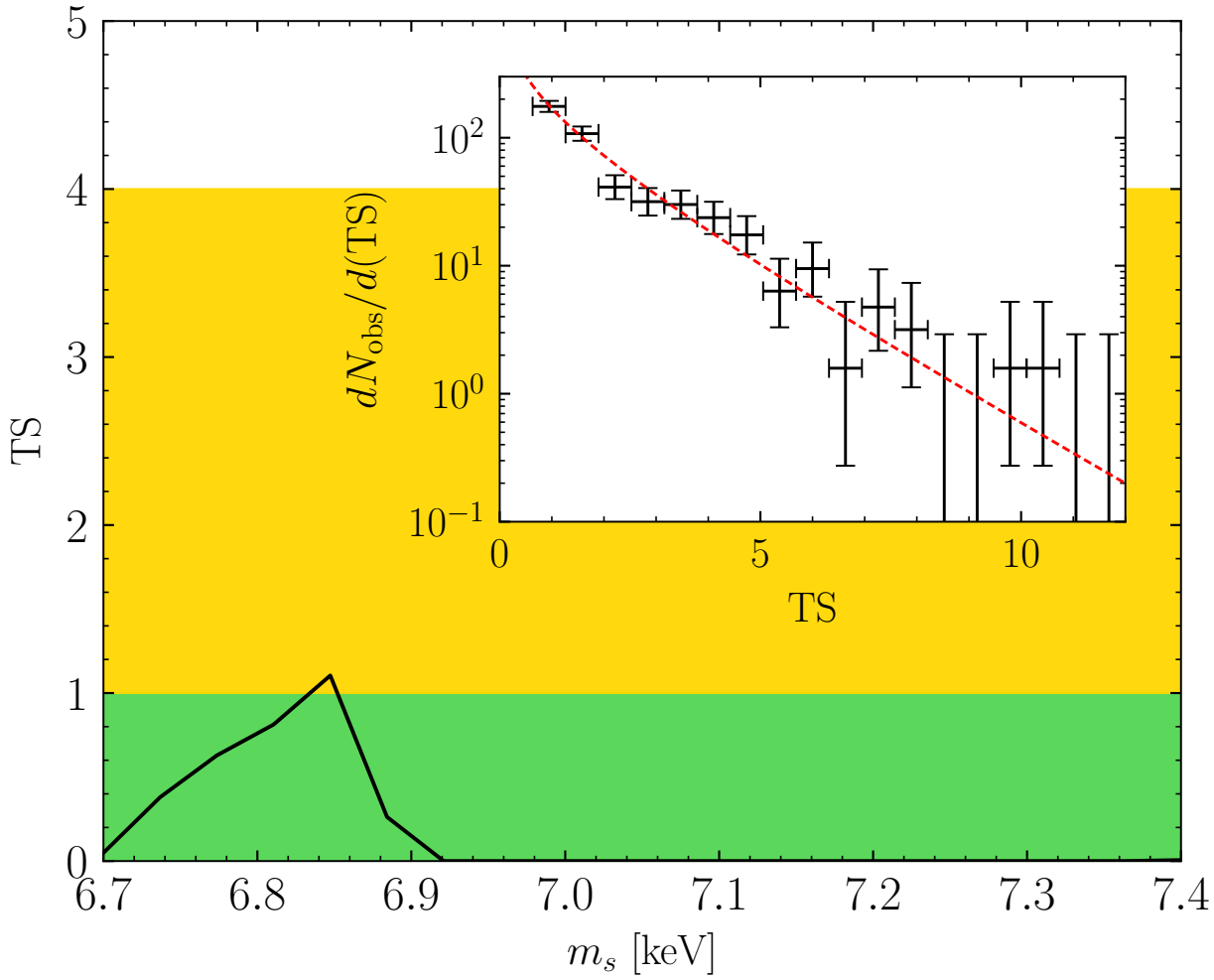

Figure 2.3: No evidence for the decaying DM interpretation of the UXL. (**A**) The TS for the UXL as a function of the DM mass m_s from the joint likelihood analysis. The black curve shows the result from the data analysis, whereas the green and yellow shaded regions indicate the 1σ and 2σ expectations, respectively, under the null hypothesis. (**B**) A histogram of the TSs from the individual exposures, with vertical error bars from Poisson counting statistics and horizontal error bars bracketing the histogram bin ranges.

Chapter 3

A Deep Search for Decaying Dark Matter with *XMM-Newton* Blank-Sky Observations

In this chapter we present one of the most sensitive searches for sterile neutrino DM, along with other DM candidates that may decay to monochromatic X-rays, over the mass range $m_\chi \in [5, 16]$ keV. We do so by searching for DM decay from the ambient halo of the Milky Way using all archival data from the *XMM-Newton* telescope collected from its launch until September 5, 2018.

This chapter builds heavily off the method developed in the previous chapter [111], which used *XMM-Newton* blank-sky observations (BSOs) to strongly disfavor the decaying DM explanation of the previously-observed 3.5 keV unidentified X-ray line (UXL). This UXL was found in nearby galaxies and clusters [88–90, 93, 95]. However the analysis performed in Chapter 1 was able to robustly rule out the DM decay rate required to explain the previous 3.5 keV UXL signals [112]. (For additional non-observations, see Refs. [96–100, 113, 114].) We extend the search in Chapter 1 to the broader mass range $m_\chi \in [5, 16]$ keV, and in doing so implement the following notable differences: (i) we use a data-driven approach to construct stacked, background-subtracted data sets in rings around the Galactic Center (GC), while previously we performed a joint-likelihood analysis at the level of individual exposures, and (ii) we use Gaussian Process (GP) modeling to describe continuum residuals, instead of parametric modeling as used in [111].

We do this for several reasons. As we increase the mass range—the previous chapter's search was over less than a keV, while this chapter's is 11 keV—it becomes more difficult to ensure all systematics are under control, so we must implement more careful treatments of the data. In the previous chapter, our background was consistent with the power-law

description of the data at the level of individual observations. As we will see, in this chapter, we find significant evidence for astrophysical and instrumental lines in our energy range of interest. The background subtraction will mitigate some of this contamination of our BSOs; the instrumental lines will be nearly fully subtracted by this procedure. Secondly, the GP modeling of the continuum allows the background significantly more freedom to describe the data, and we can analyze the full energy range at once rather than using our sliding window approach of Chapter 1. In contrast to previous searches which use parametric models of X-ray emission in plasmas (e.g. [88, 89], the GP model at any one location is not fixed by data from a far-away location, so we do not need to be as worried about background mismodeling (although we implement a number of consistency checks, detailed later in the Chapter).

As demonstrated in [111], BSO searches for DM decaying in the Milky Way halo can be both more sensitive and more robust than extra-galactic searches, because (i) the expected DM flux, even at angles $\sim 45^\circ$ away from the GC, rivals the expected flux from the most promising extra-galactic objects, such as M31 and the Perseus cluster; (ii) promising extra-galactic targets have continuum and line-like X-ray features that are confounding backgrounds for DM searches (dwarf galaxies being an exception [113, 115]), while BSOs instead focus on the lowest-background regions of the sky; (iii) extra-galactic targets require pointed observations, while in principle any observation collected by *XMM-Newton* is sensitive to DM decay in the Milky Way, opening up considerably more exposure time.

The limits presented in this chapter represent the strongest found using the *XMM-Newton* instrument over the energy range $\sim$2.5–8 keV. At higher energies our limits are superseded with those found using the NuSTAR satellite [116–120]. Ref. [118] performed a search similar in spirit to that in this chapter (though with NuSTAR) in that they looked for DM decay from the Milky Way halo near the GC ($\sim 10^\circ$ away in their case), while Ref. [120] searched for DM decay from M31 with NuSTAR.

Our results put in tension efforts to explain the abundance of DM with sterile neutrinos. For example, in the Neutrino Minimal Standard Model (νMSM) [78, 121, 122], which may simultaneously explain the observed neutrino masses, DM density, and baryon asymmetry, the Standard Model is supplemented by three heavier sterile neutrino states, the lightest of which is the DM candidate. The DM abundance is generated through the mixing of sterile and active neutrinos [79], which can further be resonantly enhanced by a finite lepton chemical potential [80, 81, 122–127], though other production mechanisms are also possible [87, 128, 129]. DM models such as axion-like-particle DM [130] and moduli DM [131] predict similar UXL signatures from DM decay.

3.1 Data reduction and processing

We process and analyze all publicly-available data collected before 5 September 2018 by the metal oxide semiconductor (MOS) and positive-negative (PN) cameras on board *XMM-Newton*. Note that in the previous chapter we focused only on the set of observations in the inner Galaxy. We subject each exposure to a set of quality cuts, which are described shortly. Those exposures satisfying the quality cuts are included in our angularly-binned data products. In particular, we divide the sky into 30 concentric annuli centered around the GC, each with a width of 6° in angular radius from the GC, $r_{\rm GC}$, where $\cos(r_{\rm GC}) = \cos(l)\cos(b)$ in terms of the Galactic longitude, l, and latitude, b. We label these from 1 to 30, starting from the innermost ring. We further mask the Galactic Plane such that we only include the region $|b| \geq 2°$. In each ring we then produce stacked spectra where, in each energy bin, we sum over the counts from each exposure whose central position lies within that annulus. We produce separate data sets for the MOS and PN cameras, which have 2400 and 4096 energy channels, respectively. In addition to stacking the counts in each ring and energy channel, we also construct the appropriately weighted detector response matrices in every ring for forward modeling an incident astrophysical flux. The full-sky maps and associated modeling data are provided as Supplementary Data [132] in both the annuli and in finer-resolution `HEALPix` binning [133]. We analyze the MOS data from 2.5 to 8 keV and the PN data from 2.5 to 7 keV, in order to exclude intervals containing large instrumental features.

3.2 Data analysis

Having constructed our data in all 30 rings, we divide the full sky into two regions of interest (ROI): a signal ROI, consisting of annuli 1 through 8 ($0° \leq r_{\rm GC} \leq 48°$ with $|b| \geq 2°$), inclusive, and the background ROI, consisting of annuli 20 through 30 ($114° \leq r_{\rm GC} \leq 180°$ with $|b| \geq 2°$). The regions are illustrated in Fig. 3.1. The MOS (PN) exposure time in the signal ROI is 25.27 Ms (5.56 Ms), whereas in the background ROI it is 62.51 Ms (17.54 Ms). The signal flux is proportional to the D-factor, which is defined by the line-of-sight integral of the Galactic DM density $\rho_{\rm DM}$, $D \equiv \int ds\, \rho_{\rm DM}$. In Fig. 3.1 we show the appropriately weighted D-factor in each annuli. The motivation for the two ROIs is that the signal should dominate in the inner regions of the Galaxy and become progressively weaker further away from the GC. The background ROI is chosen to be large enough to have significantly more exposure time than the signal ROI, so that using the background-subtracted data does not significantly broaden the statistical uncertainties. We stack the data over the full background ROI, which has D-factor $D_{\rm bkg}$, and use this as an estimate of the instrumental and astrophysical baseline

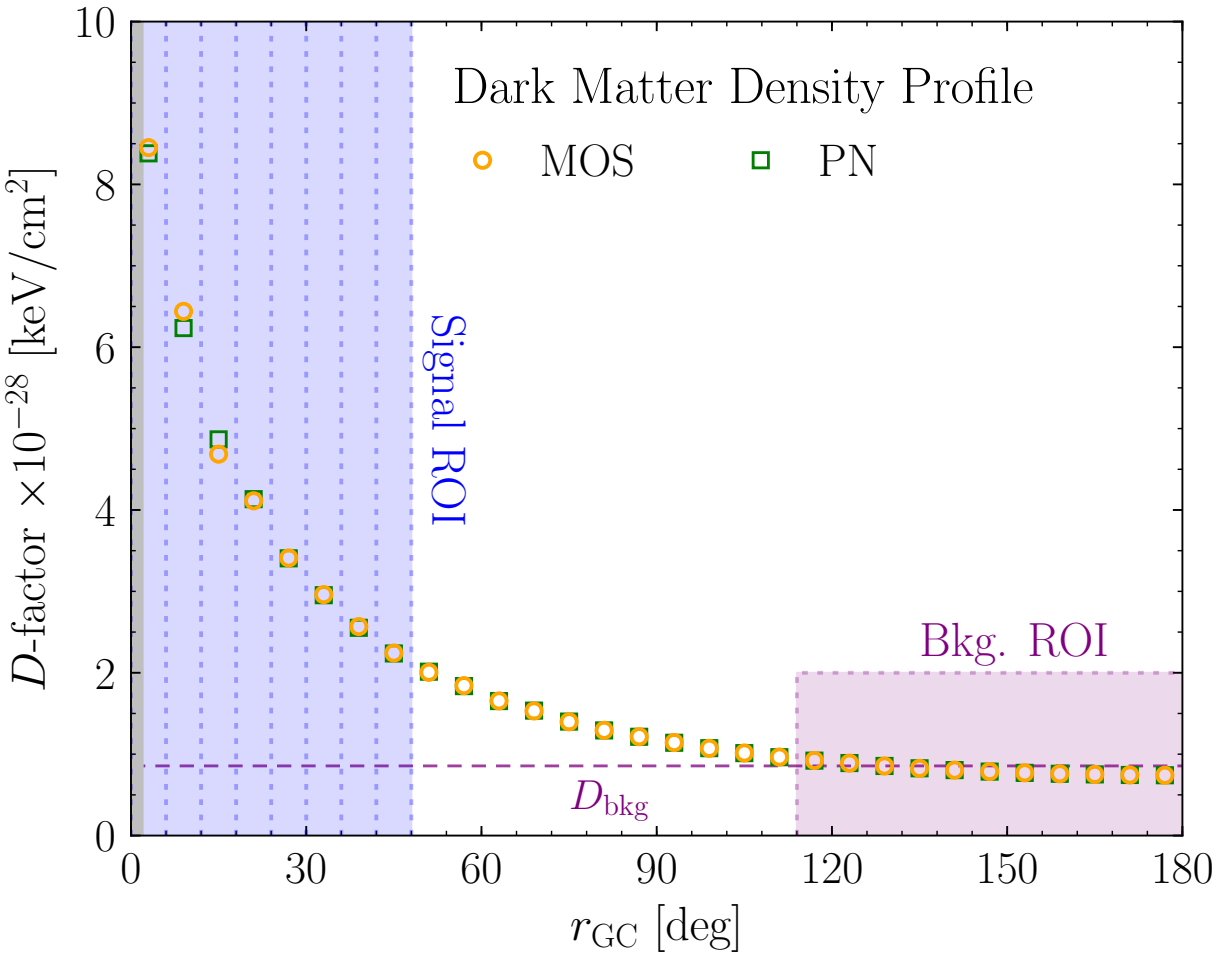

Figure 3.1: Our fiducial D-factor, which is proportional to the expected DM signal flux. Values are given in all 30 annuli, which are 6° wide in angular distance from the GC (with $|b| > 2°$), and we define a signal and background ROI as shown. In each ring, we compute the D-factor of all MOS or PN exposures, weighted according to the observation time and field of view. The horizontal line indicates $D_{\rm bkg}$, the mean D-factor in the background ROI.

fluxes by subtracting this data from the data in each ring of the signal ROI. This subtraction mostly removes large instrumental lines, as illustrated in the Appendix Fig. B.1.

We analyze the background-subtracted data in each annulus for evidence of a UXL. The data is modeled as a combination of narrow spectral features at the locations of known astrophysical and instrumental lines, and a continuum flux which we account for using GP modeling. Note that the instrumental lines need not be completely removed by the data-subtraction procedure, leaving a residual flux or flux deficit that must be modeled. Astrophysical emission lines from the Milky Way plasma should be brighter in the signal ROI, and so are also expected to appear in the background-subtracted data. For both astrophysical and instrumental lines, the lines are modeled using the forward modeling matrices for MOS

and PN. We allow the instrumental lines to have either positive or negative normalizations, while the astrophysical lines are restricted to have positive normalizations. To decide which lines to include in our residual background model we start with an initial list of known instrumental and astrophysical lines. The instrumental lines are determined from an analysis of the background ROI data, while the astrophysical lines are those expected to be produced by the Milky Way. In each ring, and for MOS and PN independently, we then determine the significance of each emission line, keeping those above $\sim 2\sigma$. As a result, every ring has a different set of lines included in the analysis. We note that it is conceivable that a UXL might be inadvertently removed by an overly-subtracted instrumental line at the same energy; however, it would be highly unlikely for such a conspiracy to occur in every ring, given the varying D-factor. The effects of sub-threshold instrumental lines are mitigated through a *spurious-signal* nuisance parameter [134], as discussed in the Appendix.

The unprecedented data volume incorporated into this analysis necessitates a flexible approach to modeling the residual continuum emission, which is accomplished with GP modeling, in order to minimize background mismodeling. As opposed to parametric modeling, where the model is specified by a specific functional form and associated list of model parameters, GP modeling is non-parametric: the model expectations for the data at two different energies, E and E', are assumed to be normally distributed with non-trivial covariance. Taking the model expectation to have zero mean, the GP model is then fully specified by the covariance kernel, $K(E, E')$. We model the mean-subtracted data using the non-stationary kernel $K(E, E') = A_{\rm GP} \exp\left[-(E - E')^2/(2EE'\sigma_E^2)\right]$, implemented in `george` [135], where σ_E is the correlation-length hyperparameter and $A_{\rm GP}$ is the amplitude hyperparameter. We fix σ_E such that it is larger than the energy resolution of the detector, which is $\delta E/E \sim 0.03$ across most energies for MOS and PN, while ensuring σ_E is kept small enough to have the flexibility to model real variations in the data. The goal is to balance two competing effects. If σ_E approaches the lower limit imposed by the energy resolution of the detector, then the GP model would have the flexibility to account for line-like features, which would reduce our sensitivity when searching for such features over the continuum background. On the other hand, if σ_E is too large then the GP continuum model may not accurately model real small-scale variations in the data. In our fiducial analysis we fix $\sigma_E = 0.3$, though in the Appendix we show that our results are robust to variations not only in this choice, but also to modifications to the form of the kernel itself. In contrast, the hyperparameter $A_{\rm GP}$ is treated as a nuisance parameter that is profiled over when searching for UXLs.

We then follow the statistical approach developed in [136], which used GP modeling to perform an improved search for narrow resonances over a continuum background in the context of the Large Hadron Collider. In particular, we construct a likelihood ratio Λ between

the model with and without the signal component, where the signal is the UXL line at fixed energy $E_{\rm sig}$. The null model is as above, the combination of a GP model with a single nuisance parameter $A_{\rm GP}$, and a set of background lines, whose amplitudes are treated as nuisance parameters. We use the marginal likelihood from the GP fit in the construction of the likelihood ratio [136]. Note that as the number of counts in all energy bins is large ($\gg 100$), we are justified in assuming normally-distributed errors in the context of the GP modeling. We then profile over all nuisance parameters. Finally, the discovery significance is quantified by the test statistic (TS) $t = -2\ln\Lambda$. We verify explicitly in the Appendix that under the null hypothesis t follows a χ^2-distribution. The 95% one-sided upper limits are constructed from the profile likelihood, as a function of the signal amplitude.

We implement this procedure and scan for a UXL from 2.5 to 8 keV in 5 eV intervals. At each test point we construct profile likelihoods for signal flux independently for each ring using the background-subtracted MOS and PN data. We then combine the likelihoods between rings – and eventually cameras – in a joint likelihood in the context of the DM model, as discussed shortly. As an example, Fig. 3.2 illustrates the signal and null model fits to the innermost MOS background-subtracted signal-annulus data for a putative UXL at 3.5 keV (indicated by the vertical dashed line). Note that while the fit is performed over the full energy range (2.5−8 keV) for clarity we show the data zoomed in to the range 3 to 4 keV. In this case the data have a deficit, which manifests itself as a signal with a negative amplitude.

3.3 DM interpretation

We combine together the profile likelihoods from the individual annuli to test the decaying DM model. In the context of sterile neutrino DM with mass m_χ and mixing angle θ, the DM decay in the Galactic halo produces an X-ray flux at energy $m_\chi/2$ that scales as $\Phi \propto m_\chi^4 D \sin^2(2\theta)$ [137]. Note that the D-factors, appropriately averaged over observations in the individual annuli, are illustrated in Fig. 3.1. Thus, at fixed DM mass m_χ we may construct profile likelihoods as functions of $\sin^2(2\theta)$ to appropriately combine the profile likelihoods as functions of flux in the individual annuli. We subtract off $D_{\rm bkg}$ from the D-factors in each signal ring since any UXL would also appear in the background ROI and thus be included in the background subtraction.

The D-factors may be computed from the DM density profile of the Milky Way. Modern hydrodynamic cosmological simulations indicate that the DM density profile in Milky Way mass halos generally have a high degree of spherical symmetry (for a review, see Ref. [138]). Further, the presence of baryons contracts the inner ∼10 kpc of the profile away from the

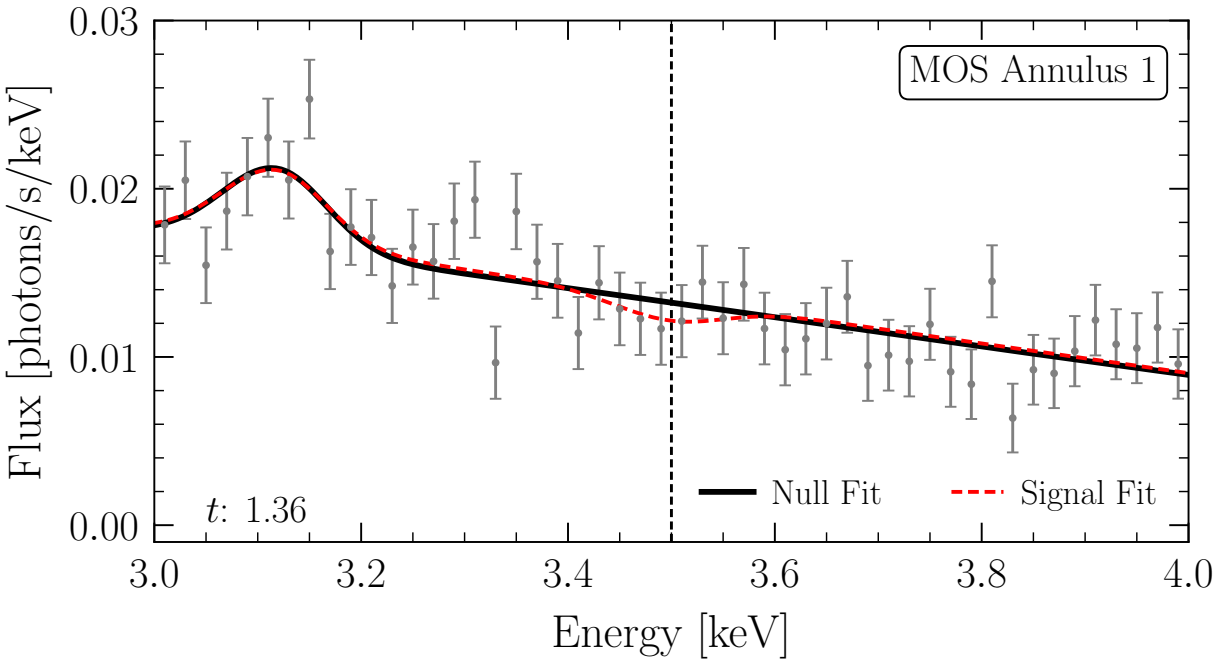

Figure 3.2: The background-subtracted MOS data for the innermost annulus, downbinned by a factor of four for presentation purposes. The indiciated best fit null and signal models, for a 3.5 keV UXL, are constructed using the GP modeling described in the text.

canonical Navarro, Frenk, and White (NFW) DM distribution [102, 139], so that there is an enhancement of the DM density at smaller radii versus the NFW expectation [140–145], though cores could develop on top of this contraction at radii $\lesssim 2$ kpc [146–149]. For example, in Milky Way analogue halos within the `Fire-2` simulations the DM-only and hydrodynamic simulations produce DM density profiles that agree within $\sim$25% at 10 kpc, but with baryons the density profiles are typically around twice as large as the NFW DM-only expectation at distances $\sim$1 kpc away from the GC [144]. To be conservative we assume the canonical NFW density profile for all radii, though in the Appendix we discuss how our results change for alternate density profiles.

The NFW profile is specified by a characteristic density ρ_0 and a scale radius r_s: $\rho_{\rm DM}(r) = \rho_0/(r/r_s)/(1+r/r_s)^2$. We use the recent results from [61], who combined *Gaia* DR2 Galactic rotation curve data [150] with total mass estimates for the Galaxy from satellite observations [151, 152]. These data imply, in the context of the NFW model, a virial halo mass $M_{200}^{\rm DM} = 0.82^{+0.09}_{-0.18} \times 10^{12}\ M_\odot$ and a concentration $c = r_{200}/r_s = 13.31^{+3.60}_{-2.68}$, with a non-trivial covariance between $M_{200}^{\rm DM}$ and c [61] such that lower concentrations prefer higher halo masses. Within the 2D 68% containment region for $M_{200}^{\rm DM}$ and c quoted in Ref. [61], the lowest DM density at $r \approx 0.5$ kpc, and thus the most conservative profile for the present analysis, is obtained for $\rho_0 = 6.6 \times 10^6\ M_\odot/{\rm kpc}^3$ and $r_s = 19.1$ kpc. We adopt these values for our

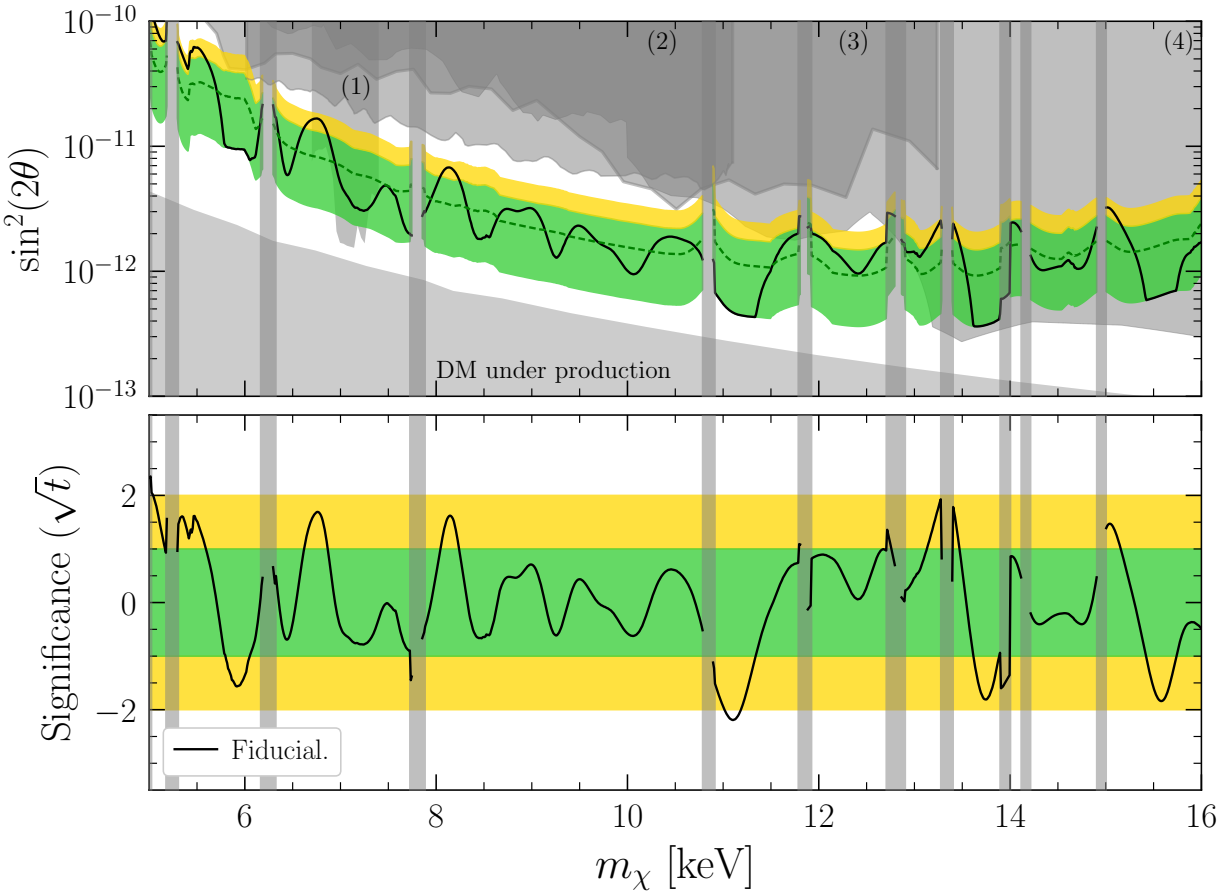

Figure 3.3: (Upper) The power-constrained 95% upper limit on the DM lifetime from this chapter, presented in the context of the sterile-neutrino mixing angle $\sin^2(2\theta)$, as a function of the DM mass m_χ. The dark grey regions correspond to theoretical bounds for DM underproduction in the νMSM or bounds from previous X-ray searches (1)–(5); see text for details. (Lower) The associated sign-weighted significance for the UXL. Vertical grey regions denote background lines and are at least partially masked. Green and gold regions indicate $1/2\sigma$ expectations under the null hypothesis. These results are shown in the context of more general DM models as constraints on the DM lifetime in SM Fig. S6.

fiducial analysis. With our choice of NFW DM parameters the local DM density, at the solar radius, is $\sim$0.29 GeV/cm^3, which is consistent with local measurements of the DM density using the vertical motion of tracer stars perpendicular to the Galactic plane, see, *e.g.*, Refs. [153, 154].

We search for evidence of decaying DM in 10 eV intervals in mass between 5−16 keV, masking 0.1 keV windows around the locations of known lines, as indicated in Fig. 3.3. We construct the joint likelihoods for the MOS and PN data sets. We test and account for additional background mismodeling in the MOS and PN analyses by looking at the distribution of best-fit mixing angles in the energy side-bands, using a technique similar to

the "spurious signal" used by ATLAS in the search for the Higgs boson [134]. This procedure is described in the Appendix and only has a small effect at low masses. We then combine, at a given mass, the resulting MOS and PN profile likelihoods to obtain the final profile likelihood used to construct the limit and discovery significance shown in Fig. 3.3. In that figure we show the one-sided 95% upper limit on $\sin^2(2\theta)$ in the upper panel, along with the 1 and 2σ expectations for the power-constrained upper limit [110] under the null hypothesis (shaded green and gold, respectively).

We find no evidence for decaying DM signals above our pre-determined significance threshold of 5σ global significance (corresponding to $\sim 6\sigma$ local significance), as shown in the bottom panel. In that figure we compare our upper limit to previous limits in the literature, adjusted to our fiducial DM model for the Milky Way where appropriate. In the context of the νMSM it is impossible to explain all of the observed DM in the region marked "DM under production" because of the big bang nucleosynthesis bound on the lepton chemical potential [81, 123, 124]. Note that the νMSM also predicts that the DM becomes increasingly warm for decreasing m_χ, which leads to tension with Milky Way satellite galaxy counts for low m_χ: data from the Dark Energy Survey and other Galactic satellite surveys [155] constrains m_χ greater than $\sim$15–20 keV in the νMSM [156] (which can be strengthened further when combined with strong lensing measurements [157]), though we note that our results apply to more general DM production mechanisms that do not predict modifications to small-scale structure. In Fig. 3.3 we also show previous X-ray limits from (1) [111], (2) a *Chandra* search for DM decay in the Milky Way [158], (3) a *Chandra* search for DM decay in M31 [96], and (4) combined *NuSTAR* searches for DM decay: in the Milky Way [116–118], the Bullet Cluster [119], and M31 [120]. Note that the results from Milky Way searches have been adjusted to use the same DM density profile as in our fiducial analysis.

3.4 Discussion

We find no significant evidence for decaying DM, which leads us to set some of the strongest constraints to-date on the DM lifetime. We confirm the results of Dessert *et al.* [111] for the non-observation of a DM decay line near 3.5 keV using a more robust and flexible analysis strategy, leaving little room for a decaying DM explanation of the previously-observed 3.5 keV anomalies [88–90, 93, 95]. (See the Appendix for further discussion.)

Given the data volume incorporated into this analysis it is unlikely that further analyses of *XMM-Newton* data, or *Chandra* data, could produce qualitatively stronger results on the DM lifetime in the mass range considered here. However, the approach taken in this chapter may lead to a powerful advancement in discovery power with future data sets from surveys

such as those by the upcoming *Athena* [159] and *XRISM* [160] telescopes. A combination of the data collected by those missions and the analysis framework introduced in this chapter may lead to the discovery of decaying DM in the few-keV mass range at lifetimes beyond those probed in this chapter.

Chapter 4

X-Ray Signatures of Axion Conversion in Magnetic White Dwarf Stars

We now switch focus to searches for the axion-like particles (ALPs) overviewed in the Introduction. The quantum chromodynamics (QCD) axion, originally proposed to solve the strong CP problem [161–164], is a well-motivated extension of the Standard Model of particle physics. The QCD axion is a light pseudoscalar particle that couples to the QCD operator $G\tilde{G}$, with G the QCD field strength. Additionally, the axion has dimension-5 couplings to electromagnetism and to matter. Studies of string compactifications show that, in addition to the QCD axion, there may exist a number of additional light pseudoscalar particles, with couplings to electromagnetism and matter but not to QCD [165, 166]. These pseudoscalars are called axion-like particles, though throughout this chapter we will refer to all such particles as axions. In this chapter we present a novel method, using X-ray observations of magnetic white dwarf (WD) stars (MWDs), to probe the existence of axions.

WDs have long been used as probes of axions by studying the possibility of energy loss from axion emission [167]. Axions are emitted by axion bremsstrahlung in electron-nucleon scattering. The extra energy loss would modify WD cooling and thus change the luminosity function of WDs. Comparisons to the observed luminosity function have been used to set stringent constraints on the axion-electron coupling [30, 168, 169]. Moreover, it has been suggested that the observed WD luminosity function actually prefers the existence of an axion [168, 169], a claim further supported by period-drift measurements of WDs undergoing pulsations [170].

In this chapter we propose to use X-ray observations of MWDs to detect the small fraction of emitted axions that convert to X-ray photons outside of the MWD in the strong

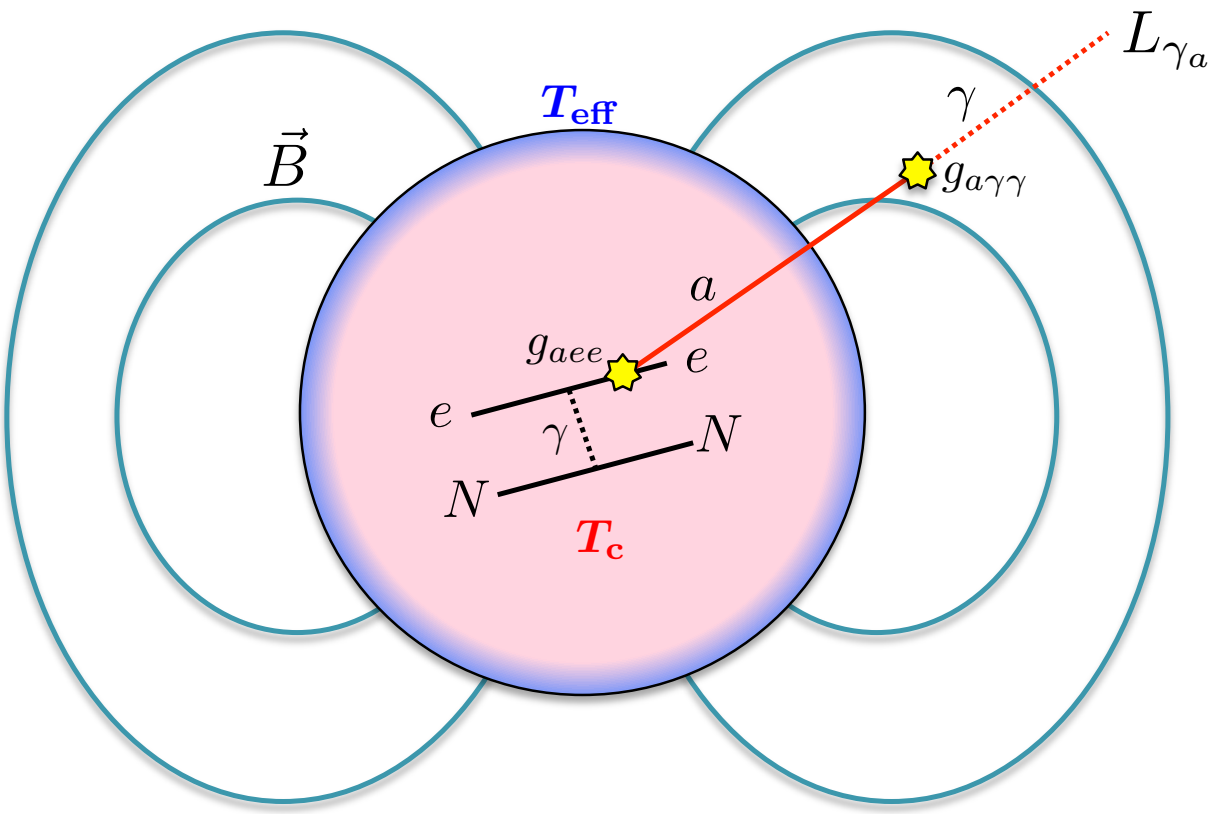

Figure 4.1: Axions are produced inside of a WD star and convert into X-ray photons as they pass through the star's magnetic field. The axion-induced X-rays have energy around the core temperature T_c, which is much higher than the WD surface temperature T_{eff}.

surrounding magnetic field, as illustrated in Fig. 4.1. The conversion of axions to photons utilizes the axion-photon coupling. The proposed method uses the following key properties of isolated MWDs. First, the surrounding magnetic fields can be quite high, $\sim 10^9$ G [20, 171], enhancing the axion-photon conversion probability. Second, while the core temperature of WDs is typically in the X-ray band, $T_c \sim 10^7\,\mathrm{K}$, the effective surface temperature is significantly lower, $T_{\mathrm{eff}} \sim 10^4\,\mathrm{K}$ (see, *e.g.*, Ref. [64]). Therefore an isolated MWD should not produce X-rays in the absence of axions. X-ray energy axions may escape the core and then convert into real X-ray photons in the magnetic field surrounding the WD, leading to a nearly thermal X-ray flux at the temperature of the core. In this chapter, we show that X-ray telescope observations of MWDs have the potential to probe a wide range of axion masses and couplings. However, as we will show, the X-ray observations are only sensitive to low-mass ALPs and not to the QCD axion, as the axion-photon conversion probability is suppressed for large axion masses.

A similar approach to axion detection was previously suggested for neutron stars (NSs) [172]. In that case, nuclear bremsstrahlung in the NS generates an outgoing flux of axions, which may convert into X-rays in the strong magnetic field surrounding the NS. However, it was pointed out in Ref. [173] that vacuum birefringence effects from quantum electrodynamics (QED), in the presence of strong magnetic fields, stymie the axion-photon conversion process. The result is that the axion-induced X-ray flux from NSs is expected to be negligible for a KSVZ [174–176] or DFSZ [177,178] QCD axion, but the flux may still be significant for ALPs [179,180]. We will discuss these QED effects for MWDs below.

In many ways our proposal is reminiscent of the CAST experiment [27,181,182], which looks for axions produced within the Sun. These keV-energy axions travel to Earth where they are converted into X-ray photons by the strong magnetic field of the CAST experiment and detected with X-ray optics. The key conceptual difference between our MWD proposal and CAST, in addition to using MWDs as the axion source instead of the Sun, is that the conversion to X-rays takes place not in the lab but rather in the magnetosphere surrounding the MWD itself. A similar approach has in fact been suggested for the Sun (see, *e.g.*, Ref. [183]), whereby one looks at spectral and morphological distortions to the solar X-ray spectrum from axion-photon conversion in the solar magnetic field, but this is complicated by the fact that the Sun is already a strong X-ray source.

We note that a host of additional astrophysical probes of axions and axion dark matter (DM) have been proposed. These include radio signatures of axion DM conversion in NSs [184–187] and radio signatures of axion decay [188], supernova cooling [189,190], energy loss in horizontal branch stars in globular clusters [191], and photon-axion oscillations leading to increased transparency of TeV gamma rays [192–195]. Axion DM is also the subject of significant laboratory efforts at present [45,196–209].

4.1 X-ray flux calculation

It is useful to recall how an axion interacts with matter (see Ref. [210] for a review). The QCD axion couples to gluons through the operator $\mathcal{L} \supset -a\alpha_s G\tilde{G}/(8\pi f_a)$, where a is the axion field, α_s is the strong fine structure constant, f_a is the axion decay constant, and G is the QCD field strength tensor. The axion may also couple to electromagnetism through the operator $\mathcal{L} \supset -g_{a\gamma\gamma} aF\tilde{F}/4$, where $g_{a\gamma\gamma}$ is the axion-photon coupling with units of GeV^{-1}, and F is the QED field strength tensor. Finally the axion can interact with electrons through the operator $\mathcal{L} \supset g_{aee}/(2m_e)\bar{e}\gamma^\mu\gamma_5 e\partial_\mu a$, where g_{aee} is the dimensionless axion-electron coupling, m_e is the

electron's mass, and e is the electron field. It is customary to write $g_{a\gamma\gamma} = C_\gamma \alpha_{\rm em}/(2\pi f_a)$ and $g_{aee} = C_e m_e/f_a$, where $\alpha_{\rm em}$ is the electromagnetic fine structure constant, and C_γ and C_e are dimensionless parameters.

The coupling of axions to matter allows axions to be emitted from WDs. WDs have dense cores that are supported by electron degeneracy pressure and consist predominantly of a hot plasma of carbon, oxygen, and electrons. The temperature of this isothermal plasma, which makes up the bulk of the matter of the WD, can be $T_c \approx 10^7$ K or higher, depending on the WD. Axions are emitted most efficiently in WDs from bremsstrahlung off of electrons in electron-nuclei scattering, through the diagram illustrated in Fig. 4.1. The luminosity radiated from a WD in axions, denoted by L_a, is calculated in Refs. [66, 167, 211] (see also Ref. [212]), and for a carbon-oxygen WD with mass density ratio 0.5 and total mass $M_{\rm WD}$, we find

$$\frac{L_a}{L_\odot} \approx 1.6 \times 10^{-4} \left(\frac{g_{aee}}{10^{-13}}\right)^2 \left(\frac{M_{\rm WD}}{1\, M_\odot}\right) \left(\frac{T_c}{10^7\ {\rm K}}\right)^4 , \tag{4.1}$$

where $L_\odot$ and $M_\odot$ are the luminosity and mass of the Sun, respectively. The energy spectrum of the axion emission is found to be thermal at temperature T_c: $dL_a/dE \propto E^3/(e^{E/T_c} - 1)$ [66].

The emitted axions may be converted into X-ray photons in the magnetic field surrounding the MWD. Under the approximation where we assume all axions travel along radial trajectories originating from the MWD center, we may derive a simple analytic expression for the conversion probability. Note that in the Appendix we derive and numerically solve the relevant equations of motion for the more general trajectories and field configurations appropriate for a realistic MWD with finite extent, but the results are similar to those found by assuming radial trajectories. The axion-photon mixing equations in the presence of an external magnetic field can be reduced to a system of first-order differential equations using a WKB approximation. This approximation assumes that the scale of variation in the magnetic field is much larger than the axion's de Broglie wavelength. By working in the Weyl gauge, $A^0 = 0$, and focusing on axion trajectories along which the angle with respect to the magnetic field does not change, these equations take the form [173]

$$\left[i\partial_r + E + \begin{pmatrix} \Delta_\parallel & \Delta_B \\ \Delta_B & \Delta_a \end{pmatrix} \right] \begin{pmatrix} A_\parallel \\ a \end{pmatrix} = 0\,, \tag{4.2}$$

where E is the axion's energy. Here $A_\parallel(r)$ denotes the vector potential component in the plane normal to the direction of propagation and parallel to the external magnetic field, as a function of the radial coordinate r, while $a(r)$ is the axion field. The probability for an axion to convert into a photon $p_{a\to\gamma}$ is determined by solving Eq. (4.2) and comparing

the magnitude squared of an initial pure axion state with the asymptotic solution for the electromagnetic vector potential. In the background magnetic field, the axion-photon interaction induces a mixing, which is parametrized by $\Delta_B(r) = (g_{a\gamma\gamma}/2)B(r)\sin\Theta$, where $B(r)$ is the strength of the magnetic field at radius r and Θ is the angle between the radial propagation direction and the magnetic field, which is r-independent. The term $\Delta_a = -m_a^2/(2E)$ incorporates the axion mass and is responsible for the slightly different momenta between the axion and photon states. Strong-field QED effects in vacuum give rise to the term $\Delta_\parallel(r) = (7/2)E\xi(r)\sin^2\Theta$, with $\xi(r) = (\alpha_{\rm em}/45\pi)[B(r)/B_{\rm crit}]^2$ with $B_{\rm crit} = m_e^2/e \approx 4.41\times10^{13}$ G the critical field strength. In general $\Delta_\parallel$ also contains a term related to the photon's effective plasma mass $\omega_{\rm pl}$, $\Delta_\parallel = -\omega_{\rm pl}^2/(2E)$, but this term is subdominant to the QED one for the systems that we consider.

Since the B field strength decreases as we move farther away from the surface of the MWD, it is important to solve the equation of motion Eq. (4.2) including the changing magnetic field profile with r. In the weak-mixing limit we can solve Eq. (4.2) using the formalism of time-dependent perturbation theory, and the axion-photon conversion probability is found to be [173, 180]

$$p_{a\to\gamma} = \left|\int_{R_{\rm WD}}^{\infty} {\rm d}r'\Delta_B(r')\, e^{i\Delta_a r' - i\int_{R_{\rm WD}}^{r'}{\rm d}r''\Delta_\parallel(r'')}\right|^2 . \tag{4.3}$$

The integral starts at the star's surface, $r = R_{\rm WD}$, since it is assumed that X-ray photons produced inside the MWD cannot escape. To first approximation we may model the magnetic field outside of the MWD as a magnetic dipole, such that $B(r) = (R_{\rm WD}/r)^3 B_0$ with B_0 the field at the surface and $r > R_{\rm WD}$. In the Appendix we consider more general magnetic field configurations, but the results are largely the same. In general, we evaluate Eq. (4.3) numerically. Note that for typical MWD parameters and asymptotically small m_a, the conversion probabilities are of order $10^{-4}\times(g_{a\gamma\gamma}/10^{-11}\ {\rm GeV}^{-1})^2$.

Having calculated both the spectrum of axion radiation, dL_a/dE, and the axion-to-photon conversion probability, $p_{a\to\gamma}$, the flux of axion-induced X-ray photons at Earth is calculated as

$$\frac{dF_{\gamma_a}}{dE}(E) = \frac{dL_a}{dE}(E)\times p_{a\to\gamma}(E)\times\frac{1}{4\pi d_{\rm WD}^2}\,, \tag{4.4}$$

where $d_{\rm WD}$ is the distance between Earth and the MWD. Note that for a typical MWD $d_{\rm WD}\approx 30$ pc away, combining Eq. (4.4) with the conversion probability estimate and the axion luminosity Eq. (4.1) leads to axion-induced X-ray fluxes of order $F_{\gamma a}\sim 10^{-15}\times(g_{aee}g_{a\gamma\gamma}/10^{-24}\ {\rm GeV}^{-1})^2$ erg/cm^2/s at low axion masses, though in practice we compute

dF_{γ_a}/dE precisely using the above formalism given the properties of the MWD under consideration. In practice we compute the integrated flux F_{2-10}, defined as the integral of Eq. (4.4) from 2 to 10 keV, to compare to data.

The only parameter that appears in Eq.(4.4) that cannot be measured directly for a given MWD is the core temperature, T_c, which affects the axion luminosity through Eq.(4.1). The core temperature is not directly observable, since the thin WD atmosphere is largely opaque to radiation. The effective temperature $T_{\rm eff}$ of the atmosphere, which determines the observed luminosity L_γ, is much smaller than the temperature of the isothermal core T_c. Understanding the relation between L_γ and T_c requires detailed modeling of the layers connecting the atmosphere to the degenerate core (see *e.g.*, Refs. [62–65]). We use the result of models presented in Ref. [64], which finds that for luminosities above $L_\gamma \sim 10^{-3.8}\ L_\odot$ and below $\sim 10^{-1.5}\ L_\odot$ the luminosity-core temperature relation is well approximated by

$$T_c \simeq \left(3 \times 10^6\ {\rm K}\right) \left(\frac{L_\gamma}{10^{-4} L_\odot}\right)^{0.4} . \tag{4.5}$$

As we discuss further in the Appendix, the WD models in Refs. [62–65] agree to within $O(10\%)$ uncertainty.

It is important to note that while the effective temperatures $T_{\rm eff}$ are often at the level of 10^4 K, the emission from the WD does not follow a pure thermal distribution at this temperature since higher frequencies probe deeper within the WD atmosphere [213]. Still, for the hot WDs we consider, the expected thermal hard X-ray flux (*e.g.*, from 2 to 10 keV) is negligible compared to the axion-induced fluxes that will be probed.

4.2 X-ray data analysis and projections

Although there are over 70000 known WD stars within approximately 100 pc of Earth [21], the total number of known MWDs with well-measured properties is only around 200 [20]. In the Appendix we list several MWDs that are expected to have the largest axion-induced X-ray flux, while in this section we focus on the most promising candidate.

The magnetic WD RE J0317-853 [214] is especially hot, has a strong magnetic field, and is relatively nearby, making it an excellent target for X-ray searches for axions. Optical and UV observations suggest an effective temperature between $T_{\rm eff} = 30000$ K and 60000 K, while at the same time being incredibly massive, $M_{\rm WD} \sim 1.3\ M_\odot$, and compact, $R_{\rm WD} \sim 0.003 - 0.004\ R_\odot$ [22, 214]. Note that the best-fit temperature presented in Ref. [214] is

$T_{\rm eff} = 4.93^{+0.22}_{-0.12} \times 10^4$ K, though a wider range was considered in Ref. [22]. The MWD rotates with a period of ∼725 s, and over this period the surface magnetic field strength is seen to oscillate. Reference [215] used time-resolved far-UV spectroscopic data from the *Hubble Space Telescope* to study the variations in the locations and magnitudes of Lyman α transition to measure the magnetic field profile. They found that the observable surface magnetic field varies between 200 and 800 MG over the WD rotation period, which is well fit by an offset dipole model [215]. They also find a best-fit temperature $T_{\rm eff} \sim 40000$ K.

In the Appendix we model in detail the magnetic field structure of this MWD and assess the sensitivity of our results to uncertainties in the value of $T_{\rm eff}$, for example. Here, however, we simply calculate the predicted X-ray flux using Eq. (4.3) with the most conservative choice of parameters for the magnetic field strength and effective temperature of RE J0317-853. We use a central dipole field with surface-field value $B_0 = 200$ MG and $\sin\Theta = 1$, corresponding to the lowest surface-field value observed in Ref. [215] anywhere on the WD surface over its period. We also take the fiducial values $T_{\rm eff} = 30000$ K, $M_{\rm WD} = 1.32\ M_\odot$, and $R_{\rm WD} = 0.00405\ R_\odot$ [22], which let us infer $L_\gamma = 0.0120\ L_\odot$ from the Stefan-Boltzmann law and $T_c = 2.0 \times 10^7$ K from Eq. (4.5). We note that higher $T_{\rm eff}$ lead to higher flux rates, and our fiducial value for $T_{\rm eff}$ is the lowest end of the range discussed in Refs. [22, 214]. Parallax measurements from *Gaia*-DR2 [21] place RE J0317-853 at a distance of $d_{\rm WD} = 29.54 \pm 0.04$ pc from Earth.

The axion-induced X-ray spectrum from RE J0317-853 should peak around $E \sim 3\,T_c \sim 5\,\text{keV}$. Observations with *Suzaku*, using approximately 60 ks of exposure time, detected no astrophysical X-ray emission from this MWD and set a flux limit in the 2-10 keV range of $F_{2-10} < 1.7 \times 10^{-13}\,\text{erg/cm}^2\text{/s}$ at 95% confidence [216]. We note that the limit in Ref. [216] required background subtraction and modeling; the limit itself is dominated by systematic uncertainties in modeling the cosmic X-ray background and the non-X-ray background. We also caution that the limit in Ref. [216] is formally only valid for an energy spectrum that resembles the above backgrounds, given the energy-dependence of the *Suzaku* effective area, though we have checked that this only induces a ∼10% difference in the predicted counts and thus can be ignored for our purposes. We translate the flux limit into a 95% constraint on the axion coupling constants $|g_{a\gamma\gamma}\, g_{aee}|$ using the fiducial values for RE J0317-853 and the formalism for axion-photon conversion developed above. Our results are presented in Fig. 4.2, which shows our constraint on the axion parameter space; the region above the blue curve is excluded at 95% confidence for the fiducial stellar parameters ($T_{\rm eff}$, B_0, etc) given above. Note that the nontrivial structure in the limit at high m_a is due to transitioning across the regime where $\Delta_a \ll \Delta_\parallel$ and then again to the regime where $\Delta_a \gg R_{\rm WD}$.

We compare our result to the previous best limits on this coupling combination. By

searching for axions produced inside of the Sun though the axion-electron coupling, the CAST experiment obtains a direct limit on $|g_{a\gamma\gamma}\, g_{aee}|$ [217]. Our constraints are approximately 2 orders of magnitude stronger than those from CAST at low axion masses. Several experiments derive upper limits on $|g_{a\gamma\gamma}|$ alone. CAST provides an upper limit on $|g_{a\gamma\gamma}|$ from axions produced in the Sun through the Primakoff process [27]. Similarly an upper bound on $|g_{a\gamma\gamma}|$ is derived from the nonobservation of a gamma ray flux coincident with SN 1987A [40], which is expected to be seen if axions are produced during the core-collapse supernova and subsequently convert into γ-ray photons in the intergalactic magnetic field. By combining these limits on $g_{a\gamma\gamma}$ with the limit $|g_{aee}| < 2.8 \times 10^{-13}$, which arises from modeling the WD luminosity function [30], we obtain a second 95% confidence upper limit, which is stronger than CAST's direct limit on $|g_{a\gamma\gamma}\, g_{aee}|$.

In Fig. 4.2 we also show the best-fit value for $g_{a\gamma\gamma} \times g_{aee}$ ("cooling hints") found in Ref. [33] from a global fit to the available stellar cooling data, which slightly favors nonzero axion-electron and axion-photon couplings. Unfortunately the global fits say little about the axion mass, since the stellar cooling probes are not sensitive to the mass of the particle causing the cooling (at least up to the temperature of the stellar cores, which are $\mathcal{O}(1$ keV). From our work we are able to say that the axion mass at these best-fit couplings needs to be above $\sim 2 \times 10^{-5}$ eV. The coupling-mass relations for the DFSZ [177, 178] and KSVZ [174–176] QCD axion models are also shown in Fig. 4.2.

The *Suzaku* observations of MWD RE J0317-853 from [216] are not ideal for searching for the proposed axion-induced X-ray signal. This is because *Suzaku* has a rather poor point-source sensitivity in the ∼2-10 keV band compared to other telescopes like *XMM-Newton* or *Chandra*. For instance, we estimate that a ∼400 ks observation with *Chandra* would yield a 95% confidence flux sensitivity in the 2-10 keV band at the level of $6 \times 10^{-16}\,\mathrm{erg/cm^2/s}$ [218], which is over 2 orders of magnitude better than the sensitivity achieved in [216] with *Suzaku*. (Specifically, this flux sensitivity estimate includes X-ray and particle backgrounds as estimated in [218] and is for the ACIS-I instrument in the timed exposure mode with no grating and with CCD *I3*, along with Very Faint telemetry.) This projected sensitivity appears in Fig. 4.2 as the red dashed curve. Note that this sensitivity projection assumes that the MWD does not produce X-ray emission in the energy range of interest at the flux levels that would be probed by *XMM-Newton* and *Chandra*. This assumption is justified because the thermal emission is exponentially suppressed in the energy range 2-10 keV and well below the levels that would be probed by future observations. Possible nonthermal emission mechanisms include synchrotron and curvature radiation in the strong magnetic field surrounding the MWD. However, these processes are suppressed by the rather large spin period of the MWD, which leads to a small accelerating potential compared to *e.g.*

the fast-spinning cataclysmic variable (CV) MWD AE Aquarii, for which pulsed nonthermal emission has been possibly observed [216, 219].

4.3 Discussion

In this chapter we used *Suzaku* observations of the nearby MWD RE J0317-853 to set the strongest limits to date on $|g_{a\gamma\gamma}\, g_{aee}|$ for axion masses $\lesssim$ meV. Dedicated observations, with existing telescopes such as *XMM-Newton*, *Chandra*, or *NuSTAR* of this MWD and others have the potential to improve the sensitivity by over an order of magnitude and perhaps more. If the previously observed stellar cooling hints are due to low-mass axion-like particles, X-ray observations of MWDs should detect excess hard X-ray flux.

If a hard X-ray signal is seen from a MWD, the first question should be if the MWD is accreting, which would be the case for a CV star. CVs, which often emit hard X-ray spectra are distinguishable from *e.g.* their variability and emission line spectra. It is also possible that some MWDs emit hard X-rays due to chromospheric activity, though this has yet to be observed [220]. Our predicted axion signal has the unique feature of having an order unity modulation fraction over the MWD period for most alignment angle configurations, as discussed more in the Appendix, which could help differentiate it from other backgrounds.

The signal discussed in this chapter requires the axion to interact with both electromagnetism and electrons. While both interactions are expected in a generic ALP theory, from an effective field theory point of view, this fact makes it hard to directly compare our sensitivity to *e.g.* the CAST limits on $g_{a\gamma\gamma}$ alone. However, in the Appendix we show that even if one assumes that the axion-electron operator is generated through the renormalization group alone due to W and Z-boson loops, the constraints from this chapter may be translated to constraints on $g_{a\gamma\gamma}$ that are comparable to those from CAST.

In addition to the axion-electron coupling, a generic axion is also expected to interact derivatively with quarks. These interactions cause NSs to radiate $\sim$keV axions, as in the WD case described in this chapter. NSs are also promising targets for axion-induced hard X-ray signals, and this will be explored in future work [221].

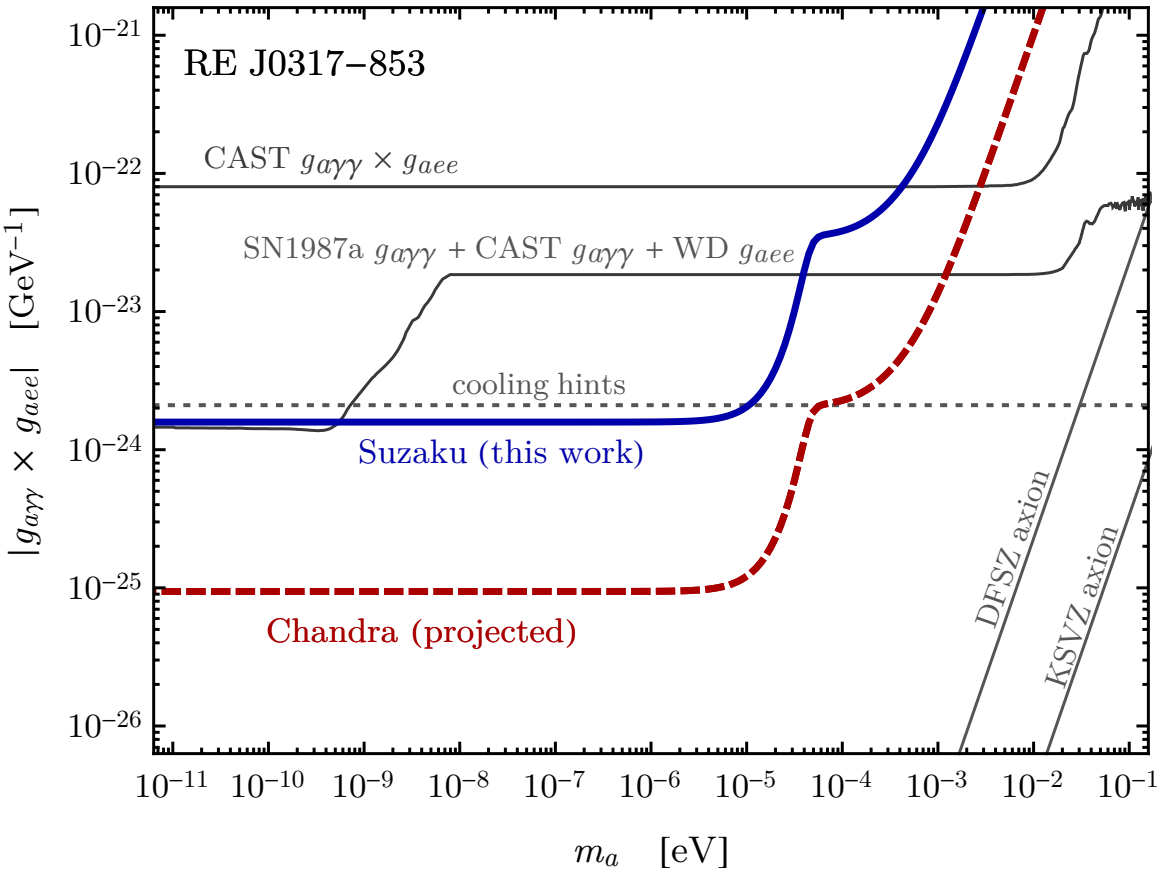

Figure 4.2: The 95% C.L. upper limit on the axion couplings $|g_{a\gamma\gamma}\, g_{aee}|$ as a function of the axion mass m_a are inferred from the nonobservation of X-ray emission from the MWD RE J0317-853 by the *Suzaku* telescope with ∼60 ks of exposure (solid blue line). We also show the 95% C.L. projected sensitivity from *Chandra* observations of the same MWD with a 400 ks exposure (dashed red line). The limits extend to $m_a = 0$ outside of the plotted range. The nontrivial structure in the limit at high m_a arises from the transition probability becoming suppressed in this regime by the axion-photon momentum mismatch (see text for details). Additionally, we show the strongest upper limit on this parameter space before this work from the nonobservation of gamma rays from SN 1987A, searches for axions with the CAST experiment, and constraints on the WD luminosity function. Stellar cooling hints suggest an axion may be present in the spectrum with $|g_{a\gamma\gamma}\, g_{aee}| \sim 2 \times 10^{-24}$, as indicated, though this interpretation is subject to large uncertainties.

Chapter 5

No Evidence for Axions from *Chandra* Observation of the Magnetic White Dwarf RE J0317-853

In the previous chapter, we pointed out that axions could produce X-ray signatures through axion-photon conversion in magnetic WD (MWD) magnetospheres [222] (see [172, 173, 179, 180, 221, 223–227] for related discussions in neutron star (NS) magnetospheres). In that chapter, we used archival data from the *Suzaku* telescope to constrain this process. However, *Suzaku* is not the optimal telescope for such a search, because it has relatively weak angular resolution and therefore point-source sensitivity. By contrast, the *Chandra* X-ray telescope boasts the leading point-source sensitivity of available X-ray telescopes. We applied to NASA and the Smithsonian Institute for time on *Chandra* to observe MWD RE J0317-853, the MWD we computed was the most axion-emissive known white dwarf in the previous Chapter. We were awarded this time and the observation was taken in December 2020. In this Chapter we analyze *Chandra* data of the MWD RE J0317-853 to look for evidence of axion production and conversion at that MWD.

The couplings of the axion a with mass m_a to electromagnetism and electronic matter are described through the Lagrangian terms

$$\mathcal{L}_{\rm int} \supset -\frac{1}{4} g_{a\gamma\gamma} a F_{\mu\nu} \tilde{F}^{\mu\nu} + \frac{g_{aee}}{2m_e} (\partial_\mu a) \bar{e} \gamma^\mu \gamma_5 e \,, \tag{5.1}$$

with F ($\tilde{F}$) the (dual) quantum electrodynamics (QED) field strength, e the electron field, and m_e the electron mass. It is convenient to parameterize the coupling constants by $g_{a\gamma\gamma} = C_{a\gamma\gamma}\alpha_{\rm EM}/(2\pi f_a)$ and $g_{aee} = C_{aee} m_e / f_a$, where the C's are dimensionless. Most laboratory and astrophysical searches for axions focus on the axion-photon coupling, with current

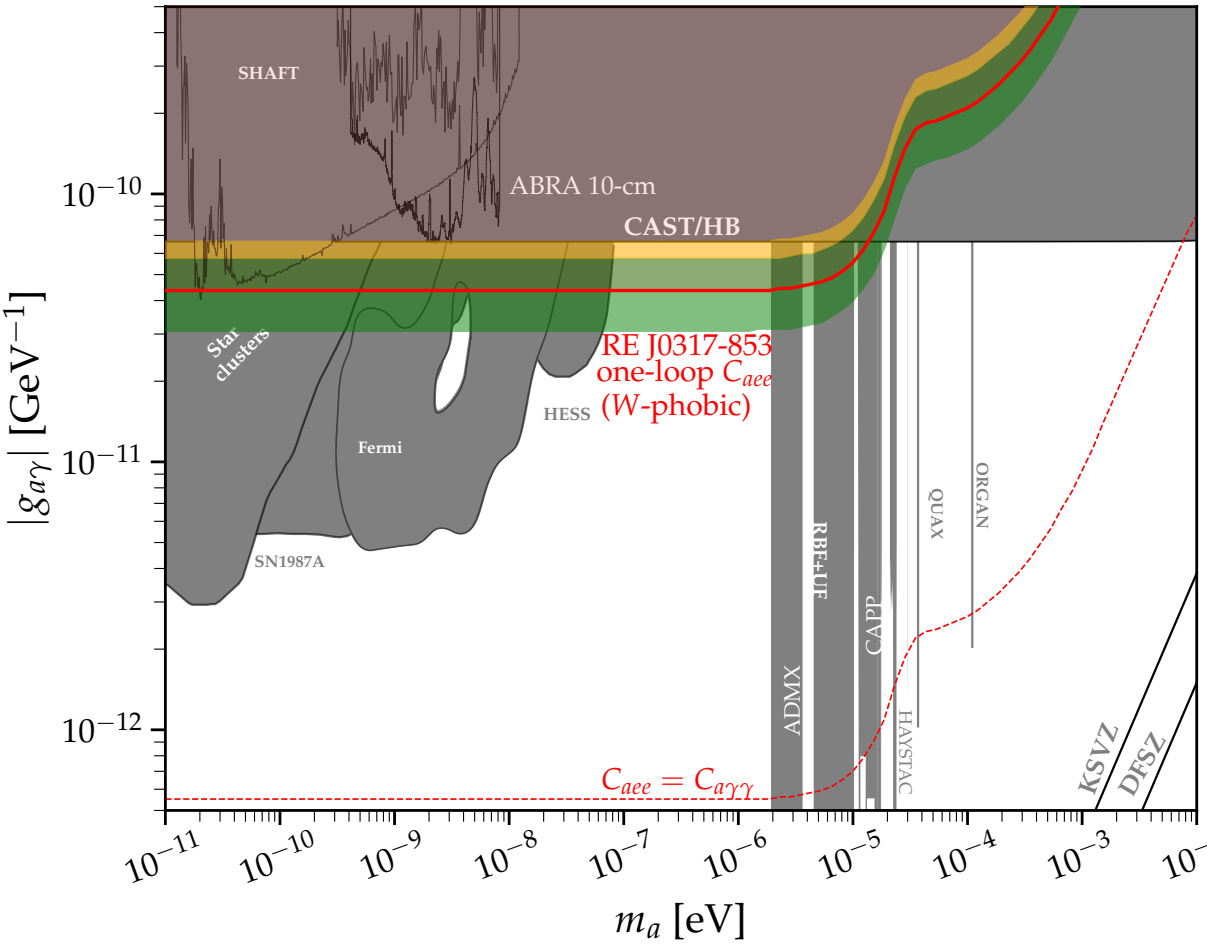

Figure 5.1: We constrain $g_{a\gamma\gamma}g_{aee} \lesssim 1.3 \times 10^{-25}$ GeV^{-1} at 95% confidence for low m_a from the non-observation of X-rays from the MWD RE J0317-853. We translate this result to constraints on $g_{a\gamma\gamma}$ assuming: (i) a tree-level axion-electron coupling with $C_{aee} = C_{a\gamma\gamma}$, and (ii) the loop-induced $C_{aee} \approx 1.6{\cdot}10^{-4} C_{a\gamma\gamma}$ that represents a conservative W-phobic axion (the loop-induced C_{aee} is generically larger). The expected 68% (95%) containment region for the power-constrained 95% upper limit is shaded in green (gold) for the W-phobic scenario. Previous constraints are shaded in grey [26].

constraints illustrated in Fig. 5.1. Low-mass constraints arise from the non-observation of photons from super star clusters (SSCs) [29] (see also [228]) and SN1987A [40] and searches for spectral modulations with *Fermi* [195], H.E.S.S. [229], and *Chandra* [37] (but see [38]). The constraints from the solar axion search with the CAST experiment [27] and from Horizontal Branch (HB) star cooling [28] are equally strong and extend over the whole mass range in Fig. 5.1, which also shows the predicted coupling-mass relations in the DFSZ [174,175] and KSVZ [177, 178] QCD axion models. The additional constraints shown in Fig. 5.1 require the axion to be dark matter [44–46, 198, 230–235] (see [26] for a summary).

As described in [222] axions may be produced within the cores of MWD stars through electron bremsstrahlung off of ions, using the g_{aee} coupling, and converted to X-rays in the stellar magnetospheres with the $g_{a\gamma\gamma}$ term in (5.1). Ref. [222] identified RE J0317-853 as being the most promising currently-known MWD because of a combination of (i) the close distance $d = 29.38 \pm 0.02$ pc, as measured by *Gaia* [236], (ii) the large magnetic field $B_{\rm pole} \sim 500$ MG, and (iii) the high core temperature $T_{\rm core} \sim 1.5$ keV. The predicted axion-induced X-ray signal is expected to be roughly thermal at the core temperature, meaning that it should peak at a few keV where *Chandra* is the most sensitive currently-operating X-ray telescope.

5.1 Analysis of *Chandra* observation of RE J0317-853

We observed the MWD RE J0317-853 on 2020-12-18 using the *Chandra* ACIS-I instrument with no grating for a total of 37.42 ks (PI Safdi, observation ID 22326). After data reduction – see the Appendix – we produce pixelated counts maps in four energy bins from 1 to 9 keV of width 2 keV each. Each square pixel in right ascension (RA) and declination (DEC) has physical length of $\sim 0\farcs492$ (note in the RA direction this is the width in RA $\times$ cos(Dec)). In Fig. 5.2 we show the binned counts over 1–9 keV in the vicinity of the MWD; note that in this region no pixel has more than one count. The figure is centered at the current location of the MWD, labeled 'Dec. 2020 (calib.)': $\mathrm{RA}_0 \approx 49^\circ\, 18'\, 37\farcs77$, $\mathrm{DEC}_0 \approx -85^\circ\, 32'25\farcs81$. Fig. 5.2 also shows intermediate source locations determined during the astrometric calibration process (see the Appendix). The 68% energy containment radius at 1 keV (9 keV) is approximately $0\farcs5$ ($0\farcs6$). The inset illustrates the expected template for emission associated with the MWD at 1 keV. No photon counts are observed near the MWD. The circle in Fig. 5.2 has radius $5''$ and is the extent of our region of interest (ROI); that is, we exclude pixels whose centers are beyond this radius in our analysis.

We analyze the pixelated data $\mathbf{d} = \{n_{i,j}\}$, with $n_{i,j}$ the number of counts in energy bin i and pixel j, in the context of the axion model, which is discussed more shortly, using the joint Poisson likelihood

$$p(\mathbf{d}|\mathcal{M}, \boldsymbol{\theta}) = \prod_{i=1}^{4} \prod_{j=1}^{\mathrm{N_{pix}}} \frac{\mu_{i,j}(\boldsymbol{\theta})^{n_{i,j}} e^{-\mu_{i,j}(\boldsymbol{\theta})}}{n_{i,j}!}\,, \tag{5.2}$$

with $\mathcal{M}$ denoting the joint signal and background model, with model parameters $\boldsymbol{\theta} = \{\mathbf{A}_{\rm bkg}, g_{aee}g_{a\gamma\gamma}, m_a\}$, and $N_{\rm pix}$ the number of spatial pixels. The model predicts $\mu_{i,j}(\boldsymbol{\theta})$ counts in energy and spatial pixel i, j. The background parameter vector $\mathbf{A}_{\rm bkg}$ consists of a

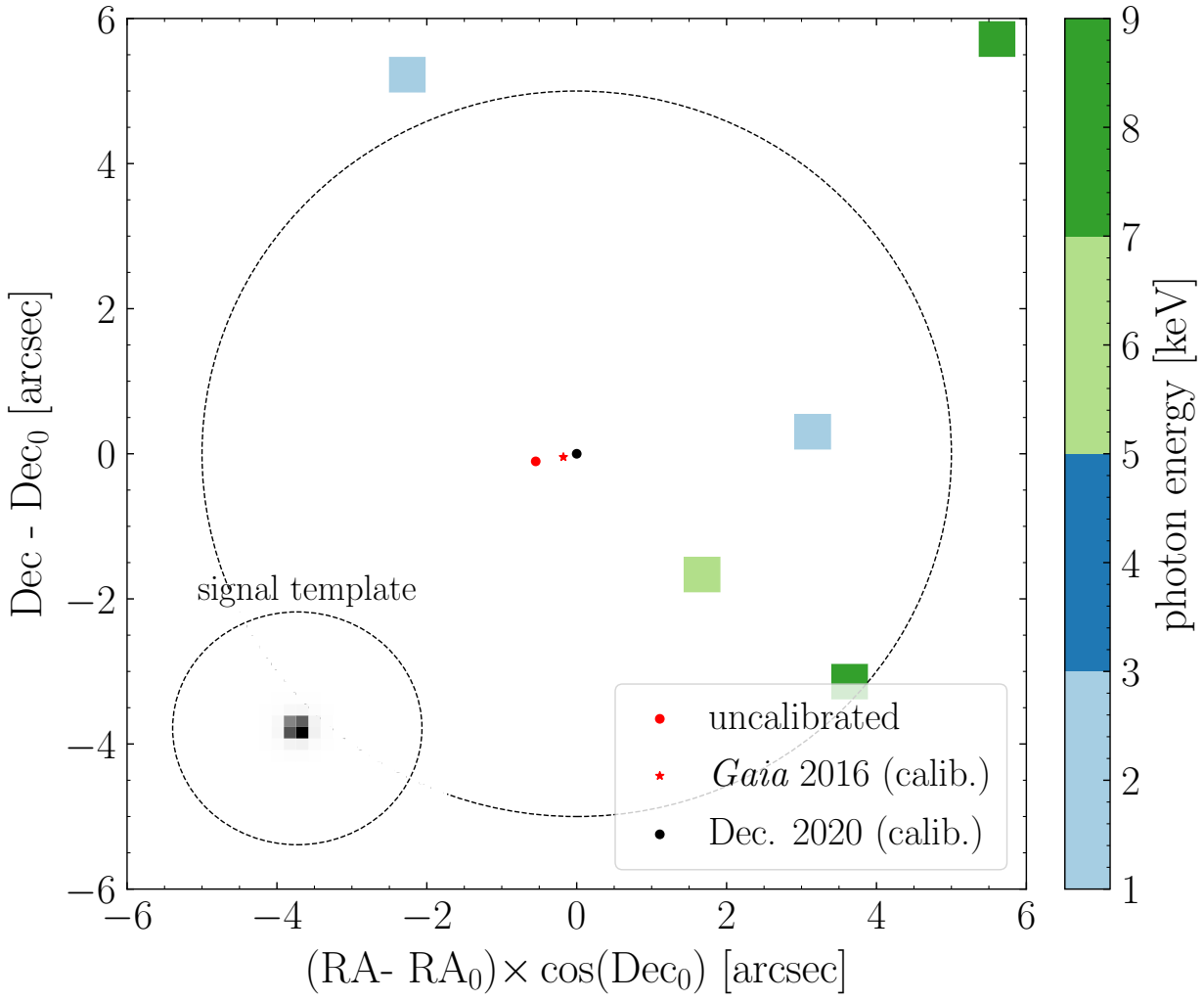

Figure 5.2: The binned counts over 1–9 keV from our ∼40 ks *Chandra* observation of the MWD RE J0317-853. No counts are observed within the vicinity of the source, whose location is indicated along with intermediate locations at various stages in the astrometric calibration process (see text for details), and also no more than one count is observed in any pixel. The dashed circle indicates the extent of the ROI used in our analysis. The inset panel illustrates the signal template in grey scale, for the first energy bin, over the analysis ROI.

single normalization parameter in each of the four energy bins that re-scales the background counts spatial template. For our background template, which we profile over, we use the exposure map, which is flat to less than 0.5% over our ROI. The signal model has the two parameters $\{g_{aee}g_{a\gamma\gamma}, m_a\}$, which predict the counts in each of the four energy bins. The signal template is centered on the MWD and accounts for the point spread function (PSF), as illustrated in the inset of Fig. 5.2.

At a fixed m_a we construct the profile likelihood for $g_{a\gamma\gamma}g_{aee}$ by maximizing the log-likelihood over $\mathbf{A}_{\rm bkg}$ at each $g_{a\gamma\gamma}g_{aee}$. Our 95% upper limit on $g_{a\gamma\gamma}g_{aee}$ is constructed directly by Monte Carlo simulations of the signal and null hypotheses instead of relying on Wilks' theorem, since we are in the low-counts limit (see *e.g.* [109] for details). A priori we decided to power constrain [110] our limits to account for the possibility of under fluctuations, though this was not necessary in practice.

We also analyze the data using the Poisson likelihood in the individual energy bins to extract the spectrum dF/dE, which is illustrated in Fig. C.6. In that figure we overlay the axion model prediction, which we now detail. For production via axion bremsstrahlung from electron-ion scattering [211, 212], we broadly follow the formalism developed in [222], though we make improvements thanks to updated WD models and luminosity data from *Gaia*. Firstly, we improve our modeling of the density profile and composition of RE J0317-853 using `MESA` [237] version `12778`. We simulate a WD of RE J0317-853's mass from stellar birth until it has cooled below RE J0317-853's observed luminosity. These simulations account for core electrostatic effects including ionic correlations and crystallization in the core that modify the profiles from that of a fully degenerate ideal electron gas, which were neglected in [222]. We find RE J0317-853 has a predominantly oxygen-neon core because it completed carbon-burning while ascending the asymptotic giant branch, typical for a WD of its mass undergoing single-star evolution. We take as our fiducial profiles those density and composition profiles from the model for which the luminosity matches the observed luminosity of RE J0317-853 (see Sec. IV of the Appendix for further details).

The second improvement we make is in estimating the core temperature of RE J0317-853. In the previous chapter we estimated the core temperature from an empirical core temperature-luminosity relation using an assumed luminosity from [238]. Ref. [238] used Hubble parallax and photometric data along with WD cooling sequences to estimate the luminosity of RE J0317-853. Here, we estimate the core temperature from WD cooling sequences [239] which predict *Gaia* DR2 band magnitudes. These cooling sequences are improved over those of [238] because they better account for ionic correlation effects than previous sequences, and our use of *Gaia* data rather than Hubble represents an improvement because of smaller uncertainties on the magnitudes, partly due to improved parallax measurements. In particular, we fit the models in [239] over cooling age and mass to the measured RE J0317-853 *Gaia* DR2 data [240]. Although previous measurements indicated a mass for RE J0317-853 of $\gtrsim 1.26\ M_\odot$, we find that the $1.22\ M_\odot$ model provides the best fit to the data. In the context of that model, we find that the *Gaia* data prefers a core temperature $T_c = 1.388 \pm 0.005$ keV. Therefore we use this model and to be conservative assume a core temperature at the lower 1σ allowed value, $T_c = 1.383$ keV, since the emissivity increases

with increasing T_c.

5.2 MWD modeling and axion interpretation

Axion emission from the stellar interior primarily results from the bremsstrahlung scattering $e + (A, Z) \to e + (A, Z) + a$ where an electron is incident on a nucleus with atomic number Z and mass number A. The electrons in a WD core are strongly degenerate with a temperature $T \ll p_F$ that is much smaller than the Fermi momentum p_F. In this regime, the axion emissivity spectrum is thermal and given by [66, 211, 212, 222]

$$\frac{d\varepsilon_a}{d\omega} = \frac{\alpha_{\rm EM}^2 g_{aee}^2}{4\pi^3 m_e^2} \frac{\omega^3}{e^{\omega/T} - 1} \sum_s \frac{Z_s^2 \rho_s F_s}{A_s u} \,, \tag{5.3}$$

which includes a sum over the species s of nuclei that are present in the plasma; Z_s is the atomic number, A_s is the mass number, ρ_s is the mass density, and $u \simeq 931.5$ MeV is the atomic mass unit. The species-dependent, order-one dimensionless factor F_s accounts for medium effects, including screening of the electric field and interference between different scattering sites. For a strongly-coupled plasma [241] we use the empirical fitting functions provided by [66]. Whereas Ref. [66] assumes a one-component plasma, we follow [242] and generalize to a multi-component plasma in (5.3) by summing over the constituent ionic species; this approach assumes that possible interference effects can be neglected. Note that the axion luminosity is given by the integral of the emissivity over the WD core.

Our fiducial WD model leads to the predicted axion luminosity $L_a \approx 8{\cdot}10^{-4} L_\odot (g_{aee}/10^{-13})^2$. Accounting for modeling uncertainties on RE J0317-853 we estimate the limit on $g_{a\gamma\gamma}$ may be $\sim$10% stronger, as illustrated in SM Fig. S4. Axions may also be produced by the $g_{a\gamma\gamma}$ coupling from electro-Primakoff production, which we compute in the Appendix, though as we show in SM Figs. S2 and S3 this process is subdominant compared to bremsstrahlung for RE J0317-853.

The axions then undergo conversion to X-rays in the MWD magnetic fields. The conversion probability $p_{a\to\gamma}$ may be calculated numerically for arbitrary magnetic field configurations and axion masses m_a by solving the axion-photon mixing equations in the presence of $g_{a\gamma\gamma}$, though it is important to incorporate the Euler-Heisenberg Lagrangian term which modifies the propagation of photons in strong magnetic fields and suppresses the mixing [173]. The magnetic field of the MWD is found to vary over the rotation period between 200 MG and 800 MG [215]; we follow [222] and assume a dipole field of strength 200 MG, to be conservative. Note that at low axion masses and high B-field values the dependence of the conversion probability on magnetic field is mild: $p_{a\to\gamma} \propto B^{2/5}$ [222]. Using the offset dipole

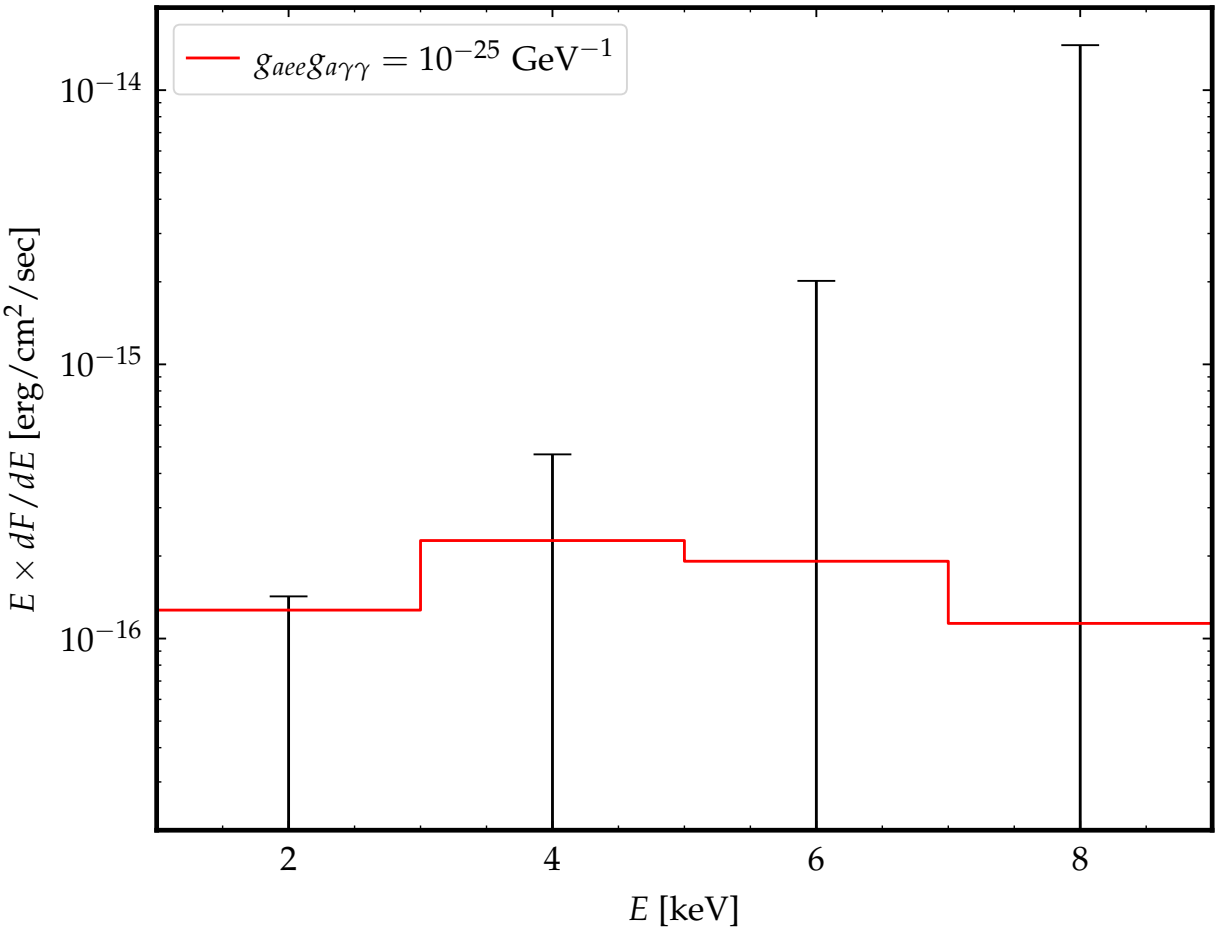

Figure 5.3: The energy spectrum found from our analysis of the *Chandra* data from the MWD RE J0317-853. In each of the four energy bins the best-fit fluxes are consistent with zero (the 68% containment intervals are shown). We also illustrate the predicted axion-induced signal that would be seen from an axion with the indicated couplings and $m_a \ll 10^{-5}$ eV.

model from [215] increases the conversion probabilities by up to ∼50% [222] at low masses, which may increase the limit by ∼10% relative to our fiducial case. Numerically the conversion probabilities are $\mathcal{O}(10^{-4}) \times \left(g_{a\gamma\gamma}/10^{-11}\,\text{GeV}^{-1}\right)^2$ for $m_a \ll 10^{-5}$ eV and drop off for higher masses. The distance is fixed at the central value measured by *Gaia* $d = 29.38$ pc [236] because the distance uncertainty only leads to a ∼0.1% uncertainty on the flux. In Fig. C.6 we illustrate the energy-binned spectrum prediction from axion-induced emission from the MWD for $m_a \ll 10^{-5}$ eV and $g_{aee}g_{a\gamma\gamma} = 10^{-25}$ GeV^{-1}. Note we neglect conversion in the Galactic magnetic fields, which we estimate to be subdominant to that in the WD magnetosphere.

We find no evidence for the axion model, with the best-fit coupling combination being zero for all masses. We thus set 95% one-sided upper limits on the coupling combination $g_{aee}g_{a\gamma\gamma}$

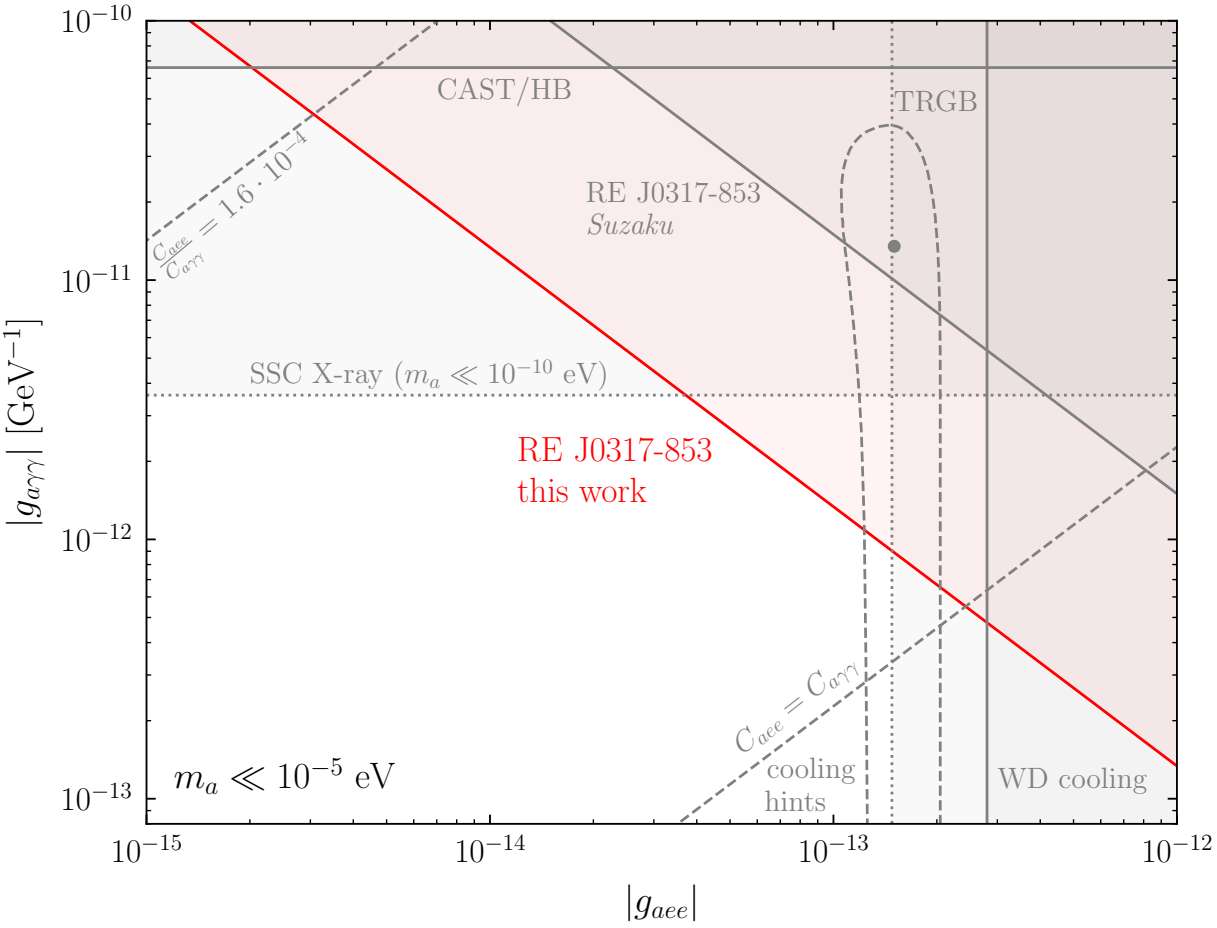

Figure 5.4: The 95% one-sided limit on the axion-photon and axion-electron coupling from this chapter $|g_{aee}g_{a\gamma\gamma}| < 1.3 \times 10^{-25}$ GeV^{-1} assuming $m_a \ll 10^{-5}$ eV. For $m_a \gtrsim 10^{-7}$ eV the leading constraint on $g_{a\gamma\gamma}$ is from the CAST experiment [27] and HB star cooling [28], while for $m_a \lesssim 10^{-10}$ eV it is from X-ray observations of SSCs [29]. The leading limits on g_{aee} are from WD cooling [30] and TRGB observations [31,32], while the 68% containment region for explaining stellar cooling anomalies [33], along with the best-fit coupling, is also indicated and in tension with our null results. In the regime that is excluded by WD cooling, our analysis should be modified to account for stellar energy loss into axions. Dashed diagonal lines show the relations $C_{aee}/C_{a\gamma\gamma} = 1$ and also $C_{aee}/C_{a\gamma\gamma} = 1.6 \times 10^{-4}$, the latter corresponding to the W-phobic loop-induced axion-electron coupling.

at fixed axion masses m_a using the profile likelihood procedure. For low masses $m_a \ll 10^{-5}$ eV the limit is $g_{aee}g_{a\gamma\gamma} \lesssim 1.3 \times 10^{-25}$ GeV^{-1}. This limit is around three orders of magnitude stronger than that set by the CAST experiment on this coupling combination [27]. Our limit also severely constrains the low-mass axion explanation of stellar cooling anomalies [33], which prefer $g_{a\gamma\gamma}g_{aee} \sim 2 \times 10^{-24}$ GeV^{-1} as illustrated in Fig. 5.4, where we show our low-mass limit in the $g_{a\gamma\gamma} - g_{aee}$ plane, along with current constraints.

It is instructive to translate our limit to one on $g_{a\gamma\gamma}$ alone by assuming a relation between the dimensionless coupling constants C_{aee} and $C_{a\gamma\gamma}$. Note that in the DFSZ QCD axion model there is a tree-level coupling between the axion and electron, such that $C_{aee} \sim C_{a\gamma\gamma}$, while in the KSVZ model no ordinary matter is charged under the Peccei-Quinn (PQ) symmetry and so $C_{aee} = 0$ at tree level, though it is generated at one loop [176]. The loop-induced value of $C_{a\gamma\gamma}$ depends on the relative coupling of the axion to $SU(2)_L$ versus hypercharge $U(1)_Y$. If the axion couples only to $SU(2)_L$ ($U(1)_Y$) then we expect, at one loop, $C_{aee} \sim 4.8 \times 10^{-4} C_{a\gamma\gamma}$ ($C_{aee} \sim 1.6 \times 10^{-4} C_{a\gamma\gamma}$) for $f_a \approx 10^9$ GeV^{-1} (see [176, 222, 243] and the Appendix). To be conservative we assume in Fig. 5.1 the W-phobic axion scenario, where the axion only couples to $U(1)_Y$ (but see SM Fig. S2). We also show the limit on $g_{a\gamma\gamma}$ for axion models with $C_{aee} = C_{a\gamma\gamma}$, which is nearly two orders of magnitude stronger than the loop-induced limit. Note, however, that assuming $C_{aee} = C_{a\gamma\gamma}$ allows constraints on g_{aee} from WD cooling [30] and tip of the red giant branch (TRGB) observations [31, 32] to be recast as constraints on $g_{a\gamma\gamma}$ at the level of few $\times\, 10^{-13}$ GeV^{-1}, which are not shown on Fig. 5.1. Couplings $C_{aee} \sim C_{a\gamma\gamma}$ may arise naturally in models with ultraviolet operators of the form $a\bar{e}\gamma_5 e$.

5.3 Discussion

Our results have strong implications for a number of astrophysical anomalies and planned laboratory experiments. For example, the WD cooling anomaly prefers $g_{aee} \sim 1.6 \times 10^{-13}$ [33]. In order for a low mass axion to explain this result and be compatible with our upper limit, one would need $C_{a\gamma\gamma} \lesssim 2.2 C_{aee}$ ($g_{a\gamma\gamma} \lesssim 8.1 \times 10^{-13}$ GeV^{-1}), which would not be able to also explain the axion-photon coupling $g_{a\gamma\gamma} \sim 10^{-11}$ GeV^{-1} suggested by the global fit to stellar cooling data [33] (see Fig. 5.4) or the TeV transparency anomalies, which prefer $g_{a\gamma\gamma} \gtrsim 2 \times 10^{-11}$ GeV^{-1} for $m_a \ll 10^{-8}$ eV [244]. Anomalous X-ray emission from nearby isolated Magnificent Seven NSs may be interpreted as low-mass ($m_a \ll 10^{-5}$ eV) axion production from nucleon bremsstrahlung in the NS cores and conversion to X-rays in the NS magnetospheres [221, 245]. The required coupling combination to explain the X-ray excesses is $g_{a\gamma\gamma} g_{aNN} \gtrsim 10^{-21}$ GeV^{-1}, with $g_{aNN} = C_{aNN} m_N / f_a$ the axion-nucleon coupling, with m_N the nucleon mass and C_{aNN} the dimensionless coupling. The non-observation of X-rays in this chapter from the MWD implies that if axions explain the Magnificent Seven excess they must be electro-phobic, with $C_{aee} \lesssim 4\, C_{aNN}$. Lastly, we note that our results are especially relevant for the upcoming ALPS II light-shining-through-walls experiment [208]. The last stage of the experiment will have sensitivity to $g_{a\gamma\gamma} \gtrsim 2 \cdot 10^{-11}$ GeV^{-1} for $m_a \lesssim 10^{-4}$ eV, meaning that much of the axion parameter space to be probed is constrained by the current

analysis (see SM Fig. S2).

As evident in *e.g.* Fig. 5.2 with ∼40 ks of *Chandra* data we are able to perform a nearly zero-background search; an additional order of magnitude in exposure time would allow us to improve the sensitivity to $g_{a\gamma\gamma}$ by a factor ∼1.5. The proposed *Lynx* X-ray Observatory [246] aims to improve the point source sensitivity by roughly two orders of magnitude compared to *Chandra*. A ∼400 ks observation with *Lynx* or a similar future telescope of RE J0317-853 (see SM Fig. S1) may be sensitive to axions with $g_{a\gamma\gamma} \sim 10^{-13}$ GeV^{-1} for $C_{aee} \sim C_{a\gamma\gamma}$, which may probe photo-philic QCD axion models [247–250] in addition to vast regions of uncharted parameter space for the hypothetical Axiverse.

Chapter 6

Hard X-ray Excess from the Magnificent Seven Neutron Stars

The Magnificent Seven neutron stars (NSs) are a group of seven nearby X-ray dim isolated NSs (XDINSs) that emit near-thermal soft X-ray emission with relatively low luminosities. They were first discovered in the *ROSAT* All Sky Survey data (RX J1856.6-3754 [251], RX J0720.4-3125 [252], RX J0806.4-4123 [253], RX J1308.6+2127 [254], RX J1605.3+3249 [255], RX J0420.0-5022 [256], and RX J2143.0+0654 [257]) and identified as a distinct class of objects by their spectral and temporal properties (see, *e.g.*, [258] for a review). Until now, no hard X-ray flux has been observed from the XDINSs. In this chapter we use archival *XMM-Newton* (hereafter *XMM*) and *Chandra* data to search for hard X-ray excesses in the 2-8 keV energy range from the XDINSs. We find that such excesses exist for the NSs RX J1856.6-3754 and RX J0420.0-5022. We characterize the spectral shapes of the hard excesses, search for evidence of variability and time dependence, and discuss possible origins of the flux.

Each of the XDINSs is radio-quiet (but see [259]) and characterized by a near-blackbody continuum in soft X-rays with distortions due to attenuation by the interstellar medium as well as potential absorption lines from the NS atmospheres. The near-thermal emission suggests we are viewing the NS surfaces, with temperatures ranging from approximately 50 eV to 100 eV. The low interstellar attenuation implies that the XDINSs are within hundreds of pcs of Earth, confirmed in some cases by parallax measurements [260]. The origin of the absorption lines is thought to be cyclotron resonance absorption [261]. Each NS also has an optical counterpart with a flux larger than expected from the Rayleigh-Jeans tail of the X-ray blackbody [36], although this may be associated with the NS atmosphere.

Six of the NSs are known to pulsate in X-rays with spin periods on the order of seconds. Assuming the NSs were born with millisecond spin periods, spin down via magnetodipole

radiation suggest large magnetic fields $\sim 10^{13}$ G and ages of around 10^6 years [262]. Coherent timing solutions have confirmed the field strengths, which roughly agree with the field strengths inferred from the absorption lines assuming they are due to cyclotron resonance by protons. The ages, along with the proper motions, point to a single birth place in the Gould Belt [263].

The hard X-ray excesses identified in this chapter could have a variety of physical origins. One exotic origin, which we discuss in the next chapter [264], is that the excesses arise due to the presence of a new ultralight particle of nature called the axion. The axions may be produced thermally in the cores of the NSs, which are expected to have temperatures of a few keV. The axions then escape the NSs and convert into X-rays in the strong magnetic fields surrounding the stars. The resulting spectrum is then nearly thermal at the core temperature, though some deviations away from the thermal spectrum are expected [173]. Less exotic explanations of the excess flux include non-thermal emission from charged-particle acceleration in the magnetospheres and X-ray emission from accretion of surrounding material. However, we point to issues with these explanations later in this chapter.

The remainder of this chapter is organized as follows. First, we describe our data reduction and analysis procedure. Then, we present detailed results for RX J1856.6-3754, the NS in which we find the most significant hard X-ray excess with a statistical significance around 5σ. Then we present our main results for the hard X-ray spectra of the remaining XDINSs, showing that while an excess is found robustly for RX J0420.0-5022 we cannot conclusively say whether similar excesses exist for the other five XDINSs. We conclude by considering possible origins of the flux.

6.1 X-ray data reduction and analysis

We use archival *XMM* and *Chandra* data to investigate the hard X-ray fluxes from the XDINSs. It is valuable to use data from both instruments because each is optimized for a different objective. A priori, *Chandra* should be the superior instrument for observation of the XDINSs with its excellent point source sensitivity in the hard X-ray range, which can be attributed to its small point spread function (PSF). However, the instrument is highly susceptible to X-ray pileup, which can artificially raise the event energies reported in an observation. This is potentially an issue when searching for hard X-ray flux in the presence of a significant soft X-ray spectrum. Meanwhile, *XMM* has the superior effective area and collectively the most exposure time of the XDINSs. Additionally, pileup is likely to be an insignificant contributor to the hard *XMM* spectra for these relatively dim NSs. However, the large PSF of *XMM* also allows for contamination due to nearby sources, which could

bias either our estimates of the signal or background spectra.

The fact that the hard XDINS spectra are consistent between the two instruments, as we show, is a promising sign that the reported excesses are not due to systematic effects. It is unlikely that a point source in the *XMM* spectra would also contaminate the *Chandra* spectra. Also, the consistency between the *XMM* and *Chandra* spectra suggests that pileup, which strongly depends on the source count rate, is not responsible for the excesses. Nevertheless, we incorporate systematic tests for these issues into our analysis.

In this section, we outline our data reduction procedures for *XMM* and *Chandra*. We further discuss our MARX simulations of the *Chandra* detector, which diagnose possible pileup effects and which we use to cut data if it appears pileup could be significant. We then discuss our analysis procedures for reconstructing the XDINS 2-8 keV spectra.

6.1.1 Data reduction

Here we describe the methods we use to process the publicly-available data from *XMM* and *Chandra* into the spectra and images analyzed in this chapter. The observation identification numbers for the observations used in this chapter are given in App. E.1, and the reduced data is given is given in App. E.2.

XMM-Newton Observations

The data products for *XMM* are downloaded from the *XMM-Newton* Science Archive. To perform the processing, we use *XMM-Newton* Science Analysis System (SAS) [265] version 17.0.

We first generate summary information for the dataset by generating the Calibration Index File (CIF) using the SAS task `cifbuild`, which locates the Current Calibration File (CCF). The CCF provides information about the state of the detector at observation time, which is necessary for future processing. We then run the task `odfingest`, which generates the Observation Data Files (ODF) containing general information on the detector.

For any individual observation, there may be multiple exposures for each camera, which are individual datasets taken during the observation time. Only a subset, called the "science exposures," are useful for analysis. The relevant science exposures for each observation ID to use for data reduction are determined from the Pipeline Processing Subsystem summary file. We only use science exposures in imaging mode, which we refer to simply as exposures for the remainder of the text.

From this information, we reprocess the ODF for the MOS and PN cameras with the tasks `emproc` and `epproc`, respectively. These tasks create calibrated and concatenated but

otherwise unfiltered event lists. We then generate the filtered event lists for each science exposure with the task `espfilt`, which filters the light-curves for soft proton (SP) contamination, which can significantly enhance the count rates for short periods of time. An observation affected by SP will have a count rate histogram that is approximately Gaussian with a peak at the unaffected rate but with a long high-count rate tail due to the contamination. `espfilt` establishes thresholds at $\pm 1.5\sigma$ of the count rate distribution and creates a good time interval (GTI) file containing the time intervals where the count rate is contained within the thresholds. `espfilt` returns a filtered event list, which contains only the events arriving during the GTIs. We then use only the filtered events in the analysis going forward.

We create images with `evselect` in the energy bins 2-4, 4-6, and 6-8 keV with the standard pixel sizes, $4.1''$ for PN and $1.1''$ for MOS. For the PN camera, we select only events with `FLAG==0` and `PATTERN<=4` (*i.e.*, single and double events) while for the MOS camera we select events with `PATTERN<=12`. We run a point source detection algorithm, `edetect_chain`, simultaneously on the images, which returns a list of point source locations. We use this source detection to determine the location of the NS in each exposure—the coordinates are subject to variations between exposures due to calibration uncertainties and the NS proper motion. In addition to a list of resolved point sources, this task returns exposure maps. We then run `rmfgen` and `arfgen`, which compute the detector redistribution matrix file (RMF) and the ancillary response file (ARF). The former accounts for the energy resolution of the detector while the latter accounts for the energy-dependent effective area. We correct the RMF for pileup in the case of the PN camera with the parameter setting `correctforpileup=yes`; however, a correction for MOS is not possible at this time. In its place, we run the task `epatplot` which estimates the amount of pileup in a spectrum. However, it is of limited use in our specific case. `Epatplot` compares the observed spectrum of the single and quadruple events in a single observation to the theoretical spectrum assuming no pileup. For the XDINSs, while there are significant counts below 2 keV, there are very few counts above 2 keV. With so few counts in individual observations, any deviations from the no pileup spectrum are not statistically significant. However, we do run the pileup test of [23], which estimates several measures of pileup in the XMM cameras.

To fit for the X-ray spectra, we begin with the image files around the NSs. We use the images created by `evselect`/`edetect_chain`. We create images for each exposure e: counts images $c_i^{p,e}$ (units [counts]) and exposure images $w_i^{p,e}$ (units [cm^2 s keV]) for each of the energy bands i, where p indexes the pixels. In the high-energy analysis we stack the images over exposures on a uniform RA-Dec grid, while for the low-energy analyses we use a joint likelihood over the individual exposures since the instrument responses are more important at low energies where the energy resolution plays an important role. To create the stacked

images, we separately stack the images in each detector (MOS or PN) over the individual exposures in each energy band in the following way. In each image, we first redefine the coordinate system such that the origin is at the source location $(\mathrm{RA}_0, \mathrm{Dec}_0)$. To correct for astrometric errors, the source location in the image is determined through PSF-based-template fitting to the counts data in the low energy data (<2 keV). Because each NS is bright in soft X-rays, this permits the localization of the NS in each image with sub-pixel accuracy. This corrects for the fact that the NS location may not be identical in each image due to a combination of calibration errors and proper motions. We then down-bin the images $I^e = \{c^e, w^e\}$ from the individual exposures into the stacked images $I = \{c, w\}$ on a uniform grid of RA and Dec according to

$$c_i^{p'} = \sum_e \sum_{p \in p'} c_i^{p,e} \tag{6.1}$$

$$w_i^{p'} = \sum_e \frac{\sum_{p \in p'} w_i^{p,e}}{\sum_{p \in p'}} , \tag{6.2}$$

where the pixel sums are over pixels p that have coordinates contained within the downbinned pixel indexed by p'.

The above stacking procedure leaves us with images in each energy band for each NS and detector with which we perform our fiducial high-energy analyses. To extract the spectra in each energy band we define a signal region R_S and a background region R_B. Extraction regions are defined relative to the energy-averaged 90% encircled energy fraction (EEF) radius. The signal region is a circle centered at the source location with radius 50% of the energy-averaged 90% EEF radius whereas the background region is an annulus centered at the source location extending from the edge of the signal region to an outer radius of 75% of the energy-averaged 90% EEF radius. We keep the background region compact to mitigate possible contamination from point sources. For the *XMM* EEF model, we use the 'Medium' mode PSF description assuming an on-axis source. Using the EEFs, we compute that in R_S there is a fraction of the signal $\chi_{S,i}$ while in R_B there is a signal fraction $\chi_{B,i}$.

Energy containment fractions are calculated by a Monte Carlo procedure in which test counts are placed with displacements from source location are drawn from the angular radius distribution specified by the PSF, then binned at our downbinned pixel resolution. The fraction of test counts placed within signal (background) region pixels defines the signal containment of the signal (background) region. Note that these fractions are energy-dependent because the region sizes are energy-independent, and that 50% of energy-averaged 90% EEF radius is inequivalent to the energy-averaged 50% EEF radius. For instance, while 100% of the energy-averaged 90% EEF radius of 0.6 arcminutes for PN corresponds to a signal

containment of 88% in the 2-4 keV bin, 50% of that energy-averaged 90% EEF radius corresponds to a signal containment of 74% in that same bin.

Chandra Observations

For the *Chandra* analyses we use the Chandra Interactive Analysis of Observations (CIAO) [266] version 4.11. We choose all ACIS `Timed Exposure` observations of the XDINSs for analysis irrespective of the grating and the spectral (-S) or imaging (-I) component. We will refer to these observations as *Chandra* observations for the remainder of the text. We use the CIAO task `download_chandra_obsid` to download the observations and reprocess them using `chandra_repro`. This task yields a filtered events file. We run `fluximage` on the events file to create images in the same bands as for *XMM*, along with exposure maps with pixel sizes of $0.492''$. We then run the source detection algorithm `celldetect` on the images, yielding the source coordinates. We use the `specextract` task to produce the detector response matrices.

We create *Chandra* images using the task `fluximage`. The signal and background regions are defined analogously to *XMM*, except that for *Chandra* the outer radius of the background region is taken to be 250% of the 90% energy-averaged EEF radius, since for *Chandra* nearby point sources are less of a concern given the superior PSF. For the *Chandra* EEF model, we use the CIAO tool `psf`.

6.1.2 MARX simulations

In this section we discuss our Model of AXAF Response to X-rays (MARX) [267] simulation framework. We use MARX version 5.4.0 to perform two simulations for each *Chandra* observation—each with the best-fit soft thermal spectrum from the data, but one with a hard X-ray tail of constant 10^{-15} erg/cm^2/s/keV and one without. To create the spectral file, we use Interactive Spectral Interpretation System version 1.6.2 [268] to generate a parameter file, and then we use the MARX tool `marxflux` to convert it to the MARX-friendly format. In order to reproduce the observation conditions as closely as possible to negate systematic errors, we simulate the NS with `marx` at the same detector coordinates and with the detector configuration as in the original observation. We create an events file and then an aspect solution file, ARF, and RMF with `marx2fits`, `marxasp`, `mkarf`, and `mkrmf`, respectively.

At this point, images can be created with `fluximage` as in the *Chandra* processing. For grating observations, the dispersed events must be order sorted with the CIAO tool `tg_create_mask` and then filtered out with `tg_resolve_events` to create events files compatible with `fluximage`. The resultant images will not include the effects of pileup. To

simulate pileup effects, we run `marxpileup` and then convert the results to an events file and image with `marx2fits` and `fluximage` as before.

6.1.3 Data analysis

We bin the data in 25 energy bins, with bin widths of 0.05 keV from 0 to 1 keV, one bin from 1 to 2 keV, and 4 bins of width 2 keV from 2 to 10 keV. Because of the energy range of the calibration on both instruments, we do not analyze data outside the range 0.5 keV to 8 keV. We also exclude observations that have a flaring time greater than 50%. In some detector operating modes (*e.g.*, `Small Window`), due to the placement of the source in the detector there is a limited extraction region available for background estimation within the vicinity of the source, and we exclude these as well. Furthermore, some *XMM* observations are excluded due to the presence of spurious source detections in the wings of the PSF.

In this subsection, we discuss our analysis of the soft spectra, including our computation of the 0.5-2 keV spectra and the analysis of the 0.5-1 keV data, in which the NSs are significantly thermally emitting. We then outline our analysis of the 2-8 keV data, in which we search for hard X-ray emission. Both analyses are of a frequentist nature.

Soft Spectral Analysis

We measure the soft X-ray spectra from 0.5-1 keV from the XDINSs both to confirm that we reproduce the previously observed spectra and so that we may fit the soft spectra and extrapolate into the hard X-ray band. That is, we fit for the soft thermal flux in order to verify that the exponential tail of the surface blackbody cannot account for the hard X-ray excesses. We find that although extrapolating the best-fit blackbody suggests the 2-8 keV bins are not contaminated by thermal surface emission, pileup of the soft photons can impact the hard spectra for some NSs and instruments. Furthermore, modeling the soft flux instead with NS atmosphere models indicates that depending on the NS and the NS surface composition, the 2-4 keV flux may be partially contaminated by thermal emission. We discuss these points later in this chapter.

For the soft analysis we use different extraction regions R_S and R_B relative to the high-energy analysis, since in the low-energy analysis we are more concerned with mismodeling the PSF than with misestimating the background. As such we take R_S to be 150% of the 90% EEF radius, and for R_B we take 250% of the 90% EEF radius, for both *XMM* and *Chandra*. We perform the following procedure for each detector (MOS, PN, or *Chandra*) independently. First we construct the NS soft spectrum from 0.5-2 keV in the following manner. We let the data in R_S in [counts] be denoted $d_S^e = \{c_{S,i}^e\}$, where i runs over the 10 relevant energy

bins and e runs over the number of exposures passing the quality cuts for a specific detector. Similarly we let the background data in [counts] be denoted $d_B^e = \{c_{B,i}^e\}$. Recall that we do not work with the images stacked over exposures in the low-energy analyses. We use this background data to compute the mean expected background counts within the signal region, $\mu_{\mathrm{B},i}^e = \frac{\Omega_S}{\Omega_B} c_{B,i}^e$, where Ω_S (Ω_B) is the solid angle of R_S (R_B).

Having obtained the source spectrum, we must now put our source spectral model in the same form. Assuming a source flux $S(E|\boldsymbol{\theta}_{\mathrm{S}})$ in [counts/cm^2/s/keV] where $\boldsymbol{\theta}_{\mathrm{S}}$ are generic model parameters describing the soft flux, we obtain the expected source counts using forward modeling

$$\mu_{S,i}^e(\boldsymbol{\theta}_{\mathrm{S}}) = t^e \int dE' \mathrm{RMF}_i^e(E') \mathrm{ARF}^e(E') S(E'|\boldsymbol{\theta}_{\mathrm{S}})\,. \tag{6.3}$$

Above we have designated t^e the observation time for the exposure in [s]. The ARF (a function of true X-ray energy E') represents the effective area of the detector in [cm^2] and the RMF (dimensionless) is a probability distribution function for the probability to observe an X-ray photon in (reconstructed) energy bin i given its true energy E'—in short, it accounts for the energy resolution of the detector.

To fit the data d we use the Poisson likelihood

$$\mathcal{L}(d|\boldsymbol{\theta}_{\mathrm{S}}) = \prod_{e,i} \frac{\left(\mu_{S,i}^e(\boldsymbol{\theta}_{\mathrm{S}}) + \mu_{\mathrm{B},i}^e\right)^{c_{S,i}^e} e^{-\left(\mu_{S,i}^e(\boldsymbol{\theta}_{\mathrm{S}}) + \mu_{\mathrm{B},i}^e\right)}}{c_{S,i}^e!} \tag{6.4}$$

joint over all exposures and energy bins. Note a slight subtlety: we may consider $\mu_{\mathrm{B},i}^e$ to be known since the background region from which it is measured is much larger than the signal region. This is not true in the high-energy analysis. In the high-energy analysis the background counts also play a more important role, so we treat them more carefully.

Except when discussing more complicated atmosphere models, we limit ourselves to the three signal parameters $\boldsymbol{\theta}_S = \{I, T, N_H\}$, which are the intensity and surface temperature of the NS in [ergs/cm^2/s] and [keV], respectively, along with the integrated hydrogen column density N_H in [atoms/cm^2]. That is, we assume a blackbody spectrum $dN/dE \sim E^2/(e^{E/T} - 1)$ with the hydrogen absorption model presented in [269]. Deviations from pure thermal spectra have been observed in the XDINSs, however, and we study this further in Sec. 6.3.2.

Hard Spectral Analysis

In the high-energy analyses we assume that the background is Poisson distributed with a flux $\{B_i\}$ in each energy bin. Assuming the source has source fluxes $\{S_i\}$, the expected

number of counts in R_B in energy bin i is $\mu_{B,i} = \sum_{p\in R_B} w_i^p B_i + \chi_{B,i} w_i^q S_i$, where q is the pixel at the source location. We compare this to the number of counts in R_B, which we denote $c_{B,i} = \sum_{p\in R_B} c_i^p$. Note that we present the explicit numbers of counts in App. E.2.

We then expect that the counts in R_S is similarly $\mu_{S,i} = \sum_{p\in R_S} w_i^p B_i + \chi_{S,i} w_i^q S_i$, where again the former is the background contribution and the latter is the signal contribution. Letting the number of counts in the signal region be $c_{S,i} = \sum_{p\in R_S} c_i^p$ leads to the joint Poisson likelihood over both R_S and R_B:

$$\mathcal{L}_{i,\text{hard}}(\{c_{S,i}, c_{B,i}\}|S_i, B_i) = \frac{(\mu_{S,i})^{c_{S,i}} e^{-\mu_{S,i}}}{c_{S,i}!} \times \frac{(\mu_{B,i})^{c_{B,i}} e^{-\mu_{B,i}}}{c_{B,i}!} \,. \tag{6.5}$$

In each energy bin, we construct the profile likelihood over the signal flux S_i treating the background flux B_i as a nuisance parameter, leading to

$$\mathcal{L}_{i,\text{hard}}(\{c_{S,i}, c_{B,i}\}|S_i) = \max_{B_i} \mathcal{L}_{i,\text{hard}}(d|S_i, B_i) \,. \tag{6.6}$$

The best-fit flux in energy bin i, which we denote by $\hat{S}_i$, is then given by the value of S_i that maximizes the profile likelihood.

6.1.4 Statistical analysis

We determine the confidence intervals on the fluxes in the individual energy bins using the test statistic (TS)

$$q_{i,\text{hard}}(S_i) = 2 \times \Big[\log \mathcal{L}_{i,\text{hard}}(\{c_{S,i}, c_{B,i}\}|\hat{S}_i) - \log \mathcal{L}_{i,\text{hard}}(\{c_{S,i}, c_{B,i}\}|S_i)\Big] \,. \tag{6.7}$$

The 1σ frequentist confidence interval for the flux is asymptotically given by the range of S_i in which the q is within one of its minimum (see, *e.g.*, [109]). Note that for consistency we must consider negative S_i values. To more accurately compute the confidence intervals we must compute the distribution of TSs from Monte Carlo, given that the number of counts may be small for some observations so that we are not in the asymptotic limit.

Away from the asymptotic limit, we wish to determine the $n\sigma$ confidence interval for a parameter of interest S with best-fit parameter $\hat{S}$. The confidence interval is defined as the range of values below the $n\sigma$ upper limit S_{+n} and above the $n\sigma$ lower limit S_{-n}. The upper limit S_{+n} is defined by the maximum value of the parameter such that simulated data

generated by the model with that parameter would satisfy the condition $P(\hat{S}' \geq \hat{S}) = \Phi(n)$, where $\hat{S}'$ denotes the best-fit values from the simulated data, Φ is the cumulative distribution function of the normal distribution, and $P(\hat{S}' \geq \hat{S})$ is the probability that $\hat{S}' \geq \hat{S}$. The lower limit S_{-n} is defined similarly.

We apply this frequentist confidence interval procedure to our data in the following way. Given our data, we maximize the likelihood profile, which is profiled over nuisance parameters $\boldsymbol{\theta}$, to determine $\hat{S}$.

To determine the upper limit, we first consider a particular value $S' \geq \hat{S}$ and maximize our likelihood at this fixed S' to find the best-fit nuisance parameters $\hat{\boldsymbol{\theta}}'$. We then generate many Monte Carlo realizations of the data under the model defined by S' and $\hat{\boldsymbol{\theta}}'$. From the simulated data we determine the distribution of the best-fit $\hat{S}'$. In this way, we are able to determine the percentile of the observed best-fit $\hat{S}$ (from the actual data) in the distribution of $\hat{S}'$ generated under $\{S', \hat{\boldsymbol{\theta}}'\}$ and ultimately determine $\hat{S}_{+n}$. An analogous procedure using $S' \leq \hat{S}$ enables the determination of $\hat{S}_{-n}$. In practice we find that this procedure reproduces the asymptotic expectation except in a few specific cases, such as those with *Chandra* data, where the number of counts is low.

In addition to determining the fluxes in the individual energy bins, we also fit power-law spectral models across energy bins. As will be described more later, these models have parameters of interest I and n, where I denotes an intensity over the full energy range and n is the spectral index. The parameters I and n may be constrained in the frequentist way by constructing the joint likelihood over the relevant energy bins and datasets. The confidence intervals on these parameters are determined using the Monte Carlo method described above, which matches the asymptotic expectation in most, though not all, cases.

When fitting the spectral models we are also interested in the evidence for the non-trivial spectral model over the null hypothesis of no hard X-ray flux from the source. To quantify the statistical significance of the model (*i.e.*, the evidence) we need to define a TS for discovery:

$$\mathrm{TS} = 2 \times \left[\log \mathcal{L}_{\mathrm{hard}}(d|\hat{I}) - \log \mathcal{L}_{i,\mathrm{hard}}(d|\mathbf{0}) \right] , \tag{6.8}$$

unless the best-fit intensity $\hat{I} < 0$ in which case $\mathrm{TS} = 0$. Note that $\mathbf{0}$ denotes the null hypothesis $I = 0$ and $\mathcal{L}_{\mathrm{hard}}(d|\hat{I})$ is the profile likelihood for the intensity over all energy bins, with the index n also profiled over, evaluated at the best-fit intensity (*i.e.*, the maximum log-likelihood for the signal hypothesis). Here d denotes the combination of datasets under consideration. In the asymptotic limit the TS may be straightforwardly interpreted in terms of significance, considering that our signal model has two model parameters of interest

(see [109]). However, as we are often away from the asymptotic limit we determine the significance directly through Monte Carlo. To do so, we first determine the best-fit null model, and then we generate Monte Carlo data from the null model parameters. We calculate the distribution of the TS on that Monte Carlo data using (6.8). The fraction of TSs generated under Monte Carlo which exceed the TS evaluated on the observed data defines a p-value with standard interpretation in terms of detection significance. Again, we find that in most (but not all) fits the recovered p-value matches the asymptotic expectation.

6.1.5 Point Source Detection

As a systematic test we consider the effect that nearby point sources might have on the recovered spectra for our sources of interest. Point sources within the signal or background extraction regions of the PN and MOS data could potentially bias our determinations of the source spectra. While in principle point sources could also be an issue for *Chandra* observations, the superior angular resolution of that detector means that the issue is much more important for *XMM*. We search for sources by first constructing a high-density (RA, Dec) grid within the vicinity of the source and background regions. At each (RA, Dec) point we determine a signal and background region as we do for our source of interest. We identify point sources by calculating a TS at each grid point for excess counts. Because point sources are expected to appear across a range of energies, we sum the counts maps over the 2-8 keV range. The point source discovery TS is defined analogously to (6.8). We join the PN and MOS TSs together to form a joint test statistic at each (RA, Dec) point. We identify point sources at those locations where the joint test statistics is greater than or equal to nine and the TS is the maximum TS on a region with an angular extent of the 50% of the 90% EEF radius. We then construct a point source mask by masking out regions with radius 50% of the 90% EEF radius centered at any location where a point source was identified. Later we demonstrate that the impact of masking point sources on the recovered spectra is relatively minor.

6.2 Hard X-ray excess in RX J1856.6-3754

In this section we show results for the NS RX J1856.6-3754, for which the hard X-ray excess is detected with the greatest significance. Note that departures from a thermal model have previously been observed around 1 keV [270]; here, we focus on the 2-8 keV range. In Fig. 6.1, we show the background-subtracted X-ray spectrum dF/dE over the energy range from 0.5 to 8 keV for PN, MOS, and *Chandra*. More precisely, what is shown is the observed number

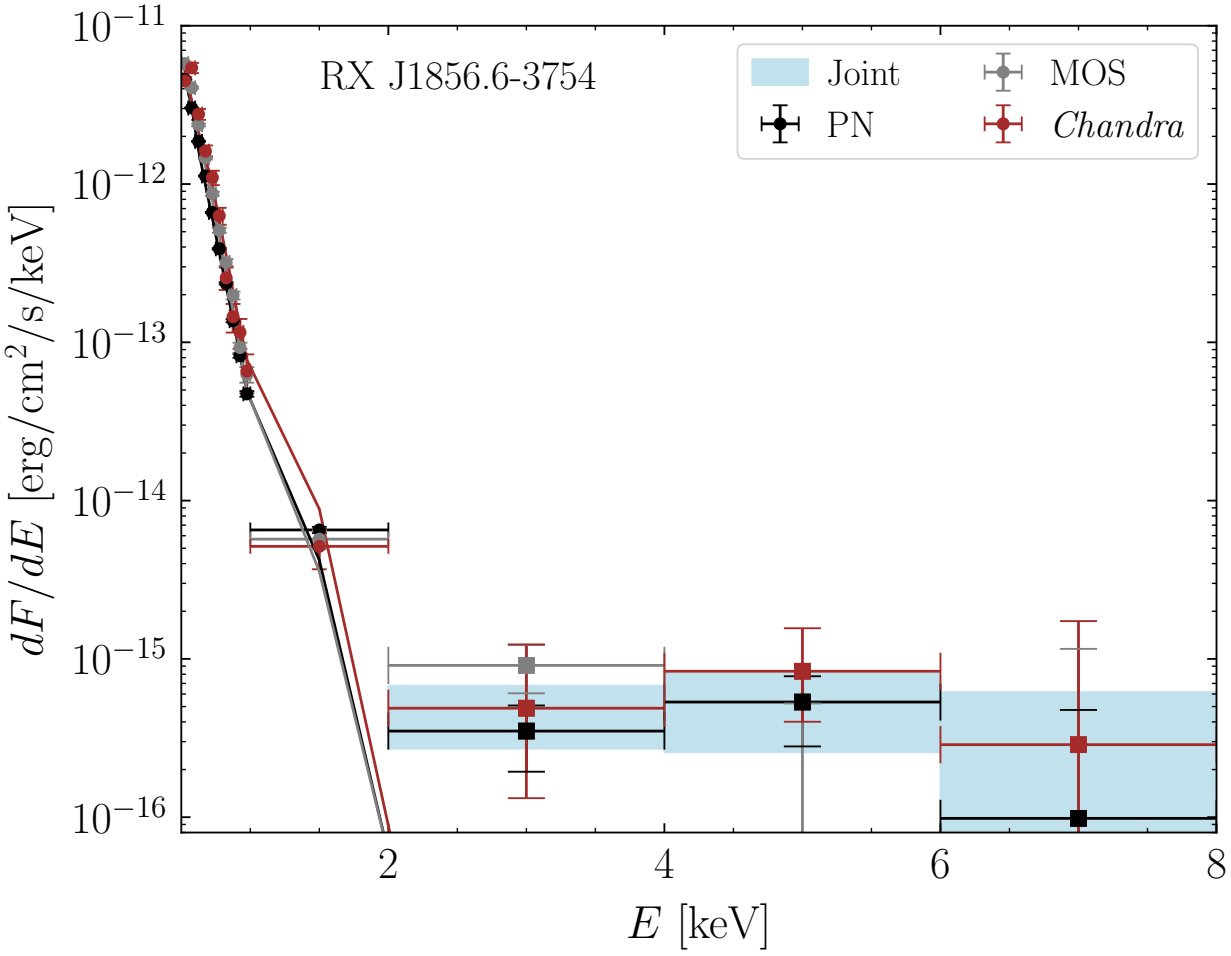

Figure 6.1: The background-subtracted X-ray spectrum of RX J1856.6-3754 for each of the three cameras individually and combined. The data points were constructed by stacking all available exposures from the source, with best-fit spectral points and associated 68% confidence intervals indicated. In all three cameras there is a clear and consistent excess above the background in the hard X-ray range of 2 keV to 8 keV, and because of the complementary strengths of the individual cameras we believe this excess is robust. The solid curves denote the best-fit thermal spectra with hydrogen absorption fit from 0.5 keV to 1 keV, and as can be seen the extrapolations of these spectra to the hard energy range does not account for the observed excess.

of counts per second in each energy channel divided by the diagonal entry on the forward modeling matrix that gives the effective area at that energy. This subtlety is important below ∼1 keV, because at these energies the observed thermal spectrum is significantly affected by the energy resolution of the detector. For this reason, it is not correct to interpret Fig. 6.1 as a plot of the true flux, since that would require inverting the forward modeling matrix which is very much not diagonal at the low energies. On the other hand, we are primarily

interested in energies above 2 keV, and at these energies with our energy binning the forward modeling matrix is effectively diagonal, so that Fig. 6.1 is effectively a plot of the true flux at these energies.

We also emphasize that these data points arise from joining all of the exposures from the individual cameras together into one single counts map per camera. This is important because, as discussed more later in this chapter, the individual exposures do not have high enough statistics to detect the hard X-ray excess. To construct this spectrum we used 40 observations for a total of 1.0 Ms of exposure for PN, 18 for a total of 0.69 Ms for MOS, and 9 for a total of 0.23 Ms for *Chandra*. We fit a thermal model, including the effect of hydrogen absorption at low energies, to the spectrum from 0.5 to 1 keV. We find best-fit temperatures $T = 71.1 \pm 0.2$ eV ($T = 66.2 \pm 0.3$ eV) ($T = 67.8 \pm 0.9$ eV) for PN (MOS) (*Chandra*). We note that these uncertainties are statistical only and do not capture possible systematic discrepancies in the true spectrum from thermal, in possible variations of the surface temperature over time, or in systematic uncertainties in the detector response. For all cameras we use the forward modeling matrices, constructed for each individual exposure, that account for both the effective area and the distribution of true flux to observed flux between energy channels in the low-energy analyses. However, only the PN forward modeling matrix includes the effect of pileup. We do not investigate the surface temperature uncertainties in more detail because it is not the main focus of this chapter. Rather, as we illustrate in Fig. 6.1, the thermal distribution, whose best-fit background-subtracted spectra are shown as solid curves, is able to account for the emission seen at and below $\sim$2 keV but is not able to account for the high-energy emission above 2 keV. We will show later on that this statement remains true even for more complicated NS atmosphere models.

Below, we provide more detail for the spectral characterization of the high-energy flux and systematic tests that investigate the robustness of the signal.

6.2.1 Spectral characterization of the RX J1856.6-3754 hard X-ray emission

We fit a power-law model $dF/dE \propto E^n$ to the data to measure both the intensity of the signal and the hardness of the signal as indicated by the spectral index n. We quantify the intensity through $I_{2-8} = \int_{2\text{ keV}}^{8\text{ keV}} dE\, dF/dE$ in units of erg/cm^2/s.[1] The statistical procedure that we use for constraining I_{2-8} and n is outlined in Sec. F.3.

The results of the spectral fits for the three different cameras are given in Table 6.1.

[1]Note that later in this chapter we will consider, for some NSs, only the energy range 4-8 keV. In these cases we will quote $I_{4-8} = \int_{4\text{ keV}}^{8\text{ keV}} dE\, dF/dE$.

Interestingly, all three cameras give consistent flux measurements for I_{2-8}, and moreover

camera	I_{2-8} [10^{-15} erg/cm^2/s]	n	σ
PN	$2.1^{+0.9}_{-0.9}$	$-0.03^{+0.89}_{-1.1}$	3.0
MOS	$1.4^{+1.1}_{-0.7}$	< -0.93	2.9
Chandra	$3.8^{+2.6}_{-1.8}$	$-0.28^{+1.71}_{-1.89}$	3.4
Joint	$1.53^{+.70}_{-.63}$	$-0.28^{+0.65}_{-0.75}$	4.6

Table 6.1: Our best-fit results for the 2-8 keV flux I_{2-8} and spectral index n assuming a power-law spectrum for the hard X-ray excess in RX J1856.6-3754. The fluxes and spectral indices are consistent between cameras, although the latter is not well constrained. We also show the results from the joint-likelihood analysis over all cameras. For the fit to the MOS data, we are only able to place upper limits on the power-law index and report the 84$^{\text{th}}$ percentile upper limit.

for PN and *Chandra* the detection is at high statistical significance. The computations of statistical significance are summarized in Sec. F.3. The consistency between the three cameras is important because each has its own strengths and weaknesses. The fact that the high-energy signal is detected in each camera thus gives confidence that the high-energy signal is real and arises from the NS itself.

The spectral index n is not well constrained by any of the individual cameras, which is perhaps not too surprising given the modest significance of the detections and the fact that we only have three independent energy bins to constrain the power-law. However, combining the results from all three cameras we find the relatively hard energy index $n = -0.28^{+0.65}_{-0.75}$. This index suggests that the emission is not the high-energy tail of the thermal surface emission, which should have a soft spectrum in this energy range.

6.2.2 Systematic tests for the RX J1856.6-3754 hard X-ray excess

The hard X-ray excess, suggesting non-thermal[2] X-ray emission from RX J1856.6-3754, is detected at high statistical significance with PN and *Chandra* and at marginal significance with MOS. However, each of these instruments is subject to systematic uncertainties, which we now examine in more detail.

Test statistic maps and nearby point sources

One of the central differences between the *Chandra* and *XMM* detectors is the significantly better angular resolution of *Chandra* as compared to *XMM*. This is important because it is

[2]More appropriately, if the spectrum is thermal then the temperature would need to be significantly higher than the NS surface temperature.

possible that the observed hard X-ray excess arises not from RX J1856.6-3754 but rather from a nearby source that is unrelated to RX J1856.6-3754 but happens to be at a similar angular position on the sky. Relatedly, it is also possible that the hard X-ray excess is the result of misinterpreting the background statistics. That is, if a significant fraction of the background flux arises from relatively bright point sources, then the assumption that we may use the observed number of counts in the background region to infer the mean number of background counts in the signal region, with the probability distribution then being Poisson distributed about this mean, could break down. It is reassuring that, for these reasons, we observe the excess both with *Chandra* and *XMM*. Still, it is worth investigating visually and quantitatively the *XMM* counts maps to make sure that they do not show significant nearby point source emission or other sources of emission that would violate our assumptions.

In Fig. 6.2 we show pixel-by-pixel χ^2 maps, with down-binned pixels, within the vicinity of the NS, which is located at RA_0 and Dec_0. The χ^2 value in pixel i is defined by $S_\chi^{-1}\left(S_p(O_i|E_i)\right)$, where E_i is the expected number of counts, O_i is the observed number of counts, S_p is the Poisson-distribution survival function, and S_χ^{-1} is the inverse survival function for the chi-square distribution with one degree of freedom. We have down-binned the maps for visualization purposes. This figure uses the sum of the counts from 2-8 keV. The background flux level is estimated from the background region, which is the region between the outer dashed circle and the inner solid circle. As a reminder, the actual pixel sizes that we use are significantly smaller than indicated for both *XMM* and *Chandra*. The predicted background flux level elsewhere in the map is calculated by assuming that the background flux is simply proportional to the exposure template (without accounting for vignetting), as would be expected if the background is predominantly from particle background. Accounting for vignetting, as would be the case if the background was dominantly from astrophysical X-rays, leads to virtually indistinguishable results since all source observations were on-axis. In a given pixel we may then compute the expected number of background counts. The higher the χ^2 value, the more likely that the photon flux within that pixel arose from source emission and not a statistical fluctuation of the background – explicitly, the p-value is given by $S_\chi(\chi^2)$, where S_χ is the survival function for the chi-square distribution with one degree of freedom.

In the right panel of Fig. 6.2, which shows the results for the *Chandra* observations, it is clearly seen that there is a significant excess of X-ray counts over the background in the central pixel within the extraction region, which is the inner circle. In this case, the extraction region is approximately $1.1''$ in radius, while the outer circle of the background region is approximately $11.5''$ in radius. The *Chandra* image strongly suggests that there is indeed excess hard X-ray flux arising from this NS between 2-8 keV. On the other hand,

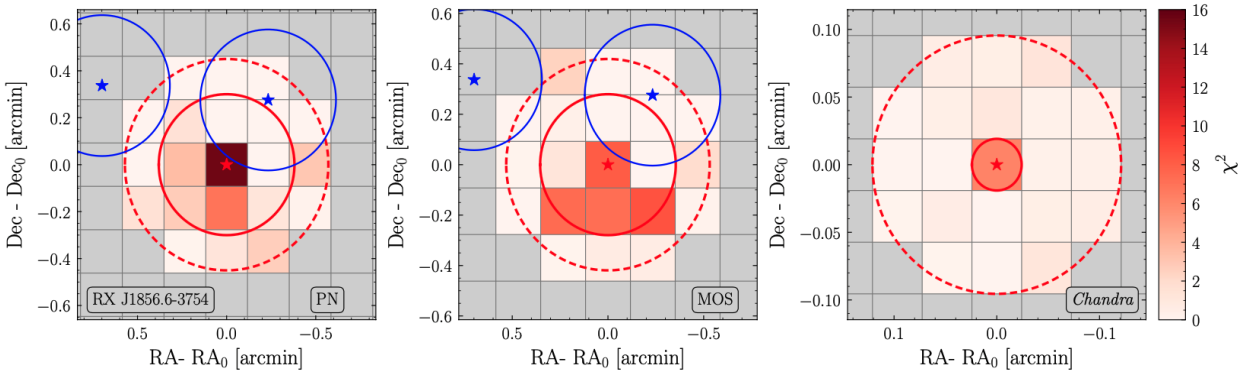

Figure 6.2: χ^2 maps (summed over 2-8 keV and all exposures) for each camera centered around the location of RX J1856.6-3754. In each case, the inner red ring denotes the radius within which the source data is extracted. The background data is extracted from the annulus between the inner and outer red rings. The maps are presented down-binned for presentation purposes only. Blue rings, where present, indicate the location of point sources identified in a joint analysis of PN and MOS data with a local TS greater than 9. Masking the identified point sources has little effect on the spectrum. Pixels that do not reside within signal or background extraction regions are displayed in grey. (*Left*) The PN data shows a significant excess in the signal region. Due to the large *XMM* PSF it is not confined to a single full-resolution pixel and is only apparent after down-binning. (*Center*) The MOS data shows a less clear excess as compared to the PN data. (*Right*) The *Chandra* data shows a central pixel excess with no other clear point sources visible in the background region appearing with approximately 3σ significance. Note that the axis scale for *Chandra* is much smaller than for the *XMM* cameras due to *Chandra*'s improved PSF: in fact, the entire *Chandra* map would fit within the *XMM* source regions.

the *Chandra* images are the most subject to pileup. As we show shortly, however, we do not believe that pileup is responsible for the *Chandra* results. It is useful, though, to examine the image for PN, which is less subject to pileup and also shows a significant excess, but has much worse angular resolution. The corresponding image for the PN data is given in the left panel. Note that in this case the source extraction region (inner circle) has a radius of $18.0''$ while the background region has an outer radius of $27.0''$. In this case, a visual excess is still observable within the signal region, as compared to the background region, which is the region between the two circles, and a less prominent excess can also be seen in the MOS image in the central panel.

Validating PN and MOS background extraction regions

Due to the comparatively worse angular resolution of the PN and MOS instruments, the signal and background extraction regions used in the analysis of PN and MOS data are

necessarily larger in angular extent than in the corresponding *Chandra* analyses. Our treatment of the background count rate, which assumes a uniform particle background resulting in a pixel-by-pixel count rate which depends only on the total exposure in each pixel, may be violated by the presence of point sources.[3] In order to validate our assumptions for the MOS and PN data, we perform a goodness-of-fit test on the pixelated counts data for both instruments.

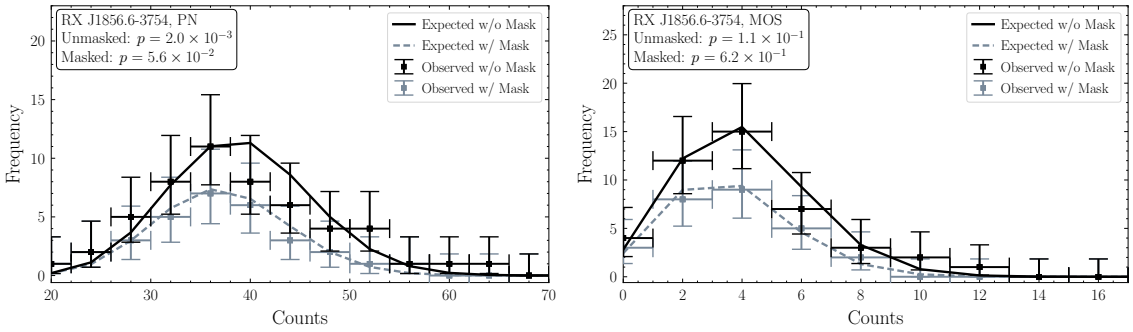

Figure 6.3: A comparison of the observed distributions of counts in the background regions summed over energies from 2 to 8 keV with the expected counts distribution under the best-fit uniform background model for PN (*left*) and MOS (*right*). Fitted distributions and observed counts are shown both with and without the application of a point source mask, and p-values are indicated.

In our goodness-of-fit test, we sum over energies to obtain the set $\{c^p\}$ of total counts over energies 2-8 keV at the p^{th} pixel in the background extraction region. Likewise, we obtain the total exposure map summed over energies 2-8 keV at each pixel, denoted $\{w^p\}$. Assuming a uniform Poisson rate for events in the background region, the best-fit expected mean number of counts in the p^{th} pixel is λw^p, with $\lambda = (\sum_p c^p)/(\sum_p w^p)$. We compute a likelihood value for the data assuming the best-fit parameter λ by

$$\mathcal{L}(\lambda|\{c^p\}) = \prod_p \frac{(\lambda w^p)^{c^p} e^{\lambda w^p}}{c^p!} \,. \tag{6.9}$$

We can then determine the p-value for the observed data by generating Monte Carlo data under the assumed background rate λ, then determining the fraction of likelihood values in the Monte Carlo ensemble which are less than the likelihood as evaluated on the observed data. This fraction then represents a p-value, where smaller values indicate a worse goodness of fit of the data under the fitted model. We emphasize that this Monte Carlo test is

[3] Later we attempt to mitigate this possibility with point source identification and masking and show that it has a minimal effect on the spectrum.

performed on the pixelated data directly, with the joint likelihood over pixels as given in (6.9), and not on the higher-level photon-count histogram data shown in *e.g.* Fig. 6.4.

In Fig. 6.3, we compare the observed and fitted counts distributions for PN and MOS data with and without the application of a point source mask, with associated p-values indicated. Note that for this test we use the high-resolution pixels and not the down-binned pixels. Some tension between the data and the fitted background is observed in the PN data without the point source mask[4]. The tension is at the $\sim 3.9\sigma$ level, although this falls to the marginal $\sim 1.9\sigma$ level after the application of the point source mask. The MOS data shows good consistency with the fitted background model both before and after the application of the mask. As we will subsequently show, the reconstructed fluxes in PN and MOS are robust with respect to the applied mask. In particular, because the excess appears in the PN data before the application of the mask, the exclusion of high count pixels from the background extraction region will only serve to increase the reconstructed intensity and associated significance of the fit to the signal model.

Systematic tests of the *XMM* *X*-ray spectrum

We test the robustness of the observed hard X-ray excesses in *XMM* data for RX J1856.6-3754 by systematically varying our analysis procedure. The results of the different analyses are shown in Fig. 6.4. In the top left panel we show our fiducial recovered spectrum for PN, MOS, and *Chandra*, along with the joint spectrum from combining all three datasets (68% confidence intervals indicated). We also indicate the p-values for the background-only fits in the background regions for the PN and MOS datasets. The other five panels consider various systematic analysis variations, which in principle should all return consistent spectra if large systematic uncertainties are not present. Indeed, we find that this is the case. In the top row middle column we change the assumption that the background is dominantly particle background to the assumption that the background is dominantly astrophysical. The difference between the two is that for the astrophysical background we include the vignetting correction. This is seen to make a minimal difference, which arises from the fact that the vignetting correction is small over our region of interest.

The top right panel of Fig. 6.4 investigates the spectrum when the point source mask is included. The spectral points move up slightly, as expected since we are masking high-flux background pixels, but the spectra are broadly consistent with the unmasked versions. Note that the background p-values improve greatly relative to the unmasked case, as previously

[4]We formally define a relation between p-values and equivalent significance as measured in standard deviations by $Z = \Phi^{-1}(1-p)$ where Φ^{-1} is the inverse of the standard normal cumulative distribution function. This does not assume statistics following an underlying standard normal distribution and merely serves the purpose of enabling easy qualitative comparison of significances.

noted. In the bottom left panel we increase the radius of the background region to 1.5 times the EEF radius. The background p-values decrease, suggesting that our recovered spectra are more susceptible to systematic biases in this case, but again the spectra become slightly larger relative to our fiducial case. Masking point sources with the large background region, as shown in the middle lower panel, increases the p-values but at the same time leads to a similar spectrum as in the unmasked case. Lastly, in the bottom right panel we consider an alternative analysis approach where we allow the background model to vary linearly in the RA and Dec directions. That is, our background model in this case has three nuisance parameters instead of one. We profile over these nuisance parameters when determining the recovered spectra. Note that we apply this analysis to the large-background region and with the point source mask. As expected, given the additional model parameters, the p-values improve relative to the case where the background model only has a single nuisance parameter. In this case the spectra becomes even larger relative to our fiducial analysis, though still consistent within uncertainties.

Note that we do not show the results of these tests on *Chandra* data since *e.g.* point sources are less of a concern in this case, though we have still checked that similar systematic analysis variations return consistent results in that case as well.

Flaring

The *XMM* satellite is subject to periods of considerable soft proton (SP) flaring when the count rate increases. Although we filter out periods of strong SP flaring, there is still residual flaring in the remaining data that can potentially affect the results. In the left panel of Fig. 6.5, we plot I_{2-8} in individual exposures against the count rate in the source region during the times excised from the data due to flaring concerns. There is no trend in the data that would indicate that the observed excess is due to SP flaring. Note that it is well known that the PN flares can be more intense than the MOS flares.

Pileup

Pileup of low-energy X-rays may generate spurious high-energy signatures if not accounted for. Pileup refers to the phenomenon in a CCD detector in which more than one photon arrives in a single frame time in the same region. The detector cannot distinguish the events and reconstructs them as a single event with energy approximately the sum of the individual photon energies. There are two major effects on a spectrum associated with pileup: event loss and spectral hardening. The former occurs for multiple reasons: first, a multiphoton event is detected as a single photon; second, the event energy may exceed the on-board

energy threshold and be rejected; third, the deposited charge-cloud shape (known as grade for *Chandra* or as pattern for *XMM*) may become inconsistent with an X-ray photon. The spectral hardening occurs because there is a loss of low-energy events along with an increase in high-energy events. Although the amount of pileup in all of the observations analyzed in this chapter is relatively low, the observed tail is potentially susceptible to influence from pileup. For this reason it is necessary to verify that the hard X-ray excess is not due to pileup, and also to verify that if a hard X-ray excess is present its observed features would not be biased by pileup effects.

The amount of pileup directly depends on the count rate—the number of photons per CCD readout frame per image region. If the hard X-ray tail is due to pileup effects, we expect to see an increase in the count rate of hard source photons with increased total count rates as we vary over exposures. In the right panel of Fig. 6.5, we plot I_{2-8} against the count rate in the central pixel from 0-2 keV for individual exposures. The wide variance in count rates is due primarily to the fact that the three different cameras have different frame times: PN ∼tens of milliseconds, MOS ∼1 second, and *Chandra* 3.2 s, depending on the observation submode. PN does have a higher effective area than the other two cameras, which somewhat increases the count rate. However, the *XMM* cameras have a much larger PSF-to-pixel-size ratio than *Chandra*, which further reduces the *XMM* count rate. For these reasons, PN is expected to be least affected by pileup while *Chandra* is the most affected. In Fig. 6.5, the *Chandra* count rates are similar to MOS because the *Chandra* exposures are in a mode that reduces the frame time. For the other NSs, *Chandra* is in the 3.2 s frame time mode and the count rates are higher than for the *XMM* exposures. In any case, we observe no significant correlation between the count rate and the reconstructed I_{2-8} in individual exposures, suggesting that pileup does not strongly influence our results for RX J1856.6-3754.

As mentioned above, we are able to generate a forward modeling matrix including pileup for the PN observations, which are also the ones that should be least affected by pileup, and we find, as seen in Fig. 6.1, that pileup is not responsible for the observed excess from 2-8 keV. On the other hand, MOS and *Chandra* are expected to be more affected by pileup than PN. Later in this section we show results for *Chandra* simulations that include the effect of pileup, and in this case we also find that pileup of the thermal spectrum is not able to generate the observed excess. Since MOS is expected to be less affected by pileup than *Chandra*, we believe that the MOS high-energy spectrum is also likely not due to pileup effects. To that end, we have used the results of [23], which provides a method to estimate pileup in the *XMM* cameras. The results, presented in Tab. E.2, support the claim that pileup is unlikely to explain the observed hard X-ray flux in RX J1856.6-3754 for both MOS

and PN.

Surface Temperature

We now investigate whether the observed excess is related to spectral variability of the surface emission of RX J1856.6-3754. Note that previous studies have found no or small variability in RX J1856.6-3754 [271]. In the bottom panel of Fig. 6.5, we plot I_{2-8} in individual exposures against the surface temperature of the NS found in that observation. To obtain the surface temperature, we fit the 0.3-2 keV data from individual observations in XSPEC [272] with an absorbed thermal model with an additional 1.5% systematic included to account for instrumental systematics such as detector location. We see no indication of a correlation between the surface temperature and the hard X-ray excess. Note that when comparing fluxes between MOS and PN, there is an additional $\sim 3\%$ systematic uncertainty in the 0.5-1 keV range, coming from cross-calibration uncertainties [273]. Note that this systematic is energy-dependent and varies between ~ 1 and 5% over that range, and thus the systematic uncertainty on the temperatures themselves is likely larger.

Chandra pileup simulation

To assess the effect of pileup on the high-energy excess observed for RX J1856.6-3754 in *Chandra*, we perform MARX simulations [267] for each observation of this source, under two assumptions for the underlying spectrum of the source. Our MARX simulation procedure is described in Sec. 6.1.2. In both cases, we use the best-fit thermal spectrum at low energies, but in one case we also include a constant spectrum $dF/dE = 10^{-15}$ erg/cm^2/s/keV. In order to separate systematic effects that may be due to pileup from statistical fluctuations, we artificially increase the exposure time to 10 Ms. We then pass the simulated data through the same analysis pipeline used on the real data.

It is important to clarify the limitations of the MARX software with regards to simulating pileup effects on a hard X-ray tail. MARX implements the John Davis pileup model [274], a probabilistic model which uses Poisson statistics to describe the probability that pileup occurs in a given frame and the probability that in the event of pileup, the piled event will be registered as an X-ray photon (due either to energy or grade migration). However, these probabilities are generally difficult to estimate due to the fact that many high-grade events are thrown out in-flight and the lack of a detailed photon-silicon interaction model. The latter probability, in particular, is entirely uncalibrated.

It is unlikely that the statistical model used here can describe the data at the accuracy level required to definitively conclude that the observed hard tail is not due to pileup. Fur-

thermore, due to these limitations, the MARX software does not assess pileup involving background photons, which could more significantly boost the event energies than the soft thermal photons. Nevertheless, the MARX simulations estimates the basic effects of pileup on the NS spectrum.

The results of these simulations are shown in Fig. 6.6. In that figure we show the spectrum measured in the real data, from 2-8 keV, in grey. The red data points show the spectrum that we extract from the simulation that includes the high-energy tail. The simulated spectrum in this case is shown as the solid red curve. We emphasize that this simulation includes the effects of pileup. The recovered spectrum is able to accurately describe the true underlying spectrum, which gives confidence that pileup does not affect our ability to measure a high-energy excess for this NS. As a second cross-check, we also perform a simulation without the high-energy tail. In this case, the recovered spectrum is shown by the blue data points. This clearly shows that an artificial high-energy tail is not generated by pileup, at least as modeled by the MARX simulation framework.

In Sec. 6.3.1 we show results of the same tests on the remaining *Chandra* XDINSs observations, and we find that for some NSs the effects of pileup are much more pronounced.

Variability

It is possible that the hard X-ray signal is strongly variable in time, which would constrain the possible production mechanisms for the excess. In order to search for signs of strong variability, we analyze the individual exposure images independently, instead of working with the combined image. We stress that this search will be most sensitive to variations on timescales of years; since both instruments were launched in 1999, our data is taken over nearly 20 years. We leave searches for variability on the timescale of the NS period, which is difficult due to the low number of signal counts, to future work. In the left panel of Fig. 6.7 we show the I_{2-8} recovered from the individual exposures versus time for PN and MOS, with the analogous result for *Chandra* shown in the right panel. In the *Chandra* case, the uncertainties are strongly one-sided because the number of signal and background counts tends to be quite low and often zero.

As before, we determine the I_{2-8} intensities by fitting the 2-8 keV spectra to a power-law. The bands in Fig. 6.7 show the best-fit intensities from the analyses on the joint images over all exposures. In the PN and *Chandra* data, we do not observe any individual exposures with a reconstructed intensity in tension with that found in the joint image analysis. We do observe that one significant intensity deficit appears in a MOS exposure at modest global significance, although this could be due to systematic effects in that particular MOS exposure such as pileup. In this exposure, we find a soft 2-8 keV spectrum in the signal region with

a typical (among other MOS exposures) spectrum in the background region. This might be expected if pileup heavily affects the observation, where in the signal region the counts are suppressed at high energies by energy or grade migration while the background region is unaffected. In fact, inspection of the `epatplot` results suggest that pileup affected the 0-2 keV spectrum of the observation, but there were not enough counts above 2 keV to make a definitive determination on whether pileup affected the hard spectrum. Overall, the evidence does not suggest that the hard X-ray excess in RX J1856.6-3754 is highly variable.

6.3 Search for hard X-ray excesses in the XDINSs

In Sec. 6.2, we analyzed in detail the hard X-ray excess in RX J1856.6-3754. We found evidence for such an excess in *Chandra* and PN data and a hint for the excess also in MOS data. In this section we investigate to what extent similar excesses exist in the rest of the XDINSs. However, it should be noted that RX J1856.6-3754 is special in that it has, by far, the most exposure time across all of the X-ray cameras that we consider. The total exposure times that we use for each of the XDINS are shown in Fig. 6.8. Note that *Chandra* data is available for RX J1308.6+2127, RX J0720.4-3125, and RX J1605.3+3249, but as we show in the next subsection we believe that these observations are too severely affected by pileup to reliably make a statement about the presence of a hard X-ray excess. On the other hand, we show that none of the PN observations should be limited by pileup. For MOS, the situation is less clear, as no pileup simulation framework is readily available and, while these observations should be less subject to pileup than *Chandra*, they should be more affected by pileup than the PN observations. To estimate the level of pileup in MOS, we use the results of [23], which also applies to PN. The results for each of the XDINSs are shown in App. E.1. We find that pileup is unlikely to explain the observed hard X-ray excesses in any case.

6.3.1 *Chandra* pileup simulations

In Sec. 6.2.2, we showed that pileup likely does not affect the high-energy tail observed for RX J1856.6-3754 with *Chandra* data. In this section we repeat this exercise for the other XDINSs which have *Chandra* observations. To perform these simulations, we first fit the thermal model to the low-energy data (0.5-1 keV). We then generate simulated datasets using this thermal spectrum, as in Sec. 6.2.2, that do and do not include a possible high-energy tail. As for RX J1856.6-3754, we model the high-energy tail as $dF/dE = 10^{-15}$ erg/cm^2/s/keV over all energies.

In Fig. 6.9 we show the results of the pileup simulations for RX J0806.4-4123 and RX

J0420.0-5022. As in Sec. 6.2.2, we artificially increase the exposure time in the simulations to 10 Ms. The NS RX J0420.0-5022, which is shown in the right panel, is the NS with the lowest 0.5-1 keV flux of all the XDINSs. This NS is, correspondingly, the least affected by pileup. The pileup simulation shows clearly that when no high-energy tail is included (blue), then no high-energy flux is recovered, and when the high-energy tail is included (red), the correct flux is recovered. The same is also true in the left panel for RX J0806.4-4123, though pileup does have a small effect on the flux in the 2-4 keV energy bin. As we discuss more later, this energy bin is excluded from the analysis for this NS because of concerns about contamination from thermal surface emission.

The simulations shown in Fig. 6.9 should be contrasted with those in Fig. 6.10, which show simulation results for the NS RX J0720.4-3125. This NS is significantly affected by pileup. Pileup generates an artificial, though rather soft, high-energy spectrum in the scenario where the true spectrum has no high-energy tail. When the high-energy tail is present in the simulation, pileup actually suppresses the flux in the energy bin from 6-8 keV. This likely arises from low-energy photons hitting the CCD in coincidence with true high-energy photons and then those photon pairs being rejected. For this reason, we are unable to use the RX J0720.4-3125 *Chandra* data for a high-energy search. The situation for RX J1308.6+2127 and RX J1605.3+3249 is similar, and so out of caution we do not analyze the *Chandra* data from any of these NSs.

6.3.2 NS surface modeling

In our fiducial analyses we assume that the 0-2 keV NS spectra are blackbody in order to verify that its extrapolation does not produce the observed 2-8 keV excesses. However, at least some of the XDINSs likely have a thin ($\sim$1 cm) atmosphere, leading to a modified spectrum (for a comprehensive review, see [275] or [276]). The surface composition is unknown, although due to the high surface gravity a hydrogen atmosphere is expected if hydrogen is present on the surface, usually due to accretion at formation. Moreover, the strong surface magnetic field significantly complicates the spectrum. The atomic binding energies increase and cause the absorption lines observed in some of the XDINSs. For the XDINSs' surface temperatures, hydrogen is expected to be partially ionized. Additionally, photons propagate preferentially along the field lines. Finally, the field will induce temperature inhomogeneities across the NS surface by suppressing the thermal conductivity perpendicular to the field. In general, the NS atmosphere can significantly harden the spectrum [277].

If no accretion occurred after the NS formation, a heavy element atmosphere or bare surface may exist instead. This may be the case for RX J1856.6-3754 and possibly RX

J0720.4-3125 and RX J1308.6+2127 [275], in which case a condensed iron surface model is appropriate. These models predict a blackbody-like spectrum with most of the deviations at low energies, and thus the hard X-ray spectrum is similar to the blackbody extrapolation. This is also the case for the thin hydrogen atmosphere model in [278] that accurately reproduces the RX J1856.6-3754 spectrum.

In this subsection, we investigate the expected contribution of the NS atmosphere spectra to the 2-4 keV bin in our analysis. We use NS magnetic atmosphere models accounting for the effects discussed above, `NSMAXG` [279–281], to fit the 0.5-1 keV spectra jointly to the phase-averaged PN spectra for each NS with the X-ray fitting software XSPEC [272]. Note that this procedure accounts for pileup through the PN response matrix. We account for the uncertainty in the surface composition by fitting four models: the hydrogen atmosphere model (`HB1300Thm90g1420` in XSPEC, hereafter referred to as model **H90**), the carbon atmosphere model `CB1300ThB00g1438`, the oxygen atmosphere model `OB1300ThB00g1438`, and the neon atmosphere model `NeB1300ThB00g1438`. Each assumes a dipolar magnetic field of 10^{13} G, although only model **H90** includes the anisotropic temperature surface distribution. Model **H90** assumes that the angle between the direction to Earth and the magnetic axis is 90°; to estimate the uncertainty associated with this assumption we also fit a mode `HB1300Thm00g1420l` where this angle is taken to be 0°. Finally, we fit hydrogen model `HB1350ThB00g1438` where the magnetic field strength is taken to be 3×10^{13} G, since the XDINSs typically have larger magnetic fields than assumed in the previous models. However, this model does not account for the surface temperature and magnetic field distributions. If any of these models predict a 2-4 keV intensity I_{2-4} greater than 10^{-16} erg/cm^2/s we exclude that bin from further analysis in each camera for that NS.

In practice, we find that model **H90** consistently suggests the highest 2-4 keV intensity I_{2-4} for each NS, so we report only these flux values. This is consistent with the fact that the mid-Z element atmospheres are known to be softer than their hydrogen counterparts [279]. In Tab. 6.2, we show the results of the predicted maximum fluxes in the 2-4 keV energy bin for each NS. We also computed the 4-6 keV intensity, but in no case was it larger than 10^{-19} erg/cm^2/s, and so we did not remove any higher energy bins from the analysis. Since the condensed iron atmospheres are similar at high energies to the blackbody spectra, we do not expect that these models would suggest $I_{2-4} \geq 10^{-16}$ erg/cm^2/s.

6.3.3 Characterization of the XDINSs' high-energy excess

We follow the same analysis procedure used for RX J1856.6-3754 to analyze the PN, MOS, and *Chandra* data from all of the XDINSs. A summary of the results of these analyses is

XDINS	I_{2-4} [10^{-16} erg/cm^2/s]
RX J1308.6+2127	4.0
RX J0420.0-5022	0.008
RX J0720.4-3125	11.8
RX J1605.3+3249	17.8
RX J0806.4-4123	4.0
RX J2143.0+0654	7.4
RX J1856.6-3754	0.01

Table 6.2: The intensity I_{2-4} in [10^{-16} erg/cm^2/s] for each of the NSs from 2-4 keV determined via a fit of model **H90** to the 0.5-1 keV PN data. If $I_{2-4} \geq 10^{-16}$ erg/cm^2/s, the 2-4 bin is discarded for the remainder of the analysis for all cameras from that NS. As such, we only analyze the 2-4 keV bin for RX J1856.6-3754 and RX J0420.0-5022.

XDINS	PN	MOS	*Chandra*	Joint
RX J0806.4-4123	1.16	0	0	0
RX J1856.6-3754	3.03	2.96	3.41	4.57
RX J0420.0-5022	3.09	1.05	2.80	3.32
RX J1308.6+2127	0.0	2.90	N/A	1.76
RX J0720.4-3125	1.14	0.0	N/A	1.0
RX J1605.3+3249	0.0	0.0	N/A	0.0
RX J2143.0+0654	1.41	N/A	N/A	N/A

Table 6.3: The joint and individual instrument discovery significances measured in σ for a hard excess at each of the seven XDINS as presented in Fig. 6.11.

shown in Fig. 6.11. In the left panel we show the best-fit intensities from the fits of the spectra to the power-law model. Note that for RX J1856.6-3754 and RX J0420.0-5022 we show I_{2-8}, since we include the 2-4 keV energy bins for these analyses, while for the other five NSs we show I_{4-8}. The significances of these detections, determined through Monte Carlo simulations as described in Sec. F.3, are given in the right panel. The spectra, along with the fits to the low-energy thermal models, are shown in Fig. C.6. Note that in Fig. C.6 only the PN thermal model has pileup accounted for in the blackbody spectra extrapolations.

Non-trivial hard X-ray flux is observed from RX J1856.6-3754 at 4.5σ significance in the joint power-law model fit over all datasets and at 2.5σ significance from RX J0420.0-5022. Below, we elaborate on the observations for each of the XDINSs, setting aside RX J1856.6-3754 which was discussed in the previous section. We also note that extended systematic

tests and analysis results for each of the XDINSs are provided in the appendices E.3, E.4, and E.5.

RX J0806.4-4123. There is no evidence for an anomalous hard X-ray excess from this NS in the 4-8 keV energy range analyzed. As seen in Fig. 6.11 with corresponding data presented in Tab. 6.3, there is modest ($<1\sigma$) evidence for an excess in the PN data but no such evidence in the *Chandra* and MOS data. The PN and *Chandra* data intensities are consistent, though the MOS intensity is recovered to be negative at marginal significance. This is the result of the negative 6-8 keV energy bin seen in Fig. C.6 for MOS. Since pileup has a larger impact on the MOS spectrum, the recovered MOS spectrum in this bin may be a result of energy or grade migration. There is a somewhat nearby point source, but the point source mask, which we do not apply in our fiducial analysis but do apply in App. E.4, only narrowly intersects the background extraction region and so its application does not affect our results.

RX J0420.0-5022. This NS is expected to be the least affected by pileup, considering that it has by-far the lowest intensity thermal flux. Varying the surface model shows that the presence of an atmosphere would not account for the observed emission in the 2-4 keV bin and so this bin is included in the analysis. The hard X-ray excess is detected from this NS from all cameras, as seen in Fig. 6.11. The best-fit spectral index for RX J0420.0-5022 combining all datasets is $n = -0.61^{+1.6}_{-2.1}$, which also suggests a hard spectrum like in RX J1856.6-3754. It is also interesting to note that the 1-2 keV datapoint for RX J0420.0-5022 is above the thermal model prediction for all three cameras, though we find that some of the mid-Z atmosphere models, particularly the oxygen atmosphere, can come close to explaining this datapoint. No nearby point source was detected for this NS.

RX J1308.6+2127. We cut the *Chandra* data due to concerns about pileup arising from the MARX simulations. We additionally cut the 2-4 keV bin in the *XMM* data due to concerns about emission from the NS atmosphere. We observe no significant excess in the remaining bins in PN, while the MOS excess is approximately $\sim 2\sigma$ in significance. The joint intensity over PN and MOS data is $I_{4-8} = 2.3^{+1.7}_{-1.7} \times 10^{-15}$ erg/cm^2/s. We detect a nearby point source, but not near enough to require any masking of the extraction regions in the masked analysis.

RX J0720.4-3125. We mask the 2-4 keV bin in our analysis and only consider PN data. Although the atmosphere models do not explain the entire flux in the 2-4 keV bin, there are other systematics to consider. It is well-established that the surface temperature of RX J0720 changes on the timescale of years from around 85 eV to 94 eV [282–284]. Since we jointly fit the spectra with the surface models, our procedure does not capture this time-dependence. The hotter observations may contribute the majority of the observed flux in

this bin. On the other hand, RX J0720.4-3125 has been previously suggested to have a condensed surface, where the NS atmosphere models do not apply. We find no evidence for a hard X-ray excess. We detect a nearby point source, but not near enough to require any masking of the extraction regions in the masked analysis.

RX J1605.3+3249. The NS atmosphere models are consistent with the entire 2-4 keV flux as observed by PN and MOS, so we mask this bin in our analysis. We find no significant hard X-ray excess. We detect a nearby point source, but not near enough to require any masking of the extraction regions in the masked analysis.

RX J2143.0+0654. Since hydrogen atmosphere models suggested a large thermal flux in the 2-4 keV bin, we eliminate this bin from our analysis despite seeing no significant excess. In the remaining two bins we find $\mathbf{I_{4-8}} = \mathbf{3.2^{+3.0}_{-3.4}} \times 10^{-15}$ erg/cm^2/s from the PN data. This NS has the least exposure time; accumulating more would help understand the nature of the excess, if any. We detect no nearby point sources.

All together, the ensemble of evidence presented strongly suggests that it is likely that at least some of the XDINSs, namely RX J1856.6-3754 and RX J0420.0-5022, produce hard X-ray flux in the energy range from 2-8 keV through a mechanism independent of the thermal surface emission. In the next section we discuss various possibilities for the source of this flux.

6.4 Possible origins of the XDINS hard X-ray excess

In this section we discuss possible production mechanisms for hard X-ray flux from the XDINSs consistent with the X-ray observations presented above. We consider only the 4-8 keV flux in all NSs for simplicity. Many pulsars are in fact observed to have two-component X-ray spectra, consisting of low-energy thermal emission from the surface and then a second harder non-thermal power-law component [285]. The non-thermal emission is commonly accepted to be rotation powered. Indeed, a tight correlation is observed between the spin-down luminosity of pulsars and the hard X-ray luminosity (see, *e.g.*, [34]), although no pulsars in the sample had spin-down luminosities less than 10^{32} erg/s. This relation includes the hard X-ray emission from a possible pulsar wind nebula [286,287]. The emission mechanism may, for example, be synchrotron emission from accelerated charge particles in the outer regions of the magnetosphere [288]. With that said, radio emission, which is also beamed, typically accompanies non-thermal X-ray emission. No radio emission has been conclusively observed from the XDINSs [35]. Under the hypothesis that the XDINSs are normal pulsars whose radio emission is not observed because we are not in the line-of-sight of the beam, then it would also be expected that no non-thermal X-ray emission would be

observed. This is supported by estimates of the viewing angles of RX J1308.6+2127 [289] and RX J0720.4-3125 [9]. Still, it is worth asking the question of whether the energetics of the hard X-ray emission observed from the XDINSs are consistent with a rotation-powered origin.

In Fig. 6.13 we show the spin-down luminosity $L_{\rm sd}$ of the XDINSs versus their observed luminosities L_{4-8} between 4 and 8 keV from this chapter. To calculate the luminosities we use the hard X-ray intensities from joint fits over the available PN, MOS, and *Chandra* data. The X-ray luminosities L_{4-8} are then calculated using the observed intensities and the distances in Tab. 9.1. Where our lower 1σ bound is above the lower limit of the plot, we show the 1σ confidence interval on the luminosity as determined by Monte Carlo; in the others we plot the 1σ upper limit. The spin-down luminosities are calculated by $L_{\rm sd} = 4\pi^2 I\dot{P}/P^3$, where I is the moment of inertia of the NS, assumed to be 10^{45} g cm^2, and P ($\dot{P}$) is the period (period derivative). A summary of the XDINSs' properties is shown in Tab. 9.1. Note that since there is no known spin period for RX J1605.3+3249, we do not include it in Fig. 6.13.

XDINS	P	$\dot{P}$	d
J0806	11.37	5.5×10^{-14}	240 ± 25
J1856	7.06	3×10^{-14}	123^{+11}_{-15}
J0420	3.45	2.8×10^{-14}	345 ± 200
J1308	10.31	1.1×10^{-13}	663 ± 137
J0720	16.8	7×10^{-14}	361^{+172}_{-88}
J1605	—	—	393 ± 219
J2143	9.43	4.1×10^{-14}	430 ± 200

Table 6.4: The properties of the XDINSs used to compute the spin-down and 2-8 keV luminosities; the NS period P is in [s], the period derivative $\dot{P}$ is unitless, and the distance d is in [pc]. There are no known pulsations in RX J1605.3+3249. Note that the distance measures for RX J0420.0-5022, RX J1308.6+2127, and RX J2143.0+0654 are uncertain from existing observations and we have estimated large errors to be maximally conservative. The data was compiled from [1–13].

Fig. 6.13 suggests that the hard X-ray excesses likely do not have non-thermal rotation-powered origins. The best-fit correlation between the spin-down and X-ray luminosity from [34] is shown as the dashed line. In that work it was shown that the 2-10 keV luminosities of pulsars (we have converted to 4-8 keV luminosities assuming a typical spectral index from that paper) typically correlate with the spin-down luminosities by that relation, with pulsars scattered typically around an order of magnitude above and below the line in

L_{4-8}. At least three of the XDINSs (RX J1856.6-3754, RX J1308.6+2127, and RX J0420.0-5022) show large deviations, at greater than 1σ, from this best-fit correlation, and we stress that RX J1856.6-3754 and RX J0420.0-5022 are high-significance ($\gtrsim 2.5\sigma$) detections, again suggesting that the hard X-ray excesses are not rotation-powered.

Since the 4-8 keV emission observed from the XDINSs is very small compared to that from the typical pulsar, we might expect that we see no radio signal because it is also small. [290] has observed a correlation between the 1400 MHz luminosity L_{1400} and the 2-10 keV X-ray luminosity of radio pulsars (again, here we convert to 4-8 keV luminosities), albeit with large scatter. In Fig. 6.14 we show the radio limits for all of the XDINSs [35] except RX J0420.0-5022 (because it has no radio luminosity measurement) and RX J1605.3+3249 (because its hard X-ray luminosity is negative at 1σ) against their measured 4-8 keV X-ray luminosities L_{4-8}. We have rescaled the limits in [35] to their values assuming the distances in Tab. 9.1. We see that the radio limits on the XDINSs would imply smaller 4-8 keV X-ray luminosities for at least RX J1856.6-3754 and RX J1308.6+2127 than those observed. This is true in particular for the NS with the highest significance hard X-ray detection, RX J1856.6-3754. This suggests that the XDINS hard X-ray excess is likely not due to magnetospheric emission with a corresponding radio counterpart.

Excesses above the Rayleigh-Jeans tail of the thermal surface emission have previously been observed in the optical and UV in all of the XDINSs [36, 291–293] by a factor 5-50. One plausible explanation of both the optical/UV and X-ray spectra is that there is a inhomogeneous temperature distribution on the surface such that cold spots explain the optical/UV emission. However, power-law fits to the optical/UV spectra deviate from the expected thermal slope, which suggests the existence of a non-thermal component. [36] notes that the extrapolation of the optical/UV data to the X-ray band, assuming a pure power-law, could potentially produce similar hard X-ray luminosities as observed here. That reference comes to the same conclusion that such luminosities are unlikely to have the magnetospheric origin common in pulsars and that there is no motivated model at present that would produce such a power-law non-thermal flux. Additionally, such power-law models are in tension with phase-resolved spectra and the absorption features; magnetized NS atmosphere models can potentially account for both the optical/UV excess and the X-ray blackbody (see, *e.g.* [278]), although this subject is still an area of debate.

In Fig. 6.15 we illustrate the optical luminosities integrated from 1500 - 4700 Å with the best-fit fluxes and spectral indices from [36], $L_{1500-4700}$, against the 4-8 keV luminosities L_{4-8}. Given the low sample size and non-detections in five of the seven, it is difficult to determine any possible correlation between the two. However, improved future measurements may reveal a connection, which would point to a unified emission mechanism. Again, we stress

that the optical/UV excesses could possibly be explained by a NS atmosphere model.

Another possible source of X-ray flux, besides from thermal surface emission and non-thermal rotation-powered emission, is X-ray emission from accretion of the interstellar medium (see, *e.g.*, [294]). The typical luminosities expected from accretion of the interstellar medium, assuming that the NS is in the accretion phase, which is itself nontrivial to achieve, are $\lesssim 10^{31}$ erg/s [294]. The emission is expected to be nearly thermal at a temperature $\sim$40 - 400 eV, depending on the luminosity, the magnetic field, and the accretion rate. If the temperature is on the higher side of this interval and the accretion luminosity is near 10^{31} erg/s, then the accretion emission could potentially contribute to the hard X-ray observations from some of the XDINSs. On the other hand, the low expected temperatures mean that the flux would, at best, be falling exponentially in the 2-8 keV energy range and only significantly contribute in the 2-4 keV energy bin. These expectations appears inconsistent with the rather hard spectra observed from *e.g.* RX J1856.6-3754. Furthermore, the high proper motions of the XDINSs make accretion unlikely to occur [7].

6.5 Discussion

In this chapter we use data from *XMM* and *Chandra* to provide evidence for hard X-ray emission from some of the XDINSs in the energy band from 2-8 keV. It is possible to extend the spectral analyses to 10 keV for *Chandra* and *XMM-Newton* (see App. E.5), though we have not included the 8-10 keV bin because of concerns about modeling the detector responses and backgrounds at these energies. Previously, the only X-ray emission seen from these NSs was at lower energies and consistent with thermal emission from the NS surfaces. No radio or hard X-ray emission has previously been observed. Our results suggest that at least RX J1856.6-3754 and RX J0420.0-5022 produce hard X-rays by some other means than thermal surface emission. The hard X-ray excess observed from RX J1856.6-3754 is the most significant and is seen with the PN, MOS, and *Chandra* cameras. It has a hard spectral index that appears inconsistent with *e.g.* being the tail of the thermal surface emission. The excess appears, as far as we are able to test, robust from pileup effects with *Chandra* and point sources with PN and MOS, though each of these concerns is real and may have a larger effect than we are able to account for in this chapter.

If the XDINS hard X-ray excesses survive further scrutiny, there appears to be no compelling astrophysical explanation for their existence at present. Rotation-powered non-thermal emission scenarios fail to explain the observed relation, or lack thereof, between the hard X-ray luminosity and the spin-down luminosity. Moreover, no radio signal has been observed from the XDINSs, which suggest that if the NSs are producing rotation-powered

non-thermal emission, this emission is not beamed towards Earth. Furthermore, the hard X-ray signal observed in this chapter is large enough that if it was rotation-powered non-thermal emission and being beamed towards Earth, a radio signal should have been observed in some of the XDINSs. The XDINSs have previously been discussed in the literature as being candidates to observe emission from accretion of the interstellar medium, but the predicted spectra from this emission is thought to be too soft to contribute substantially in the 2-8 keV energy range, especially with the spectral index observed from *e.g.* RX J1856.6-3754. In addition, the XDINSs are thought to have proper motions too large for significant accretion.

One possible exotic origin for the hard X-ray flux is the emission of hypothetical particles called axions within the NS cores and the subsequent conversion of these axions into hard X-rays in the magnetosphere. The predicted spectrum from this scenario is hard and consistent with the index observed from *e.g.* RX J1856.6-3754. This possibility was the original motivation for the analyses described in this chapter and is discussed in more depth in the next chapter [264]. On the other hand, this scenario is by far the most drastic, as it requires the existence of a new fundamental particle of nature.

Additional data would be useful to help verify or better understand the XDINS hard X-ray excess. For example, a long exposure by NuSTAR towards *e.g.* RX J1856.6-3754 could both confirm the excess below $\sim$10 keV and determine if the excess continues above 10 keV. Additional *Chandra* data would also be useful from *e.g.* RX J0806.4-4123, RX J1856.6-3754, and RX J0420.0-5022 to gather additional statistics on the hard X-ray spectra in the 2-8 keV energy ranges for these NSs.

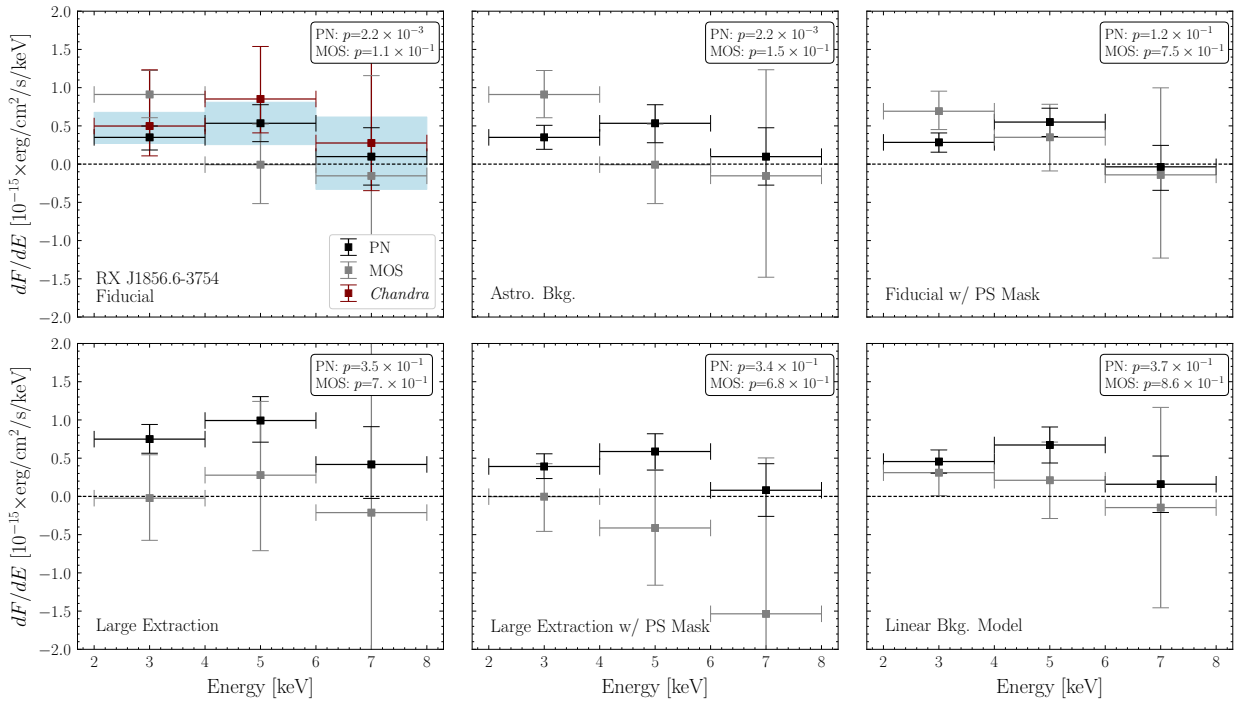

Figure 6.4: (*Upper Left*) The results of the fiducial analysis procedure. Results shown for PN, MOS, and *Chandra*, with p-values corresponding to our goodness-of-fit test of the background model in the background region in the upper right corner. The excess can be seen in all bins for PN and *Chandra*, while such an excess, if present, is not clearly visible in MOS. (*Upper Center*) Identical signal and background extraction regions as in the fiducial analysis but fitting the background using the astrophysical exposure, which accounts for vignetting, within signal and background extraction regions. (*Upper Right*) The fiducial analysis with the inclusion of a point source (PS) mask. The p-value for the goodness-of-fit in the PN data has markedly improved while the spectra remain largely unchanged. (*Lower Left*) As in the fiducial analysis, but with the signal extraction region increased to 75% of the energy-averaged 90% EEF radius. For PN and MOS, the background extraction radius is doubled but is unchanged for the *Chandra* extraction. Limits and fits do not change significantly, but the p-values for the goodness of fit in PN and MOS show tension, perhaps attributable to nearby point sources. (*Lower Center*) An analysis using the larger extraction regions and the point source mask. The p-values increase, demonstrating an improved goodness-of-fit after masking. (*Lower Right*) An analysis using the larger extraction regions and point source mask but using a background template linearly varying in RA and Dec.

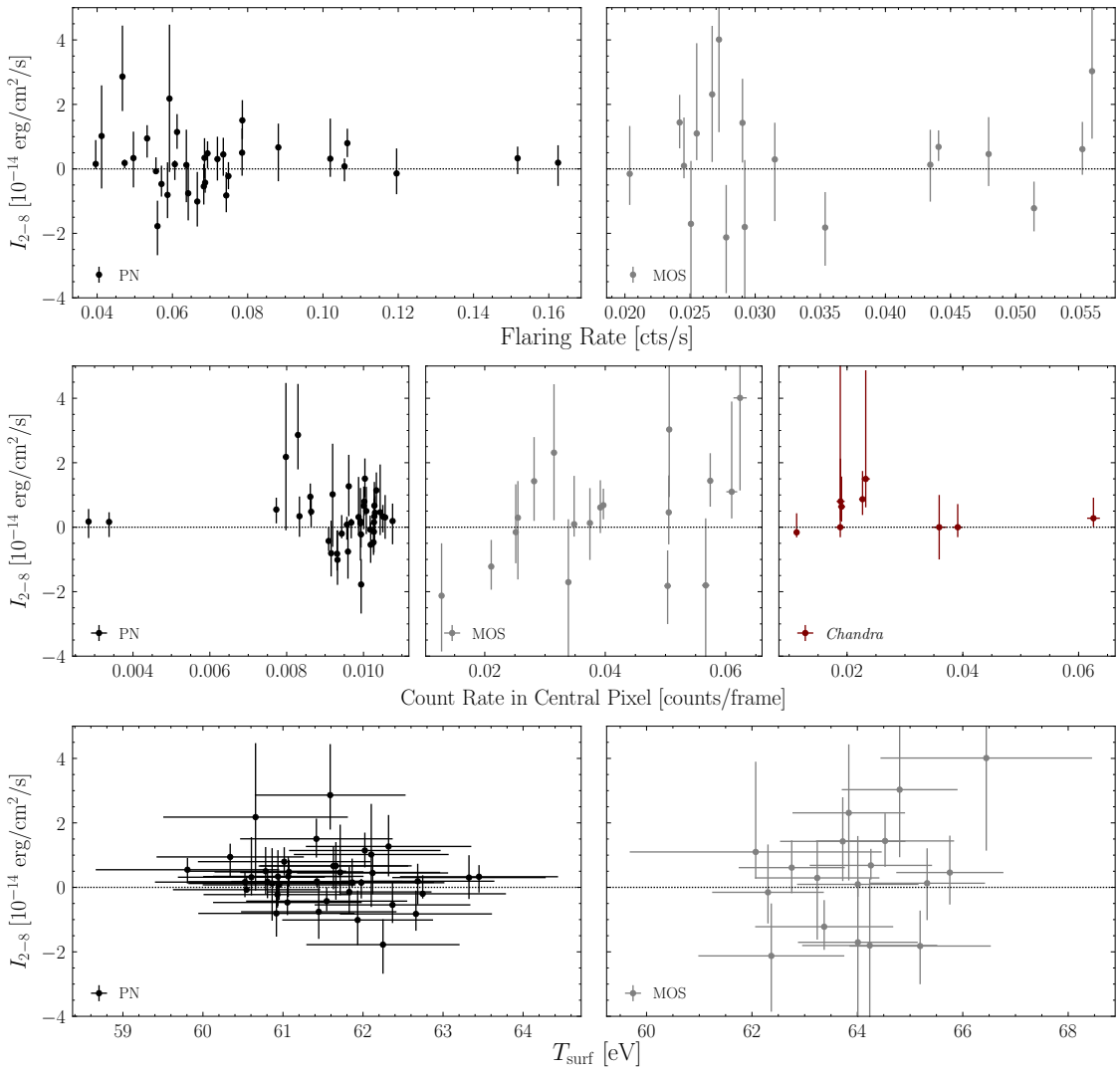

Figure 6.5: (*Top*) The best-fit I_{2-8} in [10^{-14} erg/cm^2/s] for the individual exposures (left, PN; right, MOS) for RX J1856.6-3754 plotted against the flaring rate for that exposure, if flaring was observed. (*Middle*) The best-fit I_{2-8} in [10^{-14} erg/cm^2/s] (left, PN; middle, MOS; right, *Chandra*) plotted against the count rate in the central pixel for that exposure. (*Bottom*) The best-fit I_{2-8} in [10^{-14} erg/cm^2/s] (left, PN; right, MOS) plotted against the surface temperature determined from the 0.3-2 keV data in the same exposure.

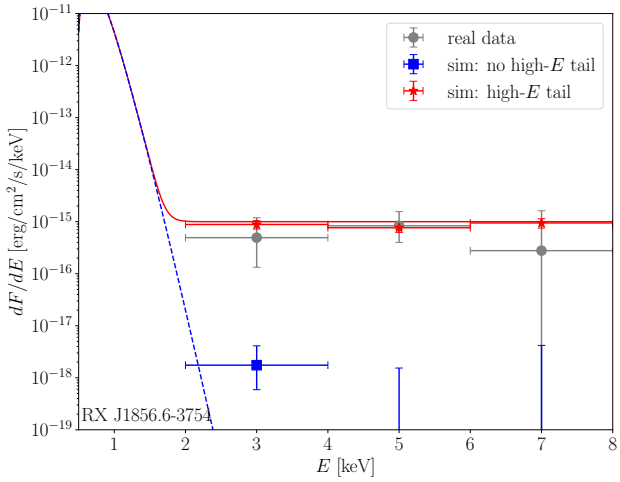

Figure 6.6: The MARX simulation results compared to the real *Chandra* data, shown in gray. The red curve shows the input spectrum to MARX with the additional flux $dF/dE = 10^{-15}$ ergs/cm^2/s/keV, from which we recover the red data points. The blue curve (with recovered blue data points) does not include this additional flux. The pileup of the soft emission does not appear to significantly impact the detection of the hard flux in this case, as we accurately recover it even with reduced statistical errors by inflating the exposure time to 10 Ms. When we input the spectrum with no high-energy tail, we again recover the input spectrum, as shown in blue. Pileup is unable to artificially reproduce the observed hard X-ray excess.

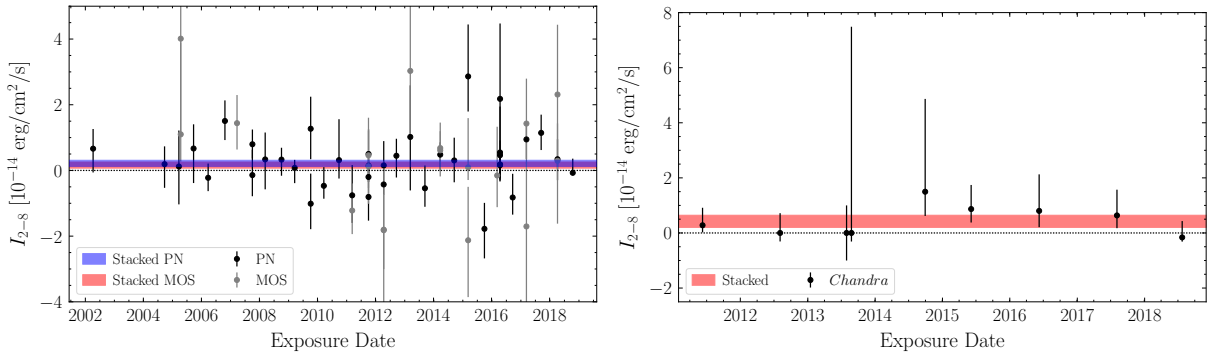

Figure 6.7: The best-fit 2-8 keV intensities for RX J1856.6-3754 in [erg/cm^2/s] in the PN and MOS cameras fit from the individual exposures. The bands cover the 1σ confidence intervals for the joint datasets. (*Left*) The PN results for the 40 individual exposures used in our analysis and the MOS results for the 18 individual exposures used in our analysis. For PN, there appears to be no evidence for variability on the timescale shown. Between approximately 2008 and 2010, the ∼five I_{2-8} values are low by approximately 1σ, but this may simply be a statistical fluctuation. It could also be due to the flaring of a source in the background region. (*Right*) The *Chandra* results for the 9 individual exposures used in our analysis. The limits are highly one-sided due to the low number of counts.

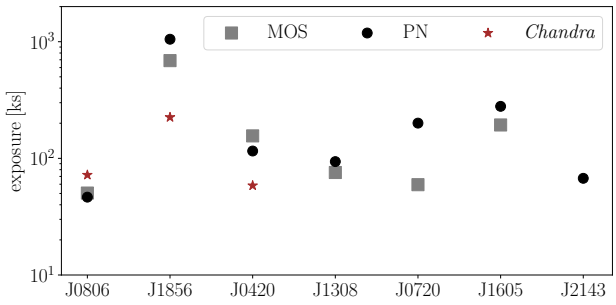

Figure 6.8: The summed exposure times in each camera for each NS in our analysis. We have chosen not to analyze *Chandra* data from NSs RX J1308.6+2127, RX J0720.4-3125, and RX J1605.3+3249 due to pileup concerns. Note that for RX J2143.0+0654 no MOS data is available that both passes our SP flaring cut and fully contains the signal and background regions in the images.

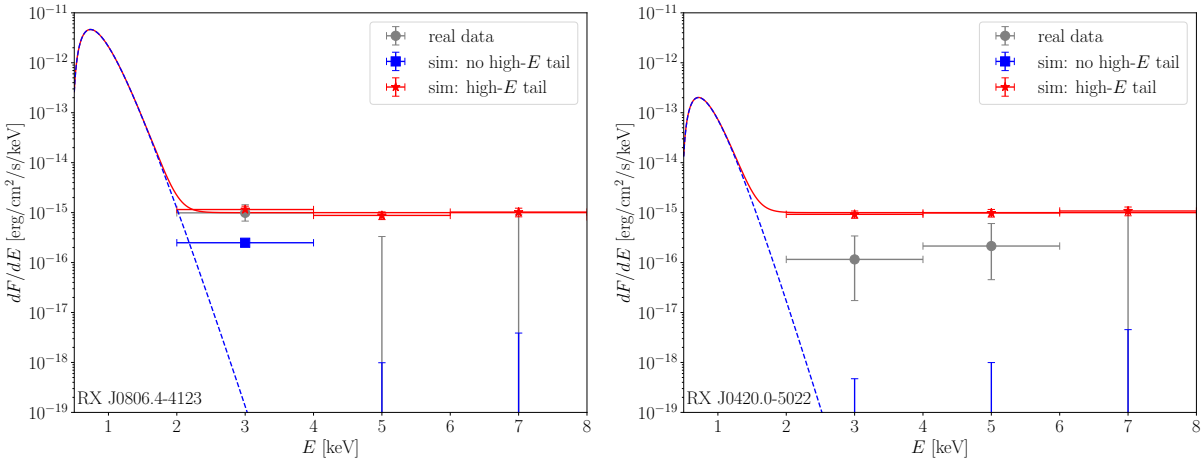

Figure 6.9: As in Fig. 6.6. (*Left*) The MARX simulation results for RX J0806.4-4123. We see that the simulation correctly recovers the true flux when the high energy tail is input into the spectrum; however, when there is no high-energy tail, pileup generates slightly more flux in the 2-4 keV bin than expected. This energy bin is excluded from our analysis, though, because of concerns about contamination from thermal emission from the NS surface. (*Right*) The MARX simulation results for RX J0420.0-5022. In this case, our analysis of both the simulation results recovers the input flux. We include all three high-energy bins in our analysis of this NS. Pileup is less of a concern for this NS because of the low thermal flux.

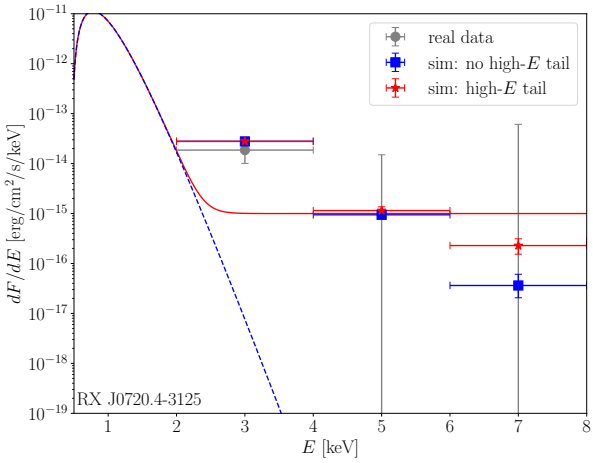

Figure 6.10: As in Fig. 6.6 but for RX J0720.4-3125. In this case, the MARX simulations indicate that pileup can generate a significant excess in the 2-4 keV bin, well above the input spectrum, regardless of the existence of a hard X-ray tail. The same is true in the 4-6 and the 6-8 keV bins, so we completely remove this NS from the *Chandra* analyses. We find similar results for MARX simulations of RX J1308.7+2127 and RX J1605.3+3249 and exclude these NSs from the *Chandra* analyses as well.

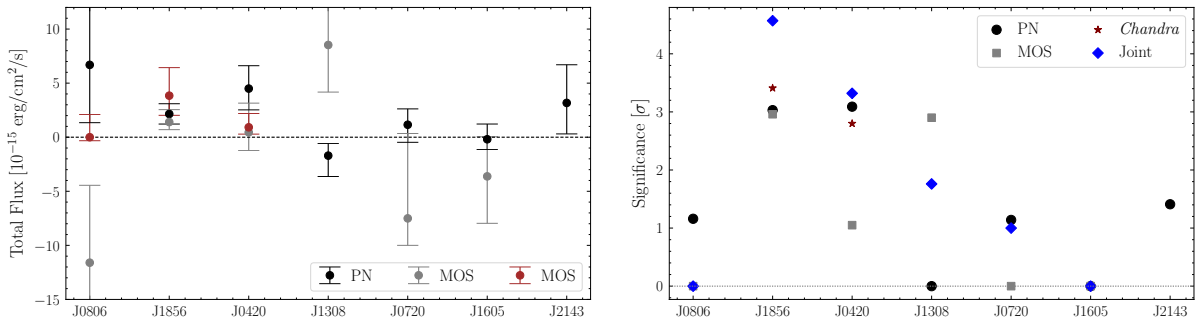

Figure 6.11: A summary of the results for all of the XDINSs. (*Left*) The total intensity in [erg/cm^2/s] recovered from the power-law fits to each of the XDINSs for the indicated instruments. For RX J1856.6-3754 and RX J0420.0-5022 we fit the model to data between 2-8 keV and so report I_{2-8}. For all other NSs, we only use data between 4-8 keV and so report I_{4-8}. Note that in all cases we show the best-fit intensities and the 68% confidence intervals. (*Right*) The significances of any intensity excesses, determined through the procedure in Sec. F.3. We also quote the significance of the joint fit across all three instruments for each NS. RX J1856.6-3754 and RX J0420.0-5022 are the two NSs where we find significant hard X-ray excesses.

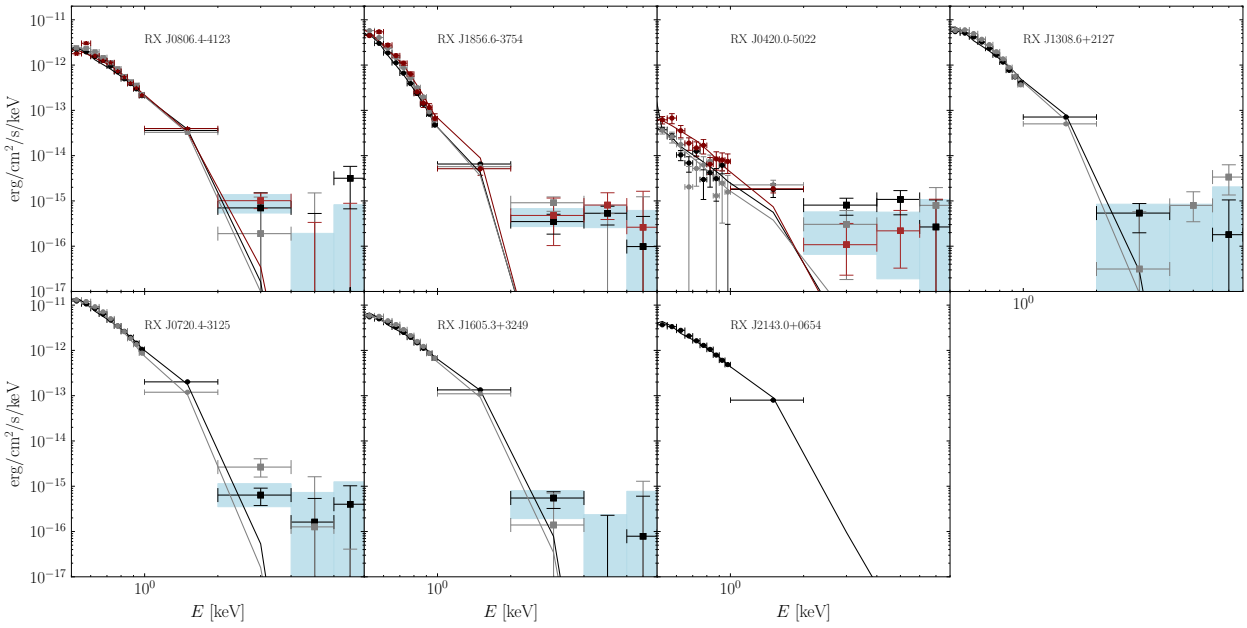

Figure 6.12: As in Fig. 6.1, but for all XDINSs. Note that the black (grey) (red) curves show the fits of the blackbody models to the low-energy (0.5-1 keV) data from PN (MOS) (*Chandra*) and extrapolated to higher energies. For the PN data only the extrapolations also include pileup. We find significant evidence for hard X-ray excesses from RX J1856.6-3754 ($\sim$4.5 σ) and RX J0420.0-5022 ($\sim$2.5 σ). Note that the joint spectra, determined from combining the data from all three cameras, are shown when more than one dataset is available. Our hard X-ray searches use either the 2-8 keV or 4-8 keV energy ranges, depending on the NS. We include the 2-4 keV energy bin for RX J1856.6-3754 and RX J0420.0-5022 but not for the other NSs because of concerns about contamination to this bin from NS atmosphere emission (see Sec. 6.3.2). However, the evidence for hard X-ray flux from RX J1856.6-3754 and RX J0420.0-5022 remains robust even without this energy bin.

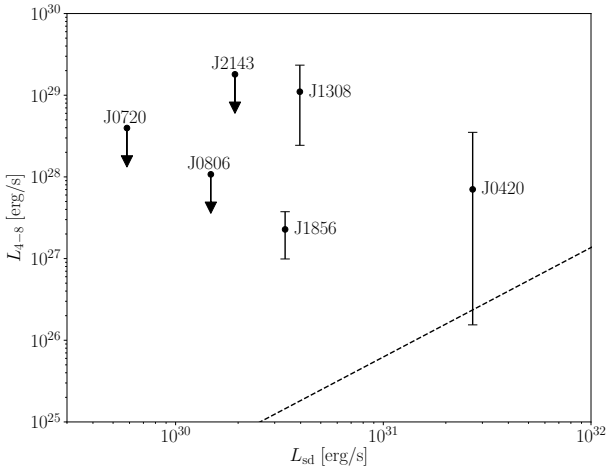

Figure 6.13: The spin-down luminosities $L_{\rm sd} = 4\pi^2 I\dot{P}/P^3$, calculated using Tab. 9.1, plotted against the joint observed 4-8 keV luminosities L_{4-8} in [erg/s]. The dotted line indicates the correlation observed in [34]. Note that we do not show RX J1605.3+3249 because its period is unknown.

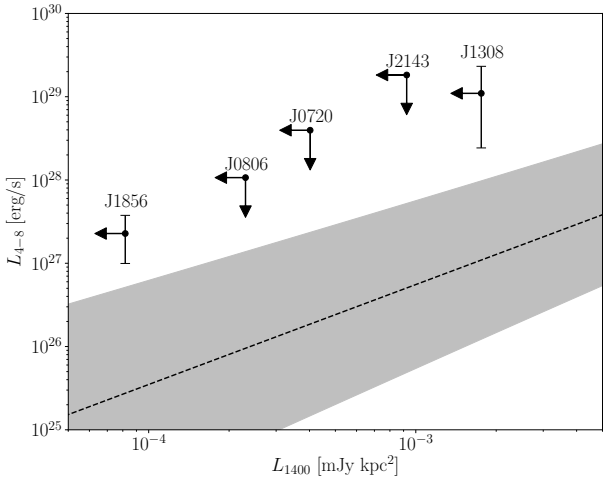

Figure 6.14: The radio luminosity limits for the XDINSs in [mJy kpc^2] plotted against the observed joint 2-8 keV luminosities L_{2-8} in [erg/s] in this chapter. The dotted line indicates the correlation observed in [35], and the shaded region indicates the 1σ uncertainty on this relation. Note that we do not show RX J1605.3+3249 because its hard X-ray luminosity is negative at over 1σ, and we do not show RX J0420.0-5022 because there are no radio measurements for this NS.

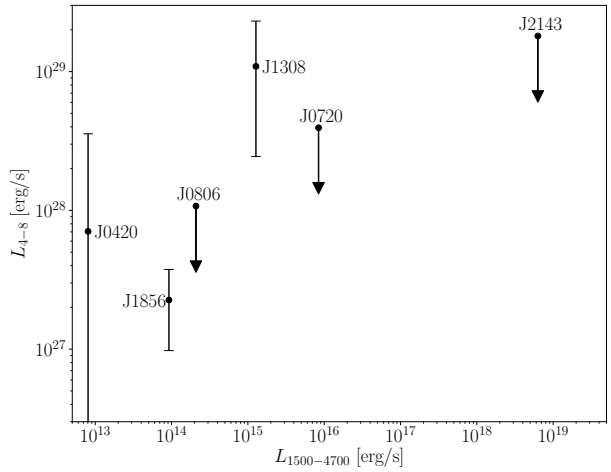

Figure 6.15: The best-fit optical/UV luminosities $L_{1500-4700}$ in [36] integrated from 1500 - 4700 Å plotted against the L_{4-8} found in this chapter. There is no observable correlation. This is perhaps not surprising considering that likely at least some of the optical/UV excess can be explained by NS atmosphere models. We note that RX J1605.3+3249 does not appear because it has a negative reconstructed hard X-ray luminosity at over 1σ.

Chapter 7

Axion Emission Can Explain a New Hard X-ray Excess from Nearby Isolated Neutron Stars

In the previous chapter, we detailed a search at the Magnificent Seven neutron stars for emission in hard X-rays. As detailed later in this Chapter, we found nontrivial evidence for hard X-ray emission that has no astrophysical explanation. In this Chapter, we outline a possible explanation in terms of axion emission and conversion to X-ray photons. Neutron stars (NSs) have long been recognized as excellent laboratories for searching for new light and weakly coupled particles of nature. This is because such particles may be produced abundantly in the hot cores of the NSs, escape, and thus provide a pathway by which the NSs may cool. Some of the strongest constraints on the ultralight pseudo-scalar particles known as axions arise from NS cooling [295–299]. Axions may be produced through nucleon bremsstrahlung in various combinations of proton and neutron scattering in the NS cores [300, 301]. It has also been suggested the axions produced in the NS cores may convert into X-rays in the magnetospheres surrounding the NSs and that these X-rays may be observable [172, 173, 179].

In this chapter we provide a consistent interpretation of the recently-observed hard X-ray excess from the nearby Magnificent Seven (M7) X-ray dim isolated NSs [15] in the context of an axion model. Ref. [15] found significant excesses of hard X-ray emission, in the 2 - 8 keV energy range, from the M7 using data from the *XMM-Newton* and *Chandra* X-ray telescopes. In particular, [15] found that the NS RX J1856.6-3754 (J1856) has around a 5σ excess, RX J0420.0-5022 (J0420) has a $\sim 3\sigma$ excess, and RX J1308.6+2127 (J1308) has a $\sim 2\sigma$ excess. The NSs RX J2143.0+0654 (J2143) and RX J0720.4-3125 (J0720) have marginal $\sim 1\sigma$ excesses, while RX J1605.3+3249 (J1605) has a small deficit and is consistent with zero

hard X-ray flux. We show that the M7 hard X-ray data may be explained in the context of an axion model where the axion couples to both nucleons and photons. The fact that hard X-ray emission is observed from some NSs and not others is consistent with the axion model because (i) the exposure times vary across the M7, (ii) the predicted fluxes at fixed axion parameters vary between NSs, given their different properties, and (iii) these properties are uncertain at present. We also provide one of the most competitive constraints to-date on the axion-photon times axion-nucleon coupling for axion masses $m_a \lesssim 10^{-4}$ eV.

The M7 were discovered in soft X-rays with the *ROSAT* All Sky Survey (see, *e.g.*, [258]). Their soft spectra are well described by near-thermal distributions with surface temperatures ∼50-100 eV. No non-thermal emission, for example in radio, has been previously observed from the NSs. As such, they are expected to produce negligible hard X-ray flux, making them background-free from the point of view of the analysis described in this chapter. Moreover, they are all observed to have strong magnetic fields [3,5,6,8,9,12,302,303] and to be relatively nearby, at distances of order hundreds of pc.

The quantum chromodynamics (QCD) axion is a hypothetical ultralight particle that solves the strong *CP* problem of the neutron electric dipole moment [161–164] and may also make up the observed dark matter [304–306]. The QCD axion and axion-like particles (ALPs) more generally also appear to be a relatively generic expectation from string compactifications [165, 166], and the ALP masses in particular may be significantly lighter than the $\sim 10^{-4}$ eV threshold relevant for this chapter (see, *e.g.*, [307, 308]). Both the QCD axion and ALPs are expected to couple derivatively to matter and also couple to electromagnetism, allowing them to be produced inside of the hot NSs and converted into photons in the strong magnetic fields surrounding the NSs. Thus in this chapter we refer to both particles simply as axions. Intriguingly, recent string theory constructions suggest that the ALP photon couplings may be slightly smaller than current limits and within reach of the search discussed in this chapter [309].

Axions have also been discussed in the context of white dwarf, red giant, and horizontal-branch (HB) star cooling [28, 30, 33, 167–170, 310–312]. In white dwarf (WD) and red giant stars the dominant production modes involve the axion-electron coupling while in HB stars the axion-photon production dominates. Recently it was proposed that X-ray observations of magnetic WD stars may probe axion scenarios, since the hot axions produced in the WD cores may convert into X-rays in the magnetic fields surrounding the WDs [222]. Axion-photon conversion within NS magnetospheres has been discussed recently in the context of dark matter axions [184, 186, 187, 313]. Axions and axion dark matter are also the subject of considerable laboratory searches [45, 197–209, 314, 315].

This chapter takes the M7 hard X-ray spectra from the previous chapter as a starting

point. Additional analysis details and systematic tests relevant for the axion model are presented in the Appendix.

7.1 Axion-induced X-ray flux from NSs

The central idea behind the proposed signal is that while the cores of the M7 are quite hot ($T \sim 1 - 10$ keV) the surfaces are relatively cool with $T \sim 0.1$ keV. Axions may be emitted from hot NS interiors, escape the NSs, and then convert into hard X-rays in the strong magnetic fields surrounding the NSs. To calculate the expected signal we both account for the axion production rate in the NS cores and the conversion probability in the magnetospheres.

The axions are produced in the NS cores through the axion couplings to fermionic matter. The coupling of the axion a to a fermion ψ_f is denoted by (see, *e.g.*, [210]) $\mathcal{L} = (C_f/2f_a)\bar{\psi}_f\gamma^\mu\gamma_5\psi_f\partial_\mu a$, with f_a the axion decay constant. Scattering amplitudes involving this operator are generally functions of the dimensionless coupling combination $g_{aff} = C_f m_f/f_a$, with m_f the fermion mass and C_f the dimensionless Lagrangian coupling (we use C_p and C_n for the proton and neutron, respectively). Note that the axion-fermion operators are generated in the infrared through the renormalization group, given an axion-photon coupling, even if such operators are absent in the ultraviolet [176, 222, 316].

The axion production mechanisms relevant for this chapter mostly occur in the NS core through axion bremsstrahlung in fully degenerate nucleon-nucleon scattering $N_1N_2 \to N_1N_2a$, where the $N_{1,2}$ are either neutrons or protons. The emissivities for these processes are functions of the couplings g_{ann}, g_{app}, the local NS core temperature T, and the neutron and proton Fermi momenta (see the Appendix and [300, 301]). As shown in [300], the local energy spectrum of axions emitted from these processes follows the modified thermal distribution $dF/dE \propto z^3(z^2+4\pi^2)/(e^z-1)$, where $z = E/T$, E is the local axion energy, and F is flux. We note that the nucleon bremsstrahlung rates may be suppressed at low temperatures, below the critical temperature for Cooper pair formation, by nucleon superfluidity [296, 317]. Recent analyses of NS cooling [14] indicate that the critical temperatures are likely too low to be relevant for this work, and so we ignore possible nucleon superfluidity in our fiducial analyses. However, given that the critical temperatures are uncertain at present, we discuss their possible effects in depth in the Appendix.

To compute the production rates in the NS cores, given the emissivity formulae, we need to know the temperature profiles in the cores, the metric, the critical temperature profiles (if including superfluidity), and the profiles of neutron and proton Fermi momenta, which all depend on the NS equation of state (EOS). We use the code package `NSCool` [318] to perform

the thermal evolution of the NSs, in full general relativity and assuming spherical symmetry. For our fiducial analysis we use the APR EOS [319] and assume NS masses of 1.4 $M_\odot$. The thermal evolution is used to obtain a relation between the effective surface temperature and the isothermal core temperature T_b^∞, which is the redshifted temperature infinitely far from the NS's potential well. The surface temperatures and associated statistical uncertainties are taken from the recent compilation in [14], which accounts for the effects of NS atmospheres in lowering the surface temperature for many NSs relative to the observed single-blackbody temperature.

The relation between the surface and core temperatures is known to be strongly affected by accretion and magnetic fields, and moreover strong magnetic fields may make the surface temperature inhomogeneous (see, *e.g.*, [320]). In fact it is the anisotropic surface temperatures that are thought to lead to the observed X-ray pulsations of the M7 [321]. Additionally, NS atmospheres may distort the spectra away from perfect blackbodies [275, 276]. We account for these possibilities through a systematic uncertainty on the core temperatures, as described in the Appendix. We combine all T_b^∞ uncertainties, statistical and systematic, into single Gaussian priors, with standard deviations given in Tab. 7.1, with the restriction that $T_b^\infty > 0$.

The core temperatures may also be estimated from the kinematic ages of the NSs. The local temperature at the outer boundary of the core T_b is expected to evolve as $T_b \approx 10^9 (t/\mathrm{yr})^{-1/6}$ K over times $t \gg$ yr, neglecting effects such as ambipolar diffusion, which may provide additional heating to the core [322]. The kinematic core temperature estimates agree with those in Tab. 7.1 within uncertainties when the NS ages are available, though there are minor differences which, as shown in Supp. Fig. S8, lead to slightly lower inferred axion couplings when using core-temperature priors from age estimates.

We then consider the conversion of the axions into X-rays in the NS magnetic fields. Here we follow closely the framework outlined in [222] for axion-photon conversion in WD magnetospheres. The axion-photon mixing is induced through the operator $\mathcal{L} = -g_{a\gamma\gamma} a F \tilde{F}/4$, where F is the electromagnetic field strength tensor, $\tilde{F}$ is its dual field, and $g_{a\gamma\gamma}$ is the axion-photon mixing parameter. The parameter $g_{a\gamma\gamma}$ is related to f_a through the relation $g_{a\gamma\gamma} = C_\gamma \alpha_{\mathrm{EM}}/(2\pi f_a)$, with α_{EM} the fine structure constant and C_γ a dimensionless coupling constant. In the presence of a strong magnetic field this operator may cause an initially pure axion state to rotate into an electromagnetic wave polarized parallel to the external magnetic field. However, the axion-photon conversion is suppressed by the Euler-Heisenberg term for strong field quantum electrodynamics [173].

In the limit of low axion mass, which for our applications is roughly $m_a \lesssim (\omega R_{\mathrm{NS}}^{-1})^{1/2}$ (and approximately 10^{-4} eV at axion frequencies $\omega \sim$ keV and NS radii $R_{\mathrm{NS}} \sim 10$ km), the

Name	B_0	T_s^∞	T_b^∞	d	I_{x-8}	Refs.
J0806	5.1	100 ± 10	15 ± 9	240 ± 25	$0.0^{+1.6}_{-0.3}$	[2, 303, 323]
J1856	2.9	50 ± 14	5 ± 3	123 ± 13	$1.5^{+0.7}_{-0.6}$	[3, 4, 270, 278, 324]
J0420	2.0	45 ± 10	3 ± 2	345 ± 200	$0.7^{+1.0}_{-0.5}$	[2, 5, 323]
J1308	6.8	70 ± 20	8 ± 6	380 ± 30	$2.3^{+1.8}_{-1.7}$	[6, 7, 289]
J0720	6.8	92 ± 10	13 ± 8	286 ± 25	$0.9^{+1.1}_{-1.6}$	[9, 325]
J1605	2.0	78 ± 42	9 ± 11	174 ± 52	$-0.5^{+1.3}_{-0.7}$	[12, 326]
J2143	4.0	72 ± 32	8 ± 8	430 ± 200	$3.1^{+3.0}_{-3.4}$	[2, 302, 327]

Table 7.1: The M7 properties used in this chapter. The magnetic field strength at the pole B_0 is in 10^{13} G; the surface temperature at infinity T_s^∞ is in eV; the core boundary temperature at infinity T_b^∞ is in keV; the distance d is in pc; the hard X-ray intensity I_{x-8} is in 10^{-15} erg/cm^2/s, integrated from x keV to 8 keV, with $x = 4$ for all NSs but J0420 and J1856, for which $x = 2$. We obtain the NS properties from the catalog of cooling NSs [14], and the I_{x-8}'s from Ref. [15].

conversion probability $p_{a\to\gamma}$ is approximately [173, 179, 222]

$$p_{a\to\gamma} \approx 1.5 \times 10^{-4} \left(\frac{g_{a\gamma\gamma}}{10^{-11}\ \text{GeV}^{-1}}\right)^2 \left(\frac{1\ \text{keV}}{\omega}\right)^{4/5} \left(\frac{B_0}{10^{13}\ \text{G}}\right)^{2/5} \left(\frac{R_{\text{NS}}}{10\ \text{km}}\right)^{6/5} \sin^{2/5}\theta\,, \tag{7.1}$$

independent of the axion mass. Above, B_0 is the surface magnetic field strength at the magnetic pole, assuming a dipole field configuration, and θ is the polar angle from the magnetic axis. At large axion masses the conversion probability becomes additionally suppressed and must be computed numerically (see, *e.g.*, [222]).

We assume dipolar magnetic field strengths calculated from the spindown of the NSs [3, 5, 6, 8, 9, 302, 303] via magneto-dipole radiation. (Note that the statistical uncertainties on the dipole field strengths are sub-leading.) In the case of J1605, there is no spin-down measurement and we adopt 2×10^{13} G as considered in [12]. Measurements of the magnetic field from spectral fitting of cyclotron resonance lines or atmosphere models generally predict larger fields, which we consider in the Appendix. We account for the unknown alignment angle θ by profiling over θ with a flat prior.

7.2 Data analysis

Ref. [15] analyzed all available archival data from *XMM-Newton* and *Chandra* towards each of the M7 for evidence of hard X-ray emission. For *XMM-Newton* they reprocessed data from both the MOS and PN cameras and treated these datasets independently, since they are subject to different sources of uncertainty from *e.g.* pileup. The data were binned into three high-energy bins from 2 - 4, 4 - 6, and 6 - 8 keV. Ref. [15] computed likelihood profiles for flux from the M7 in each one of these energy bins; these likelihoods are provided as Supplementary Data in [15] and are the starting points for the analyses presented in this chapter. As an illustration, in Fig. 7.1 we show the energy spectrum from J1856, which is

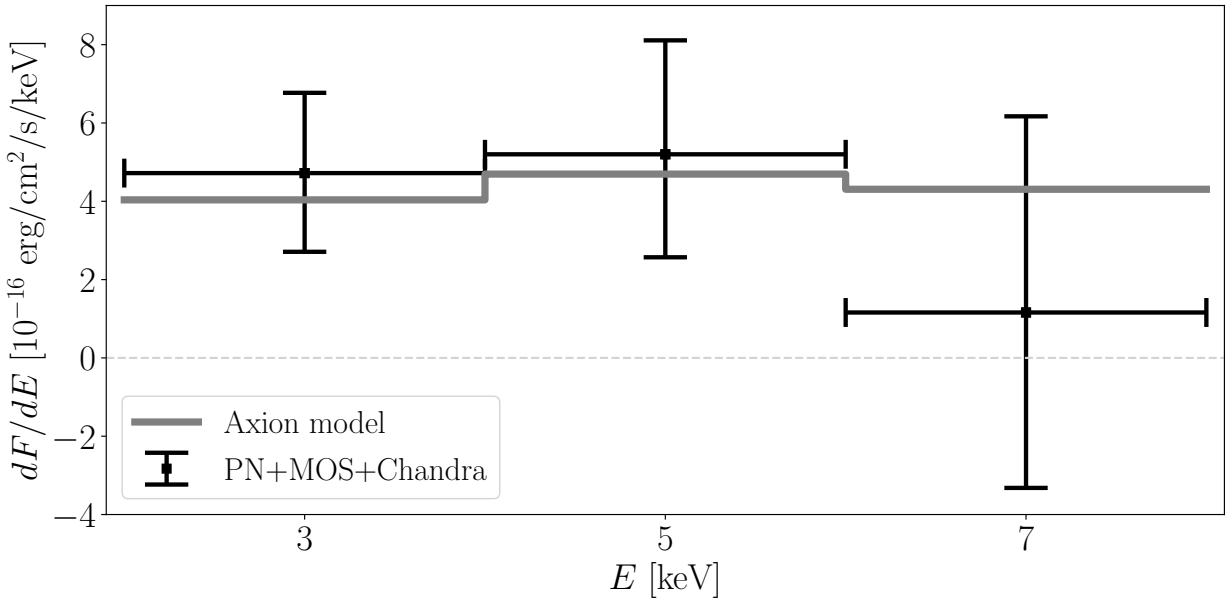

Figure 7.1: The energy spectrum from 2 to 8 keV for NS J1856 as measured by combining PN, MOS, and *Chandra* data, with 68% statistical uncertainties [15]. We also show the best-fit axion model spectrum from a fit to this NS only, with the core temperature fixed to the central value in Tab. 7.1.

the NS with the most significant hard X-ray excess. Note that we show the best-fit fluxes and associated 68% confidence intervals from the joint analyses over all three cameras.

Ref. [15] showed that the $2-4$ keV energy bin may be contaminated by the high-energy tail of the thermal emission from the NS surfaces, depending on the atmosphere model, for all NSs except J1856 and J0420. The predicted thermal surface emission is negligible for all NSs in the last two energy bins. As such in this analysis we use all three available energy bins for J1856, which has by far the most exposure time of all M7, and J0420, but only the last two energy bins for the other five NSs. Ref. [15] only provides *Chandra* data for J1856,

J0420, and J0806, because for the other NSs they found that pileup may affect the observed high-energy spectrum. For J2143 only PN data is available.

We interpret the M7 hard X-ray spectra in the context of the axion model by using a joint likelihood over all of the M7 and available datasets with a frequentist profile likelihood analysis procedure. Our parameters of interest are $\{m_a, g_{a\gamma\gamma}, g_{ann}, g_{app}\}$ and our nuisance parameters, which describe uncertain aspects of the NSs, are the set of parameters $\{\theta, d, T_b^\infty\}$ for each NS, where d is distance. Each of the nuisance parameters is taken to have a Gaussian prior with uncertainty given in Tab. 7.1, except for θ, which is given a flat prior from 0 to π. Uncertainties arising from the NS superfluidity model are described in the Appendix. For our fiducial analysis we fix $g_{app} = g_{ann}$. We construct a joint likelihood over all of the M7 and available datasets, and we use this likelihood to constrain our parameters of interest.

7.3 Results

The resulting best-fit parameter space in the m_a-$g_{a\gamma\gamma}g_{ann}$ plane and 95% one-sided upper limit are shown in Fig. 7.2. Interpreting the data in the context of the axion model, we find

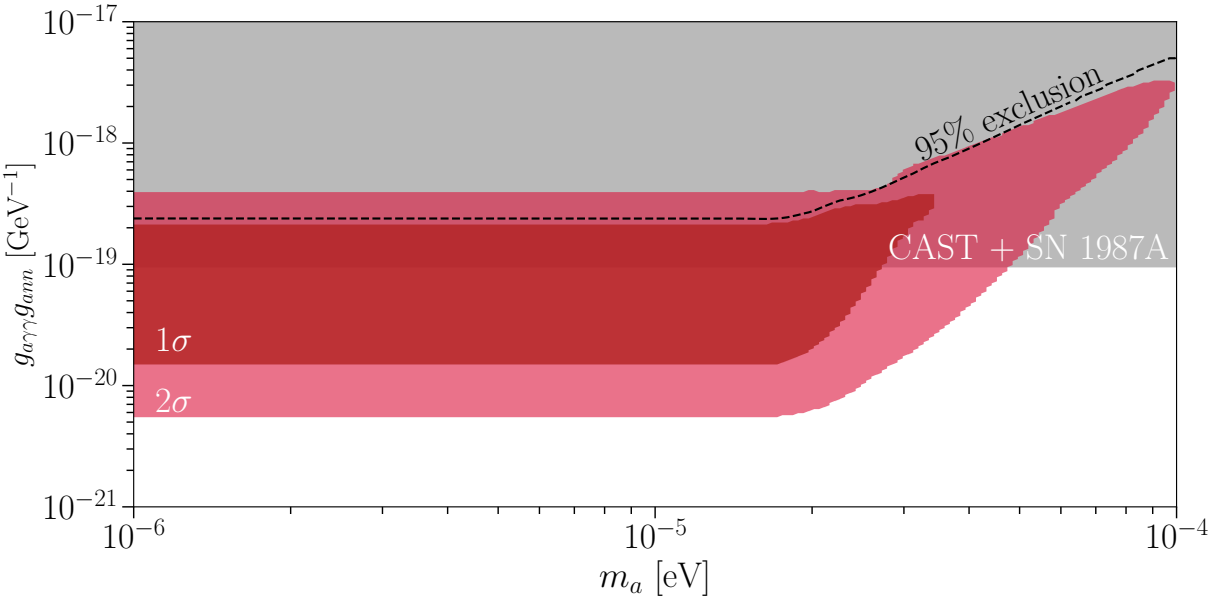

Figure 7.2: 95% exclusion limit and best fit 1 and 2σ regions from a joint likelihood analysis over all of the M7 and combining PN, MOS, and *Chandra* data. We compare our result to existing limits from CAST2017+NS cooling. All curves and regions continue to arbitrarily small m_a. Note that the QCD axion model is too weakly coupled to appear in this figure. Accounting for systematic uncertainties may allow for smaller values of $g_{a\gamma\gamma}g_{ann}$, by approximately an order of magnitude, as discussed in the Appendix.

approximately 5σ evidence for the axion-induced flux over the null hypothesis of no non-thermal hard X-ray flux from the M7. The global fit prefers a low axion mass and a coupling at and slightly below previous limits, which are also indicated. In particular we combine the CAST constraints on $g_{a\gamma\gamma}$ ($g_{a\gamma\gamma} < 6.6 \times 10^{-11}$ GeV^{-1} at low masses) [27] with the SN 1987A constraints on g_{ann}, taking $g_{app} = g_{ann}$, $g_{ann} < 1.4 \times 10^{-9}$ [328] (but see [329] which questions these constraints). Constraints on g_{ann} from cooling of the NS Cas A [296, 298, 299] may all be relevant, though these constraints are subject to both instrumental [24] and theoretical systematic uncertainties. Thus the current constraints on $g_{a\gamma\gamma}g_{ann}$ in Fig. 7.2 should be taken as suggestive.

It is interesting to investigate whether the high-energy flux observed between the individual NSs is consistent with the expectation from the axion hypothesis. In Fig. 7.3 we show the observed intensities I_{2-8} (I_{4-8}) between 2 - 8 keV (4 - 8 keV) for each of the M7 after combining the MOS, PN, and *Chandra* datasets. These intensities are determined by fitting the low-mass axion spectral model uniquely to the data from each NS, with model parameters T_b^∞ and I_{2-8} (I_{4-8}). Note that for the NSs where we include the 2 - 4 keV energy bin we report I_{2-8}, while for those where we do not include this bin we instead report I_{4-8}. (We obtain qualitatively similar results if we only use the 4 - 8 keV bins for all NSs, as shown in the Appendix.) The green (yellow) bands indicate the 68% (95%) confidence intervals for the intensities from the X-ray measurements. The black and gray error bands, on the other hand, denote the 68% and 95% confidence intervals for the axion model predictions, fixing the axion model parameters at the best-fit point from the global fit, $g_{a\gamma\gamma}g_{ann} \approx 4 \times 10^{-20}$ GeV^{-1} with $m_a \ll 10^{-5}$ eV, and profiling over the nuisance parameters. The uncertainties in the model prediction arise primarily from the nuisance parameters describing the unknown properties of the M7, as described above, while the uncertainties on the measured intensity values are purely statistical in nature.

The observed intensities are consistent with expectations from the axion model. Additionally, there are sources of uncertainty on the axion model predictions for the individual NSs beyond those shown in Fig. 7.3, arising from for example nucleon superfluidity, the EOS, and the inference of the core temperatures. For example, as we show in the Appendix with alternate core-temperature models, based on ages rather than surface temperatures, the best-fit couplings could be as low as $g_{a\gamma\gamma}g_{ann} \approx 2 \times 10^{-21}$ GeV^{-1}.

We also investigate whether the observed spectra from the two high-significance detections in J1856 and J0420 are consistent with the axion model expectation. In Fig. 7.4 we show the best-fit core temperatures T_b^∞ measured from fitting the axion-model, with $m_a \ll 10^{-5}$ eV, to the X-ray data between 2 and 8 keV. We note that the NS with the best-determined spectral shape is J1856, which has the most significant detection. In Fig. 7.1 we show the

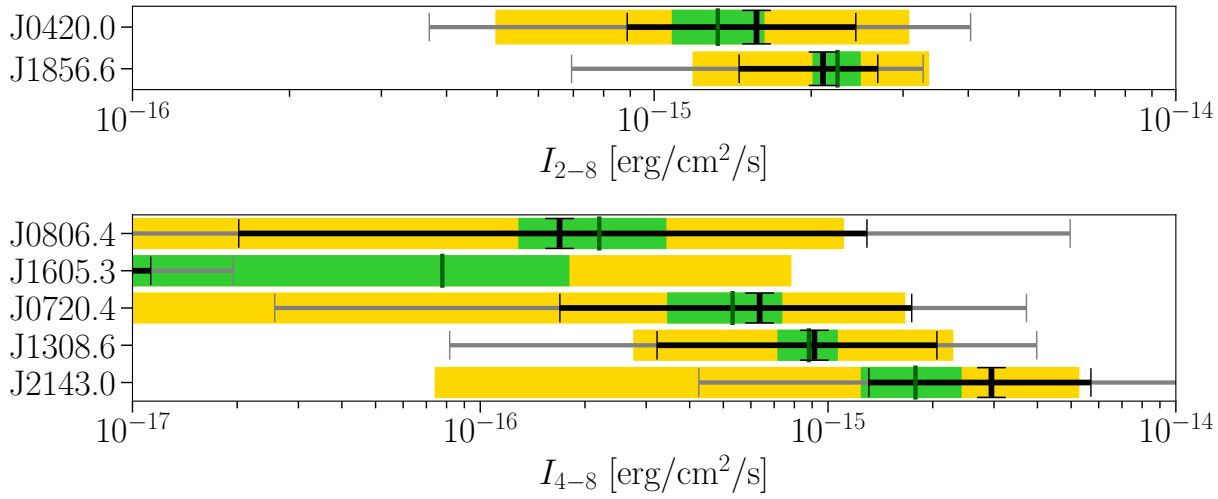

Figure 7.3: Best-fit intensities I_{2-8} and I_{4-8} for all M7. The green (yellow) bands indicate the 68% (95%) confidence intervals from the X-ray intensity measurements, with best-fit intensities marked by vertical green lines. Black and gray error bands denote the 68% and 95% confidence intervals for the axion model predictions at the global best-fit coupling $g_{a\gamma\gamma}g_{ann}$ and $m_a \ll 10^{-5}$ eV, with uncertainties arising from uncertain aspects of the NSs.

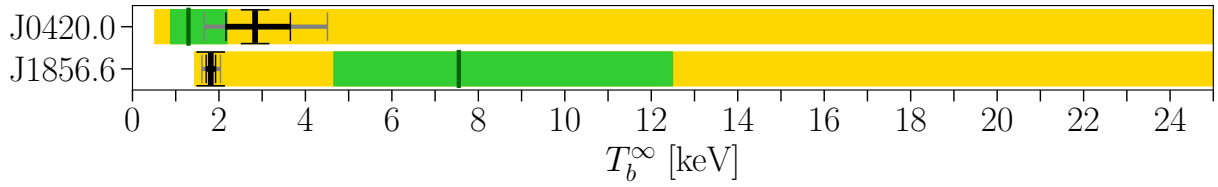

Figure 7.4: As in Fig. 7.3 but for the best-fit core temperature T_b^∞ for J1856 and J0420.

best-fit model prediction for this NS compared to the observed spectrum. The axion model appears to reproduce the spectral shape found in the data.

7.4 Discussion

In this chapter we presented results of a search for hard X-ray emission arising from axions in the M7 NSs. We showed that the M7 hard X-ray excess observed in [15] may be interpreted in the context of the axion model.

Alternative explanations for the hard X-ray emission exist, but they are not compelling [15]. For example, some of the observations may be affected by pileup due to the high flux of soft, thermal X-rays, though these effects seem insufficient to explain the observed

hard X-ray flux [15]. For the *XMM-Newton* data in particular, unresolved astrophysical point sources near the source of interest could also bias the observed spectrum, though the fact that consistent spectra are observed with *Chandra*, which has over an order of magnitude better angular resolution, provides evidence that this is at least not the sole explanation for the excess. Hard non-thermal X-ray emission is observed generically from pulsars, and one possibility is that the observed hard X-ray flux from the M7 arises from the traditional non-thermal emission mechanisms (*e.g.*, synchrotron emission) that are present in other pulsars. On the other hand, this emission is often accompanied by non-thermal radio emission, which is not observed for the M7 [330], and also the spin-down luminosity seems insufficient for most of the M7 for this to be an appreciable source of flux [15]. Accretion of the interstellar medium may also be a source of X-rays from the M7, though this is typically thought to produce flux at much softer energies if at all (see, *e.g.*, [294]).

Observations at higher energies by *e.g. NuSTAR* of J1856 and J0420 in particular may help discriminate the axion explanation of the excess from other explanations. This is because the predicted axion spectrum in the energy range from $\sim$10-60 keV is unique and potentially includes a significant enhancement due to Cooper pair-breaking-formation processes, depending on the superfluidity model. (See the Appendix for details, where we also show that the Cooper pair processes could enhance the flux below 10 keV as well.) The axion-induced flux should also pulsate at the NS period, and this may be measurable with future instruments such as *Athena* that can acquire better statistics. *Athena* will have similar angular resolution to *Chandra* while also being significantly less affected by pileup [331]. X-ray observations of magnetic white dwarf stars [222], the magnetized intracluster medium [37], or nearby bright galaxies [332] could also help constrain or provide additional evidence for the best-fit axion from this chapter. The best-fit axion parameter space from this chapter may also be probed with next-generation light-shining-through-walls experiments like ALPS II [333] and helioscopes like IAXO [334]. In summary, if the M7 hard X-ray excess is due to axions, then a variety of near-term measurements should be able to conclusively establish a discovery.

Chapter 8

X-ray Searches for Axions from Super Star Clusters

In the previous chapters on axion searches, we required axion couplings to matter in order to produce the axions inside the star. In this chapter, we choose a target that can instead produce the axion through the same operator that converts the axion to a photon in a background magnetic field, so that we can place limits on the axion-photon coupling alone.

Axions may interact electromagnetically through the operator $\mathcal{L} = -g_{a\gamma\gamma} a F_{\mu\nu} \tilde{F}^{\mu\nu}/4$, where a is the axion field, F is the electromagnetic field-strength tensor, with $\tilde{F}$ its Hodge dual, and $g_{a\gamma\gamma}$ is the dimensionful coupling constant of axions to photons. This operator allows both the production of axions in stellar plasmas through the Primakoff Process [335,336] and the conversion of axions to photons in the presence of static external magnetic fields. Strong constraints on $g_{a\gamma\gamma}$ for low-mass axions come from the CERN Axion Solar Telescope (CAST) experiment [27], which searches for axions produced in the Solar plasma that free stream to Earth and then convert to X-rays in the magnetic field of the CAST detector. CAST has excluded axion couplings $g_{a\gamma\gamma} \gtrsim 6.6 \times 10^{-11}$ GeV^{-1} for axion masses $m_a \lesssim 0.02$ eV at 95% confidence [27]. Primakoff axion production also opens a new pathway by which stars may cool, and strong limits ($g_{a\gamma\gamma} \lesssim 6.6 \times 10^{-11}$ GeV^{-1} at 95% confidence for $m_a \lesssim$ keV) are derived from observations of the horizontal branch (HB) star lifetime, which would be modified in the presence of axion cooling [28].

In this chapter, we produce some of the strongest constraints to-date on $g_{a\gamma\gamma}$ for $m_a \lesssim 10^{-9}$ eV through X-ray observations with the Nuclear Spectroscopic Telescope Array (NuSTAR) telescope [337] of super star clusters (SSCs). The SSCs contain large numbers of hot, young, and massive stars, such as Wolf-Rayet (WR) stars. We show that these stars, and as a result the SSCs, are highly efficient at producing axions with energies ∼10–100 keV through the Primakoff process. These axions may then convert into photons in the Galactic magnetic

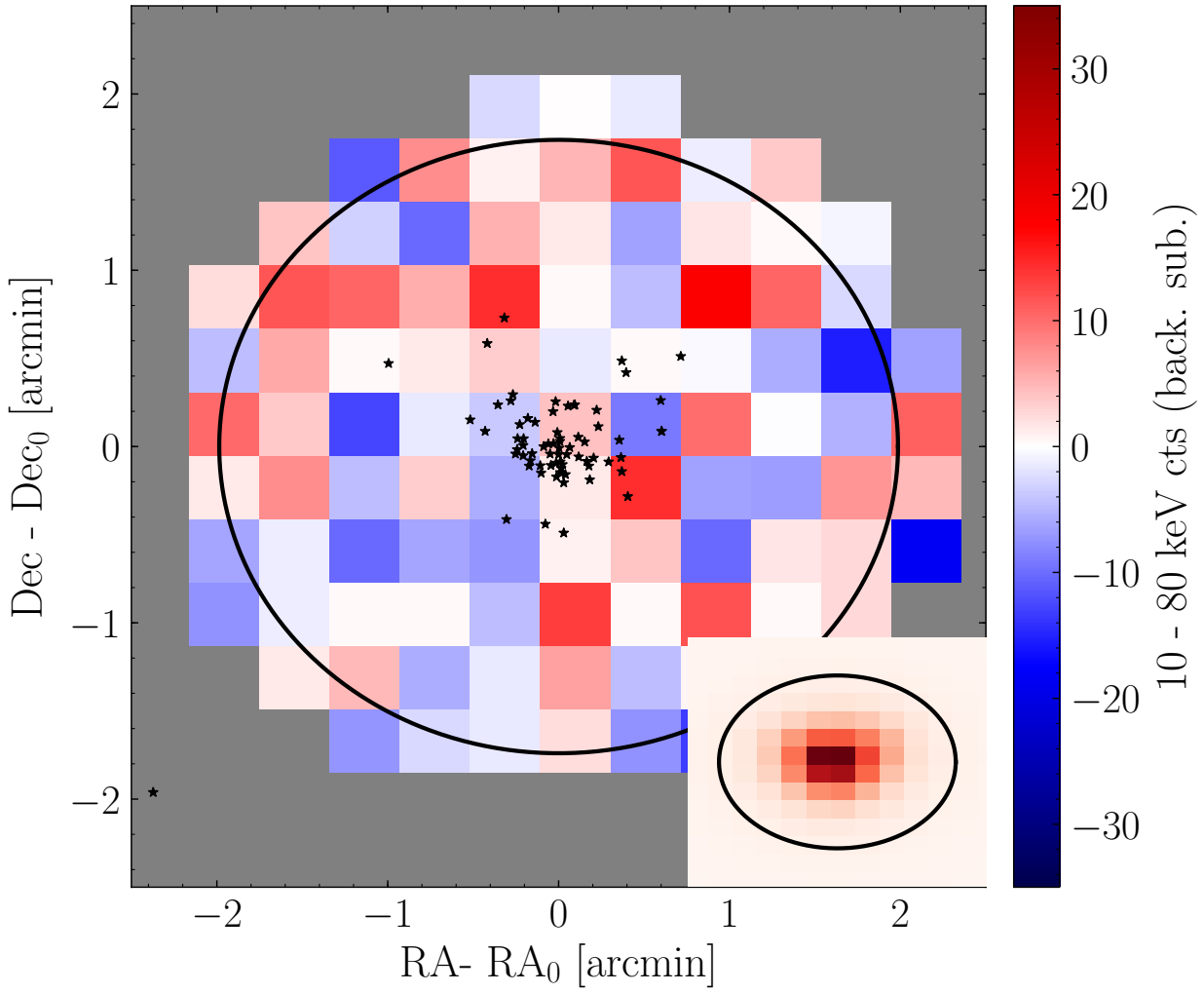

Figure 8.1: The stacked and pixelated background-subtracted count data (10 - 80 keV) from the NuSTAR observations of the Quintuplet SSC. The locations of the stars are indicated in black, while the 90% energy containment region for emission associated with the SSC is indicated by the black circle, accounting for the NuSTAR point spread function (PSF). RA_0 and DEC_0 denote the locations of the cluster center. We find no evidence for axion-induced emission from this SSC, which would follow the spatial counts template illustrated in the inset panel.

fields, leading to signatures observable with space-based X-ray telescopes such as NuSTAR. We analyze archival NuSTAR data from the Quintuplet SSC near the Galactic Center (GC) along with the nearby Westerlund 1 (Wd1) cluster and constrain $g_{a\gamma\gamma} \lesssim 3.6 \times 10^{-12}$ GeV^{-1} at 95% confidence for $m_a \lesssim 5 \times 10^{-11}$ eV. In Fig. 10.2 we show the locations of the stars within the Quintuplet cluster that are considered in this chapter on top of the background-subtracted NuSTAR counts, from 10 - 80 keV, with the point-spread function (PSF) of NuSTAR also indicated. In the Appendix we show that observations of the Arches SSC

yield similar but slightly weaker limits.

Our work builds upon significant previous efforts to use stars as laboratories to search for axions. Some of the strongest constraints on the axion-matter couplings, for example, come from examining how HB, white dwarf (WD), red giant, and neutron star (NS) cooling would be affected by an axion [28, 30, 33, 167–170, 310–312]. When the stars have large magnetic fields, as is the case for WDs and NSs, the axions can be converted to X-rays in the stellar magnetospheres [179, 221, 222, 245]. Intriguingly, in [221, 245] observations of the Magnificent Seven nearby isolated NSs found evidence for a hard X-ray excess consistent with the expected axion spectrum from nucleon bremsstrahlung. This chapter extends these efforts by allowing the axions to convert to X-rays not just in the stellar magnetic fields but also in the Galactic magnetic fields [338–340].

8.1 Axion production in SSCs

During helium burning, particularly massive stars may undergo considerable mass loss, especially through either rotation or binary interaction, which can begin to peel away the hydrogen envelope, revealing the hot layers underneath and reversing the cooling trend. Stars undergoing this process are known as WR stars, and these stars are the most important in our analyses. If the star has a small (<40% abundance) remaining hydrogen envelope, it is classified as a WNh star; at <5% hydrogen abundance it is classified as a WN star; otherwise, it is classified as WC or WO, which indicates the presence of >2% carbon, and oxygen, respectively, in the atmosphere.

Axions are produced through the photon coupling $g_{a\gamma\gamma}$ in the high-mass stars in SSCs through the Primakoff process $\gamma + (e^-, Z) \rightarrow a + (e^-, Z)$. This process converts a stellar photon to an axion in the screened electromagnetic field of the nucleons and electrons. The massive stars are high-temperature and low-density and therefore form nonrelativistic nondegenerate plasmas. The Primakoff emission rate was calculated in [336,341] as a function of temperature, density, and composition, and is described in detail in the Appendix.

To compute the axion luminosity in a given star, we use the stellar evolution code Modules for Experiments in Stellar Astrophysics (MESA) [342,343] to find, at any particular time in the stellar evolution, radial profiles of temperature, density, and composition. The simulation states are specified by an initial metallicity Z, an initial stellar mass, an initial rotation velocity, and an age. The initial metallicity is taken to be constant for all stars. In the Appendix we show that the Quintuplet and Arches clusters, which are both near the GC, are likely to have initial metallicities in the range $Z \in (0.018, 0.035)$, consistent with the conclusions of previous works which place the initial metallicities of these clusters near solar

(solar metallicity is $Z \approx 0.02$) [67, 344]. Note that higher metallicities generally lead to the stars entering the WR classifications sooner, when their cores are cooler. Rotation may also cause certain massive stars to be classified as WR stars at younger ages. We model the initial rotation distribution as a Gaussian distribution with mean $\mu_{\rm rot}$ and standard deviation $\sigma_{\rm rot}$ for non-negative rotation speeds [345, 346]. Refs. [345, 346] found $\mu_{\rm rot} \approx 100$ km/s and $\sigma_{\rm rot} \approx 140$ km/s, but to assess systematic uncertainties we vary $\mu_{\rm rot}$ between 50 and 150 km/s [345].

We draw initial stellar velocities from the velocity distribution described above (from 0 to 500 km/s) and initial stellar masses from the Kroupa initial mass function [347] (from 15 to 200 $M_\odot$). We use MESA to evolve the stars from pre-main-sequence (pre-MS)–before core hydrogen ignition–to near-supernova. At each time step we assign each stellar model a spectroscopic classification using the definitions in [348,349]. We then construct an ensemble of models for each spectroscopic classification by joining together the results of the different simulations that result in the same classification for stellar ages within the age range for star formation in the cluster; for Quintuplet, this age range is between 3.0 and 3.6 Myr [350]. Note that each simulation generally provides multiple representative models, taken at different time steps. In total we compute 10^5 models per stellar classification.

Quintuplet hosts 71 stars of masses $\gtrsim 50 M_\odot$, with a substantial WR cohort [350]. In particular it has 14 WC + WN stars, and we find that these stars dominate the predicted axion flux. For example, at $g_{a\gamma\gamma} = 10^{-12}$ GeV^{-1} we compute that the total axion luminosity from the SSC (with $Z = 0.035$ and $\mu_{\rm rot} = 150$ km/s) is $2.1^{+0.7}_{-0.4} \times 10^{35}$ erg/s, with WC + WN stars contributing ∼70% of that flux. Note that the uncertainties arise from performing multiple (500) draws of the stars from our ensembles of representative models. In the 10 - 80 keV energy range relevant for NuSTAR the total luminosity is $1.7^{+0.4}_{-0.3} \times 10^{35}$ erg/s. We take $Z = 0.035$ and $\mu_{\rm rot} = 150$ km/s because these choices lead to the most conservative limits. For example, taking the metallicity at the lower-end of our range ($Z = 0.018$) along with $\mu_{\rm rot} = 100$ km/s the predicted 10 - 80 keV flux increases by ∼60%. At fixed $Z = 0.035$ changing $\mu_{\rm rot}$ from 150 km/s to 100 km/s increases the total luminosity (over all energies) by ∼10%, though the luminosity in the 10 - 80 keV range is virtually unaffected.

The Wd1 computations proceed similarly. Wd1 is measured from parallax to be a distance $d \in (2.2, 4.8)$ kpc from the Sun [351], accounting for both statistical and systematic uncertainties [352]. Wd1 is estimated to have an age between 4.5 and 7.1 Myr from isochrone fitting, which we have broadened appropriately from [353] accounting for expanded distance uncertainties. In our fiducial analysis we simulate the stars in Wd1 for initial metallicity $Z = 0.035$ and $\mu_{\rm rot} = 150$ km/s as this leads to the most conservative flux predictions, even though it is likely that the metallicity is closer to solar for Wd1 [354], in which cases

the fluxes are larger by almost a factor of two (see the Appendix). We model 153 stars in Wd1 [353], but the axion flux is predominantly produced by the 8 WC and 14 WN stars. In total we find that the 10 - 80 keV luminosity, for $g_{a\gamma\gamma} = 10^{-12}$ GeV, is $9.02^{+1.2}_{-1.1} \times 10^{35}$ erg/s, which is $\sim$5 times larger than that from Quintuplet.

8.2 Axion conversion in Galactic fields

The axions produced within the SSCs may convert to X-rays in the Galactic magnetic fields. The axion Lagrangian term $\mathcal{L} = g_{a\gamma\gamma} a \mathbf{E} \cdot \mathbf{B}$, written in terms of electric and magnetic fields $\mathbf{E}$ and $\mathbf{B}$, causes an incoming axion state to rotate into a polarized electromagnetic wave in the presence of an external magnetic field (see, *e.g.*, [173]). The conversion probability $p_{a\to\gamma}$ depends on the transverse magnetic field, the axion mass m_a, and the plasma frequency $\omega_{\rm pl} \approx 3.7 \times 10^{-12} (n_e/10^{-2}\ {\rm cm}^{-3})^{-1/2}$ eV, with n_e the free-electron density (see the Appendix for an explicit formula). Note that hydrogen absorption towards all of our targets is negligible, being at most $\sim$5% in the 15-20 keV bin of the Quintuplet analysis [355].

To compute the energy-dependent conversion probabilities $p_{a\to\gamma}$ for our targets we need to know the magnetic field profiles and electron density distributions along the lines of sight. For our fiducial analysis we use the regular components of the JF12 Galactic magnetic field model [356, 357] and the YMW16 electron density model [358] (though in the Appendix we show that the `ne2001` [359] model gives similar results), though the JF12 model does not cover the inner kpc of the Galaxy. Outside of the inner kpc the conversion probability for Quintuplet is dominated by the out-of-plane (X-field) component in the JF12 model. We conservatively assume that the magnitude of the vertical magnetic field within the inner kpc is the same as the value at 1 kpc ($|B_z| \approx 3\ \mu$G), as illustrated in Supp. Fig. S6. In our fiducial magnetic field model the conversion probability is $p_{a\to\gamma} \approx 2.4 \times 10^{-4}$ (7×10^{-5}) for $g_{a\gamma\gamma} = 10^{-12}$ GeV^{-1} for axions produced in the Quintuplet SSC with $m_a \ll 10^{-11}$ eV and $E = 80$ keV ($E = 10$ keV). Completely masking the inner kpc reduces these conversion probabilities to $p_{a\to\gamma} \approx 1.0 \times 10^{-4}$ ($p_{a\to\gamma} \approx 3.2 \times 10^{-5}$), for $E = 80$ keV ($E = 10$ keV). On the other hand, changing global magnetic field model to that presented in [360] (PTKN11), which has a larger in-plane component than the JF12 model but no out-of-plane component, leads to conversion probabilities at $E = 80$ and 10 keV of $p_{a\to\gamma} \approx 4.9 \times 10^{-4}$ and $p_{a\to\gamma} \approx 4.2 \times 10^{-5}$, respectively, with the inner kpc masked.

The magnetic field is likely larger than the assumed 3 μG within the inner kpc. Note that the local interstellar magnetic field, as measured directly by the *Voyager* missions [361], indirectly by the Interstellar Boundary Explorer [362], inferred from polarization measurements of nearby stars [363], and inferred from pulsar dispersion measure and the rotation measure

data [364], has magnitude $B \sim 3$ μG, and all evidence points to the field rising significantly in the inner kpc [365]. For example, Ref. [366] bounded the magnetic field within the inner 400 pc to be at least 50 μG, and more likely 100 μG (but less than $\sim$400 μG [367]), by studying non-thermal radio emission in the inner Galaxy. Localized features in the magnetic field in the inner kpc may also further enhance the conversion probability beyond what is accounted for here. For example, the line-of-sight to the Quintuplet cluster overlap with the GC radio arc non-thermal filament, which has a $\sim$3 mG vertical field over a narrow filament of cross-section $\sim$(10 pc)^2 (see, *e.g.*, [368]). Accounting for the magnetic fields structures described above in the inner few hundred pc may enhance the conversion probabilities by over an order of magnitude relative to our fiducial scenario (see the Appendix).

When computing the conversion probabilities for Wd1 we need to account for the uncertain distance d to the SSC (with currently-allowable range given above). In the JF12 model we find the minimum $p_{a\to\gamma}/d^2$ (for $m_a \ll 10^{-11}$ eV) is obtained for $d \approx 2.6$ kpc, which is thus the value we take for our fiducial distance in order to be conservative. At this distance the conversion probability is $p_{a\to\gamma} \approx 2.4 \times 10^{-6}$ ($p_{a\to\gamma} \approx 1.5 \times 10^{-6}$) for $E = 10$ keV ($E = 80$ keV), assuming $g_{a\gamma\gamma} = 10^{-12}$ GeV^{-1} and $m_a \ll 10^{-11}$ eV. We note that the conversion probabilities are over 10 times larger in the PTKN11 model (see the Appendix), since there is destructive interference (for $d \approx 2.6$ kpc) in the JF12 model towards Wd1. We do not account for turbulent fields in this analysis; inclusion of these fields may further increase the conversion probabilities for Wd1, although we leave this modeling for future work.

8.3 Data analysis

We reduce and analyze 39 ks of archival NuSTAR data from Quintuplet with observation ID `40010005001`. This observation was performed as part of the NuSTAR Hard X-ray Survey of the GC Region [369, 370]. The NuSTAR data reduction was performed with the HEASoft software version 6.24 [371]. This process leads to a set of counts, exposure, and background maps for every energy bin and for each exposure (we use data from both Focal Plane Modules A and B). The astrometry of each exposure is calibrated independently using the precise location of the source 1E 1743.1-2843 [372], which is within the field of view. The background maps account for the cosmic X-ray background, reflected solar X-rays, and instrumental backgrounds such as Compton-scattered gamma rays and detector and fluorescence emission lines [373]. We then stack and re-bin the data sets to construct pixelated images in each of the energy bins. We use 14 5-keV-wide energy bins between 10 and 80 keV. We label those images $d_i = \{c_i^p\}$, where c_i^p stands for the observed counts in energy bin i and pixel p. The pixelation used in our analysis is illustrated in Fig. 10.2.

For the Wd1 analysis we reduced Focal Plane Module A and B data totaling 138 ks from observation IDs 80201050008, 80201050006, and 80201050002. This set of observations was performed to observe outburst activity of the Wd1 magnetar CXOU J164710.2–45521 [374], which we mask at $0.5'$ in our analysis. (The magnetar is around 1.5' away from the cluster center.) Note that in [374] hard X-ray emission was only detected with the NuSTAR data from 3 - 8 keV from CXOU J164710.2–45521 – consistent with this, removing the magnetar mask does not affect our extracted spectrum for the SSC above 10 keV. We use the magnetar in order to perform astrometric calibration of each exposure independently. The Wd1 exposures suffer from ghost-ray contamination [375] from a nearby point source that is outside of the NuSTAR field of view at low energies (below ∼15 keV) [374]. (Ghost-ray contamination refer to those photons that reflect only a single time in the mirrors.) The ghost-ray contamination affects our ability to model the background below 15 keV and so we remove the 10 - 15 keV energy bin from our analysis.

In each energy bin we perform a Poissonian template fit over the pixelated data to constrain the number of counts that may arise from the template associated with axion emission from the SSC. To construct the signal template we use a spherically-symmetric approximation to the NuSTAR PSF [376] and we account for each of the stars in the SSC individually in terms of spatial location and expected flux, which generates a non-spherical and extended template. We label the set of signal templates by S_i^p. We search for emission associated with the signal templates by profiling over background emission. We use the set of background templates described above and constructed when reducing the data, which we label B_i^p.

Given the set of signal and background templates we construct a Poissonian likelihood in each energy bin:

$$p_i(d_i|\{S_i, A_B\}) = \sum_p \frac{(\mu_i^p)^{c_i^p} e^{-\mu_i^p}}{c_i^p!}\,, \tag{8.1}$$

with $\mu_i^p = S_i S_i^p + A_B B_i^p$. We then construct the profile likelihood $p_i(d_i|\{S_i\})$ by maximizing the log likelihood at each fixed S_i over the nuisance parameter A_B. Note that when constructing the profile likelihood we use the region of interest (ROI) where we mask pixels further than 2.0' from the SSC center. The 90% containment radius of NuSTAR is ∼1.74', independent of energy, as indicated in Fig. 10.2. We use a localized region around our source to minimize possible systematic biases from background mismodeling. However, as we show in the Appendix our final results are not strongly dependent on the choice of ROI. We also show in the Appendix that if we inject a synthetic axion signal into the real data and analyze the hybrid data, we correctly recover the simulated axion parameters.

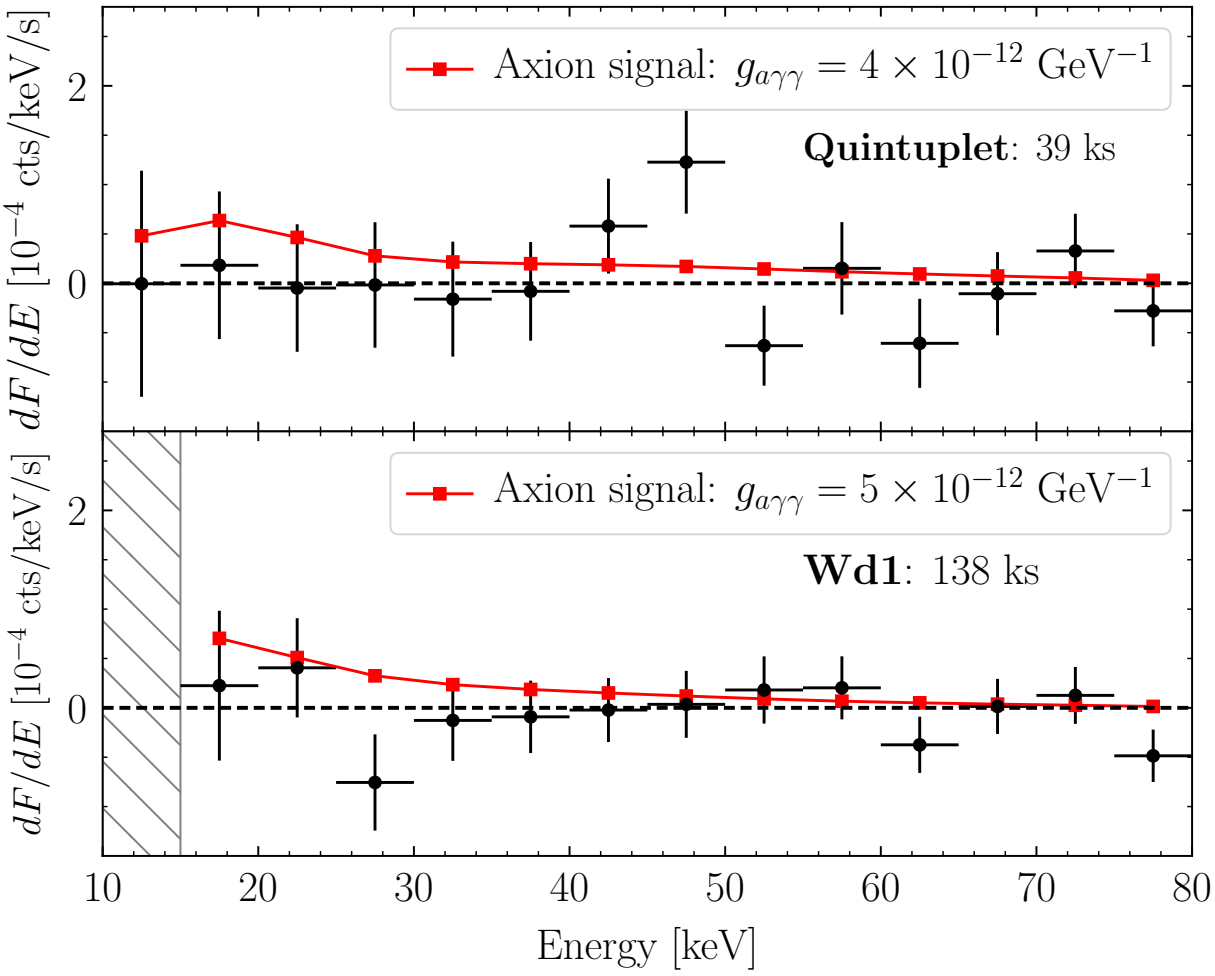

Figure 8.2: The spectra associated with the axion-induced templates from the Quintuplet and Wd1 SSCs constructed from the NuSTAR data analyses, with best-fit points and 1σ uncertainties indicated. In red we show the predicted spectra from an axion with $m_a \ll 10^{-11}$ eV and indicated $g_{a\gamma\gamma}$. Note that for Wd1 we do not analyze the 10 - 15 keV energy bin because of ghost-ray contamination.

The best-fit flux values and 1σ uncertainties extracted from the profile likelihood procedure are illustrated in Fig. 8.2 for the Quintuplet and Wd1 data sets. We compare the spectral points to the axion model prediction to constrain the axion model. More precisely, we combine the profile likelihoods together from the individual energy bins to construct a joint likelihood that may be used to search for the presence of an axion signal: $p(d|\{m_a, g_{a\gamma\gamma}\}) = \prod_i p_i\big[d_i|R_i(m_a, g_{a\gamma\gamma})\big]$, where $R_i(m_a, g_{a\gamma\gamma})$ denotes the predicted number of counts in the i^{th} energy bin given an axion-induced X-ray spectrum with axion model parameters $\{m_a, g_{a\gamma\gamma}\}$. The values $R_i(m_a, g_{a\gamma\gamma})$ are computed using the forward-modeling matrices constructed during the data reduction process.

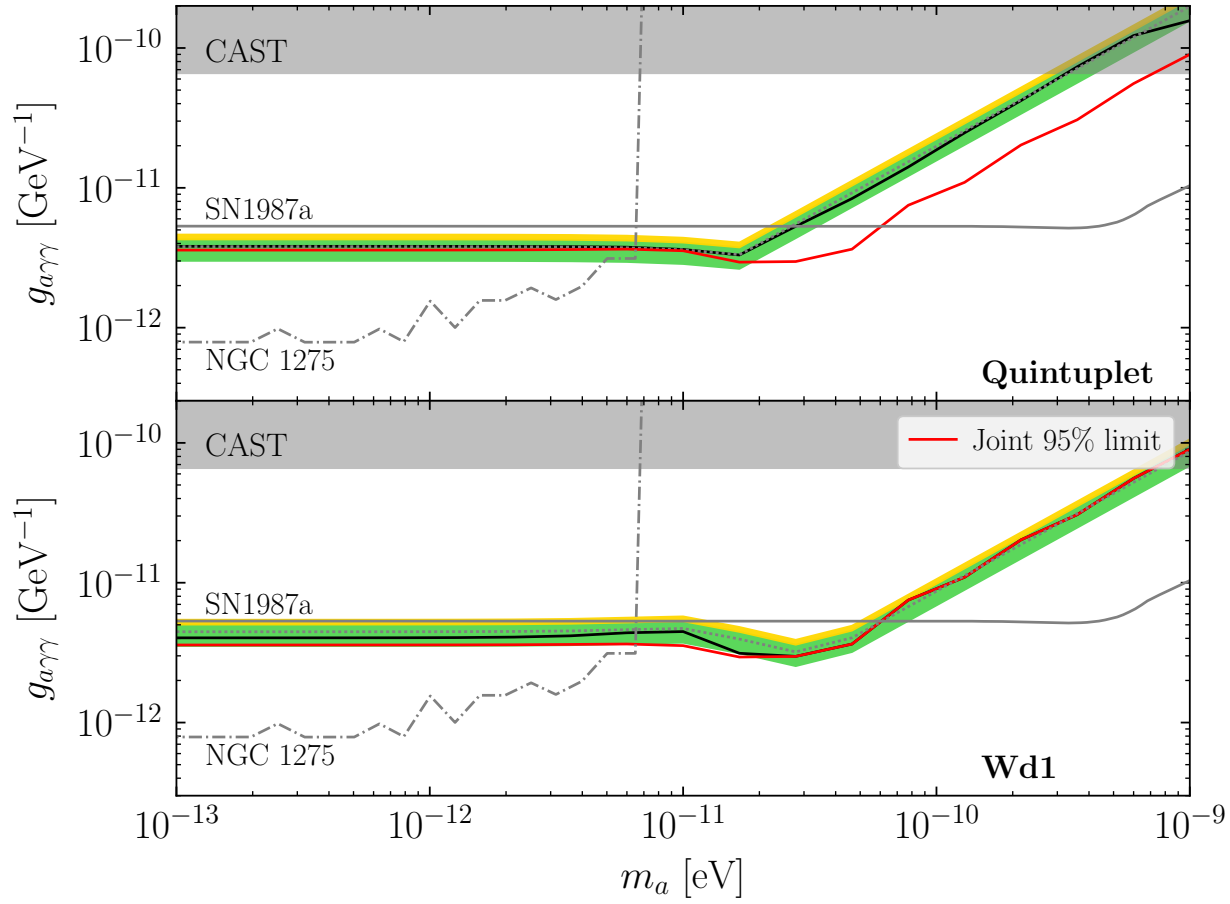

Figure 8.3: The 95% upper limits (black) on $g_{a\gamma\gamma}$ as a function of the axion mass from the Quintuplet and Wd1 data analyses. We compare the limits to the 1σ (green band) and 2σ (yellow band) expectations under the null hypothesis, along with the median expectations (dotted). The joint 95% upper limit, combining Quintuplet and Wd1, is also indicated (expected joint limit not shown). At low masses our limits may be surpassed by those from searches for X-ray spectral modulations from NGC 1275 [37], though we caution that those limits have been called into question recently, as discussed further in the text [38].

In Fig. 8.3 we illustrate the 95% power-constrained [110] upper limits on $g_{a\gamma\gamma}$ as a function of the axion mass m_a found from our analyses. The joint limit (red in Fig. 8.3), combining the Quintuplet and Wd1 profile likelihoods, becomes $g_{a\gamma\gamma} \lesssim 3.6 \times 10^{-12}$ GeV^{-1} at low axion masses. At fixed m_a the upper limits are constructed by analyzing the test statistic $q(g_{a\gamma\gamma}|m_a) \equiv 2\ln p(d|\{m_a, g_{a\gamma\gamma}\}) - 2\ln p(d|\{m_a, \bar{g}_{a\gamma\gamma}\})$, where $\bar{g}_{a\gamma\gamma}$ is the signal strength that maximizes the likelihood, allowing for the possibility of negative signal strengths as well. The 95% upper limit is given by the value $g_{a\gamma\gamma} > \bar{g}_{a\gamma\gamma}$ such that $q(g_{a\gamma\gamma}|m_a) \approx 2.71$ (see, *e.g.*, [109]). The 1σ and 2σ expectations for the 95% upper limits under the null hypothesis, constructed from the Asimov procedure [109], are also shown in Fig. 8.3. The evidence in

favor of the axion model is $\sim 0.3\sigma$ (0σ) local significance at low masses for Quintuplet (Wd1).

We compare our upper limits with those found from the CAST experiment [27], the non-observation of gamma-rays from SN1987a [40] (see also [189, 212, 377] along with [329], who recently questioned the validity of these limits), and the NGC 1275 X-ray spectral modulation search [37]. It was recently pointed out, however, that the limits in [37] are highly dependent on the intracluster magnetic field models and could be orders of magnitude weaker, when accounting for both regular and turbulent fields [38]. The CAST limits are stronger than ours for $m_a \gtrsim 10^{-9}$ eV and rely on less modeling assumptions, since CAST searches for axions produced in the Sun, though we have made conservative choices in our stellar modeling.

8.4 Discussion

We present limits on the axion-photon coupling $g_{a\gamma\gamma}$ from a search with NuSTAR hard X-ray data for axions emitted from the hot, young stars within SSCs and converting to X-rays in the Galactic magnetic fields. We find the strongest limits from analyses of data towards the Quintuplet and Wd1 clusters. Our limits represent some of the strongest and most robust limits to-date on $g_{a\gamma\gamma}$ for low-mass axions. We find no evidence for axions. Promising targets for future analyses could be nearby supergiant stars, such as Betelgeuse [338, 378], or young NSs such as Cas A.

Chapter 9

Upper Limit on the QCD Axion Mass from Isolated Neutron Star Cooling

For the first time in this thesis we discuss a search for the quantum chromodynamics (QCD) axion, which is a well-motivated beyond-the-Standard-Model particle candidate that may explain the absence of the neutron electric dipole moment [161–164] and the dark matter (DM) in our Universe [304–306]. However, the axion remains remarkably unconstrained experimentally and observationally, despite nearly 45 years of effort dedicated to axion searches (see [379] for a review). The QCD axion is primarily characterized by its decay constant f_a, which sets both its mass [380] $m_a \approx 5.7\ \mu\text{eV}\left(10^{12}\,\text{GeV}/f_a\right)$ and its interaction strengths with matter. Requiring f_a below the Planck scale implies $m_a \gtrsim 10^{-12}$ eV. The axion mass is currently bounded from above by supernova (SN) and stellar cooling constraints at the level of tens of meV, subject to model dependence and astrophysical uncertainties that are discussed further below. This chapter aims to improve upon these upper bounds by studying the cooling of old neutron stars (NSs) with ages $\sim 10^5$–10^6 yrs.

The NS constraints presented in this chapter are part of a broader effort to probe the QCD axion over its full possible mass range. Black hole superradiance disfavors QCD axion masses $m_a < 2 \times 10^{-11}$ eV [166, 381, 382], while the ADMX experiment has reached sensitivity to Dine-Fischler-Srednicki-Zhitnitsky (DFSZ) [174, 175] QCD axion DM over the narrow mass range $m_a \sim 2.66$–$3.31\ \mu$eV by using the axion-photon coupling [47, 48]. Apart from these constraints, and additional narrow-band constraints from the ADMX [383] and HAYSTAC [384] experiments at the level of the more strongly-coupled Kim-Shifman-Vainshtein-Zakharov (KSVZ) [177, 178] axion, there is nearly a decade of orders of magnitude of parameter space open for the axion mass that is un-probed at present. On the other hand, near-term plans exist to cover experimentally most of the remaining parameter space for QCD axion DM, including ABRACADABRA [45, 46, 203], DM-Radio [206], and CASPEr [207, 385, 386] at

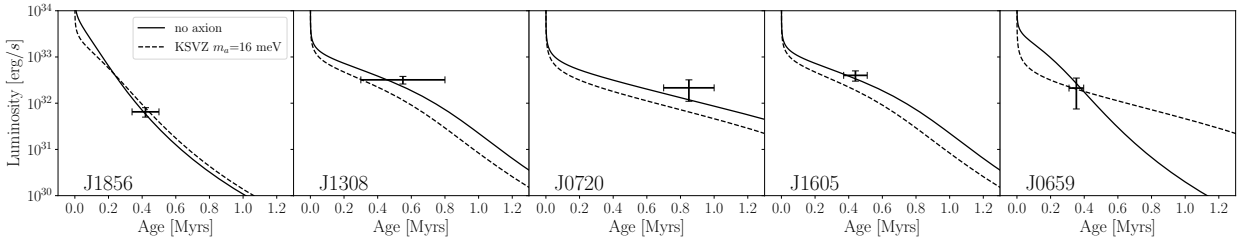

Figure 9.1: The luminosity and age data for each of the NSs considered in this chapter (see Tab. 9.1). We show the best-fit cooling curves computed in this chapter for each of these NSs under the null hypothesis and with the axion mass fixed to $m_a = 16$ meV, which is our 95% upper limit on the QCD axion mass in the context of the KSVZ model.

axion masses $m_a \ll \mu$eV, ADMX and HAYSTAC at axion masses $m_a \sim 1$–100 μeV, and MADMAX and plasma haloscopes at masses $\sim$40–400 μeV [315, 387]. However, astrophysical searches such as that presented in this chapter play an important role in constraining higher axion masses near and above the meV scale. Axions with $m_a \gtrsim$ meV are difficult to probe in the laboratory, even under the non-trivial assumption that the axion is DM (but see [388–390] for proposals). While it was previously thought that the QCD axion cannot explain the entirety of DM at masses at and above $\sim$meV masses, this assumption has been challenged recently (see, *e.g.*, [391, 392]), further motivating the search for meV-scale axions.

The fundamental idea behind how axions may modify NS cooling is that these particles, just like neutrinos [393], may be produced in thermal scattering processes within the NS cores and escape the stars due to their weak interactions [300, 394]. Most previous studies of axion-induced NS cooling have focused on either proto-NSs, like that from SN 1987A [189, 395–398], that are seconds old or young NSs like Cas A [297, 399–403], which has an age $\sim$300 yrs. In this chapter we show that robust and competitive constraints on m_a may be found from analyses of older NS cooling, focusing on NSs with ages $\sim 10^5$–10^6 yrs (see [298, 299] for related studies of older NSs). This is important when considering the possible issues that affect the SN 1987A and Cas A constraints, such as the lack of fully self-consistent 3D simulations [395] for SN 1987A and uncertainties related to the formation of the proto-NS [329]. Axion constraints from Cas A arise by using the observed temperature drop of the young NS over the past $\sim$two decades by the *Chandra* telescope, but it was realized recently that this drop may be due in large part to a systematic evolution of the energy calibration of the detector over time [24]. Moreover, the Cas A constraints are typically derived under the assumptions of specific superfluidity and equation of state (EOS) models, which are themselves uncertain. It is clear that additional, independent probes are needed to robustly disfavor or detect the QCD axion at masses above a few meV.

9.1 Isolated NS data and modeling

In this chapter we use luminosity and kinematic age data from four of the seven Magnificent Seven (M7) NSs, which are those where kinematic age data is available (see Tab. 9.1 and Fig. 9.1 for their relevant data). We add to this list PSR J0659, identified with the Monogem Ring, as it also has an age above 10^5 yrs known from kinematic considerations [14, 404] and a thermal luminosity measurement. The NSs with ages $\sim 10^5$ yrs live at a unique era, as illustrated in Fig. 9.2, where cooling from axion bremsstrahlung emission is maximally important; at lower ages neutrino emission plays a more important role since the the neutrino (axion) emissivity scales as $\propto T^8$ (T^6) with temperature T, while at older ages the thermal surface emission dominates the energy loss. We discuss NSs with ages less than 10^5 yrs, including Cas A, in the Appendix. The age data have been determined by tracing the NSs back to their birthplaces. A measured NS orbit is run backwards in the Galactic potential and a parent stellar cluster is identified in each case. J1856 and J1308 are found to originate in the Upper Scorpius OB association [7, 405]. J0720 was likely born in the Trumpler association [325]. J1605 can be associated with a runaway former binary companion, which was disrupted in a supernova [406].

The thermal luminosity data for these NSs are measured from spectral fitting of NS surface models to the X-ray spectra. The strong magnetic fields create localized temperature inhomogeneities on the surfaces, so the total thermal luminosity is a more robust observable for our purposes since it is less affected by the temperature inhomogeneities than direct temperature measurements. For this reason we use the luminosity data in this chapter rather than surface temperature measurements [407]. Typically, one of a NS atmosphere model or a double-blackbody model is fit to the X-ray spectral data. For J1856, a thin partially ionized hydrogen atmosphere model suggests our lower luminosity bound $\sim 5 \times 10^{31}$ erg/s [278] while a double blackbody model suggests the upper bound $\sim 8 \times 10^{31}$ erg/s [324]. For J1308, the same models suggest $(3.3 \pm 0.5) \times 10^{32}$ erg/s and 2.6×10^{32} erg/s, respectively [289]. For J0720, both types of models give similar luminosities $\sim 2 \times 10^{32}$ erg/s [325]. A double blackbody fit yields the luminosity $(4 \pm 1) \times 10^{32}$ erg/s for J1605, which we adopt in our analysis [326]. The J0659 luminosity was determined with a double blackbody model including a power law, since it emits non-thermally in hard X-rays as it is a pulsar [408]. We assume Gaussian priors on the NS luminosities and ages that include all measurements at 1σ. Note that the M7 have previously been the subject of searches for axion-induced hard X-ray emission [221, 245].

In this chapter we build off of the one-dimensional NS cooling code `NSCool` [318] to simulate NS cooling curves with axion energy losses. `NSCool` solves the energy balance and transport equations in full General Relativity in the core and crust of the NS. An envelope

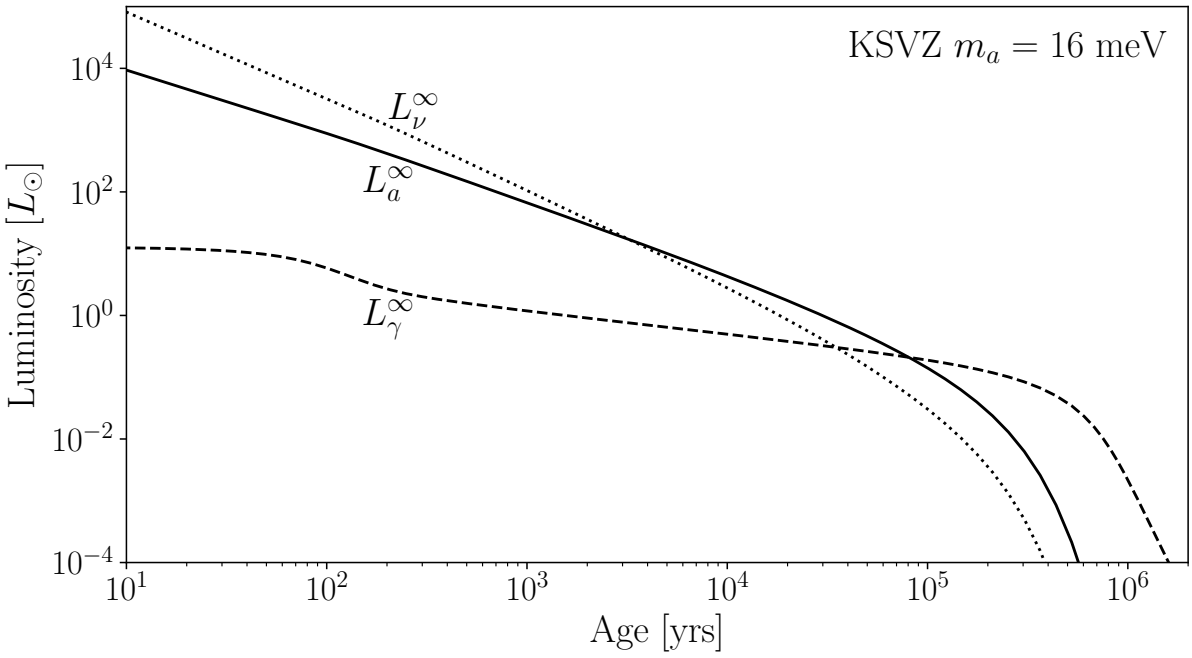

Figure 9.2: The luminosity production from neutrinos, axions, and surface radiation for an example NS with the KSVZ axion at $m_a = 16$ meV. The NS parameters have been chosen to be those found in the profile likelihood procedure for J1605 with this axion mass: the BSk22 EOS, `SBF-0-0` superfluidity model, $M_{\rm NS} = 1.0\ M_\odot$, and $\Delta M/M_\odot = 10^{-12}$.

model $T_s(T_b)$ that relates the interior and surface temperatures, T_b and T_s respectively, is glued to the exterior of the crust. After thermal relaxation, so that the NS has a uniform core temperature, integrating the energy balance equation over the interior of the NS leads to the cooling equation

$$L_\gamma^\infty = -C\frac{dT_b^\infty}{dt} - L_\nu^\infty - L_a^\infty + H\,, \tag{9.1}$$

where $L_\gamma^\infty = 4\pi R_{*,\infty}^2 (T_s^\infty)^4$ is the photon luminosity, and t is time. (Throughout this chapter, the infinity superscript will indicate that the value is taken to be that as measured by a distant observer.) The heat capacity of the NS is C, L_ν^∞ is the neutrino luminosity, L_a^∞ is the axion luminosity, and H accounts for possible heating sources, such as from magnetic field decay (see Fig. 9.2 for an illustration). Note that we include important corrections to the neutrino emissivities relative to those in `NSCool` [318], which we discuss shortly, and we also assume that $H = 0$, since magnetic field induced heating likely plays a subdominant role in constraining L_a^∞ (see the Appendix). The solution of this equation yields the NS cooling curve $L_\gamma^\infty(t, \boldsymbol{\theta})$, where $\boldsymbol{\theta}$ parameterizes the particular choices of axion and NS properties. The axion is parameterized by its mass m_a and coupling constants to nucleons, while for the NS we need to know (i) the NS mass $M_{\rm NS}$, (ii) the equation of state (EOS), (iii) the

superfluidity model $\Delta(T_b)$, and (iv) the envelope model parameterized by the mass of light elements ΔM.

The axion energy losses from nucleon scattering processes are determined by the axion-neutron and axion-proton dimensionless coupling constants C_p and C_n, respectively, in addition to f_a; the axion-nucleon interactions are of the form $\mathcal{L} \supset (C_N/2f_a)\bar{\psi}_N\gamma^\mu\gamma_5\psi_N\partial_\mu a$ with $N = p, n$, ψ_N the nucleon fields, and a the axion field. In the KSVZ axion model $C_p = -0.47 \pm 0.03$ and $C_n = -0.02 \pm 0.03$ [380], while in the DFSZ model C_p and C_n are functions of $\tan\beta$, which is the ratio of the vacuum expectation values of the up- to down-type Higgs doublets in that theory: $C_n = (-0.160 \pm 0.025) + 0.414\sin^2\beta$, $C_p = (-0.182 \pm 0.025) - 0.435\sin^2\beta$ [380]. Additional axion models are also possible [409], for which it is useful to define the dimensionless coupling constants $g_{aNN} = C_N m_N/f_a$, with m_N the nucleon mass. Note that the uncertainties on the KSVZ and DFSZ axion couplings arise from lattice QCD [380]; to make contact with previous literature we assume the central values.

When computing the axion luminosities we account for axion bremsstrahlung [300, 394] from nucleons and axion production from Cooper pair breaking and formation (PBF). If the NS core temperature is below the superfluid critical temperature, nucleons form Cooper pairs and condense into a superfluid phase. These Cooper pairs can liberate energy in the form of neutrinos [410, 411] or axions [296, 298] when breaking and forming. The PBF processes may dominate the axion luminosity at temperatures near the superfluid transition temperature, while the bremsstrahlung processes are exponentially suppressed at lower temperatures. To evaluate the axion and neutrino emission rates, for both PBF and bremsstrahlung production, we account for the medium-dependent axion-nucleon and pion-nucleon couplings [412, 413], which have not been included in earlier work on axion emission from compact stars or supernovae. These corrections are density dependent, varying throughout the interior of the star, and at the highest densities the overall effect is a $\sim$30% suppression of the axion emission rate and a $\sim$50% enhancement of the neutrino rate. See the Appendix for details.

We make one additional modification to `NSCool` to help quantify the effects of astrophysical uncertainties. The addition of light elements (hydrogen, helium, and carbon) in the NS envelope changes the expected relation between the surface and core temperatures, which in turn affects the observed surface luminosity even for the same internal state. We incorporate the analytic formulae in [414] into `NSCool` in order to cool a NS with a mass ΔM of light elements layered on top of the default iron surface. Values for ΔM can span from $0\,M_\odot$, such that the NS has a pure iron surface, to $\sim 10^{-7} M_\odot$, which is the mass of the entire envelope. In practice, we modify the equation $T_s(T_b)$ to account for the addition of light

Name	L_γ^∞ [10^{33} erg/s]	Age [Myr]	Refs
J1856	0.065 ± 0.015	0.42 ± 0.08	[278, 324, 405]
J1308	0.32 ± 0.06	0.55 ± 0.25	[7, 289]
J0720	0.22 ± 0.11	0.85 ± 0.15	[9, 325]
J1605	0.4 ± 0.1	0.44 ± 0.07	[326, 406]
J0659	0.28 ± 0.14	0.35 ± 0.044	[404, 408]

Table 9.1: The properties of the NSs considered in this chapter – RX J1856.6−3754, RX J1308.6+2127, RX J0720.4−3125, RX J1605.3+3249, PSR J0659+1414 – which we abbreviate throughout this chapter. We include all known NSs with ages above 10^5 yrs and robust age and luminosity measurements (see *e.g.* [14]). Younger NSs are discussed in the Appendix.

elements, which can change the photon luminosity of the NS by up to a factor $\sim$5 before the photon cooling stage and $\gtrsim$100 after. Since each ΔM value requires a dedicated `NSCool` simulation, we use a discrete number eight of equally log-spaced values for $\Delta M/M_\odot$ ranging from $10^{-20} M_\odot$ to $10^{-6} M_\odot$. Similarly, we discretize the NS mass range with six equally spaced masses between $1 M_\odot$ and $2 M_\odot$; we show in the Appendix that our results are not strongly dependent on this mass range.

We simulate NSs for five distinct EOSs: APR [415], BSk22, BSk24, BSk25, and BSk26 [416]. The APR EOS is constructed using variational methods to model the two-nucleon interaction incorporating the effects of many-body interactions and with the input of nucleon-nucleon scattering data. The BSk family of EOSs are generated by fitting the Skyrme effective interaction to atomic mass data. The distinct BSk EOSs are constructed with different assumed values of the Skyrme symmetry energy. These EOSs phenomenologically characterize the range of possible stiffnesses of the EOSs. Recently, data from the *NICER* telescope has allowed for the simultaneous measurements of the mass and radius of two NSs, PSR J0030 [69] and PSR J0740 [68], which can be used in conjunction with gravitational wave observations of NS mergers to constrain the EOS [68]. As we show in SM Fig. S3, only the BSk22, BSk24, and BSk25 EOS are consistent with the mass-radius data to within 1–2σ significance. We thus restrict ourselves to this set of EOS in the main chapter, though we discuss how our results change with the APR and BSk26 EOS in the Appendix.

We consider three distinct superfluidity models, denoted in `NSCool` and here as `0-0-0`, `SFB-0-0`, and `SFB-0-T73`. The first model assumes no superfluidity by setting the gaps to zero. The second model turns on the $^1S_0$ neutron pairing gap from [417], and the third model additionally turns on the $^1S_0$ proton pairing gap from [418]. Neutron $^3P_2$-$^3F_2$ pairing may also be possible (we will refer to this as $^3P_2$ for brevity), but the estimate of this gap is more complicated in part because it appears at higher density where many-body interactions are

more important (see, *e.g.*, [419]). However, in the Appendix we show that the $^3P_2$ superfluid would only increase the strength of our limit, though many $^3P_2$ gap models are inconsistent with the isolated NS data.

9.2 Data analysis and results

Given the set of cooling curves, we can compare them to the observed data in Tab. 9.1. For a given QCD axion model, under the assumption of a particular NS EOS and superfluidity model $\Delta(T_b)$, let us label the present-day luminosity of a NS by $L(m_a, \boldsymbol{\theta})$. The luminosity of NS i is then jointly determined by the axion mass m_a and the nuisance parameters $\boldsymbol{\theta}^i = \{M^i_{\rm NS}, \Delta M^i, t^i\}$ that characterize the NS. We can now write the likelihood for a single NS i as

$$\begin{aligned}\mathcal{L}_i(\boldsymbol{d}_i|m_a, \boldsymbol{\theta}^i) =& \mathcal{N}(L(m_a, \boldsymbol{\theta}^i) - L^i_0, \sigma^i_L) \\ &\times \mathcal{N}(t^i - t^i_0, \sigma^i_t)\,,\end{aligned} \tag{9.2}$$

where we have introduced the NS data set $\boldsymbol{d}_i = \{L^i_0, \sigma^i_L, t^i_0, \sigma^i_t\}$, where L^i_0 is the measured luminosity of the NS with uncertainty σ^i_L. Similarly, t^i_0 is the measured age of the NS with uncertainty σ^i_t. The probability of observing a value x under the zero-mean Gaussian distribution with standard deviation σ is denoted by $\mathcal{N}(x, \sigma)$. The joint likelihood $\mathcal{L}(\boldsymbol{d}|m_a, \boldsymbol{\theta})$ over all five NSs is constructed by taking the product of (9.2) over the NSs. Note that the total list of model parameters is denoted by $\boldsymbol{\theta} = \{\boldsymbol{\theta}^i\}^5_{i=1}$. The best-fit axion mass $\hat{m}_a$ and nuisance parameters $\hat{\boldsymbol{\theta}}$ can be determined for a given choice of EOS and superfluidity model by maximizing the joint likelihood. To test for systematic mismodeling we allow $m_a < 0$, with the axion luminosity multiplied by $\text{sign}(m_a)$.

Additionally, given the large number of nuisance parameters, many of which have non-trivial degeneracy with the signal parameter m_a, we determine the 95% upper limit on m_a, defined by m^{95}_a, by the Neyman construction of the 95% confidence interval for m_a through a Monte Carlo (MC) procedure rather than by invoking Wilks' theorem. Similarly, we determine the significance of the axion model over the null hypothesis through MC simulations of the null hypothesis, instead of relying on Wilks' theorem. (See the Appendix for details.)

For each combination of EOS and superfluidity model we determine m^{95}_a, $\hat{m}_a$, and the significance of the axion model over the null hypothesis of $m_a = 0$ meV. We choose the 95% upper limit over the ensemble of nine EOS and superfluidity combinations that gives the most conservative limit. For the KSVZ axion model we find that $m^{95}_a \approx 16$ meV with the

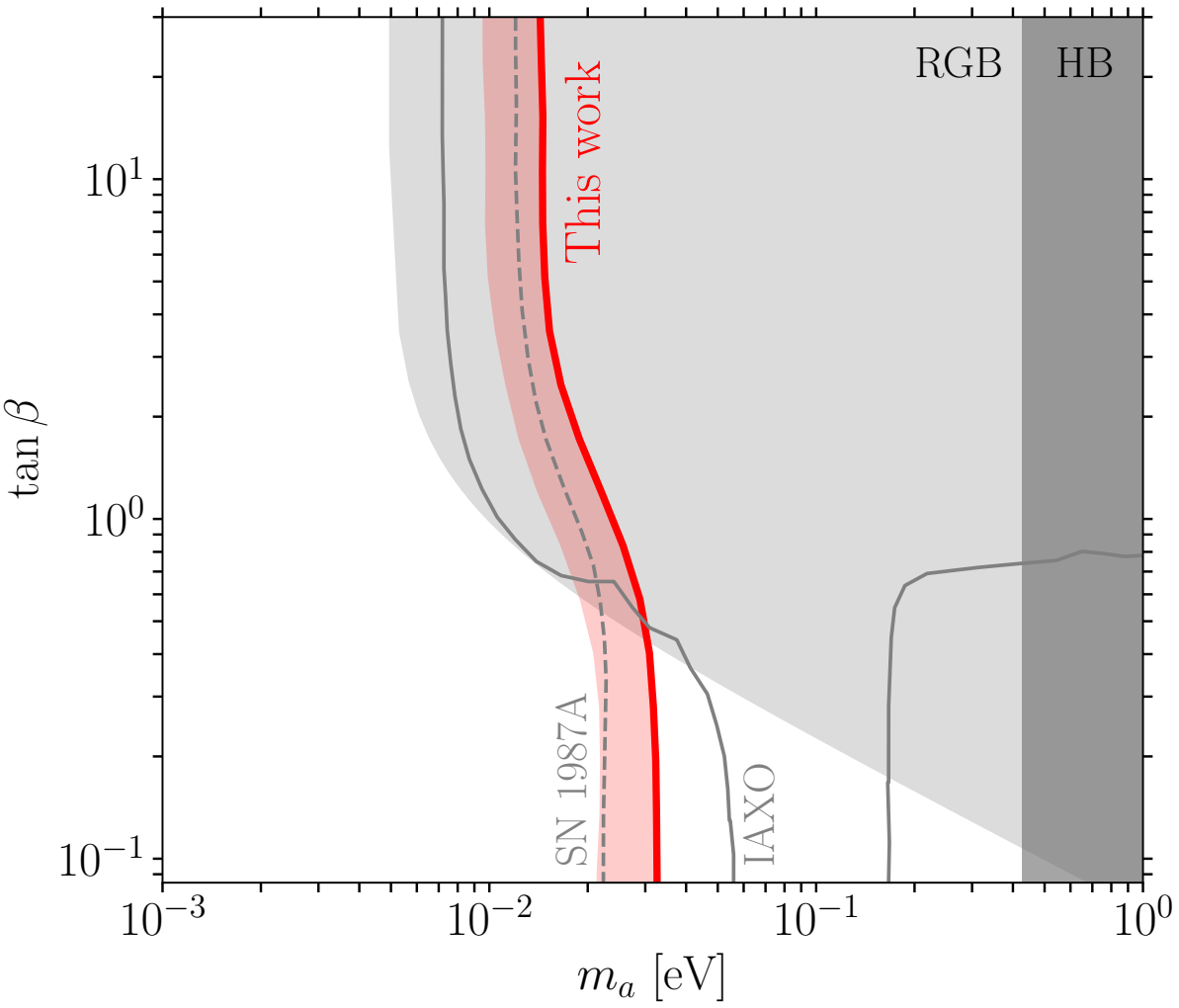

Figure 9.3: Upper limit from this chapter on the DFSZ axion mass m_a as a function of $\tan\beta$, which controls the relative coupling of the axion to neutrons and protons. The width of the shaded red band reflects the uncertainty on the upper limit by varying over superfluidity and EOS models. We compare our upper limits to existing constraints and the projected IAXO discovery sensitivity.

BSk22 EOS model and the `SFB-0-0` superfluidity model; the strongest constraint over all combinations is $m_a^{95} \approx 6$ meV with the BSk25 EOS and the `SFB-0-T73` model. With that said, the `SFB-0-T73` model is the worst fit to the data, with the best-fit axion mass being negative at $\sim 1.6\sigma$ significance. The best-fitting model is that with the BSk22 EOS and no superfluidity, for which the limit is $m_a^{95} \approx 14$ meV and the best-fit axion mass being negative at $\sim 0.36\sigma$. From these results we conclude that the NS cooling data show no evidence for the KSVZ axion and also no significant evidence for a preference for a particular EOS or superfluidity combination; the isolated NS data appear well described by the null hypothesis.

For the DFSZ axion the results depend on the value of $\tan\beta$. In Fig. 9.3 we show m_a^{95} as a function of $\tan\beta$, with the shaded band showing the range of limits found over all EOS and superfluidity combinations. DFSZ axion masses to the right of the exclusion curve are disfavored at 95% confidence. The weakest limit (bold) is achieved for all $\tan\beta$ for the no superfluidity model with the BSk22 EOS. We compare these upper limits to those from horizontal branch (HB) [28, 420], red giant branch (RGB) [31, 32], and SN 1987A [397] cooling. Note, however, that the SN 1987A limit is approximate, since *e.g.* it arises from the rough requirement $L_a^\infty < L_\nu^\infty$ for the proto-NS, and also it does not account for the density-dependent couplings for axions and neutrinos, which we estimate should weaken the SN 1987A limit by a factor ∼1.3–1.6, depending on the EOS. We also show the projected discovery reach for the future IAXO experiment [421]; our results leave open a narrow mass range ∼10 meV where IAXO may discover the QCD axion. In the axion model with only an axion-neutron (axion-proton) coupling we constrain $|g_{ann}| < 1.3 \times 10^{-9}$ ($|g_{app}| < 1.5 \times 10^{-9}$) at 95% confidence.

9.3 Discussion

In this chapter we present a search for the QCD axion from NS cooling, comparing NS cooling simulations with axions to luminosity and kinematically-determined age data from five NSs. Four of the five NSs are part of the M7, which are unique in that they only emit radiation thermally and thus have well-measured thermal luminosities. The NSs that are most important for our analysis are J0720, J1605, and J1308, as further highlighted in the Appendix.

Our upper limits disfavor at 95% QCD axions with masses $m_a \gtrsim 10-30$ meV, depending on the axion model, which constrains the axion interpretation of the previously-observed stellar cooling anomalies [33, 422]. The limits may be stronger if $^3P_2$ superfluidity is active in the NS cores, as we discuss in the Appendix, though large $^3P_2$ gaps appear disfavored by the isolated NS data. Many-body nuclear techniques should provide improved estimates of the energy gaps of the $^1S_0$ (neutron), $^1S_0$ (proton), and $^3P_2$ (neutron) pairings in the future [419]. On the other hand, more work should be done to rigorously assess the possible impact of heating mechanisms such as magnetic field decay on the axion limits, for example using fully self-consistent simulations along the lines of those in [423, 424]. Axions may also be produced from more exotic forms of matter in the NS interiors, such as hyperon superfluids and pionic and kaonic Bose Einstein condensates, and these channels should be investigated as the NS EOS and composition becomes better understood.

Chapter 10

Upper Limit on the Axion-photon Coupling from Magnetic White Dwarf Polarization

In this Chapter, we return to probing the axion solvely through its electromagnetic coupling. In particular, an axion a may interact with electromagnetism through the Lagrangian term $\mathcal{L} = g_{a\gamma\gamma} a \mathbf{E} \cdot \mathbf{B}$, where $\mathbf{E}$ and $\mathbf{B}$ are the electric and magnetic fields, respectively, and $g_{a\gamma\gamma} \propto 1/f_a$ is the coupling constant. In this chapter, we set some of the strongest constraints to-date on $g_{a\gamma\gamma}$ for low-mass axions using white dwarf (WD) polarization measurements.

Axions are notoriously difficult to probe experimentally due to their feeble interactions with the Standard Model. The most powerful approach at present to probe ultralight axions purely in the laboratory is that employed by light shining through walls experiments, which leverage the fact that photons and axions mix in the presence of strong magnetic fields; the ALPS [425] experiment has constrained $|g_{a\gamma\gamma}| \lesssim 5 \times 10^{-8}$ GeV^{-1} at 95% confidence for axion masses $m_a \lesssim$ few $\times 10^{-4}$ eV. The upcoming experiment ALPS-II [208] may reach sensitivity to $|g_{a\gamma\gamma}| \lesssim 2 \times 10^{-11}$ GeV^{-1} for a comparable mass range. Going to lower coupling values, however, requires making use of astrophysical axion sources in order to access strong magnetic fields, longer distances, and higher luminosities. For example, the CAST [27] experiment (see Fig. 10.1) has set strong constraints on $g_{a\gamma\gamma}$ by looking for axions produced in the Sun and then converting to X-rays in the magnetic field of their detector, and the followup project IAXO [426] may be able to cover significant unexplored parameter space ($|g_{a\gamma\gamma}| \lesssim 4 \times 10^{-12}$ GeV^{-1} for $m_a \lesssim 5 \times 10^{-3}$ eV). Purely astrophysical probes currently set the strongest constraints on $g_{a\gamma\gamma}$ at ultra-low axion masses. Observations of horizontal branch (HB) star cooling [28] constrain $g_{a\gamma\gamma}$ at a level comparable to CAST ($|g_{a\gamma\gamma}| \lesssim 6.6 \times 10^{-11}$ GeV^{-1}, as illustrated in Fig. 10.1, for axion masses less than the keV scale). The non-observation of

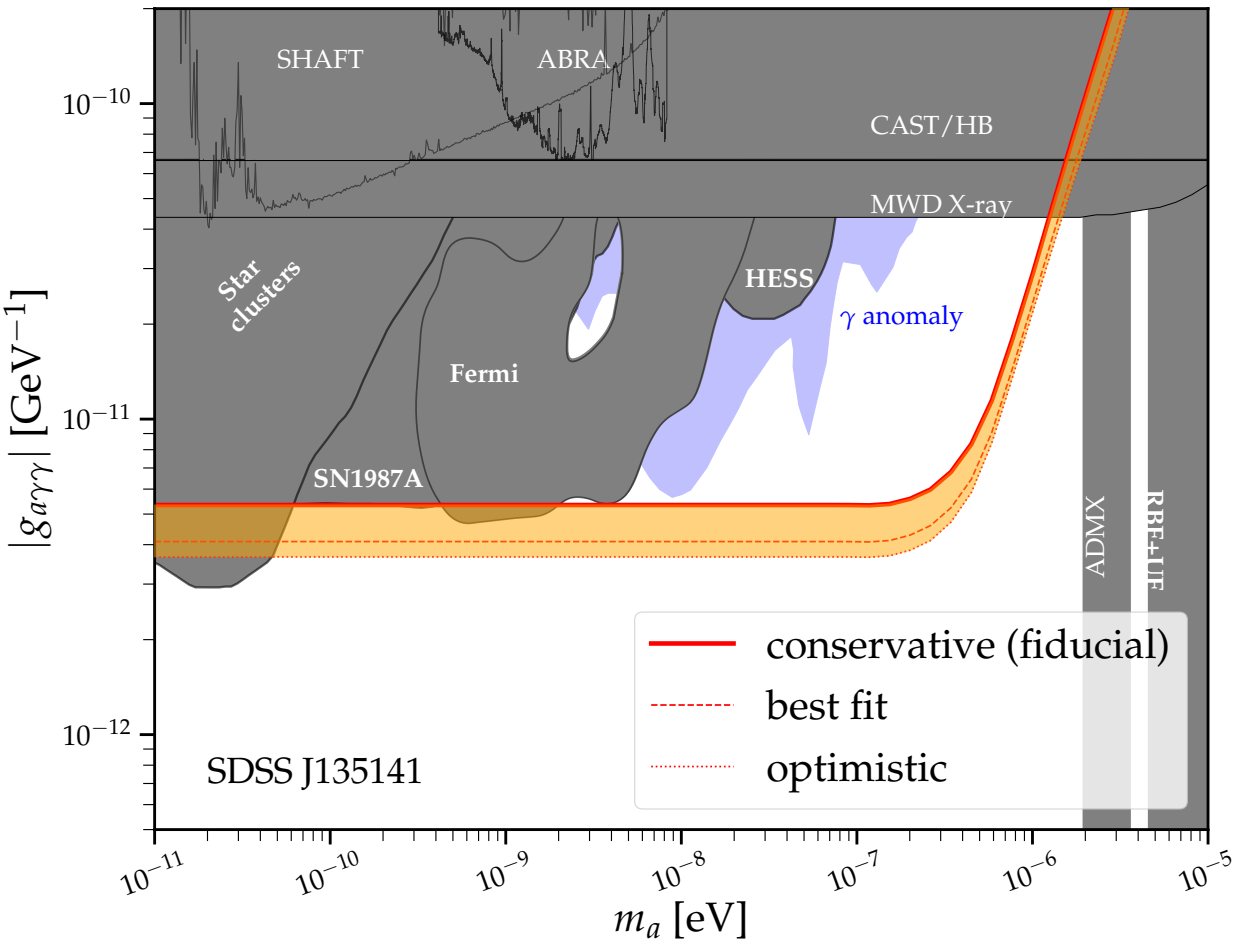

Figure 10.1: Constraints on the axion-photon coupling $g_{a\gamma\gamma}$ arise from searches for axion-induced X-rays from super star clusters [29] and a nearby MWD [39] in addition to gamma-rays from SN1987A [40], searches for spectral irregularities with Fermi-LAT [41, 42] and H.E.S.S. [43], the CAST axion helioscope [27], HB star cooling [28], and constraints from SHAFT [44], ABRACADABRA [45, 46], ADMX [47, 48], and RBF+UF [49, 50] that are contingent on the axion being dark matter. The fiducial 95% upper limit from this chapter from the non-observation of linear polarization from SDSS J135141 is computed assuming the most conservative (at 1σ) magnetic field strength, MWD radius, and orientation. The shaded orange region shows how the limits change when considering astrophysical uncertainties; the dominant uncertainty is the inclination angle. The limit found using the best-fit astrophysical parameters for the MWD is also indicated.

gamma-rays from SN1987A — which would be produced from Primakoff production in the supernova core and converted to photons in the Galactic magnetic fields — leads to the limit $|g_{a\gamma\gamma}| \lesssim 5.3 \times 10^{-12}$ GeV^{-1} for $m_a \lesssim 4.4 \times 10^{-10}$ eV [40] (but see [329]). The non-observation of X-rays from super star clusters, which may arise from axion production in the stellar cores and conversion in Galactic magnetic fields, leads to the limit $|g_{a\gamma\gamma}| \lesssim 3.6 \times 10^{-12}$

GeV^{-1} for $m_a \lesssim 5 \times 10^{-11}$ eV [29]. Ref. [37] claims to constrain $|g_{a\gamma\gamma}| \lesssim 8 \times 10^{-13}$ GeV^{-1} for $m_a \lesssim 10^{-12}$ eV using searches for X-ray spectral irregularities from the active galactic nucleus NGC 1275, though the magnetic field models in that work, and thus the resulting limits, are subject to debate [38, 427].

There are a number of astrophysical anomalies that favor axions at $|g_{a\gamma\gamma}|$ below current constraints. For example, the unexplained transparency of the Universe to TeV gamma-rays may be explained by the existence of axions with $g_{a\gamma\gamma} \sim 10^{-12} - 10^{-10}$ GeV^{-1} and $m_a \sim 10^{-9} - 10^{-8}$ eV (see Fig. 10.1) [244, 428–432] (but see [433, 434]). The high-energy gamma-rays would convert to axions in the magnetic fields surrounding the active galactic nuclei sources and then reconvert to photons closer to Earth in the inter-galactic magnetic fields, effectively reducing the attenuation of gamma-rays caused by pair-production off of the extragalactic background light. The gamma-ray transparency anomalies are constrained in-part by searches for spectral irregularities from gamma-ray sources with the H.E.S.S [43] and Fermi-LAT [41, 42] telescopes (but see [38]).

Magnetic WDs (MWDs) are natural targets for axion searches because of their large magnetic field strengths, which can reach up to $\sim 10^9$ G at the surface. Ref. [39] recently constrained the coupling combination $|g_{a\gamma\gamma} g_{aee}|$, with g_{aee} the axion-electron coupling, using a *Chandra* X-ray observation of the MWD RE J0317-853. Axions would be produced from electron bremsstrahlung within the MWD cores and then converted to X-rays in the magnetosphere. Depending on the relation between g_{aee} and $g_{a\gamma\gamma}$ the constraint on $g_{a\gamma\gamma}$ alone could vary from $|g_{a\gamma\gamma}| \lesssim \text{few} \times 10^{-13}$ GeV^{-1} to $|g_{a\gamma\gamma}| \lesssim 4.4 \times 10^{-11}$ GeV^{-1} for $m_a \lesssim 5 \times 10^{-6}$ eV; the most conservative constraint from that work is illustrated in Fig. 10.1. (See [179, 180, 221, 227] for similar searches using neutron stars (NSs) as targets.) Note that WD cooling provides one of the most sensitive probes of the axion-electron coupling alone, since the axions produced by bremsstrahlung within the stellar cores provide an additional pathway for the WDs to cool [167].

Refs. [223, 435] were the first to propose using MWD polarization measurements to constrain $g_{a\gamma\gamma}$. The basic idea behind this proposal, which is the central focus of this chapter, is illustrated in Fig. 10.2. The MWD radiates thermally at its surface temperature. The thermal radiation is unpolarized, but it may effectively acquire a linear polarization when traversing the magnetosphere because photons polarized parallel to the transverse magnetic fields may convert to axions, which are unobserved, while the orthogonal polarization direction is unaffected. Ref. [435] claimed that MWD linear polarization measurements of the MWDs PG 1031+234 and Sloan Digital Sky Survey (SDSS) J234605+38533 may be used to constrain $|g_{a\gamma\gamma}| \lesssim (5 - 9) \times 10^{-13}$ GeV^{-1} for $m_a \lesssim \text{few} \times 10^{-7}$ eV. Here we critically reassess the upper limits from these MWDs and show that, while strong, the upper

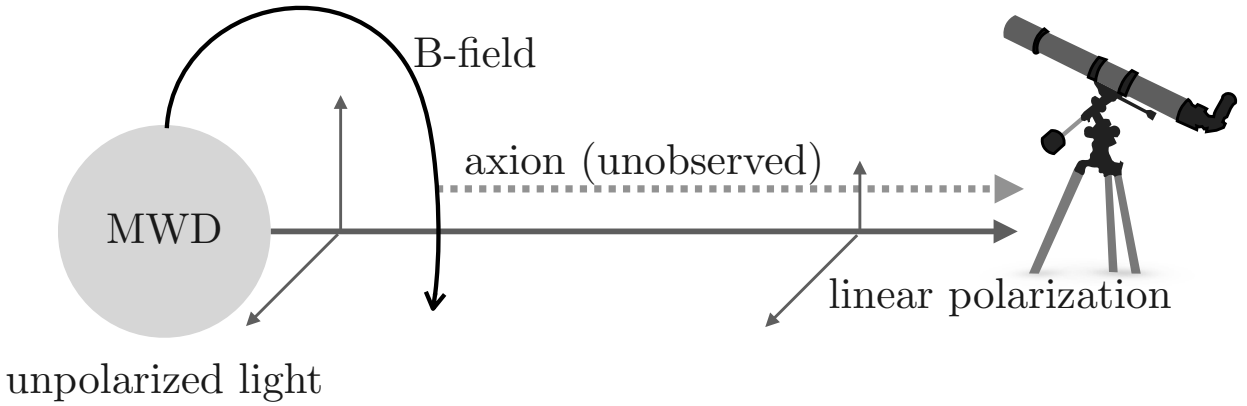

Figure 10.2: The MWD emits thermal, unpolarized light, but this light may acquire a linear polarization when traversing the magnetosphere by photon-to-axion conversion. Photons polarized along the direction of the transverse magnetic field may convert to axions, while those polarized in the orthogonal direction are unaffected. Note that the conversion process may take place well away from the MWD surface.

limits on $g_{a\gamma\gamma}$ from these MWDs are around an order of magnitude weaker than claimed in [435], when accounting for astrophysical uncertainties on the magnetic field and its geometry. Additionally, we identify two other MWDs — SDSS J135141.13+541947.4 (hereafter SDSS J135141) and Grw 70°8247 — whose linear polarization measurements lead to strong constraints on $g_{a\gamma\gamma}$. The upper limits on $g_{a\gamma\gamma}$ from this chapter represent the strongest to-date for few $\times\, 10^{-9}$ eV $\lesssim m_a \lesssim 10^{-6}$ eV. We show that the axion-induced polarization signal is determined only by the magnetic field strength and geometry far away from the MWD surface, outside of the atmosphere, where the free-electron plasma does not play an important role.

In contrast, the astrophysical polarization originates in the atmosphere from the scattering of starlight by bound and free electrons. Through a simplified radiative transfer analysis, we estimate the effect of the astrophysical polarization following standard MWD polarization modeling techniques. In particular, we extend a first-order linear Zeeman approximation of the bound-free cross-section at low ($B \ll 100$ MG) magnetic fields to the regime where the Zeeman and Coulomb interactions are comparable ($100\,\mathrm{MG} \lesssim B \lesssim 5000\,\mathrm{MG}$). This is because the exact cross sections have not yet been computed. On the other hand, we exactly account for the quadratic Zeeman shifting of hydrogen bound-state energy levels and for the quantization of free electrons into Landau levels. We find a strong frequency dependence in the astrophysical polarization that allows the astrophysical polarization to be distinguished from the relatively frequency-independent axion-induced polarization. Lastly, we identify future MWD targets whose polarization observations could further constrain $g_{a\gamma\gamma}$ or lead to

evidence for axions at currently un-probed coupling strengths. We begin, in Sec. 10.1, by outlining the formalism for how to compute the axion-induced polarization signal.

10.1 Axion-Induced Polarization

In this section we outline the formalism for computing polarization signals from astrophysical sources due to axion-photon mixing. While we ultimately focus on MWDs in this chapter, we begin with a more general survey of possible astrophysical targets. The basic idea behind this chapter is to focus on sources where the initial electromagnetic emission is known to be unpolarized but where the radiation must traverse regions of large magnetic field strengths before reaching Earth. Since photons polarized along the directions of the transverse magnetic fields may convert to axions, the presence of axions in the spectrum of nature will effectively induce a level of linear polarization whose degree depends on the strength of the axion-photon coupling. This process is illustrated for MWDs in Fig. 10.2, where the relevant magnetic field is that directly surrounding the MWD.

The idea of searching for axion-induced polarization signals has been discussed in three main contexts: MWDs [223,435], NSs [223,226], and quasars [436–443]. In the first two cases the star is the source of both the initially-unpolarized photons and the strong magnetic fields. In the latter case, the magnetic fields are much weaker but they act over larger distances. In this section we focus on polarization signals of the former type, where the star provides both the source of photons and magnetic fields, but first we briefly discuss the results of the quasar searches. Ref. [441] claims to constrain $|g_{a\gamma\gamma}| \lesssim \text{few} \times 10^{-13}$ GeV^{-1} for $m_a \lesssim \text{few} \times 10^{-14}$ eV in order to not overproduce the measured optical polarization signals from distant quasars; this upper limit would be the most stringent to-date on low mass axions. However, the results in [441] are dependent on the strength of the assumed magnetic fields and plasma density profiles over distances $\sim$20 Mpc away from the sources. Ref. [441] assumed supercluster magnetic fields $\sim 2\mu$G in strength and coherent over $\sim$100 kpc distances within 20 Mpc of the quasars. On the other hand, simulations of supercluster magnetic fields [444–448] find that the fields are filamentary and typically orders of magnitude smaller than those assumed in [441] at such large distances away from the clusters. The field strengths increase in the clusters themselves, but so too does the free-electron density, which suppresses photon-to-axion conversion. At present it seems likely that our knowledge of the supercluster-scale magnetic fields and plasma density profiles are not robust enough to claim a bound on $g_{a\gamma\gamma}$, which is why we focus on stellar sources for which the magnetic field profiles may be measured more precisely using *e.g.* the Zeeman effect and for which, as we will show, knowledge of the free-electron density is not necessary.

10.1.1 Analytic aspects of axion-induced polarization

Consider an unpolarized monochromatic beam of photons with frequency ω propagating through a medium with magnetic field profile $\mathbf{B}(s)$ and plasma-frequency profile $\omega_{\rm pl}(s)$, with s the distance along the propagation direction. The plasma frequency is sourced by free electrons for our purposes. We will track the Stokes parameters, which in terms of the complex electric field $\mathbf{E}$ are defined by

$$\begin{aligned} I &= |E_1|^2 + |E_2|^2\,, \qquad Q = |E_1|^2 - |E_2|^2 \\ U &= 2{\rm Re}\,(E_1 E_2 *)\,, \qquad V = -2{\rm Im}\,(E_1 E_2 *)\,, \end{aligned} \tag{10.1}$$

with $\mathbf{x}_1 - \mathbf{x}_2$ the transverse directions to the propagation direction $\mathbf{x}_3$. The linear polarization fraction is conventionally defined by

$$L_p \equiv \frac{\sqrt{Q^2+U^2}}{I}\,, \tag{10.2}$$

while the circular polarization fraction, which we will discuss less in this chapter, is $C_p \equiv V/I$. The linear polarization is also specified by an angle in the $\mathbf{x}_1 - \mathbf{x}_2$ plane χ, with $\tan 2\chi = U/Q$. Note that we are interested in time-averaged quantities. Thus, implicitly when we write quantities like I and Q we are referring to $\langle I\rangle$ and $\langle Q\rangle$, where the brackets refer to time averages over intervals much longer than $2\pi/\omega$.

As a first example let us consider the simple case of a static magnetic field $\mathbf{B} = B_0\mathbf{x}_2$ extending over a length L in the $\mathbf{x}_3$ direction, such that $s \in (0, L)$. We also take $\omega_{\rm pl}(s) = \omega_{\rm pl}$ to be independent of distance. The point of this exercise is to gain familiarity with how competing effects contribute to L_p before turning to the case of interest of conversion in stellar magnetospheres. Under the assumption that the photon wavelength is much smaller than the length L ($2\pi/\omega \ll L$), one may use a WKB approximation (see, *e.g.*, [173]) to reduce the second-order axion-photon mixing equations to first-order mixing equations:

$$\left[i\partial_s + \begin{pmatrix} \Delta_{||} + \Delta_{\rm pl} & \Delta_B \\ \Delta_B & \Delta_a \end{pmatrix}\right] \begin{pmatrix} A_2 \\ a \end{pmatrix} = \mathbf{0}\,, \tag{10.3}$$

with $A_2 = E_2/(i\omega)$ the corresponding component of the vector potential in Weyl gauge ($A_0 = 0$), $\Delta_a = -m_a^2/\omega$, $\Delta_{\rm pl} = -\omega_{\rm pl}^2/\omega$, $\Delta_B = g_{a\gamma\gamma}B_0/2$, and $\Delta_{||} = (7/2)\omega\xi$, with $\xi = (\alpha_{\rm EM}/45\pi)(B/B_{\rm crit})^2$, arising from the non-linear Euler-Heisenberg Lagrangian in strong-field quantum electrodynamics, with $B_{\rm crit} = m_e^2/e \approx 4.41\times 10^{13}$ G [449].

Throughout this chapter we are interested in the weak mixing regime where the photon-

to-axion conversion probabilities ($p_{\gamma\to a}$) and axion-to-photon probabilities ($p_{a\to\gamma}$) are much less than unity, so that we may work to leading non-trivial order in $g_{a\gamma\gamma}$. We may then solve (10.3) in perturbation theory, treating the Δ_B mixing term as a perturbation, since without this term the mixing matrix in (10.3) is diagonal. We consider the initial state, at $s = 0$, to be specified by the vector potential $\mathbf{A} = (A/\sqrt{2})\,(a_1\hat{\mathbf{x}}_1 + a_2\hat{\mathbf{x}}_2)$ for an arbitrary real A, where a_1 and a_2 are complex random variables that obey the relations: $\langle a_1 a_1 * \rangle = \langle a_2 a_2 * \rangle = 1$, with $\langle a_1 a_1 \rangle = \langle a_2 a_2 \rangle = \langle a_1 a_2 \rangle = \langle a_1 a_2 * \rangle = 0$. Referring to (10.1), and recalling that all such quantities are subject to expectation values $\langle \dots \rangle$, we see that at $s = 0$ we have $I = A^2$, while $Q = U = V = 0$, implying that the initial state is unpolarized. The perturbative solution to the equations of motion at $s > 0$ is then, up to unimportant phases and to second-order in perturbation theory,

$$\mathbf{A}(s) = \frac{A}{\sqrt{2}}\left[a_1\hat{\mathbf{x}}_1 + a_2\hat{\mathbf{x}}_2\left(1 - \int_0^s ds\Delta_B \int_0^{s'} ds''\Delta_B e^{-i\int_0^{s''} ds'''\Delta_{\rm tr}}\right)\right], \tag{10.4}$$

where in general (10.4) would hold even if the mixing terms were s-dependent, though they are not in this simple example. Note that we have defined $\Delta_{\rm tr} \equiv \Delta_{||} + \Delta_{\rm pl} - \Delta_a$. Performing the integration in (10.4) out to $s = L$ we find that

$$\begin{aligned} I &= A^2\left(1 - \frac{\Delta_B^2[1-\cos(L\Delta_{\rm tr})]}{\Delta_{\rm tr}^2}\right), \\ L_p &= \frac{\Delta_B^2}{\Delta_{\rm tr}^2}[1-\cos(L\Delta_{\rm tr})], \\ C_p &= 0, \end{aligned} \tag{10.5}$$

to leading non-trivial order in Δ_B, with the polarization angle $\chi = 0$. Note that by the same logic the axion-to-photon conversion probability, for a pure initial axion state, is given by

$$p_{a\to\gamma} = \left|\int_0^L ds'\Delta_B e^{-i\int_0^{s'} ds''\Delta_{\rm tr}}\right|^2 = 2\frac{\Delta_B^2}{\Delta_{\rm tr}^2}[1-\cos(L\Delta_{\rm tr})], \tag{10.6}$$

such that we may infer, at least for this example, that $L_p = p_{a\to\gamma}/2$ to leading order in Δ_B. This should not be surprising in light of the physical picture of the underlying mechanism that produces the linear polarization. The photons polarized in the $\hat{\mathbf{x}}_1$ direction are unaffected by the axion. However, those in the $\hat{\mathbf{x}}_2$ direction have a probability to convert to axions, $p_{\gamma\to a}$, which is equal to $p_{a\to\gamma}$. The photon survival probability is then $p_{\gamma\to\gamma} = 1 - p_{a\to\gamma}$. Then, referring to (10.1) and (10.2), it is clear that $L_p = p_{a\to\gamma}/2$.

There are a few interesting points to be made about the expression for L_p. If $|L\Delta_{\rm tr}| \ll 1$

then $L_p \approx \frac{1}{2}\Delta_B^2 L^2$; the quadratic growth of L_p with L is related to the fact that the axion and photon remain in-phase during the mixing. As $|L\Delta_{\rm tr}|$ becomes comparable to and greater than unity we begin to notice the different dispersion relations between the axion and photon over the distance L. The difference of dispersion relations suppresses mixing. Indeed, one surprising aspect of (10.5) is that if we assume $|\Delta_{||}| \gg |\Delta_a|, |\Delta_{\rm pl}|$ and $L|\Delta_{||}| \gg 1$, which would be the case appropriate for photons propagating over a large distance through a strongly magnetized region with low plasma density and an ultra-light axion in the spectrum, then the dependence of L_p on B_0 is $L_p \propto 1/B_0^2$. This is surprising because it suggests that when the Euler-Heisenberg term dominates $\Delta_{\rm tr}$, strong magnetic fields actually suppress mixing compared to weaker magnetic fields.

Let us now generalize the example above to consider dipole magnetic fields. This is instructive because the magnetic fields surrounding many stars, such as the MWDs that are the main topic of this chapter but also the fields surrounding NSs and to a large extent main sequence stars as well, may be described – at least to first approximation – by dipole fields. Indeed, at distances far away from the star the field should approach that of a dipole, since the higher multipole field components fall off faster with distance. Let us assume that the star has a radius $R_{\rm star}$ such that unpolarized emission radiates from the surface and then propagates to infinity. For the purpose of this example we will assume that $\mathbf{B}(s) = B_0 \hat{\mathbf{x}}_2 [R_{\rm star}/(R_{\rm star}+s)]^3$, and we will compute L_p with $s \to \infty$. This magnetic field profile is that seen by radial emission at the magnetic equator, where $\mathbf{B}(s)$ remains perpendicular to the propagation direction for all s. Moreover, we will make the assumption for this example that $|\Delta_{||}|$ dominates $\Delta_{\rm tr}$, which is the case appropriate for low-mass axions and low plasma densities. In this case we may use (10.4) to compute, to leading non-trivial order in Δ_B,

$$\begin{aligned} L_p \approx & 1.4 \times 10^{-4} \left(\frac{g_{a\gamma\gamma}}{10^{-12}\ \text{GeV}^{-1}}\right)^2 \left(\frac{B_0}{100\ \text{MG}}\right)^{2/5} \left(\frac{1\ \text{eV}}{\omega}\right)^{4/5} \left(\frac{R_{\rm star}}{0.01\ R_\odot}\right)^{6/5} \times \\ & \frac{\text{Abs}\left\{\text{Re}\left[(-1)^{2/5} e^{-i\frac{7}{10}R_{\rm star}\xi_0\omega}\left(\Gamma\left(\frac{4}{5}\right) - \Gamma\left(\frac{4}{5}, -\frac{7}{10}iR_{\rm star}\xi_0\omega\right)\right)\right]\right\}}{0.022}, \end{aligned} \tag{10.7}$$

with ξ_0 denoting the value at the surface such that

$$R_{\rm star}\xi_0\omega \approx 9 \cdot 10^{-3} \left(\frac{R_{\rm star}}{0.01\,R_\odot}\right)\left(\frac{\omega}{1\,\text{eV}}\right)\left(\frac{B_0}{100\,\text{MG}}\right)^2. \tag{10.8}$$

Note that when $R_{\rm star}\xi_0\omega \ll 1$, which is a limit applicable to many MWD in this chapter, we

may expand (10.7) to write

$$L_p \approx 1.4 \times 10^{-4} \left(\frac{g_{a\gamma\gamma}}{10^{-12}\ \mathrm{GeV}^{-1}}\right)^2 \left(\frac{B_0}{100\ \mathrm{MG}}\right)^2 \times \left(\frac{R_{\rm star}}{0.01\ R_\odot}\right)^2 , \qquad R_{\rm star}\xi_0\omega \ll 1 \,. \quad (10.9)$$

On the other hand, when $R_{\rm star}\xi_0\omega \gg 1$, the term appearing in the second line of (10.7) oscillates, with a typical magnitude around unity. That is, at very large magnetic field values, when the Euler-Heisenberg term dominates, $L_p \propto B_0^{2/5}$, while in the low-field limit the polarization scales more rapidly with magnetic field as $L_p \propto B_0^2$.

There are a number of important points to be made regarding the formulae (10.7) and (10.9). The MWDs in this chapter will have field values $\lesssim$1000 MG, and we will typically be considering energies $\omega \sim$ eV; thus, except in extreme cases – such as high energies and high field values – the Euler-Heisenberg term will not significantly affect L_p. On the other hand, consider the searches in [39,450] for hard X-rays arising from axion production in the cores of MWDs and converting to photons in the magnetospheres. In those works the typical axion energies are $\omega \sim$ keV, and thus we see that for the same MWDs the Euler-Heisenberg term is important to accurately describe the axion-to-photon conversion at those energies. On the other hand, consider an optical polarization signal arising from a strongly magnetic NS, with $R_{\rm star} \sim 10$ km, $\omega \sim$ eV, and $B_0 \sim 10^{14}$ G. Since $R_{\rm star}\xi_0\omega \gg 1$ in that case we may infer that $L_p \approx 5 \times 10^{-5} (g_{a\gamma\gamma}/10^{-12}\ \mathrm{GeV}^{-1})^2$. Additionally, NS surface temperatures are typically much larger than an eV, with $\omega \sim 100$ eV being a more appropriate reference energy, which further suppresses L_p. We thus arrive at the surprising conclusion that despite their lower magnetic field values, MWDs are more powerful probes of ultralight axions, with polarization probes, than NSs because the Euler-Heisenberg term suppresses axion-photon mixing in NS magnetospheres.

We may also use (10.9) to verify that MWDs are more efficient at producing linear polarization than non-compact stars. The Sun, for example, has a dipole magnetic field strength $B_0 \sim 10$ G. Thus, for unpolarized emission emanating from the non-active Sun we expect $L_p \sim 10^{-14} \left(g_{a\gamma\gamma}/10^{-12}\ \mathrm{GeV}^{-1}\right)^2$. Note that one of the most magnetized non-compact stars is HD 215441, which hosts a dipole magnetic field of strength $\sim$30 kG and a radius $\sim$2 $R_\odot$ [451]. The axion-induced linear polarization fraction from this star would be $L_p \sim 5 \cdot 10^{-7} \left(g_{a\gamma\gamma}/10^{-12}\ \mathrm{GeV}^{-1}\right)^2$, which is still subdominant compared to the MWD expectation.

Indeed, we may make a general argument that, at least for $\omega \sim$ eV, strongly-magnetic MWDs are the optimal targets for axion-induced linear polarization searches. Stellar evolution approximately conserves magnetic flux across a surface far away from the star, such that the dipole field strength B_f in a final stellar evolution stage is related to the initial field

strength B_i by $B_f \approx B_i(R_i/R_f)^2$, where R_i (R_f) is the initial (final) stellar radius. Note that with this approximation we may re-scale the magnetic field of HD 215441 down to WD-radii stars ($R_{\rm star} \approx 0.01\,R_\odot$) to estimate that the most strongly magnetized MWDs should have field strengths $B \sim 1000$ MG, which is approximately correct. Similarly, using this argument we may correctly infer that NSs can reach magnetic field values $\sim 10^{15}$ G. Using the flux conservation argument and assuming that we remain in the limit where we may neglect the Euler-Heisenberg term, we may relate the final-stage axion-induced polarization fraction L_p^f to the initial-stage polarization fraction L_p^i: $L_p^f \approx L_p^i(R_i/R_f)^2$. This estimate suggests that more compact stars, such as MWDs, will be more efficient at producing axion-induced linear polarization than less compact stars. On the other hand, this argument stops being true as soon as the Euler-Heisenberg term becomes important: at that point, the larger-radius star will produce a larger L_p. As strongly-magnetic MWDs may achieve $R_{\rm star}\xi_0\omega \sim 1$, we see that these are thus the optimal targets for axion-induced polarization studies. For this reason, we will focus on these targets in this chapter.

So far we have neglected the possible effects of non-zero $\Delta_{\rm pl}$. We now justify this approximation for MWD magnetospheres. The free electron density in the interstellar medium away from the Galactic Center may be as much as $n_e \sim 10^{-1}/{\rm cm}^3$, though in the outer parts of the Galaxy near the MWDs that are studied in this chapter it is typically lower [359]. The plasma frequency associated with a free electron density $n_e = 10^{-1}/{\rm cm}^3$ is $\omega_{\rm pl} = \sqrt{4\pi\alpha_{\rm EM} n_e/m_e} \approx 10^{-11}$ eV, with m_e the electron mass. Referring back to *e.g.* (10.5), the relevant dimensionless quantity to compute to assess the importance of the plasma mass term is $|R_{\rm star}\Delta_{\rm pl}| \approx 4 \times 10^{-9}$ for the above n_e estimate, $\omega = 1$ eV, and $R_{\rm star} = 0.01 R_\odot$ appropriate for a WD. Note that the plasma mass term would be important for $|R_{\rm star}\Delta_{\rm pl}| \gtrsim 1$. Thus, even accounting for a significantly enhanced interstellar free-electron density near the MWD, it is unlikely that the $\Delta_{\rm pl}$ term would be important at optical frequencies. On the other hand, within the MWD atmosphere the free-electron density may be significantly higher, perhaps as high as $n_e \approx 10^{17}/{\rm cm}^3$ [435]. However, the MWD atmosphere is expected to have a density profile that falls exponentially with a characteristic scale height $\sim$100 m. Considering that a typical WD radius is $\sim 7 \times 10^6$ m, we see that the atmosphere only extends non-trivially over a very small fraction of the stellar radius away from the surface. The photon-to-axion conversion takes place continuously over a characteristic distance of order the MWD radius away from the stellar surface. Thus, the effect of the atmosphere on the axion-induced contribution to L_p is negligible. More precisely, the effect of the atmosphere on the conversion probability is suppressed by the ratio of the MWD atmosphere thickness to the MWD radius; this ratio is 10^{-5}.

In contrast to the axion-induced polarization signal, the standard astrophysical contribu-

tions to L_p and C_p arise solely within the atmosphere from anisotropic cyclotron absorption and bound-free transitions [452, 453]. In general, the degree of polarization is proportional to the optical depth of the atmosphere [452], so that the generation of astrophysical linear polarization is dominantly localized to within a characteristic scale height from the surface of the MWD. We discuss the astrophysical contributions to the linear polarization in Sec. 10.1.3, as they are a possible confounding background for the axion search.

Faraday rotation within the MWD magnetosphere and in the interstellar medium could in principle reduce the linear polarization fraction, though we estimate numerically that Faraday rotation is small (rotation angles up to $\sim 10^{-10}$) for nearby MWDs with $B \lesssim 10^3$ MG and free electron densities of order those in the interstellar medium.

Returning to the axion-induced polarization signal, in the limit where we may neglect the Euler-Heisenberg term, we may also integrate (10.3) for a dipole magnetic field including the Δ_a term, but neglecting $\Delta_{\rm pl}$ for the reasons given above. In this case, we find

$$L_p \approx 2 \times 10^{-8} \left(\frac{g_{a\gamma\gamma}}{10^{-12}\ \text{GeV}^{-1}}\right)^2 \left(\frac{B_0}{100\ \text{MG}}\right)^2 \times \left(\frac{\omega}{1\ \text{eV}}\right)^2 \left(\frac{10^{-5}\ \text{eV}}{m_a}\right)^4 , \tag{10.10}$$

which is valid for $|r_0 \Delta_a| \gg 1$. Interestingly, L_p is independent of $R_{\rm star}$ in the high axion mass limit. Nevertheless, the transition from the low mass to high mass region is dependent on $R_{\rm star}$, and in practice, the large-mass condition $|r_0 \Delta_a| \gg 1$ is satisfied for

$$m_a \gg 1.7 \times 10^{-7}\ \text{eV} \sqrt{\left(\frac{\omega}{1\ \text{eV}}\right)\left(\frac{0.01\ R_\odot}{R_{\rm star}}\right)} . \tag{10.11}$$

Thus, we expect that MWD polarization studies to be insensitive to the axion mass for $m_a \lesssim 10^{-7}$ eV, while for masses much larger than this the sensitivity to $g_{a\gamma\gamma}$ should drop off quadratically with increasing m_a. Next, we present the generalized mixing equations for non-radial trajectories including the Euler-Heisenberg Lagrangian.

10.1.2 General axion-photon mixing equations

In this chapter we numerically solve the axion-photon mixing equations including the Euler-Heisenberg terms and also integrating over emission across the surface of the MWD. That is, we assume that the MWD surfaces are isothermal (but see [454], which would introduce $\mathcal{O}(10\%)$ corrections to our results), such that the emission we see on Earth originates from across the full Earth-facing hemisphere of the MWD. However, this means that photons that originate from across this surface that reach Earth will generically travel along non-radial trajectories, and this requires us to generalize the mixing equations in (10.3) to include

mixing of the axion with both transverse modes:

$$\left[i\partial_s + \begin{pmatrix} \Delta_{11} & \Delta_{12} & \Delta_{B_1} \\ \Delta_{12} & \Delta_{22} & \Delta_{B_2} \\ \Delta_{B_1} & \Delta_{B_2} & \Delta_a \end{pmatrix} \right] \begin{pmatrix} A_1 \\ A_2 \\ a \end{pmatrix} = \mathbf{0}\,. \tag{10.12}$$

Above, we assume that the photon travels along a straight trajectory in the direction $\hat{\mathbf{s}}$, with coordinate s, with $\hat{\mathbf{x}}_1$ and $\hat{\mathbf{x}}_2$ spanning the transverse directions. We also neglect plasma terms because, as discussed above, they play a subdominant role. The terms appearing in the mixing Hamiltonian in (10.12) arise from axion-photon mixing, the Euler-Heisenberg Lagrangian, and the axion mass, and those that differ from the terms in (10.3) are defined by [173]

$$\begin{aligned} \Delta_{11} &= \frac{2\alpha_{\rm EM}\omega}{45\pi}\left[\frac{7}{4}\left(\frac{B_1}{B_{\rm crit}}\right)^2 + \left(\frac{B_2}{B_{\rm crit}}\right)^2\right] \\ \Delta_{22} &= \frac{2\alpha_{\rm EM}\omega}{45\pi}\left[\frac{7}{4}\left(\frac{B_2}{B_{\rm crit}}\right)^2 + \left(\frac{B_1}{B_{\rm crit}}\right)^2\right] \\ \Delta_{12} &= \frac{3}{4}\frac{2\alpha_{\rm EM}\omega}{45\pi}\left(\frac{B_1 B_2}{B_{\rm crit}^2}\right), \quad \Delta_{B_i} = \frac{1}{2} g_{a\gamma\gamma} B_i\,, \end{aligned} \tag{10.13}$$

with $i = 1, 2$ in the last line. Above, B_1 and B_2 are the magnetic field values in the transverse directions, and they are generically functions of s.

When applying the formalism above to predict the axion-induced L_p from a MWD, we begin by discretizing the surface of the hemisphere of the Earth-facing MWD. We consider initially unpolarized emission from each surface element propagating in the $\hat{\mathbf{x}}_3$ direction, with the final A_1 and A_2 being the appropriate sum of the contributions from the different surface elements. This is accomplished by letting the initial vector potential of each surface element i be labeled as $\mathbf{A}^i = (A^i/\sqrt{2})\big(a_1^i \hat{\mathbf{x}}_1 + a_2^i \hat{\mathbf{x}}_2\big)$, where the a_1^i and a_2^i are uncorrelated random variables such that $\langle a_1^i a_1^{j\,*}\rangle = \delta^{ij}$ with all other correlators vanishing. We adjust the normalization parameter A^i such that $A^i \propto \sqrt{0.7 + 0.3\cos\theta_i}$, with θ_i being the angle between the normal vector to the sphere at pixel i and the $\hat{\mathbf{x}}_3$ axis. This scaling reproduces the limb darkening law for the intensity adopted in [455], who confirmed this scaling through radiative transfer calculations.

Magnetic white dwarf magnetic field models

' The magnetic field profile around a compact star will generically approach that of a dipole configuration far away from the stellar surface, since higher-harmonic contributions to the vacuum solutions to the Maxwell equations fall off faster with radius. In this chapter, we will consider both pure dipole profiles and profiles containing higher harmonic modes, which have been fit to luminosity and circular polarization data from specific MWDs. The dipole solution may be written as

$$\mathbf{B}(\mathbf{r}) = \frac{B_p}{2}\left(\frac{R_{\rm star}}{r}\right)^3 \left[3\hat{\mathbf{r}}(\hat{\mathbf{m}}\cdot\hat{\mathbf{r}}) - \hat{\mathbf{m}}\right] , \tag{10.14}$$

where $\hat{\mathbf{m}}$ points along the polarization axis in the direction of the magnetic north pole and $\hat{\mathbf{r}}$ is the position unit vector, with distance r from the center of the star. The field strength B_p is the polar value at the surface of the star.

The general solution to the Maxwell equations in vacuum may be written in terms of spherical harmonics; the associated magnetic scalar potential ψ, defined such that $\mathbf{B} = -\nabla\psi$, is given by

$$\psi = -R_{\rm star}\sum_{\ell=1}^{\infty}\sum_{m=0}^{\ell}\left(\frac{R_{\rm star}}{r}\right)^{\ell+1}\left[g_\ell^m\cos m\phi + h_\ell^m \sin m\phi\right] P_\ell^m(\cos\theta) , \tag{10.15}$$

where the coefficient g_ℓ^m and h_ℓ^m have dimensions of magnetic field strength. The angle θ is the angle away from the polarization axis $\hat{\mathbf{m}}$, such that $\hat{\mathbf{m}}\cdot\hat{\mathbf{r}} = \cos\theta$, and the angle ϕ is the rotation angle about $\hat{\mathbf{m}}$. The P_ℓ^m are the associated Legendre polynomials. Note that the terms in (10.15) at $\ell = 1$ are simply those in (10.14) for the dipole configuration. Ref. [52] provides a fit of the harmonic solution in (10.15) to MWD circular polarization and spectra data for Grw+70°8247 up through $\ell \leq 4$; we will make use of this fit later in this chapter.

It is convenient to define an inclination angle i that is the angle between the magnetic axis $\hat{\mathbf{m}}$ and the direction towards Earth. For definiteness, throughout this chapter we define the coordinate system centered at the MWD center with $\hat{\mathbf{z}}$ pointing towards the Earth and with $\hat{\mathbf{m}} = \cos i\hat{\mathbf{z}} + \sin i\hat{\mathbf{y}}$. Note that for a dipole field configuration the linear polarization must vanish as $i \to 0$, since in this limit there is no preferred direction for the linear polarization to point.

10.1.3 Astrophysical contributions to the linear polarization

Astrophysical mechanisms exist within the MWD atmospheres for polarizing the outgoing radiation. Like the axion mechanism that is the focus of this chapter, the astrophysical

mechanisms also rely on the polarizing effects of the magnetic field. Here, we overview the calculation of the astrophysical polarization, as astrophysical emission serves as a background contribution in the axion searches that we discuss later in this chapter. As we will see one crucial difference between the two sources of linear polarization is that the astrophysical mechanisms lead to strong wavelength dependence of the polarization fraction, while the axion-induced polarization depends less strongly on wavelength. This difference helps constrain the axion-induced linear polarization fraction even in the presence of an unconstrained astrophysical polarization fraction, which in principle could partially interfere with the axion signal at certain wavelengths.

In what follows we assume that the MWD atmosphere is composed primarily of hydrogen, which is the case for the MWDs we consider in this chapter. The bound electrons in the MWD atmosphere can be considered in the Paschen-Back regime, where the Hamiltonian is given by

$$H = \frac{p^2}{2m_e} - \frac{\alpha_{\rm EM}}{r} + \frac{1}{2}\Omega_C L_z + \frac{1}{8} m_e \Omega_C^2 r^2 \sin^2\theta \,, \tag{10.16}$$

with the third term accounting for the linear Zeeman effect and the fourth term the quadratic Zeeman effect. The electron mass is m_e, the cyclotron frequency is $\Omega_c = eB/m_e$, r is the atomic radial distance, and $\theta = 0$ points along the magnetic field. At the fields under consideration $B \gtrsim 100$ MG, the quadratic Zeeman effect is important or dominant. However, in this chapter we use an approximation for fields $B \lesssim 100$ MG to model the astrophysical linear polarization, given by Ref. [452] and Ref. [456]. The reason is that the bound-free transition cross sections have not yet been computed with sufficient resolution for the modeling of MWD polarization at high field values. Recent advances in solving the Hamiltonian of (10.16) have led to numerical cross sections for a limited number of these transitions, but they were not reported on a fine enough grid of magnetic fields strengths for astrophysical modeling [457–459].

Here, we first describe the generation of polarization for low fields, where the quadratic Zeeman effect is negligible. There are two main astrophysical processes that contribute to continuum linear and circular polarization of MWD starlight: (1) the ionization of a bound electron in a hydrogen atom (bound-free polarization) and (2) the absorption of a photon by an ionized electron (free-free polarization) [452]. Bound-bound transitions of the hydrogen atom can produce localized features in the MWD spectra, and the observation of these features are used to estimate the surface magnetic fields of MWD, as the bound state energies of the hydrogen atom have been solved. Bound-bound transitions can also contribute to the polarization continuum, but these effects are washed-out by the large variation in the

field on the MWD surface. We discuss the bound-bound transitions further in the context of SDSS J135141 in Sec. 10.2.1.

The MWD starlight is produced unpolarized deep within the atmosphere as blackbody radiation. The polarization is generated as the light propagates through the thin atmosphere and ionizes bound electrons and scatters on free electrons. Because the atmosphere is thin compared to the coherence length of the magnetosphere, to a good approximation the magnetic field is constant throughout the atmosphere at a given point on the surface of the MWD. This surface magnetic field preferentially selects a direction for the absorption to occur, which polarizes the blackbody radiation. The bound-free transitions must satisfy the dipole selection rules $q = 0, \pm 1$, where q is the difference between the initial and final magnetic quantum numbers, m_i and m_f, respectively, of the transition. The transitions with $q = \pm 1$ preferentially absorb photons polarized perpendicular to the magnetic field and therefore polarizes the starlight parallel to the magnetic field. On the other hand, the transitions with $q = 0$ preferentially absorb photons of the opposite polarization, so that these transitions polarize the starlight perpendicular to the magnetic field. To determine the overall effect of bound-free absorption, there is a competition between these two terms. Over the majority of the photon energy range, the $q = \pm 1$ transitions are stronger such that the starlight is polarized parallel to the magnetic field. Only for photon energies near the hydrogen absorption edges does the polarization flip so that the linear polarization points perpendicular to the magnetic field. Finally, for free-free absorption, light is preferentially absorbed in the plane perpendicular to the magnetic field because the cyclotron motion of the free electrons restricts them to this plane, and therefore this absorption polarizes the light parallel to the magnetic field. If the axion-induced polarization is perpendicular to the astrophysical polarization direction then the two signals may partially destructively interfere.

Quantitatively, the effect of the bound-free and free-free absorption may be captured though the transfer equation describing the evolution of the photon polarization state matrix (effectively a photon density matrix),

$$\mathcal{F} = \begin{pmatrix} E_1 \\ E_2 \end{pmatrix} \begin{pmatrix} E_1^* & E_2^* \end{pmatrix} = \frac{1}{2} S^\mu \sigma_\mu \,, \tag{10.17}$$

where $S^\mu = (I, Q, U, V)$ and $\sigma_\mu = (\mathbb{1}, \sigma_z, \sigma_x, \sigma_y)$ are the Stokes and Pauli vectors, respectively. In the anisotropic atmospheric plasma of the MWD, the transfer equations take the form [452],

$$\frac{d\mathcal{F}}{ds} = -\frac{1}{2}(T\mathcal{F} + \mathcal{F}T^\dagger) + \mathcal{E} \,, \tag{10.18}$$

where the transfer matrix $T = \mathcal{K} - 2i\mathcal{R}$ describes absorption ($\mathcal{K}$) and refraction ($\mathcal{R}$), while $\mathcal{E}$ describes emission. Equation (10.18) can be solved analytically under the approximation that the initially unpolarized blackbody radiation emanating from the MWD experiences a constant magnetic field while traversing the thin, cold, atmosphere. As shown in [452], under these assumptions, the solution to (10.18) as expressed in terms of the final polarization state of starlight leaving the MWD atmosphere of thickness δs is given in terms of the Stokes parameters by [452]

$$\begin{aligned} I &= 1 - \frac{\delta s}{2}\mathrm{tr}(\mathcal{K})\,, \quad Q = -\frac{\delta s}{2}\mathrm{tr}(\sigma_z\mathcal{K})\,, \\ U &= -\frac{\delta s}{2}\mathrm{tr}(\sigma_x\mathcal{K})\,, \quad V = -\frac{\delta s}{2}\mathrm{tr}(\sigma_y\mathcal{K})\,. \end{aligned} \tag{10.19}$$

For dipole transitions like bound-free and cyclotron absorption, $\mathcal{K}$ is diagonal in the complex spherical basis with matrix elements

$$\mathcal{K}_q(\omega) = n\sigma_q(\omega)\,, \tag{10.20}$$

where n is the number density of the absorbing species and σ_q the associated frequency-dependent cross-section, with ω the radiation frequency.

The astrophysical linear polarization follows from (10.19) and (10.20) and is given by

$$L_{p,\mathrm{astro}} = \frac{|Q|}{I} = \frac{\delta s}{4}|2\mathcal{K}_0 - \mathcal{K}_+ - \mathcal{K}_-|\sin^2\theta\,, \tag{10.21}$$

since $U = 0$ in this basis. As in (10.16), θ is the angle between the surface magnetic field and the light propagation direction, and $\mathcal{K}$ in general includes bound-bound, bound-free, and free-free absorption contributions, although we do not consider bound-bound transitions.

Note that (10.21) holds for any MWD magnetic field strength. However, for MWDs with high fields where the linear Zeeman effect breaks down ($B \gtrsim 100$ MG), the bound-free absorption cross-section become difficult to calculate. In this chapter we use an approximation that is common in the literature. For bound-free collisions where the quadratic Zeeman effect is unimportant ($B \lesssim 100$ MG), $\mathcal{K}_q$ can be calculated analytically under the approximation that the wavefunction of the bound electron is unaffected by the perturbing external magnetic field while its energy shifts linearly by $m_i\Omega_C$. Under these approximations, the bound-free absorption cross-section was derived first in [452].

We use the improved approximation [456] that accounts for the energies of the hydrogen absorption edges ϵ_{nlmq} as a function of magnetic field, $\epsilon_{nlmq} \equiv E_{nlm}(B) + \Theta\left(m_f\Omega_C\right)$ for Θ the Heaviside step function. The first term accounts for the fact that the bound state energies

of hydrogen in the quadratic Zeeman regime depend on all three quantum numbers $\{n,l,m\}$ and the magnetic field strength B, because the Hamiltonian of (10.16) breaks spherical symmetry. These bound state energies $E_{nlm}(B)$ are tabulated in [460]. We also account for the quantization of the free electrons into Landau levels, which yields the second term. Then the bound-free absorption coefficients are given by

$$\mathcal{K}_{q,\mathrm{bf}}(\omega) = n_{\mathrm{H}} \frac{\omega}{\omega - q\Omega_C} \sum_{nlm}^{n\leq 4} \exp\left(\frac{-E_{nlm}(B)}{T}\right) \times \begin{cases} \sigma_n^{\mathrm{bf}}(\omega - q\Omega_C), & \omega \geq \epsilon_{nlmq} \\ 0, & \omega < \epsilon_{nlmq} \end{cases} . \tag{10.22}$$

We weight the states with the Boltzmann factor, under the assumption of the fixed surface temperature $T = 15000$ K, appropriate for the MWDs we consider in this chapter. $\sigma_n^{\mathrm{bf}}(\omega) \propto n^{-5}\omega^{-3}$ is the cross section for a photon of energy ω to ionize an electron of principal quantum number n at zero magnetic field. The dependence on $\omega - q\Omega_C$ is derived in the linear Zeeman regime. For the optical spectra we consider in this chapter, we only need to consider $n \leq 4$.

The free-free absorption matrix is proportional to the cyclotron absorption cross-section

$$\mathcal{K}_{q,\mathrm{ff}}(\omega) = \begin{cases} n_e \sigma^{\mathrm{ff}} & q = +1 \\ 0 & q \neq +1 \end{cases} , \tag{10.23}$$

where n_e the number density of free electrons. We take the cyclotron absorption cross-section σ^{ff} as given in [452]. Only the $q = 1$ component is nonzero due to selection rules that enforce energy and angular momentum conservation along $\mathbf{B}$ [461], and this cross section is strongly peaked around $\omega = \Omega_C$.

At low magnetic fields $B \lesssim 100$ MG, the cyclotron frequency is much smaller than the optical frequencies, so that we do not need to consider cyclotron absorption contributions to the atmospheric opacity. Thus, only the bound-free absorption cross-section (10.22) contributes to the polarization. Furthermore, the hydrogen absorption edges are close to their zero-field values 13.6 eV$/n^2$. Then, for energies far away from the absorption edges (10.21) reduces to [452]

$$L_{p,\mathrm{astro}}(\omega) \propto \frac{\Omega_C^2}{\omega^5} \sin^2\theta \,. \tag{10.24}$$

The proportionality constant of (10.24) depends on the line-of-sight integrated bound electron density in the MWD atmosphere. Since $\Omega_C \propto B$, we see that in this regime the astrophysical linear polarization scales as the transverse magnetic field strength squared like that induced by the axion. However, the astrophysical polarization points parallel to the magnetic field while the axion-induced polarization points perpendicular to the field, which

means that the two contributions may partially cancel each other depending on their relative magnitudes.

By contrast, even at low magnetic fields, the linear polarization displays strong localized features near the absorption edges. The linear polarization becomes much larger in magnitude and switches direction blueward of the edge so that it points perpendicular to the magnetic field, in the same direction as the axion-induced polarization.

However, in this chapter we consider MWDs with large magnetic fields $B \gtrsim 100$ MG. In this case, the cyclotron frequency enters the optical, so that we must include the cyclotron absorption contribution to the linear polarization. The bound-free absorption also becomes more complex than at lower fields. The absorption edges cover nearly the entire optical spectrum. Furthermore, the hydrogen bound state energies depend strongly on the magnetic field strength, and the magnetic field strength on the surface of the MWD may span more than a factor of two, which additionally broadens the absorption edge features. Under the approximation used in this chapter (10.22), which assumes the bound-free cross section is simply that at zero-field shifted by $q\Omega_C$, we find that most of the linear polarization spectrum is dominated by the absorption edge features rather than by the simple power law scaling of (10.24). The exact cross sections have been previously computed numerically for a limited number of transitions [457–459]. In these results there are additional oscillatory features near Landau thresholds, where the photon energy matches the energy difference between a Rydberg bound state and a Landau level. We thus expect that the eventual incorporation of the numerical cross sections into MWD linear polarization calculations will introduce additional features in the spectra due to these resonances, although these features will be smeared out due to the range of field strengths on the MWD surface.

At still higher magnetic fields $B \gtrsim 5000$ MG, the situation becomes less complicated. The quadratic Zeeman term dominates the Coulomb term in (10.16). The approximation that the Coulomb field is a perturbation on the background magnetic field becomes more appropriate, and in this limit, we find, following [462], that $\sigma^{\rm bf}$ scales as ω^{-3} away from absorption edges as in the low-field case.

Despite the uncertainties described above, essentially any energy dependence in the astrophysical polarization is sufficient to distinguish it from the axion-induced polarization for the purpose of setting an upper limit on the axion-induced polarization contribution, which is approximately energy independent, given spectropolarimetric data. As discussed further in Sec. 10.2.1, this is because given some amount of energy dependence in the astrophysical background, the axion and astrophysical contributions would not completely destructively interfere across the full analysis energy range. On the other hand, in order to claim evidence for an axion signal, the astrophysical linear polarization signal should be better understood in

the high-field regime. This is because without a full understanding of how the astrophysical polarization emerges in the high field regime, one cannot be confident that a putative signal arises from axions and not the imprecisely known astrophysical polarization mechanisms.

10.2 Upper Limits on $g_{a\gamma\gamma}$ from Magnetic White Dwarfs

In this section we apply the formalism developed in the previous section to set upper limits on $|g_{a\gamma\gamma}|$ from linear polarization data towards the MWDs SDSS J135141 (Sec. 10.2.1) and GRW+70°8247 (Sec. 10.2.2). These MWDs are unique in that they have strong but well-characterized magnetic field profiles in addition to dedicated linear polarization data. We discuss additional MWDs that are promising but have somewhat incomplete data at present in Sec. 10.2.3.

10.2.1 SDSS J135141

The MWD SDSS J135141 has one of the largest magnetic fields of all known MWDs. Ref. [16] measured the polar magnetic field strength in the context of the dipole model to be $B_p = 761.0 \pm 56.4$ MG, with an inclination angle $i = 74.2° \pm 21.7°$.[1] In the below analysis we consider the dipole model, and we compute the 95% upper limit on $|g_{a\gamma\gamma}|$ considering the range of allowable magnetic field parameters. In particular, we take our fiducial limit to be the weakest one across the range of allowable magnetic field parameters, allowing the parameters to vary within their 1σ ranges, while we calculate the 95% confidence level statistical upper limit on the data itself.

Absorption lines and magnetic field model

In this section we overview the determination of the SDSS J135141 magnetic field strength. To date, this determination has been made only through spectra rather than polarimetry, although the addition of polarimetery would be beneficial to further constraining the magnetic field profile on the surface. The spectrum of a MWD is that of a thermal distribution at the temperature of the MWD surface, but with absorption features at wavelengths at which bound-bound transitions occur in the atmosphere. The transition wavelengths are very strongly dependent on the local magnetic field; therefore, the absorption lines are broadened by the range of magnetic field strengths on the MWD surface. In many cases the features are entirely washed out because the transition wavelengths are highly dependent on the local magnetic field, but a few transitions are nearly stationary because they encounter local

[1] Note that Ref. [16] also considered an offset dipole model, but we do not consider this model here.

extrema. The primary method for determining the magnetic field strength of MWDs is to search for these stationary features in the spectrum. The bound-bound transitions and dipole transition strengths of the hydrogen atom in a strong magnetic field are given in Ref. [463].

In Fig. 10.3 we show the wavelength dependence as a function of magnetic field for the stationary bound-bound $3d_{-1} - 2p_0$ transition in the upper panel. The transition is nearly stationary around across the full range of field strengths present on the surface of SDSS J135141, assuming the 761 MG dipolar field. In the middle panel, we show the expected line templates for two cases (i) the best-fit dipolar field of 761 MG [16] and inclination angle $i = 74.2°$, and (ii) a dipolar field of 400 MG with best-fitting i for that field strength. To compute these templates, we histogram the wavelengths of the transition on the visible hemisphere of the MWD and weight each contribution by the dipole transition strength. We also incorporate the limb darkening law mentioned previously from Ref. [455], which weights the intensities between pixels on the sphere such that $I \propto 0.7 + 0.3\cos\theta$, with θ the angle of the normal to the $\hat{\mathbf{x}}_3$ axis that points towards Earth. Note that due to the symmetry present in a dipole field, it is only the limb darkening rule that changes the spectral shape of the template with inclination angle i. The template is then convoluted with a Gaussian that has standard deviation $\sigma_{\rm stark}$. This broadening is due to the Stark effect, accounting for the electric field that is also present on the MWD surface, and is the dominant broadening effect for these lines. We treat $\sigma_{\rm stark}$ as a nuisance parameter that is determined by maximum likelihood estimation.

For the 761 MG case, the absorption line appears at approximately the same location across the entire hemisphere, so that the resulting feature is highly localized around 8530 $\mathring{A}$. On the other hand, if the MWD had a lower field strength of 400 MG, the feature would be significantly broadened because the transition is not stationary at those field strengths, and additionally the feature would appear at shorter wavelengths $\sim 8200 - 8600$ $\mathring{A}$. In the lower panel, we fit expected flux models for each case to the SDSS data [16]. The models are a power law background with free index and normalization with the multiplicative absorption template as shown in the middle panel. For the 761 MG case, we see that the model prefers an absorption line, indicating that the 761 MG dipole is a reasonable fit to the data. On the other hand, for the 400 MG case, the fit finds no evidence for a line. Following a similar procedure SDSS J135141 was determined to have a 761.0 ± 56.4 MG field [16], although that work fit to the broad-band flux spectra over a much larger wavelength range encompassing many absorption lines. In fact, Ref. [16] did not include the wavelength range shown in Fig. 10.3 in their fit; the fact that their best-fit model from lower wavelengths also explains the $3d_{-1} - 2s_0$ absorption line feature provides non-trivial evidence that the magnetic fields on the surface of the MWD are ∼400-700 MG.

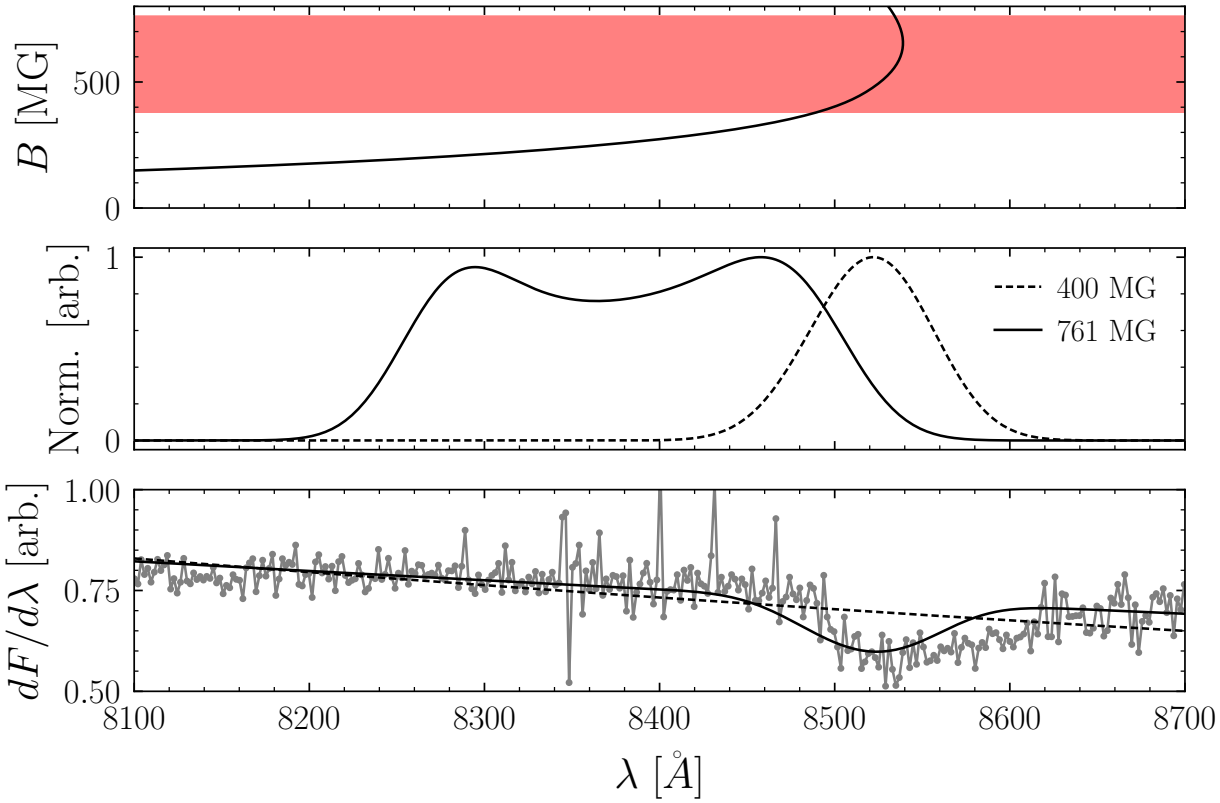

Figure 10.3: (Top) The wavelength of the $3d_{-1} - 2p_0$ absorption line as a function of magnetic field. The red shaded region indicates the range of field strengths present on the surface, assuming the best-fit dipole field of 761 MG from [16]. (Middle) In solid black is the $3d_{-1} - 2p_0$ line template for a 761 MG dipolar field; in dashed black for 400 MG. (Bottom) The flux of SDSS J135141 as measured by SDSS DR7 (gray). In solid black is the best fit spectrum assuming a 761 MG dipole field. In dashed black is the best fit spectrum assuming a 400 MG dipole field.

Polarization data

The linear polarization of SDSS J135141 was measured in 2007 by [51] using the Special Astrophysical Observatory (SAO) 6-m telescope with the Spectral Camera with Optical Reducer for Photometric and Interferometrical Observations (SCORPIO) focal reducer [464]. Across the wavelength range 4000 $\mathring{A}$ to 6500 $\mathring{A}$ the linear polarization fraction was measured to be $L_p = 0.62\% \pm 0.4\%$. The uncertainty on L_p is dominated by the systematic uncertainty, arising from effects such as scattered light and ghosts [464], though the exact systematic uncertainty accounting that goes into the L_p measurement is not detailed in [51]. The linear polarization fraction data from [51] is reproduced in Fig. 10.4.

An upper limit on the average axion-induced polarization fraction over the wavelength

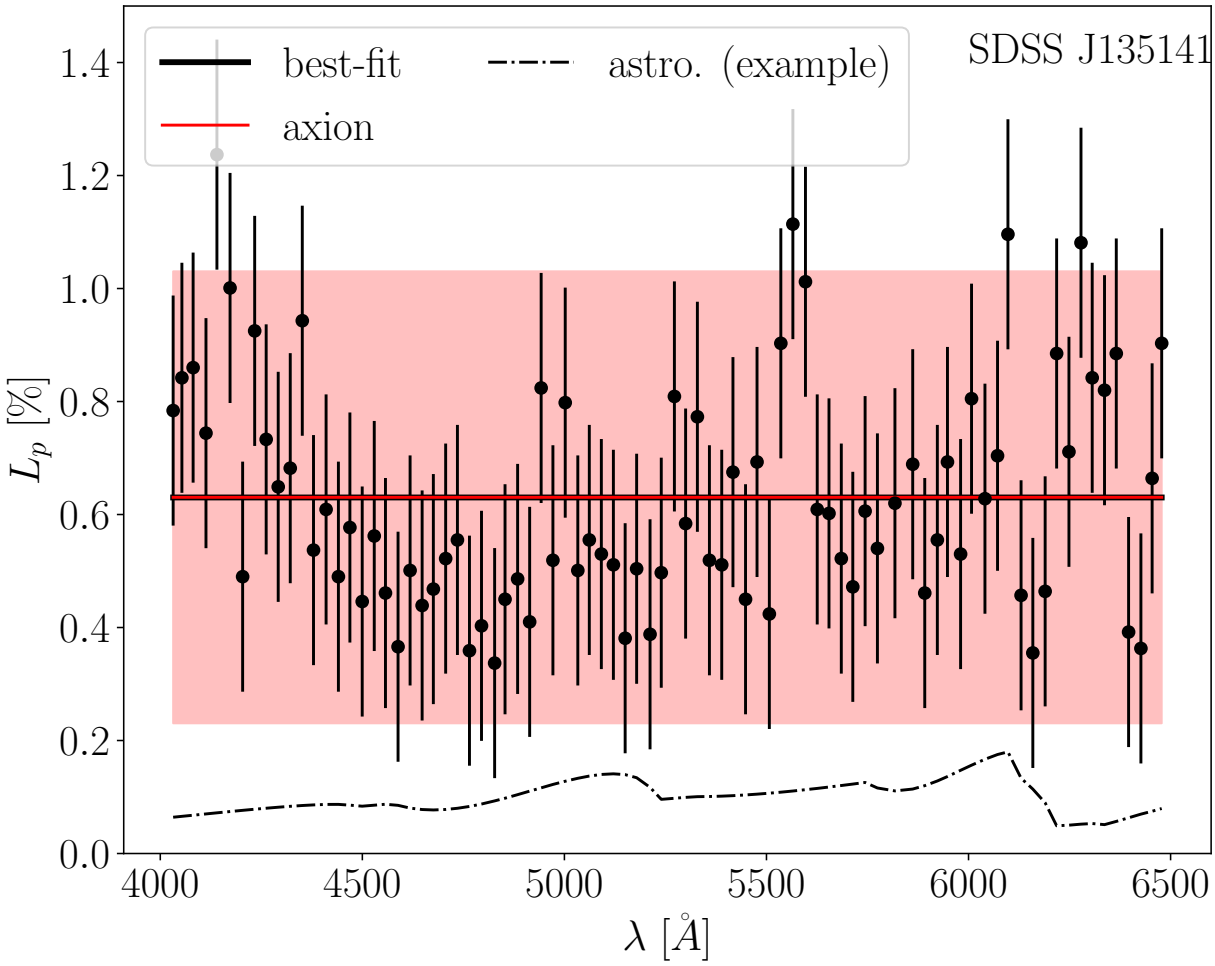

Figure 10.4: The linear polarization data as a function of wavelength towards the MWD SDSS J135141 as observed by [51] with the SAO 6-m telescope. We use a Gaussian likelihood to fit a model to the data with three components: (i) the axion signal, (ii) the astrophysical background, and (iii) an instrumental systematic contribution. We assume that the axion signal and the instrumental systematic are wavelength-independent, while the astrophysical background depends on wavelength as described in Sec. 10.2.1. The axion signal and the instrumental systematic contributions would be completely degenerate, given that the systematic normalization parameter can take either sign, but for the prior on the systematic nuisance parameter. The best fit model, along with the axion contribution to that model, are illustrated, along with the best-fit statistical uncertainties on the data; the statistical uncertainty is treated as a hyperparameter that is determined by maximum likelihood estimation. The red band illustrates the allowed axion contribution at 1σ confidence. At the best-fit point the astrophysical normalization is zero. Still, we illustrate the astrophysical linear polarization model, with an arbitrary normalization.

range $L_{p,\mathrm{axion}}$ may be estimated by the requirement that axions not overproduce the observed polarization, which at 95% confidence and assuming Wilks' theorem implies $L_{p,\mathrm{axion}} \lesssim$

$0.62\% + \sqrt{2.71} \times 0.4\% \approx 1.28\%$ [109]. This upper limit is very close to that we will derive below making use of the wavelength dependent data and incorporating the astrophysical background model. This point illustrates that the astrophysical polarization contribution is not a limiting background for constraining the axion-induced polarization, at least for this example. This is fundamentally because the astrophysical background and the axion signal are polarized in the same direction over the wavelength range relevant for this search. Our polarization upper limit is also consistent with that found in [465], who performed spectropolarimetric observations of the MWD using the Steward Observatory 2.3 m telescope in 1993 and state that the linear polarization of SDSS J135141 in the wavelength range 4100 $\mathring{A}$ to 7280 $\mathring{A}$ was found to be less than 1%, though the confidence level of that statement is not given in [465].

To analyze the wavelength dependent data, we adopt a Gaussian likelihood function that incorporates the systematic uncertainty in a straightforward way, though the following analysis could likely be improved in the future with a better understanding of the origin of the systematic uncertainty. The likelihood we adopt is given by

$$p(\mathbf{d}|\mathcal{M}, \boldsymbol{\theta}) = \left(\prod_i \frac{1}{\sigma} e^{\frac{-(d_i - L_p(\boldsymbol{\theta}))^2}{2\sigma^2}} \right) e^{\frac{-A_{\rm sys}^2}{2\sigma_{\rm sys.}^2}} , \tag{10.25}$$

where we leave off unimportant numerical normalization factors and where i labels the wavelength bins (there are 83 different wavelength bins, as illustrated in Fig. 10.4). The data $\boldsymbol{d}$, with entries d_i, are the observed polarization values, while the model $\mathcal{M}$ has parameters $\boldsymbol{\theta} = \{A_{\rm axion}, A_{\rm astro}, A_{\rm sys}, \sigma\}$. The signal parameter $A_{\rm axion}$ controls the normalization of the axion-induced polarization and, physically, is a proxy for $g_{a\gamma\gamma}$, at fixed m_a. The parameter $A_{\rm astro}$ controls the amplitude of the unknown astrophysical background. The instrumental (*e.g.*, systematic) contribution to the polarization is characterized by the nuisance parameter $A_{\rm sys}$. The parameter σ may be interpreted as the uncorrelated statistical uncertainty on the linear polarization data. We treat σ as a hyperparameter that is determined by maximum likelihood estimation.

Both the astrophysical and axion contributions to the polarization in principle have nontrivial wavelength dependence; in the axion case, the wavelength dependence is found by numerically solving the axion-photon mixing equations, while for the astrophysical contribution we use (10.21). For all of the magnetic field models, only bound-free absorption contributes, as the cyclotron wavelength is not in the wavelength range of the data. We compute the Stokes parameters by averaging them over $\sim 10^5$ points on the MWD surface in each wavelength bin. The full list of absorption edges and associated wavelength ranges that contribute to features in the astrophysical linear polarization model are given in

$nl_{\rm m}$	q	ϵ_{nlmq} ($\mathring{A}$)
$2p_1$	-1	5860+
$3p_{-1}$	$0, \pm 1$	4630—5290
$3p_0$	$0, -1$	5800—6270
$3p_1$	0	4630—5270
$3d_0$	$0, -1$	6090—6730
$4d_{-2}$	$0, \pm 1$	5420—6480
$4d_2$	0	5420—6440
$4f_{-2}$	$0, \pm 1$	3650—4580
$4f_2$	0	3650—4560

Table 10.1: The list of absorption edges that contribute to features in the SDSS J135141 astrophysical linear polarization model, assuming the fiducial magnetic field model. The first column shows the initial hydrogen state labeled by the zero-field quantum numbers nlm; the second column labels the transition by q, the difference between the initial and final magnetic quantum numbers. The absorption edge features for each respective transition appear in the wavelength range listed in the third column in $\mathring{A}$. This wavelength range is equivalent to the range of ϵ_{nlmq} over the magnetic field strengths present on the surface, $353 - 705$ MG.

Tab. 10.1. Accounting for the uncertainty on the magnetic field strength and orientation, the edges may shift by ~ 100 $\mathring{A}$. Note that over the range of magnetic field models and wavelengths analyzed, the axion and astrophysical model contributions to the linear polarization point in the same direction.

$A_{\rm sys}$ is given a zero-mean Gaussian prior distribution in (10.25), with variance $\sigma^2_{\rm sys}$. This prior breaks the degeneracy between the axion signal and the contribution from $A_{\rm sys}$. We set $\sigma_{\rm sys} = 0.4\%$ since this is the uncertainty quoted in [51] on the average linear polarization over this wavelength range and since the uncertainty in [51] is systematics dominated.

We fix $A_{\rm axion}$ and $A_{\rm astro}$ to be positive, since as discussed above these two contributions are polarized in the same direction for this MWD and wavelength range, while $A_{\rm sys}$ is allowed to be both positive and negative. This means that, for example, the axion and systematic contributions may completely cancel each other, up to the prior contribution from $A_{\rm sys}$.

We compute the profile likelihood for $A_{\rm sig}$, profiling the likelihood over the nuisance parameters $\{A_{\rm astro}, A_{\rm sys}, \sigma\}$ for each fixed value of $A_{\rm sig}$. We then assume Wilks' theorem such that the one-sided 95% upper limit on $A_{\rm sig}$ is defined through the test statistic t

$$t(A_{\rm axion}) \equiv -2 \left[\log p(\mathbf{d}|\mathcal{M}, \{A_{\rm axion}, \hat{A}_{\rm astro}, \hat{A}_{\rm sys}, \hat{\sigma}\}) - \log p(\mathbf{d}|\mathcal{M}, \hat{\boldsymbol{\theta}}) \right] , \tag{10.26}$$

by $t(A_{\rm axion}) \approx 2.71$ for $A_{\rm sig} > \hat{A}_{\rm sig}$ (see, *e.g.*, [109]). Here, hatted quantities denote the values that maximize the likelihood. In the first term in (10.26) the hatted nuisance parameters are those at fixed values of $A_{\rm axion}$. Performing this analysis on the data illustrated in Fig. 10.4 we find $L_{p,\rm axion} \lesssim 1.25\%$, where $L_{p,\rm axion}$ is the average axion-induced polarization over the wavelength range. We adopt this upper limit for our analysis. Note that the best-fit astrophysical normalization parameter is in fact zero. In the case where the axion signal has wavelength dependence $L_p \propto \lambda^{-2}$, as expected in the large-m_a limit, the limit on $L_{p,\rm axion}$ is strengthened to $L_{p,\rm axion} \lesssim 0.9\%$. However, even in the large m_a limit we adopt the upper limit of 1.25% to account for the possibility that the true wavelength dependence of the systematic contribution to the polarization is more complicated than that assumed here.

In Fig. 10.4 we illustrate the best-fit model contributions to the data, along with the inferred statistical uncertainty σ. The shaded red region shows the allowed values that the axion contribution to L_p could take at 1σ significance. The best-fit model (solid black) has clear evidence of mismodeling; for example, the model systematically under-predicts the data at low λ while it over-predicts the data at other wavelengths. This mismodeling may be from the systematic contribution to the linear polarization having more complicated wavelength dependence than the assumed flat contribution that we take in our analysis. Still, as the magnitude of the systematic deviations of the best-fit model from the data is smaller, by a factor of a few, than our upper limit on $L_{p,\rm axion}$, we hypothesize that a more careful understanding of the instrumental systematic contributions to L_p would be unlikely to significantly affect our estimate of the upper limit. As mentioned previously, the best-fit astrophysical normalization is zero for polarization from bound-free absorption, which we expect to dominate in this wavelength range. We thus conclude that the observed polarization is likely systematic in nature. For illustration purposes, we show in Fig. 10.4 the linear polarization signal from bound-free emission for the best-fit magnetic field and inclination angle, with an arbitrary normalization.

A better understanding of the astrophysical background and systematic contributions would be needed to claim evidence for an axion signal. For this reason we focus in this chapter only on producing upper limits on $|g_{a\gamma\gamma}|$ and not on looking for evidence for the axion model over the null hypothesis of astrophysical emission only.

WD radius from *Gaia* photometry

From (10.9) we see that $L_p \propto R_{\rm star}^2$ at low axion masses, so that the limit on $g_{a\gamma\gamma}$ will scale linearly with $R_{\rm star}$. WDs have radii $\sim 0.01 R_\odot$, but as there is scatter from star-to-star it is important to determine the radii on a per-star basis. We infer the WD radius from *Gaia* Early Data Release 3 (EDR3) photometry [466]. *Gaia* has measured SDSS J135141's apparent

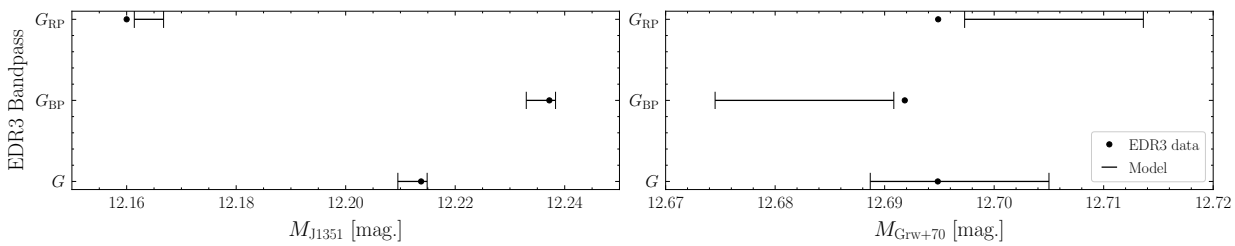

Figure 10.5: (Left) The *Gaia* EDR3 data set in the three bandpasses (dots), G, $G_{\rm BP}$, and $G_{\rm RP}$, for SDSS J135141. The model from cooling sequences is shown as error bars in each bandpass at the best fit WD mass of 0.7 $M_\odot$ and age. (Right) The same as the left panel, but now for Grw+70°8247 at the best fit WD mass of 1.0 $M_\odot$.

magnitudes to be $G = 16.4621 \pm 0.0007$, $G_{\rm BP} = 16.486 \pm 0.004$, $G_{\rm RP} = 16.414 \pm 0.005$.

To infer the WD radius from these data, we use WD cooling sequences [467] for WD masses between 0.3 and 1.2 $M_\odot$ in steps of 0.1 $M_\odot$. These sequences provide the expected EDR3 magnitudes as the WD cools, along with a WD radius. For each mass, we infer the WD radius for SDSS J135141 with a joint Gaussian likelihood over the three bands as a function of age. At a fixed WD mass, we maximize this likelihood over the WD age. To account for possible systematic issues, we additionally maximize over a common uncertainty for G, $G_{\rm BP}$, and $G_{\rm RP}$. That is, we assume that the uncertainties on the magnitudes have a common systematic component, which is added in quadrature with the statistical components and then treated as a nuisance parameter. We then use the age-radius relation supplied by the cooling sequence to obtain a radius estimate. In the left panel of Fig. 10.5, we show the *Gaia* EDR3 data in each of these bands in absolute magnitudes. We also show the model from the cooling sequence at the best fit WD mass and age.

The best-fit mass for SDSS J135141 is 0.7 $M_\odot$. Within the context of this WD model, the expected radius is 0.0111336 ± 0.0000003 $R_\odot$, where the 1σ error bars are computed by solving for the ages where the $\Delta\chi^2$ increases by 1 on either side. The WD radius is not highly dependent on age; rather, it is more strongly dependent on mass. Therefore, although the 0.6 and 0.8 $M_\odot$ models are disfavored by the *Gaia* data by $\sim 4\sigma$, to be conservative we adopt as the radius uncertainties those from assuming the nearby WD masses provided in the cooling sequences. (Ideally, we would use cooling sequences at higher mass resolution than provided in [467].) Using this procedure we infer the radius of SDSS J135141 as $R_{\rm star} = 0.011 \pm 0.001$ $R_\odot$. Within the uncertainties the most conservative low-mass axion limit is then achieved for $R_{\rm star} = 0.01$ $R_\odot$.

Predicted axion-induced polarization signal

For simplicity we begin by fixing $m_a = 0$ eV and considering how the predicted axion-induced polarization signal varies as a function of the uncertain MWD parameters. The goal of this exercise is to understand the importance of various sources of modeling uncertainty on the final $g_{a\gamma\gamma}$ upper limit and to determine the most conservative set of fiducial model parameters for computing the upper limit. In performing these calculations we follow the formalism described in Sec. 10.1.2; specifically, we discretize the surface of the MWD and for each discrete point we solve the mixing equations in (10.12) to determine the linear polarization contribution for initially unpolarized rays that leave the surface at that point. The final polarization signal is the appropriately weighted sum of polarization vectors across the ensemble of all surface points on the hemisphere facing Earth. We use 10^4 points on the hemisphere in performing our calculations.

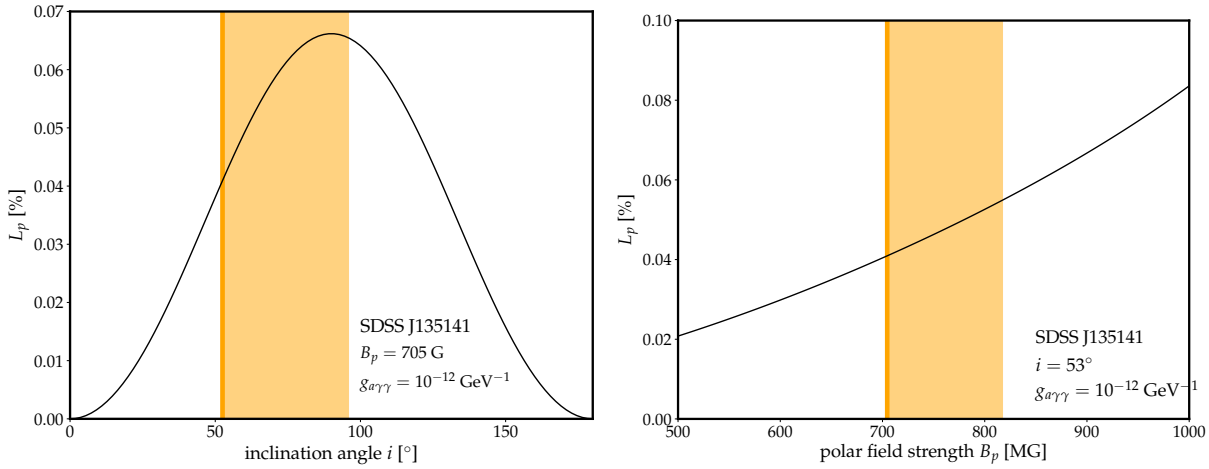

Figure 10.6: (Left) The axion-induced linear polarization fraction L_p for SDSS J135141 as a function of the inclination of the magnetic dipole moment relative to the line-of-sight. The polarization fraction vanishes for $i = 0°$ and $180°$ because in these cases there is no preferred direction for the linear polarization to point. We highlight in orange the inclination angles preferred at 1σ by the analysis in [16]. In our fiducial analysis we fix the inclination angle at the value, indicated by vertical orange, within the 1σ band that leads to the weakest limit. Note that in the figure we also fix the magnetic field at the lowest value allowed at 1σ, and also the polarization fraction is illustrated for the indicated value of $g_{a\gamma\gamma}$. Since $L_p \ll 1$, however, the polarization fraction scales approximately quadratically with $g_{a\gamma\gamma}$. (Right) As in the left panel, but illustrating the dependence of L_p on the dipole magnetic field strength. Note that the inclination angle is fixed at the conservative value indicated in the left panel. The shaded orange region is that preferred at 1σ by [16]; in our fiducial analysis we fix the magnetic field at the value corresponding to the lower edge of this region to be conservative. In both panels that axion mass is $m_a \ll 10^{-7}$ eV such that L_p is independent of m_a.

In Fig. 10.6 we show how the axion-induced polarization faction from SDSS J135141 varies as functions of the inclination angle i (left panel) and the polar magnetic field strength B_p (right panel). Note that for this example we fix $R_{\rm star} = 0.01 R_\odot$ and $g_{a\gamma\gamma} = 10^{-12}$ GeV^{-1}, though since $L_p \ll 1$ the scaling with $g_{a\gamma\gamma}$ is simply $L_p \propto g_{a\gamma\gamma}^2$. The L_p are computed averaging over the wavelength range 4000 $\mathring{A}$ to 6500 $\mathring{A}$ in order to match the polarization data from [51]. The right panel shows, as expected, that increasing field strengths increase the predicted L_p; the scaling is roughly quadratic over the range shown. Shaded in orange is the 1σ confidence interval for the polar field strength in the centered dipole model from [16]. The most conservative B field strength in this model is, at 1σ, $\sim$705 MG, as indicated by the solid vertical orange line. The left panel fixes the polar field strength at this value and shows how L_p varies as a function of the inclination angle i. Unsurprisingly, L_p is minimized for $L_p = 0^\circ$ (or 180°); the reason, as mentioned previously, is that in these limits for the dipole model there is no preferred direction for the linear polarization to point, so it must vanish. Thus, the most conservative value of i at 1σ is that closest to zero, which is $i \approx 53^\circ$.

Note that the axion-induced L_p may be approximately a factor of two larger than it is with our fiducial choices, if the B-field model parameters are in fact at more fortuitous points in the 1σ parameter space. However, using the most pessimistic allowed magnetic field parameters produces more robust upper limits on $g_{a\gamma\gamma}$. It is also important to keep in mind that the Zeeman-split lines observed in the spectra give a robust indication of the field strengths on the surface of the MWD on the Earth-facing hemisphere. The orientation information may be extracted more precisely, however, using circular polarization data, but Ref. [16] only used spectral data. Thus, the orientation determination in the context of the inclination angle measured in Ref. [16] is that needed to get the correct distribution of magnetic fields strengths on the Earth-facing hemisphere accounting for the limb darkening. Analyses of the circular polarization data for this MWD would be useful to better constrain the magnetic field geometry.

In Fig. 10.1 we illustrate the 95% upper limit on $|g_{a\gamma\gamma}|$ determined from the non-observation of axion-induced polarization from SDSS J135141. Our fiducial limit is illustrated in solid red and is that obtained with the most pessimistic magnetic field model parameters allowed at 1σ from the fits presented in [16] ($i \approx 53^\circ$ and $B_{\rm p} = 705$ MG). In shaded orange we assess the systematic uncertainty from mismodeling the magnetic field by showing the inferred 95% limits over the full allowable 1σ parameter space for the magnetic field strength and orientation (note that the MWD radius uncertainty is subdominant). The limit labeled "best-fit" is that obtained with the best-fit dipole model parameters in [16]; the most aggressive limit (labeled optimistic) is found in the offset dipole model by taking the magnetic field at its largest allowed value and $i = 90^\circ$.

10.2.2 Grw+70°8247

The MWD Grw+70°8247 is thought to have a smaller magnetic field than SDSS J135141, with typical surface field values ∼300 MG, but it is an interesting target for axion-induced polarization searches because: (i) modern linear polarization data is available [468], and (ii) the magnetic field profile has been well modelled in the context of a harmonic expansion out to $\ell \leq 4$ [52]. In particular, Ref. [468] used the ISIS spectropolarimeter at the William Herschel Telescope to measure the linear polarization of Grw+70°8247 in 2015 and 2018. The linear polarization was measured accross two bands: (i) a blue band (B) from 3700 to 5300 $\mathring{A}$, and (ii) a red band (R) from 6100 to 6900 $\mathring{A}$. The linear polarization L_p was found to be non-zero at high significance in the B band, at a level ∼3%, but in the R band the polarization was consistent with zero in both 2015 and 2018. This trend is consistent with that found in earlier observations of L_p, going back to 1972 [469], where it is consistently found that the linear polarization is non-zero for wavelengths shorter than ∼5000 $\mathring{A}$ and consistent with zero at lower frequencies. Note that an axion-induced linear polarization signal would be non-zero across the full wavelength range; thus, we may use the R filter data to set a constraint on the possible contribution to the linear polarization from axions.

The R filter linear polarization was measured to be $L_p = 0.24\% \pm 0.08\%$ in 2015 and $L_p = 0.44\% \pm 0.14\%$ in 2017 [468], with uncertainties reflecting photon noise only. Systematic uncertainties were estimated at ∼0.1-0.2% [468]. Assuming the systematic uncertainty is correlated and maximal between the two observing dates, we may combine these results to estimate $L_p = 0.29\% \pm 0.07_{\rm stat}\% \pm 0.2_{\rm sys}\%$. Then, we assume Wilks' theorem to estimate $L_p \lesssim 0.29\% \pm \sqrt{2.71}(0.07 + 0.2)\% \approx 0.73\%$ at 95% confidence. Given that the within the R band there is no significant evidence for wavelength dependence [468], we use our intuition from the analysis in Sec. 10.2.1 to estimate that the 95% upper limit on the axion-contribution to L_p, accounting for systematic and astrophysical contributions, will be comparable to the estimate above on the total linear polarization limit. Thus, below we assume $L_{p,\rm axion} \lesssim 0.73\%$ at 95% confidence.

The MWD Grw+70°8247 was the first identified MWD [469, 470] and thus its magnetic field profile is well studied [52, 456, 468, 469, 471–474]. Additionally, the MWD is known to have a long period, with $P \gtrsim 20$ yrs [468]. Ref. [52] fit a spherical harmonic magnetic field model including modes with $\ell \leq 4$ to the flux and circular polarization data from Grw+70°8247; the result was a field profile of comparable magnitude to the dipole profile but a more non-trivial and twisted spatial distribution. Interestingly, the dipole and harmonic fits in [52] predict nearly identical flux spectra, since the Zeeman effect is only a function of the absolute magnetic field, but the circular polarization prediction from the harmonic model provides a significantly improved fit to the polarization data than the dipole model,

since the circular polarization depends on the orientation of the magnetic field.

The best-fit dipole model from a fit to the flux and circular polarization data for Grw+70° 8247 was found in [52] to have dipole field strength $B_p \approx 347$ MG at an inclination angle $i \approx 56°$. By contrast, the best-fit harmonic model has $i \approx 75.9°$ and non-trivial g_ℓ^m and h_ℓ^m through $\ell = 4$ that may be found in [52]; for example, $g_{10} = 183$ MG, $g_{20} = -40.58$ MG, $g_{30} = 1.39$ MG, and $g_{40} = +1.45$ MG, in the notation of (10.15).

The Grw+70°8247 polarization data may naturally be explained by cyclotron absorption. Under the best-fit dipole model, cyclotron absorption will contribute to linear polarization in the range $\sim 3090 - 6170$ $\mathring{A}$. This range lies predominantly in the B band. Thus, we expect the linear polarization to be much larger in the B band than in the R band, as observed in the data.

Ref. [52] found that in detail the dipole model does not provide a satisfactory fit to the circular polarization data. The harmonic model provided an improved fit to the circular polarization data in [52], though we note that the linear polarization data was not included in their fit. Under the harmonic model, the cyclotron absorption contributes to the linear polarization over the full range of both the B and R bands, but the bulk of the support is in the B band (we compute that the mean linear polarization predicted in the B band is ∼2 times higher than that in the R band in this model). Therefore, we expect that cyclotron absorption accounts for the fact that higher linear polarization is observed in the B band compared to the R band. On the other hand, note that we do not expect cyclotron absorption to contribute to the linear polarization of the MWD SDSS J135141 in the wavelength range of the data, $4000 - 6500$ $\mathring{A}$, because the field is much larger than that of Grw+70°8247. For a dipole field strength of 705 MG, as in the most conservative case for SDSS J135141, cyclotron polarization appears only in the wavelength range $\sim 1520 - 3040$ $\mathring{A}$. For larger polar field strengths, the cyclotron absorption wavelength range shifts blueward, so that we do not need to consider cyclotron absorption in our analysis of SDSS J135141.

It is interesting to compare the predicted axion-induced polarization signals between the harmonic and dipole models in order to understand the sensitivity of the polarization signal to the magnetic field geometry at the surface of the star. Note, however, that the photon-to-axion conversion takes place at distances of order multiple $R_{\rm star}$ away from the surface, where the field is dominated by the dipole contribution since the higher-harmonic terms fall off faster with distance from the star. We infer $R_{\rm star}$ for Grw+70°8247 in the same way as we do for SDSS J135141, and we obtain $R_{\rm star} = 0.0078 \pm 0.0011$ $R_\odot$ corresponding to $M_{\rm star} = 1.0 \mp 0.1$; to be conservative, we fix $R_{\rm star} = 6.7 \times 10^{-3}$ $R_\odot$ throughout this analysis. We show the *Gaia* data and best-fit cooling sequence model in the right panel of Fig. 10.5.

In Fig. 10.7 we show the predicted axion-induced linear polarization fraction for $g_{a\gamma\gamma} =$

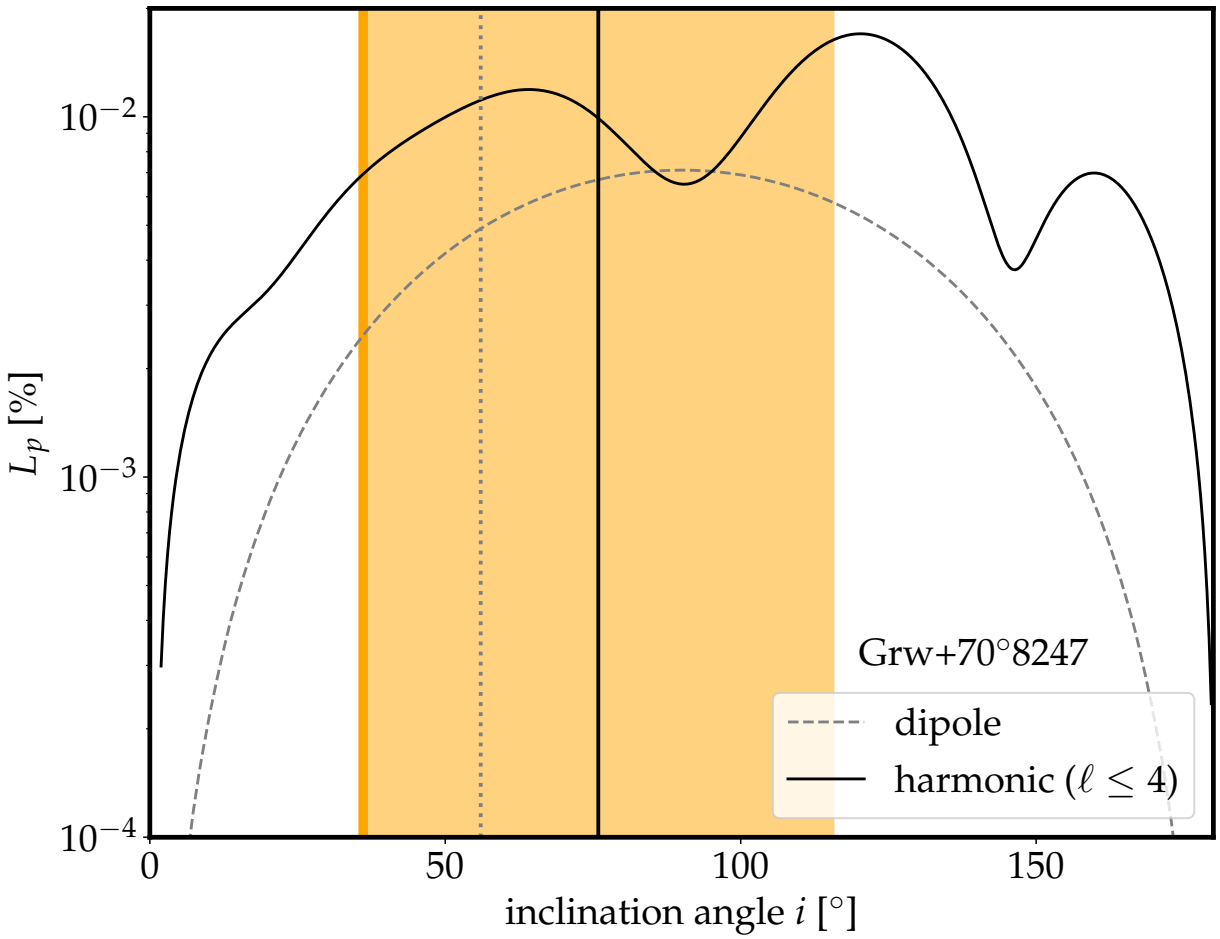

Figure 10.7: As in the left panel of Fig. 10.6 but for the MWD Grw+70°8247. As in Fig. 10.6 we fix $g_{a\gamma\gamma} = 10^{-12}$ GeV^{-1}. We illustrate the dependence of L_p on the inclination angle for both the dipole fit presented in [52], which has polar field strength $B_p = 347$ MG, and for the best-fit harmonic model (out through $\ell \leq 4$) from [52]. The best-fit inclination angles for both fits are indicated by the vertical lines (solid for harmonic and dashed for dipole). Note that the harmonic model does not lead to vanishing L_p at $i = 0°$ and $i = 180°$ because their magnetic field profile is not symmetric about the magnetic axis in this case. Ref. [52] does not present uncertainties on their fit parameters, so we estimate that the leading uncertainty arises from the inclination angle. We estimate this uncertainty using the difference between the inclination angles from the dipole and harmonic fits. In particular, we take the uncertainty on the inclination angle to be twice the difference between the inclination angles measured between the dipole and harmonic fits. To be conservative we then, in our fiducial analysis, fix the inclination angle in the harmonic model at the indicated value (solid, vertical orange) that leads to the smallest value of L_p.

10^{-12} GeV^{-1} as a function of the inclination angle i, with all other parameters of the dipole and harmonic magnetic field profiles fixed at the best-fit values provided in [52]. Note

that [52] does not provide uncertainties on the inferred model parameters. As we observe in the previous section when studying SDSS J135141, the dominant uncertainty is likely that arising from the inclination angle. The best-fit inclination angles quoted in [52] are indicated by solid and dashed vertical lines for the harmonic and dipole models, respectively. We estimate an uncertainty on the harmonic-fit inclination angle i using the difference between the inclination angle measured from the harmonic fit and the dipole fit. In particular, we take the uncertainty $\sigma_i = 40^\circ$ to be twice the difference between the best-fit inclination angles measured between the two different magnetic field profiles. Note that this choice of uncertainty is somewhat arbitrary, but it allows us to estimate the possible uncertainty that may arise from mismodeling in the absence of the actual measurement uncertainties. Additionally, note that in Fig. 10.7 the linear polarization is relatively flat as a function of i for the harmonic fit, except for inclination angles near 0° and 180° where the dipole and $m = 0$ modes do not contribute. Indeed, it interesting to contrast the harmonic model with the dipole model; the harmonic model generically predicts a larger linear polarization fraction, and the polarization fraction is less sensitive to i in the harmonic case. The latter point is explained by the fact the dipole model gives rise to vanishing L_p for magnetic axes aligned with the line of sight, while the harmonic model does not because it need not be azimuthally symmetric about the magnetic axis. To be conservative we compute our upper limits on $g_{a\gamma\gamma}$ by fixing $i = 36^\circ$ with the harmonic model, which is the inclination angle over our uncertainty region that gives rise to the lowest L_p.

In Fig. 10.8 we illustrate the 95% upper limit on $g_{a\gamma\gamma}$ as a function of the axion mass m_a, as in Fig. 10.1, for the Grw+70°8247 analysis. We compute the 95% upper limit under three assumptions: (i) the harmonic model with $i = 36^\circ$, which is our fiducial limit; (ii) the harmonic model at the best-fit $i \approx 75.9^\circ$, and (ii) the harmonic model with $i \approx 116^\circ$, which is the inclination angle within our 1σ band that gives rise to the maximal L_p prediction. The shaded band in Fig. 10.1 covers this range of possibilities and is an estimate of the systematic uncertainty from magnetic field mismodeling.

10.2.3 Additional MWDs

In this section we comment on additional promising MWDs where linear polarization data is already available or where acquiring polarization data should be a priority for the future. First note that Ref. [435] suggests upper limits on $g_{a\gamma\gamma}$ at the level of $|g_{a\gamma\gamma}| \lesssim (5-9) \times 10^{-13}$ GeV^{-1} using the linear polarization data from the MWDs PG 1031+234 and SDSS J234605+38533. We begin by revisiting these MWDs to assess the robustness of the upper limits from these stars.

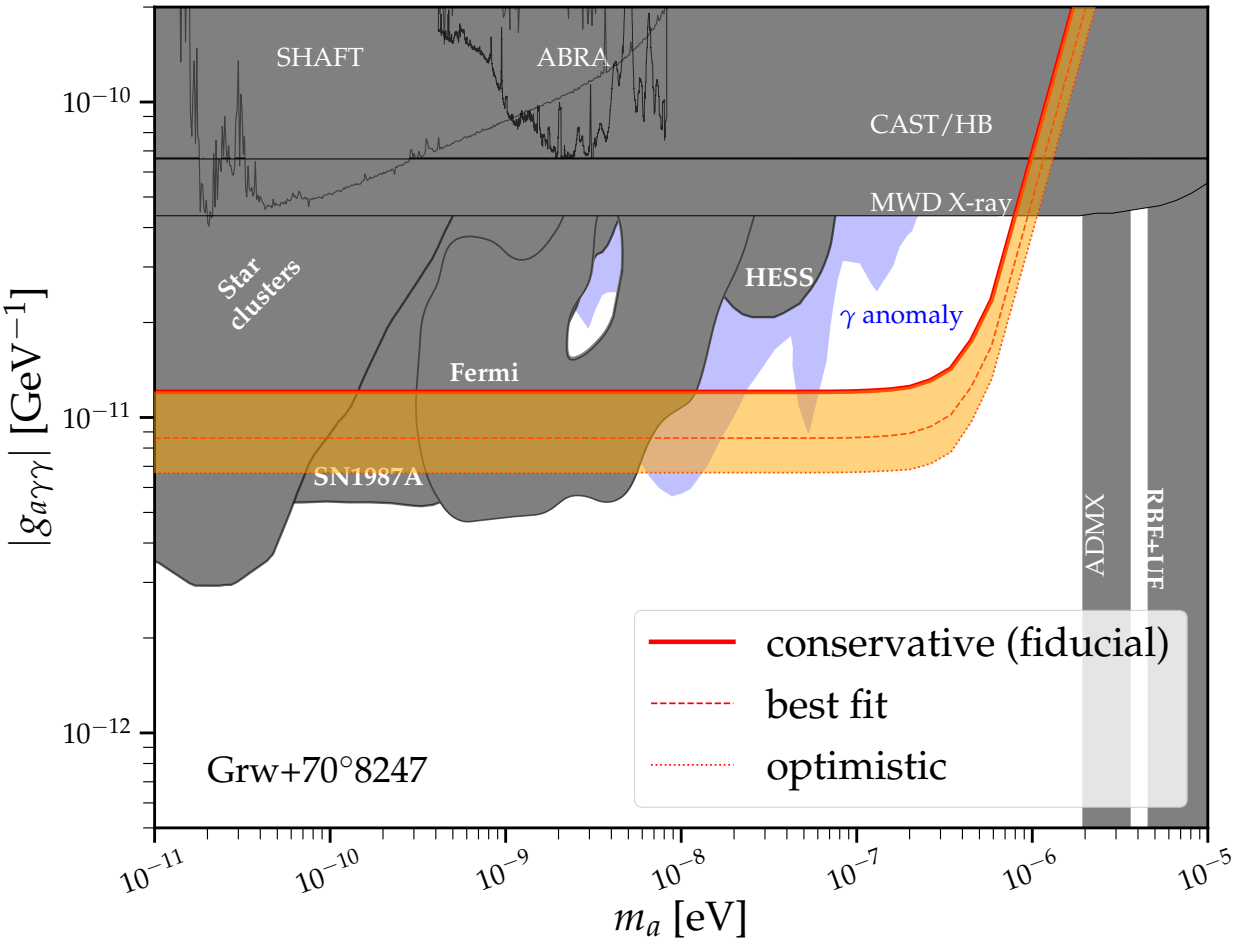

Figure 10.8: As in Fig. 10.1 but for the MWD Grw+70°8247. We compute the upper limit on $g_{a\gamma\gamma}$ using the harmonic magnetic field model. The orange region arises from varying the inclination angle over the region shown in Fig. 10.7; the fiducial upper limit is that computed with the inclination angle shown in solid vertical in that figure. The upper limit computed with the best-fit inclination angle in [52] is also indicated. Note that we fix the MWD radius at $R_{\rm star} = 6.7 \times 10^{-3}\ R_\odot$, which is the smallest value allowed at 1σ in our analysis, in order to be conservative.

A fit of the centered dipole magnetic field model to the intensity spectra for the MWD SDSS J234605+38533 measured by the SDSS resulted in a polar field strength $B_p = 798 \pm 164$ and inclination angle $i = 2.5° \pm 1.1°$ [16]. Note, however, that this analysis only consider intensity spectra and not circular polarization, and so the orientation angle is only constrained by producing the correct distribution of surface field strengths not directly by the orientation of the magnetic field structure. Indeed, in the context of the offset dipole model a comparable magnetic field strength was found but for $i = 87° \pm 15°$ [16]. Ref. [475] measured a linear polarization from SDSS J234605+38533 of $L_p \approx 1.33\%$, though with no uncertain-

ties quoted, across the wavelength range 4200 $\AA$ to 8400 $\AA$ using the SPOL instrument on the Steward Observatory Bok Telescope and the Multiple Mirror Telescope (MMT) on Mt. Hopkins (see [476] for details). Without uncertainties on the L_p measurement, it is difficult to estimate the 95% upper limit on the linear polarization. For concreteness, let us imagine that the upper limit is $L_p \lesssim 2\%$ over this wavelength range. To set a conservative upper limit, we take $i = 1.4°$ for the centered dipole with $B_p = 634$ MG, since this is the most conservative scenario consistent within the 1σ uncertainties for B_p and i. We also fix $R_{\rm star} = 0.01\ R_\odot$ for definiteness. For $m_a \ll 10^{-6}$ eV we find that this then translates into a limit $|g_{a\gamma\gamma}| \lesssim 2.1 \times 10^{-11}$ GeV^{-1}, though it is important to remember that this is an estimate since no rigorous upper limit on L_p is available. This upper limit is comparable to the conservative upper limit from Grw+70°8247, weaker than the conservative upper limit from SDSS J135141, and significantly weaker than the $|g_{a\gamma\gamma}| \lesssim (5-9) \times 10^{-13}$ GeV^{-1} upper limit quoted from this MWD and PG 1031+234 in [435]. However, it is possible that the limit from SDSS J234605+38533 could be improved with a better determination of the magnetic field geometry, since *e.g.* the off-set dipole model prefers much larger inclination angles.

Next, we consider PG 1031+234, which was the second MWD from [435] that led to the proposed upper limit $|g_{a\gamma\gamma}| \lesssim (5-9) \times 10^{-13}$ GeV^{-1} for low axion masses. This MWD is unique relative to the MWDs considered so far in this chapter in that it has a period ∼3 hr 24 min that leads to observable oscillations in the polarization and flux spectra [53,477]. The linear polarization data from [53] stacked over the rotational phase of the MWD in the band 3200–8600 $\AA$ is illustrated in Fig. 10.9; the left (right) panel shows the Stokes parameter ratio Q/I (U/I). These ratios are inferred from the data in [53] using the linear polarization data and the polarization angle. The uncertainties in Fig. 10.9 are estimated during the model fitting process, as described shortly.

The MWD PG 1031+234 was modeled in [53] as having a centered dipole field with a polar field strength ∼500 MG and a small magnetic hot-spot that has a much larger field strength $\sim 10^3$ MG. More specifically, Ref. [53] showed that the following magnetic field model was able to explain the major features observed in the flux, circular polarization, and linear polarization data by using radiative transfer models to estimate to the polarization and absorption signals at different points on the MWD surface. Their model included a centered dipole with polar field strength $B_c \approx 400$ MG and magnetic axis inclined by 35° relative to the rotation axis. The rotation axis is at an inclination angle of $i = 60°$ relative to the line of sight. The magnetic hot-spot is modeled by an offset dipole with magnetic axis inclined at 55° relative to the rotation axis, polar surface field strength of 10^3 G, and offset $z_{\rm off} = 0.4\ R_{\rm star}$ along the magnetic axis. The magnetic hot-spot precedes the centered dipole by a phase of 120°. In Fig. 10.9 we adjust the phase such that zero corresponds to

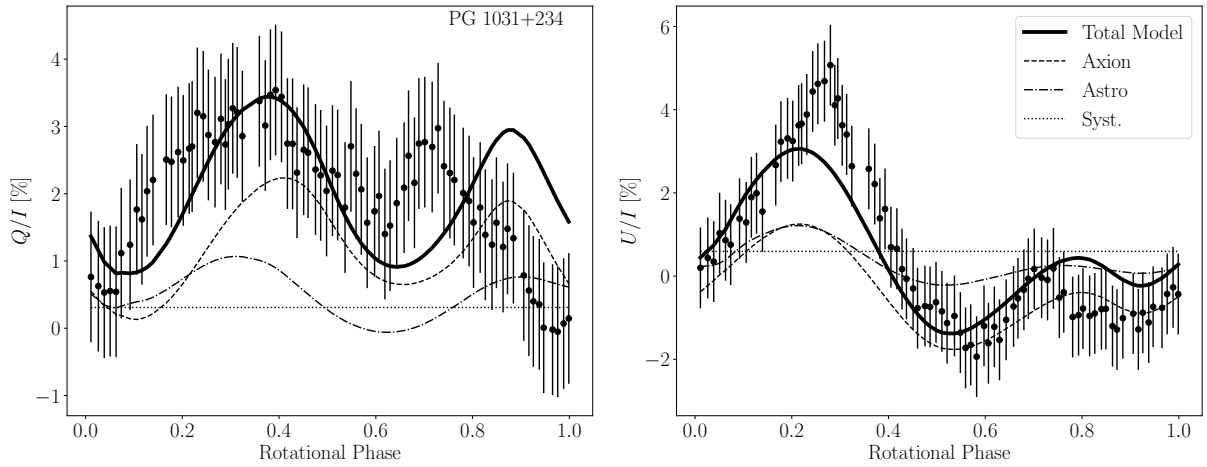

Figure 10.9: The linear polarization data from [53] for PG 1031+234 presented as ratios of the Stokes parameters Q (left) and U (right) relative to the intensity I. We fit a model consisting of an axion, astrophysical, and systematic contributions to the joint Q/I and U/I data, treating the statistical uncertainty as a nuisance parameter. We display the best-fit joint model, in addition to the best-fit components. The uncertainties on the data points are the best-fit uncertainties from maximum likelihood estimation of the associated hyperparameter. The magnetic field model consists of two dipoles, with one being offset, and thus the axion and astrophysical contributions have varying phase differences over the rotational phase of the MWD. We estimate the constraint $|g_{a\gamma\gamma}| \lesssim 8.8 \times 10^{-12}$ GeV^{-1} at 95% confidence for $m_a \ll 10^{-7}$ eV, subject to the caveat that the magnetic field model is fixed at the best-fit model from [53]. The best-fit axion coupling, corresponding to the illustrated curve, is $g_{a\gamma\gamma} \approx 7.4 \times 10^{-12}$ GeV^{-1}.

the transit of the centered dipole. The radiative transfer calculation in [53] using this model was able to explain the broad features observed in both the circular and linear polarization data, though an axion signal would only contribute to the linear polarization.

We compute the astrophysical contribution to the linear polarization using a similar method to that in [53]. In particular, we use the formalism in [452], including both the bound-free and cyclotron contributions to the polarization, as cyclotron absorption is expected to contribute in the wavelength band of the observations. We compute the astrophysical Stokes parameters averaged over wavelengths and over $\sim 10^5$ points on the observable hemisphere at a fixed phase. We repeat this process over all of the rotational phases of the MWD. Note that we assign the astrophysical model two unconstrained nuisance parameters that independently normalize the amplitudes of the linear polarization contributions from bound-free and cyclotron absorption.

We compute the axion-induced linear polarization signal for the magnetic field model described above assuming $m_a \ll 10^{-7}$ eV. The polarization signal is illustrated in Fig. 10.9

for the best-fit coupling $g_{a\gamma\gamma} \approx 7.4 \times 10^{-12}$ GeV.

In addition to the astrophysical and axion contributions to the polarization, we separately add in phase-independent systematic contributions to Q/I and U/I. These contributions are to allow for instrumental effects that could bias Q/I or U/I away from zero. We then construct a joint likelihood over the Q/I and U/I data, with the axion and astrophysical models contributing to both ratios. Since we do not know the alignment of the MWD on the sky, we allow for an additional nuisance parameter that rotates the projection of the MWD on the sky. Note, however, that the astrophysical and axion contributions rotate by the same amount for a given orientation. Lastly, we determine the uncertainties on the data in a data-driven way by assigning the uncertainties to be hyperparameter that is treated as a nuisance parameter and determined by maximum likelihood estimation, as in *e.g.* (10.25). In total, we thus have our signal parameter $g_{a\gamma\gamma}$ and six additional nuisance parameters.

The best fit of the joint signal and background model is illustrated in Fig. 10.9, along with the best-fit component contributions. Note that while the model is able to describe the broad features in the data, there is clear evidence for mismodeling across the phase of the MWD. On the other hand, our goal here is not to derive a precise limit, since for example we do not account for uncertainties on the magnetic field model, but rather to illustrate key points behind the phase-resolved analysis and to roughly estimate the magnitude of the limit that may emerge from a more careful analysis.

Importantly, the Q/I and U/I axion and astrophysical contributions vary independently over the phase of the MWD, since they depend differently on the observable magnetic field geometry. Thus, large cancellations between the axion and astrophysical contributions are not possible across all phases and for both Q/I and U/I. This leads to the result that the 95% upper limit on $g_{a\gamma\gamma}$, as determined from the profile likelihood, is estimated as $|g_{a\gamma\gamma}| \lesssim 8.8 \times 10^{-12}$ GeV^{-1}, which is relatively close to the best-fit axion coupling of $g_{a\gamma\gamma} \approx 7.4 \times 10^{-12}$ GeV^{-1}. We caution, however, that this upper limit should be treated with caution, since it does not account for uncertainties on the magnetic field profile and since the fits in Fig. 10.9 show evidence for mismodeling. Still, it is striking that our estimate for the upper limit around an order of magnitude weaker than the upper limit estimate in [435] for the same MWD.

The example of PG 1031+234 highlights how rotational-phase resolved data may be useful in the context of the axion-induced linear polarization search. This example motivates, in particular, a search for axion-induced polarization from the MWD RE J0317-853. This MWD is rotating quickly with a period ∼725 s [214]. The magnetic field varies across the surface over the rotation period between ∼200 – 800 MG [215]. Moreover, Ref. [215] presented a model for the magnetic field structure in terms of a harmonic expansion through

MWD Name	B_p [MG]
RE J0317-853	$\sim 200 - 800$
SDSS J033320.36+000720.6	849 ± 42
SDSS J002129.00+150223.7	531 ± 64
SDSS J100356.32+053825.6	672 ± 119
HE 1043-0502	~ 820
SDSS J120609.80+081323.7	761 ± 282
ZTF J190132.9+145808.7	$\sim 600 - 900$

Table 10.2: MWDs without existing linear polarization data but which would be promising targets for future axion searches, due to their large magnetic fields. The magnetic fields for these targets were determined by Refs. [16–18].

$\ell \leq 3$ with a magnetic axis offset from the rotation axis, which is at a non-zero angle to the line-of-sight. Unfortunately, no linear polarization data is available for RE J0317-853 at present, but acquiring such data and interpreting it in the context of the axion model should be a priority. We note that [39] recently used X-ray data from RE J0317-853 to search for axion-induced hard X-ray signals. A list of MWDs which do not currently have linear polarization data but with large magnetic fields, including RE J0317-853, is in Tab. 10.2. In addition to high-resolution linear polarization data from the MWDs, circular polarization data would be useful in order to better constrain the magnetic geometries of these MWDs using radiative transfer theory.

10.3 Discussion

In this chapter we model how axions may induce polarization signals in the otherwise unpolarized thermal emission from MWD surfaces. We show that MWDs are optimal targets for axion-induced polarization searches because they have large magnetic fields but not so large that the Euler-Heisenberg Lagrangian suppresses the photon-to-axion conversion probability. Larger stars with lower magnetic field strengths have reduced conversion probabilities because of the axion-to-photon mixing term, while the more compact NSs, which have stronger magnetic fields, are in the regime where the Euler-Heisenberg term suppresses the mixing by modifying the photon dispersion relation relative to that of the axion. At the same time, the predicted astrophysical backgrounds to the linear polarization from MWDs are minimal, relative to *e.g.* those from NSs, and induced by polarization-dependent radiative transfer processes for initially unpolarized surface emission propagating through the thin, magnetized MWD atmospheres.

The axion-induced polarization signal from MWDs was previously discussed in [223,435], where it was claimed that linear polarization data from the MWDs SDSS J234605+38533 and PG 1031+234 may already constrain the axion-photon coupling to $|g_{a\gamma\gamma}| \lesssim (5-9)\times 10^{-13}$ GeV^{-1} for low axion masses $m_a \ll 10^{-7}$ eV. We provide a simple formalism for predicting the axion-induced polarization signal, which only involves the field configuration far away from the MWD surface, and we show that these previous limits are likely overstated. However, we present analyses from two MWDs with dedicated linear polarization data and well-measured magnetic field distributions: SDSS J135141 and GRW+70°8247. The conservative upper limit from SDSS J135141, which is $|g_{a\gamma\gamma}| \lesssim 5.4 \times 10^{-12}$ GeV^{-1}, is the strongest to-date over a large region of axion masses and strongly disfavors the axion interpretation of the previously-observed gamma-ray transparency anomalies. Future linear polarization measurements, in conjunction with dedicated modeling efforts for the magnetic field geometries and astrophysical linear polarization backgrounds, towards promising targets such as RE J0317-853 could further strengthen these limits and perhaps unveil evidence for low-mass axions.

Chapter 11

Red-Giant Branch Stellar Cores as Macroscopic Dark Matter Detectors

Dark matter (DM) is known to exist from a multitude of gravitationally-based evidence accumulated over a century of observation [478]. Much of the unconstrained DM mass range, which spans from $\sim 10^{-22}$ eV fuzzy dark matter [479] to $\sim 5M_\odot$ MACHOs [480–482], lies above the mass scales involved in the Standard Model (SM). Elementary DM can exist below the Planck scale, however, more massive DM must be a bound state, typically thought of as comprising new particles. In this case the DM sector should have a particle-antiparticle asymmetry to allow bound state coalescence. A wide and continuous range of interactions can generate DM bound states with masses ranging from very large nuclei, $m \lesssim M_{Pl}$ [483–485], to nuggets of mass 10^{-7} g $\lesssim m \lesssim 10^{23}$g [486], and up to substructure of mass $\gtrsim M_\odot$ [487,488]. Macroscopic DM can also be comprised of SM particles or contain SM charges if the bound state is energetically prevented from decaying to nucleons [489–491].

Macroscopic DM candidates have sufficiently low event rates as to render microscopic direct detection experiments, with exposure times $\sim$1 kT yr, ineffective. However, massive, old astrophysical objects can act as DM detectors with exposure times $\sim M_\odot \times$Gyr $\approx 10^{33}$ kT yr. For example, it is well known that the passage of macroscopic DM through white dwarfs (WD) can deposit sufficient energy in a local region to ignite a Type 1a supernova [492]. Similarly, macroscopic DM passage in neutron stars can ignite superbursts [55]. In stars, supersonic DM can dissipate energy in the form of shockwaves, which travel to the surface, releasing transient UV radiation [493]. Macroscopic DM has also been probed through a host of additional mechanisms that do not require such extreme exposure times, albeit at lower masses [494–500].

In this chapter, we demonstrate that macroscopic DM can ignite helium fusion in red-giant branch (RGB) stellar cores. An RGB star is a low-mass star which has completed

hydrogen burning on the main sequence but has not yet begun helium burning. It has an inert electron-degenerate pure-helium core surrounded by a hydrogen-fusing shell. In the absence of macroscopic dark matter, shell fusion will continue to heat the core for ~ 0.5 Gyr, over which time the luminosity of the RGB star rises — this continues until the critical temperature for helium ignition is reached in the core. Because degeneracy pressure is independent of temperature, the energy released heats the core, further increasing the fusion rate. The entire core ignites in a runaway reaction known as the "helium flash" (HF). The only outwardly observable signal is the essentially instantaneous drop in luminosity of the star over $\sim 10 - 50$ kyrs, due to expansion and subsequent cooling. The transition of the RGB star onto the next stage of stellar evolution, the horizontal branch (HB), then takes place over ~ 2 Myrs.

The HF can occur prematurely if significant energy is deposited in the core. When a macroscopic DM particle traverses the degenerate core of an RGB star, elastic collisions between DM and the stellar material can generate enough heat to initiate local helium fusion, in an early-onset HF. The star undergoes the transition to the HB which in the extreme would entirely eliminate the RGB as a phase of stellar evolution. To capture cases in which only some fraction of RGB stars are subject to a DM-induced HF, we constrain DM using the measured RGB luminosity function (LF), which is the observed number of RGB stars as a function of their luminosity.

The RGB core temperatures and densities increase with time, so the high-luminosity RGB stars already closest to undergoing the standard HF are more easily ignited by DM. The presence of macroscopic DM steepens the LF, since fewer high-luminosity stars survive. To probe this new mechanism, we use the MESA code [501] to simulate the evolution of the RGB stars in the globular cluster (GC) M15 and compute theoretical LFs to compare to the M15 LF computed in Ref. [502]. Old GCs such as M15 are good targets for this search because they are well-studied and host many RGB stars which were formed in similar conditions, *e.g.* in similar metallicity environments. We focus on M15 because it is the only GC for which an LF has been directly constructed and presented. The LF can be computed for many other GCs using their Hertzsprung-Russell diagrams, but this is beyond the scope of this chapter. Additionally, as we will discuss, if the GC formation was seeded by an early universe DM overdensity, then the surviving DM density may be orders of magnitude greater than the Milky Way (MW) density at that location. We assume the standard Milky Way DM halo density for our fiducial constraint, but discuss the much stronger limit obtained if future measurements determine that M15 hosts its own DM halo.

In Sec. 11.1, we examine the physics of the HF and the DM-induced ignition mechanism. In Sec. 11.2, we detail the MESA simulations of the M15 RGB stars used in this chapter. In

Sec. 11.3, we discuss the computation of the DM-induced HF rate. In Sec. E.2, we discuss our construction of the LFs and show the 95% limits on macroscopic DM parameters from the observed M15 LF. Finally, we conclude and discuss additional targets and methods to improve detection prospects in Sec. 11.5.

11.1 Inducing the HF in Red Giants

In order to prematurely ignite the helium core, DM must deposit enough energy to initiate helium fusion before that energy diffuses away. The ignition of significant helium fusion in a large region will generate a stable flame-front, or deflagration [503]. In this chapter, we assume that such an energy deposition occurs through SM elastic scattering off macroscopic DM with sufficient interaction strength that the resulting cross section is geometric.

For such a DM candidate undergoing elastic scattering, the average energy transfer per nuclei is $\mathcal{O}(m_n v_\chi^2)$, giving a linear energy deposition rate of [504]

$$\frac{dE}{dx} = \sigma_{\chi n} \rho_\star v_\chi^2. \tag{11.1}$$

Where ρ_* is the stellar density, which varies strongly throughout the star, and v_χ the DM velocity at that depth in the star. The DM deposits energy in a cylinder with length a substantial portion of the star, and cross-sectional area given by the geometric cross section. This energy deposition has only local effects, and is hence unobservable (but see [493]), unless it ignites a runaway fusion reaction. A runaway reaction will occur when the local energy generation rate by fusion exceeds the energy loss rate, which is dominated by diffusion. To estimate these rates, we must assume a temperature profile immediately after the DM impact. We work in cylindrical coordinates where the longitudinal axis points along the direction of the DM path and r is the distance from the center of the DM path. We assume the energy deposition is linearly increasing from the edge of the cylinder ($r = \sqrt{\sigma_{\chi n}/\pi}$) to the center, yielding

$$\frac{dE}{dV} = \frac{3}{\sigma_{\chi n}} \left(1 - \frac{r}{\sqrt{\sigma_{\chi n}/\pi}}\right) \frac{dE}{dx}. \tag{11.2}$$

This profile is just one example of a heat deposition profile. We vary the energy deposition profile and find that if they are not sharply peaked at the center, the effect on the ignition parameter can be $\mathcal{O}(1)$; see Appendix I.2 for further discussion. We then compute the temperature $T_{\rm hot}$ that the energy deposition heats the stellar material to, via numerically

solving

$$\frac{dE}{dx} = \rho\sigma_{\chi n}\int_{T_*}^{T_{\rm hot}} c_v dT. \tag{11.3}$$

We use analytic approximations for the heat capacities of the electrons, ions and photons, which are

$$c_v^{e^-} = \begin{cases} \dfrac{7\pi^2}{15}\dfrac{k_B^4}{\hbar^3c^3}\dfrac{T^3}{\rho_*} & T > 10^9 K \\ \dfrac{3k_B}{m_{^4\rm He}} & T_{degen} < T < 10^9 K \\ \dfrac{4k_B^2 T}{m_{^4\rm He}E_F\pi^2} & T < T_{degen}, \end{cases} \tag{11.4}$$

$$c_v^{\gamma} = \frac{4}{15}\pi^2\frac{k_B^4}{\hbar^3c^3}\frac{T^3}{\rho_*}, \tag{11.5}$$

$$c_v^{ion} = \frac{3k_B}{2m_{^4\rm He}}. \tag{11.6}$$

where $T_{degen} = 3E_F/\pi^2 k_B$, for E_F the Fermi energy, and 10^9 K approximates the transition to a relativistic electron gas. We neglect the relativistic degenerate electron regime because the electron contributes negligibly to the heat capacity when it applies.

The dominant fusion process is helium fusion, specifically through the triple-alpha process, wherein three ^{4}He fuse through the resonant Hoyle state to create a ^{12}C nucleus. The triple-alpha energy generation rate is [503]

$$\dot{S}_{3\alpha} = 5.1\left(\frac{\rho_*(r)}{10^4\ \mathrm{g/cm^2}}\right)^2\left(\frac{X(\mathrm{He})}{T_9(r)}\right)^3 e^{-4.4/T_9(r)}\frac{\mathrm{ergs}}{\mathrm{s\ g}}, \tag{11.7}$$

where $T_9(r) \equiv T(r)/(10^9\ \mathrm{K})$. Electron screening enhances the rate at low temperatures, however this effect is $\lesssim 5\%$ at 5×10^8 K, where the nuclear generation rate is already quite low and so is neglected. Note that carbon fusion, which operates at similar temperatures, is suppressed in the initial ignition by the low carbon abundance. Thus we use Eq. (11.7) to determine the local energy generation rate, which can be expressed as

$$\frac{d\dot{E}_{\rm nuc}}{dx} = 2\pi\int \dot{S}(r)\rho_* r dr. \tag{11.8}$$

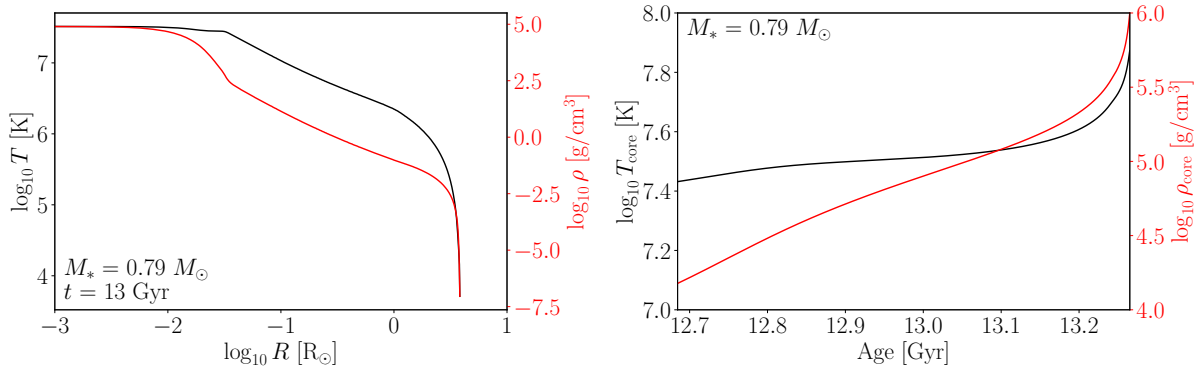

Figure 11.1: **Left Panel** The internal temperature (black) and density (red) profiles of the 0.79 $M_\odot$ star when it is 13 Gyr old. **Right Panel** The central temperature (black) and central density (red) of the 0.79 $M_\odot$ star as a function of time during the RGB phase, which spans the x-axis of the plot.

The heated region cools off via diffusion at a rate of

$$\frac{d\dot{E}_{\rm diff}}{dx} = -2\pi k r \frac{dT}{dr}\bigg|_{r=\sqrt{\sigma/\pi}} \tag{11.9}$$

where k is the thermal conductivity. Runaway nuclear fusion will occur if the generated heat is greater than that lost through diffusion. To see this explicitly, we define an ignition parameter, ζ, as

$$\zeta \equiv \frac{d\dot{E}_{\rm nuc}/dx}{d\dot{E}_{\rm diff}/dx}. \tag{11.10}$$

Ignition occurs for $\zeta > 1$. We will see that for typical points in our constrained region, this ratio is far greater than 1.

11.2 MESA Simulations of M15 RGB stars

In this section, we describe our MESA simulations of the RGB stars in the GC M15. We use MESA version 12115 [501] to simulate the evolution of the RGB stars. The age of M15 is 13 ± 1 Gyr [502]; we fix its age at 13 Gyr. Under this assumption, the masses of the RGB stars in M15 range from $0.785 M_\odot$ (just ascending the RGB) to $0.795 M_\odot$ (at the end of the RGB phase). The metallicity of the M15 GC is [Fe/H] $= -2.1$ [502], which corresponds to an average isotopic abundance of [Z] $= -1.57$ [505] — we fix this to be the initial abundance in the MESA simulations.

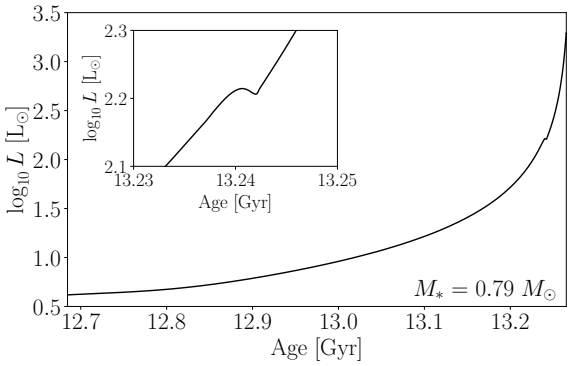

Figure 11.2: **Main Plot** The luminosity of the 0.79 $M_\odot$ star as a function of time during the RGB phase, which spans the x-axis of the plot. **Inset** The same as the main plot but zoomed in around the red giant bump.

We simulate stars of initial mass M_* between 0.785 and 0.795$M_\odot$ in steps of 0.001$M_\odot$ from the pre-main sequence through the beginning of central helium ignition. The MESA simulations return one-dimensional (radial) profiles of temperature T, density ρ, and isotopic compositions at many time points throughout the evolution, along with bulk properties of the star: age t, luminosity $L(t)$, effective temperature $T_{\rm eff}(t)$ and surface gravity $g(t)$. We use these stellar models to (i) compute the expected DM-induced HF rate in each star and (ii) compute the theoretical LFs under the null and signal hypotheses.

In the left panel of Fig. 11.1, we show the temperature and density profiles, at $t = 13$ Gyr, of the star with mass $\overline{M}$ in the center of the range, $\overline{M} \equiv 0.790\ M_\odot$. Over the full mass range we focus on in this chapter, the stellar properties in the RGB phase are the same as those shown here to $< 1\%$. The helium core occupies $\sim$1% of the stellar radius, when the temperature and density sharply drop traversing farther out of the star. The vast majority of the star by volume is the low-density stellar envelope, which at this time extends out to $\sim 4\ R_\odot$, though the envelope will continue to expand in size until the HF. In the right panel, we show the time-evolution of the central temperature and density, which sharply increase as the star nears the flash. The lower and upper x-limit of the plot corresponds to when the star enters the RGB phase at $\sim$12.68 Gyr and when the HF occurs at $\sim$13.27 Gyr, corresponding to a total RGB duration for this star of $T_{\rm RGB}^{\overline{M}} = 590$ Myr. We parameterize the fraction of the RGB branch ascended by the star by τ,

$$\tau \equiv \frac{t - t_{\rm TAMS}}{T_{\rm RGB}}, \tag{11.11}$$

where $t_{\rm TAMS}$ is the terminal age main sequence, the age at which the star begins to ascend the RGB, and $T_{\rm RGB}$ is the length of the RGB phase. Therefore $\tau = 0$ defines when the star

begins the RGB phase and $\tau = 1$ when the standard HF occurs and the star moves onto the HB. Note that the explicit mapping between t and τ depends on the stellar mass through $t_{\rm TAMS}$ and $T_{\rm RGB}$.

In Fig. 11.2, we show the luminosity evolution of the star. Based on this plot, we can reconstruct the two basic features of the LF by making the approximation that there are the same number of stars in each age interval. Firstly, because the luminosity increases faster with increasing age, there will be more stars at lower luminosities. Therefore, the LF will sharply increase towards lower luminosities. Secondly, at ∼13.24 Gyr, the luminosity abruptly stops increasing for a few Myr (see the inset). As the hydrogen-burning shell expands outwards, it reaches a composition discontinuity created by the first dredge-up, which leads to a brief halt in the luminosity increase. Because of this, stars spend a longer time at this luminosity level. This is known as the red giant bump [506, 507], and indeed in the LF there is a small bump at this luminosity.

11.3 The DM-Induced He-ignition Rate

The rate at which DM trajectories ignite a given stellar core depends sensitively on the details of the DM distribution. There are two basic assumptions one can make; either the GC formed within a DM overdensity that survives today, or that it did not and the only DM around is that of the Milky Way (MW) halo. This first assumption is nominally the expectation of the standard model of cosmology, and would give a DM density orders of magnitude above the MW halo density. However, there is a lack of supporting observational evidence. In [508] a prototypical GC was found to contain very little DM under modest assumptions, and [509] found that GCs closer than 100 kpc to the Galactic Center typically have halos that have already merged with the galaxy halo (M15 is $\sim$ 10 kpc from the Galactic Center). Numerical simulations of the GC DM halo scenario find that tidal stripping can significantly reduce the amount of DM, however this still would likely leave some portion of the DM within the tidal radius [509–512], and this scenario is often assumed in the literature [493, 513, 514].

Due to the lack of a complete consensus, we place our fiducial limits assuming the DM density in M15 is purely that of the MW DM halo, and defer our analysis including a GC DM halo to App. I.1.

We model the MW halo with the NFW profile [102, 139] from [515] with scale factor $r_s = 20$ kpc, normalized such that distance of Earth to the Galactic Center is 8.12 kpc [516]. In the context of this profile, we infer a MW halo DM density at the location of M15 today, 10.76 kpc from the Galactic Center [517], of $\rho_{\rm DM} = 0.35 \pm 0.10$ GeV cm^{-3}, and we assume the lower 1σ value 0.25 GeV cm^{-3} in our analysis. However, M15 has a galactic orbital

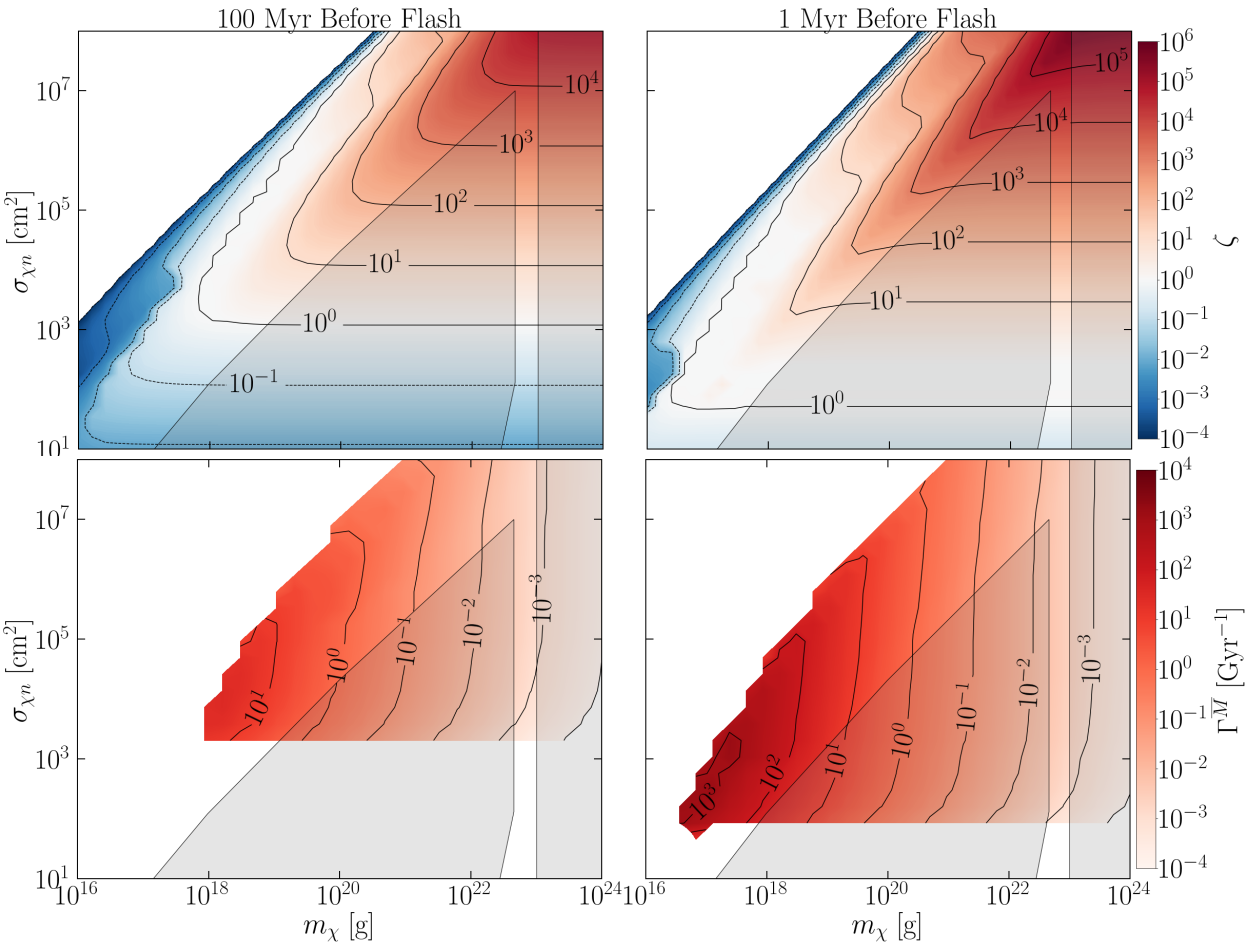

Figure 11.3: **Top Panels:** The maximum ignition parameter, ζ, described in Eq.(11.10), for a simulated DM trajectory assuming an initial angular momentum $\ell_0 = 10^{-4}c \times 10^{10}$ cm, where 10^{10}cm $= 0.14\ R_\odot$, and the benchmark mass $\overline{M}$ star. In light grey are constraints from non-observation of DM-induced Type Ia supernova in WDs [54, 55](triangular shape) and from microlensing [56] (vertical line). **Top Left:** 100 Myr before the expected HF (total RGB phase duration is $T_{\rm RGB} \sim 590$ Myr). **Top Right:** 1 Myr remaining in the RGB phase. **Bottom Panels:** The rate of DM induced HF ignition $\Gamma^{\overline{M}}$[Gyr^{-1}], with correction factor $c(t)$ set to 1 for comparison purposes, see Eq. (11.13). **Bottom Left:** 100 Myr before the nominal HF. **Bottom Right:** Ignition rate 1 Myr before HF.

period of ∼140 Myr with a $\sim 3.7 - 4$ kpc periapsis, so that its local DM density periodically changes by a factor ∼4.8 over the length of the RGB phase, ∼600 Myr. This orbit was computed numerically in Ref. [518] by evolving the M15 orbital trajectory backwards in the galactic gravitational potential in [519], and in our analysis we assume the best-fit orbit

provided. We assume the DM velocity distribution is given by the standard halo model,

$$f(\mathbf{v},t) = N\exp\left(-\frac{(\mathbf{v}+\mathbf{v_{GC}}(t))^2}{2\sigma_{vr}^2}\right) \times \Theta(v_{esc} - |\vec{v}+\vec{v}_{GC}(t)|). \tag{11.12}$$

for normalization N, radial velocity dispersion given by the upper 1σ value from [515], $\sigma_{vr} = 167$ km s^{-1}, and a MW escape velocity v_{esc} of 544 km s^{-1}. The stellar velocity within M15 is ≈ 10 km s^{-1}, thus to a good approximation all stars move at the GC velocity. At the present location of M15, we find $v_{GC} = 123 \pm 1.1$ km s^{-1}.

The depth to which the DM must penetrate is to the ignition radius of the star $R_{\zeta=1}(\tau)$, where again τ is the proportion of the RGB branch a given star in M15 has gone through. For DM with initial velocity v_0, the rate of impacts within radius $R_{\zeta=1}$ is enhanced by a gravitational focusing factor of $\left(1+(v^*_{\rm esc}(r)/v_0)^2\right)$, where r is the distance of the DM from the center of the star. The $v_{\rm esc}$ at the core is $\sim 10^3$ km s^{-1}, so we approximate this effect with $(v_{*\rm esc}(r)/v_0)^2$.[1] These effects can be analytically integrated, which we show in App. I.3. We divide these contributions to the DM-induced ignition rate into contributions that depend only on stellar evolution (*i.e.*, the time-dependence is given only by τ) and those that depend on the GC location throughout the galaxy, where the time-dependence is on t directly.

$$\Gamma(t,\tau) = \Gamma_0 \times c(t, v_{GC}, v_{\rm esc}) \tag{11.13}$$

$$\Gamma_0(\tau) = 2\sqrt{2\pi}\frac{\rho_{DM}(t_0)}{m_\chi} R^2_{\zeta=1}(\tau)\sigma_{vr} \times \frac{v^2_{*\rm esc}(R_{\zeta=1}(\tau))}{2\sigma^2_{vr}} \tag{11.14}$$

Where t_0 implies evaluation at the position of M15 today. The correction factor $c(t, v_{GC}, v_{\rm esc})$ includes the finite MW escape velocity, and the variation of v_{GC} and ρ_{DM} over time as the GC orbits the MW. It varies within $c(t)\ \epsilon\ [0.87, 2.47]$ with large values occuring when the GC passes near the galactic center and its higher DM density. We detail its computation in App. I.3 and show our results in Fig. I.3.

The value of $R_{\zeta=1}$ is determined by simulation of a DM infall to the benchmark star $\overline{M} = 0.79\ M_\odot$. We use MESA generated profiles of the stellar density as a function of radius, and the friction force derived from Eq. (11.1). We simulate DM trajectories starting at infinity with varying impact parameters b, scanning over signal parameters $\boldsymbol{\theta}_s$ and at multiple stellar ages t. For each point in the scan, $R_{\zeta=1}$ is defined as the largest radius at which the trajectory ignites the star, typically of order 10^9 cm. We implement Fehlberg's $4^{th}(5^{th})$ order method and use an error tolerance per step of 10 m and $10^{-9}c$. We verified

[1] One may also think there is a gravitational focus from the GC potential, however this effect is not independent of the stellar focusing and including this effect increases the rate only by $v^2_{GC\rm esc}/v^2_{*\rm esc} \sim 10^{-4}$.

this procedure by checking that in selected cases the global error estimate was within 10%.

An important simplification is that the DM trajectory depends only on the initial angular momentum per unit mass, $\ell = b v_0^{\max}$, rather than individually on b, and velocity at infinity, v_0, within $\sim 10\%$ below $v_0 \approx 5 \times 10^{-3} c$. Further, the rate of stellar ignition depends only on the maximum angular momentum, $\ell^{\max}$, defined by the largest ℓ that satisfies our ignition condition, $\zeta > 1$. Trajectories directly towards the star, defined by small ℓ_0, impact both deeper in the core and at higher velocities, leading to larger ζ, see Eq. (11.10). Trajectories with larger initial angular momentum may result in DM which only skims the core, or in extreme cases undergoes multiple orbits, resulting in lower ζ. Thus all smaller ℓ_0 will also ignite. This allows us to eliminate a dimension from our parameter scan. Thus explicitly what we determine from simulation is the maximum $\ell = R_{\zeta=1} v_{*\mathrm{esc}}(R_{\zeta=1})$ that causes ignition, yielding a rate of

$$\Gamma^{\overline{M}}(\boldsymbol{\theta}_s, t) = \sqrt{2\pi} \frac{\rho_{DM}(t_0)}{m_\chi} \frac{\ell_{\max}(\boldsymbol{\theta}_s, \tau)^2}{\sigma_{v_r}} \times c(t, v_{GC}, v_{\mathrm{esc}}) \tag{11.15}$$

for our benchmark star.

In the top panels of Fig. 11.3 we simulate DM trajectories for fixed initial angular momentum, plotting the maximum ignition ratio ζ for each m_χ and $\sigma_{\chi n}$. The left and right panels are for two stars of the same mass $\overline{M}$ but of different ages, corresponding to 100 and 1 Myr before the standard HF respectively. The triangular shape of each ζ contour can be understood simply. The series of "hypotenuses" mark where the DM loses significant kinetic energy in the stellar envelope. The white region begins where the DM loses all initial kinetic energy before reaching the core. The slope of these lines are close to unity as the acceleration from friction is $\propto \sigma_{\chi n}/m_\chi$. Moving perpendicularly away from the hypotenuse towards larger m_χ and smaller $\sigma_{\chi n}$ increases the depth at which the DM penetrates. Far away from this line, friction is irrelevant so the only relevant parameter for ζ is $\sigma_{\chi n}$, where lower cross section corresponds to decreased energy deposition by Eq. (11.1), until ignition is no longer possible. We can see from the relative location of the $\zeta = 1$ contour in the left and right panels that as the star approaches the standard HF, smaller cross sections may ignite the star, consistent with Eq. (11.2).

In the bottom panels we plot the simulated rate of igniting DM impacts on a star in M15 for the same two ages. The minimum igniting cross section decreases over time, following the $\zeta = 1$ contour in the top panels. Near the minimum $\sigma_{\chi n}$ the contours turn sharply due to the rapid decrease in the portion of the core with sufficient temperature and density to be ignited by a given cross section. Where the rate is non-zero in both left and right panels, we see the overall rate increases with time due to the larger maximum igniting impact parameter

for stars closer to their nominal HF.

11.4 Constraints on Macroscopic DM

In this section, we outline our modeling of the theoretical LFs under the dark matter hypothesis and assess their goodness-of-fit to the measured M15 LF.

Although previously in Sec. 11.2 we had qualitatively discussed the LF as a function of L, the observable is the apparent V-magnitude. M15 was observed three times between 2002 and 2004 by the Hiltner 2.4m telescope at the Michigan-Dartmouth-MIT Observatory at Kitt Peak, Arizona. Ref. [502] used that data to construct the LF between apparent visual magnitudes $V \in [13.94, 17.94]$ (except V between 14.34 and 14.74) by [502], shown in Fig. 11.4, and we fit our theoretical LFs to that data in this chapter. Explicitly, we start with the number of stars N_i in bin i corresponding to apparent visual magnitude V_i with bin widths of 0.2 magnitudes. We will refer to this data as $\boldsymbol{d} = \{N_i\}$. In particular, the red-giant bump is visible around 15.5 V-magnitudes. We mask the four data points between 15.14 and 15.94 V, where the model in [502] did not accurately capture all of the physics of the red-giant bump (our null model, also in Fig. 11.4, is nearly identical to that found in [502]). The relation between L and V is given by

$$V(t; M_*) = -2.5 \log\left(\frac{L(t; M_*)}{L_\odot}\right) \tag{11.16}$$

$$+ 4.74 + \mu - BC_{\rm V}(t, T_{\rm eff}, g) \tag{11.17}$$

where μ is the dereddened distance modulus with best fit $\hat{\mu} = 14.86$ [502] and we compute bolometric corrections in the V-band $BC_{\rm V}$ with the python package `isochrones` [520].

To construct a theoretical LF for the cluster, we need to know the DM-induced flash rate and the V as a function of time for the range of possible stellar initial masses in the cluster. The former we have detailed the calculation of in Sec. 11.3 for the $\overline{M}$ model. To compute the latter, we start from the luminosity-age relations $L(t; M_*)$ generated by MESA and compute $V(t; M_*)$ as in Eq. (11.17).

We now make the assumption that the GC evolution is coeval [502, 521]. Then the stellar ages are all $t_{\rm M15} = 13$ Gyr, with V magnitudes $V(t_{\rm M15}; M_*)$. Finally, we invert this relation to obtain the initial stellar mass as a function of V magnitude today, $M_*(V)$. For a particular signal model $\boldsymbol{\theta}_s$, the expected number of stars in V magnitude bin i spanning magnitudes $V_i^{\rm min}$ to $V_i^{\rm max}$ is

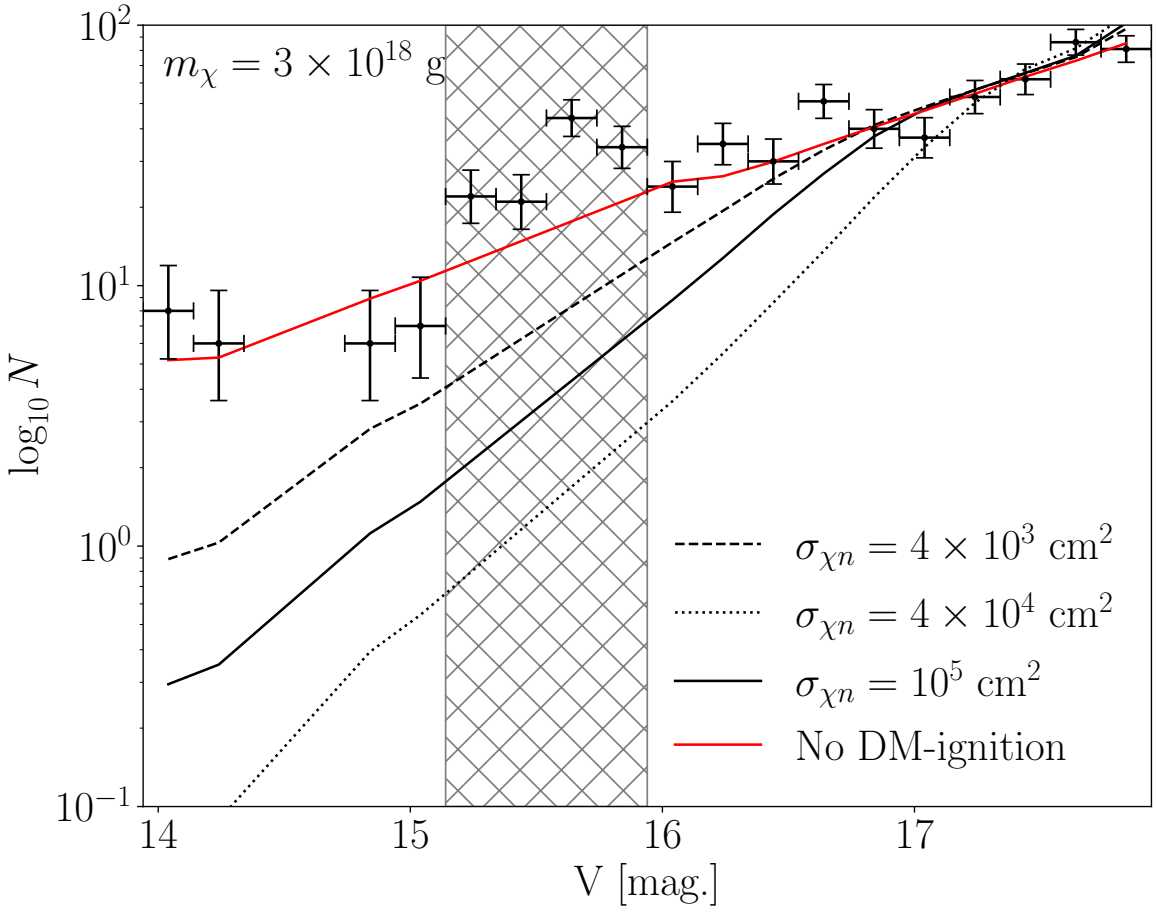

Figure 11.4: The M15 LF (black data points) with uncertainties given by $\sqrt{N_i}$. In red, we show the best-fit LF with no DM ignition. In black, we show the LFs with $m_\chi = 3 \times 10^{18}$ g and $\sigma_{\chi n} = 4 \times 10^3$ cm^2 (dashed), $\sigma_{\chi n} = 4 \times 10^4$ cm^2 (dotted), $\sigma_{\chi n} = 10^5$ cm^2 (solid). The hatched region indicates those four bins around the RGB bump which are masked in the analysis.

$$\lambda_i(\boldsymbol{\theta}_s) = A \times C_i \int_{M_*(V_i^{\rm min})}^{M_*(V_i^{\rm max})} dM \frac{dN}{dM}(M) P_{\rm surv}(\boldsymbol{\theta}_s, M) \tag{11.18}$$

where A is an arbitrary normalization constant to be fit to the data and C_i is the completeness factor in bin i computed via artificial star tests in [502]. $dN(M)/dM$ is the initial mass function, which we take to have a Salpeter form $dN(M)/dM \propto M^{-2.35}$ [522]. The integration limits are entirely determined by stellar physics, while the DM physics is only captured in the survival probability $P_{\rm surv}(\boldsymbol{\theta}_s, M)$, which we compute as follows. As detailed in Sec. 11.3, we have simulated the DM-induced ignition rate $\Gamma^{\overline{M}}(\boldsymbol{\theta}_s, t, \tau)$ for the mass $\overline{M}$ star. Then

$$P_{\rm surv}(\boldsymbol{\theta}_s, M_*) = \exp\left(-\int_0^{t_{\rm M15}} dt\ \Gamma^{M_*}(\boldsymbol{\theta}_s, t, \tau)\right), \tag{11.19}$$

which implicitly assumes that the DM-induced ignition rates are equal across stellar masses at fixed percentage of time completed on the RGB stage τ. Note that the rates are always zero unless the star is on the RGB.

In Fig. 11.4 we show the theoretical LFs $\lambda = \{\lambda_i(\boldsymbol{\theta}_s)\}$ for three separate cases, along with the measured completeness-corrected LF of M15. The LF with no DM-ignition has the shallowest slope, and the red giant bump is clearly visible in the bin around $V = 15.6$ magnitudes. We then show three curves under the model assumption $m_\chi = 3 \times 10^{18}$ g, at $\sigma_{\chi n} = \{4 \times 10^3\ \text{cm}^2, 4 \times 10^4\ \text{cm}^2, 10^5\ \text{cm}^2\}$. Tracing these curves from high to low V, they tend to follow the no DM-ignition line at until a particular V at which DM-ignition turns on, which sharpens the slope of the LF. Recall that stars with lower V are more highly evolved, and so have smaller survival probabilities. The DM model with the smallest cross section $\sigma_{\chi n} = 4 \times 10^3\ \text{cm}^2$ is in the region where increasing cross section decreases the survival probability, because the increased cross section increases the energy deposition in the core. The model with the largest cross section $\sigma_{\chi n} = 10^5\ \text{cm}^2$ lies in the region where increasing cross section increases the survival probability because the DM has lost significant kinetic energy in the stellar envelope. The model with middling cross section $\sigma_{\chi n} = 4 \times 10^4\ \text{cm}^2$ delineates the boundary between these two regions, and as such has the minimum survival probability for any DM with that mass. The LFs for other DM masses display similar behavior.

With the model in the same form as the data, we can write down the joint likelihood over V magnitude bins

$$\mathcal{L}(\boldsymbol{d}|\boldsymbol{\theta}_s, \boldsymbol{\theta}_{\rm nuis}) = \prod_i \mathcal{N}(\lambda_i(\boldsymbol{\theta}_s) - N_i, \sqrt{N_i}) \tag{11.20}$$

where the nuisance parameters $\boldsymbol{\theta}_{\rm nuis} = \{A, \mu\}$. A, as mentioned previously, is a normalization parameter that sets the total number of RGB stars in M15. μ is the distance modulus for M15, which we let float around its central value $\hat{\mu}$. $\mathcal{N}(x, \sigma_x)$ is the Gaussian likelihood with a mean x and standard deviation σ_x.

We construct the profile likelihood at fixed mass m_χ as a function of the cross section $\sigma_{\chi n}$, given by

$$\mathcal{L}(\boldsymbol{d}|\boldsymbol{\theta}_s) = \mathcal{L}(\boldsymbol{d}|\boldsymbol{\theta}_s, \hat{\boldsymbol{\theta}}_{\rm nuis}) \tag{11.21}$$

where $\hat{\boldsymbol{\theta}}_{\rm nuis}$ denotes the values of $\boldsymbol{\theta}_{\rm nuis}$ that maximize the likelihood at that $\boldsymbol{\theta}_s$. To define the region ruled out by this analysis, we construct the test statistic [109]

$$q(\boldsymbol{\theta}_s) = \begin{cases} 2\left[\ln \mathcal{L}(\boldsymbol{d}|m_\chi, \hat{\sigma}_{\chi n}) - \ln \mathcal{L}(\boldsymbol{d}|\boldsymbol{\theta}_s)\right] & \hat{\sigma}_{\chi n} \leq \sigma_{\chi n} \\ 0 & \hat{\sigma}_{\chi n} > \sigma_{\chi n} \end{cases} \tag{11.22}$$

where $\hat{\sigma}_{\chi n}$ is the value of the cross section that maximize the likelihood at that mass. We exclude at 95% confidence the cross sections for which $q(\boldsymbol{\theta}_s) > 2.71$. We additionally apply the Asimov procedure to the null hypothesis to compute the expected limits [109], and power-constrain the reported limits [110], although the latter was not necessary in practice. We do not find any evidence of DM-induced He flash events in this analysis.

We show the 95% limit on macroscopic DM from this search in Fig. 11.5, and compare with the expected sensitivity under the null hypothesis from the Asimov procedure. The analogous plot assuming a GC overdensity is shown in Appendix Fig. I.1. At fixed m_χ, the limits cut off at small $\sigma_{\chi n}$ below which the DM deposits too little energy to ignite helium fusion in the core. As $\sigma_{\chi n}$ increases, the signal increases until the cross section is so large that the DM is slowed by the stellar envelope. In that case, when the DM reaches the stellar core, it has too little kinetic energy remaining to ignite fusion, which cuts off the bounded region at large $\sigma_{\chi n}$. At high masses, the sensitivity decreases because the DM number density is too low for collisions to occur in the lifetime of the RGB stars. Nominally the above arguments suggest that the shape of the excluded region should be a right triangle, as discussed in Sec. 11.3. However, the time-dependence of the star over the RGB lifetime distorts this simple picture. At lower DM masses, the DM flux increases, so that we have increased sensitivity to DM-induced ignition in older stars. These stars can be ignited by DM with lower cross sections than their younger counterparts. Therefore, the bottom of the excluded region is slanted upwards rather than flat like the DM-induced ignition rates as in Fig. 11.3.

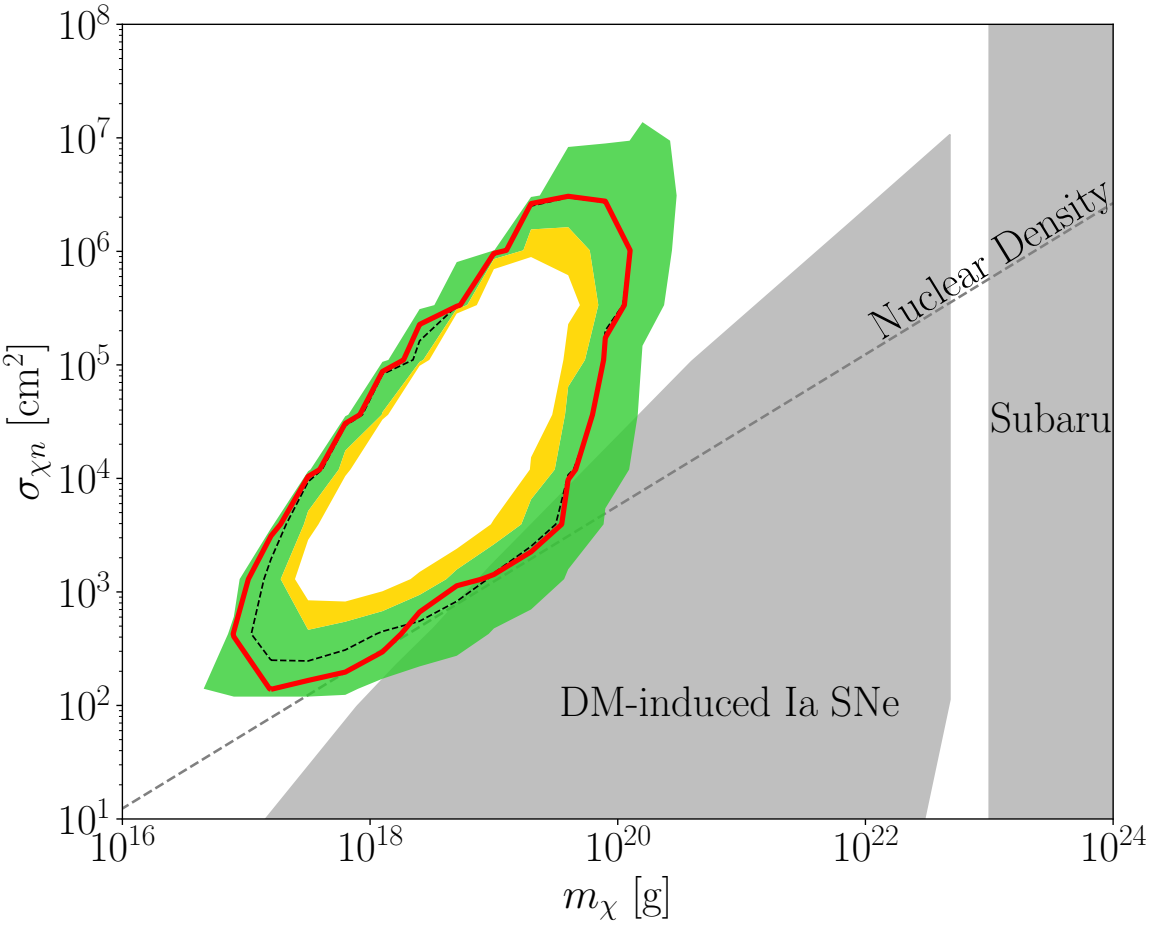

Figure 11.5: The red line is the 95% limit on macroscopic DM from the non-observation of DM-induced He flashes in the GC M15 LF; the region inside this line is excluded. The dashed line is the Asimov expectation with green (yellow) bands denoting the 1σ (2σ) containment region. We assume that the M15 DM is dominantly from the MW halo. We additionally show constraints from the non-observation of DM-induced Type Ia supernova in WDs [54, 55] and from microlensing [56]. Macroscopic DM is bounded from above from CMB observations [57] and the non-observations of gas cloud heating [58], although at too large cross-section to be shown on this plot. We also show as a dotted line where the DM is nuclear density $\rho_0 = 2 \times 10^{14}$ g/cm^3.

11.5 Discussion

We have outlined a process wherein macroscopic DM can collide with an RGB star core, depositing sufficient energy to ignite helium fusion. The result is the premature end to the RGB stage of stellar evolution for that star. The RGB luminosity function is a sensitive probe of this process; we use the LF of the GC M15 to constrain macroscopic DM properties.

A crucial assumption in our proposal is that the the DM-baryon scattering is purely elastic

with geometric cross section. The elastic assumption breaks down if the binding energy of DM constituents is of order of the typical energy transfer $\sim$ MeV. This would unbind the DM, resulting in a smaller penetration depth, but increased local energy deposition as the DM breaks up. Even in the elastic scattering regime, whether or not the cross section is geometric depends on the DM substructure, the resulting form factor and the mean free path within the DM. It is left for future work to see how relaxing these assumptions could modify our constraints. For example, primordial black holes clearly do not obey this assumption [523], though we do not constrain black hole densities in any case.

There are GC targets with improved sensitivity to this mechanism, although without existing LF data as in the case of M15. If a GC is found to host a DM halo, that GC would likely provide the strongest bound on macroscopic DM from this mechanism (see App. I.1 for an application of this scenario to M15). But we need not rely on the possibility of GC DM substructure. In particular, the GC M54 has a much larger DM density than that of M15 because it is located at the center of the Sagittarius dwarf galaxy. Ref. [187] estimated that the Sagittarius DM density at the location of M54 is $\sim$7 GeV cm^{-3}, although if the DM profile is cusped the density could be orders of magnitude larger. Future measurements of the LF in M54 would have improved discovery potential over that of M15, in particular at high DM masses $m_\chi > 10^{21}$ g. The star clusters in the Galactic Center may also be sensitive probes of DM-induced HFs, given the extreme DM densities reached there. In fact, there is a lack of luminous RGB stars in the central $\sim$0.3 pc relative to expectations [524, 525], where there may be a DM spike around Sagittarius A [526]. Qualitatively, the missing red giants may be explained by DM-induced helium ignition, although we leave a quantitative assessment to future work and note that more standard explanations have been suggested [527–533].

In this chapter we elected not to use the well studied tip of the red-giant branch to constrain the mechanism. The LF is more sensitive in the faint-signal regime where only a small percentage of high-luminosity RGB stars have been struck by DM; the slope of the LF can significantly increase even though the TRGB may be similar to that in the null case, for example if some RGB stars survive to undergo the standard HF. However, there can be some cases where the TRGB is affected, which would affect the calibration of the Hubble constant so that its value is dependent on the DM density in the vicinity of the RGB population.

In future work, we will investigate additional probes of this mechanism. For instance, the early ignition of the HF leads to HB stars with smaller helium cores than typical of HB stars. Therefore, there may be a set of sub-HB stars at lower luminosity than the normal HB, consisting of stars which did not ascend the full RGB due to DM impacts. Additionally, the DM impacts may simultaneously ignite fusion in the whole core at once, whereas in the standard scenario the HF ignites in a series of layers over a longer timescale, which may

affect direct observations of individual stars. However, observations have not yet resolved this transitionary period and distinguishing such stars from RGB or HB stars would likely prove difficult.

In principle, one can also study a HF triggered by the accumulation and annihilation of DM. However, this mechanism is suppressed relative the analogous bound in WDs [492] for two reasons. Firstly, RGB stars have a much lower DM capture rate than WDs due to their low core densities. Secondly, pure helium matter ignition requires a larger energy injection than the ignition of the carbon/oxygen matter of WDs. Then the annihilating DM must be more massive than in the WD case, so the DM number density is also suppressed.

Chapter 12

Conclusion

In this thesis, I have developed novel statistical frameworks to probe interesting, well-motivated parameter space for physics beyond the Standard Model, focusing primarily on two hypothetical degrees of freedom, sterile neutrino dark matter and axion-like particles.

In that process, I showed that the 3.5 keV line, a potential signature of sterile neutrino dark matter decays, is not due to beyond the Standard Model physics. To do so, I developed a new technique for dark matter decay searches, that can be generalized to searches in other wavelength bands and for other dark matter candidates. In follow-up work, I set constraints on more generic sterile neutrino parameter space, introducing new methodologies that will pave the way to probe the full parameter space of the resonantly-produced sterile neutrino with the upcoming X-ray telescope *XRISM*, which will have unprecedented energy resolution.

Furthermore, I detailed a promising mechanism by which one could detect axions at isolated stars with X-ray observations: axions can be produced in stellar cores, free-stream out of the star, and convert to an X-ray photon in the magnetic field surrounding the star. By analyzing 20 years of observations of the Magnificent Seven neutron stars from the *XMM-Newton* and *Chandra* X-ray telescopes, I uncovered a potential X-ray excess at these stars that may be consistent with an axion undergoing the aforementioned process. On the other hand, a similar search I performed at the white dwarf RE J0317-853 returned null results. Due to those constraints, if an axion is producing the Magnificent Seven hard X-ray excess, then it must be electrophobic or nucleophilic such that $\sqrt{C_{aee}/C_{ann}} \lesssim 0.1$. More generically one would expect this ratio of dimensionless couplings to be $\mathcal{O}(1)$, so this does dampen the likelihood that the excess is due to an axion. However, neutron stars are complicated objects, and could be emitting axions through emission mechanisms not explored in this thesis—for example, through synchrotron radiation off of charged species, or via exotic states in the inner core, such as meson condensates or a quark-gluon plasma. Additionally, future observations of both the Magnificent Seven and of white dwarfs will

continue to probe these possibilities. In particular, NuSTAR observations of RX J1856.6-3754 at high energies $\gtrsim$ 10 keV would have the required sensitivity to probe axion models in the case that the inner neutron star core is superfluid, and would be more discriminatory between axion and astrophysical origins than additional observations $\lesssim 10keV$. Excitingly, I will observe RX J1856.6-3754 with NuSTAR for 40 ks, and also two additional magnetic white dwarfs with *Chandra* for 40 ks each, all within the next year. We will be able to answer these questions more definitively in the near future.

It is possible or even likely that the new physics model realized in nature lives in a region of the parameter space that is as of yet inaccessible, but will be possible to probe in the near future. There is already a wealth of archival data which can be analyzed in hopes of discovery of the first signal of new physics; I have analyzed only a small fraction of that data in this thesis. Within the next few years multiple new telescopes and experiments will come online that have unprecedented sensitivities to new physics. Perhaps at that time we will finally obtain an solution to the microscopic nature of dark matter.

Appendix A

The Dark Matter Interpretation of the 3.5-keV Line is Inconsistent with Blank-Sky Observations

A.1 Materials and Methods

A.1.1 Data Reduction

The data products were downloaded from the *XMM-Newton* Science Archive and processed into the X-ray spectra and QPB flux estimates used in the main chapter. This process is applied to each exposure individually. We have applied our data reduction pipeline to all 6,350 observations within 90° of the Galactic Center, collected by *XMM-Newton* up to 2018 September 5 (the instrument collected a total of 12,044 observations in that time). The data reduction process uses the *XMM-Newton* Extended Source Analysis Software (ESAS) package for modeling extended objects and the diffuse X-ray backgrounds. The ESAS package is part of the *XMM-Newton* Science Analysis System (SAS) [265]; we used version 17.0.

After selecting an observation, we obtain summary information for this dataset and its associated exposures. The Calibration Index File (CIF) is generated using the task `cifbuild`, which locates the Current Calibration File (CCF). The CCF provides information about the state of the detector at observation time; for example, it supplies the location of bad pixels on the detector. Next, the task `odfingest` is used to generate the Observation Data Files (ODF), which contains uncalibrated summary files in addition to general information on the observation including data quality records. The relevant science exposures for each observation ID to use for data reduction are determined from the Pipeline Processing Subsystem summary file. Only PN exposures in submodes `Full Frame` and `Extended Full Frame` were

chosen to ensure an accurate estimate of the instrumental Quiescent Particle Background (QPB).

From this information, a set of filtered events is then created for both MOS and PN cameras for each available science exposure. The PN pipeline is as follows. The task `epchain` is first used to generate an event list. The list of out-of-time events, which are events recorded while the CCD is being read out, is generated with `epchain withoutoftime=true`. After obtaining the list of events, the task `pn-filter` is called to record only those events that occurred during a good time interval (GTI). This task calls the SAS routine `espfilt` to filter the light-curves for periods of soft proton (SP) contamination. An observation affected by SP will typically have a count rate histogram with a peak at the unaffected rate, and a long tail due to the contamination. `espfilt` establishes thresholds at $\pm 1.5\sigma$ of the count rate distribution, and then creates a GTI file containing the time intervals where the data is contained within those limits. The MOS pipeline is analogous to that for PN, requiring the tasks `emchain` and `mos-filter`.

Now that the data has been cleaned, we identify regions of the dataset we wish to mask. The routine `cheese` is applied to search for any point sources in the field of view for the energy range $3 - 4$ keV. The resulting mask is then used to exclude these sources from further analysis. Applying this mask also removes the necessity of a pile-up correction, as for extended source analyses this is only a concern near point sources. In addition, MOS CCDs flagged as anomalous are disregarded. For example, a suspected micrometeorite impact caused the loss of MOS1 CCD6 on 2005 March 12, and a similar event caused the loss of MOS1 CCD3 on 2012 December 11. These CCDs are excluded from analysis for observations made after these dates.

With the cleaned data masked, the final step is the production of the spectra and QPB data. For the PN and MOS cameras this is achieved with the tasks `pn-spectra` and `mos-spectra` respectively. These tasks use the filtered event files to create the photon-count data, the QPB data, the Ancillary Response File (ARF), and the source count weighted Redistribution Matrix File (RMF), for the masked region but otherwise the full field of view (FOV). The ARF and RMF account for the detector response, and will be described in more detail in the following subsection.

A.1.2 Data Analysis

For a given exposure, we model the observed number of X-rays as originating from a combination of instrumental effects and conventional astrophysical sources, which we consider backgrounds, and a putative DM decay line as our signal hypothesis. The DM in the Milky

Way is sufficiently non-relativistic ($v \sim 10^{-3}$ in natural units where v is velocity of the DM) that we treat the decay signal as a zero-width line at an energy $m_s/2$. The line-width generated by the finite velocity dispersion of DM within the Milky Way is small compared to the energy resolution of the detector. The flux of this line in counts $\mathrm{cm}^{-2}\mathrm{s}^{-1}\mathrm{sr}^{-1}\mathrm{keV}^{-1}$, averaged over the full region of interest (ROI) for this observation, is given by

$$\frac{d\Phi}{dE} = \frac{d\Phi_{\rm pp}}{dE} \times D\,, \tag{A.1}$$

where the particle physics and D-factor contributions are given by

$$\frac{d\Phi_{\rm pp}}{dE} = \frac{\Gamma}{4\pi\, m_s}\,\delta(E - m_s/2)\,, \qquad D = \int ds\,\rho_{\rm DM}(s,\Omega)\,. \tag{A.2}$$

Above, $\Gamma = \tau^{-1}$ is the DM decay rate (the inverse of the DM lifetime τ), s is an integration variable along the line-of-sight, and $\rho_{\rm DM}$ is the Milky Way DM distribution, which will be discussed further below. For our searches for DM decay in the ambient MW, we may compute D using any angular position within the ROI, and use this as an estimate for the average D factor. This is because variations in the line-of-sight integral through the Milky Way halo are negligible (at most $\sim$2% for the regions we consider) over the small *XMM-Newton* field-of-view. However, if the DM density varies over the scale of the ROI, as is the case when considering extragalactic sources such as galaxy clusters, then the D-factor needs to be averaged over the ROI, accounting for the vignetting of the instrument. Note the D-factor here is the Decay analogue of the J-factor, which is used for DM annihilation. For the specific case of sterile-neutrino DM, the decay rate can be related to the mixing angle between active and sterile neutrinos, θ, as [86]

$$\Gamma = 1.361 \times 10^{-29}\ \mathrm{s}^{-1} \left(\frac{\sin^2 2\theta}{10^{-7}}\right) \left(\frac{m_s}{1\ \mathrm{keV}}\right)^5 . \tag{A.3}$$

This expression is valid for a Majorana neutrino, for a Dirac neutrino it is a factor of 2 smaller.

For each observation, we only included the contribution from the MW halo DM column density. Each region will also include a large column density from extragalactic DM. We can neglect the extragalactic contribution because an extragalactic line emitted over cosmological distances will be smeared out by redshifting, and the resulting smooth emission will be more than an order of magnitude smaller than the line from the MW halo.

We have concentrated on sterile neutrino DM, but our results apply to any model of decaying DM which produces an X-ray line. Alternate models for the 3.5 keV UXL have

been proposed, however, that involve the decay of DM into an ultralight axion-like particle, which converts to photons within the galactic and/or cluster magnetic fields [534]. Our results do not directly apply to these models because the spatial morphology of the signal is a convolution of the DM density distribution and the magnetic field distribution. Estimating the size of the effect [535] indicates that our results also constrain this DM.

By restricting our attention to relatively blank regions of the sky and a narrow energy range, we reduce the number of backgrounds that need to be considered. As discussed in the main chapter, we model the contributions to the X-ray counts using a power-law instrumental QPB rate and a power-law astrophysical spectrum, which may also describe the soft proton background if present [536]. In principle, the soft proton background an unfolded power-law that has not been passed through the instrument response, however we find that including such an additional model has minimal impact on our results. Physical astrophysical emission may be present within the ROIs from the cosmic X-ray background, extended emission regions, or unresolved populations of Galactic sources. We model the QPB spectrum using a power-law in counts, while the astrophysical emission is modeled by a power-law in flux. A flux power-law is, in principle, not directly equivalent to a counts power-law because of the energy-dependent detector response. However, over the narrow energy ranges we consider the distinction is small. Still, for consistency we model the spectra in these different ways.

Given the signal and astrophysical background models, we calculate the predicted number of model counts in each of the camera channels. Let us define $S(E, \theta^e_{\mathbf{phys}})$ in units of counts $\mathrm{cm}^{-2}\mathrm{s}^{-1}\mathrm{sr}^{-1}\mathrm{keV}^{-1}$, as the signal and astrophysical background spectrum, as a function of energy E. Within this expression, the index e is used to enumerate the different exposures. The parameters $\theta^e_{\mathbf{phys}}$ denote the astrophysical background parameters and the signal parameters for the given exposure e. The signal parameters can be separated out by writing $\theta^e_{\mathbf{phys}} = \{m_s, \Gamma, \theta^e_B\}$, where θ^e_B are the background astrophysical power-law parameters. The QPB is not included here but will be incorporated separately, as described below. By using Γ we keep our discussion appropriate for a general decaying DM scenario, but the analysis can immediately be specialized to the sterile neutrino scenario using equation (S3). For the decaying DM hypothesis the DM parameters do not vary throughout the Milky Way or over time, and thus must be identical across exposures, so they do not carry an index e. The background parameters do vary between exposures and thus must be treated independently. Explicitly, the expected flux can be written as follows:

$$S(E, \theta^e_{\mathbf{phys}}) = \frac{\Gamma\, D}{4\pi\, m_s}\delta(E - m_s/2) + A^e_{\mathrm{astro}}\left(\frac{E}{1\ \mathrm{keV}}\right)^{n^e_{\mathrm{astro}}} . \tag{A.4}$$

To compare this predicted spectrum to the observed number of X-rays in counts, we use forward modeling to incorporate the instrument response. The predicted number of counts in a given energy bin indexed by i is given by

$$\mu^e_{i,\mathrm{phys}}(\theta^e_{\mathbf{phys}}) = t^e \Delta\Omega^e \int dE'\, \mathrm{RMF}^e_i(E')\, \mathrm{ARF}^e(E')\, S(E', \theta^e_{\mathbf{phys}})\,, \tag{A.5}$$

where t^e is the observation time for the given exposure in s, $\Delta\Omega^e$ is the angular area of the ROI, the ARF provides the effective area of the detector as a function of energy in cm^2, and the dimensionless RMF accounts for the energy resolution and detector gain effects. All of these detector quantities vary between exposures and so carry an explicit e index. We now add to equation (A.5) the contribution from the QPB rate as a power law in reconstructed (rather than true) energy

$$\mu^e_{i,\mathrm{QPB}}(\theta^e_{\mathbf{QPB}}) = A^e_{\mathrm{QPB}} \times E_i^{n^e_{\mathrm{QPB}}}\,, \tag{A.6}$$

where $\theta^e_{\mathbf{QPB}} = \{A^e_{\mathrm{QPB}},\, n^e_{\mathrm{QPB}}\}$ are the model parameters defining the power-law. The separate treatment for the QPB arises as its flux is not folded with the detector response.

For the given exposure we now have the total predicted model counts μ^e_i in each energy bin as a function of the model parameters $\theta^e = \{\theta^e_{\mathbf{phys}},\, \theta^e_{\mathbf{QPB}}\}$:

$$\mu^e_i(\theta^e) = \mu^e_{i,\mathrm{phys}}(\theta^e_{\mathbf{phys}}) + \mu^e_{i,\mathrm{QPB}}(\theta^e_{\mathbf{QPB}})\,. \tag{A.7}$$

The data collected in this exposure can be identically binned, such that we can represent the X-ray dataset for each exposure by a set of integers $d^e_{\text{X-ray}} = \{k^e_i\}$, where explicitly k^e_i is the number of X-rays in energy bin i for this exposure. With the data and model in identical forms, we can now compare the two by constructing a joint likelihood over all energy bins as follows

$$\mathcal{L}^e_{\text{X-ray}}(d^e_{\text{X-ray}}|\theta^e) = \prod_i \frac{\mu^e_i(\theta^e)^{k^e_i} e^{-\mu^e_i(\theta^e)}}{k^e_i!}\,. \tag{A.8}$$

The above likelihood accounts for the X-ray data collected during a given exposure, but there is additional information collected by the cameras that we incorporate into our model. This arises in the form of an estimate for the QPB background during the given exposure, as determined from pixels on the CCD that were shielded and therefore unexposed to direct X-rays. The ESAS tools provide this information as the mean and standard deviation on the (non-integer) QPB counts in each energy bin, which we denote by $\lambda^e_{i,\mathrm{QPB}}$ and $\sigma^e_{i,\mathrm{QPB}}$ respectively. We then construct a Gaussian likelihood for the QPB dataset $d^e_{\mathrm{QPB}} = \{\lambda^e_{i,\mathrm{QPB}},\, \sigma^e_{i,\mathrm{QPB}}\}$

as

$$\mathcal{L}^e_{\rm QPB}(d^e_{\rm QPB}|\theta^e_{\mathbf{QPB}}) = \prod_i \frac{1}{\sigma^e_{i,\rm QPB}\sqrt{2\pi}} \exp\left[-\frac{(\mu^e_{i,\rm QPB}(\theta^e_{\mathbf{QPB}}) - \lambda^e_{i,\rm QPB})^2}{2(\sigma^e_{i,\rm QPB})^2}\right]. \tag{A.9}$$

To account for both the X-ray and QPB data simultaneously, we form the joint likelihood as

$$\mathcal{L}^e(d^e|m_s,\Gamma,\theta^e_B) = \mathcal{L}^e_{\text{X-ray}}(d^e_{\text{X-ray}}|\theta^e_{\mathbf{phys}}) \times \mathcal{L}^e_{\rm QPB}(d^e_{\rm QPB}|\theta^e_{\mathbf{QPB}}), \tag{A.10}$$

where $d^e = \{d^e_{\text{X-ray}}, d^e_{\rm QPB}\}$ and where θ^e_B denotes the four model parameters that describe the background astrophysical power-law and the power-law QPB model.

In a similar manner we can construct likelihoods for each exposure, recalling that the signal parameters will not vary between them. We therefore remove these background parameters at the level of individual exposures, using the standard frequentist technique of profiling. At fixed m_s we construct the profile likelihood as a function of Γ [537]. The profile likelihood is given by

$$\mathcal{L}^e(d^e|m_s,\Gamma) = \mathcal{L}^e(d^e|m_s,\Gamma,\hat{\theta}^e_B), \tag{A.11}$$

with $\hat{\theta}^e_B$ denoting the value of each of the background parameters that maximizes the likelihood for the specific values of m_s and Γ under consideration. This technique does not involve fixing the background to its value under the null hypothesis or the signal hypothesis. Instead, we determine a new value for θ^e_B for each value of Γ considered, at fixed m_s using `minuit` [538].

We construct a profile likelihood for each exposure, leaving a likelihood depending only on the DM parameters. The information from each of these exposures can then be combined into the joint likelihood, which depends on the entire dataset $d = \{d^e\}$:

$$\mathcal{L}(d|m_s,\Gamma) = \prod_e \mathcal{L}^e(d^e|m_s,\Gamma). \tag{A.12}$$

We reiterate that the signal parameters do not vary between exposures.

Using the likelihood in equation (A.12) we perform hypothesis testing between a signal model containing a DM decay line at fixed m_s and the null hypothesis without the DM line. Following frequentist standards, we will quantify the significance of any excess using a test statistic (TS) for discovery

$$\text{TS}(m_s) = \begin{cases} 2\left[\ln\mathcal{L}(d|m_s,\hat{\Gamma}) - \ln\mathcal{L}(d|m_s,\Gamma=0)\right] & \hat{\Gamma} \geq 0, \\ 0 & \hat{\Gamma} < 0. \end{cases} \tag{A.13}$$

Here $\hat{\Gamma}$ is the value of Γ that maximizes the likelihood at fixed m_s, and asymptotically

$\mathrm{TS}(m_s) = \sigma^2$, where σ is the significance of the excess. We may also construct a test statistic appropriate for establishing one-sided limits on Γ for a fixed m_s. Note that Γ is physically constrained ($\Gamma \geq 0$), though for consistency we must consider negative values of Γ as well, so we define [109]

$$q(m_s, \Gamma) = \begin{cases} 2\left[\ln \mathcal{L}(d|m_s, \hat{\Gamma}) - \ln \mathcal{L}(d|m_s, \Gamma)\right] & \hat{\Gamma} \leq \Gamma\,, \\ 0 & \hat{\Gamma} > \Gamma\,. \end{cases} \tag{A.14}$$

This statistic then allows us to determine the one-sided 95% limit on the decay rate $\Gamma_{95\%}$ by solving $q(m_s, \Gamma_{95\%}) = 2.71$. We also power-constrain the limits, to avoid setting stronger limits than expected due to statistical fluctuations [110], as discussed in the main chapter. To obtain the expected value for $q(m_s, \Gamma)$, we apply the Asimov procedure [109] to the null hypothesis. The interpretation of the square root of the discovery TS as being the significance of the line and the precise TS threshold used to calculate the one-sided 95% limit rely on the TS in equation (A.13) following a one-sided χ^2 distribution under the null hypothesis. This is justified by the fact that our photon statistics are sufficient to invoke Wilks' theorem.

A.2 Supplementary Text

In this section, we provide extended results for the fiducial analysis presented in the main chapter and test variations to the procedure. This section is organized as follows. First, we subject our fiducial analysis to a key statistical test by injecting a synthetic signal into the data. Then, we present results from individual exposures and determine which observations contribute most to our limits. In the following section, we consider how our limits depend on assumptions for the DM profile of the Milky Way. In the final sub-section we explore how our sensitivity varies for different selection criteria on the exposures.

A.2.1 Synthetic Signal

The limit on decaying DM, shown in Fig. 1, is tighter than in previous studies. We therefore subject our analysis to test that it is statistically meaningful. For example, it is possible that systematic effects cause the limit to appear stronger than it should be and that a real signal, if present, would be excluded by our analysis. To test this possibility, we add a synthetic signal to the real data and verify that our limit does not exclude the signal that we inject.

We perform this analysis for our fiducial selection criterion described in the main chapter. The results of the test, for three different assumed DM masses, are shown in Fig. A.1. That

figure shows the value of the mixing angle for the synthetic signal injected into the data, $\theta_{\rm inj}$, and the mixing angle recovered by our analysis, $\theta_{\rm rec}$. The 95% one-sided limits are computed as the injected signal strength is varied. The limits never fall below the true value of the injected signal for any of the mass points shown. The mean, 1 and 2σ expectations for the 95% one-sided limit under the signal hypothesis were computed from the Asimov procedure [109]. Our limits are consistent with the real data being a realization of the null hypothesis and the only signal contribution comes from that which we inject.

There is no inconsistency in that the lower 2σ band for the 95% one-sided limit falls below the injected value. This is expected because the one-sided 95% limit and the 2σ bands for the 95% limit have different statistical interpretations, because the 2σ band is a 2-sided interval while the one-sided 95% limit is a statement about a one-sided interval. Figure A.1 also shows that the lower 2σ bands flatten at low injected mixing angles. This is because we are showing power-constrained limits [110], and those values reach the constraints.

We also test the effect of assuming the wrong DM density profile. We consider how our limits change for different assumed DM profiles below. Here, we address the question of whether the evidence for a real DM-induced line may be obscured if an incorrect DM profile is used in the profile likelihood analysis. We follow the same procedure described above to construct a hybrid dataset consisting of the real data and a synthetic signal at $m_s = 7.0$ keV. That synthetic signal is constructed assuming our canonical NFW DM profile. We then analyze the synthetic data assuming the DM profile follows the alternative Burkert DM profile [539, 540]. That profile is an extreme departure from the NFW DM profile, in that it has a roughly 9 kpc core. The difference between the spatial morphologies of the NFW profile and the Burkert profile encapsulate the largest mismatch between the DM profiles we test in this chapter and the real profile of the Milky Way.

In Fig. A.2 we show the resulting TS in favor of DM as a function of the synthetic injected mixing angle, for an analysis that assumes the NFW DM profile and one that assumes the Burkert DM profile, with the NFW DM profile injected. The two TS curves are extremely similar, so we conclude that a real signal is not going undetected because we do not have the correct DM density profile. In both cases the D-factor does not change appreciably between different exposures in our region of interest. In both cases the TS at $\sin^2(2\theta_{\rm inj}) \approx 10^{-10}$ is $\sim 10^3$, meaning that at this signal strength a DM-induced line would have been detected at approximately 30σ.

If the DM profile used in the analysis is not correct then the limit will be systematically biased. However, Fig. A.2 shows the true limit, constructed with the correct DM profile, may be obtained by rescaling the limit obtained with an incorrect DM profile by the appropriate ratio of mean D-factors, where the means are constructed from the ensemble of exposures

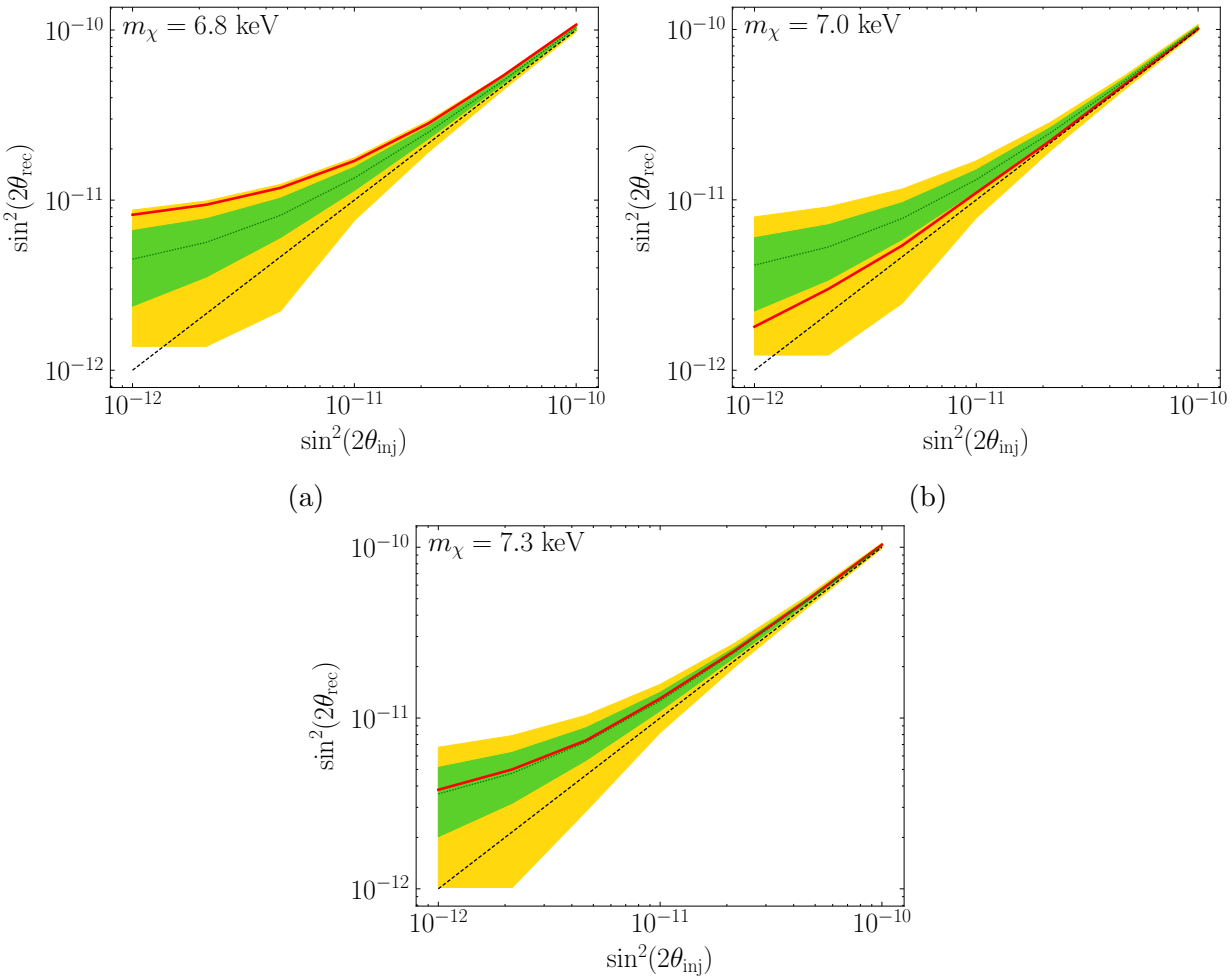

Figure A.1: Results of the synthetic signal test. We inject an artificial DM signal to the data, with mixing angle $\sin^2(2\theta_{\rm inj})$ as indicated on the x-axes, and recover values $\sin^2(2\theta_{\rm rec})$, shown on the y-axes. In (A), we show the results for 6.8 keV; (B), for 7.0 keV; (C), for 7.3 keV. The red curves show the power-constrained 95% one-sided upper limits that we find on the analysis of the hybrid datasets, consisting of the real data plus the synthetic signal. The bands show the mean (black), 1σ (green) and 2σ (yellow) expectations for the 95% one-sided upper limit. The injected signal strength is never excluded, as indicated by the red line never dropping below the dashed black diagonal line.

used in the joint-likelihood analysis.

As an additional cross-check, below we compute the limit on the DM-induced line in regions consisting of narrow annuli centered around the Galactic Center. For all the DM profiles considered, these annuli are small enough that the DM density does not change appreciably between exposures in these subregions.

A.2.2 Individual Exposures

Our fiducial result relied on the construction of the joint likelihood over 1,397 independent exposures. We now consider the sensitivity of the most constraining individual exposures, and their individual properties. We begin by describing how the individual exposures in our fiducial analysis are distributed.

Spatial Distribution of exposures

Fig. A.3 shows the spatial distribution of the exposures included in the fiducial analysis about the Galactic Center. In cases where there are multiple exposures at the same location, we have only shown the highest exposure case. This can be compared with Fig. A.4, which shows the TS at three different mass points for the exposures illustrated in Fig. A.3. The high-TS exposures do not correlate with distance from the Galactic Center and appear randomly distributed about the region.

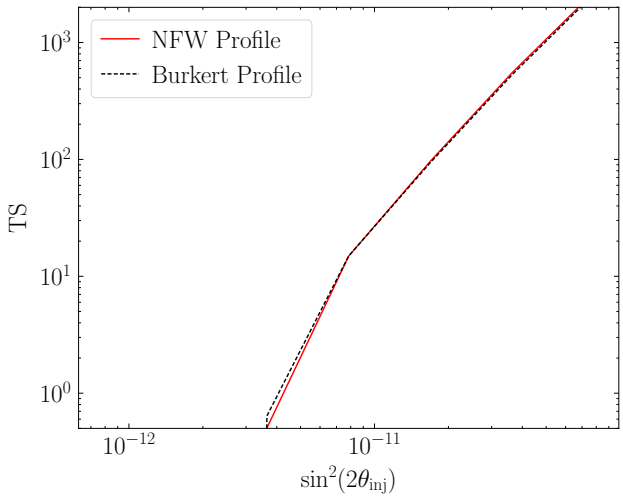

Figure A.2: The effects of a different DM profile. As in Fig. A.1, we add a fake DM signal to the real data, with mixing angle $\sin^2(2\theta_{\rm inj})$ as indicated on the x-axis. Here we have fixed $m_s = 7.0$ keV. We show the TS assuming the NFW DM profile (red), which was used in the production of the synthetic signal, and the Burkert profile (black dashed) with a 9 kpc core. The TS is almost insensitive to the DM profile assumed.

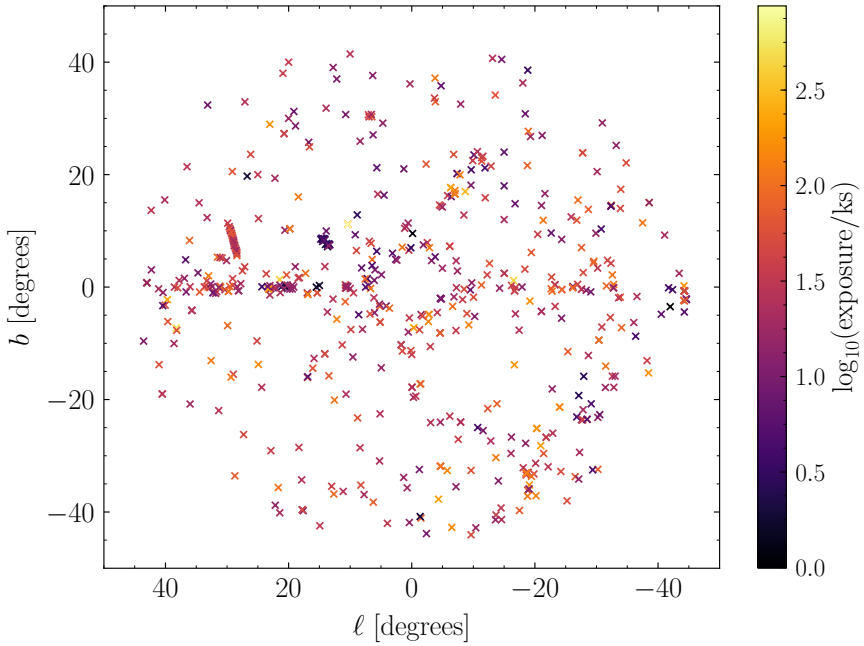

Figure A.3: A map of the exposure times. Exposure times for the exposures included in the fiducial analysis on a map of galactic coordinates, where l is longitude and b is latitude. In cases where multiple exposures occur at the same position, we only show the longest exposure time.

Goodness of fit for individual exposures

We quantify the goodness of fit for an individual exposure through the $\delta\chi^2$ per degree of freedom. In calculating $\delta\chi^2$ we only include the X-ray count data, and we also take the degrees of freedom to be the number of data points minus two to account for the two degrees of freedom in the astrophysical power-law. We assume that the QPB model parameters are already fixed by the QPB data, for the purpose of counting model parameters. There are typically ∼100 energy bins in the 0.5 keV energy window around the putative line energy considered in the analysis. The exact number of energy bins varies slightly as a function of the line energy. We present results for $m_s = 7.1$ keV, though the results at other masses are similar. In this case, there are 100 energy bins included in the MOS analyses and 97 in the PN analyses. Thus, we take 98 (95) degrees of freedom for the MOS (PN) exposures.

In Fig. A.5 we show the distribution of $\delta\chi^2$ per degree of freedom (DOF) over all of the MOS and PN exposures in the fiducial analysis. The vertical error bars show the 1σ Poisson counting uncertainties. The data histograms are consistent with expectations under the null hypothesis. Under the null hypothesis these distributions should follow the χ^2 distribution with the appropriate number of degrees of freedom.

Top 10 Exposures

We show the limits obtained from the top 10 exposures individually in Fig. A.6. These exposures are listed in Table A.1, ranked in order of the strongest predicted limit under the null hypothesis, from the Asimov analysis at $m_s = 7.0$ keV. None of the top 10 exposures were proposed to search for extended emission. These ten observations were all looking at specific astrophysical sources, which we mask in our analysis.

Fig. A.6A shows the one-sided 95% power-constrained limits obtained from these exposures. Many of these top 10 exposures are themselves strong enough to independently disfavor the decaying DM interpretation of the UXL. None of these exposures show evidence for an UXL. This is illustrated in Fig. A.6B, which shows the TSs as a function of mass for the top 10 exposures. There is only one exposure whose TS exceeds the 2σ expectation. This, however, is not surprising, considering that there are 10 independent exposures and each exposure has roughly three independent mass points across the mass range considered.

Profile Likelihood for the Top Exposure

We describe in detail our most constraining exposure, observation ID 0653550301 in Table A.1. Our goal is to illustrate the profile likelihood procedure at the level of the individual

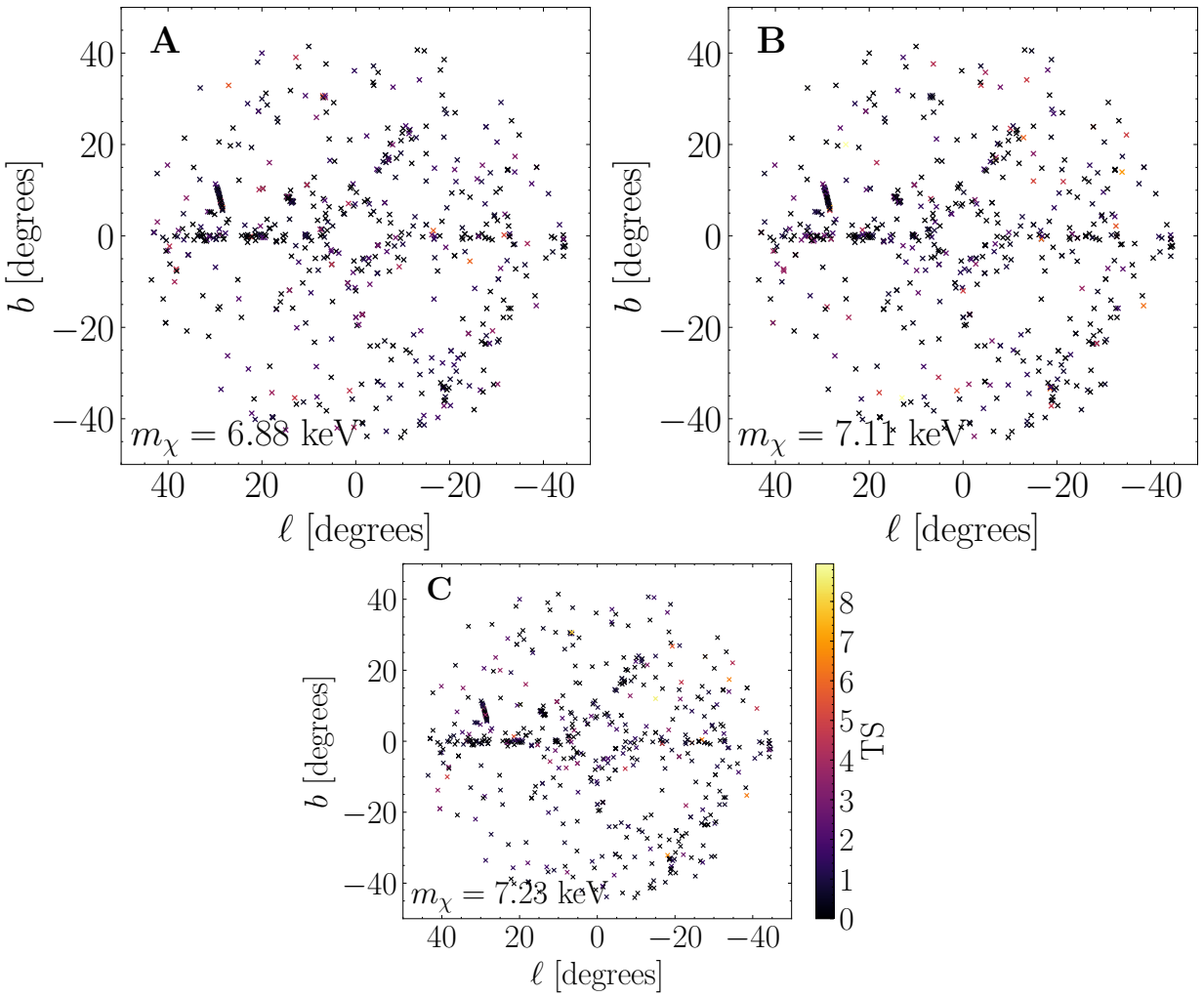

Figure A.4: Maps of the maximum TSs. The maximum TSs for the individual exposures illustrated in Fig. A.3 at three different mass points 6.88 keV (A), 7.11 keV (B), and 7.28 keV (C). The high-TS exposures appear randomly distributed about the region.

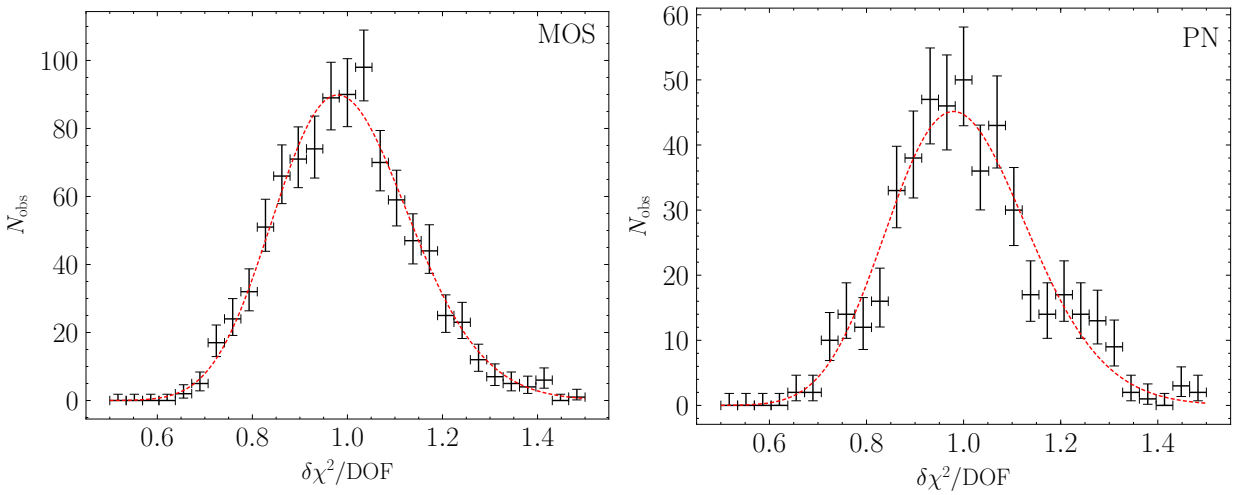

Figure A.5: The distribution of $\delta\chi^2$/DOF for the MOS (A) and PN (B) exposures considered in our fiducial analysis for $m_s = 7.1$ keV. The number of degrees of freedom is 98 (95) for the MOS (PN) exposures. Under the null hypothesis, these distributions should follow the appropriate χ^2-distributions, which are shown in dashed red. The vertical error bars on the black data points are the 1σ Poisson counting uncertainties, while the horizontal error bars show the bin ranges. The observed data are consistent with the null hypothesis model.

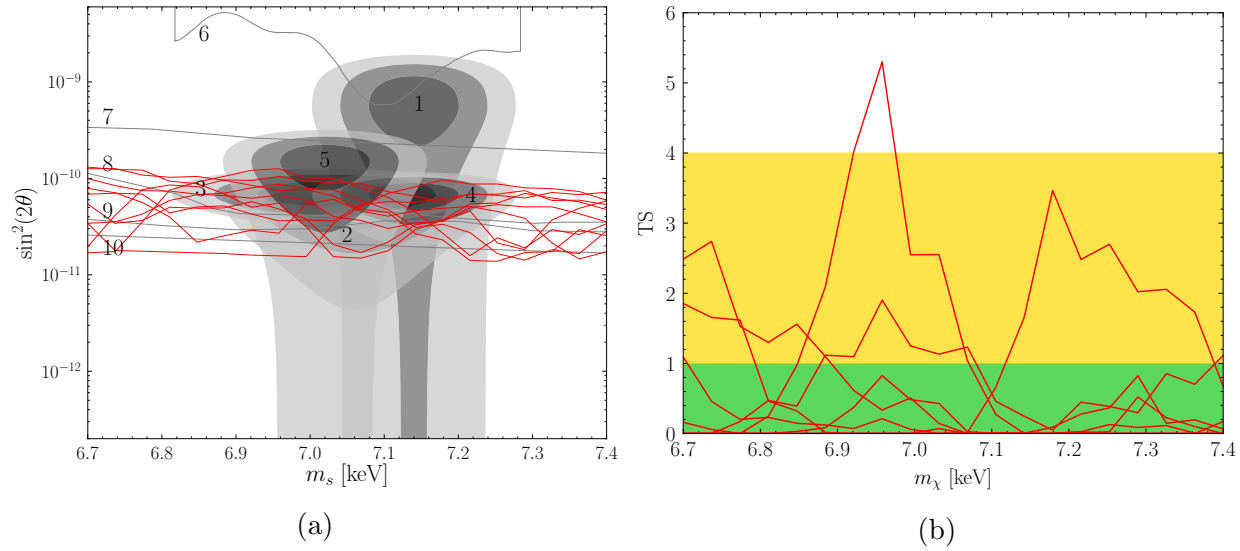

Figure A.6: Limits from individual exposures. (A) The one-sided power-constrained 95% limits (red) from the 10 most constraining exposures, which are listed in Table A.1. The shaded regions and pre-existing constraints are as labeled in Fig. 1. (B) The maximum TSs (red) for the 10 exposures. The distribution of TSs observed is consistent with the null hypothesis. The green and yellow regions indicate 1σ and 2σ detections, respectively.

Table A.1: The 10 most constraining *XMM-Newton* exposures in the fiducial analysis. The exposures are ranked by their predicted limits under the null hypothesis at $m_s = 7.0$ keV from the Asimov analysis. The "Identifier" column denotes the specific exposure within an observation. LMXRB stands for "low-mass X-ray binary."

Observation ID	Camera	Identifier	Exposure [ks]	l [deg]	b [deg]	Target Type
0653550301	PN	S003	63.2	5.1	-6.2	Quiescent Novae
0203750101	PN	S003	33.7	-2.8	-4.9	LMXRB Black Hole
0152750101	PN	S001	30.1	1.6	7.1	Dark Cloud
0203750101	MOS2	S002	43.4	-2.8	-4.9	LMXRB Black Hole
0781760101	PN	S003	46.0	-2.7	-6.1	LMXRB Burster
0761090301	PN	S003	95.2	-8.7	17.0	B2III Star
0206610101	PN	S003	35.4	-2.9	7.0	Dark Cloud
0412601501	MOS2	S002	90.2	-1.4	-17.2	Neutron Star
0727760301	MOS2	S003	67.9	-1.4	-17.2	Neutron Star
0761090301	MOS2	S002	107.4	-8.7	17.0	B2III Star

exposures.

The X-ray count and QPB data for this exposure are shown Fig. A.7A. The data are shown over a 0.5 keV energy range centered around the example line energy of 3.55 keV. The figure also shows the best-fitting QPB and astrophysical models under the assumption of no signal. The models match the data within the statistical noise, which can be quantified by calculating the χ^2 per degree of freedom: $\chi^2/\text{DOF} \approx 1.016$. We then construct the profile likelihood for the putative line signal at 3.55 keV. In constructing the profile likelihood we re-fit for the best-fitting nuisance parameters for each value of the line signal strength, as is mandated by the profile likelihood procedure. The resulting profile likelihood is shown in Fig. A.7B. We show the profile likelihood as twice the difference in log likelihood with the convention $2\Delta \ln \mathcal{L} = 2[\ln \mathcal{L}(\sin^2(2\hat{\theta})) - \ln \mathcal{L}(\sin^2(2\theta))]$, where $\hat{\theta}$ is the value of θ that maximizes the likelihood. Note that the best-fitting mixing angle is slightly negative in this case. To convert from counts to flux to $\sin^2(2\theta)$ within this exposure and for $m_s = 3.55$ keV, we use the following properties. First, the average D-factor within this region for the fiducial NFW profile is 9.15×10^{28} keV/cm^2. Second, the channel bin widths are 0.015 keV wide because this is a PN exposure. And third, a spectral value of 1 count/cm^2/s/sr/keV at 3.55 keV produces, on average, $\sim$22 counts, distributed across a $\sim$0.2 keV-wide window in channels about 3.55 keV, due to the energy resolution of the camera.

We compare the $2-10$ keV intensity and the QPB rate for this exposure to sets of cuts on our fiducial analysis. Under the null hypothesis, we infer $F_{2-10} \approx 3.47 \times 10^{-11}$ erg/cm^2/s/deg^2 and a QPB rate that is in the lower 57% percentile, with a rate of $\sim$0.127 QPB counts/s.

A.2.3 Dependence on the Dark Matter Profile

Here we consider how our results depend on the assumed DM profile for the Milky Way. For our fiducial analysis we used the NFW DM profile [102, 139] for the DM density $\rho_{\text{DM}}(r)$

$$\rho_{\text{NFW}}(r) = \frac{\rho_0}{r/r_s \, (1 + r/r_s)^2} \,, \tag{A.15}$$

with r the distance from the Galactic Center and r_s the scale radius. The density normalization parameter ρ_0 is fixed to give the measured local DM density ρ_{local} at the solar radius $r_\odot$. In our fiducial analysis, we took $\rho_{\text{local}} = 0.4$ GeV/cm^3, $r_\odot = 8.13$ kpc, and $r_s = 20$ kpc.

We consider the effects of departing from the assumed NFW profile. One possibility is that baryonic feedback in the inner regions of the Milky Way leads to the formation of a dark matter core in the inner part of the DM halo. Hydrodynamic simulations of Milky Way size galaxies suggest that feedback could increase DM density [144], which would increase

our sensitivity. Taking the more pessimistic scenario, we consider the possibility that within the inner 1 kpc of the Milky Way, the DM density profile is flat:

$$\rho_{\rm core}(r) = \begin{cases} \rho_{\rm NFW}(r) & r > r_c\,, \\ \rho_{\rm NFW}(r_c) & r \leq r_c\,, \end{cases} \tag{A.16}$$

where $r_c = 1$ kpc is the core radius. Figure A.8 compares the limit we obtain with this DM profile to our fiducial limit; the difference between the two limits is small. This is because we mask the inner 5° of the Milky Way, which covers almost the entire region that would be affected by the 1 kpc core. Varying other fiducial NFW parameters has little impact. For example, using $r_s = 16$ kpc and $\rho_0 = 0.47$ GeV/cm^3 [59], we find only minor impact on our results.

We also consider the Burkert DM profile [539, 540]:

$$\rho_{\rm Burk}(r) = \frac{\rho_0}{(1 + r/r_c)(1 + (r/r_c)^2)}\,, \tag{A.17}$$

where r_c is the core radius and again ρ_0 is fixed by matching $\rho_{\rm local}$. To be conservative, we take the core radius to be $r_c = 9$ kpc [59], which effectively corresponds to coring the DM density profile within the solar radius. While there is no evidence that this density profile describes our own Milky Way, we consider it the largest plausible deviation from the NFW profile. The limit is also shown in Fig. A.8. Even with such an extreme DM profile we still find that the best-fitting parameters for DM to explain the UXL remain inconsistent with our results. Changing between the NFW and Burkert profiles has a small effect on the limit, as within our fiducial region the difference between the D-factors computed between the two profiles is relatively small.

A.2.4 MOS and PN Independent Analyses

We analyze the data from the MOS and PN cameras separately to test for systematic issues in the cameras. Because these are different detectors, we also expect their instrumental systematic uncertainties (such as effective area uncertainties and possible instrumental lines) to also be largely independent. In Fig. A.9 we show the limits and TS distributions from independent analyses of the MOS and PN datasets, as compared to the joint (fiducial) analysis. Neither dataset shows evidence for DM decay, and both constrain the decaying DM interpretation of the UXL. A low-significance feature (TS $\sim$1) is seen in both datasets at $m_s \sim 6.8$ keV. While this feature could be a statistical fluctuation, it is also possible that it is due to a common systematic, such as a feature in the background emission, that affects

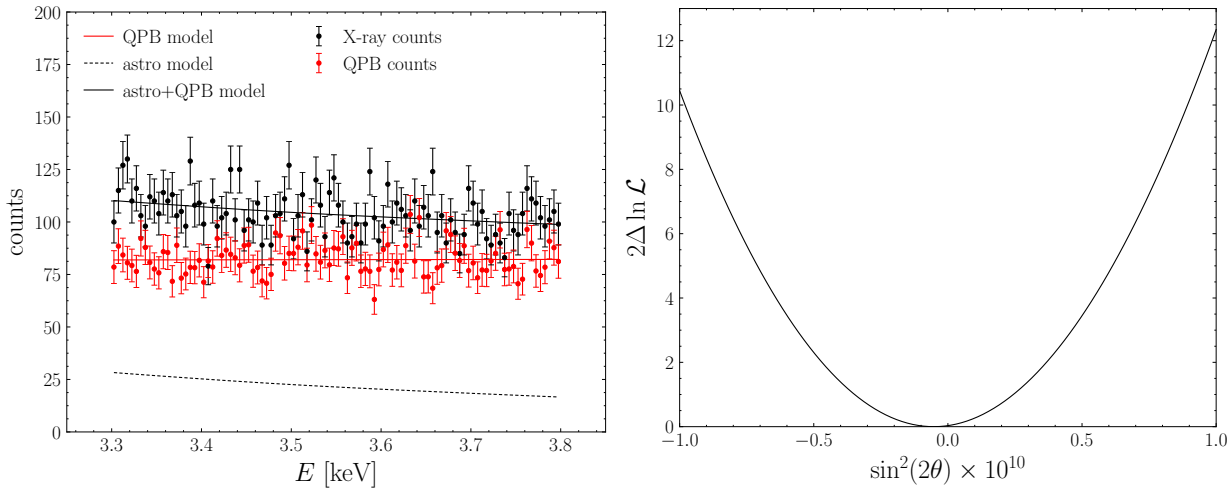

(a) (b)

Figure A.7: Results for our most constraining exposure. (A) An example spectrum obtained from the PN camera of observation ID 0653550301, our most constraining exposure, as listed in Table A.1. In addition to the data (black circles) we show the best-fitting QPB and astrophysical models (red line and dashed black line respectively), under the assumption of no UXL. The energy range shown corresponds to that in our fiducial analysis, and the individual energy bins are 0.015 keV wide. (B) The profile likelihood for the strength of the 3.55 keV signal for the dataset shown on the left, in terms of the mixing angle.

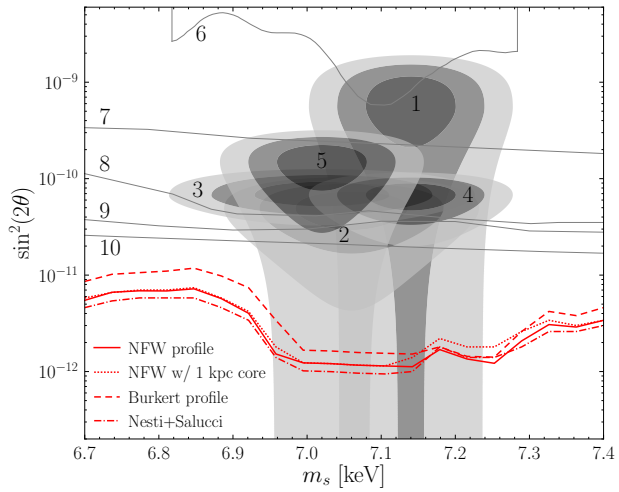

Figure A.8: Limits with different DM density profiles. The parameter space from Fig. 1, compared to our limits for different assumptions about the DM density profile. In additon to the fiducial NFW profile (solid red), we consider the NFW profile with a 1 kpc core (dot-short dashed red), an NFW with $r_s = 16$ kpc and $\rho_0 = 0.47$ GeV/cm^3 [59] (dot-long dashed red), and the Burkert profile with a 9 kpc core (dashed red). See text for details.

both analyses. Nevertheless, this feature is not distinguishable from statistical fluctuations.

A.2.5 Variations to Selection Criteria

We tested how our limits change when we vary the selection criteria for the exposures used to produce the joint likelihood. We summarize the various combinations of the criterion that we consider in Table A.2. The region of interest extends from $r_{\rm min}$ to $r_{\rm max}$ from the Galactic Center, with the Galactic plane masked at $|b|_{\rm min}$. We include all exposures with 2-10 keV intensity less than $I^{\rm max}_{2-10}$. Similarly, we include exposures with QPB rates in the lower $F^{\rm max}_{\rm QPB}$ percentile, separately determined for MOS and PN exposures. For two of the analyses, we mask either the northern or southern hemispheres as well.

In Fig. A.10 we show the limits obtained with the criteria given in Table A.2. Our main conclusion – that the decaying DM interpretation of the UXL is inconsistent with our results – is insensitive to these variations in the selection criterion.

A.2.6 Energy binning

In our fiducial analysis we used the default energy binning recommended by the *XMM-Newton* analysis software. The PN forward modeling matrix uses 15 eV input energy bins, for physical flux, in our energy range of interest and outputs predicted detector counts in 5 eV output energy channels. The MOS forward modeling matrix maps 5 eV input energy bins to 5 eV output energy channels. Because the output energy channel widths are much smaller than the detector energy resolution, our results should not depend on the energy binning. We test this by down-binning the detector responses to lower energy resolutions.

As a demonstration, we focus on the individual PN observation with observation ID 0653550301 used in Fig. A.7. In our fiducial analysis there are 97 output energy channels across the 0.5 keV energy window of the analysis. However, the energy resolution of the PN camera, which is captured by the forward modeling procedure that we use, is around 0.1 keV. Thus we expect that down-binning the forward modeling matrix to $\sim$5 energy channels, each of 0.1 keV, should have little effect on the resulting profile likelihood for the putative UXL. This is demonstrated in Fig. A.11, which shows the X-ray and QPB data down-binned to 5 $\sim$0.1 keV energy channels, with the best-fitting astrophysical power-law and QPB power-law models from the joint likelihood fit using the down-binned data. The profile likelihood for the UXL at 3.55 keV is shown compared to the fiducial profile likelihood. The differences between the two profile likelihoods are small, with the fiducial profile likelihood being slightly more sensitive. This is because the 0.1 keV energy bins are at the limit of the detector energy resolution.

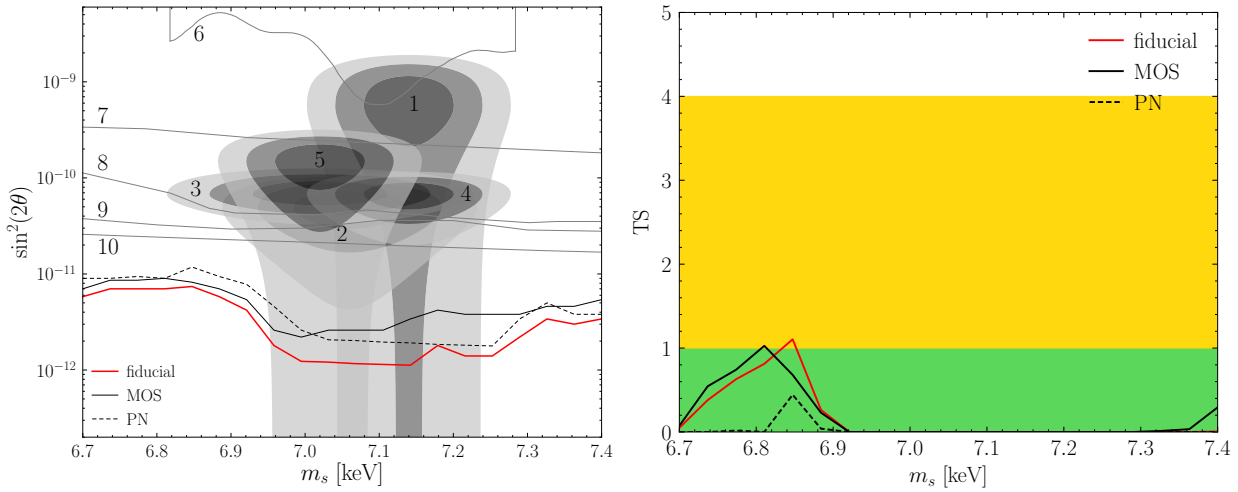

(a) (b)

Figure A.9: Exploring the results from individual cameras. Variations to the limit (A) and TS (B) arising from performing independent analyses on the MOS (solid black) and PN (dashed black) datasets, to test for possible systematic effects present in one camera but not in the other. These can be compared to the fiducial results (red). We find that both limits are independently inconsistent with the decaying DM interpretation of the UXL.

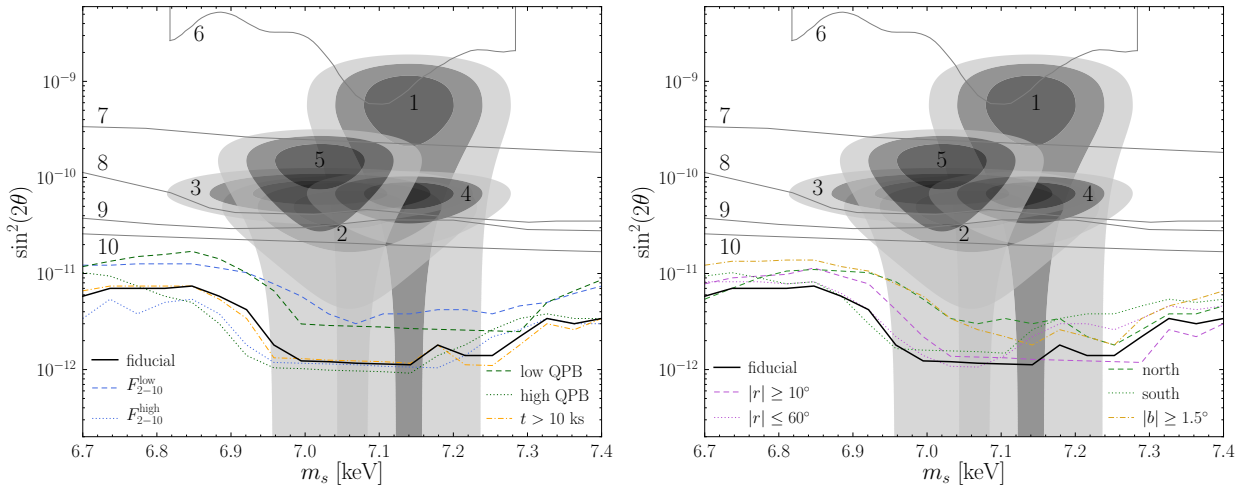

(a) (b)

Figure A.10: Variations to the limits arising from different selection criteria that determine which exposures are included in the joint likelihood. In (A) we vary the cuts on the exposures while in (B) we vary the regions considered. The various criteria are summarized in Table A.2. In all cases the decaying DM origin of the UXL is inconsistent with the resulting limits.

Table A.2: The different selection criteria that we test in Fig. A.10. These are variations to the cuts we have chosen in our fiducial analysis.

	$r_{\rm min}$ [deg]	$r_{\rm max}$ [deg]	$\lvert b\rvert_{\rm min}$ [deg]	$I^{\rm max}_{2-10}$ [erg/cm^2/s/deg^2]	$F^{\rm max}_{\rm QPB}$ [%]	Exposure [Ms]	other
fiducial	5	45	0	10^{-10}	68	30.6	-
$r \geq 10^\circ$	10	45	0	10^{-10}	68	27.9	-
$r \leq 60^\circ$	5	60	0	10^{-10}	68	56.9	-
$b \geq 1.5^\circ$	5	45	1.5	10^{-10}	68	24.8	-
north	5	45	0	10^{-10}	68	12.5	mask $b < 0^\circ$
south	5	45	0	10^{-10}	68	18.1	mask $b > 0^\circ$
$F^{\rm low}_{2-10}$	5	45	0	5×10^{-11}	68	18.8	-
$F^{\rm high}_{2-10}$	5	45	0	5×10^{-10}	68	35.7	-
low QPB	5	45	0	10^{-10}	16	6.3	-
high QPB	5	45	0	10^{-10}	95	45.6	-
$t > 10$ ks	5	45	0	10^{-10}	68	28.2	require $t^e > 10$ ks

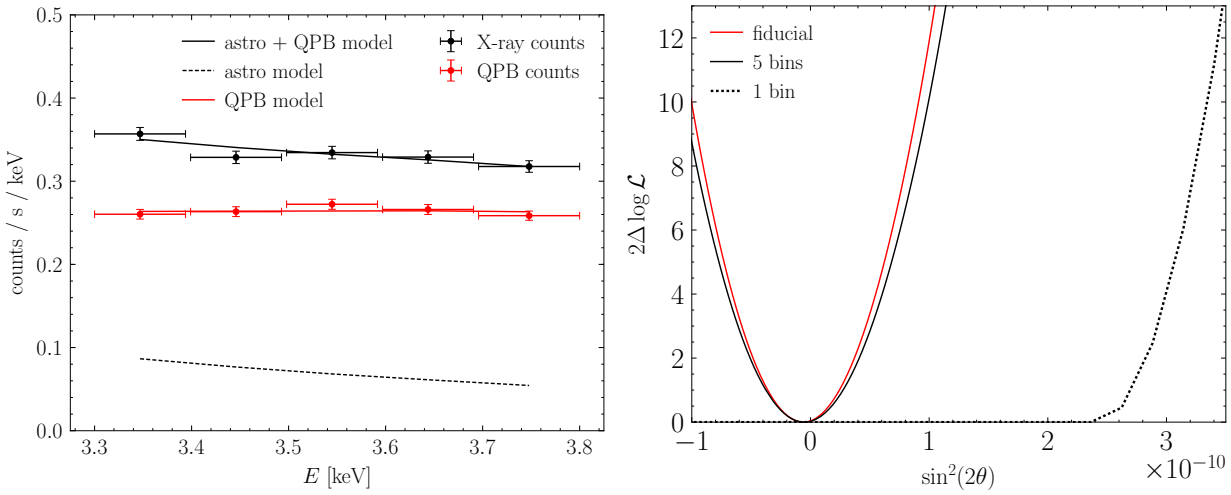

(a) (b)

Figure A.11: The effects of down-binning the data. As in Fig. A.7, except here we have down-binned the output energy channels of the PN detector forward modeling matrix. (A) we down-bin to to 0.1 keV output energy channels across the 0.5 keV energy window and show the fitted model. In red we show the QPB counts as data points and the model as a solid line, respectively. The X-ray data we show as black data points, and we show the model for the astronomical counts in dotted black. The sum of the two models, which is fitted to the X-ray counts, is shown in solid black. (B) we compare the profile likelihood for a UXL at 3.55 keV obtained from this analysis (solid black line), compared to the fiducial profile likelihood in Fig. A.7 (red). The two profile likelihoods are very similar, as expected given that the PN energy resolution is ∼0.1 keV. We also show the result of using a single 0.15 keV wide output energy bin (dotted black line) centered at 3.55 keV.

Down-binning further leads to a large decrease in sensitivity, since the UXL then becomes degenerate with the other (nuisance) model parameters. As an extreme example, we show the single-bin profile likelihood in Fig. A.11B, where we have adopted a single output energy bin with a width of 0.15 keV centered around 3.55 keV. Because we are using a single energy bin, the UXL model parameter is completely degenerate with the model parameters describing the QPB and X-ray power-laws. As such, it would not be possible to find evidence for a UXL with this analysis, but the limit obtained is maximally conservative. The limit is $\sin^2(2\theta) \lesssim 2.8 \times 10^{-10}$ at 95% confidence, so any larger value of $\sin^2(2\theta)$ would overproduce the entire observed X-ray data in this energy bin, without any modeling. The profile likelihoods in Fig. A.11 show that the fiducial and 5-bin likelihoods are symmetric and quadratic about their minimum, the 1-bin profile likelihood is zero at low $\sin^2(2\theta)$ and then rises steeply at high $\sin^2(2\theta)$. Any model flux from the UXL that is below the observed X-ray counts can be compensated by the nuisance models (astrophysical and QPB models), which implies that all such models will fit the data equally well. As $\sin^2(2\theta)$ becomes arbitrarily negative the other models are allowed to become arbitrarily large to compensate. However, as $\sin^2(2\theta)$ increases and the UXL model flux begins to surpass the observed data counts, the flux from the nuisance parameters is driven to zero (the nuisance astrophysical and QPB models are restricted to positive flux). Comparing the 1-bin profile likelihood to the fiducial profile likelihood, we see that modeling the astrophysical and QPB emission improves the limit on the UXL by almost an order of magnitude in this case.

A.2.7 Additional Degrees of Freedom in the Background Model

We test how our limits are impacted if there are additional degrees of freedom in the background model. We consider the possibility of two lines in the energy range of interest, at 3.31 keV and 3.69 keV. The existence of a weak instrumental line at 3.31 keV was suggested in PN data by [541] and of both lines in the MOS data [115]. The existence of these lines has not been conclusively established, nevertheless we can test the impact their inclusion would have on our analysis.

Analysis of *XMM-Newton* data in a region of the inner Galaxy that partially overlaps with ours [60] found evidence for sterile neutrino DM at a mixing angle $\sin^2(2\theta) \sim 2 \times 10^{-11}$ and mass $m_s \approx 7.0$ keV. That work used a broad energy range in their analysis of the stacked data and included additional lines in their background model in the vicinity of 3.5 keV, at 3.12 keV, 3.31 keV, 3.69 keV, and 3.90 keV. We analyze how our results change with the addition of these lines. We only include the lines at 3.31 keV and 3.69 keV because these are the relevant lines for DM masses in the vicinity of 7.0 keV when restricting to a narrow

energy range 0.5 keV wide about the line center.

Generically, as we include more degrees of freedom in the background model we expect the limits to weaken, as there is more potential for degeneracy between the signal model and background model, which we profile over. As an extreme illustration, consider the possibility that the background model has a spectral template that is identical to the signal spectral template and that the normalization of the background spectral template is allowed to float negative in the profile likelihood process. Then, for a fixed signal value S the signal template can always be completely canceled by the background model with a background signal template normalization of $-S$. This means that the likelihood profile as a function of S will be completely flat for all S. We can never find evidence for DM with this background model, but we will also set limits that are arbitrarily weak, meaning that we will not rule out a real signal if one were present. The background model we use with the addition of the two extra lines, whose normalizations are allowed to go negative, does not have a complete degeneracy with the signal model, but there is a partial degeneracy which leads to weaker limits as compared to the power-law model we use in our fiducial analysis.

We illustrate the difference between the two background models with a simple example. We generate Monte Carlo data using the best-fitting background model shown in Fig. A.7 for the PN camera of observation ID 0653550301, our most constraining exposure, as given in Table A.1. The Monte Carlo is generated under the null hypothesis, so there is no signal in the data. We then analyze the simulated data for a signal at $m_s = 7.1$ keV with our fiducial background model and with the background model that has two extra lines at 3.31 keV and 3.69 keV. The profile likelihoods for these different analyses are shown in Fig. A.12A. The profile likelihood with extra lines is broader than the fiducial profile likelihood. As a result, the limit obtained with the background model containing extra lines is weaker by approximately a factor of two in this case.

The degeneracy between the signal and background model in the profile likelihood is illustrated in Fig. A.13, where we show the best-fitting models for fixed signal fluxes with both the fiducial background model and the background model including the extra lines. In the presence of a signal, the analysis including the extra lines still recovers the injected signal strength, but the significance of the detection is reduced because the background model is semi-degenerate with the signal. Fig. A.12B shows the profile likelihoods for analyses of the same simulated datasets used in the example but now with the addition of a synthetic signal with $\sin^2(2\theta) = 1.8 \times 10^{-10}$. Both the fiducial analysis and the analysis including the extra lines find the injected signal strength within 68% confidence, but the significance of the detection is reduced for the analysis with extra lines, as may be seen from the likelihood profile being broader in this case.

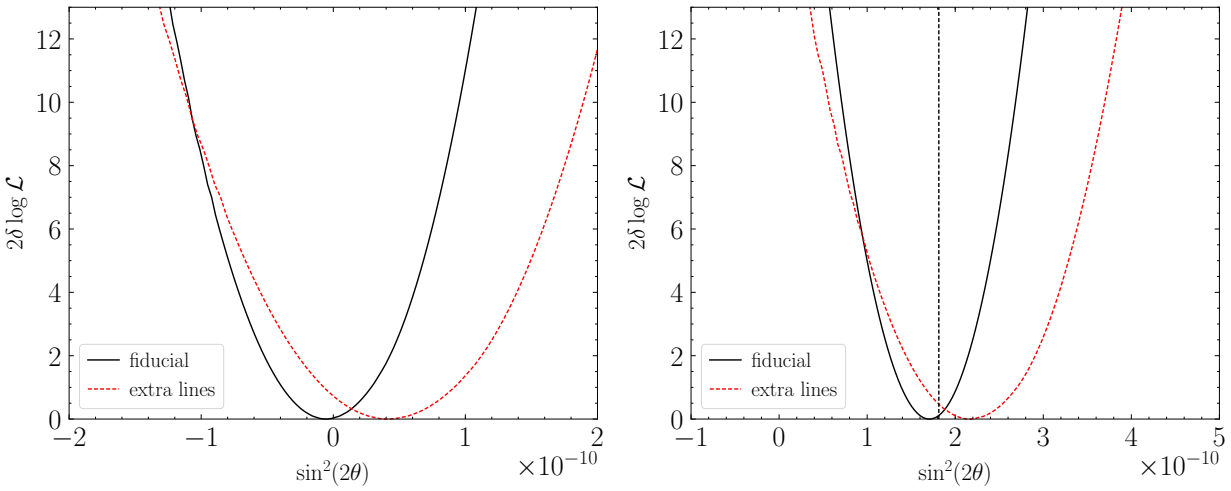

Figure A.12: The effects of adding extra lines on the profile likelihood. (A) The profile likelihood for a Monte Carlo-generated dataset with no DM decay signal. The solid black line indicates the results using our fiducial analysis, while the dotted red line indicates the results when including the lines at 3.31 keV and 3.69 keV. The analysis with extra lines sets weaker limits on the sterile-active mixing angle, due to the partial degeneracy between the background and signal models. (B) The profile likelihood for a Monte Carlo-generated dataset with an injected signal of $\sin^2(2\theta) = 1.8 \times 10^{-10}$, indicated by the vertical dotted black line. Again, the analysis with the extra lines sets weaker limits.

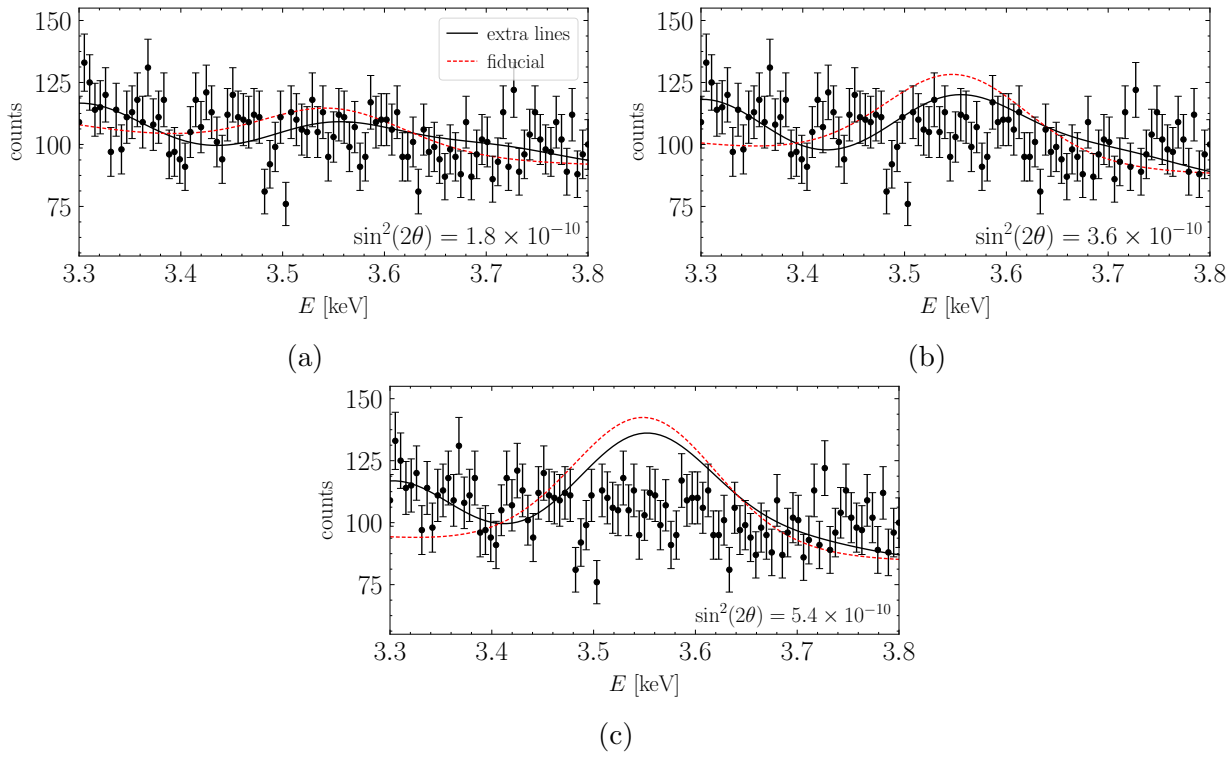

Figure A.13: The effects of adding extra lines on the fitted model. The best-fitting models assuming a DM mass of 7.1 keV for fixed signal strengths (A, $\sin^2(2\theta) = 1.8 \times 10^{-10}$; B, $\sin^2(2\theta) = 3.6 \times 10^{-10}$; C, $\sin^2(2\theta) = 5.4 \times 10^{-10}$) for the fiducial background model (red line) and the background model with extra lines (black line). The data shown (black points) is the Monte Carlo data analyzed in the left side of Fig. A.12.

We perform this analysis across our ensemble of exposures and present the limits in Fig. A.14A. We show the limits for the MOS datasets, the PN datasets, and the combination of both datasets (joint). We show the MOS and PN limits separately to account for the possibility that the extra lines affect one detector but not the other. As expected, the limits are weaker when including the extra lines in the background model. However, the limits (from both MOS and PN datasets independently) remain inconsistent with the DM interpretation of the UXL and the best-fitting parameters from the blank-sky analysis in [60]. In the vicinity of 7.0 keV we find no evidence for DM, as in shown in Fig. A.14B. For this analysis we restrict the exposure times of the individual exposures to be greater than 10 ks to ensure the model fitting of the individual exposures is well converged. This reduces the total exposure time to ∼27.2 Ms, which does not substantially affect the projected sensitivity.

We investigate whether the model fitting favors the background model with the two extra lines over the fiducial model. Adding two extra degrees of freedom to the background model should lead to an improved fit to the data. If the data is well described by the fiducial background model then we might expect that using the model with extra lines, which has two extra degrees of freedom, would cause a decrease in the χ^2 for the best-fitting background model that follows a χ^2-distribution with two degrees of freedom. This is what we observe, as is shown in Fig. A.15 for the particular case of $m_\chi = 7.1$ keV. We show the average χ^2 difference, over all of the exposures included in the analysis, between the fiducial background model and the model with two extra lines, for the MOS and PN datasets independently and combined. The distributions follow the appropriate χ^2-distributions with two degrees of freedom.

A.2.8 Analysis of Disjoint Regions

We performed our analysis separately in multiple disjoint regions. We determine the TS in favor of DM within each region, and investigate whether it is consistent with the null hypothesis. Figure 3B shows the distribution of TSs for the individual exposures combined into the joint likelihood used in our fiducial analysis. However, in the presence of a small signal of strength near our limiting value, this distribution may resemble the null hypothesis χ^2 distribution, because the effect on each individual exposure is small. Here we extend this check, by determining the TS distribution in different regions.

Our fiducial analysis includes exposures within 5° and 45° of the Galactic Center. We now consider dividing the region between 5° and ∼90° into four approximately equal exposure regions, with the first region being our fiducial region, the second region extending from 45° to 62.2°, the third region from 62.2° to 74.0°, and the fourth from 74.0° to 83.4°. All of

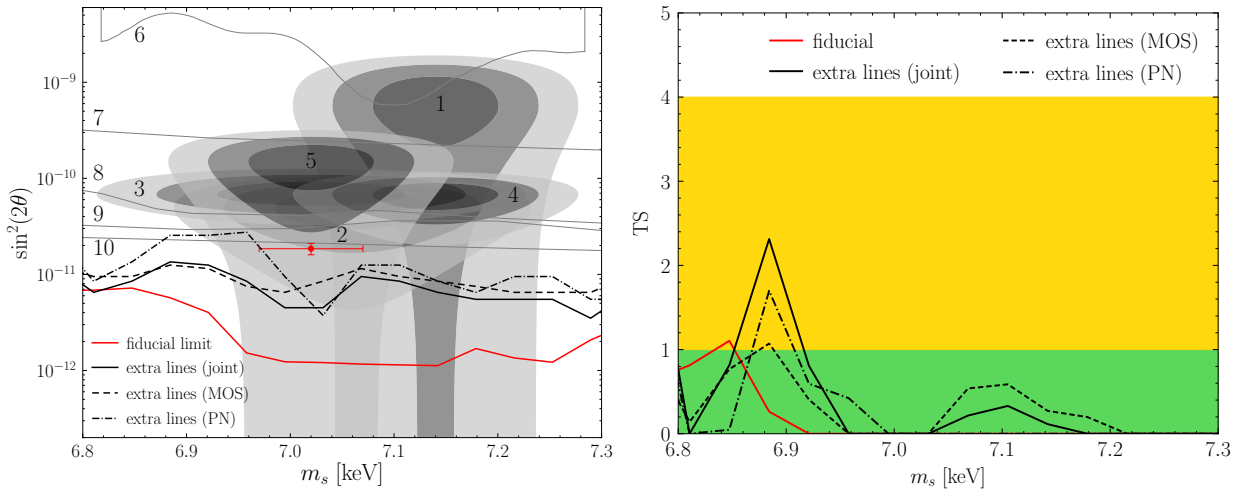

Figure A.14: The effects of adding extra lines on the limits and TS. (A) The one-sided power-constrained 95% limits on $\sin^2(2\theta)$ as a function of the DM mass m_s with the analysis with extra lines, compared to the fiducial limit and the parameter space from Fig 1. We show the extra-line limits for the MOS and PN datasets independently and combined. The fiducial limit is stronger than the limit when including the extra lines. Nevertheless, the latter limit remains inconsistent with the detections shown in Fig. 1, and the best-fitting parameters in [60] (red point). Our conclusions are not dependent on our choice of background model. (B) The test statistic (TS) in favor of a decaying DM interpretation of the UXL as a function of the DM mass m_s with the analysis with extra lines (black), compared to the fiducial TS (red). The green and yellow regions indicate 1σ and 2σ detections, respectively. No evidence for decaying DM in either analysis is found.

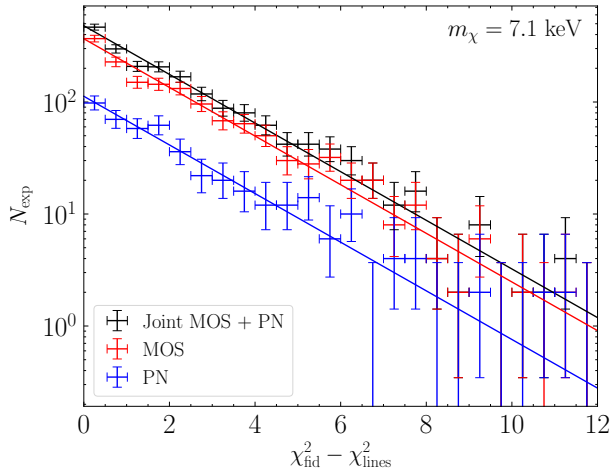

Figure A.15: The effects of adding extra lines on the χ^2 . For the 7.1 keV mass point, we show a histogram of the individual $\chi^2_{\rm fid} - \chi^2_{\rm lines}$ values from each individual exposure in our fiducial analysis, with error bars calculated from Poisson statistics. We show the MOS (red) and PN (blue) data separately and our fiducial data (black) from Fig. 3B, with the appropriate χ^2 distributions with 2 degrees of freedom illustrated by the solid curves.

these regions have approximately 30.6 Ms of exposure, by construction. These regions would also be approximately equal area, though in practice we see that the area of the concentric circular regions decreases with distance from the Galactic Center. This is due to our flux cut on individual exposures, which is less frequently satisfied for observations closer to the Galactic Center. We compute the TS for analyses in each of these regions for three different mass points: $m_s = 6.9$, 7.1, and 7.3 keV. We use the three independent mass points to improve the statistics when constructing the TS distribution. We then combine the TSs from the different mass points; the resulting distribution of TSs is shown in Fig. A.16. The distribution TSs follows the one-sided χ^2 distribution, as expected under the null hypothesis, though the number of independent analyses $N_{\rm anal}$ is limited. This disfavors the presence of large systematic uncertainties, indicating that our uncertainty is is dominated by statistical variations. The bin with TS = 0 is not shown in Fig. A.16; instead, we state it here. We expect that half of our 12 analyses should produce TS = 0 and find $7^{+3.8}_{-2.6}$, consistent with the predicted number of 6.

In Fig. A.16B, we show how, at $m_s = 7.1$ keV, our best-fitting mixing angle $\sin^2(2\theta)$ changes between the analyses in the four independent regions. We show the expectations under the null hypothesis; for statistical consistency, we must include the possibility of negative $\sin^2(2\theta)$. If our background model systematically under predicts the counts at energies $\sim m_s/2$, but also a real signal is present, the evidence for that real signal could be obscured. However, in that case regions further from the Galactic Center would have a smaller signal contribution, so we would expect the best-fit mixing angle to become more and more negative. This is not what we see (there is a slight trend in the other direction). This indicates that our analysis is statistically limited and that there is not a systematic effect at $m_s/2$ obscuring the presence of a signal.

By choosing regions with similar exposure times as our fiducial analysis, the number of regions considered above $N_{\rm anal}$ is limited. We can seek to find an intermediary regime between this result and Fig. 3B by decreasing the size of our concentric regions. This, however, comes at the cost of reduced sensitivity, because each individual analysis does not have as much exposure. In the extreme limit of individual exposures, the limits obtained are shown in Fig. A.6. As an illustration, we consider taking 45 approximately equal-exposure regions, with the first region extending from 5° to 10°, the second from 10° to 15.4°, and the last from 88.6° to 88.9°. All of the sub-regions have approximately 3 Ms of exposure. The distribution of TSs at $m_s = 6.9$ keV, 7.1 keV, and 7.3 keV over these analyses is shown in the right panel of Fig. A.17B. The TS distribution is consistent with the expectation under the null hypothesis. This again indicates that the dominant source of uncertainty is statistical and not systematic. The limits obtained from the inner four rings are shown in Fig. A.17A.

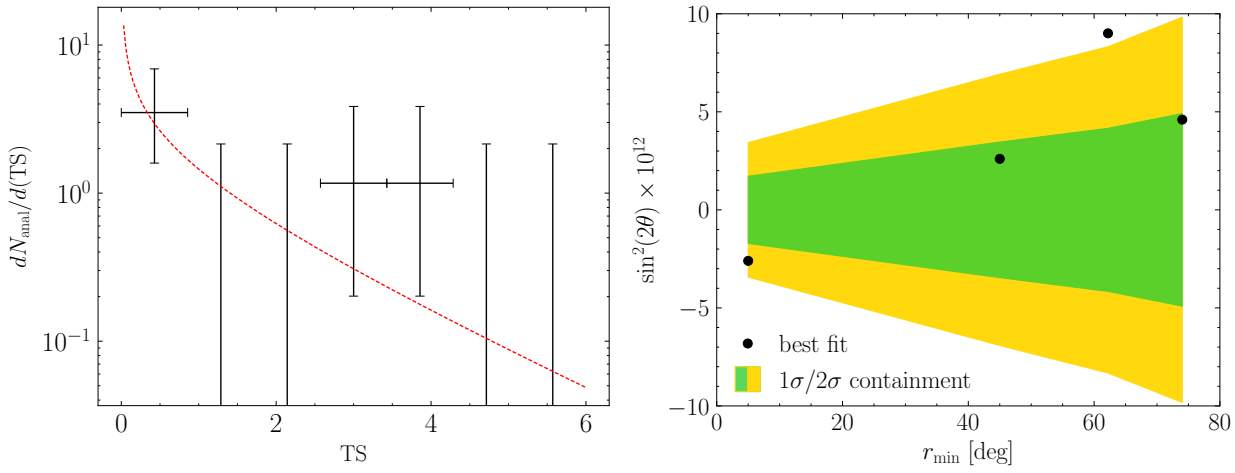

(a) (b)

Figure A.16: Dividing the analysis into 4 concentric regions around the Galactic Center. (A) Distribution of TS values obtained from four independent regions, with three mass points considered for each, are shown in black, with error bars from Poisson statistics. The different regions are our fiducial region used in the main chapter, as well as observations with $45^\circ < r < 62.2^\circ$, $62.2^\circ < r < 74.0^\circ$, and $74.0^\circ < r < 83.4^\circ$, where r is the angle from the Galactic Center. These regions have approximately 30.6 Ms of exposure each, with our fiducial set of flux and QPB cuts. We also show in red the expectation from statistical fluctuations of the null hypothesis, as determined by the χ^2 distribution. Note the bin with TS = 0 is excluded from the figure, but the values are stated in the text. (B) The best fitting values (black circles) of $\sin^2(2\theta)$ for each of our four regions, identified by their minimum angle from the Galactic Center, for $m_s = 7.1$ keV. The green and yellow regions indicate 1σ and 2σ containment for these values, respectively.

While these limits are slightly weaker than in our fiducial analysis, they are each inconsistent with the decaying DM interpretation of the 3.5 keV line.

A.2.9 Analysis of Stacked Data

Our fiducial data analysis is based on the joint likelihood that combines the profile likelihoods from the disjoint analyses of the individual exposures. An alternative analysis, as described in the main chapter, is to instead stack the data from the individual exposures and then analyze the stacked data. The limits obtained from this procedure are consistent with those obtained from our fiducial data analysis and, in particular, are in tension with the DM interpretation of the UXL. In this section we provide additional details behind this analysis.

The stacked MOS and PN datasets are shown in Fig. 2 (see also Figs. A.18A and B) from 3.3 keV to 3.8 keV. These datasets are constructed by summing the individual spectra. We then fit models to these stacked spectra that consist of a null hypothesis component to describe the smooth background emission and a signal component to model the contribution from a putative UXL at *e.g.* 3.55 keV. We independently fit models to the MOS and PN data, since these instruments have different instrument responses, in order to construct profile likelihoods for the UXL flux as determined by the two cameras. We then join these two profile likelihoods together in order to obtain our final constraint on the 3.55 keV UXL. Note that since all of the energy bins shown in Fig. 2, for both the MOS and PN data, have over 10^3 counts, we use a Gaussian likelihood instead of a Poisson likelihood.

The red curves in Fig. 2 are the best sums of the best-fit null hypothesis models from the analyses of the individual exposures. While each of the curves that goes into the sum is modeled as a combination of two power-law components, the combined spectrum does not need to follow a simple power-law. However, as shown below, we find that a quadratic background model with three model parameters is able to describe the data at the level of statistical noise. In particular, we take the background model for the stacked data analysis to be $dN/dE(E, \theta_{\rm nuis}) = A + B\,(E/1\text{ keV}) + C\,(E/1\text{ keV})^2$, where dN/dE are the fluxes appearing in Fig. 2 in units of counts $\text{s}^{-1}\text{keV}^{-1}$, and where $\theta_{\rm nuis} = \{A, B, C\}$ are the nuisance parameters. The signal component is as shown in Fig. 2 and is obtained by forward modeling the 3.55 keV UXL through the detector responses from each individual exposure and then summing the resulting spectra. As seen in Fig. 2, the effect of the UXL is to produce a spectral feature with a width $\sim$200 eV, though that feature is narrower for the MOS data than for the PN data.

Fitting the quadratic background plus signal model to the PN (MOS) data produces a fit with a χ^2/DOF, for $50 - 4$ DOF, of 1.14 (0.81). The expected 68% containment

interval for the χ^2/DOF with 46 DOF under the null hypothesis is $\sim$[0.79, 1.21]; this interval contains the values measured for both the PN and MOS data. We then compute the profile likelihood for the signal-model flux parameter $\sin^2(2\theta)$ by profiling over the background nuisance parameters. The profile likelihood is shown in Fig. A.18C. We show the profile likelihoods for the PN and MOS data analyzed separately and also for the combination. The 95% upper limit is found by taking the upper value for $\sin^2(2\theta)$ under the condition $2\Delta \log \mathcal{L} \approx 2.71$; this leads to the upper limit $\sin^2(2\theta) < 5 \times 10^{-12}$, which strongly constrains the DM interpretation of the 3.5 keV UXL.

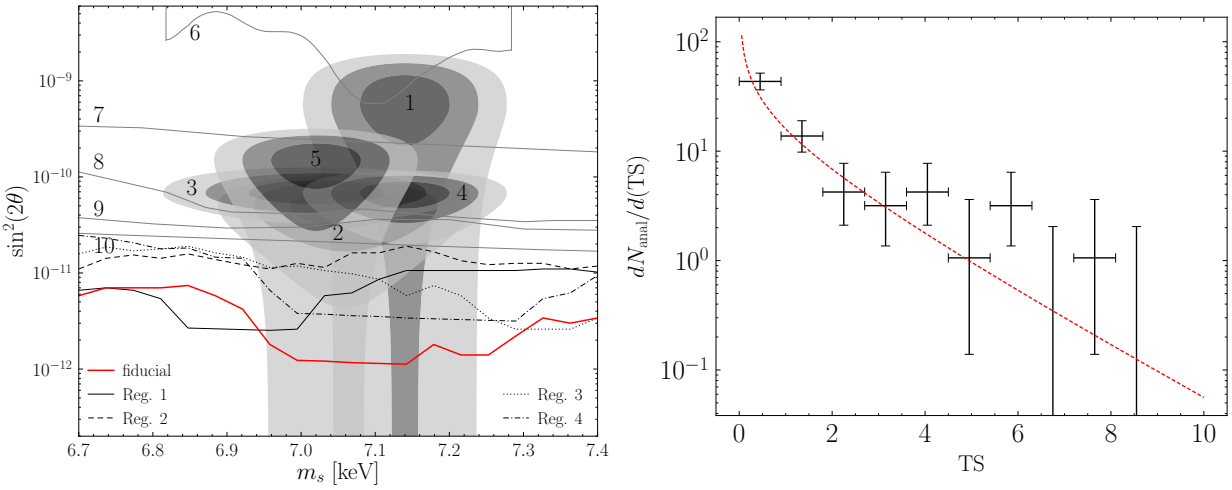

Figure A.17: Dividing the analysis into 45 concentric regions around the Galactic Center. (A) The limits from the inner four rings, obtained from analyses in sub-regions consisting of concentric rings starting at 5° from the Galactic Center that have approximately 3 Ms of exposure per ring, compared with the parameter space from Fig 1. The limits from the first ring is presented in solid black, the second in dashed black, the third in dotted black, and the fourth in dashed-dotted. These can be compared to our fiducial limit, plotted in red. (B) As in A.16, but for analyses in the concentric circle sub-regions used in the left panel.

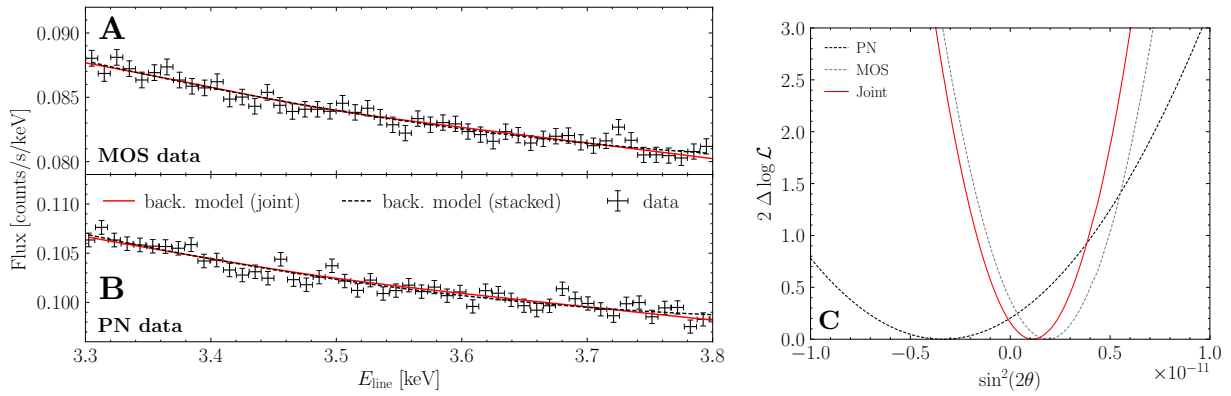

Figure A.18: Analysis of stacked data. The stacked MOS (A) and PN (B) data as presented in Fig. 2. The red curves are the sums of the best-fit null-hypothesis models from the analyses of the individual exposures, as presented in Fig. 2, while the dashed black curves are the best-fit null-hypothesis models from fits of the quadratic background model to the stacked data. (C) The profile likelihoods as functions of the signal-strength parameter $\sin^2(2\theta)$, including negative values, from analyses of the stacked data with the quadratic background model. Results are shown for MOS and PN individually as well as combined.

Appendix B

A Deep Search for Decaying Dark Matter with *XMM-Newton* Blank-Sky Observations

This chapter is organized as follows. In Sec. D.2 we provide additional details behind our data reduction and analysis procedure. In Sec. H.3 we provide additional results from the main analysis presented in the main chapter. Sec. B.3 presents non-trivial checks of our analysis procedure using synthetic signals. Lastly, in Sec. B.4 we perform multiple analysis variations to demonstrate the robustness of our main results.

B.1 Data Reduction and Analysis

In this section, we detail our process for data reduction and analysis.

B.1.1 Data Reduction

We selected all *XMM-Newton* observations performed until September 5, 2018. For each of these observations, we retrieved the raw data products from the XMM-Newton Science Archive. For data reduction, we used the *XMM-Newton* Extended Source Analysis Software (ESAS) package, which is a part of the Science Analysis System [542] (SAS) version 17.0, and used for modeling sources covering the full *XMM-Newton* field-of-view and diffuse backgrounds.

The data reduction process is described in detail in Ref. [111]; here, we summarize the important steps and point out any differences. To reduce a given observation, we obtain the list of science exposures (i.e. pointings taken in a mode usable for scientific purposes) from

the summary files. For each exposure (independent of camera), we generate an event list and filter this list to only include events which were recorded during a period of low-background, which cuts contamination from soft-proton flares. We then mask point sources in the field of view which contribute in any energy range (c.f. Ref. [111] where we only masked point sources in the 3-4 keV range). We also mask data from CCDs operating in anomalous states. From the filtered and masked data products we create the photon-count data, the ancillary response file (ARF), and the redistribution matrix file (RMF).

The reduced data contains 11,805 observations, with 21,388 and 8,190 individual MOS and PN exposures, totaling 438 Ms and 109 Ms of data. Given our focus is on searching for DM emission in otherwise dark regions of the sky, we place a cut on these data sets to isolate the astrophysically quietest amongst them. In particular, we construct the integrated flux from $2 - 10$ keV in all exposures, and determine the median value for MOS and PN separately as 0.09 photons/keV/s and 0.39 photons/keV/s. All observations with integrated fluxes higher than these median values are excluded. This cut will remove observations with above average astrophysical emission, but also those where there is large instrumental or quiescent particle background (QPB) emission (c.f. Ref. [111] where a separate cut on the QPB emission was performed). For regions of the sky that are not focused on a bright Galactic or extra-galactic source, the QPB counts should dominate over the extra-galactic X-ray background [105]. However, the QPB is time-dependent and will vary over exposures because of *e.g.* flaring activity (which, as described in this chapter, we filter for). Further, we emphasize that even in the most optimistic scenario, a DM UXL will only provide an exceptionally small contribution to the total integrated flux, and thus this cut will not bias against a potential signal. In addition to removing these bright exposures, we place two additional cuts. Firstly, all exposures with less than 500s of data are removed, as the flux in such short exposures can be poorly characterized. Finally, we exclude all observations within 2° of the plane of the Milky Way, which excises only a small amount of the expected DM signal, but a much larger fraction of the expected astrophysical emission associated with emission from our own galaxy. The cuts leave 215 Ms (57 Ms) of the total 438 Ms (109 Ms) of full-sky ($|b| \geq 2^\circ$) exposure time for MOS (PN).

Exposure passing all three cuts are then divided into 30 rings, each of width 6° from the GC as described in the main chapter. The rings, numbered 1-30 starting from the GC, are used to form our signal ROI (rings 1-8) and background ROI (rings 20-30).

B.1.2 Public Data Products

The processed data used to perform the analysis in this chapter is made fully publicly available at github.com/bsafdi/XMM_BSO_DATA. There we provide all the data required to reproduce our results. In particular, we provide the data after the cuts described above in each ring for the MOS and PN cameras separately. The instrument response files, appropriately weighted across the exposures in each ring, are provided.

B.1.3 Analysis

In this section we provide additional details behind the analysis framework used to interpret the data products described above in the context of the decaying DM model. First, we describe how we analyze the flux data in the individual annuli, and then we detail how those results are joined together to constrain the DM lifetime. Lastly, we describe how we test for and incorporate systematic uncertainties.

Construction of the profile likelihood

Let us first focus on the analysis of the (either MOS or PN) data in an individual ring $k \in [1, 8]$. The data set d^k in this ring consists of background subtracted count rates d_i^k in each energy channel i. The count rates have units of cts/s/keV, as illustrated in *e.g.* Fig. B.1, with Poisson counting uncertainties σ_i^k that arise from combining the statistical uncertainties in the signal and background data sets in the large-count limit, where the uncertainties become normally distributed. Our goal is then to compute the log-likelihood $\log p(d_k|\theta)$ as a function of the model parameters $\theta = \{A_{\rm sig}, \theta_{\rm nuis}\}$, which consist of our parameter of interest, $A_{\rm sig}$, and our nuisance parameters $\theta_{\rm nuis}$. The nuisance parameters include background line amplitudes, A_j, with j indexing the different lines at energies E_j, and also hyperparameters for the GP model. In our fiducial analysis the only GP model hyperparameter is the amplitude of the double-exponential kernel $A_{\rm GP}$. Note that, as described shortly, in determining the instrumental line list we also assign nuisance parameters to the locations of the lines. Our goal is to construct the profile likelihood $\log p(d_k|A_{\rm sig}) = \max_{\boldsymbol{\theta}_{\rm nuis}} \log p(d_k|\boldsymbol{\theta})$.

Before describing the log-likelihood function in detail, we note that because we are in the large-count limit, so that the statistical fluctuations are normally distributed, we may interchangeably use the concept of modeling the data as the sum of model components and subtracting model components from the data and considering the residuals. In the small-count limit, where the Poisson fluctuations are not nearly Gaussian, this approach would not be appropriate.

The log-likelihood function that we use is a modification of the zero-mean GP marginal likelihood. The modification that we implement incorporates the background lines and the signal line of interest. For a given set of model parameters $\{A_{\rm sig}, A_j\}$ we construct the modified data vector[1]

$$y_i^k(\boldsymbol{\theta}) \equiv d_i^k - A_{\rm sig}\mu_{{\rm sig},i}^k - \sum_j A_j \mu_{j,i}^k - \left\langle d_i^k - A_{\rm sig}\mu_{{\rm sig},i}^k - \sum_j A_j \mu_{j,i}^k \right\rangle_i , \tag{B.1}$$

where $\mu_{\rm sig}$ is the spectral template of the signal line of interest, with fixed normalization, as obtained by appropriately summing the forward modeling matrices of the individual exposures that compose the observations within the ring of interest, k. Similarly, $\mu_{j,i}^k$ denotes the fixed-normalization spectral template of the $j^{\rm th}$ background line, at energy E_j, in ring k (recall that i labels the detector energy channel). The quantity $\langle \cdots \rangle_i$ in (B.1) denotes the average over energy bins i, which implies that by construction the $y_i^k(\boldsymbol{\theta})$ have zero mean when averaged over the full energy range of the analysis. We postulate that the y_i^k are described by GP models, so that we may use the GP marginal likelihood to compute the hyperparameter $A_{\rm GP}$:

$$\log p(d_k|\boldsymbol{\theta}) = -\frac{1}{2}\mathbf{y}^{k\,T}\left[\mathbf{K} + (\sigma^k)^2\mathbf{I}\right]^{-1}\mathbf{y}^k - \frac{1}{2}\log|\mathbf{K} + (\sigma^k)^2\mathbf{I}| - \frac{n}{2}\log(2\pi)\,. \tag{B.2}$$

Above, n is the number of energy channels, and all matrix operations are taken in the space of energy channels, with $(\sigma^k)^2\mathbf{I}$ denoting the diagonal matrix with entries $(\sigma_i^k)^2$. The matrix $\mathbf{K}$ denotes the GP kernel. We implement the non-stationary kernel

$$K(E, E') = A_{\rm GP}\exp\left[-\frac{(E-E')^2}{2EE'\sigma_E^2}\right] , \tag{B.3}$$

which has the hyperparameters $A_{\rm GP}$ and σ_E. Note that later in this chapter we show that similar results are obtained using the more standard double exponential kernel, but we chose the form of the kernel in (B.3) for reasons discussed below.

It is worth emphasizing that we have made the choice to describe the residuals of the background-subtracted data, after also subtracting the contributions from the instrumental lines, by a zero-mean GP model. An alternative strategy would be to allow the GP model to have an energy-dependent mean. Equivalently, we could include a parametric model component (such as a power-law or exponential) to model the clear upward trend in the data at low energies observed in *e.g.* Fig. B.1, with the GP model then describing fluctuations

[1]Note that the line energies E_j are fixed in all analyses except those of the background ROI data for constructing our lists of instrumental lines; in those analyses only, the E_j are also model parameters.

about that parametric component. Such an approach would likely result in smaller values of the hyperparameter $A_{\rm GP}$ and, potentially, increased sensitivity. Such a hybrid parametric plus GP modeling approach could be explored in future work.

Our goal is to look for narrow lines on top of a smooth continuum flux. We know that even a narrow line will manifest itself as a broader feature in the detector-level data due to the detector response. So the correlation-length of the GP kernel has a lower-bound set by the detector resolution. Because the energy resolution δE of *XMM-Newton* increases linearly with energy (*i.e.*, $\delta E/E$ is roughly constant), a stationary kernel with a fixed correlation length is not adequate and a kernel of the form in (B.3) is more natural. However, we expect the continuum to be much smoother, even before the smearing induced by the detector resolution. A common approach in GP literature when the hyperparameters are not motivated from some other considerations is to fit them to the data. This approach leads to the best-fit values $\sigma_E \approx 0.608$ ($\sigma_E \approx 0.77$) for MOS (PN) in the first annulus, with comparable results in the annuli further from the Galactic Center. However, we chose to fix $\sigma_E = 0.3$ because this is an intermediate value between the lower-bound of a narrow line given by the energy resolution and the best-fit result reflecting the smoothness of the observed continuum. This choice leads to more conservative limits, since for smaller values of σ_E the GP model is able to capture smaller-scale fluctuations in the data, absorbing what would otherwise be attributed to narrow lines.

Lastly, note that while the marginal likelihood in (B.2) is defined within the context of Bayesian statistics, as it is obtained by integrating the likelihood times prior distribution for the formal GP model parameters, we will use the likelihood to perform frequentist parameter inference. This approach is called the "hybrid approach" in [136]. As noted in [136], the asymptotic expectations for the distribution of the TS constructed from the marginal likelihood may differ from the frequentist expectations [109], because of the use of the Bayesian marginal likelihood, and so in principle the p-values and upper-limit criteria should be calibrated on Monte Carlo (MC). However, as we show below, we find through MC simulations that in our examples the TS statistical distributions follow the asymptotic frequentist expectations to high accuracy. With that in mind, we briefly review the asymptotic expectations for translating discovery TS values to p-values and forming 95% one-sided upper limits.

As discussed in the main chapter, the TS in favor of the signal model is given by

$$t = -2\Big[\max_{\boldsymbol{\theta}} \log p(d_k|\boldsymbol{\theta}) - \max_{\theta_{\rm nuis}} \log p(d_k|\{A_{\rm sig} = 0, \boldsymbol{\theta}_{\rm nuis}\}\Big] \,, \tag{B.4}$$

where the second term is the maximum marginal likelihood for the null model without a signal line. When searching for evidence of DM, the discovery TS is set to zero for unphysical

model parameters (in that case, $\sin^2(2\theta) < 0$), but for the purpose of testing for systematic uncertainties it is useful to allow for both positive and negative signal amplitudes. The discovery TS is asymptotically χ^2 distributed with one degree of freedom under the null hypothesis (see, *e.g.*, [109]). In addition to searching for evidence of the signal model over the null hypothesis using t, we also set 95% one-sided upper limits using the likelihood ratio. We define the profile likelihood ratio $q(A_{\rm sig})$ by

$$q(A_{\rm sig}) = -2\Big[\max_{\boldsymbol{\theta}_{\rm nuis}} \log p(d_k|\{A_{\rm sig}, \boldsymbol{\theta}_{\rm nuis}\}) - \max_{\boldsymbol{\theta}} \log p(d_k|\boldsymbol{\theta})\Big]\,, \tag{B.5}$$

where in the first term we maximize the log-likelihood over the nuisance parameters $\boldsymbol{\theta}_{\rm nuis}$ at fixed signal parameter $A_{\rm sig}$. Let $\hat{A}_{\rm sig}$ be the best-fit signal parameter; *i.e.*, $q(\hat{A}_{\rm sig}) = 0$. Then, the 95% one-sided upper limit $A_{\rm sig}^{95\%}$ is given by the value $A_{\rm sig}^{95\%} > \hat{A}_{\rm sig}$ which satisfies $q(A_{\rm sig}^{95\%}) \approx -2.71$ [109].

Note that the profile likelihood in (B.5) is computed as a function of the signal normalization $A_{\rm sig}$ at fixed UXL energy (or, equivalently, fixed DM mass). All of the analyses presented in the main chapter are performed in this way (*i.e.*, we have a grid of different UXL energies to probe and then for each fixed energy we compute the profile likelihood as a function of the signal-strength amplitude). In SM Sec. B.3.1, however, we consider our ability to localize a putative signal in m_a and $\sin^2(2\theta)$ using synthetic data. In that analysis, and that analysis only, we simultaneously constrain the mass and the signal strength.

Instrumental and astrophysical background lines

Several instrumental and astrophysical background spectral lines are expected to contribute to the observed flux spectra. Here, we outline the procedure by which we obtain our candidate instrumental and astrophysical background lines, with the complete list of included lines for MOS and PN presented in Tab. B.1 and Tab. B.2, respectively.

We adopt an initial instrumental line list for PN and MOS from Refs. [543,544]. We then analyze the stacked data, for MOS and PN independently, in the background ROI in order to test for the presence of each candidate line. We use an analysis framework analogous to that we use in the background-subtracted signal ROI data: in particular, our analysis of the background ROI data incorporates GP modeling for the continuum emission, in addition to the set of putative instrumental lines. We test for known instrumental lines in the vicinity of: 4.51 keV (Ti $K\alpha$), 5.41 keV (Cr Kα), 5.90 keV (Mn Kα), 5.95 keV (Cr Kβ), 6.40 keV (Fe Kα), 6.49 keV (Mn Kβ), 7.06 keV (Fe Kβ), 7.47 keV (Ni Kα), 8.04 keV (Cu Kα). During this process, we allow the central location of the background lines to float by up to 25 eV. Lines which are detected with $t > 16$ (4σ local significance) in the background data analysis

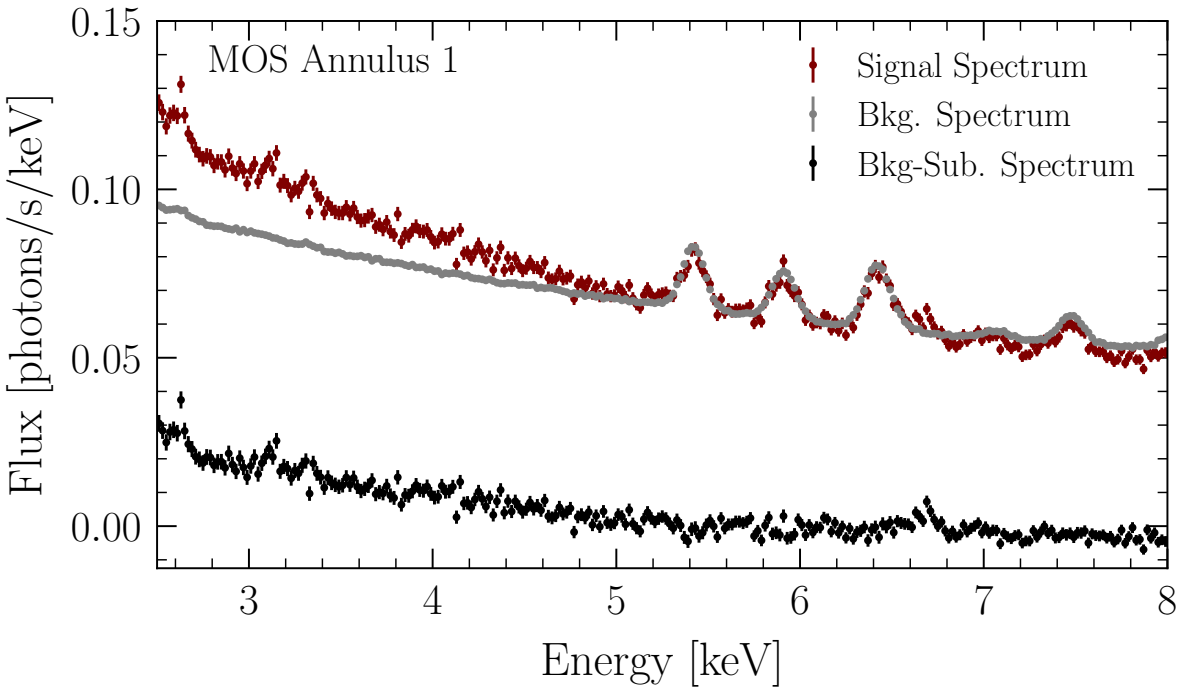

Figure B.1: Examples of the signal region spectra for MOS (top panels) and PN (bottom panels) in Ring 1 (left panels) and Ring 8 (right panels) with and without background subtraction in red and black, respectively. The background-region spectra are shown in grey. Many of the large instrumental features that are removed when looking at the background-subtracted data. Note that for visual clarity these spectra have been down-binned by a factor of 4.

are accepted at their best-fit energy as a new component of our residual background model. In MOS, we accept instrumental lines at energies: 5.42 keV, 5.915 keV, 6.425 keV, 7.07 keV, 7.485 keV, and 8.06 keV. In PN, we accept instrumental lines at 4.52 keV , 5.42 keV, 5.95 keV, and 6.39 keV.

After constructing our list of instrumental background lines we include them in our analyses of the signal-ROI background-subtracted data sets. In particular, each line is given an intensity nuisance parameter in each ring. Given our procedure of subtracting the background flux from the signal region, variability in the instrumental lines between observations can result in the best fit instrumental line intensity in our data set having a positive or negative normalization. Accordingly, we allow the normalization of the instrumental lines to be either positive or negative.

We also develop an initial list of candidate astrophysical background lines following [88], by selecting those with emissivities greater than 5×10^{-19} photons/cm^3/s at a temperature of 1 keV, which is the approximate temperature of the hot component of the Galactic Center, using the AtomDB database [545]. We include additional iron lines that are known to

$E_{\rm line}$	Origin	Type	Ring 1	Ring 2	Ring 3	Ring 4	Ring 5	Ring 6	Ring 7	Ring 8
2.46	S	Astro.	**12.5**	0.7	**7.2**	0.7	2.0	**5.5**	0.9	**5.4**
2.62	S	Astro.	**36.8**	**7.6**	**4.3**	1.9	0.0	2.1	0.0	**6.1**
3.12	Ar	Astro.	**15.0**	1.1	**8.8**	2.8	0.0	**3.5**	0.0	0.9
3.90	Ca	Astro.	0.3	0.0	0.0	**9.8**	0.0	0.2	**4.1**	0.0
5.42	Cr	Inst.	**8.9**	**7.7**	**22.1**	0.1	0.0	1.2	**7.2**	0.0
5.92	Mn	Inst.	1.8	1.0	**3.6**	0.3	0.4	2.5	**10.0**	1.7
6.42	Fe	Inst.	0.1	**7.1**	**82.0**	0.3	1.5	0.0	2.7	**7.2**
6.67	Fe	Astro.	**55.4**	1.7	0.0	**4.3**	**5.9**	2.5	0.0	0.0
6.97	Fe	Astro.	**5.9**	0.0	0.5	**4.3**	0.3	0.2	0.4	0.2
7.08	Fe	Inst.	1.5	0.0	**4.1**	0.2	2.1	1.3	0.0	2.2
7.48	Ni	Inst.	2.0	0.1	**11.9**	0.1	0.0	0.1	**3.1**	**4.7**
8.06	Cu	Inst.	1.1	0.9	0.3	0.1	0.0	0.2	0.4	0.1

Table B.1: The list of spectral lines of instrumental and astrophysical origins which are included in our background model for the MOS camera. For the line in each ring, we provide the value of $\Delta\chi^2$ associated with the addition/removal of the line from the best-fit background model which is obtained after our line-dropping procedure. Bolded values indicate the inclusion of a line in a ring's background model.

produce emission in the inner Galaxy [546]. Taking this preliminary list, we then inspect the innermost ring and determine all lines which appear with TS $t > 3$ in either PN or MOS. If such a line meets this criteria in either PN or MOS then we add it to our list of putative astrophysical lines for both instruments. As with their instrumental counterparts, the astrophysical lines are treated with independent nuisance parameters describing their intensity in each annuli. However, for astrophysical background lines, we restrict intensities to values greater than or equal to zero.

The procedure described above leads to a list of astrophysical and instrumental lines, which are shown in Tabs. B.1 and B.2. However, this does not mean that we included all of the those lines in every ring when performing our UXL search. In each annulus we analyze the background-subtracted data to determine which of the lines in Tabs. B.1 and B.2 are detected with moderate significance (we use the criteria $t > 3$) in the background-subtracted data set. Note that in Tabs. B.1 and B.2 we indicate whether the line is included in each annulus. To determine the significance of a given line we proceed iteratively, starting with the full list of lines and then calculating the change in the maximum likelihood when a given line is removed from the model.

$E_{\rm line}$	Origin	Type	Ring 1	Ring 2	Ring 3	Ring 4	Ring 5	Ring 6	Ring 7	Ring 8
2.46	S	Astro.	**15.3**	0.7	**12.5**	**3.9**	0.0	**3.5**	1.1	**6.8**
2.62	S	Astro.	**19.0**	**4.5**	**9.1**	**5.1**	0.0	0.0	0.1	**4.4**
3.12	Ar	Astro.	**6.4**	2.8	**6.5**	**13.7**	0.0	1.1	0.0	0.0
3.90	Ca	Astro.	**3.9**	0.0	0.5	**3.8**	0.0	**6.0**	0.2	0.5
4.52	Ti	Inst.	0.6	0.7	0.8	0.6	0.1	0.3	0.5	0.0
5.42	Cr	Inst.	0.7	0.0	0.4	**7.3**	0.7	1.9	2.4	**6.6**
5.93	Cr	Inst.	0.8	1.0	0.5	**4.7**	0.1	1.7	**3.6**	0.7
6.39	Fe	Inst.	0.0	0.1	**3.2**	1.2	0.0	1.6	**9.3**	0.0
6.67	Fe	Astro.	**79.2**	**5.5**	**8.9**	2.8	0.8	2.3	0.3	2.3
6.97	Fe	Astro.	0.0	0.0	0.4	0.0	0.3	0.0	0.7	0.0

Table B.2: The list of spectral lines of instrumental and astrophysical origins which are included in our background model for the PN camera. For the line in each ring, we provide the value of $\Delta\chi^2$ associated with the addition/removal of the line from the best-fit background model which is obtained after our line-dropping procedure. Bolded values indicate the inclusion of a line in a ring's background model.

In Fig. B.2 we illustrate example fits for our fiducial analyses to the data without the inclusion of an UXL. These fits are to the same background-subtracted data as illustrated in Fig. B.1, as labeled. In black we show the combined best-fit model, which is the sum of the GP model contribution (dark red) and the contributions from the individual astrophysical and instrumental lines (colored curves). Note that the number of background lines differs between each of the annuli because the important background lines are determined independently for each annulus.

The joint likelihood and background mismodeling

After constructing the profile log likelihoods $q_k(A_{\rm sig})$ in each energy annulus ($k = 1, 2, \cdots, 8$) we then convert from $A_{\rm sig}$, which has units of cts/cm^2/s/sr, to $\sin^2(2\theta)$ using the relation

$$\Phi \approx 0.26\,\text{photons/cm}^2\text{/s/sr} \times \left(\frac{m_\chi}{7.0\,\text{keV}}\right)^4 \left(\frac{D}{10^{29}\,\text{keV/cm}^2}\right) \left(\frac{\sin^2(2\theta)}{10^{-10}}\right) . \tag{B.6}$$

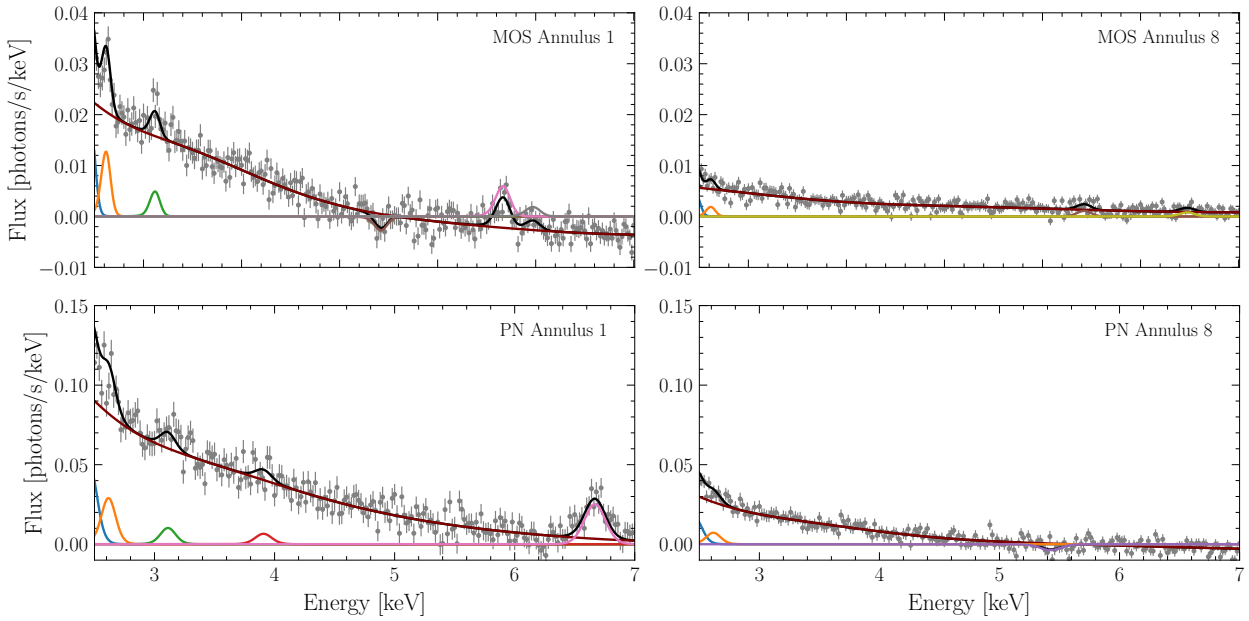

Figure B.2: The same background-subtracted data sets illustrated in Fig. B.1 (also down-binned), but now shown along with their best-fits under the null hypothesis. The best-fit model prediction is shown in black, which may be decomposed into the contribution from the GP model (dark red) and the contributions from the individual background lines (colored curves). Note that the background lines to include in the analysis are determined independently in each annulus, as described in the text.

To do so we use the background-subtracted D-factors, as discussed in the main chapter. Then, at each test mass point for the DM model we construct the joint profile likelihood

$$q_{\text{joint}}\big(\sin^2(2\theta)\big) = \sum_{k=1}^{8} q_k\big(\sin^2(2\theta)\big)\,, \tag{B.7}$$

for both MOS and PN independently. Later, we will also combine the MOS and PN profile likelihoods to construct our final joint profile likelihood that we use to search for evidence of decay DM. First, however, we analyze the joint MOS and PN profile likelihoods independently for evidence of background mismodeling.

We test and account for possible background mismodeling by extending the background model to include a component that is totally degenerate with the signal. This is a conservative approach that would remove all sensitivity to a UXL if the amplitude for this additional signal-like component were left free. Therefore we penalize the amplitude of such a signal like feature in the background model with a zero-mean Gaussian likelihood with variance hyperparameter σ^2_{spur} . The approach we follow was developed and implemented in [547–549] within the context of searches for narrow spectral features in γ-ray astronomy and in the

context of the Higgs boson search by the ATLAS experiment, where it is called the "suprious signal" [134]. We extend the likelihood to include two "spurious signal" nuisance parameters, one for the MOS data and one for the PN data. The MOS and PN likelihoods are then combined to produce the joint likelihood that we use for probing the DM model.

After extending the background model to include a signal-like component constrained by $\sigma^2_{\rm spur}$, the resulting profile likelihood (for either the MOS or PN data) is given by

$$\tilde{q}_{\rm joint}\big(\sin^2(2\theta)\big) = \max_{A_{\rm spur}} \left[q_{\rm joint}\big(\sin^2(2\theta) + A_{\rm spur}\big) - \frac{(A_{\rm spur})^2}{\sigma^2_{\rm spur}} \right] , \tag{B.8}$$

where $q_{\rm joint}$ is defined in (B.7). Note that the profile likelihood now depends on the hyperparameter $\sigma^2_{\rm spur}$, which determines the strength of the spurious-signal nuisance parameter For example, in the limit $\sigma^2_{\rm spur} \to 0$ the nuisance parameter becomes fixed at zero ($A_{\rm spur} \to 0$) and the modified profile likelihood $\tilde{q}$ approaches the un-modified likelihood q. However, in the opposite limit $\sigma^2_{\rm spur} \to \infty$ we completely lose constraining power and $\tilde{q}_{\rm joint}\big(\sin^2(2\theta)\big) \to 0$ for all $\sin^2(2\theta)$.

In practice, we determine the value of the hyperparameter at each test mass point independently. The philosophy is that if there is evidence that the background model is not properly describing the data in the immediate energy side-bands around a mass point of interest, then we should account for the possibility, through $A_{\rm spur}$, of similar background mismodeling at our mass point of interest. Specifically, we implement the following approach. At a given mass point m^m_χ, where m is the index that labels the mass point, we consider the subset of test mass points in a 2 keV window around m^m_χ, masking: (i) a 0.4 keV window in mass around m^m_χ and (ii) masking 0.1 keV windows around the locations are all background lines that were included in the analyses of the annuli. Each test mass point within this side-band window has a best-fit $\sin^2(2\theta)$ from the likelihood analysis without the inclusion of the spurious-signal nuisance parameter. The ensemble of best-fit points in the side-band window is denoted by $\{\sin^2(2\theta)\}_m$. We compute the variance over this ensemble of best-fit points, $\text{Var}\left[\{\sin^2(2\theta)\}_m\right]_{\rm observed}$. The observed variance is then compared to the expected variance $\text{Var}\left[\{\sin^2(2\theta)\}_m\right]_{\rm expected}$, and specifically we set

$$\sigma^2_{\rm spur,m} = \max\left[0, \text{Var}\left[\{\sin^2(2\theta)\}_m\right]_{\rm observed} - \text{Var}\left[\{\sin^2(2\theta)\}_m\right]_{\rm expected}\right] , \tag{B.9}$$

where $\sigma^2_{\rm spur,m}$ denotes the hyperparameter at the mass point m^m_χ. The expected side-band best-fit variance $\text{Var}\left[\{\sin^2(2\theta)\}_m\right]_{\rm expected}$ is computed from 500 MC simulations of the null hypothesis. The null hypothesis model is that given by the fit of the background model to the data without any extra UXL signal components.

We expect $\sigma^2_{\rm spur,m}$ to be non-zero if there is background mismodeling in the energy side-band, which increases the variance of observed best-fit points relative to the expectation under the null hypothesis. However, sometimes $\sigma^2_{\rm spur,m}$ will be non-zero simply because of statistical fluctuations in the observed side-bands, in which case the nuisance parameter will weaken the limits more than intended. However, this occasional weakening of the limits is worth the advantage of having an analysis framework that is more robust to mismodeling. Indeed, we know that there is an opportunity for some degree of background mismodeling because we have chosen to only include background lines that pass some significance threshold, and thus the aggregate effect of the sub-threshold lines could lead to mismodeling that could be partially mitigated by $A_{\rm spur}$.

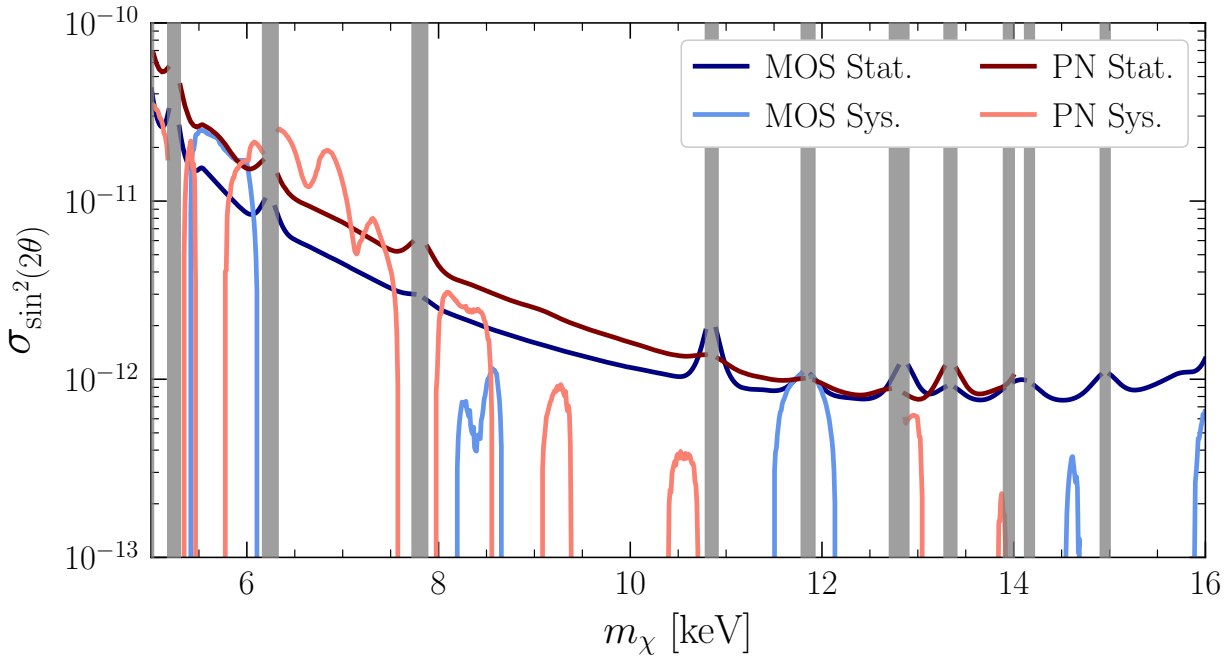

Figure B.3: The spurious-signal hyperparameter $\sigma^2_{\rm spur,m}$ (labeled MOS Sys. and PN Sys.), as computed in (B.9), as a function of the DM mass. For both MOS and PN the nuisance parameter $A_{\rm spur}$ is predominantly active at low energies, and it plays a more significant role in PN than in MOS. We compare the hyperparameter to the statistical uncertainties (labeled MOS Stat. and PN Stat.), which are computed from the Hessian of the log-likelihood (without the spurious-signal) about the best-fit mixing angle at a fixed energy. We note that several of the sharp variations of the expected sensitivity shown in Fig. 3.3 arise as a result of the variations of the spurious signal hyperparameter shown here.

In Fig. B.3 we illustrate the values of $\sigma^2_{\rm spur,m}$ (labeled MOS Syst. and PN Syst.) that we find from the data analyses of the MOS and PN data. We compare the hyperparameter to the statistical uncertainty on $\sin^2(2\theta)$, labeled MOS Stat. and PN Stat. Note that the statistical uncertainties are computed from the Hessian of the log-likelihood, for that data

set, about the best-fit coupling at a fixed UXL energy, without the inclusion of $A_{\rm spur}$. For both MOS and PN we see that the background mismodeling uncertainties, as captured by $A_{\rm spur}$, may dominate the statistical uncertainties at some low energies, though the nuisance parameter appears more important for PN than for MOS.

It is interesting to consider the ensemble of discovery TSs in favor of the DM model across all tested mass points. We denote this distribution of TSs without the spurious-signal by $\mathbf{T}$, while with the inclusion of the spurious-signal nuisance parameter we call this distribution $\mathbf{T}_{\rm sys}$. We expect $\mathbf{T}_{\rm sys}$ to have fewer high-TS points than $\mathbf{T}$. In the left and center panels of Fig. B.4 we illustrate the distributions of TSs for both $\mathbf{T}$ (labeled Data) and $\mathbf{T}_{\rm sys}$ (labeled Data w/ Nuisance Parameter) for MOS and PN, respectively. More specifically, in that figure we illustrate the survival fractions for the distributions, which show the faction of TSs in $\mathbf{T}$ or $\mathbf{T}_{\rm sys}$ with a value above the TS indicated on the x-axis. Asymptotically we expect, up to the caveat that we used the Bayesian marginal likelihood of the GP to define our TSs, that the TSs should be χ^2 distributed [109]. The survival function of the χ^2 distribution is shown in Fig. B.4. We verify with a large number of MC simulations that the that the null-distribution of TSs is indeed χ^2-distributed for both MOS and PN datasets. The results of these tests are labeled "Monte Carlo" in Fig. B.4 and overlap with the χ^2 distribution, providing evidence that we are in the asymptotic regime [109].

Because there are a finite number of samples in $\mathbf{T}$ and locations spaced within the detector energy resolution are correlated, the survival function for the observed data is not expected to follow the χ^2-distribution exactly. The green and gold bands in Fig. B.4 show the 68% and 95% containment regions for the survival fraction computed over 500 MC realizations of $\mathbf{T}$. We expect that the data should fall within these bands if no signal is present, which is analogous to the green and gold bands for the significance in Fig. B.5. In the left and center panels of Fig. B.4 we may see that the distributions of $\mathbf{T}$ for MOS and PN are broadly consistent with the MC expectations. The distributions of $\mathbf{T}_{\rm sys}$, as expected, fall off slightly faster at large values of the TS. The right panel of Fig. B.4 shows the survival fraction for the combined analysis where we combine the MOS and PN profile likelihoods, with and without the spurious-signal. The most significant test point has a significance slightly above 2σ local significance, which is less than 1σ in global significance. Thus, we conclude that there is no evidence for decaying DM in our analysis above our 5σ global predetermined detection threshold.

The effect of the spurious-signal nuisance parameter on the individual MOS and PN limits is illustrated in Fig. B.5. The inclusion of the nuisance parameter slightly decreases the discovery TSs at low masses and also causes a slight weakening of the limits. Note that the expectations under the null hypothesis are indicated for the spurious-signal-corrected

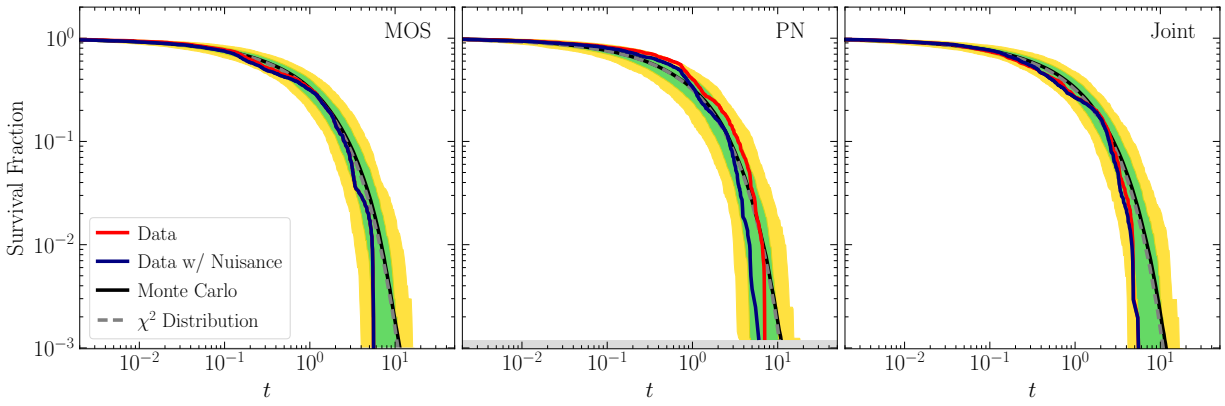

Figure B.4: (Left) The survival function of the test statistic for discovery in the analysis of the MOS data. Under the null hypothesis, and for a large number of samples, the survival fractions are expected to follow the χ^2 distribution, as verified by MC (as labeled). At a finite number of samples the expected chi-square distributions are found from MC to be expected to be contained within the green and gold shaded regions at 68% and 95% confidence, respectively. The negligible effect of the systematic nuisance parameter can be seen by comparing the survival function without the nuisance parameter (red, labelled "Data") and with the nuisance parameter (blue, labeled "Data w/ Nuisance Parameter"). (Center) As in the left panel, but for the PN analysis. (Right) The survival function for the joint analysis of MOS and PN data. In blue, the survival function for the joined PN and MOS analysis without systematic nuisance parameters; in red, the survival function for the joint analysis when the PN and MOS results are corrected by their independently-tuned systematic nuisance parameters prior to joining.

analysis in that figure.

B.2 Extended Results

In this section we present extended results for the analyses that go into producing Fig. 3.3. First, we provide a measure of the goodness-of-fit of our null model to the data, quantified through the χ^2 per degree of freedom (dof), in each annulus for the PN and MOS data sets in Tab. B.3. Note that we also quote the p-value associated with the χ^2 per dof, with smaller numbers indicating a worse null-model fit. We observe acceptable p-values ($p \gtrsim 0.1$) in all rings except for Ring 3 of the PN data set, which realizes a p-value associated with the χ^2/dof of $p \approx 5.7 \times 10^{-6}$. We would not expect to observe a p-value this small in any of the 16 rings. For example, Fig. B.3 shows some evidence for mild systematic uncertainties at low energies in the PN data, though these are captured through our spurious-signal formalism. We also note that there is some indication that the poor χ^2/dof in PN Ring 3 arises from statistical fluctuations on scales much smaller than the detector energy resolution; for example, down-

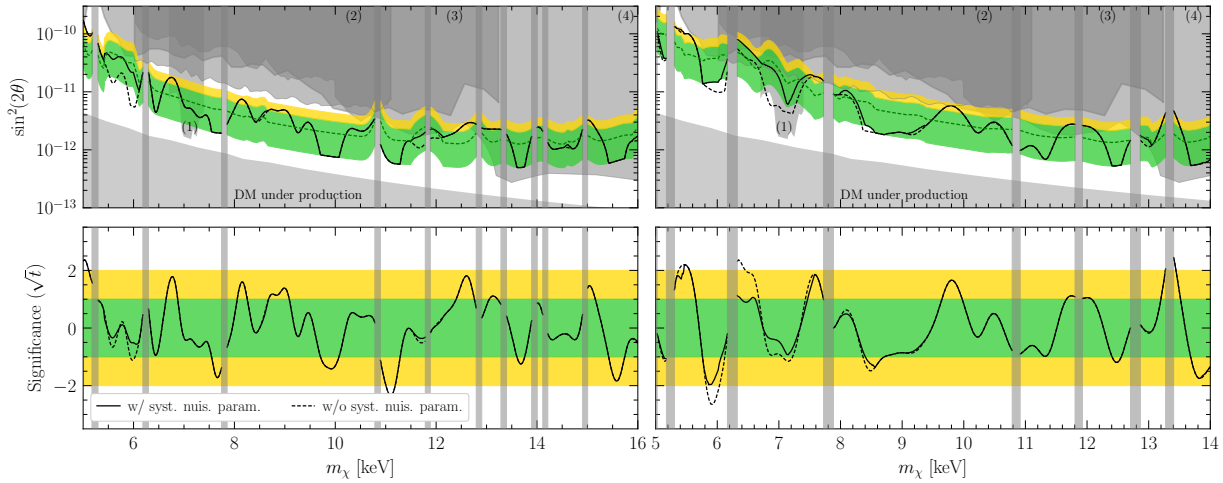

Figure B.5: As in Fig. 3.3, but for the MOS (left panel) and PN (right panel) analyses individually and with and without the spurious-signal nuisance parameter. The 1σ and 2σ expectations are shown only for the case with the spurious-signal nuisance parameter. The limits without the nuisance parameter are slightly stronger at low masses. The sharp variations in the expected sensitivity, especially visible in the PN results, arise from how the spurious-signal hyperparameter is determined through the sliding window procedure.

binning that data set to bins of width 45 eV, which is still smaller by a factor of a few relative to the energy resolution across the full energy range, improves the p-value associated with the χ^2/dof to $p \approx 4 \times 10^{-3}$. As an additional test, we compare the results obtained without the spurious-signal formalism in the joint analysis of the PN data with and without the inclusion of the data in Ring 3. These results are presented in Fig. B.6, and are qualitatively unchanged by the inclusion or exclusion of the PN Ring 3 data set. We also provide best-fit normalizations for our GP kernels, presented in Tab. B.4.

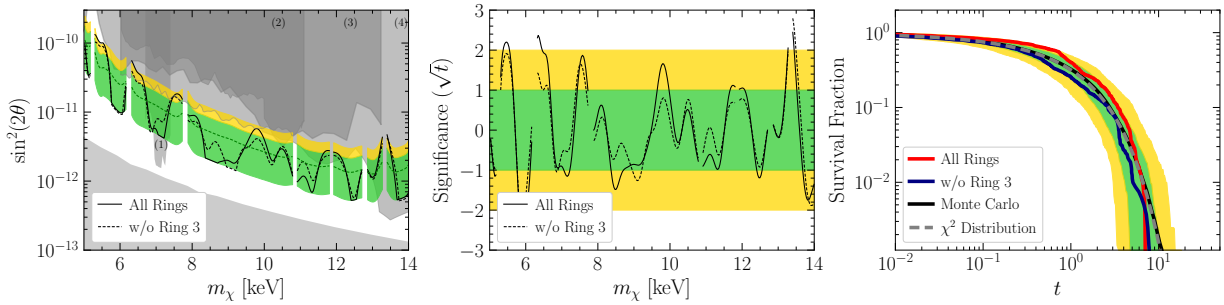

Figure B.6: A comparison of all results obtained in the joint analysis of PN data with and without the inclusion of Ring 3, which may be subject to systematic mismodeling. Note that for this comparison we do not profile over the spurious-signal nuisance parameter.

In Fig. B.7 we present the main result in Fig. 3.3 in terms of the DM lifetime instead of in terms of $\sin^2(2\theta)$. The result in Fig. B.7 is more general than in Fig. 3.3 since it holds

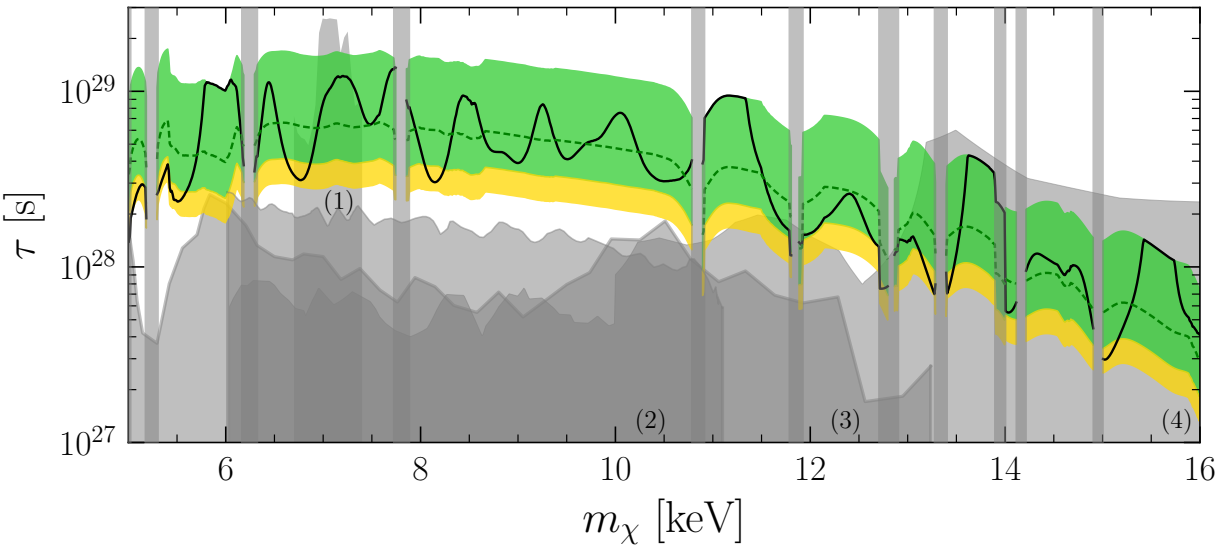

Figure B.7: As in Fig. 3.3, but interpreted as limits on the DM lifetime. This figure applies for DM whose decays produce a single mono-energetic photon at energy $m_\chi/2$. If the DM decay produces two photons (as in an axion model), then the lifetime limits are twice as strong.

for more general DM models beyond the sterile neutrino model. Note, however, that this figure applies to DM whose decays produces one mono-energetic photon at energy $m_\chi/2$. Axion-like models produce two photons during the decay, in which case the limits are twice as strong as those shown in Fig. B.7.

Instrument	Ring 1	Ring 2	Ring 3	Ring 4	Ring 5	Ring 6	Ring 7	Ring 8
MOS	0.19	0.71	0.02	0.34	0.10	0.69	0.59	0.45
PN	0.77	0.89	10^{-5}	0.65	0.34	0.25	0.92	0.68

Table B.3: The goodness-of-fit of the null model fit in each annulus for PN and MOS data sets as measured by the p-value. With the exception of Ring 3 of the PN data set, this measure indicates an acceptable goodness-of-fit to the data under the null (see text for details).

Next, we show our results from the analyses to the individual MOS and PN annuli. In Figs. B.8 through B.15 we show the best-fit fluxes and significances (times the sign of the excess or deficit) for the UXLs for all of the annuli and for both MOS and PN. Note that the shaded grey regions denote the masks that we use to avoid searching for UXLs in the direct vicinity of background lines included in the analyses.

The distribution of discovery TSs that we observe in the individual annuli all appear consistent with expectations from MC, as illustrated in Fig. B.16 for MOS and Fig. B.17 for PN. These figures illustrate the survival fractions of TSs, as in Fig. B.4, but at the

Instrument	Ring 1	Ring 2	Ring 3	Ring 4	Ring 5	Ring 6	Ring 7	Ring 8
MOS	6.9	1.6	1.1	3.4	0.7	1.9	0.9	1.5
PN	23	5.3	5.7	9.1	2.0	4.2	0.2	11

Table B.4: The best fit normalization of the GP kernel for each ring in PN and MOS. We present $\sqrt{A_{\rm GP}}$ in units of 10^{-3} photons/cm^2/s/keV for $A_{\rm GP}$ defined in (B.3).

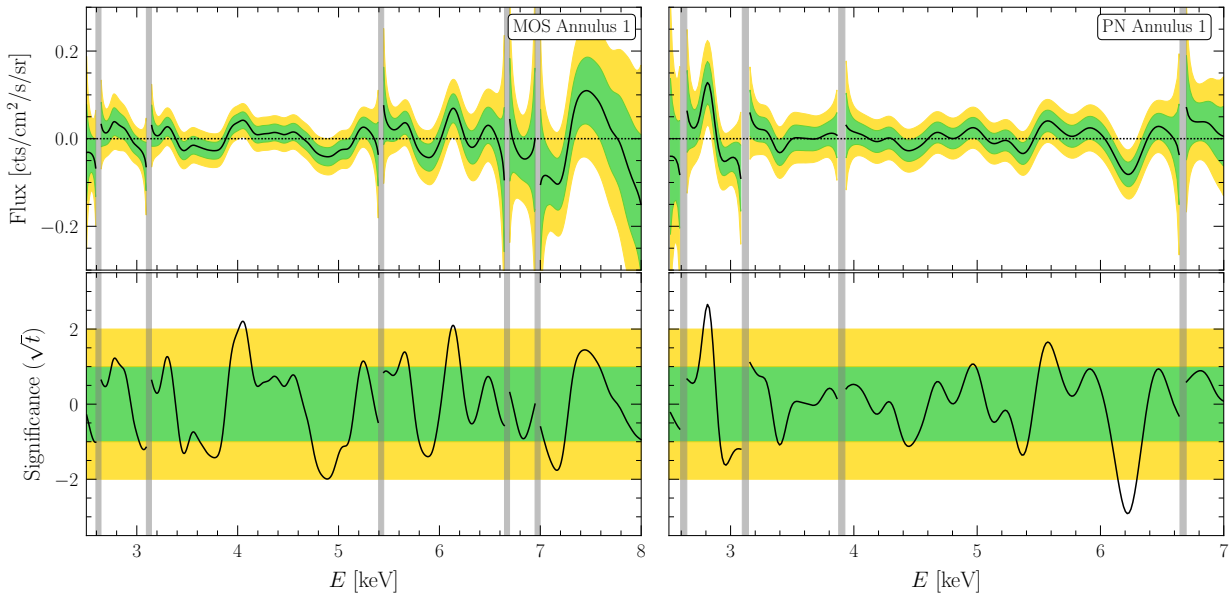

Figure B.8: (Upper Left) The best-fit signal flux, and 1 and 2σ uncertainties, as a function of the central UXL energy across our full energy range for the innermost MOS ring. (Lower Left) The corresponding significance in favor of the signal model, multiplied by the sign of the best fit UXL normalization at that energy, along with the $1/2\sigma$ expectations under the null hypothesis. (Right Panel) As in the left panel but for the innermost PN annulus.

level of the individual annuli instead of the joint analysis. Note that the MC expectations are constructed independently for each annulus and each data set. These results do not include the systematic nuisance parameter since that is only included at the level of the joint likelihood, after combining the results from all of the individual annuli.

B.3 Synthetic signal tests for the fiducial analysis

In this section we verify that our analysis framework has the ability to discover real signals if they are present in the data. We do so by injecting a synthetic signal into the real data and analyzing the hybrid data set with our full analysis. We also demonstrate the full analysis as applied to fully synthetic data generated with varying injected signal strengths.

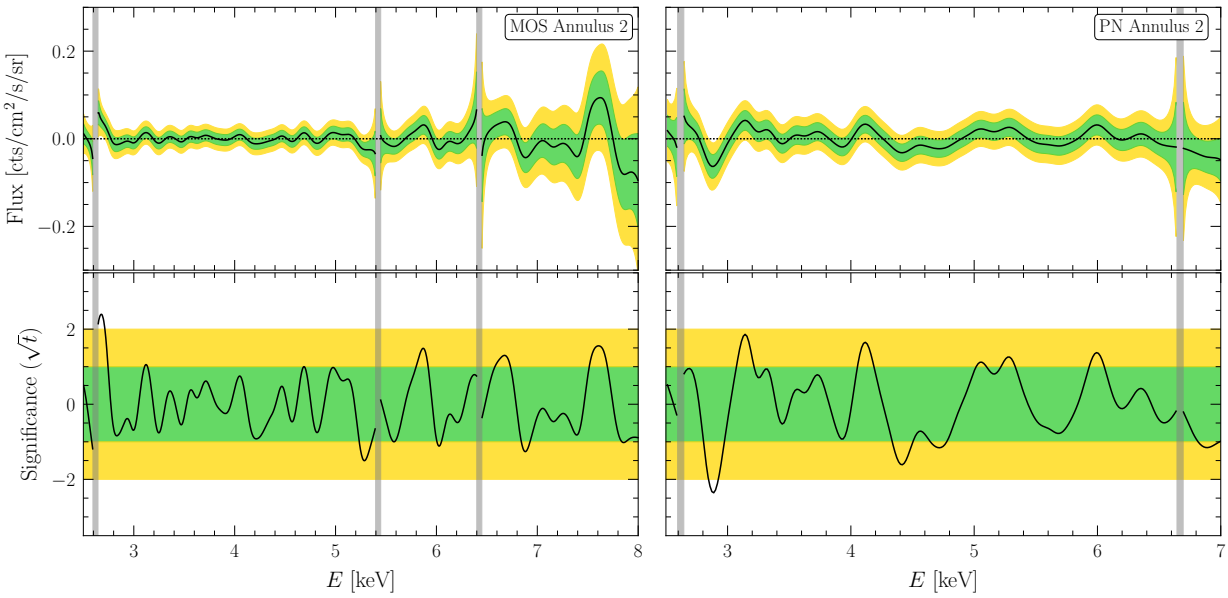

Figure B.9: As in Fig. B.8 but for annulus 2.

B.3.1 Signal injection in real data

For injection tests in the real data, we chose a DM mass $m_\chi = 7.0$ keV and a mixing angle $\sin^2(2\theta) = 2.5 \times 10^{-11}$. We chose this mixing angle because we expect such a signal to be detected at approximately 5σ significance. We forward model this signal through the appropriate MOS and PN detector responses, draw Poisson counts, and then add these counts to the actual data sets. The results of the data analysis of the hybrid data are illustrated in Fig. B.18. In the top panel we show the 95% upper limits for MOS, PN, and the joint analysis, with and without the systematic nuisance parameter. Note that the injected signal is indicated by the red star. The upper limits weaken at the injected signal point, as expected, and do not exclude the injected signal coupling. In the second row we show the corresponding detection significances. The signal is detected at nearly 5σ in MOS alone and at around 2σ in PN. The systematics nuisance parameter slightly reduces the significance of the discovery, but by a minimal amount since we mask a 0.4 keV window around the test mass when determining the systematics nuisance parameter. In the third row we show how the discovery of the injected signal extends the survival function to higher TS values. Lastly, in the bottom row we show the 1, 2, and 3 σ best-fit regions in the m_χ-$\sin^2(2\theta)$ plane for the DM candidate. In red we mark the location of the injected signal, which is recovered appropriately.

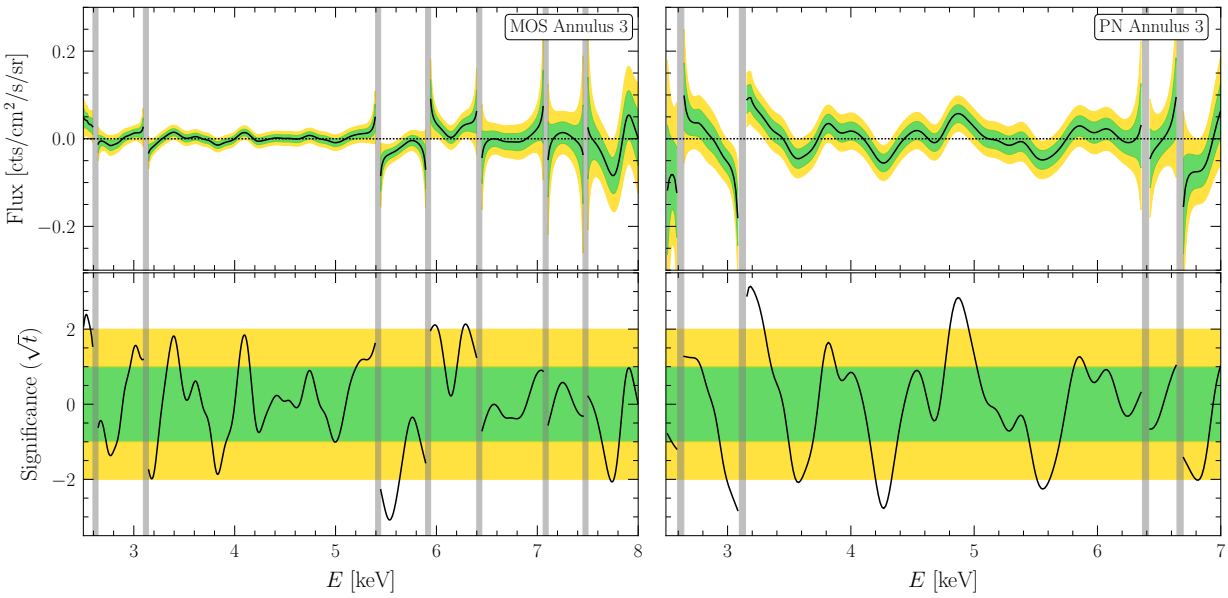

Figure B.10: As in Fig. B.8 but for annulus 3.

B.3.2 Signal injection in synthetic background data

For injection tests on the real data, we first generate synthetic data according to the best-fit null models for each of the eight rings studied in MOS and PN data sets. We then inject a synthetic signal at a specified value of $\sin^2(2\theta)$ on top of the null-model realizations using the same procedure as applied for the signal injection on the real data and repeat our full analysis procedure in search of the injected signal with the exception that we do not apply a nuisance parameter tuning and correction. We perform 1000 independent realizations and analyses for each value of $\sin^2(2\theta$, and we repeat this procedure for 30 values of $\sin^2(2\theta)$ between 10^{-13} and 10^{-10} for two different neutrino masses: 7.0 keV and 11.5 keV. The results of the data analysis of the hybrid data are illustrated in Fig. B.19. In the top row, we show ensemble statistics for the 95% upper limits as a function of injected signal strength for the two neutrino masses studied in this test. In the bottom row, we show the ensemble statistics of the recovered detection test statistic as a function of the injected signal strength. The upper limits weaken with increasing injected signal strength without excluding the true value of the injected signal. Moreover, the detection test statistic smoothly increases as a function of increasing injected signal strength. Critically, at large injected signal strength, the test statistic safely exceeds $TS \approx 30$, which is the approximate threshold for a 5σ detection after correcting for the look-elsewhere effect.

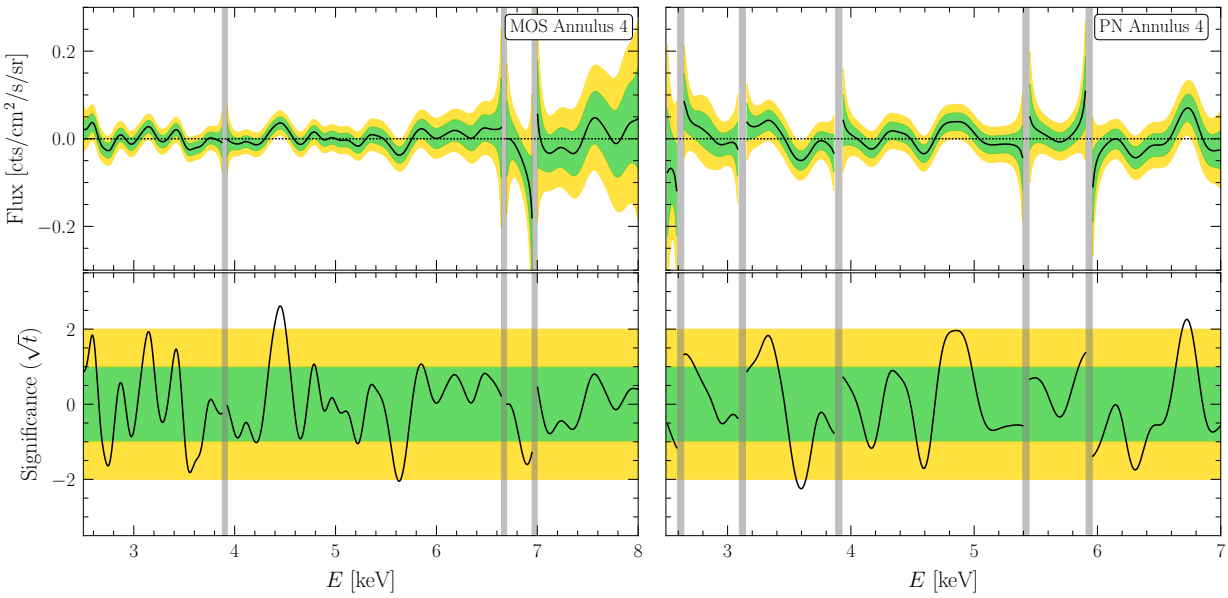

Figure B.11: As in Fig. B.8 but for annulus 4.

B.4 Systematic Analysis Variations

Our fiducial result, which is illustrated in Fig. 3.3, made a number of physics-level and analysis-level choices. These choices are justified in the main chapter and the supplementary results of the proceeding sections of this chapter. Still, it is worthwhile to consider how our results change for different physics and analysis assumptions and choices, as this gives an indication of the robustness of the limits and significances shown in Fig. 3.3.

B.4.1 Alternate DM Density Profiles

In the main chapter, and in particular in Fig. 3.3, we adopted the conservative DM profile that was shown in Fig. 3.1. As already described, the present expectation is that in the absence of baryons, the DM halo is well described by an NFW profile. Baryons are then expected to contract this profile, increasing the DM density towards the GC, and potentially also introducing a core on top of this. For our fiducial analysis we conservatively assumed an uncontracted NFW halo, using the most conservative parameters determined within the 68% best fit region of [61]. In particular, we used an NFW profile with $r_s = 19.1$ kpc and normalized to a local DM density of $\rho_{\rm DM} = 0.29$ GeV/cm^3.

In Fig. B.20, we show our main results if instead we repeat the analysis for the best fit NFW profile determined in Ref. [61], which corresponds to $r_s = 15.6$ kpc and $\rho_{\rm DM} = 0.31$ GeV/cm^3, as well as showing results for the more realistic contracted profile. There is not a parametric form for the contracted profile, however, Ref. [61] provides a best fit model

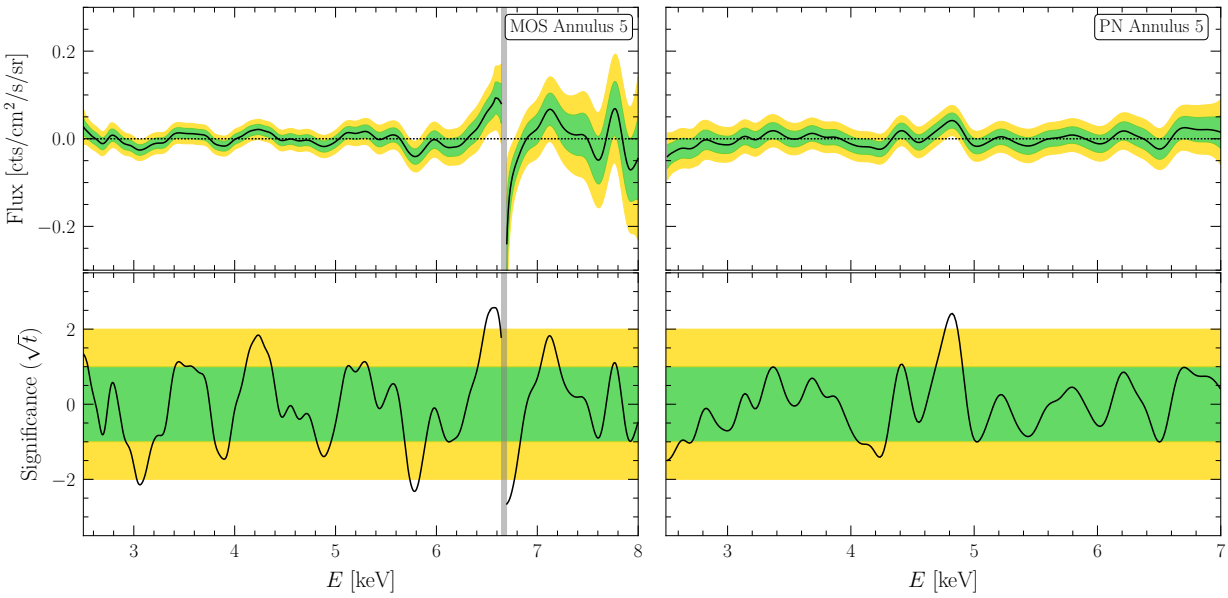

Figure B.12: As in Fig. B.8 but for annulus 5.

for the DM mass distribution, which we use to infer the density and then D-factor. The model only provides an estimate down to 1 kpc from the GC, within which we conservatively assume the density profile is completely cored.

As the figure demonstrates, adopting a more realistic contracted DM profile strengthens our limits by roughly a factor of 2. Importantly, however, changing the profile does not appreciably change the distribution of significance, and we continue to see no clear evidence for an UXL.

B.4.2 Dependence on the GP model

For our fiducial analysis we use the GP kernel given in (B.3) with the choice $\sigma_E = 0.3$. This choice was made so that the residual background model has the ability to adjust on scales around one order of magnitude larger in scale than the energy resolution of the detectors, which are $\delta E/E \sim 0.03$. In this section we verify that our results do not depend in detail upon the particular value chosen.

First, we consider a small modification to our default analysis by taking $\sigma_E = 0.2$ and $\sigma_E = 0.4$. The results of these analyses are shown in Figs. B.21 and B.22. As a further modification of our GP modeling procedure, we repeat our analysis with the relative scale of our kernel promoted to a nuisance parameter that we independently profile in each annulus in both instruments between the range of 0.15 and 0.9. We report the resulting best-fit GP scales in Tab. B.5. Results for this analysis are shown in Fig. B.23. In those figures we show

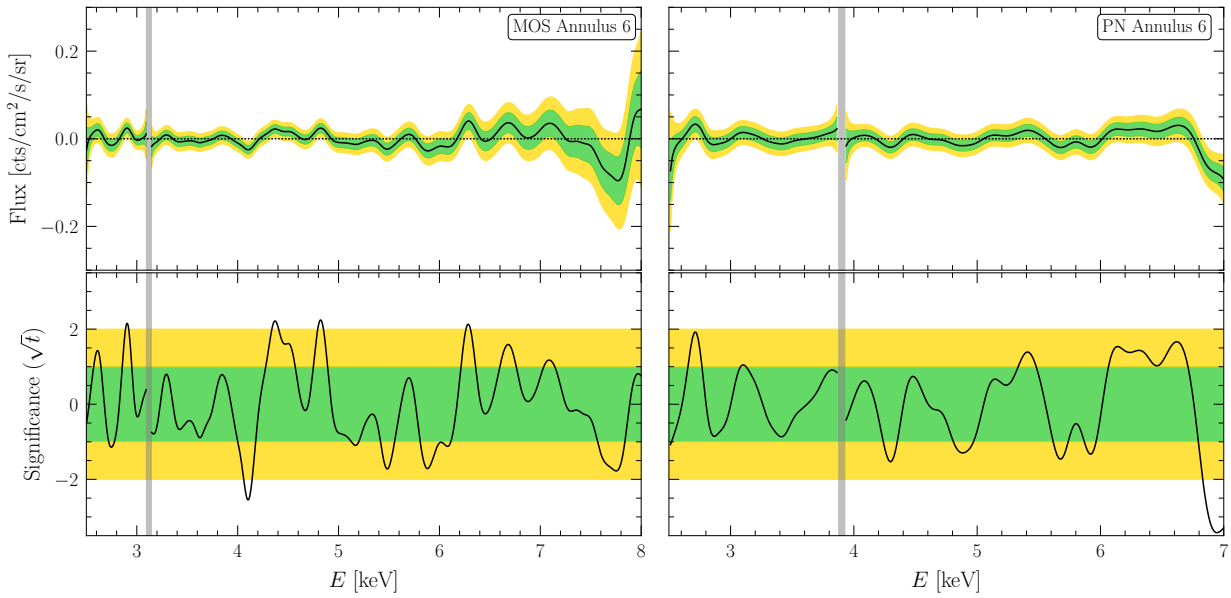

Figure B.13: As in Fig. B.8 but for annulus 6.

the 95% upper limits (upper panel), significances (middle panel), and survival fraction of significances (bottom panel). We give the results both with an without nuisance parameters. There is a slight trend where increasing σ_E leads to a corresponding strengthening of the sensitivity, though this difference is minor compared to other choices in the analysis. In general, the results appear robust to the choice of σ_E.

Instruments	Ring 1	Ring 2	Ring 3	Ring 4	Ring 5	Ring 6	Ring 7	Ring 8
MOS	0.60	0.90	0.90	0.34	0.81	0.90	0.42	0.90
PN	0.77	0.84	0.59	0.90	0.66	0.28	0.90	0.54

Table B.5: The best-fit scale σ_E, determined under the null model, when this scale is treated as profiled nuisance parameter. In all cases except Ring 6 of PN data, the best-fit scale is larger than the scale of the kernel used in our fiducial analysis, indicating that our fiducial choice of $\sigma_E = 0.3$ was conservative and endowed the GP model with sufficient flexibility.

Next, we consider changing the GP modeling more significantly by adopting an alternate kernel. In particular, we consider the standard (and stationary) double exponential kernel

$$K(E, E') = A_{\mathrm{GP}} \exp\left[-\frac{(E - E')^2}{2\sigma^2}\right], \tag{B.10}$$

which has the hyperparameter σ^2. Note that our fiducial kernel, given in (B.3), has the property whereby the correlation length increases with the energy resolution of the detector. The kernel in (B.10), on the other hand, has a fixed correlation length as a function of energy.

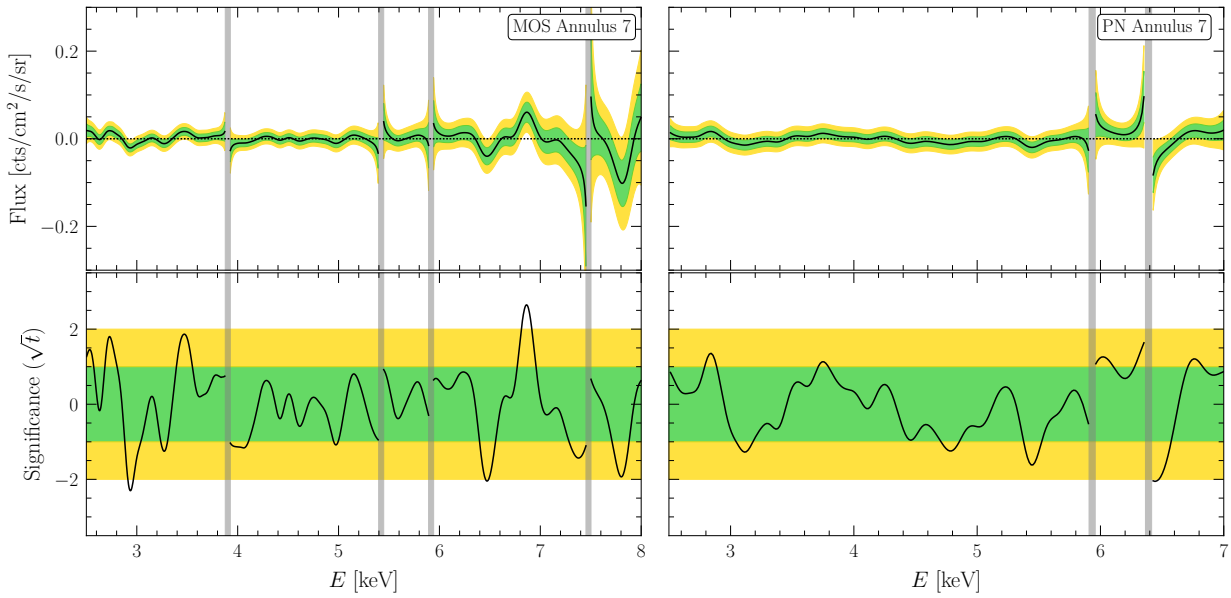

Figure B.14: As in Fig. B.8 but for annulus 7.

In Figs. B.24 and B.25 we show the results of using the double exponential kernel with scale length $\sigma^2 = 0.5$ keV^2 and $\sigma^2 = 1.0$ keV^2, respectively. As with our fiducial kernel, in this case we also find that increasing σ slightly increases the limits. However, the differences between the double-exponential kernel results and our fiducial results are minor and most evident at high DM masses, m_χ, where the two kernels predict the largest differences. In particular, we find no evidence for decaying DM with the alternate kernels and similar 95% upper limits. The systematic uncertainty associated with this choice is generally less than other aspects of the analysis such as our assumptions regarding the DM density profile.

A full comparison of the limits obtained under all the described GP kernel modeling choices is presented in Fig. B.26. The choice of GP kernel and treatment of its scale as a fixed or profiled parameter is shown to have a marginal impact on our limit-setting procedure.

B.4.3 Unmodeled lines in the vicinity of 3.5 keV

Our results have a significant impact on the decaying DM interpretation of the previously-observed 3.5 keV line from nearby galaxies and galaxy clusters [88–90, 93, 95]. Ref. [111] used a similar method to that presented in this chapter to argue that the non-observation of the UXL in *XMM-Newton* BSOs excluded the decaying DM origin of the 3.5 keV line. However, subsequent works [550, 551] questioned the validity of the results in [111] for three primary reasons: (i) the use of a narrow energy range, (ii) the possible importance of instrumental or astrophysical lines in the analysis region, (iii) the D-factor profile chosen with a local DM

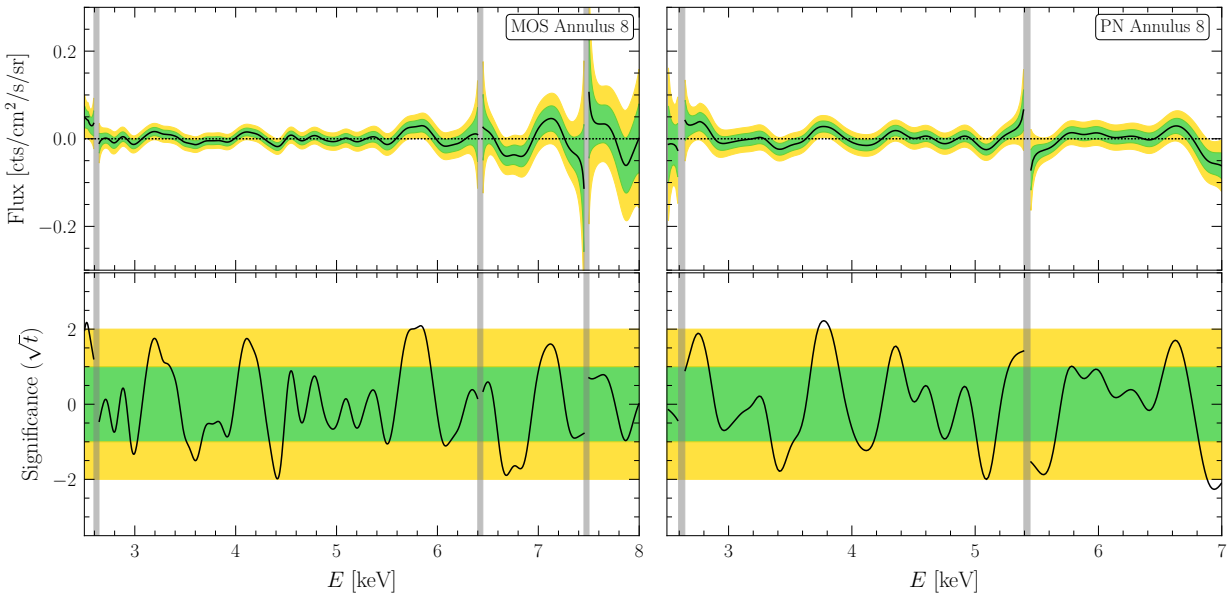

Figure B.15: As in Fig. B.8 but for annulus 8.

density of 0.4 GeV/cm^3. These points were addressed extensively in the response [112], and we do not review the arguments here for how these points are addressed within the context of the analysis in [111].

Here we point out that the analysis in this chapter provides a probe of the decaying DM origin of the 3.5 keV line that is more robust to systematic uncertainties than [111] and that the null results from this chapter strongly disfavor the decaying DM interpretation of the 3.5 keV line. Ref. [111] performed a similar analysis to this work, but the analysis focused on the limited mass range from 6.7 to 7.4 keV. As in this chapter [111] used *XMM-Newton* blank sky data, with a comparable exposure time within the signal ROI to that in this chapter. As mentioned in the main chapter, Ref. [111] used a joint likelihood over individual exposures, as opposed to this chapter where we stack the data in rings and construct the joint likelihood in individual rings. Use of the ringed data facilitates our background subtraction and GP modeling procedures, in part because the number of counts in each ring is large enough that we may make the Gaussian approximation to the Poisson likelihood. This chapter also performs a more systematic accounting of astrophysical and instrumental lines that are not fully removed by the background subtraction process. Because we analyze a wide energy range in this analysis, we are able to use energy side-bands to determine the hyperparameter for the spurious-signal contribution to the likelihood, which accounts for residual mismodeling. Thus while the limit presented in this chapter in Fig. 3.3 is slightly weaker than the fiducial limit from [111], it is more robust to mismodeling. Furthermore, we use a more conservative D-factor profile in this chapter, though astrophysical uncertainties

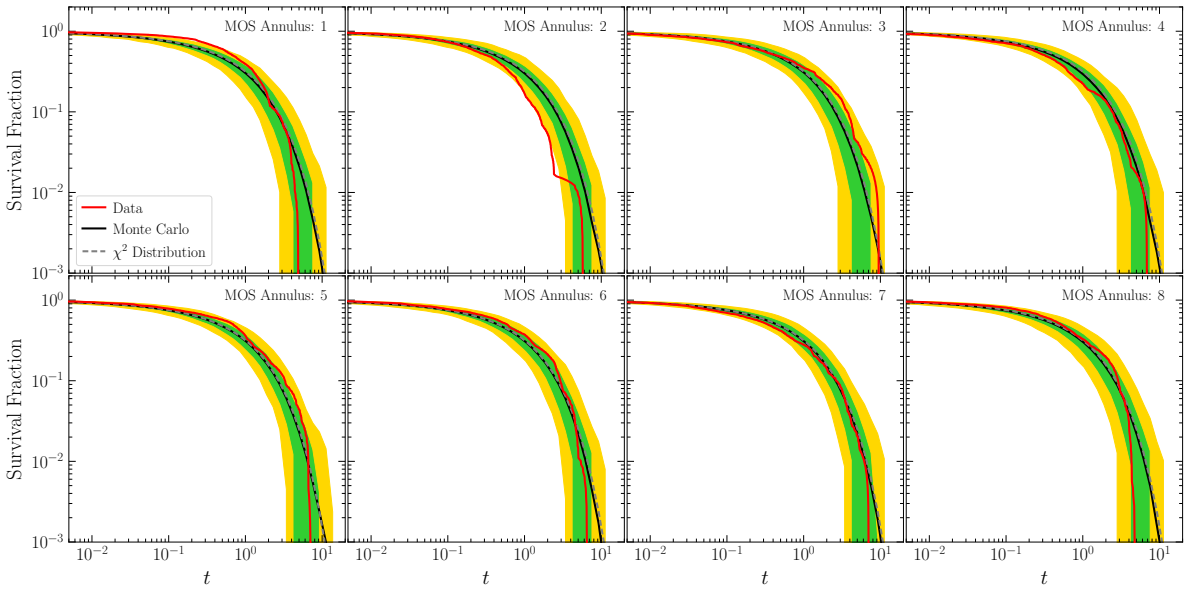

Figure B.16: As in Fig. B.4 but for the individual MOS annuli. Note that the systematic nuisance parameter has not been applied since that is only incorporated in the joint likelihood that combines the results from the individual annuli.

on the DM density profile are not sufficiently large to explain why a decaying DM signal would have appeared in nearby galaxies and clusters but not in this chapter (see [112] for a discussion of this point).

Still, in this section we investigate the potential for mismodeling in the vicinity of 3.5 keV. In particular, [60] argued that lines may be present near 3.32 and 3.68 keV in both the MOS and PN data. Note that in [111] these possible lines were tested for and their inclusion did not change the central conclusion of that work. Moreover, there is no robust evidence to-date for these lines in the MOS and PN data sets. For completeness, however, we investigate how the inclusion of these lines affects the results of the analysis in this chapter. Importantly, following our normal line-dropping procedure neither the 3.32 nor the 3.68 keV lines meet our criterion for inclusion in any of the rings for either MOS or PN. This itself serves as evidence for the non-importance of these line candidates on our conclusions. However, as a systematic test we perform an analysis where we include these two lines in all of our rings for both MOS and PN, while performing the normal line-dropping procedure for the rest of the background lines. We treat the amplitude of these lines as a nuisance parameter which is allowed to take arbitrarily large positive or negative values.

A summary of the full results of the analysis which includes these additional lines is provided in Fig. B.27. No new detections are made. The limits obtained by this analysis in the 6-8 keV range are compared with the results obtained in our fiducial analysis in Fig. B.28, which reveals small but unimportant changes in our limits.

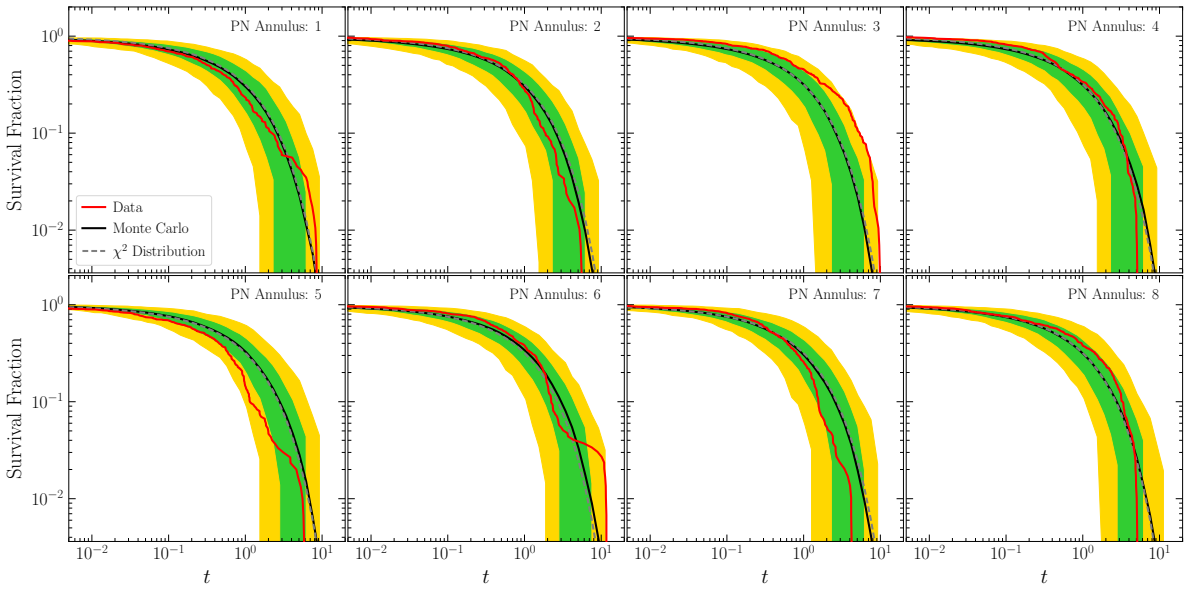

Figure B.17: As in Fig. B.16 but for the PN data sets.

B.4.4 Analysis of Fully Stacked Data

In the main chapter, we divided our signal ROI into rings and modeled the flux independently in each ring. The motivation behind this choice was to incorporate spatial information into the analysis, particularly as we expect the flux of an actual DM decay signal to steadily increase towards the GC. Here we show the results of an alternative approach where instead of modeling the data ring-by-ring, we instead combine the data in the innermost three rings of the signal ROI and model that directly. We effectively are then left with a single combined ring, which we analyze using our fiducial procedure.

In Fig. B.29 we show the resulting limit in the case where we also subtract the background-ROI flux from the stacked signal region data. While there are small differences, the resulting sensitivity and limits from this simpler approach are in good qualitative agreement to those of our default analysis. In detail, the result here are slightly weaker, which is as expected because there is less information in the signal ROI (we use fewer rings and by stacking the spatial information is partially erased).

Next, in Fig. B.30 we repeat this procedure but without subtracting the background flux. The differences are now more noticeable - the expected and resulting limit undergoes larger fluctuations and there are several mildly significant excesses. This emphasizes the importance of the background subtraction procedure in simplifying the data, particularly around bright instrumental lines.

B.4.5 Parametric Modeling without Background Subtraction

In this section, we detail an alternate analysis to the one presented in the main chapter and provide a comparison between the fiducial and alternate analysis in a representative example over the 8-9 keV mass range. The alternate framework uses the same data as used in our primary analysis. However, a more traditional approach is adopted for the background modeling. Firstly, we consider the unsubstracted data in each ring within the signal ROI. The flux within each annulus is then modeled as follows. The background and putative signal lines are treated identically to our fiducial approach, but the smooth background contribution is modeled parametrically using an unfolded second order polynomial, rather than with a GP model. The three parameters that define the quadratic background component are treated as nuisance parameters and profiled over. As the quadratic background has less freedom than the GP model, we restrict to a smaller energy range. Specifically, we determine the energy range by fitting a Gaussian to the detector response at a given putative signal energy, and we define our energy range to extend 5 standard deviations out from the signal energy in either direction. In the 8-9 keV DM mass range, this corresponds to an approximate energy range of 0.60 keV. Furthermore, background lines within 7 standard deviations of the signal energy are included in the model. Thus, in the 8-9 keV mass range, the only line included is the 4.52 keV instrumental line for all PN annuli. We do not include the systematic nuisance parameter modeling for this example.

While our background modeling is significantly different in this case, we find again that our results are qualitatively unchanged compared to our fiducial analysis. To provide a representative example, in Fig. B.31 we show the comparison between our fiducial analysis (without the systematics nuisance parameter to facilitate the comparison) and this alternate approach over the mass range 8-9 keV. As can be seen, the expected sensitivity of the two approaches is almost identical. This is a significant further demonstration that our specific choice of background model is not underpinning our sensitivity.

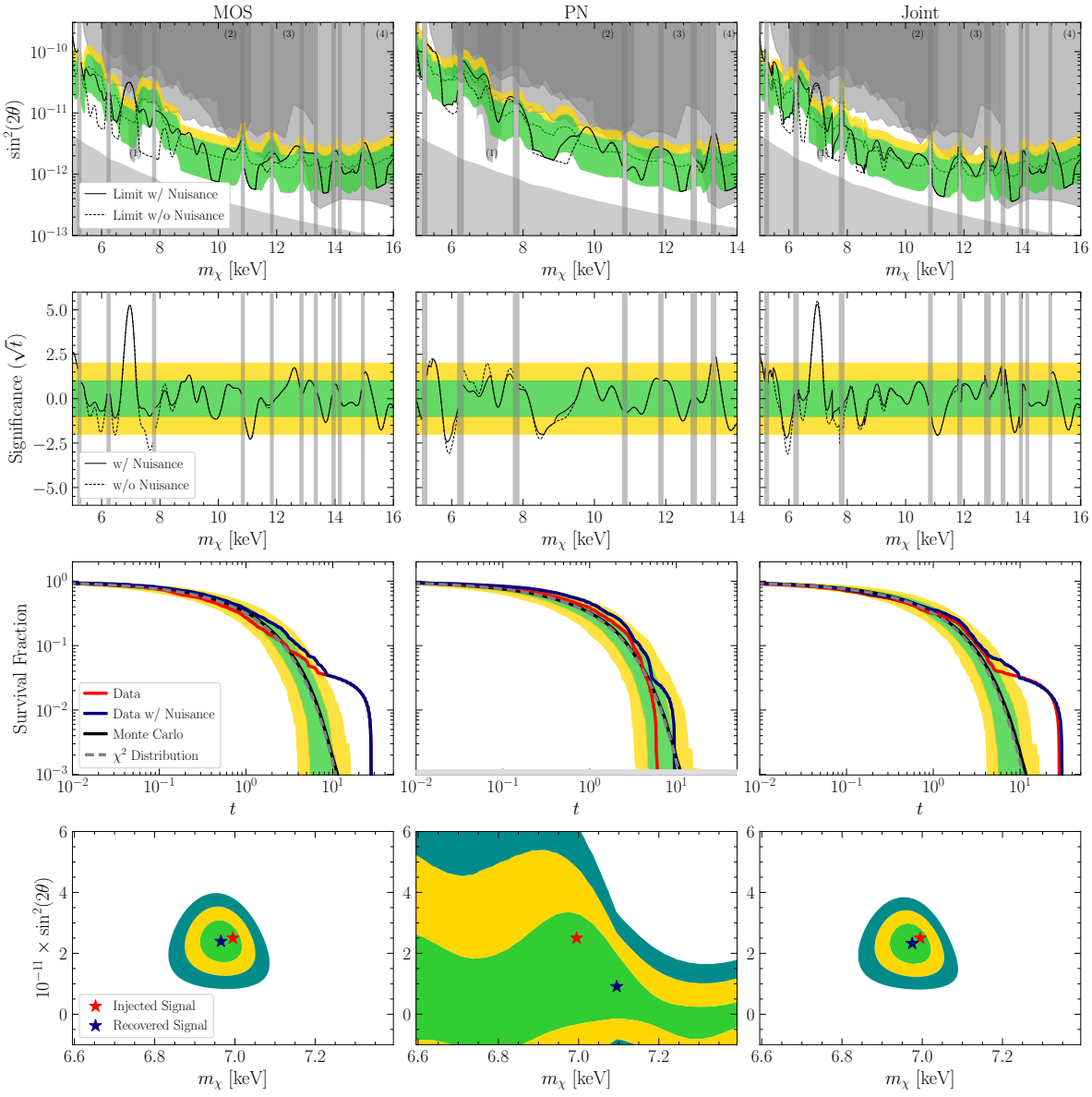

Figure B.18: The results of the analysis of the hybrid data that consists of the real MOS and PN data plus a synthetic DM signal. The DM signal is generated with mass $m_\chi = 7.0$ keV and mixing angle $\sin^2(2\theta) = 2.5 \times 10^{-11}$ as described in the text. The top, middle, and third rows are analogous to Figs. B.4 and B.5, but for the hybrid data set. The last row shows the 1, 2, and 3 σ recovered parameter space for the signal in the mass and mixing angle plane. The best-fit recovered signal is indicated in dark blue, while the red star denotes the true value injected. The synthetic signal is appropriately recovered, adding confidence that our analysis procedure has the ability to detect real DM signals if present in the data.

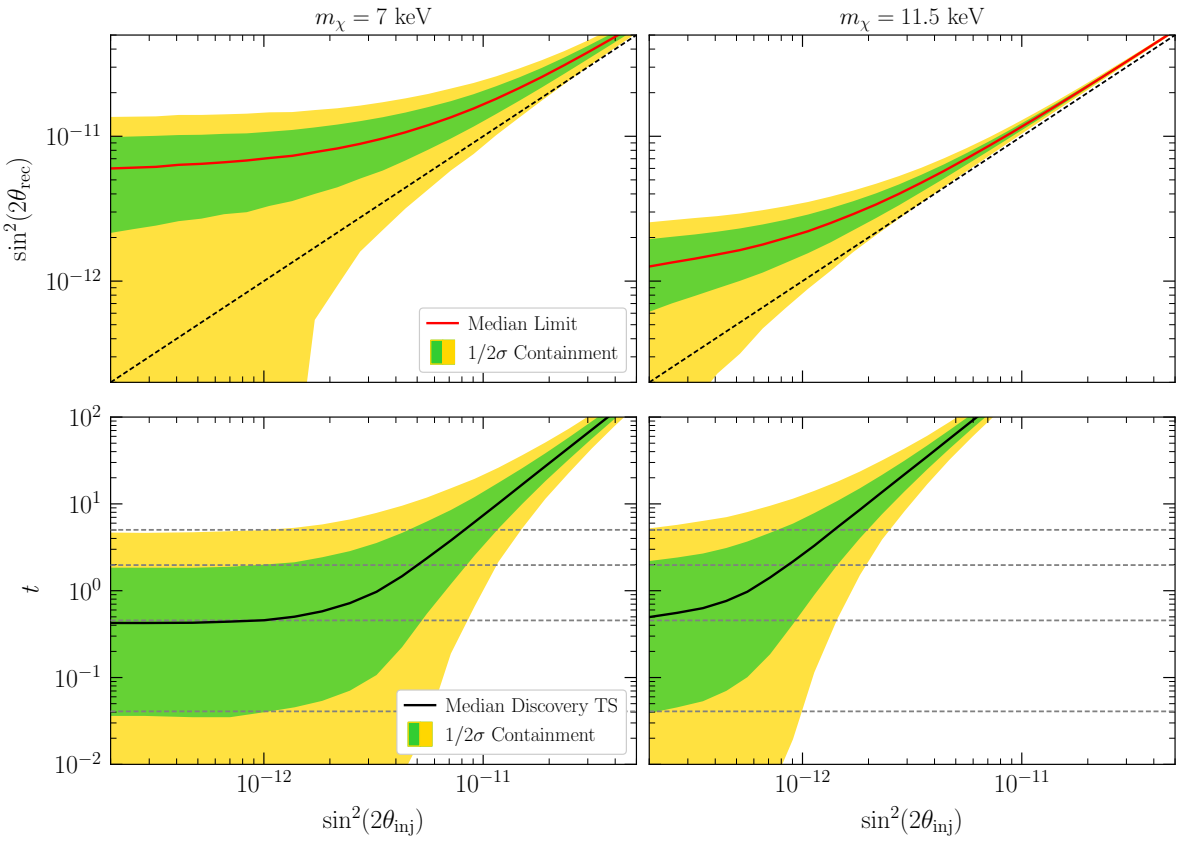

Figure B.19: (*Top Row*) In red, the median 95$^{\rm th}$ percentile upper limit on the recovered signal as a function of the injection signal strength at two neutrino masses evaluated on synthetic data. We additionally indicate the 1 and 2σ containment intervals for the ensemble of upper limits realized at each injected signal strength. Note that these upper limits are not power constrained. These results demonstrate that our analysis framework places robust upper limits that do not rule out an injected signal. (*Bottom Row*) In black, the median recovered detection test statistic for a signal injected in the synthetic data as a function of the injected signal strength, with the 1 and 2σ containment intervals also indicated. Under the null hypothesis, the detection test statistic should follow a χ^2-distribution; the median and 1σ and 2σ percentile values of the χ^2-distribution are indicated by dashed grey lines. These results demonstrate that our detection test statistic follows its theoretically expected distribution under the null hypothesis ($\sin^2(2\theta_{\rm inj}) = 0$) and that our analysis framework can robustly identify a signal which is present in the data. The results are smoothed with a Savitzky–Golay filter for clarity.

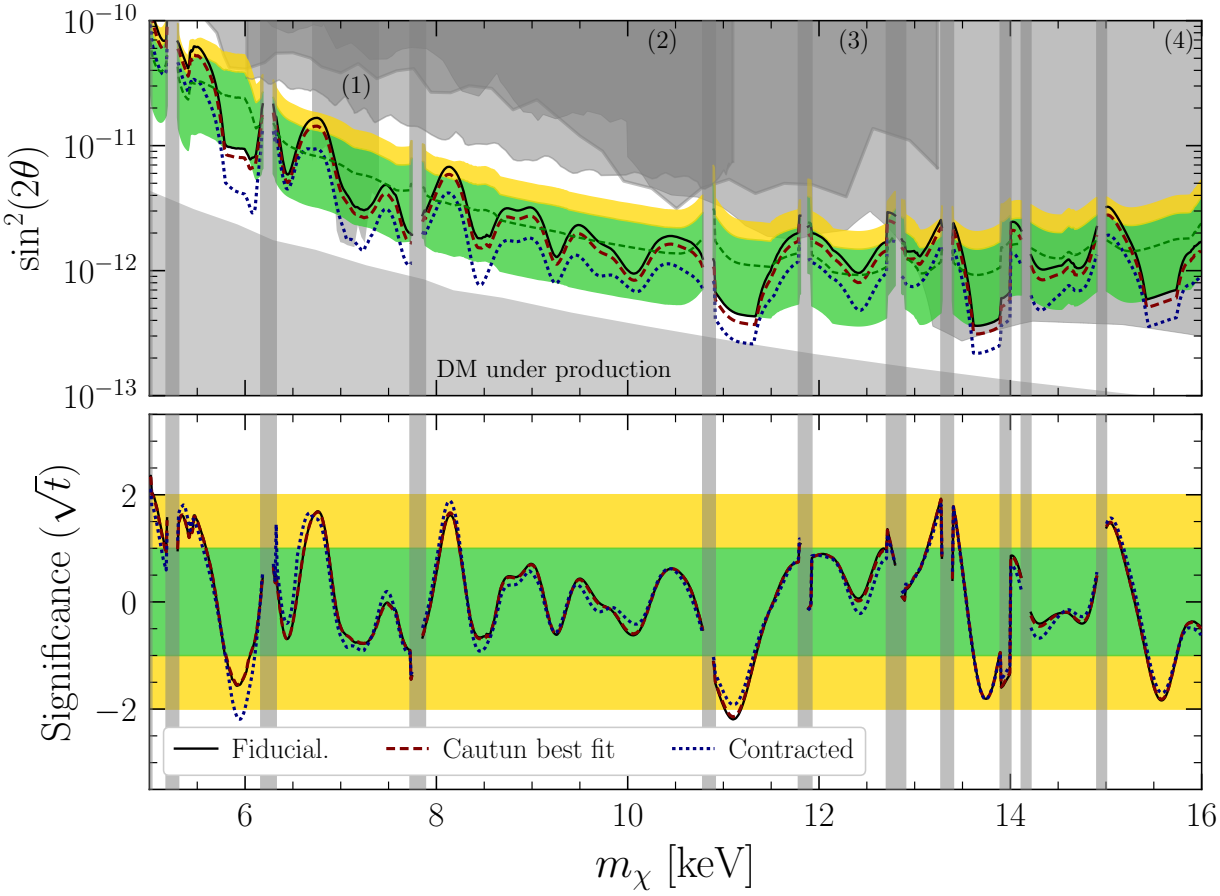

Figure B.20: As in Fig. 3.3, but for three different DM density profiles, all based upon Ref. [61]. In solid curve we show our fiducial results, corresponding to the uncontracted NFW profile with a conservative density. The dashed curve then shows our results using the best fit NFW profile, whereas in dashed we show the stronger limits that would be obtained with a contracted DM distribution. Details of the distributions are provided in the text.

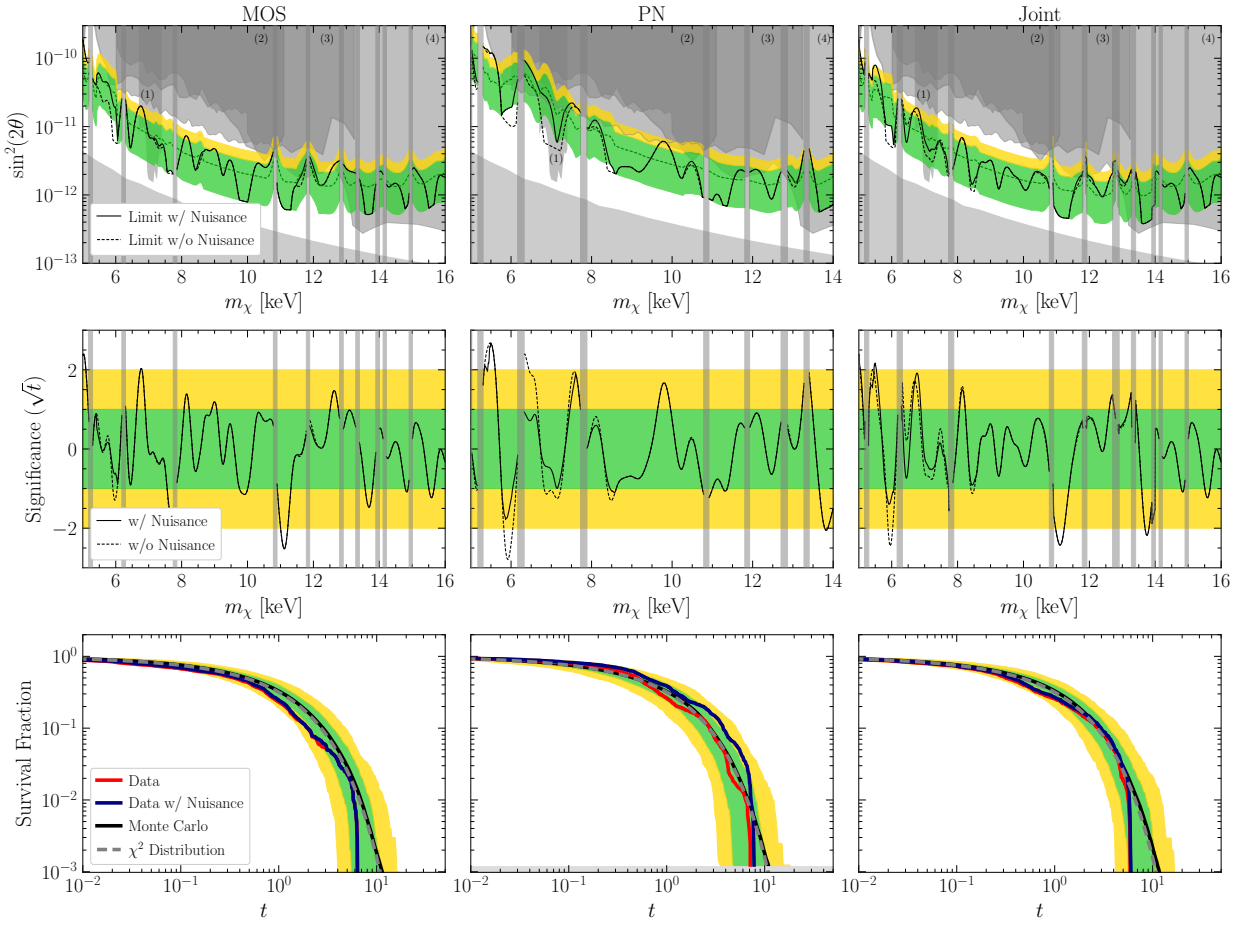

Figure B.21: The analogues of Figs. B.4 and B.5, but changing the kernel correlation length to $\sigma_E = 0.2$ (c.f. our fiducial value of $\sigma_E = 0.3$). The differences between the $\sigma_E = 0.2$ and 0.3 results are minor.

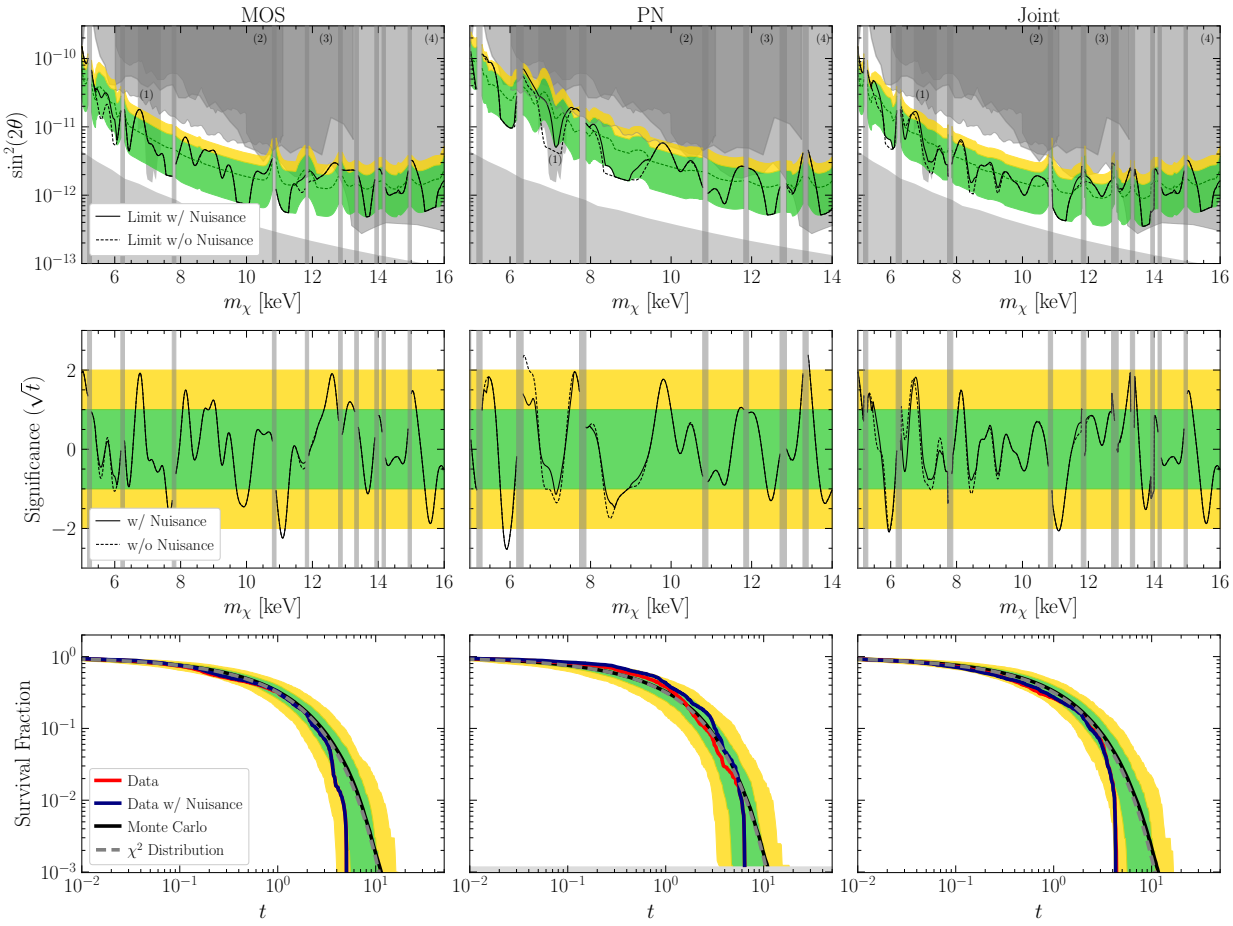

Figure B.22: As in Fig. B.21 but with $\sigma_E = 0.4$. The limit is slightly strengthened, although again the differences are not significant.

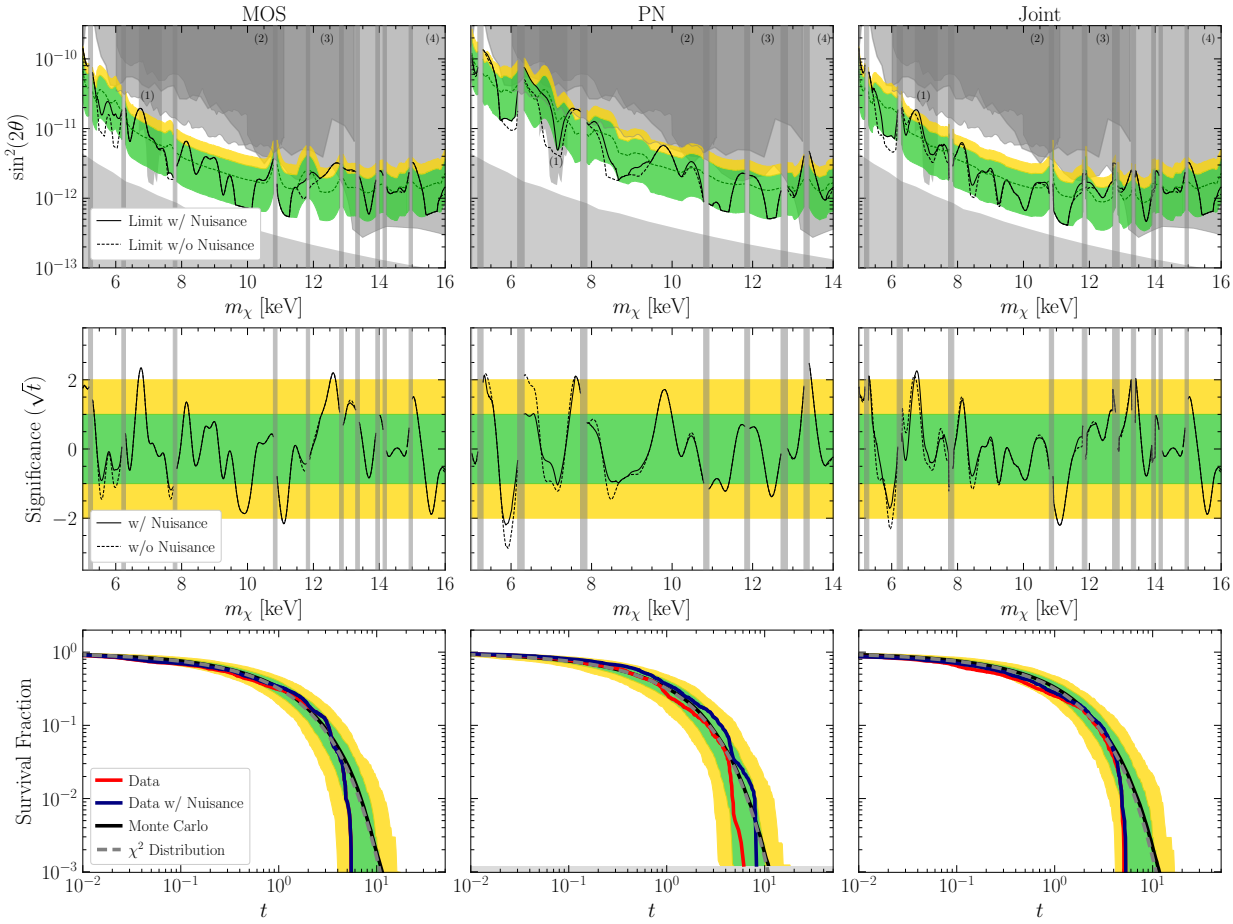

Figure B.23: As in Fig. B.21 but with σ_E treated as a profiled nuisance parameter. The results demonstrate that even providing our background model this additional freedom does not have a significant impact on the limit.

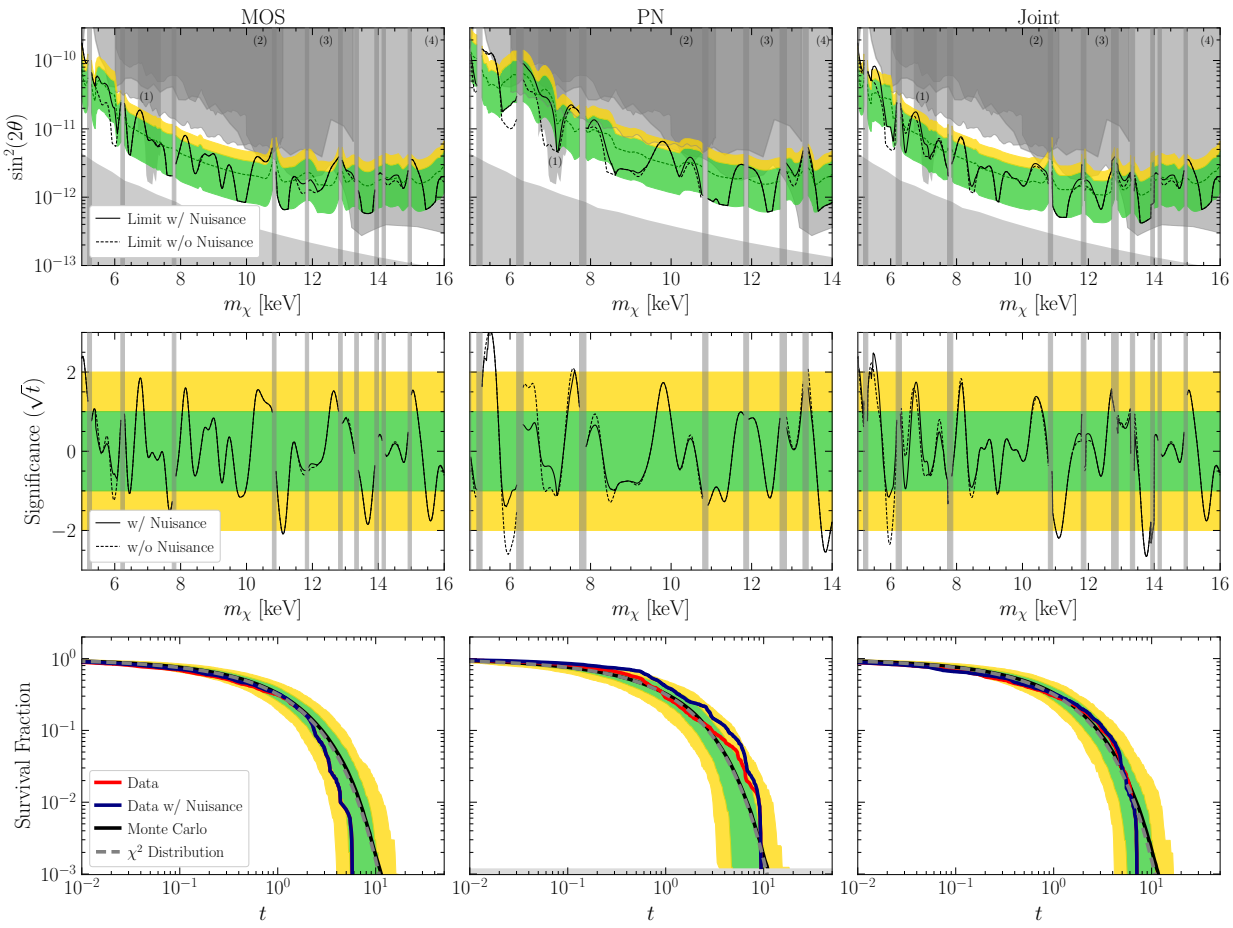

Figure B.24: As in Fig. B.21 but with the alternate GP kernel, in (B.10), with $\sigma^2 = 0.5$ keV^2.

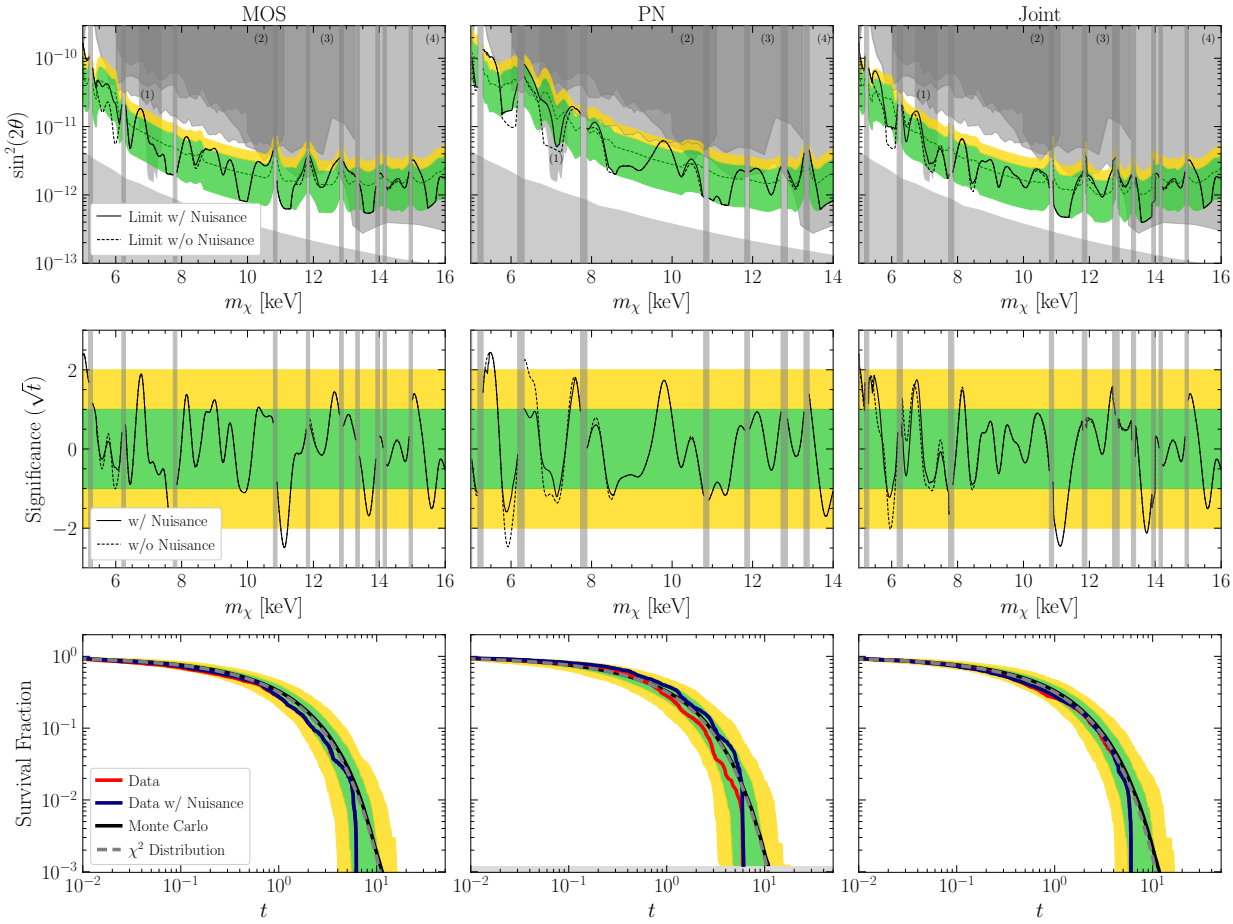

Figure B.25: As in Fig. B.24 but with $\sigma^2 = 1.0$ keV^2. Adopting a large scale length again slightly strengthens the limits, although again the systematic variation of our results with the kernel is relatively small.

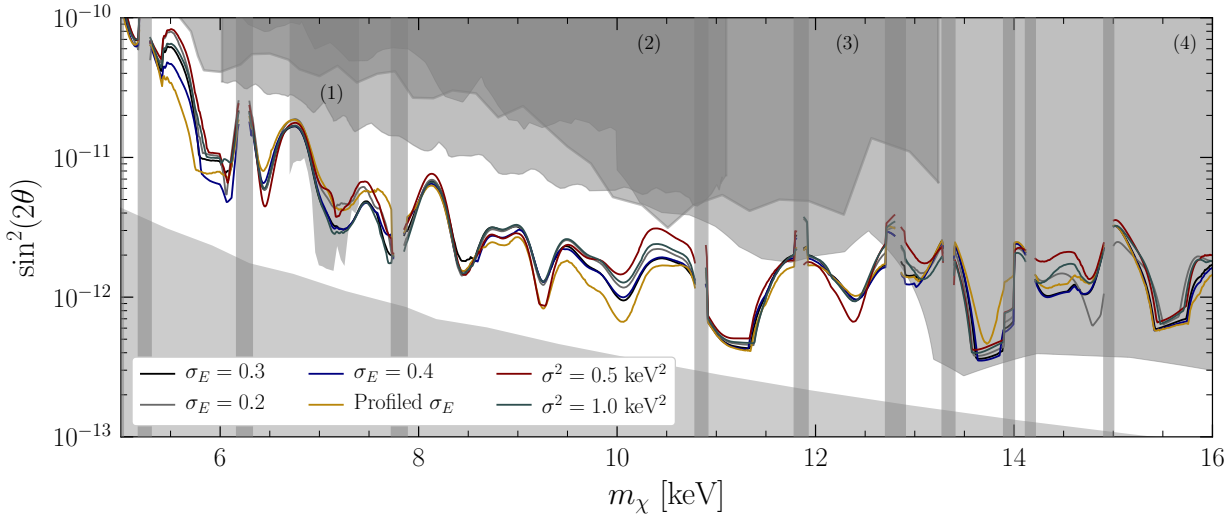

Figure B.26: A comparison of the limits obtained across the full mass range for each variation of the GP correlation-length hyperparameter considered. In particular we show results for variations of the relative-scale and fixed-scale kernels (denoted σ_E and σ^2 respectively), as well as the relative-scale kernel where the scale profiled independently in each annulus.

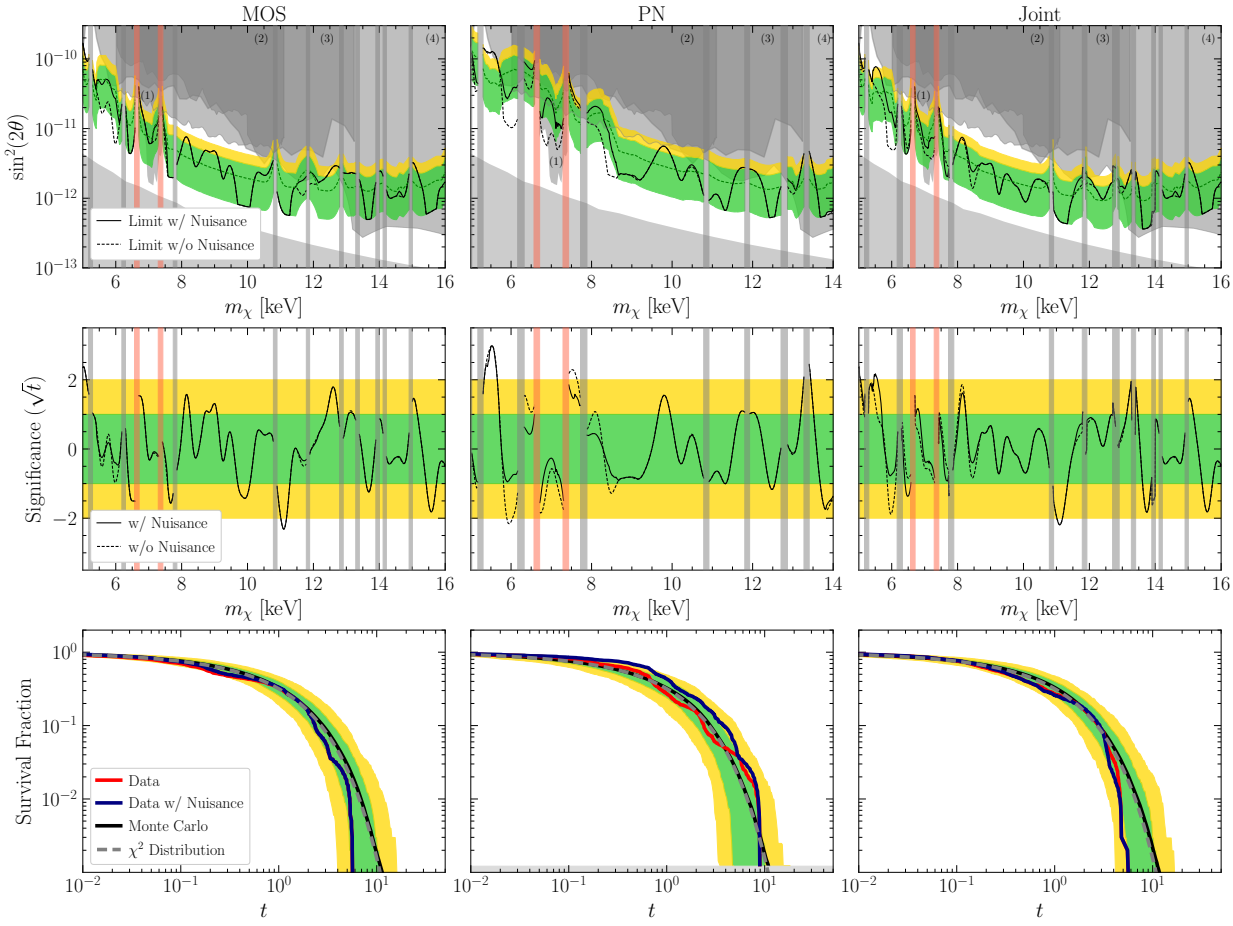

Figure B.27: As in Fig. B.21, but with the fiducial GP kernel at $\sigma_E = 0.3$ and the inclusion of 3.32 and 3.68 keV lines in all analyzed annuli. The newly masked region associated with these two lines is highlighted in light red.

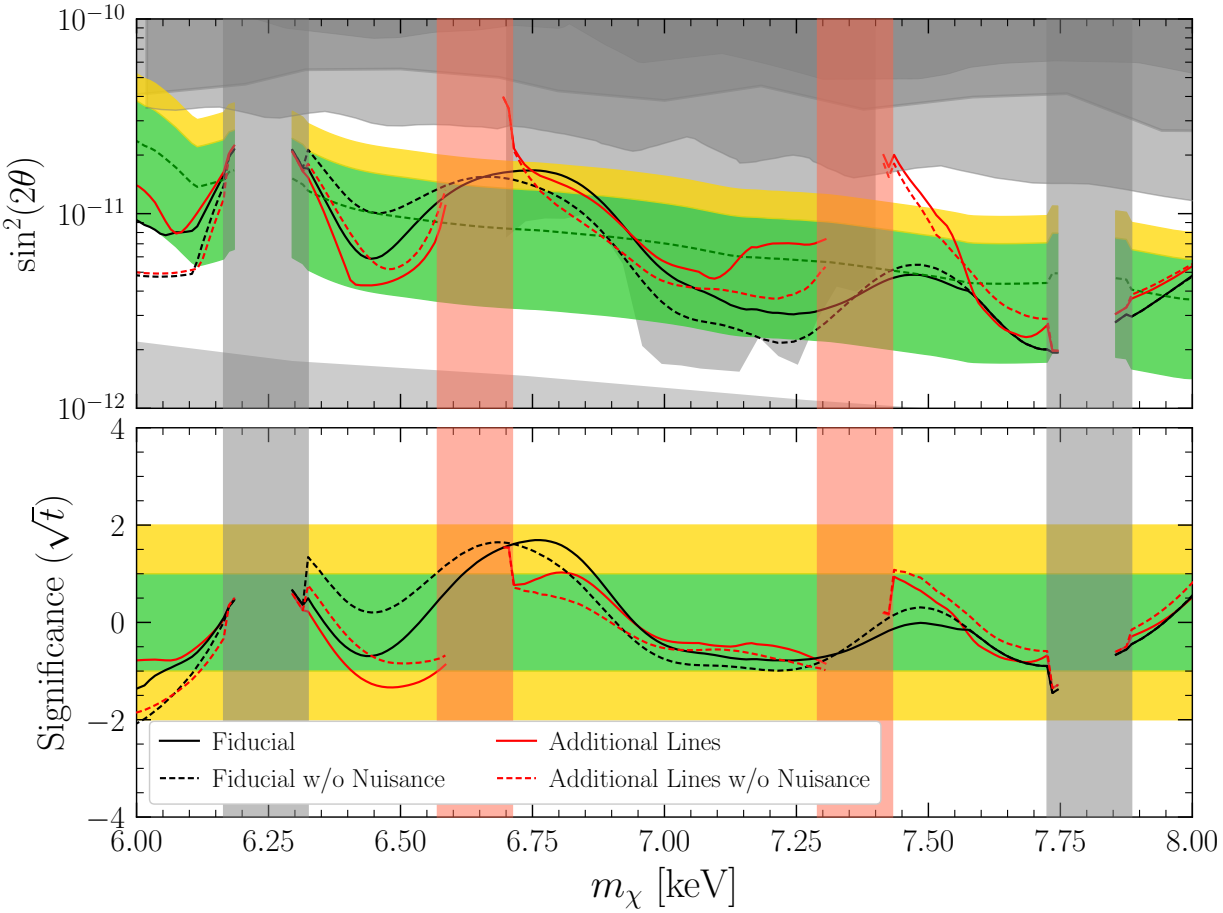

Figure B.28: A close inspection of the limits set in our fiducial analysis and the modified analysis that includes a 3.32 and 3.68 keV line in each annulus. We compare the limits set in these two analyses both with (solid lines) and without (dashed lines) the inclusion of our systematic nuisance parameter designed to test for and correct possible mismodeling.

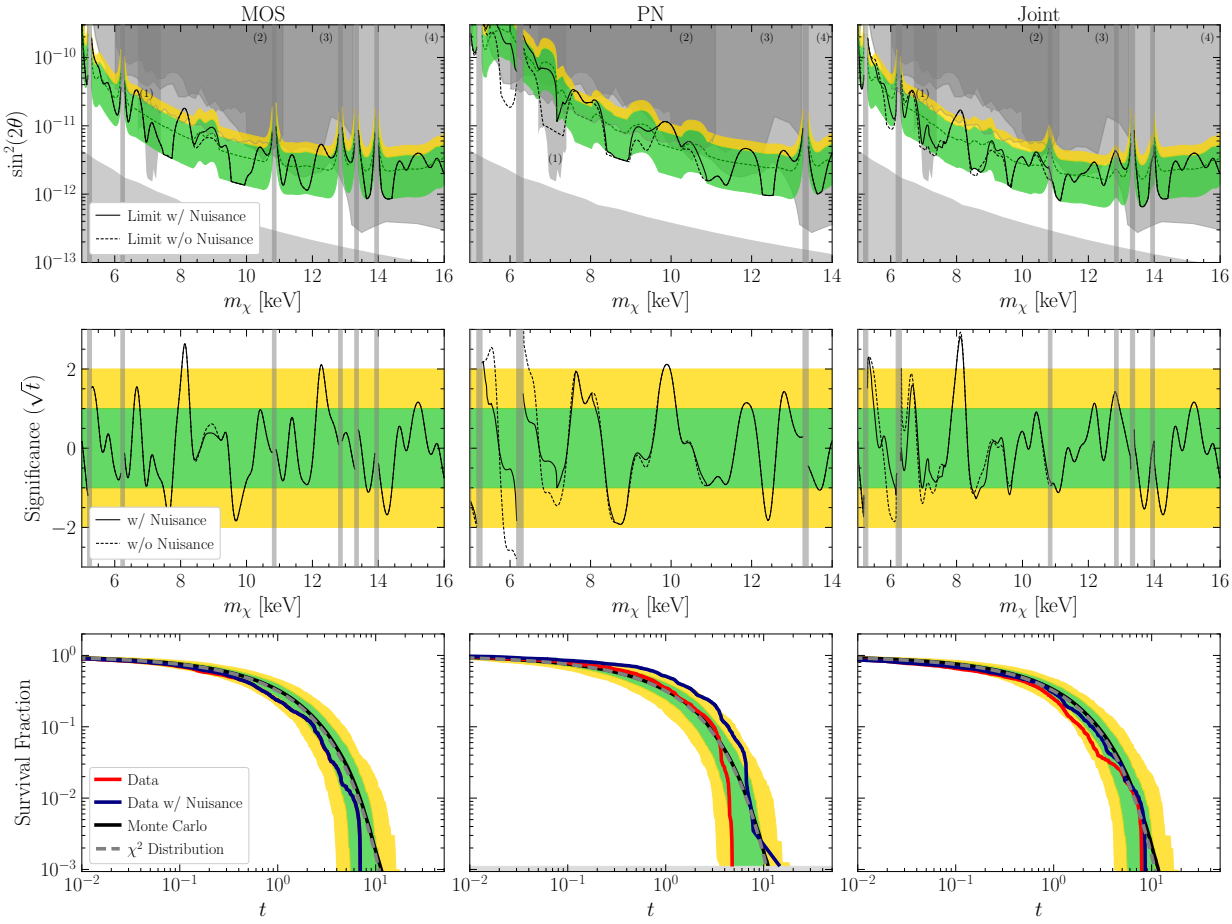

Figure B.29: The same results as presented in Figs. B.4 and B.5, however on a modified data set where instead of analyzing the signal ROI divided into eight individual rings, we stack the inner three rings into a single annulus. As in our primary approach, we subtract the background ROI flux from the signal-region data. The results are comparable to, although slightly weaker than, those from our fiducial approach, consistent with the reduced information available.

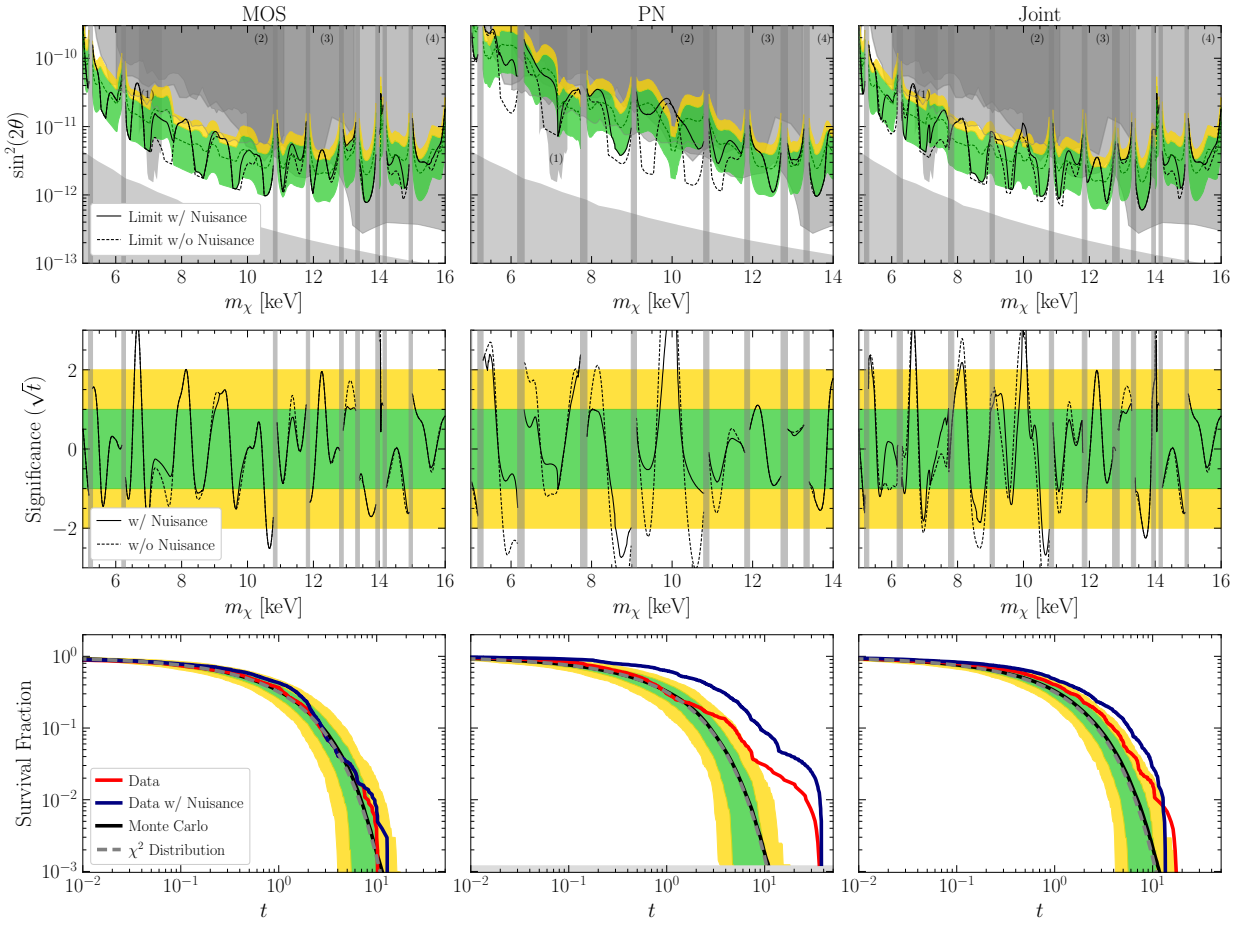

Figure B.30: As in Fig. B.29, however considering the stacked signal ROI without subtracting the background. The limit is noticeably worse, and several excesses appear, highlighting the importance of the background subtraction.

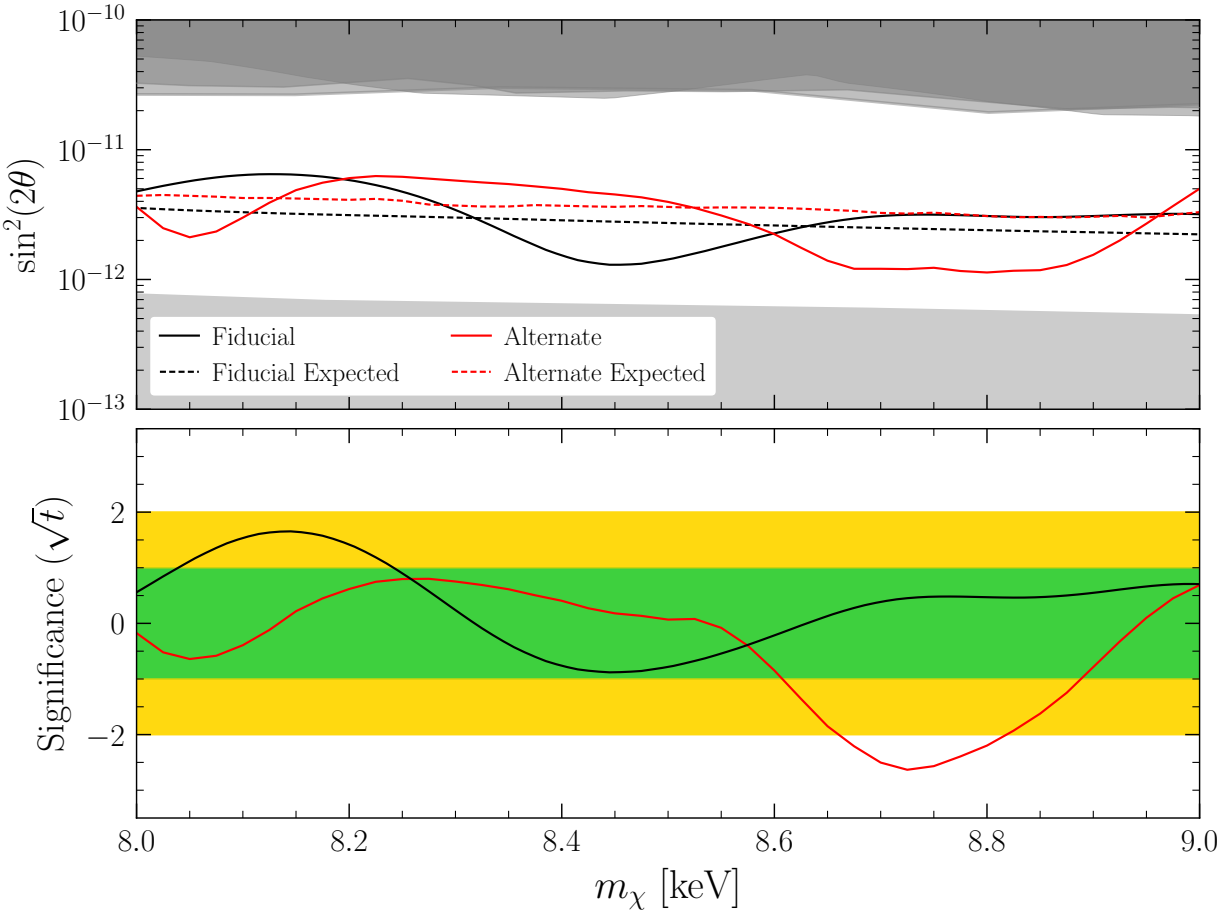

Figure B.31: Here we compare our fiducial results using a GP model, shown in black, to the result of an approach where the continuum background contribution is modeled with a second order polynomial, shown in red, as described in the text. Both results are shown without imposing a systematic nuisance parameter. While our fiducial approach uses the background-subtracted signal-ROI data, the alternate approach uses the un-subtracted data. We see that in both cases the expected and resulting limits are in qualitative agreement, demonstrating that our choice of GP modeling in our fiducial analysis does not drive the sensitivity of our results.

Appendix C

X-Ray Signatures of Axion Conversion in Magnetic White Dwarf Stars

This Supplementary Material is organized as follows. Section C.1 includes a list of several MWD stars that are expected to be promising candidates for observations of axion-induced X-ray flux. In Sec. C.2 we present a more general formalism for calculating the axion-to-photon conversion probability to account for the fact that the axions are emitted isotropically and homogeneously throughout the WD core. In Sec. C.4 we perform a more detailed study of the X-ray emission from RE J0317-853, including a more accurate modeling of its magnetic field structure, an assessment of uncertainties in its temperature measurements, and an evaluation of its X-ray spectrum. Finally Sec. C.5 presents the radiatively-induced axion-electron coupling that arises from the axion-photon coupling, which allows us to recast our limit on $|g_{a\gamma\gamma}\, g_{aee}|$ in terms of the axion-photon coupling alone.

C.1 Additional MWD candidates for X-ray observation

In the main chapter we have focused our analysis on the MWD star RE J0317-853, since it is expected to have a particularly strong X-ray flux, and because X-ray data is already available from *Suzaku*. However, there are over 200 MWD stars with well-measured field strengths, temperatures, and distances. For each of these stars, we calculate the expected axion-induced X-ray flux in the $2-10$ keV energy window, denoted by F_{2-10}, assuming $m_a = 10^{-9}$ eV and $g_{a\gamma\gamma}g_{aee} = 10^{-24}$ GeV^{-1}. The flux is insensitive to the axion mass in

the limit $m_a \to 0$, and more generally the flux has an overall scaling with the couplings, $F_{2-10} \propto (g_{a\gamma\gamma} g_{aee})^2$.

Our results are summarized in Table C.1, which shows the ten MWDs with the largest predicted X-ray flux, F_{2-10}. We constructed a full list by merging the SDSS DR7 magnetic WD catalog [19], a review MWD catalog [20], and Gaia DR2 WD catalog [21]. The former two provide the magnetic field strengths and temperatures of the WDs, while the latter provides distances, luminosities, masses, and radii, if known. Since the mass and radius of WD 2010+310 are not known, we take its mass to be $M_{\rm WD} = 1\,M_\odot$, and we infer its radius from the Stefan-Boltzmann law.

Table C.1: MWD stars that make good candidates for measurement of their secondary, axion-induced X-ray flux. The columns correspond to the star's mass in solar masses, radius in solar radii, luminosity in solar luminosities, effective temperature in Kelvin, magnetic field strength in mega-Gauss, distance from Earth in parsecs, and predicted X-ray flux from $2 - 10\,\text{keV}$ in erg/cm^2/s, calculated assuming $m_a = 10^{-9}\,\text{eV}$ and $g_{a\gamma\gamma} g_{aee} = 10^{-24}\ \text{GeV}^{-1}$. The parameters were obtained by merging the catalogs in Refs. [19–21]. We infer the mass and radius of WD 2010+310 as discussed in the text.

	$M_{\rm WD}$	$R_{\rm WD}$	L_γ	$T_{\rm eff}$	B	$d_{\rm WD}$	F_{2-10}
RE J0317-853	1.32	0.00405	0.0120	30000	200	29.54	6.8×10^{-14}
WD 2010+310	1*	0.00643*	0.00566	19750	520	30.77	4.4×10^{-14}
WD 0041-102 (Feige 7)	1.05	0.00756	0.00635	18750	35	31.09	3.0×10^{-14}
WD 1031+234	0.937	0.00872	0.0109	20000	200	64.09	2.3×10^{-14}
WD 1533-057	0.717	0.0114	0.0121	18000	31	68.96	1.3×10^{-14}
WD 1017+367	0.730	0.0111	0.0082	16500	65	79.24	7.1×10^{-15}
WD 1043-050	1.02	0.00787	0.00388	16250	820	83.33	5.4×10^{-15}
WD 1211-171	1.06	0.00754	0.00992	21000	50	92.61	5.4×10^{-15}
SDSS 131508.97+093713.87	0.848	0.00968	0.01347	20000	14	101.7	3.5×10^{-15}
WD 1743-520	1.13	0.00681	0.00184	14500	36	38.93	2.9×10^{-15}

C.2 The probability for axion-photon conversion in a general magnetic field background

In this section we present a more general formalism to calculate the axion-photon conversion probability, and in the following section we apply this calculation to study the X-ray emission from RE J0317-853 in more detail. Interactions between the axion and photon are described

by the following Lagrangian:

$$\begin{aligned}\mathcal{L} = &\frac{1}{2}(\partial_\mu a)^2 - \frac{1}{2}m_a^2 a^2 - \frac{1}{4}F_{\mu\nu}F^{\mu\nu} + \frac{1}{2}m_A^2 A_\mu A^\mu \\ &- A_\mu j^\mu - \frac{1}{4}g_{a\gamma\gamma}\, a\, F_{\mu\nu}\tilde{F}^{\mu\nu} + \frac{\alpha_{\rm em}^2}{90\, m_e^4}\Big[\big(F_{\mu\nu}F^{\mu\nu}\big)^2 + \frac{7}{4}\big(F_{\mu\nu}\tilde{F}^{\mu\nu}\big)^2\Big]\,,\end{aligned} \tag{C.1}$$

where m_a is the axion's mass, m_A is the photon's effective mass, j^μ is the electromagnetic current density, $g_{a\gamma\gamma}$ is the axion-photon coupling, $\alpha_{\rm em}$ is the electromagnetic fine structure constant, and m_e is the electron's mass. An environment with a nonzero electron density, n_e, gives rise to an effective mass, $m_A = \omega_{\rm pl} = \sqrt{4\pi\alpha_{\rm em} n_e/m_e}$, and although this term will be negligible for our calculation, we retain it here for the sake of generality. The last term in (C.1), known as the Euler-Heisenberg term, describes the photon's self-interaction that arises at energies below the electron's mass, where the electron can be integrated out of the theory.

One can derive the field equations for $a(\boldsymbol{x},t)$ and $A_\mu(\boldsymbol{x},t)$ by applying the variational principle to (C.1). It is customary to work in the Weyl gauge, $A_0 = A^0 = 0$ [173]. Upon writing $A_i = -A^i = -\boldsymbol{A}_i$ and $j^\mu = (\rho, \boldsymbol{j})$, the field equations are expressed as

$$\ddot{a} - \nabla^2 a + m_a^2 a = -g_{a\gamma\gamma}\, \dot{\boldsymbol{A}}\cdot(\boldsymbol{\nabla}\times\boldsymbol{A}) \tag{C.2a}$$

$$\begin{aligned}-\boldsymbol{\nabla}\cdot\dot{\boldsymbol{A}} = &\rho - g_{a\gamma\gamma}\,\boldsymbol{\nabla}a\cdot(\boldsymbol{\nabla}\times\boldsymbol{A}) \\ &+ \frac{16\alpha_{\rm em}^2}{45\, m_e^4}\boldsymbol{\nabla}\cdot\Big[\frac{1}{2}\big(|\dot{\boldsymbol{A}}|^2 - |\boldsymbol{\nabla}\times\boldsymbol{A}|^2\big)\dot{\boldsymbol{A}} \\ &\qquad + \frac{7}{4}\dot{\boldsymbol{A}}\cdot(\boldsymbol{\nabla}\times\boldsymbol{A})(\boldsymbol{\nabla}\times\boldsymbol{A})\Big]\end{aligned} \tag{C.2b}$$

$$\begin{aligned}\ddot{\boldsymbol{A}} - \nabla^2\boldsymbol{A} + \boldsymbol{\nabla}(\boldsymbol{\nabla}\cdot\boldsymbol{A}) + m_A^2\boldsymbol{A} = &\boldsymbol{j} + g_{a\gamma\gamma}\,\dot{a}\,\boldsymbol{\nabla}\times\boldsymbol{A} - g_{a\gamma\gamma}\,\boldsymbol{\nabla}a\times\dot{\boldsymbol{A}} \\ &- \frac{16\alpha_{\rm em}^2}{45\, m_e^4}\partial_t\Big[\frac{1}{2}\big(|\dot{\boldsymbol{A}}|^2 - |\boldsymbol{\nabla}\times\boldsymbol{A}|^2\big)\dot{\boldsymbol{A}} \\ &\qquad + \frac{7}{4}\dot{\boldsymbol{A}}\cdot(\boldsymbol{\nabla}\times\boldsymbol{A})(\boldsymbol{\nabla}\times\boldsymbol{A})\Big] \\ &- \frac{16\alpha_{\rm em}^2}{45\, m_e^4}\boldsymbol{\nabla}\times\Big[\frac{1}{2}\big(|\dot{\boldsymbol{A}}|^2 - |\boldsymbol{\nabla}\times\boldsymbol{A}|^2\big)(\boldsymbol{\nabla}\times\boldsymbol{A}) \\ &\qquad - \frac{7}{4}\dot{\boldsymbol{A}}\cdot(\boldsymbol{\nabla}\times\boldsymbol{A})\dot{\boldsymbol{A}}\Big]\,.\end{aligned} \tag{C.2c}$$

Here $\partial_0 = \partial_t$ is denoted by a dot, and $\partial_i = \boldsymbol{\nabla}_i$.

To study axion-photon conversion, we are interested in the field equations for linearized

perturbations around static background fields. This motivates us to write

$$\rho(\boldsymbol{x},t) = \bar{\rho}(\boldsymbol{x})\ , \quad \boldsymbol{j}(\boldsymbol{x},t) = \bar{\boldsymbol{j}}(\boldsymbol{x})\ , \quad a(\boldsymbol{x},t) = \bar{a}(\boldsymbol{x}) + \delta a(\boldsymbol{x},t)\ ,$$
$$\text{and} \quad \boldsymbol{A}(\boldsymbol{x},t) = \bar{\boldsymbol{A}}(\boldsymbol{x}) + \delta\boldsymbol{A}(\boldsymbol{x},t)\,, \tag{C.3}$$

where $\bar{a}(\boldsymbol{x})$ and $\bar{\boldsymbol{B}}(\boldsymbol{x}) = \boldsymbol{\nabla}\times\bar{\boldsymbol{A}}$ are the background axion and magnetic fields. In particular, we are interested in systems for which $\bar{a} = 0$ and $\bar{\boldsymbol{B}}$ can be approximated as a magnetic dipole.

We assume that gradients in the background field, $\bar{\boldsymbol{B}}$, are small compared to the wavenumber of the axions, $k = |\boldsymbol{k}|$, which lets us apply the WKB approximation. Consider the trajectory $\boldsymbol{x}(z) = \boldsymbol{x}_0 + z\,\hat{\boldsymbol{k}}$ where $\boldsymbol{x}_0$ is a point inside the WD, $z \geq 0$ parametrizes the distance, and the unit vector $\hat{\boldsymbol{k}} = \boldsymbol{k}/k$ is the trajectory's orientation. If gradients in the directions transverse to $\hat{\boldsymbol{k}}$ are small, then we are motivated to adopt the plane-wave Ansatz

$$\delta a(\boldsymbol{x},t) = a(z) + \text{c.c.} \tag{C.4a}$$
$$\text{with} \qquad a(z) = \tilde{a}(z)\,e^{-i\omega t + ikz}$$
$$\delta\boldsymbol{A}(\boldsymbol{x},t) = -i\big[A_x(z)\,\hat{\boldsymbol{e}}_x + A_y(z)\,\hat{\boldsymbol{e}}_y + A_z(z)\,\hat{\boldsymbol{e}}_z\big] + \text{c.c.} \tag{C.4b}$$
$$\text{with} \qquad A_a(z) = \tilde{A}_a(z)\,e^{-i\omega t + ikz}\,.$$

For relativistic particles, it is an excellent approximation to take the natural frequency as $\omega \approx k$. We choose a set of orthonormal basis vectors, $\{\hat{\boldsymbol{e}}_x, \hat{\boldsymbol{e}}_y, \hat{\boldsymbol{e}}_z\}$, such that $\hat{\boldsymbol{e}}_z = \hat{\boldsymbol{k}}$ and therefore $\hat{\boldsymbol{e}}_x \cdot \hat{\boldsymbol{k}} = \hat{\boldsymbol{e}}_y \cdot \hat{\boldsymbol{k}} = 0$. We can also write $B_x(z) = \bar{\boldsymbol{B}} \cdot \boldsymbol{e}_x$, $B_y(z) = \bar{\boldsymbol{B}} \cdot \boldsymbol{e}_y$, $B_T(z) = [B_x^2 + B_y^2]^{1/2}$, $B_L(z) = \bar{\boldsymbol{B}} \cdot \hat{\boldsymbol{k}}$, and $B(z) = |\bar{\boldsymbol{B}}| = [B_T^2 + B_L^2]^{1/2}$. In the WKB approximation, we assume that the background changes slowly along the axion's trajectory. This lets us drop derivatives of the background field and also second derivatives of the perturbations. With these simplifications, the Weyl-gauge field equations (C.2) become

$$\left[i\partial_z + k + \begin{pmatrix} \Delta_x & \Delta_{xy} & \Delta_{ax} \\ \Delta_{xy} & \Delta_y & \Delta_{ay} \\ \Delta_{ax} & \Delta_{ay} & \Delta_a \end{pmatrix}\right] \begin{pmatrix} A_x(z) \\ A_y(z) \\ a(z) \end{pmatrix} = 0\,, \tag{C.5}$$

where we have defined

$$\Delta_a \equiv \frac{1}{2k}\left(\omega^2 - k^2 - m_a^2\right) \tag{C.6a}$$

$$\Delta_x \equiv \frac{1}{2k}\left(\omega^2 - k^2 - m_A^2\right) + \frac{8\alpha_{\rm em}^2}{45\, m_e^4}\left(\frac{7}{4}\frac{\omega^2}{k}B_x^2 + kB_y^2\right) \tag{C.6b}$$

$$\Delta_y \equiv \frac{1}{2k}\left(\omega^2 - k^2 - m_A^2\right) + \frac{8\alpha_{\rm em}^2}{45\, m_e^4}\left(\frac{7}{4}\frac{\omega^2}{k}B_y^2 + kB_x^2\right) \tag{C.6c}$$

$$\Delta_{ax} \equiv \frac{1}{2}g_{a\gamma\gamma}\frac{\omega}{k}B_x \tag{C.6d}$$

$$\Delta_{ay} \equiv \frac{1}{2}g_{a\gamma\gamma}\frac{\omega}{k}B_y \tag{C.6e}$$

$$\Delta_{xy} \equiv \frac{8\alpha_{\rm em}^2}{45\, m_e^4}\left(\frac{7}{4}\frac{\omega^2}{k} - k\right)B_xB_y\,. \tag{C.6f}$$

In deriving (C.5), we have dropped terms that are nonlinear in the perturbations. The wavefunction $\tilde{A}_z$ is not dynamical, meaning that its field equation is algebraic rather than differential, and we can remove it from the system of equations. We regain (4.2) in the main chapter by taking $z = r$, $\omega = k$, $m_A = 0$, and by focusing on isotropic field configurations for which $B_x = 0$, $B_y(r) = B(r)\sin\Theta$, and $B_z(r) = B(r)\cos\Theta$.

The axion-to-photon conversion probability is calculated by solving (C.5). We assume that photons produced inside of the star, $r < R_{\rm WD}$, will be unable to escape as X-ray emission, and therefore we are only interested in conversions that occur outside of the star. Along a given trajectory, let $z = z_0$ denote the surface of the star. We solve (C.5) along with the initial condition $a(z_0) = a_0$, $A_x(z_0) = 0$, and $A_y(z_0) = 0$, and then the axion-to-photon conversion probability is given by $p_{a\to\gamma} = \left(|A_x(\infty)|^2 + |A_y(\infty)|^2\right)/a_0^2$. Since (C.5) is linear, the initial condition a_0 cancels when calculating $p_{a\to\gamma}$.

C.3 Analytic approximations to the conversion probability

In order to develop our intuition, let us consider axion-photon conversion in a constant magnetic field, $B(r) = B$, which extends for a distance $\Delta r = R_{\rm WD}$ outside of the MWD, with $R_{\rm WD}$ the star's radius. Then (4.2) may be solved exactly, and the axion-photon conversion probability is found to be

$$p_{a\to\gamma} = \sin^2 2\theta\ \ \sin^2(\Delta_{\rm osc}R_{\rm WD}/2)\,, \tag{C.7}$$

where the mixing angle, θ, and the oscillation length scale, $\Delta_{\rm osc}^{-1}$, can be written as

$$\tan 2\theta = \frac{2\Delta_B}{\Delta_\parallel - \Delta_a}\,, \qquad \Delta_{\rm osc} = \frac{\Delta_\parallel - \Delta_a}{\cos 2\theta}\,. \tag{C.8}$$

Note that $\Delta_\parallel - \Delta_a$ is always positive.

We will generally be interested in the weak-mixing regime where $\theta \ll 1$, and for the sake of illustration let us also focus on the regime where the axion mass is low, such that $|\Delta_a| \ll \Delta_\parallel$. With these assumptions, (C.7) becomes $p_{a\to\gamma} \approx 4(\Delta_B^2/\Delta_\parallel^2)\,\sin^2(\Delta_\parallel R_{\rm WD}/2)$. If the magnetic field is weak, such that $\Delta_\parallel R_{\rm WD} \ll 1$, then the conversion probability becomes $p_{a\to\gamma} \approx \Delta_B^2 R_{\rm WD}^2 \propto g_{a\gamma\gamma}^2 B^2$. Alternatively, if the magnetic field is very strong, such that $1 \ll \Delta_\parallel R_{\rm WD}$, then we have instead $p_{a\to\gamma} \propto g_{a\gamma\gamma}^2/(BE)^2$. Here we see that the conversion probability is suppressed in the strong-magnetic field regime, which is a consequence of the QED birefringence effects, as anticipated in [173]. The axion-photon conversion probability is maximal for $\Delta_{\rm osc} R_{\rm WD} \sim 1$. In practice, for frequencies $E \sim 1$ (10) keV, this transition occurs for magnetic fields around $\sim 10^7$ ($\sim 5\times 10^6$) G. The dipole magnetic fields around the MWDs fall with distance from the WD surface, which leads to the result that if the magnetic field at the surface of the WD is high, the conversion probability is suppressed until the field drops to where $\Delta_{\rm osc} R_{\rm WD} \sim 1$.

As we increase the axion mass, we enter the regime where $\Delta_\parallel \ll |\Delta_a|$ and $p_{a\to\gamma} \approx 4(\Delta_B^2/\Delta_a^2)\,\sin^2(\Delta_a R_{\rm WD}/2)$. For asymptotically large axion masses we have also $|\Delta_a| R_{\rm WD} \gg 1$, in which case $p_{a\to\gamma} \propto g_{a\gamma\gamma}^2 B^2 E^2/m_a^4$. Thus, contrary to the search for low-mass axions, searches for high-mass axions benefit from the largest magnetic fields and largest frequencies available.

With the dipole field configuration we instead need to compute the integral given in (4.3). While in general this must be done numerically, we note that an analytic approximation is available in the regime of small axion mass, such that $|\Delta_a| \ll \Delta_\parallel$, where we find

$$p_{a\to\gamma} \approx \frac{(\Delta_{B,0} R_{\rm WD})^2}{(\Delta_{\parallel,0} R_{\rm WD})^{\frac{4}{5}}} \left| \frac{\Gamma(\frac{2}{5}) - \Gamma(\frac{2}{5}, -\frac{i}{5}\,\Delta_{\parallel,0} R_{\rm WD})\big]}{5^{\frac{3}{5}}} \right|^2 , \tag{C.9}$$

with $\Gamma(z)$ the gamma function, $\Gamma(a,z)$ is the incomplete gamma function, $\Delta_{B,0} = \Delta_B(R_{\rm WD})$, and $\Delta_{\parallel,0} = \Delta_\parallel(R_{\rm WD})$.

To help illustrate the different regimes for the conversion probability, in Fig. C.1 we illustrate the conversion probability computed using (C.9) as a function of the transverse magnetic field $B_{T,0}$ at $r = r_{\rm WD}$ for an axion with an arbitrary small mass, a reference $g_{a\gamma\gamma} = 10^{-11}$ GeV^{-1}, and a MWD with $R_{\rm WD} = 0.00405\ R_\odot$. For definiteness we show the conversion probability for $E = 10$ keV. At small values of $B_{T,0}$ the conversion probability

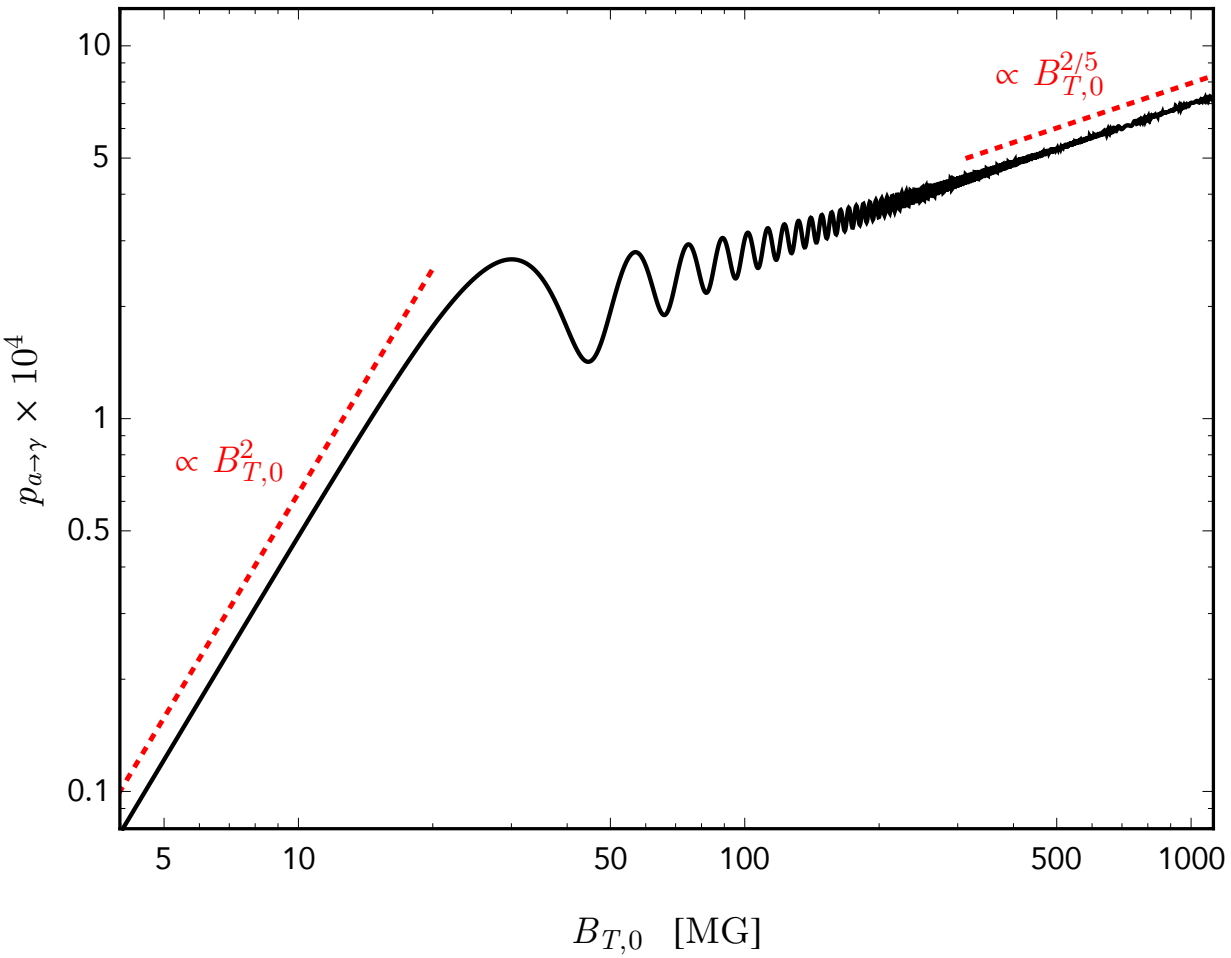

Figure C.1: The probability $p_{a\to\gamma}$ for axion to convert into X-ray photons in the presence of a dipole magnetic field with surface transverse field strength $B_{T,0}$. We use (C.9) with $m_a = 0$, $g_{a\gamma\gamma} = 10^{-11}$ GeV^{-1}, $R_{\rm WD} = 0.00405\ R_\odot$, and $E = 10$ keV. In general $p_{a\to\gamma} \propto g_{a\gamma\gamma}^2$.

rises like $B_{T,0}^2$. However, the Euler-Heisenberg term becomes important for $B_{T,0} \gtrsim 10$ MG, causing the conversion probability to scale less strongly with $B_{T,0}$ beyond this point.

C.4 A detailed analysis of the axion-induced X-ray flux from RE J0317-853

Our analysis of the X-ray flux from RE J0317-853 in the main chapter makes several simplifying assumptions. In this section we revisit and refine these assumptions.

C.4.1 Magnetic field structure

In the main chapter we calculated the probability for axions to convert into X-ray photons in a background magnetic field by assuming that the background field is isotropic along the axion's trajectory and decreases with propagation distance like $B \sim r^{-3}$. This is a reasonable assumption for a dipole field configuration if axions propagate on radial trajectories, as if they were produced at the star's center. However, in general the axion's trajectory will not originate at the origin and, moreover, the background field will deviate from a simple dipole configuration. Here we assess the effect of relaxing these assumptions.

Let us first understand how our results depend on the axion's trajectory through the magnetosphere. Consider a dipolar magnetic field centered on the center of the star. Such a field can be written as

$$\bar{\boldsymbol{B}} = \frac{|\boldsymbol{m}|}{4\pi}\frac{1}{r^3}\Big(3(\hat{\boldsymbol{m}}\cdot\hat{\boldsymbol{x}})\,\hat{\boldsymbol{x}} - \hat{\boldsymbol{m}}\Big) \qquad \text{for} \qquad r > R_{\rm WD}\,, \tag{C.10}$$

where $\boldsymbol{m} = |\boldsymbol{m}|\,\hat{\boldsymbol{m}}$ is the magnetic dipole moment, $|\boldsymbol{m}|/4\pi = B_0 R_{\rm WD}^3/2$ is the relationship with the polar field B_0, $\boldsymbol{x} = r\,\hat{\boldsymbol{x}}$ is the spatial coordinate, and $r = |\boldsymbol{x}|$ is the distance from the center of the MWD. Note that here B_0 is the value of the magnetic field at the star's surface in the direction of the magnetic pole, whereas in the main chapter below (4.3) we used B_0 to denote the value at the surface in any arbitrary direction. Note that the orientation of $\bar{\boldsymbol{B}}$ along a radial trajectory is invariant, which allows us to calculate the axion-photon conversion probability, $p_{a\to\gamma}$, using (4.3), in this case. The result is presented in the left panel of Fig. C.2 as the blue curve, where we show the conversion probability as a function of the angle between the magnetic pole and the viewing angle, $\hat{\boldsymbol{m}}\cdot\hat{\boldsymbol{x}} = \cos\theta$. As one expects, the probability vanishes at $\theta = 0$ and π where the transverse magnetic field vanishes, and the probability peaks at $\theta = \pi/2$ where the transverse magnetic field, $B_T = B\,\sin\theta$, is maximal. It is a rough approximation to suppose that axions only propagate on radial trajectories, and more accurately we should allow the axion's trajectory to originate anywhere inside the MWD. In general the field direction is not invariant along such a trajectory, and we cannot use (4.3) to calculate $p_{a\to\gamma}$, but rather we must solve (C.5) directly. Doing so leads to the red-dashed curve in the left panel of Fig. C.2, where we have sampled 3,000 points in the star's interior, uniformly distributed in $\boldsymbol{x}$ with $|\boldsymbol{x}| < R_{\rm WD}$. The effects of this averaging are to remove the oscillatory behavior and enhance the probability at $\theta = 0, \pi$. However, the rough approximation is reliable up to an order unity correction factor.

Let us finally address the specific magnetic field structure in our MWD candidate, RE J0317-853. Using phase-resolved far-ultraviolet spectroscopy data, [215] constructed several models for the field configuration of RE J0317-853. It was found that the observa-

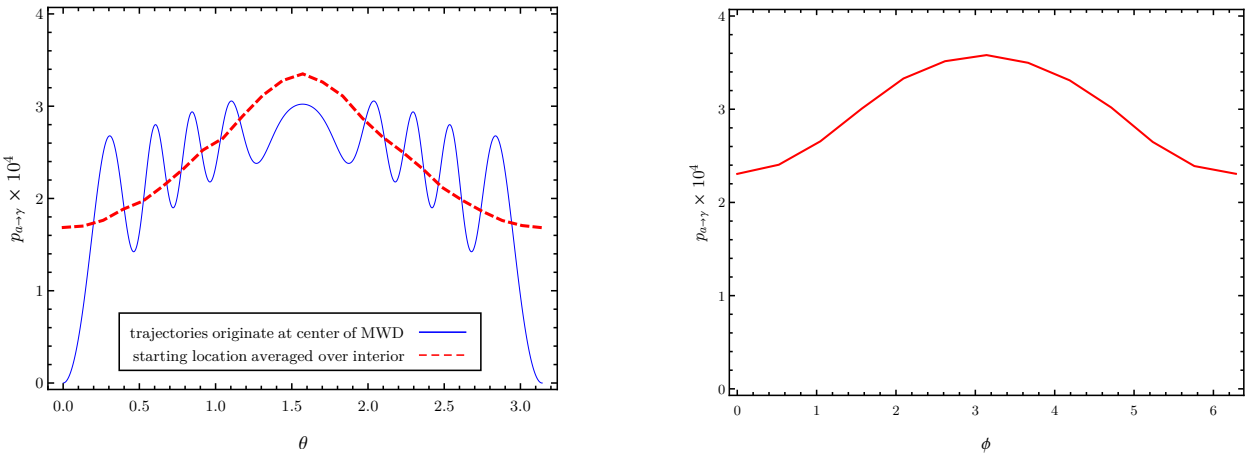

Figure C.2: The axion-photon conversion probability, $p_{a\to\gamma}$, for different models of the magnetic field around RE J0317-853. *Left:* We assume a magnetic dipole field with polar field strength $B_0 = 400\,\mathrm{MG}$ (200 MG at $\theta = \pi/2$), and we calculate $p_{a\to\gamma}$ for axion trajectories that propagate radially outward from the star's center (blue) as a function of the angle θ between the magnetic pole and the propagation direction. We also show an average over trajectories that originate throughout the star's interior (red, dashed). *Right:* We assume the offset-dipole model of [22] and calculate the trajectory-averaged conversion probability as a function of the azimuthal angle ϕ measured from the star's rotation axis, which corresponds to the phase over the ∼725 s period. For both panels, we have taken $m_a = 10^{-9}\,\mathrm{eV}$, $g_{a\gamma\gamma} = 10^{-11}\,\mathrm{GeV}^{-1}$, $\omega = 10\,\mathrm{keV}$, and $R_{\mathrm{WD}} = 0.00405\,R_\odot$.

tions are well described by a magnetic dipole, with a polar field strength of $B_0 = 363\,\mathrm{MG}$, which is offset from the star's center along the magnetic axis by 19% of R_{WD}, which is misaligned with the star's rotation axis by an angle of 20^o, and which is viewed from an angle of 51^o to the rotation axis. We have calculated the axion-photon conversion probability for this field configuration by solving (C.5) and averaging over 5000 trajectories. Our results appear in the right panel of Fig. C.2. Since the polar viewing angle is known, we vary the azimuthal angle, ϕ, instead. Here we see that the axion-to-photon conversion probability experiences an $O(50\%)$ variation as the star revolves, which corresponds to a period of ∼725 s for RE J0317-853, and this translates into a corresponding modulation of the X-ray flux. Note that across all masses we find that when integrating out in radius r to compute the conversion probability the probability has researched its asymptotic values by $r \sim 10 \times R_{\mathrm{WD}}$.

Finally let us compare our limit on $|g_{a\gamma\gamma}\, g_{aee}|$, calculated using two different models for the background magnetic field. In the main chapter we used a configuration with $B(r) = (r/R_{\mathrm{WD}})^{-3}\, B_0$ for $B_0 = 200\,\mathrm{MG}$, and we obtained the limit appearing in Fig. 4.2. If we perform the same calculation using the offset dipole configuration described above, then we obtain instead the limit appearing in Fig. C.3 as the brown curve. Note that the limit derived

in the main chapter is reliable up to an $O(1)$ factor, but it is also a conservative estimate. At small values of the axion mass, we find that the two limits are comparable. This result is consistent with Fig. C.2 where we see $p_{a\to\gamma} \simeq 3.0 \times 10^{-4}$ at $\theta = \pi/2$ in the left panel while $\langle p_{a\to\gamma} \rangle \approx 2.9 \times 10^{-4}$ in the right panel after averaging over ϕ. We note, though, that improved sensitivity may be obtained by using an analysis procedure that incorporates the expected non-trivial light curve, in the case of the displaced dipole model.

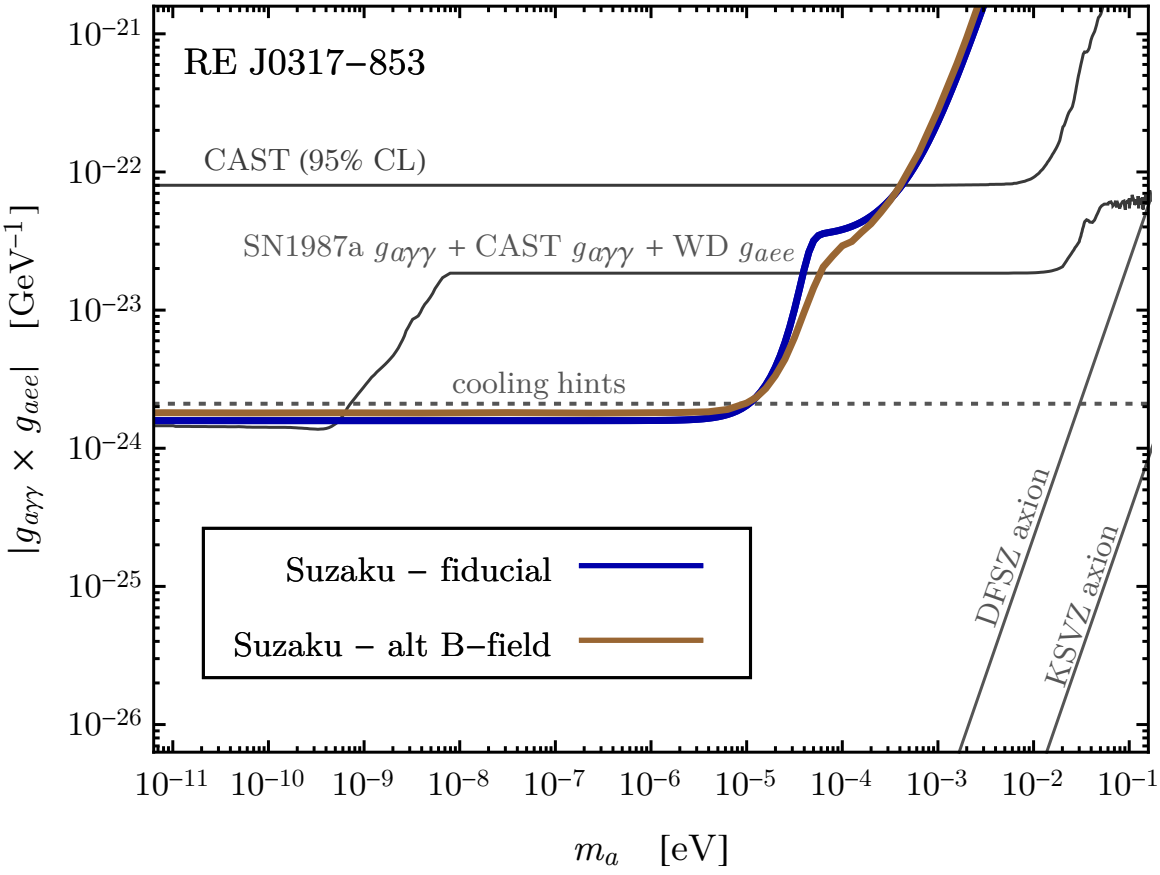

Figure C.3: The limit on $|g_{a\gamma\gamma}\, g_{aee}|$, calculated using two different models for the background magnetic field. The alternate B-field model, with the displaced dipole, gives a comparable result at low axion masses and slightly improved sensitivity at high axion masses, due to the increased magnetic field strength.

C.4.2 Effective temperature uncertainties

The MWD RE J0317-853 has garnered significant interest, due in part to its high effective temperature, which takes a value in the range from 30,000 to 55,000 K [214]. This uncertainty

Table C.2: The X-ray flux of RE J0317-853 is calculated for different values of $M_{\rm WD}$ [$M_\odot$], $R_{\rm WD}$ [$0.01\,R_\odot$], and $T_{\rm eff}$ [K], which were determined by [22]. The luminosities, L_γ [$L_\odot$], are inferred from the Stefan-Boltzmann law. We calculate F_{2-10} for $m_a = 10^{-9}\,\text{eV}$ and $g_{a\gamma\gamma}g_{aee} = 10^{-24}$ GeV^{-1} in erg/cm^2/sec. We also list the polar magnetic field strength B [MG] and the distance from Earth $d_{\rm WD}$ [pc].

	$M_{\rm WD}$	$R_{\rm WD}$	L_γ	$T_{\rm eff}$	B	$d_{\rm WD}$	F_{2-10}
CO-low-T	1.32 ± 0.020	0.405 ± 0.011	0.0120	30000	200	29.54	6.8×10^{-14}
CO-high-T	> 1.46	0.299 ± 0.008	0.0503	50000	200	29.54	2.4×10^{-13}
ONe-low-T	1.28 ± 0.015	0.416 ± 0.011	0.0126	30000	200	29.54	7.2×10^{-14}
ONe-high-T	1.38 ± 0.020	0.293 ± 0.008	0.0483	50000	200	29.54	2.2×10^{-13}

in $T_{\rm eff}$ translates into an uncertainty in our predicted X-ray flux, F_{2-10}, and therefore an uncertainty in our constraint on the axion's parameter space. In order to quantify this uncertainty we compare our fiducial model from the main chapter with four benchmark models, given by Table 6 of [22]. The results are summarized in Tab. C.2, which shows that the predicted X-ray flux can vary by a factor of ~ 4 depending on the specific stellar model parameters used to describe RE J0317-853. Since the flux depends on the axion's couplings through $F_{2-10} \propto (g_{a\gamma\gamma}g_{aee})^2$, the effect on our limit is a factor of ~ 2. The flux uncertainty follows primarily from the uncertainty in $T_{\rm eff}$. In Fig. C.4 we show how these uncertainties translate into the uncertainty in the 95% limit from *Suzaku* observations and (projected) *Chandra* observations. The bands encompass the range of limits obtained by cycling through the parameters presented in Tab. C.2.

C.4.3 Core temperature model uncertainties

Since the WD's core temperature is not directly observable, it is necessary to have a model for the WD interior in order to relate T_c to an observable quantity like the luminosity, L_γ. Moreover, since the axion emission depends sensitively on the WD core temperature, with the axion luminosity going as $L_a \sim T_c^4$ in (4.1), it is therefore important to quantitatively assess how our prediction for the axion-induced X-ray signal depends on this modeling. In this section we specifically investigate how the modeling uncertainties affect our limits on the axion parameter space for RE J0317-853.

The physics of WD cooling is a balance between the energy stored in the hot core and the transparency of the envelope. The transport of thermal energy also depends on various physical inputs including the thermal conductivity of the degenerate matter, neutrino emission rates, and chemical diffusion. The cooling of old hydrogen-rich DA WDs has been studied extensively, and we summarize the relevant results of several prominent studies [62–65] in

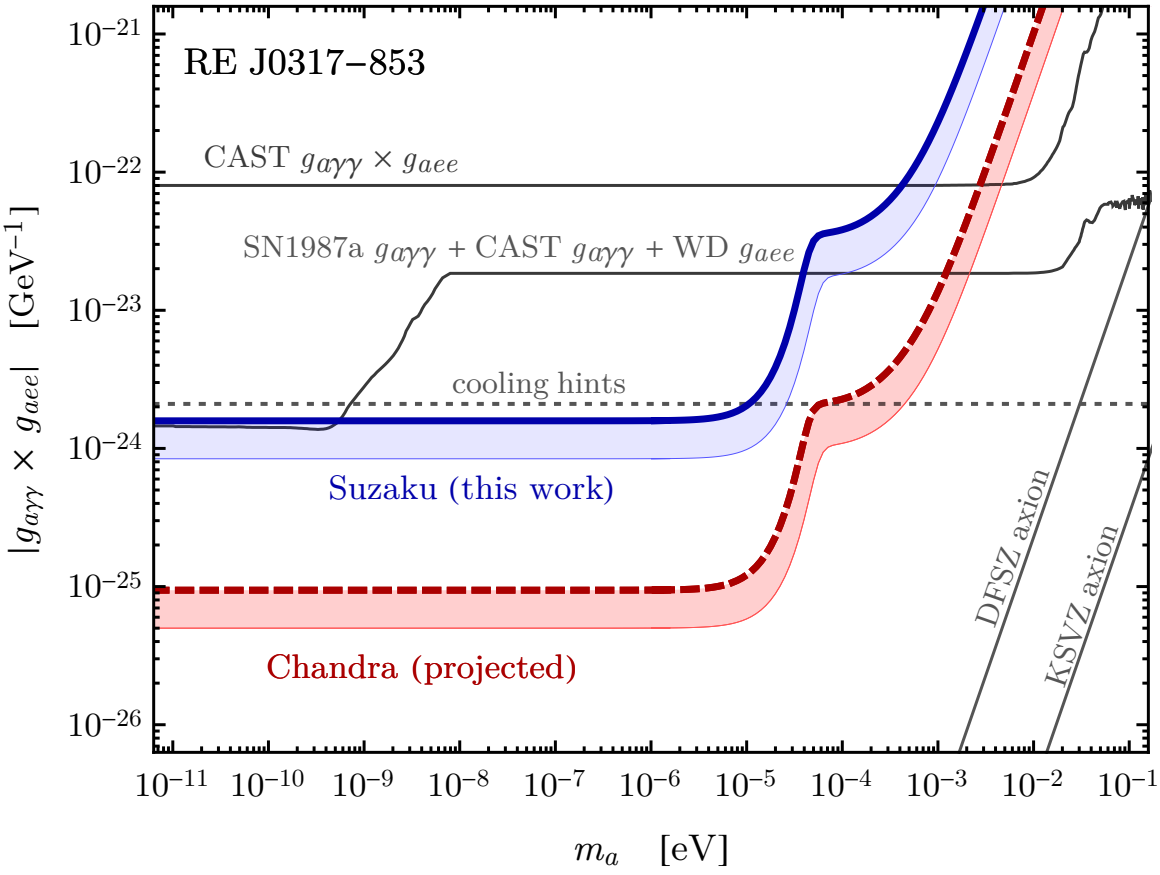

Figure C.4: As in Fig. 4.2, except we have broadened the *Suzaku* and (projected) *Chandra* limits to encompass the systematic uncertainty that follows from the uncertainty in the WD parameters, such as temperature, and as described in Tab. C.2.

Fig. C.5. In particular we are interested in the predicted relation between the core temperature and surface luminosity. The left panel of Fig. C.5 shows that all four models agree very well with our fiducial formula (4.5) for $10^{-4} \lesssim L_\gamma/L_\odot \lesssim 10^{-1}$.

At the fiducial luminosity of RE J0317-853, $L_\gamma = 0.012\ L_\odot$, the predictions for the core temperature vary from $T_c \simeq 1.8$ to 2.0×10^7 K, and thus we can associate the WD cooling model with an $O(10\%)$ uncertainty on T_c. Since the axion luminosity goes as $L_a \sim T_c^4$, we infer that the WD cooling model leads to an $O(40\%)$ uncertainty on our axion-induced X-ray flux signal and an $O(20\%)$ uncertainty on our axion parameter space limits for RE J0317-853 since $|g_{a\gamma\gamma} \times g_{aee}| \sim T_c^2$. This is illustrated in the right panel of Fig. C.5.

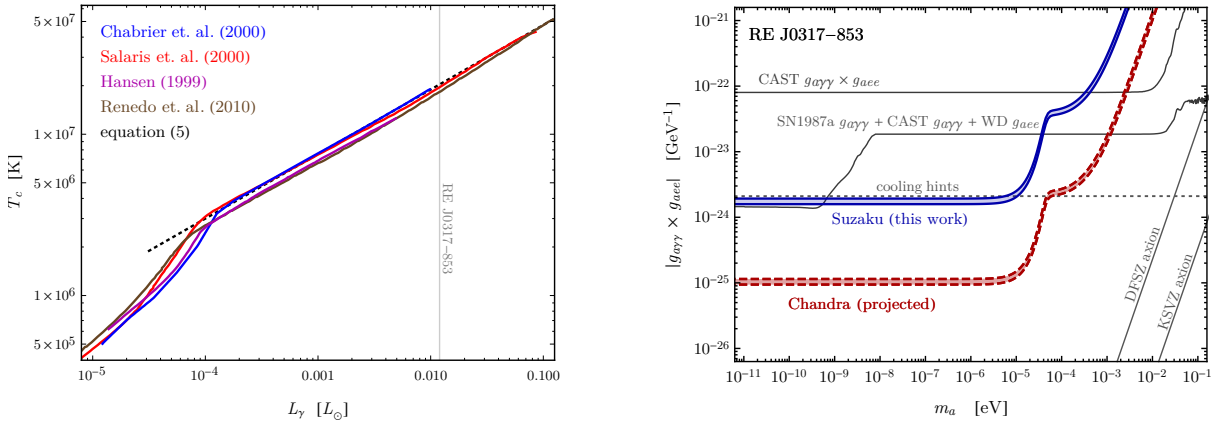

Figure C.5: A quantitative assessment of the robustness of our results under various WD cooling models. *Left:* The models in [62–65] predict the WD core temperature, T_c, in terms of its photon luminosity, L_γ. Additionally the black-dashed line shows (4.5) and the vertical gray line indicates the fiducial luminosity for RE J0317-853. *Right:* As in Fig. 4.2, except that we have broadened the limit curves to reflect the uncertainty in the WD model that we use to infer T_c from the measured L_γ for RE J0317-853.

C.4.4 Spectrum

Fig. C.6 shows the predicted spectra of axion and photon emission from our candidate MWD star, RE J0317-853. The shape of the axion spectrum (blue curve) is very well approximated by a blackbody at temperature $T_c \simeq 2 \times 10^7\,\mathrm{K} \simeq 1.7\,\mathrm{keV}$ whereas the amplitude of the spectrum is set by the magnitude of the axion-electron coupling according to (4.1). To draw the blue curve we take $g_{aee} = 10^{-13}$. The spectrum of secondary, axion-induced photons (red curve) tracks the thermal spectral shape up to an additional energy dependence coming from the axion-photon conversion probability (4.3). To draw the red curve we take $m_a = 10^{-9}\,\mathrm{eV}$ and $g_{a\gamma\gamma} = 10^{-11}\,\mathrm{GeV}^{-1}$, such that the product $|g_{a\gamma\gamma}\, g_{aee}| = 10^{-24}$ is marginally consistent with the *Suzaku* limit. We assume that all axions are emitted isotropically and homogeneously from throughout the interior of the WD core, and the axion-photon conversion probability is calculated using (C.5).

C.5 The running of the axion-electron coupling and sensitivity to $g_{a\gamma\gamma}$

In the main chapter we have shown the limit on $|g_{a\gamma\gamma}\, g_{aee}|$ that follows from X-ray observations of MWD stars. Here we would like to translate this into a limit on simply $g_{a\gamma\gamma}$. For

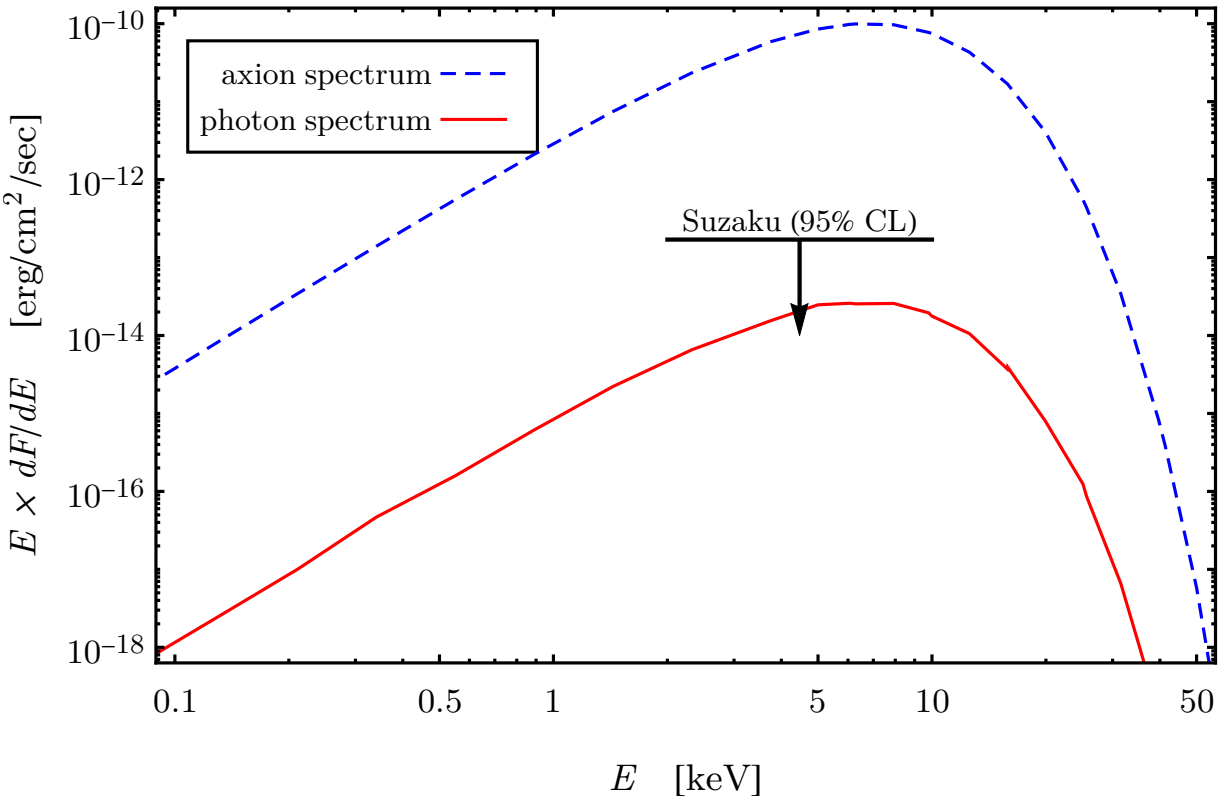

Figure C.6: The predicted emission spectra of primary axions (dashed blue) and secondary X-rays (red) from RE J0317-853 with $g_{aee} = 10^{-13}$, $m_a = 10^{-9}$ eV and $g_{a\gamma\gamma} = 10^{-11}\,\mathrm{GeV}^{-1}$.

any value of $g_{a\gamma\gamma}$ there is a "reasonable range" of values for g_{aee}: it is bounded from above by direct observation, and it is bounded from below because an axion-electron coupling can be induced radiatively from an axion-photon coupling. In this section we estimate the lower bound.

Consider an axion-like particle, which does not couple to QCD. The effective theory describing the interactions of this axion with the Standard Model electroweak gauge fields is generated at a high scale, which we denote by $\Lambda \sim f_a \sim 10^{10}$ GeV, and the corresponding Lagrangian can be written as

$$\mathcal{L}_{a,\Lambda} \supset -\frac{1}{4} g^{\Lambda}_{aWW} a W\tilde{W} - \frac{1}{4} g^{\Lambda}_{aBB} a B\tilde{B} + \frac{C^{\Lambda}_e}{2} \frac{\partial_\mu a}{f_a} \bar{e}\gamma^\mu\gamma_5 e\,, \tag{C.11}$$

where $W \equiv W^a_{\mu\nu}$ is the $SU(2)_L$ field strength tensor, $B \equiv B_{\mu\nu}$ is the $U(1)_Y$ field strength tensor, $g^{\Lambda}_{aWW} = C^{\Lambda}_W \alpha_W/(2\pi f_a)$, and $g^{\Lambda}_{aBB} = C^{\Lambda}_B \alpha_B/(2\pi f_a)$. The fine structure constants can be written as $\alpha_W = \alpha_{\rm em}/s_w^2$ and $\alpha_B = \alpha_{\rm em}/c_w^2$ where the electromagnetic fine structure

constant is $\alpha_{\rm em} \simeq 1/137$ and the weak mixing angle's sine and cosine are $s_w = \sin\theta_w \simeq 0.48$ and $c_w = \cos\theta_w \simeq 0.88$. The parameters C_W^Λ, C_B^Λ, and C_e^Λ are dimensionless constants that parameterize the UV theory. We are interested in how these parameters evolve, under the renormalization group, to scales $\mu \ll \Lambda$, since the physical processes we consider are at much lower energies. We assume that the scale μ is larger than the electroweak scale $\Lambda_{\rm EW} \sim 100$ GeV so that the Lagrangian (C.11) is the correct description of the axion-gauge-boson interactions. Below this scale we should instead map to the axion-photon coupling, and we will return to this point shortly.

The one-loop diagrams that contribute to the running of C_e were computed in [176, 316] and consist of triangle diagrams with electron and axion final states connected by a loop of $SU(2)_L$ or $U(1)_Y$ gauge bosons. Evaluating the divergent part of these diagrams and applying the renormalization procedure gives the beta function for the axion-electron coupling. The running coupling at the scale μ, denoted by C_e^μ, is given by [316]

$$C_e^\mu = C_e^\Lambda + \frac{3}{8\pi^2}\alpha_{\rm em}^2 \left(\frac{3}{8}\frac{C_W^\Lambda}{s_w^4} + \frac{5}{8}\frac{C_B^\Lambda}{c_w^4}\right) \log\frac{\Lambda^2}{\mu^2}\,, \tag{C.12}$$

which illustrates how the axion-electron coupling is induced radiatively from the axion-gauge couplings in (C.11). Evaluating (C.12) at the electroweak scale, $\mu = \Lambda_{\rm EW} \simeq 100$ GeV gives

$$C_e^\mu \approx C_e^\Lambda + (5.2\times 10^{-4})\, C_W^\Lambda + (7.9\times 10^{-5})\, C_B^\Lambda\,, \tag{C.13}$$

for typical values of $\Lambda \sim 10^{10}$ GeV.

Below the scale of electroweak symmetry breaking we are interested in the axion-photon coupling, $\mathcal{L} \supset -g_{a\gamma\gamma} a F\tilde{F}/4$ with $g_{a\gamma\gamma} = C_\gamma \alpha_{\rm em}/(2\pi f_a)$. To leading order we have $C_\gamma = C_W^\Lambda + C_B^\Lambda$, which illustrates how the axion-photon interaction arises at low energies from the axion-W_μ^a and/or axion-B_μ interactions in the UV. Thus, barring any accidental cancellations between the C_W and C_B terms, we anticipate a relation between the axion-electron and axion-photon couplings, which is

$$|C_e^\mu| \sim (5\times 10^{-4})\, |C_\gamma| \tag{C.14}$$

in the IR for theories where the axion-electron coupling is not present in the UV. Running the axion-electron coupling from the weak scale down to the electron mass scale, further enhances C_e by a factor of ∼1-2. Additionally, the case of the QCD axion is slightly more complicated since C_γ receives an IR contribution from pion mixing in that case. Therefore we simply use (C.14) for the following estimates.

In Fig. 4.2 we expressed our sensitivity in terms of $|g_{a\gamma\gamma}\, g_{aee}|$, and now by using the expression for C_e^μ from (C.14), we can map the sensitivity onto $g_{a\gamma\gamma}$ directly. A reasonable range of values for the axion-electron coupling is given by

$$(2 \times 10^{-4})\ |g_{a\gamma\gamma}|\ \text{GeV} \ < \ |g_{aee}| \ < \ 2.8 \times 10^{-13}\,. \tag{C.15}$$

The lower limit follows from (C.14) since $g_{aee} = C_e m_e / f_a$ and $g_{a\gamma\gamma} = \alpha_{\rm em} C_\gamma / 2\pi f_a$. The upper limit is an empirical 95% confidence constraint from modeling the WD luminosity function [30]. Using this range of values for g_{aee}, our sensitivity curves from Fig. 4.2 translate into bands, which are shown in Fig. C.7. We also show the CAST experiment's limit on the axion-photon coupling [27], and the predictions of the KSVZ and DFSZ models of the QCD axion. For $m_a \lesssim 10^{-5}$ eV our limit is comparable to the CAST 95% CL exclusion, even under the "pessimistic" assumption that g_{aee} is "minimal" as in (C.14), which leads to the weakest limit on $g_{a\gamma\gamma}$. On the other hand, dedicated *Chandra* observations would lead to a conservative upper limit on $g_{a\gamma\gamma}$ that is significantly stronger than the CAST bound at low masses. We also show an upper bound on $|g_{a\gamma\gamma}|$ from gamma-ray flux associated with SN1987a [40].

Our results also constrain the axion explanations of the very-high-energy gamma-ray transparency anomalies previously observed with Cherenkov telescope data [244, 430]. The gamma-ray observations indicate that the Universe is more transparent than previously thought to high-energy gamma-rays, and one explanation is that gamma-rays could oscillate into axions in astrophysical magnetic fields. The allowed parameter space from [244] to fit these anomalies is indicated in shaded gray in Fig. C.7, though we note that stringent constraints from *e.g.* the *Fermi* Large Area Telescope [195] and H.E.S.S. [229] also exist below $\sim$few $\times 10^{-8}$ eV. Furthermore, the transparency anomalies are subject to uncertainties from assumptions about galactic magnetic field models. Future dedicated observations of MWDs by *e.g. XMM-Newton* or *Chandra* would be able to probe much of the motivated parameter space to explain these anomalies.

For low-mass axions with $m_a \lesssim 10^{-6}$ eV, the upper limits on axion-matter couplings become insensitive to the axion's mass, m_a. We summarize these limits in Fig. C.8, where we also compare our limit with previous limits on the axion's coupling to photons, $g_{a\gamma\gamma}$ and the axion's coupling to electrons, g_{aee}.

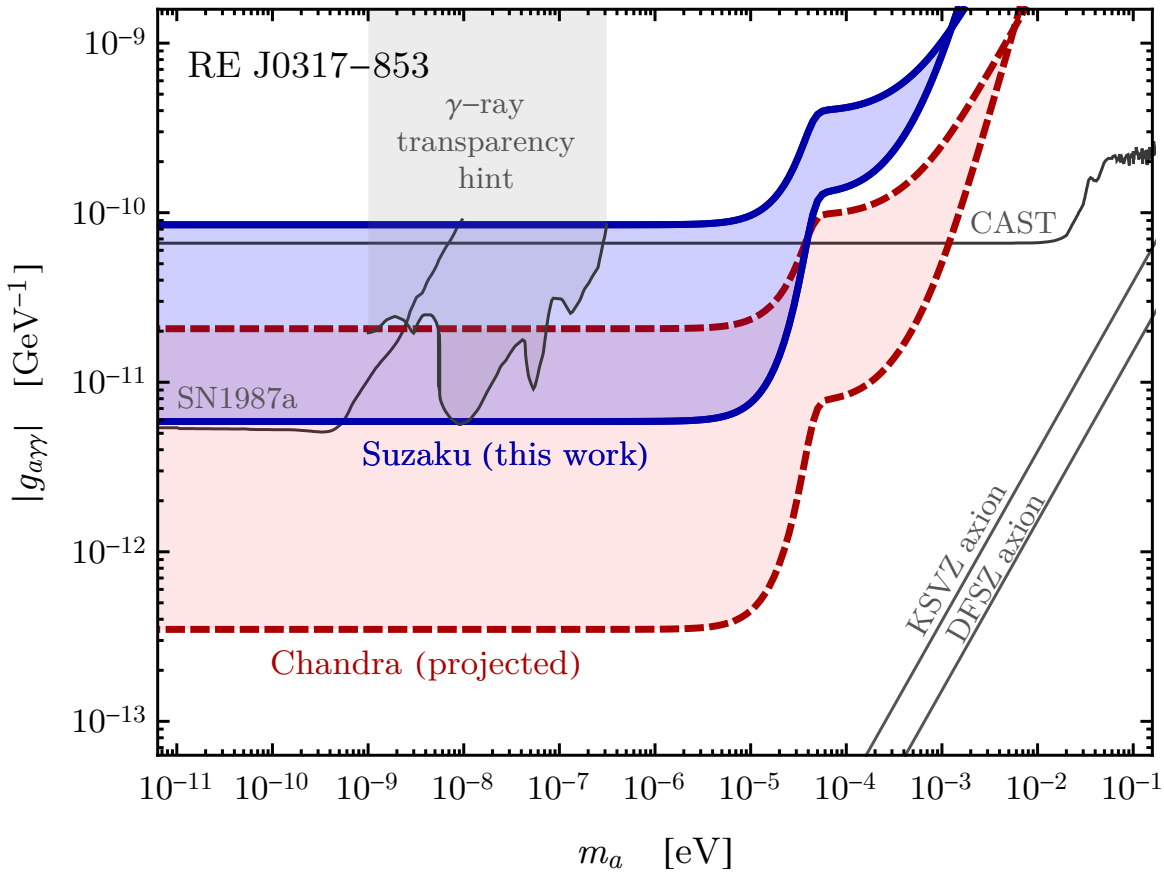

Figure C.7: Our upper limits (from *Suzaku* data and projected) on $|g_{a\gamma\gamma}\, g_{aee}|$ from the main chapter are expressed here as upper limits on $|g_{a\gamma\gamma}|$ alone by assuming a reasonable range of values for g_{aee}. For instance, the blue band is our upper limit on $|g_{a\gamma\gamma}|$ derived from *Suzaku* observations of RE J0317-853, which did not observe any X-ray flux. The upper (lower) edge of the band corresponds to the smaller (larger) value of g_{aee} in (C.15).

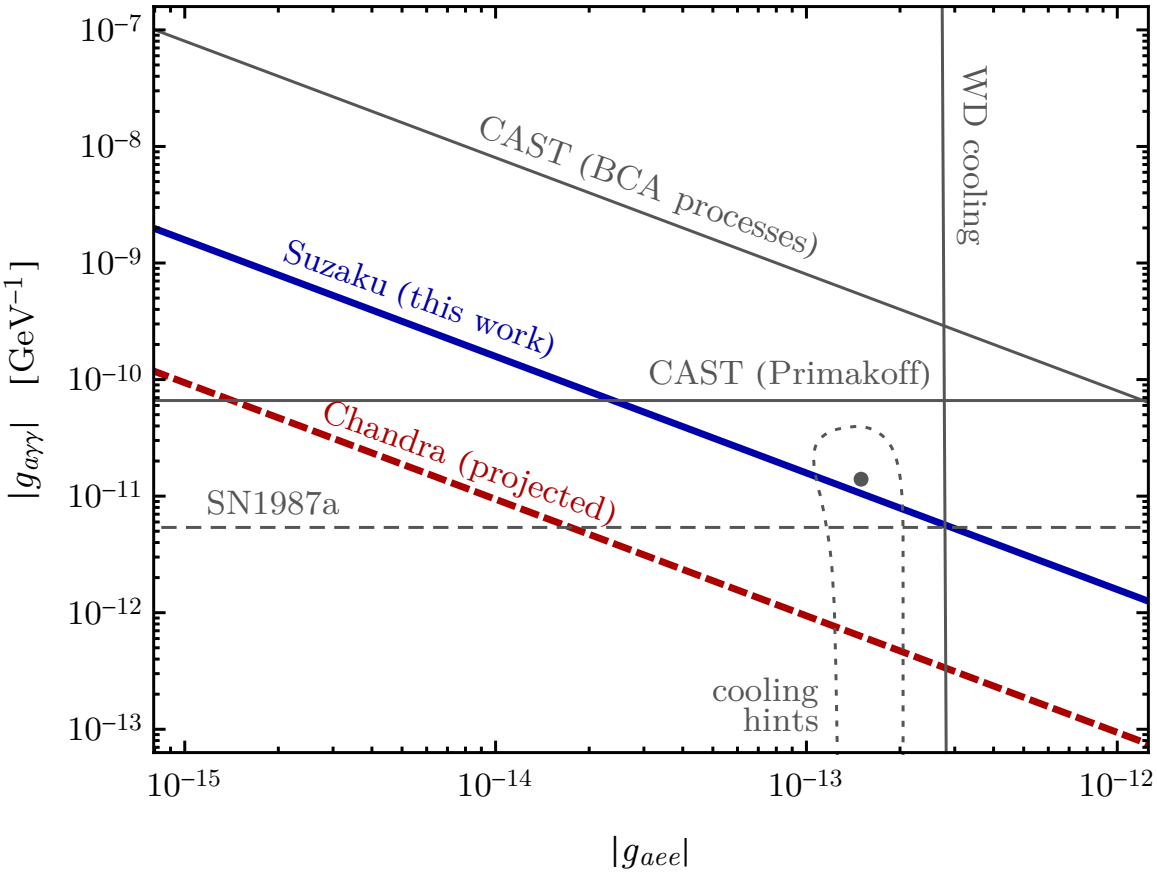

Figure C.8: This figures summarizes upper limits on the couplings of axions with photons and electrons for low mass axions where these limits become insensitive to m_a. The CAST helioscope provides both an upper limit on $|g_{a\gamma\gamma}|$ from axions produced in the Sun through the Primakoff process, as well as an upper limit on $|g_{a\gamma\gamma}g_{aee}|$ from axions produced through the BCA processes: bremstrahlung, Compton, and axio-recombination. We also highlight the region of parameter space that is favored by the various stellar cooling hints [33] with the best-fit point indicated with a gray dot, and the 1σ confidence region indicated by a gray-dotted curve. Observations of SN1987a [40] imply an upper limit on $|g_{a\gamma\gamma}|$ for $m_a < 10^{-9}$ eV at the level shown by the gray-dashed line, but this limit becomes weaker than the CAST limit above $m_a \approx 10^{-8}$ eV.

Appendix D

No Evidence for Axions from *Chandra* Observation of the Magnetic White Dwarf RE J0317-853

This chapter is organized as follows. Sec. D.1 provides Supplementary Figures that are referenced in the main chapter. Sec. D.2 gives further information on our data reduction and calibration procedure. In Sec. D.3 we review the renormalization group evolution of the axion-electron coupling to justify the values taken in the main chapter. In Sec. D.4 we describe our modeling procedure for the MWD in more detail. Sec. D.5 presents our calculation of the Electro-Primakoff axion production rate.

D.1 Supplementary Figures

In this section we illustrate Figs. D.1, D.2, D.3, and D.4, which are cited and described in the main chapter.

D.2 Data reduction and calibration

The data from the 37.42 ks *Chandra* ACIS-I `Timed Exposure` observation of RE J0317–853 (PI Safdi, observation ID `22326`) is reduced as follows. For the data reduction process, we use the Chandra Interactive Analysis of Observations (CIAO) [266] version 4.11. We reprocess the observation with the CIAO task `chandra_repro`, which produces an events file filtered for flares and updated for the most recent calibration. We create counts and exposure images (units [$\mathrm{cm}^2\mathrm{s}$]) with pixel sizes of $0\farcs492$ with `flux_image`.

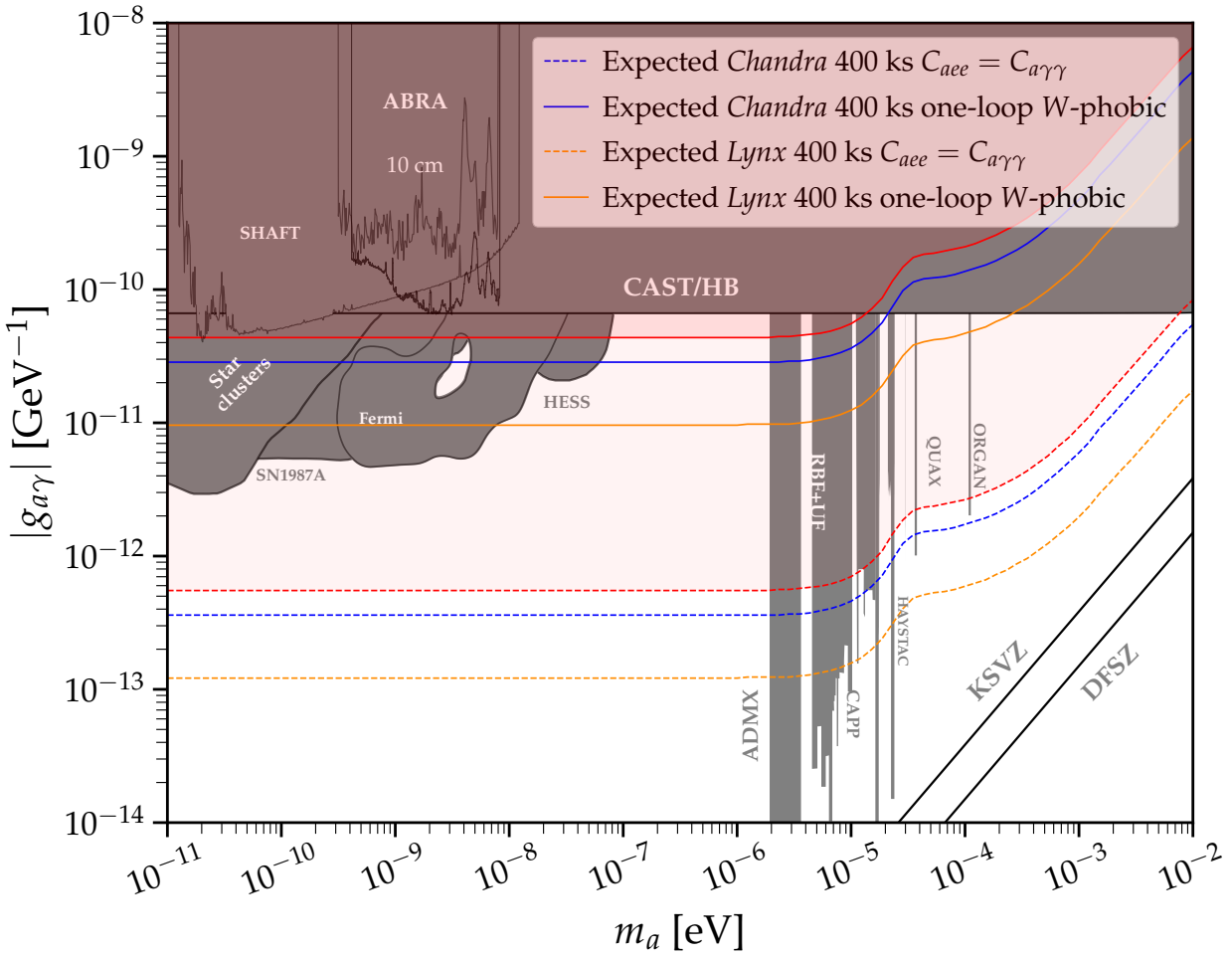

Figure D.1: As in Fig. 5.1 but projecting future sensitivity from deeper observations of RE J0317-853. A factor of 10 increase in *Chandra* exposure time would lead to the projected expected 95% upper limits indicated, while in the future the *Lynx* X-ray observatory will allow for a significant increase in sensitivity. Note that in this figure the axion-induced luminosity scales with the axion-photon coupling as $g_{a\gamma}^4$, so that in the no-background limit a factor of 10 increase in exposure time strengthens the limit by a factor $\sim$1.8. To generate the *Lynx* projections, we use the package SOXS to generate expected counts maps, exposure maps, and the *Lynx* PSF. We then run our *Chandra* pipeline with the *Lynx* files.

We account for the astrometric uncertainty of *Chandra*, which is expected to be on the order of 0.″5 [552], through the following procedure: we (i) run the point source (PS) finding algorithm `celldetect` on the full *Chandra* image to find high-significance PSs ($\gtrsim 10\sigma$ significance), and then (ii) cross-correlate these sources with the *Gaia* early data release 3 (EDR3) catalog [236] evolved to the Dec. 2020 epoch. (Note that there are no already-known X-ray sources within the field of view to use as references.) Two of the high-significance sources have nearby matches with *Gaia* sources (*Gaia* source IDs 4613614905421384320 and

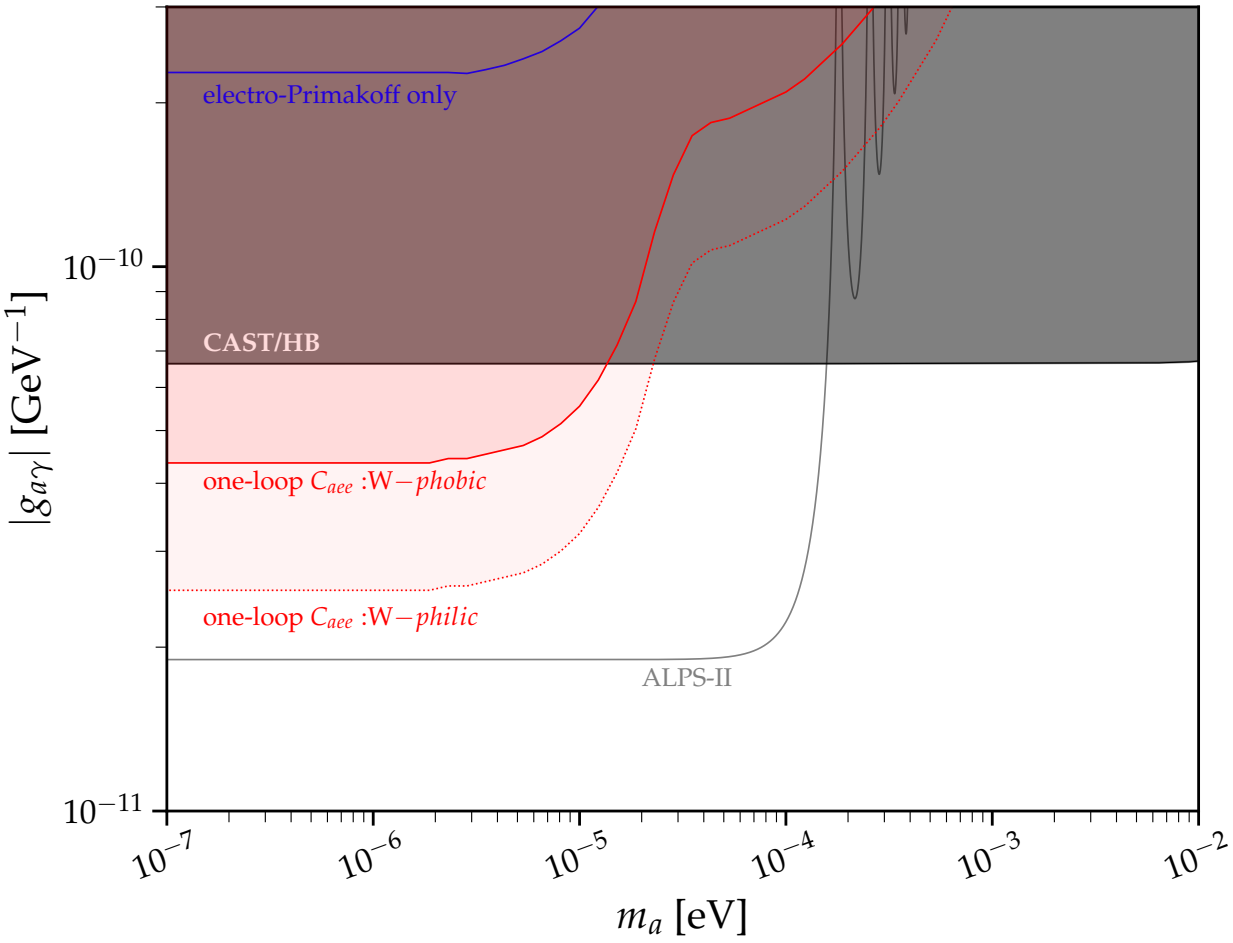

Figure D.2: As in Fig. 5.1 but showing the 95% upper limits from this chapter interpreted in the context of limits on $g_{a\gamma\gamma}$ assuming loop-induced couplings to C_{aee} for the W-phobic ($C_{aee} = 1.6 \times 10^{-4} C_{a\gamma\gamma}$) and W-philic ($C_{aee} = 4.8 \times 10^{-4} C_{a\gamma\gamma}$) UV completions. Models that couple to both $SU(2)_L$ and $U(1)_Y$ will generically have loop-induced couplings between these two extremes, assuming no fine-tuned cancellations (for example, models that couple in a way that preserve the Grand Unification group symmetry may have $C_{aee} \approx 2.7 \times 10^{-4} C_{a\gamma\gamma}$). Note that UV contributions to C_{aee} may also exist. We compare these limits to the projected sensitivity from the ALPS-II experiment. We also show our limits only accounting for the electro-Primakoff process, which does not involve C_{aee} – this process is seen to be subdominant compared to the bremsstrahlung process.

4613614974140862464). Although we were not able to verify the identity of these two sources from our observation, the Gaia sources both appear in the WISE catalog on active galactic nuclei [553], as J031629.01-852836.0 and J031821.59-852751.5 respectively. Both sources are localized by `celldetect` to within $\sim 0\farcs2$. However, both *Chandra* sources are displaced from their *Gaia* matches by $\sim 0\farcs6$ in approximately the same direction (the offset is $(0\farcs53, 0\farcs25)$ for

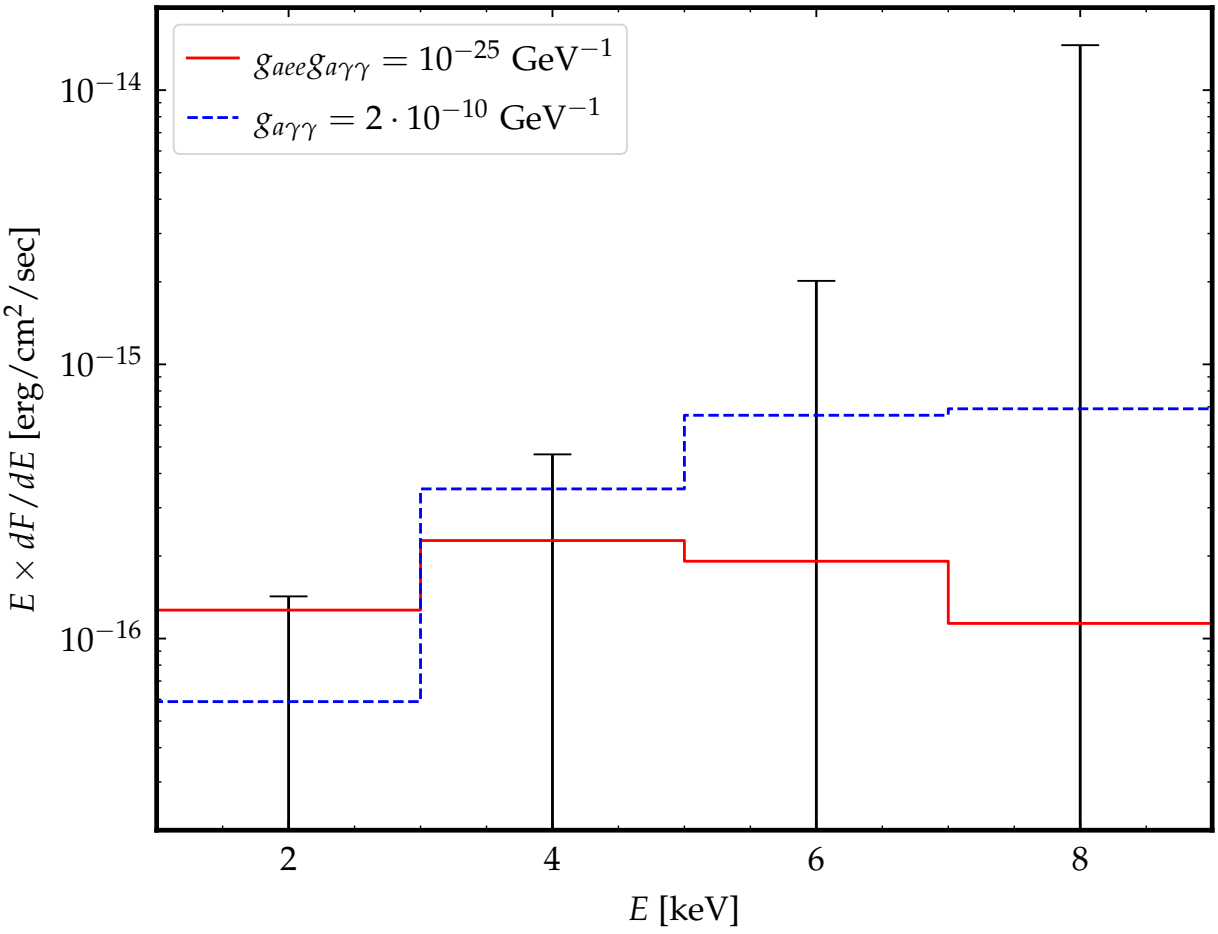

Figure D.3: As in Fig. C.6 but comparing the bremsstrahlung (red) and electro-Primakoff (dashed blue) production rates, for the indicated couplings.

one source and $(0''.57, -0''.05)$ for the other, in $(\mathrm{RA}\cos(\mathrm{DEC}), \mathrm{DEC})$. We average these two offsets to determine our overall calibration and shift all RA, DEC values accordingly. The uncalibrated location is shown in Fig. 5.2. Note that we cannot exclude the possibility that the *Chandra* PSs are falsely matched with the *Gaia* sources, though this appears less likely given that the two position offsets are nearly the same. Additionally, using the uncalibrated source location produces nearly identical results to using the calibrated location, since the calibration error is relatively minor and there are no photons in the vicinity of either location.

In addition to the calibration, we also account for the proper motion of the WD. In particular, RE J0317-853 was observed by *Gaia* in the EDR3 with location RA $\approx 49^\circ\, 18'\, 42''.51$, DEC $\approx -85^\circ\, 32'25''.75$ at the reference epoch of J2016.0 [236]. We use the proper motion measurements from *Gaia* to infer the position in December 2020, which accounts for the small shift between *Gaia* 2016 and Dec. 2020 shown in Fig. 5.2.

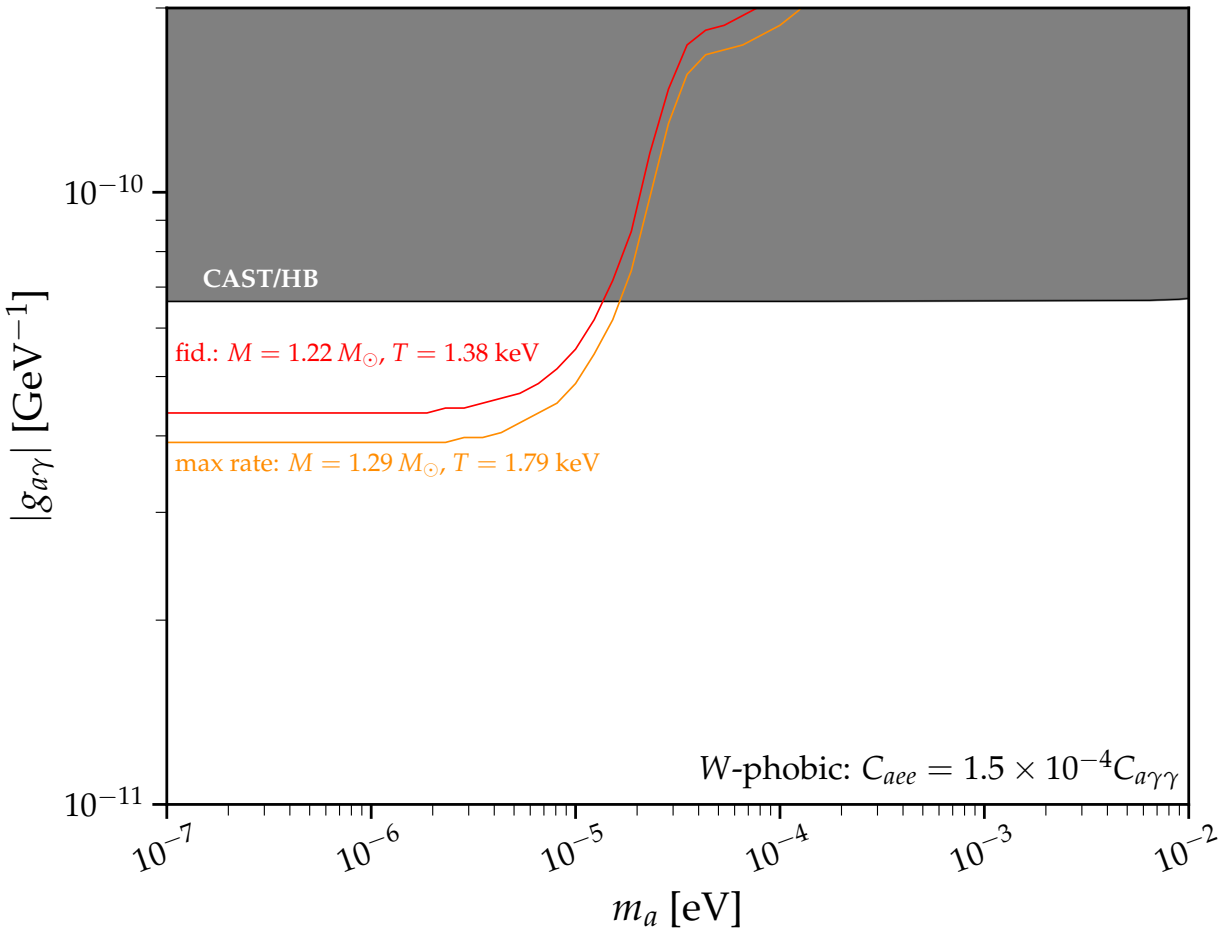

Figure D.4: As in Fig. 5.1 but comparing the W-phobic loop-induced upper limit (red) for our fiducial stellar model to that for the alternate stellar model that differs in two ways: (i) the MWD mass in assumed to be higher at 1.29 $M_\odot$, and (ii) the temperature is taken at the upper value of the 1σ containment interval from fitting the stellar model to the *Gaia* luminosity data. The difference between these two limits gives an estimate for the magnitude of the astrophysical uncertainties, which are around 10%.

D.3 Loop-induced axion-electron coupling

In this section we review the loop-induced axion-electron coupling in order to justify the fiducial values taken in the main chapter for the W-phobic and W-philic axion with no ultraviolet (UV) axion-electron coupling. Consider an axion-like particle that does not couple to QCD. The interactions of this axion with the Standard Model electroweak gauge fields and electrons are described by the effective field theory

$$\mathcal{L}_{a,\Lambda} \supset -\frac{1}{4} g^{\Lambda}_{aWW} a W\tilde{W} - \frac{1}{4} g^{\Lambda}_{aBB} a B\tilde{B} + \frac{C^{\Lambda}_e}{2} \frac{\partial_\mu a}{f_a} \bar{e}\gamma^\mu\gamma_5 e \,, \tag{D.1}$$

where the scale of new physics is denoted by $\Lambda \sim 4\pi f_a \sim 10^{10}$ GeV. Additionally $W \equiv W^a_{\mu\nu}$ is the $\mathrm{SU}(2)_L$ field strength tensor with coupling g, $B \equiv B_{\mu\nu}$ is the $\mathrm{U}(1)_Y$ field strength tensor with coupling g', $g^\Lambda_{aWW} = C^\Lambda_W g^2/(8\pi^2 f_a)$, and $g^\Lambda_{aBB} = C^\Lambda_B g'^2/(8\pi^2 f_a)$. The parameters C^Λ_W, C^Λ_B, and C^Λ_e are dimensionless constants that parameterize the UV theory. Recall that under the renormalization group and at energy scales $\mu > M_Z$, with M_Z the mass of the Z-boson,

$$\frac{\mu\, dC^\mu_e}{d\mu} = -\frac{3}{64\pi^4}\left(\frac{3}{8}g^4 C^\Lambda_W + \frac{5}{8}g'^4 C^\Lambda_B\right), \tag{D.2}$$

where C^μ_e is the dimensionless axion-electron coupling at energy scale $\mu < \Lambda$, with Λ the UV cutoff [176, 222, 243, 554]. These beta functions can be derived from the Feynman graphs in Fig. D.5. The dimensionless axion couplings to weak isospin and hypercharge are denoted by C^Λ_W and C^Λ_B, respectively. Note that these couplings are topologically protected and do not evolve under the renormalization group.

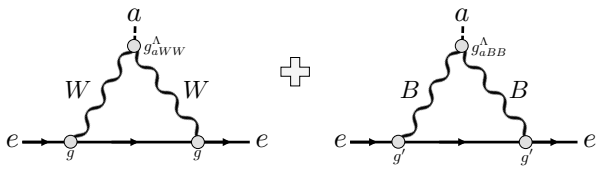

Figure D.5: Feynman graphs used to evaluate the loop-induced axion-electron coupling. A sum over the SU(2) isospin index is performed.

It is common to integrate (D.2) down to M_Z and yet take g and g' to be their low-energy values, at scales well below M_Z. Below M_Z the axion-electron coupling continues to evolve under the renormalization group equation

$$\frac{\mu\, dC^\mu_e}{d\mu} = -\frac{3}{4\pi^2}\alpha^2_{\mathrm{EM}}(C^\Lambda_W + C^\Lambda_B)\,, \tag{D.3}$$

and this contribution to C_e at the scale $\mu = m_e$ is also typically found by integrating (D.3) and taking α_{EM} to be the value at the scale m_e. Here, we do not complete a full two-loop computation of C_e but we try to be slightly more precise by accounting for the running of α_{EM}, g, and g'. To one-loop and within the Standard Model these couplings evolve as

$$\frac{\mu\, dg_i}{d\mu} = \frac{b_i}{(4\pi)^2} g_i^3\,, \tag{D.4}$$

with $g_1 = \sqrt{5/3}g'$, $g_2 = g$, $b_1 = 41/10$, and $b_2 = -19/6$. Integrating (D.2) in conjunction

with (D.4) from the UV scale Λ down to the electroweak scale M_Z leads to the result

$$C_e^{M_Z} = C_e^{\Lambda} + \frac{3}{128\pi^4} \log \frac{\Lambda^2}{M_Z^2} \left(\frac{3}{8} C_W^{\Lambda} \left[g(M_Z) g(\Lambda) \right]^2 + \frac{5}{8} C_B^{\Lambda} \left[g'(M_Z) g'(\Lambda) \right]^2 \right) , \tag{D.5}$$

where $g(M_Z)$ denotes the coupling at energy scale M_Z, while $g(\Lambda)$ is the coupling at the UV scale and similarly for g'. At the Z-pole $\alpha_{\rm EM}(M_Z) \approx 1/127$ and $\sin^2\theta_W \approx 0.231$, with θ_W the Weinberg angle. Taking a benchmark value $\Lambda = 10^9$ GeV we then find

$$C_e^{M_Z} \approx C_e^{\Lambda} + 4.2 \times 10^{-4} C_W^{\Lambda} + 9.8 \times 10^{-5} C_B^{\Lambda} \, . \tag{D.6}$$

Accounting for the running of $\alpha_{\rm EM}$ from M_Z down to the electron mass we then find

$$C_e^{m_e} \approx C_e^{\Lambda} + 4.8 \times 10^{-4} C_W^{\Lambda} + 1.6 \times 10^{-4} C_B^{\Lambda} \, . \tag{D.7}$$

Note that the axion-photon coupling is defined by $C_{a\gamma\gamma} = C_W^{\Lambda} + C_B^{\Lambda}$. To be conservative, in our fiducial loop-induced model we consider a "W-phobic" axion and take $C_W^{\Lambda} = 0$ such that $C_{aee} \approx 1.6 \times 10^{-4} C_{a\gamma\gamma}$. We do note, though, with some amount of fine tuning the loop-induced contribution could be made smaller. For example, if $C_W^{\Lambda} \approx -0.33\, C_B^{\Lambda}$ then the two contributions to $C_e^{m_e}$ would roughly cancel each other. We do not consider this possibility further because it would require a conspiracy between the UV and IR contributions to the running. Note, also, that the relations in (D.7) could be modified by the existence of beyond the Standard Model physics below the UV cutoff $\sim 10^9$ GeV. We also remark that an axion-photon coupling $C_{a\gamma\gamma} \sim C_{aee}$ can be generated from a UV pseudoscalar axion-electron coupling of the form $\mathcal{L}_{\rm int} \propto a \bar{e} \gamma_5 e$ (see, *e.g.*, [554]).

Lastly, note that the arguments in this section are specific to axion-like particles with no couplings to QCD. In particular, the minimal KSVZ axion model has no infrared axion-electron coupling but a non-zero infrared axion-photon coupling, seemingly violating the arguments presented in this section. However, this is because in that model there is no UV coupling of the axion to electroweak bosons; the coupling between the axion and the photon arises below the QCD confinement scale from mixing between the axion and the neutral pion. Axion-like-particle models, on the other hand, necessarily have ultraviolet couplings to electroweak gauge bosons.

D.4 Modeling RE J0317–853

In this section we detail our modeling of the interior of RE J0317-853. To compute the axion luminosity, we need to know the core temperature, the density profile, and the composition profiles. Note that we assume the core temperature is uniform throughout the interior due to the high thermal conductivity of the degenerate matter, while the density and composition can change throughout the interior.

We analyze WD cooling sequences [239] to infer the core temperature of RE J0317-853. These cooling sequences are improved over older ones in that they take ionic correlations into account, which are expected to be important for RE J0317-853 due to its high mass and low surface temperature. Included with the sequences are corresponding *Gaia* DR2 G, $G_{\rm BP}$, and $G_{\rm RP}$ band absolute magnitudes as a function of cooling age. The sequences are available for WD masses of 1.10, 1.16, 1.22, and $1.29 M_\odot$.

RE J0317-853's measured apparent magnitudes in the DR2 *Gaia* dataset [240] are

$$\begin{aligned} G &= 14.779 \pm 0.005 \\ G_{\rm BP} &= 14.565 \pm 0.017 \\ G_{\rm RP} &= 14.987 \pm 0.012 \end{aligned} \tag{D.8}$$

where we have converted linear errors on flux to linear errors on magnitude. For reference, the G-band covers wavelengths between ∼300 and ∼1100 nm, $G_{\rm BP}$ between ∼300 and ∼700 nm, and $G_{\rm RP}$ between ∼600 and ∼1100 nm, although with wavelength-dependent efficiencies. Note we use EDR3 astrometric and distance data elsewhere in this chapter, but there do not yet exist cooling sequences incorporating EDR3 bands. We infer the core temperature T_c of RE J0317-853 with a joint Gaussian likelihood over the three bands as a function of cooling age t for each WD mass available. We find that the $1.22 M_\odot$ model provides the best fit to the data, as shown in the left panel of Fig. D.6. Note that this is a lower mass for RE J0317-853 than previously inferred, but it is a conservative choice with respect to the $1.29 M_\odot$ model, which is closer to previous mass estimates [238].

In the right panel of Fig. D.6, we show the resulting likelihood profile as a function of T_c for the best-fit $1.22 M_\odot$ model. The $\pm 1\sigma$ ages are extracted by solving for the age where $\Delta\chi^2$ increases by 1 on each side of the best-fit point. We find $t = 0.369 \pm 0.003$ Gyr, corresponding to a core temperature $T_c = 1.388 \pm 0.005$ keV. We adopt the lower 1σ value of $T_c = 1.383$ keV in our fiducial analysis to be conservative. We also show the axion luminosity, for which changes are minor over the range considered.

The 1.29 $M_\odot$ model is disfavored in our analysis relative to the 1.22 $M_\odot$ model at a level

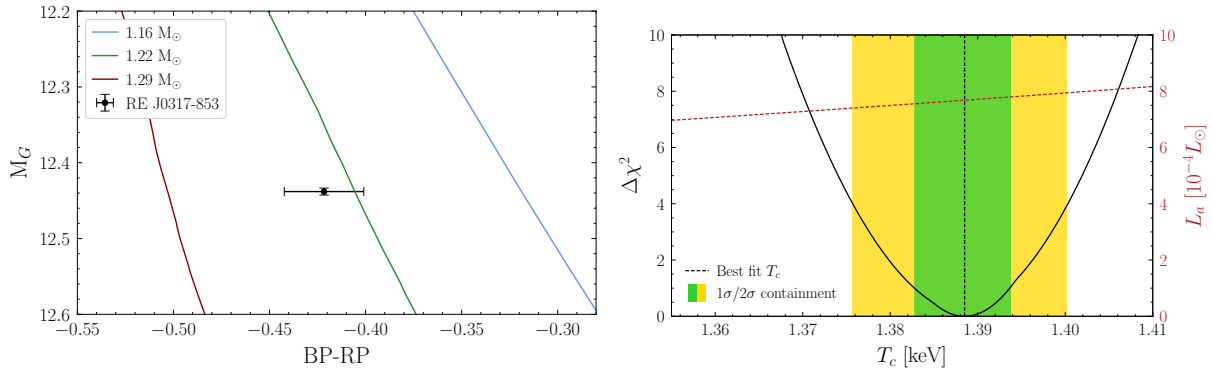

Figure D.6: (Left) A color-magnitude diagram with RE J0317-853's *Gaia* DR2 data shown with the black error bars. We show the curves predicted by the cooling simulation for three masses: 1.16, 1.22, and $1.29 M_\odot$. Note that M_G refers to the absolute G-band magnitude, while the color $\mathrm{BP} - \mathrm{RP} = G_{\mathrm{BP}} - G_{\mathrm{RP}}$. (Right) The likelihood profile for the $1.22 M_\odot$ model as a function of T_c. The best fit T_c is shown as the dashed vertical line, while the 1 and 2σ containment regions on T_c are shown as green and yellow bands, respectively. We also show, on the right y-axis, the axion luminosity (dashed red) as a function of T_c for $g_{aee} = 10^{-13}$.

$\sim 5\sigma$ (the measured G_{BP} and G_{RP} are in tension with the model expectations). Therefore, when we determine the properties of RE J0317-853 in the context of the 1.29 $M_\odot$ model, we broaden the likelihood profile so that at the best-fit point, $\Delta\chi^2/\mathrm{dof} = 1$. We find a lower cooling age of 0.301 ± 0.008 Gyr and a higher $T_c = 1.77 \pm 0.02$ keV by following the same procedure. SM Fig. D.4 compares our limits computed using the fiducial model and the 1.29 $M_\odot$ model, with T_c at the upper end of the 1σ band; the differences are seen to be minor, indicating that our results are likely not significantly affected by astrophysical mismodeling.

We run simulations with MESA from which we determine the density and composition profiles for RE J0317-853. MESA is a 1-dimensional modular stellar modeling code that outputs these profiles, along with others, as a function of time since stellar birth. We use the default parameters from the test suite inlist `make_o_ne_wd`, but change the initial stellar mass to 11.1 (11.9) $M_\odot$, which produces a 1.22 (1.29) $M_\odot$ WD. We evolve the star through the pre-WD stages and allow it to cool until its luminosity reaches $10^{-3} L_\odot$.

We then select the model for which the stellar luminosity matches the observed value and choose the profiles corresponding to this model, shown in Fig. D.7, to be our fiducial density and composition profiles. We find that the core is predominantly oxygen and neon as expected for an isolated WD of its mass, and reaches densities $\rho > 10^6$ g/cm^3, which means that the electron gas is strongly correlated. For $\rho \gtrsim 10^7$ g/cm^3, the interior transitions to the lattice phase, which tends to reduce the axion emissivity. In the left panel of Fig. D.8, we show the value of F as defined in (5.3) across the profile of the star for the four dominant

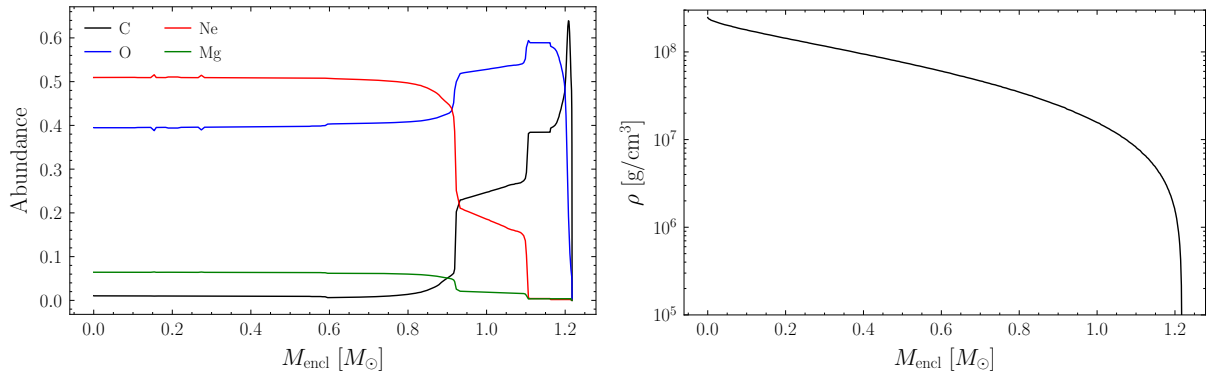

Figure D.7: (Left) The carbon, oxygen, neon, and magnesium mass abundances in the MESA simulation for the model most closely matching the observed luminosity of RE J0317-853. The x-axis is the mass coordinate *i.e.*, enclosed mass. (Right) The density profile in [g/cm^3] for the same model as a function of mass coordinate.

ions in our WD model. The discontinuities in the profiles (except carbon) are due to the transition from the liquid phase to the lattice ion structure in the inner core of the WD. In general, F decreases with increasing density, although because the axion emissivity $\varepsilon_a \sim \rho F$, the center of the star is still the most emissive. Note that in the analytic fitting formulas of [66] to F_s in a multi-component mixture there is a choice to be made in whether the density is taken to be ρ or ρ_s; we conservatively assume the former as the latter leads to an $\sim$18% increase in axion luminosity.

Note that our choice of test suite is not the driving force behind why our WD is modeled as having an oxygen-neon core–this is simply because, under the assumption of single-star evolution, the initial stellar mass of the WD progenitor is high enough so that the star depletes its core carbon on the asymptotic giant branch (this is the case for WDs with masses $\gtrsim 1.1 M_\odot$ [239, 467]). If the star has evolved from a binary channel, then it may host a carbon-oxygen core instead. However, we consider this to be unlikely, as [238] finds that if RE J0317-853 has an effective temperature $\lesssim$40000 K, the single-star evolution is more likely. Indeed, our *Gaia* analysis prefers an effective temperature 25570 ± 50 K. Note that although RE J0317-853 has a binary companion, they are too far apart to have interacted [238].

Given the core temperature, the density profile, and composition profiles, we have the tools to compute the axion luminosity of RE J0317-853 due to both axion bremsstrahlung and electro-Primakoff. We compute the axion emissivity at each radial slice in the MESA-generated profiles and integrate over the star to obtain the axion luminosity spectrum $dL_a/d\omega$ (in, *e.g.*, ergs/s/keV) as

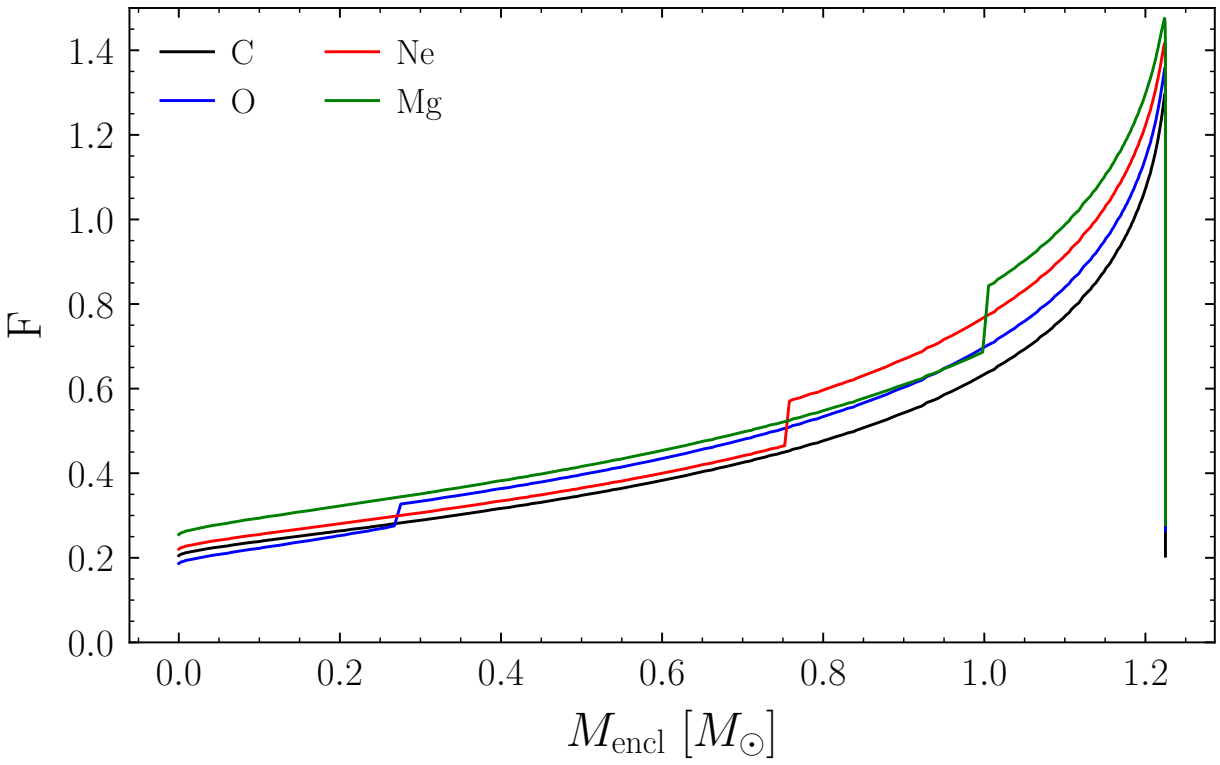

Figure D.8: (Left) The F-profile evaluated for the 1.22 $M_\odot$ star, evaluated using the parametrization provided by [66], considered in our emissivity calculation. (Right) The sum in (5.3) evaluated for both mass models (1.22 $M_\odot$ and 1.29 $M_\odot$).

$$\frac{dL_a}{d\omega}(\omega) = 4\pi \int_0^R r^2 dr \frac{d\varepsilon_a}{d\omega}(r) \tag{D.9}$$

for a stellar radius R. For axion bremsstrahlung, $d\varepsilon_a/d\omega$ is computed using (5.3); for electro-Primakoff, (D.30). Because of the geometric factors in the integrand in (D.9) that suppress the contribution from the stellar core, the axion luminosity profile dL_a/dr peaks around half the WD radius.

For our fiducial analysis, we model the magnetic field as a dipole field of strength 200 MG at the pole. To compute the axion-photon conversion probability $p_{a\to\gamma}(\omega)$, we follow the formalism developed in [222]. The axion-induced photon flux $dF_{\gamma_a}/d\omega$ at Earth is then

$$\frac{dF_{\gamma_a}}{d\omega}(\omega) = \frac{dL_a}{d\omega}(\omega) \times p_{a\to\gamma}(\omega) \times \frac{1}{4\pi d_{\rm WD}^2}. \tag{D.10}$$

In Fig. D.9 we show the expected signal for fiducial values of the axion-photon and axion-electron couplings in the four energy bins. The upper left panel shows the axion energy spectrum from the WD at the fiducial parameters in our analysis $M_{\rm WD} = 1.22 M_\odot$, $T_{\rm core} = 1.38$ keV, and $B_0 = 200$ MG for a massless axion with $g_{aee} = 10^{-13}$. The upper right panel shows the conversion probability for the same parameters with $g_{a\gamma\gamma} = 10^{-12}$ GeV^{-1}. In the lower left panel, we plot the average effective area of the *Chandra* telescope in each bin. Finally, the lower right panel plots the expected count rate in our observation at the combination of the two couplings $g_{aee} g_{a\gamma\gamma} = 10^{-25}$ GeV^{-1}.

D.5 Electro-Primakoff Axion Production

This section provides a derivation of the axion emissivity from the core of a WD from the electro-Primakoff production mechanism. Note that while the bremsstrahlung process dominates for our MWD, the electro-Primakoff process may be important for WDs with higher core temperatures, and this computation has not appeared elsewhere. We broadly follow the approach presented in [212] for similar emissivity calculations.

D.5.1 Cross section

Consider the scattering of an electron e and a nucleus $N = (A, Z)$ that results in the emission of an axion a:

$$e(\boldsymbol{p}_1, s_1) + N(\boldsymbol{p}_2, s_2) \to e(\boldsymbol{p}_3, s_3) + N(\boldsymbol{p}_4, s_4) + a(\boldsymbol{k}) \,. \tag{D.11}$$

If the axion-photon coupling is dominant, then axion production is dominated by the electro-Primakoff channel. The leading-order Feynman graph is shown in Fig. D.10, and the corresponding matrix element is

$$\begin{aligned} \mathcal{M} = &\left[\bar{u}_e(p_3, s_3)(+ie)\gamma^\mu u_e(p_1, s_1)\right]\left[-\frac{i g_{\mu\rho}}{(p_1 - p_3)^2 + i\epsilon}\right]\left[-i g_{a\gamma\gamma}\epsilon^{\rho\sigma\alpha\beta}(p_1 - p_3)_\alpha (p_2 - p_4)_\beta\right] \\ &\times \left[-\frac{i g_{\sigma\nu}}{(p_2 - p_4)^2 + i\epsilon}\right]\left[\bar{u}_N(p_4, s_4)(-iZe)\gamma^\nu u_N(p_2, s_2)\right] \,. \end{aligned} \tag{D.12}$$

Note that the amplitude vanishes as $\omega = k^0 \to 0$, since 4-momentum conservation implies $\epsilon^{\rho\sigma\alpha\beta}(p_1 - p_3)_\alpha (p_2 - p_4)_\beta = \epsilon^{\rho\sigma\alpha\beta}(p_1 - p_3)_\alpha k_\beta$. The spin-averaged, squared matrix element is given by $\overline{|\mathcal{M}|^2} = (g_e g_N)^{-1} \sum_s |\mathcal{M}|^2$ where $g_e = g_N = 2$ counts the two spin states of the electron and the nucleus.

The differential cross section for axion emission is calculated from the squared matrix element as

$$\mathrm{d}\sigma = \frac{1}{4F_{aN}(p_1,p_2)}\,\mathrm{d}\Pi_e(\boldsymbol{p}_3)\,\mathrm{d}\Pi_N(\boldsymbol{p}_4)\,\mathrm{d}\Pi_a(\boldsymbol{k})\;(2\pi)^4\,\delta(p_1+p_2-p_3-p_4-k)\;|\mathcal{M}|^2 \tag{D.13}$$

where the Lorentz-invariant flux factor is $F_{aN}(p_1,p_2) = [(p_1\cdot p_2)^2 - m_e^2 m_N^2]^{1/2}$, and where the Lorentz-invariant phase space volume element is $\mathrm{d}\Pi_s(\boldsymbol{p}) = \mathrm{d}^3\boldsymbol{p}/(2\pi)^3/2E_s(\boldsymbol{p})$ for $s = e, N, a$. All 4-momenta are evaluated on shell with $p^0 = E_s(\boldsymbol{p}) = [\boldsymbol{p}^2 + m_s^2]^{1/2}$.

D.5.2 Thermal-averaging

The thermal environment leads to Pauli-blocking and Bose-enhancement of the final-state particles. We take this into account by defining the thermally-suppressed/enhanced differential cross section

$$\mathrm{d}\tilde{\sigma} = \mathrm{d}\sigma\;\big(1-f_e(\boldsymbol{p}_3)\big)\,\big(1-f_N(\boldsymbol{p}_4)\big)\,\big(1+f_a(\boldsymbol{k})\big) \tag{D.14}$$

where f_e, f_N, and f_a are the phase space distribution functions for electrons, nuclei, and axions, respectively. The electrons are in equilibrium and their distribution function (in the rest frame of the plasma) is given by the Fermi-Dirac distribution

$$f_e(\boldsymbol{p}) = \big(e^{[E_e(\boldsymbol{p})-\mu_e]/T_e}+1\big)^{-1}\;, \tag{D.15a}$$

where T_e and μ_e are the electrons' temperature and chemical potential. The nuclei are also in thermal equilibrium, and we could also write their distribution function as a Fermi-Dirac distribution. However, since their temperature is so low, $T_N \ll m_N$, it turns out that the nuclei are effectively at rest $v_N \sim \sqrt{T/m_N} \ll 1$. To a good approximation we can write the nuclei phase space distribution function (in the rest frame of the plasma) as

$$f_N(\boldsymbol{p}) = \frac{n_N}{g_N}\;(2\pi)^3\delta(\boldsymbol{p})\;, \tag{D.15b}$$

where n_N is the total number density of nuclei and $g_N = 2$ counts the two spin states. This also lets us approximate $1 - f_N \approx 1$ in (D.14). Finally the axions are out of thermal equilibrium, and their distribution function satisfies

$$f_a(\boldsymbol{p}) \ll 1 \,, \tag{D.15c}$$

and we can approximate $1 + f_a \approx 1$ in (D.14).

D.5.3 Axion emissivity

Using the differential cross section from (D.14), we construct the thermally-suppressed/enhanced differential scattering rate density, which is

$$\mathrm{d}\tilde{\gamma} = \frac{\mathrm{d}\tilde{\sigma}}{g_e\, g_N}\, v_{\mathrm{Mol}}\, \mathrm{d}n_e(\boldsymbol{p}_1)\, \mathrm{d}n_N(\boldsymbol{p}_2)\,, \tag{D.16}$$

where the Moller velocity is $v_{\mathrm{Mol}}(\boldsymbol{p}_1, \boldsymbol{p}_2) = F_{aN}(p_1, p_2)/E_a(\boldsymbol{p}_1)E_N(\boldsymbol{p}_2)$, where the thermally-weighted differential number density of incident particles is $\mathrm{d}n_s(\boldsymbol{p}) = g_s \mathrm{d}^3\boldsymbol{p}\, f_s(\boldsymbol{p})/(2\pi)^3$ for $s = e, N$, and where $g_e = g_N = 2$ counts the redundant internal degrees of freedom (spin). The differential axion emissivity (in the rest frame of the plasma) is

$$\mathrm{d}\varepsilon_a = \sum_{\text{spins}} \mathrm{d}\tilde{\gamma}\; E_a(\boldsymbol{k})\,, \tag{D.17}$$

where we multiply by the axion energy and sum over the spins of all the particles. Using the expression for $\mathrm{d}\tilde{\gamma}$ gives

$$\begin{aligned}
\mathrm{d}\varepsilon_a = \frac{g_e g_N}{32} & \frac{\mathrm{d}^3\boldsymbol{p}_1}{(2\pi)^3} \frac{\mathrm{d}^3\boldsymbol{p}_2}{(2\pi)^3} \frac{\mathrm{d}^3\boldsymbol{p}_3}{(2\pi)^3} \frac{\mathrm{d}^3\boldsymbol{p}_4}{(2\pi)^3} \frac{\mathrm{d}^3\boldsymbol{k}}{(2\pi)^3} \\
& \times (2\pi)\, \delta\big(E_e(\boldsymbol{p}_1) + E_N(\boldsymbol{p}_2) - E_e(\boldsymbol{p}_3) - E_N(\boldsymbol{p}_4) - E_a(\boldsymbol{k})\big) \\
& \times (2\pi)^3\, \delta(\boldsymbol{p}_1 + \boldsymbol{p}_2 - \boldsymbol{p}_3 - \boldsymbol{p}_4 - \boldsymbol{k}) \\
& \times f_e(\boldsymbol{p}_1)\, f_N(\boldsymbol{p}_2)\, \big(1 - f_e(\boldsymbol{p}_3)\big)\, \big(1 - f_N(\boldsymbol{p}_4)\big)\, \big(1 + f_a(\boldsymbol{k})\big) \\
& \times \frac{\overline{|\mathcal{M}|^2}}{E_e(\boldsymbol{p}_1)\; E_N(\boldsymbol{p}_2)\; E_e(\boldsymbol{p}_3)\; E_N(\boldsymbol{p}_4)}
\end{aligned} \tag{D.18}$$

where the factors of E_a have cancelled, and all 4-momenta are on-shell.

D.5.4 Evaluating phase space integrals

To calculate the emissivity, we evaluate the phase space integrals as follows. First, we use the momentum-conserving Dirac delta function to evaluate the integral over the recoiling nucleus's momentum, which sets $\boldsymbol{p}_4 = \boldsymbol{p}_1 + \boldsymbol{p}_2 - \boldsymbol{p}_3 - \boldsymbol{k}$. Next we write $\boldsymbol{p}_1$, $\boldsymbol{p}_3$, and $\boldsymbol{k}$ in polar coordinates,

$$\begin{aligned} \mathrm{d}^3\boldsymbol{p}_1 &= p_1^2 \mathrm{d}p_1 \, \mathrm{d}\Omega_1 = p_i \, E_i \, \mathrm{d}E_i \, \mathrm{d}\Omega_i \\ \mathrm{d}^3\boldsymbol{p}_3 &= p_3^2 \mathrm{d}p_3 \, \mathrm{d}\Omega_3 = p_f \, E_f \, \mathrm{d}E_f \, \mathrm{d}\Omega_f \\ \mathrm{d}^3\boldsymbol{k} &= k^2 \mathrm{d}k \, \mathrm{d}\Omega_a = k \, \omega \, \mathrm{d}\omega \, \mathrm{d}\Omega_a \end{aligned} \tag{D.19}$$

where i denotes the initial-state electron, f denotes the final-state electron, and $\omega = E_a(\boldsymbol{k})$. We use the remaining Dirac delta function to evaluate the integral over E_f, which gives

$$\begin{aligned} \mathrm{d}\varepsilon_a = \frac{g_e g_N}{128\pi^5} \, \mathrm{d}E_i \, \frac{\mathrm{d}\Omega_i}{4\pi} \, \frac{\mathrm{d}^3\boldsymbol{p}_2}{(2\pi)^3} \, \frac{\mathrm{d}\Omega_f}{4\pi} \, \mathrm{d}\omega \, \frac{\mathrm{d}\Omega_a}{4\pi} \\ \times f_e(E_i) \, f_N(\boldsymbol{p}_2) \left(1 - f_e(E_f)\right) \left(1 - f_N(\boldsymbol{p}_4)\right) \left(1 + f_a(\omega)\right) \\ \times \frac{p_i \, p_f \, k \, \omega}{E_N(\boldsymbol{p}_2) \, E_N(\boldsymbol{p}_4)} \, \overline{|\mathcal{M}|^2} \, . \end{aligned} \tag{D.20}$$

Next we make use of the distribution functions in (D.15). These let us approximate $1 - f_N \approx 1$ and $1 + f_a \approx 1$. Additionally, $f_N \propto \delta(\boldsymbol{p})$ and the $\boldsymbol{p}_2$ integral sets $\boldsymbol{p}_2 = 0$. Finally we note that the scattering is statistically isotropic, since the distributions of incident particles have no preferred direction. It suffices to suppose that Ω_f and Ω_a are measured with respect to Ω_i, which is then treated as the orientation of the polar axis. Then the integral over Ω_i reduces to the trivial integral over the polar axis (net rotation of the whole system), which just gives $\int \mathrm{d}\Omega_i = 4\pi$, and

$$\mathrm{d}\varepsilon_a = \frac{g_e n_N}{128\pi^5} \, \mathrm{d}E_i \, \frac{\mathrm{d}\Omega_f}{4\pi} \, \mathrm{d}\omega \, \frac{\mathrm{d}\Omega_a}{4\pi} \, f_e(E_i) \left(1 - f_e(E_f)\right) \, \frac{p_i \, p_f \, k \, \omega}{m_N \, E_N(\boldsymbol{p}_4)} \, \overline{|\mathcal{M}|^2} \, . \tag{D.21}$$

To evaluate the squared matrix element, we approximate $m_a \approx 0$ implying $\omega \approx |\boldsymbol{k}|$. We can also approximate the recoiling nucleus as non-relativistic, implying $E_4 \approx m_N + \boldsymbol{p}_4^2/(2m_N)$, and here it is important to keep the sub-leading term in the energy expansion, since the would-be leading order contribution to the squared matrix element cancels. Then the squared

matrix element reduces to

$$\overline{|\mathcal{M}|^2} \approx \frac{(Z g_{a\gamma\gamma} e^2)^2}{g_e\, g_N}\, \frac{32 m_N^2 \omega^2}{q_{13}^4\, q_{24}^4} \Big[\big(2c_{if}c_{ia}c_{fa}p_i^2p_f^2 - 2c_{fa}^2 p_i^2 p_f^2 - c_{if}p_i^3 p_f s_{ia}^2 + 2p_i^2p_f^2 s_{ia}^2 - c_{if}p_i p_f^3 s_{fa}^2\big) + m_e^2\big(2c_{if}p_ip_f - 2c_{ia}c_{fa}p_ip_f - p_i^2 s_{ia}^2 - p_f^2 s_{fa}^2\big) + E_iE_f\big(-2c_{if}p_ip_f + 2c_{ia}c_{fa}p_ip_f + p_i^2 s_{ia}^2 + p_f^2 s_{fa}^2\big)\Big] \tag{D.22}$$

where we have dropped terms that are $O(m_N^1)$. Here we have also written $\boldsymbol{p}_1 \cdot \boldsymbol{p}_3 = p_i p_f c_{if}$ and $\boldsymbol{p}_1 \cdot \boldsymbol{k} = p_i \omega c_{ia}$ and $\boldsymbol{p}_3 \cdot \boldsymbol{k} = p_f \omega c_{fa}$. The momentum transfers are

$$\begin{aligned} q_{13}^2 &= (p_1 - p_3)^2 = (E_1 - E_3)^2 - |\boldsymbol{p}_1 - \boldsymbol{p}_3|^2 = (E_i - E_f)^2 - p_i^2 - p_f^2 + 2p_ip_fc_{if} \\ q_{24}^2 &= (p_2 - p_4)^2 = (E_2 - E_4)^2 - |\boldsymbol{p}_2 - \boldsymbol{p}_4|^2 \approx -p_f^2 - \omega^2 - p_i^2 - 2p_f\omega c_{fa} + 2p_ip_fc_{if} + 2p_i\omega c_{ia}\,. \end{aligned} \tag{D.23}$$

Putting the squared matrix element into (D.21) yields the axion emissivity

$$\begin{aligned} \mathrm{d}\varepsilon_a = n_N\, \frac{8Z^2\alpha_{\rm EM}^2\alpha_{a\gamma\gamma}}{\pi^2}\, \mathrm{d}E_i\, \frac{\mathrm{d}\Omega_f}{4\pi}\, \mathrm{d}\omega\, \frac{\mathrm{d}\Omega_a}{4\pi}\, f_e(E_i)\,\big(1 - f_e(E_f)\big) \\ \times \frac{1}{q_{13}^4\, q_{24}^4} \Big[\big(2c_{if}c_{ia}c_{fa}p_i^2p_f^2 - 2c_{fa}^2 p_i^2 p_f^2 - c_{if}p_i^3 p_f s_{ia}^2 + 2p_i^2p_f^2 s_{ia}^2 - c_{if}p_i p_f^3 s_{fa}^2\big) \\ + m_e^2\big(2c_{if}p_ip_f - 2c_{ia}c_{fa}p_ip_f - p_i^2 s_{ia}^2 - p_f^2 s_{fa}^2\big) \\ + E_iE_f\big(-2c_{if}p_ip_f + 2c_{ia}c_{fa}p_ip_f + p_i^2 s_{ia}^2 + p_f^2 s_{fa}^2\big)\Big]\,. \end{aligned} \tag{D.24}$$

We have also used $e^2 = 4\pi\alpha_{\rm EM}$ and ${g_{aee}}^2 = 4\pi\alpha_{aee}$ and set $g_e = g_N = 2$. Note that our assumption $E_N(\boldsymbol{p}_4) \approx m_N$ implies the simple relation $E_f \approx E_i - \omega$.

If the plasma is degenerate, $T \ll p_F = \sqrt{E_F^2 - m_e^2}$, then the thermal factor can be approximated as

$$f_e(E_i)\,\big(1 - f_e(E_f)\big) \approx \frac{1}{e^{\omega/T} - 1}\, \Theta(E_F - E_i)\, \Theta(E_i - E_F - \omega)\,. \tag{D.25}$$

Then the integral over E_i sets $E_i \approx E_F$ and $E_f \approx E_F - \omega$ and gives $\mathrm{d}E_i \approx \omega$. This lets us write

$$\mathrm{d}\varepsilon_a = n_N\, \frac{Z^2\alpha_{\rm EM}^2\alpha_{a\gamma\gamma}}{2\pi^2}\, \frac{(m_e^2 + p_F^2)\,\omega^5\,\mathrm{d}\omega}{m_e^2\, p_F^2}\, \frac{1}{e^{\omega/T} - 1}\, \tilde{F}\,, \tag{D.26}$$

where we have defined

$$\tilde{F} \equiv \frac{m_e^2}{m_e^2 + p_F^2} \int \frac{\mathrm{d}\Omega_f}{4\pi} \int \frac{\mathrm{d}\Omega_a}{4\pi} \left[4\big(1 - c_{if} - c_{ia}^2 - c_{fa}^2\big) + \big(c_{ia} + c_{fa}\big)^2 \big(1 + c_{if}\big) \right] \frac{16 p_F^8}{\boldsymbol{q}^8} \ , \quad \text{(D.27)}$$

which contains the angular integrals. The momentum transfer factors have become

$$q_{13}^2 \approx q_{24}^2 \approx -\boldsymbol{q}^2 + O(\omega p_F) \qquad \text{where} \qquad \boldsymbol{q}^2 \equiv -2p_F^2\big(1 - c_{if}\big) \ , \quad \text{(D.28)}$$

and we neglect the ω-suppressed terms.

D.5.5 Emissivity and luminosity

Now generalizing to a plasma with multiple species of ions, labeled by s, the emissivity spectrum is written as

$$\frac{d\varepsilon_a}{d\omega} = \frac{\alpha_{\rm EM}^2 \alpha_{a\gamma\gamma}}{2\pi^2} \frac{\omega^5}{e^{\omega/T} - 1} \left(\frac{1}{m_e^2} + \frac{1}{p_F^2} \right) \sum_s \frac{Z_s^2 \rho_s \tilde{F}_s}{A_s u} \ , \quad \text{(D.29)}$$

where we have used $n_s = \rho_s/u$ and $u \approx 931.5$ MeV is the atomic mass unit, and we have assumed that all species have a common temperature $T_s = T$. Note that the emissivity spectrum, $d\varepsilon_a/d\omega_a$, is almost a thermal spectrum, except that there's an additional factor of ω^2, which follows from the momentum-dependent axion-photon coupling. The integral over ω evaluates to $8\pi^6 T^6/63$, and the total emissivity is found to be

$$\varepsilon_a = \frac{4\pi^4}{63} \alpha_{\rm EM}^2 \alpha_{a\gamma\gamma} T^6 \left(\frac{1}{m_e^2} + \frac{1}{p_F^2} \right) \sum_s \frac{Z_s^2 \rho_s \tilde{F}_s}{A_s u} \ . \quad \text{(D.30)}$$

Note that these relations hold for either relativistic or non-relativistic electrons; i.e., $p_F \approx E_F \gg m_e$ or $p_F \ll E_F \approx m_e$.

In the derivation above, we have neglected medium effects, which are now taken into account following Ref. [212]. Free electrons in the medium will screen the photon propagator, introducing an effective photon mass $k_{\rm TF}^2 = 4\alpha_{\rm EM} p_F E_F/\pi$, which is the Thomas-Fermi screening scale. Additionally interference and correlation effects are captured by the static structure factor $S_{\rm ions}(|\boldsymbol{q}|)$, which is why $\tilde{F}_s$ depends on the ionic species. We absorb these effects into the dimensionless coefficient $\tilde{F}_s$, which is no longer evaluated using (D.27). Instead, for a strongly-coupled plasma, such as the one in a WD core, the static structure factor has been calculated in Refs. [66, 211], and the factor $\tilde{F}_s$ is also evaluated for axion emission

via electron-bremsstrahlung scattering. As a rough estimate, we simply carry over that estimate of $\tilde{F}_s$ here, though future work using this result should calculate $\tilde{F}_s$ more precisely. For instance, Refs. [66,211] assume a one-component plasma with a single ionic species. We generalize to a multi-component plasma by summing over the constituent ionic species, as in (D.29). This approach assumes that possible interference effects can be neglected.

The axion luminosity is evaluated by integrating $L_a = \int \mathrm{d}V\, \varepsilon_a$ over the volume of the WD star. To a good approximation, the core temperature $T \approx T_c$ is approximately uniform throughout the star, due to the degenerate matter's high thermal conductivity. On the other hand, the medium factors $\tilde{F}_s$ and mass fractions $R_s = \rho_s/\rho_{\rm tot}$ have radial-dependent profiles. To provide a rough estimate, we neglect these effects and the volume integral gives $\int \mathrm{d}V\, \rho_{\rm tot} = M$, which is the mass of the star. Then the axion luminosity is

$$\begin{aligned} L_a &\approx \frac{4\pi^4}{63}\, \alpha_{\rm EM}^2 \alpha_{a\gamma\gamma} \frac{T_c^6 M}{m_e^2 u} \left(1 + \frac{m_e^2}{p_F^2}\right) \sum_s \frac{Z_s^2 R_s \tilde{F}_s}{A_s} \\ &\simeq \left(7.6 \times 10^{-12}\, L_\odot\right) \left(\frac{g_{a\gamma\gamma}}{10^{-11}\ \mathrm{GeV}}\right)^2 \left(\frac{T_c}{1\ \mathrm{keV}}\right)^6 \left(\frac{M}{1\ M_\odot}\right) \left(1 + \frac{m_e^2}{p_F^2}\right) \sum_s \frac{Z_s^2 R_s \tilde{F}_s}{A_s}\,, \end{aligned} \tag{D.31}$$

Compared with axion bremsstrahlung emission, the luminosity here is suppressed by a factor of $\alpha_{a\gamma\gamma} T_c^2/\alpha_{aee}$. The electro-Primakoff emission spectrum and resulting limits are illustrated in Figs. D.2 and D.3.

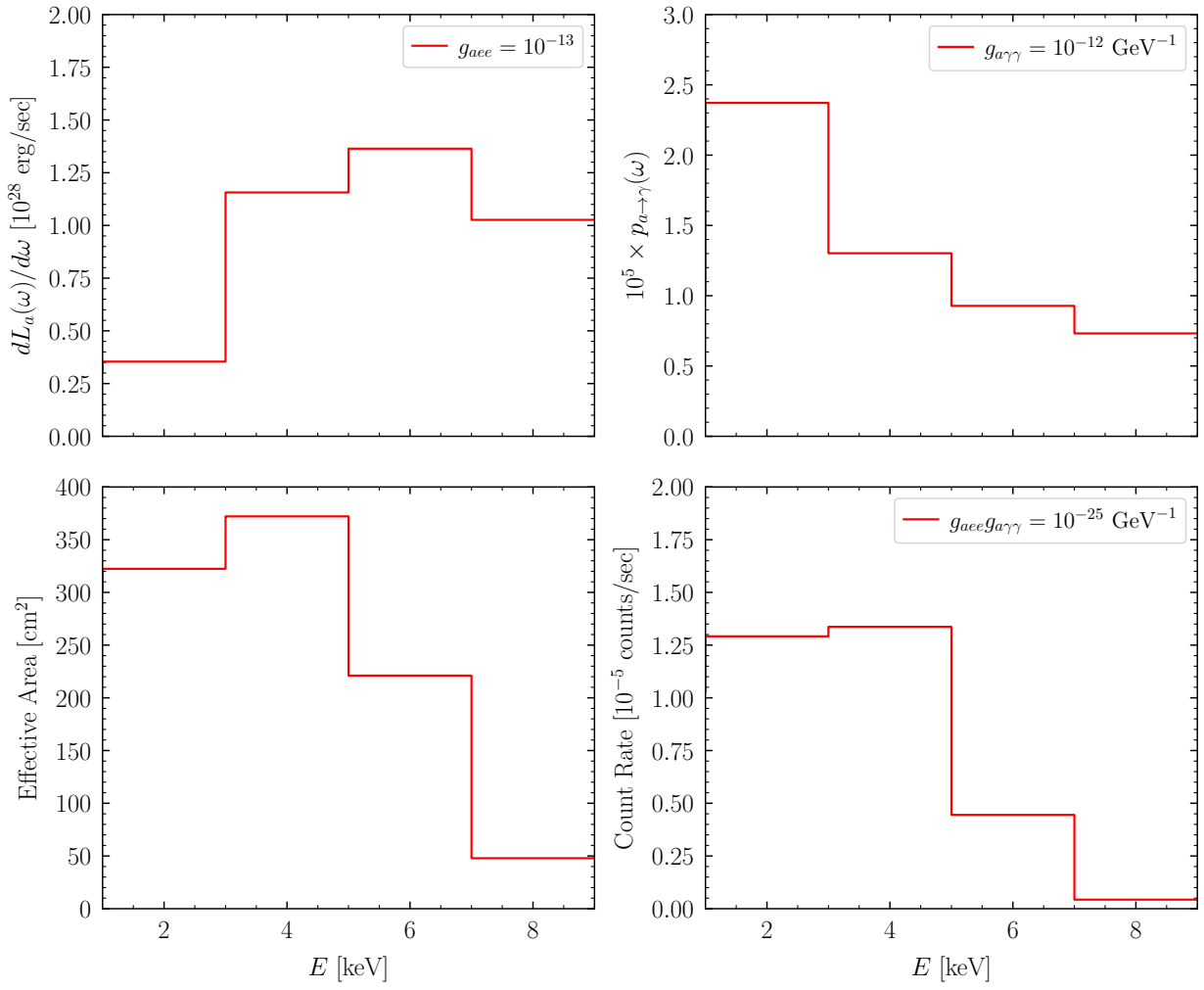

Figure D.9: (Upper left) The axion bremsstrahlung luminosity spectrum in erg/s emitted from the WD at the fiducial parameters in our analysis and $g_{aee} = 10^{-13}$. (Upper right) The conversion probability as a function of energy at the fiducial parameters in our analysis and $g_{a\gamma\gamma} = 10^{12}$ GeV^{-1}. (Lower left) The *Chandra* effective area as a function of energy. (Lower right) The expected *Chandra* count rate from axion bremsstrahlung in our observation at $g_{aee}g_{a\gamma\gamma} = 10^{-25}$ GeV^{-1}.

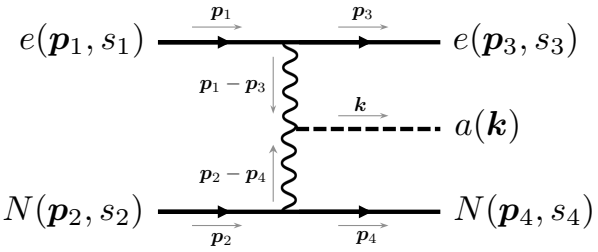

Figure D.10: The Feynman graph for axion production via the electro-Primakoff channel.

Appendix E

Hard X-ray Excess from the Magnificent Seven Neutron Stars

E.1 Observations used in the analyses

Here we list the observation identification numbers, by NS and instrument, which are used in the analyses presented in this chapter. In addition, we show the instrument used to make the observation, including the grating for *Chandra*, and the mode the instrument was in at observation time. For MOS the possible modes are Full Frame (FF) and Large Window (LW), while for PN we have also included Small Window (SW) data. For *Chandra* the mode records the subarray the observation was taken in (FF, 1/2, 1/4, or 1/8). We also show the exposure time of the observation t_{exp} in ks. For the *XMM* observations, we additionally show several estimates of pileup. The singles and doubles columns indicate the ratio of observed to expected events in the 0.5-2 keV range with singles and doubles patterns, respectively. Deviations from 1.0 indicate possible pileup. We additionally show estimates of the spectral distortion (SD) and flux loss (FL) in percent due to pileup [23].

The former pileup estimate, SD, is particularly important for our case. For the two NSs in which we find an excess, RX J1856.6-3754 and RX J0420.0-5022, we find that the SD is much lower than would be required for the thermal flux to produce the observed hard X-ray emission. This is not so surprising, as the count rates are around two orders of magnitude lower than the conservative limits on the count rate from [23]. In particular, we compute the required SD to produce the hard X-ray emission via pileup for each NS and camera. Here we assume that every piled-up photon below 2 keV contributes to the flux above 2 keV. Note that this is significantly conservative as most of these photons will contribute only to the flux below 2 keV. Nevertheless, we find that the SD required to reproduce the RX J1856.6-3754

hard flux is 0.78% (1.00%) for MOS (PN), while the observed values are ∼0.04% (∼0.07%). To reproduce the RX J0420.0-5022 hard flux, we find 20.8% (32.7%) for MOS (PN), while the observed values are ∼0.01% (∼0.00%). The RX J0420.0-5022 values are larger because the count rate is lower. Therefore, we conclude that pileup is not significantly contributing to the observed hard X-ray emission in these NSs.

RX J0806.4-4123

Exposure ID	Mode	t_{exp}	Singles	Doubles	SD	FL
0106260201PNS001	FF	4.1	0.974 ± 0.036	1.099 ± 0.061	0.19	0.48
0141750501PNU002	FF	12.4	0.967 ± 0.020	1.130 ± 0.035	0.20	0.51
0552210201PNS003	SW	5.9	0.996 ± 0.031	1.014 ± 0.046	0.03	0.04
0552210401PNS003	SW	3.7	0.998 ± 0.039	0.998 ± 0.058	0.03	0.04
0552210901PNS003	SW	3.7	1.039 ± 0.040	0.876 ± 0.055	0.03	0.04
0552211001PNS003	SW	6.4	0.995 ± 0.030	1.017 ± 0.046	0.03	0.04
0552211101PNS003	SW	5.4	1.011 ± 0.032	0.981 ± 0.048	0.03	0.04
0552211601PNS003	SW	3.2	1.005 ± 0.043	0.975 ± 0.064	0.03	0.04
0672980201PNS001	SW	5.4	1.008 ± 0.033	0.983 ± 0.048	0.03	0.04
0672980301PNS001	SW	3.8	1.040 ± 0.040	0.893 ± 0.055	0.03	0.04
0106260201MOS1S002	FF	8.3	1.053 ± 0.052	0.817 ± 0.081	0.15	0.42
0106260201MOS2S003	FF	8.7	1.053 ± 0.051	0.818 ± 0.079	0.15	0.44
0141750501MOS1U002	FF	16.6	1.057 ± 0.038	0.801 ± 0.058	0.14	0.39
0141750501MOS2U002	FF	16.9	1.057 ± 0.037	0.802 ± 0.057	0.15	0.43
2789 ACIS-I/NONE	FF	17.7	—	—	—	—
5540 ACIS-I/NONE	FF	19.7	—	—	—	—
16953 ACIS-I/NONE	FF	34.7	—	—	—	—

Table E.1: The exposures (Exposure ID) used in our fiducial analyses for RX J0806.4-4123 along with supplementary data. We list the instrument's operating mode and the length of the observation t_{exp} in ks along with four pileup metrics. The singles and doubles columns refer to the observed to expected events with singles and doubles fractions in the 0.5-2 keV range. The spectral distortion (SD) and flux loss (FL) [%] are additional metrics for pileup described in [23]. Note we do not show these metrics for *Chandra* as in that case we perform dedicated simulations.

RX J1856.6-3754

Exposure ID	Mode	t_{exp}	Singles	Doubles	SD	FL
0791580301PNS001	SW	4.0	0.967 ± 0.033	1.116 ± 0.055	0.04	0.05

0791580501PNS001	SW	4.3	0.983 ± 0.034	1.066 ± 0.055	0.03	0.04
0791580201PNS001	SW	6.3	0.989 ± 0.028	1.030 ± 0.044	0.03	0.04
0791580601PNS001	SW	9.5	0.979 ± 0.024	1.086 ± 0.039	0.04	0.05
0791580101PNS001	SW	12.5	0.998 ± 0.030	1.016 ± 0.047	0.03	0.03
0791580401PNS001	SW	12.7	0.993 ± 0.023	1.030 ± 0.036	0.03	0.03
0165971601PNS003	SW	21.6	0.982 ± 0.014	1.067 ± 0.023	0.04	0.05
0165971901PNS003	SW	10.9	0.977 ± 0.022	1.090 ± 0.036	0.04	0.05
0165972001PNS003	SW	17.9	0.985 ± 0.017	1.057 ± 0.027	0.04	0.05
0106260101PNS001	SW	38.3	0.986 ± 0.011	1.054 ± 0.018	0.04	0.05
0412600601PNU002	SW	41.1	0.985 ± 0.011	1.057 ± 0.017	0.04	0.05
0412600701PNS003	SW	45.4	0.970 ± 0.011	1.107 ± 0.018	0.04	0.05
0412601101PNU002	SW	43.8	0.982 ± 0.011	1.065 ± 0.018	0.03	0.04
0165972101PNS003	SW	47.0	0.981 ± 0.011	1.067 ± 0.017	0.04	0.05
0412600301PNS003	SW	14.7	0.991 ± 0.018	1.029 ± 0.029	0.04	0.05
0412600301PNU002	SW	9.2	0.983 ± 0.024	1.066 ± 0.038	0.04	0.05
0727761301PNS001	SW	20.4	0.982 ± 0.018	1.065 ± 0.028	0.04	0.05
0727761101PNS001	SW	31.9	0.979 ± 0.015	1.075 ± 0.024	0.04	0.04
0727761001PNS001	SW	45.5	0.974 ± 0.011	1.093 ± 0.018	0.04	0.05
0727760101PNS001	SW	43.5	0.972 ± 0.011	1.099 ± 0.018	0.04	0.05
0412600101PNS003	SW	47.9	0.984 ± 0.010	1.062 ± 0.016	0.04	0.05
0412600901PNS003	SW	30.5	0.986 ± 0.013	1.057 ± 0.021	0.04	0.05
0412602201PNS003	SW	46.5	0.960 ± 0.011	1.138 ± 0.018	0.04	0.05
0412600401PNU002	SW	25.1	0.983 ± 0.014	1.066 ± 0.023	0.04	0.05
0810840101PNS001	SW	35.2	0.982 ± 0.012	1.064 ± 0.020	0.04	0.04
0727760201PNS001	SW	33.5	0.985 ± 0.014	1.058 ± 0.021	0.04	0.05
0727760401PNS001	SW	33.9	0.958 ± 0.013	1.148 ± 0.023	0.04	0.05
0727761201PNS001	SW	26.6	0.958 ± 0.013	1.145 ± 0.023	0.04	0.05

0412601401PNS003	SW	20.5	0.970 ± 0.017	1.111 ± 0.027	0.04	0.05
0412601401PNU002	SW	4.2	0.994 ± 0.035	1.016 ± 0.053	0.04	0.05
0727760301PNS001	SW	48.2	0.973 ± 0.009	1.098 ± 0.016	0.04	0.05
0412602301PNS003	SW	47.0	0.965 ± 0.010	1.125 ± 0.017	0.04	0.05
0412600801PNS003	SW	4.2	1.007 ± 0.036	0.969 ± 0.054	0.04	0.05
0412600801PNU002	SW	34.0	0.984 ± 0.012	1.058 ± 0.019	0.04	0.05
0727760501PNS001	SW	42.6	0.972 ± 0.011	1.103 ± 0.018	0.04	0.05
0412601301PNS003	SW	28.6	0.986 ± 0.014	1.059 ± 0.022	0.04	0.05
0412601501PNS600	SW	16.9	0.982 ± 0.018	1.070 ± 0.029	0.04	0.05
0412601501PNS601	SW	15.9	0.977 ± 0.019	1.085 ± 0.031	0.04	0.05
0412601501PNS602	SW	13.8	0.958 ± 0.019	1.148 ± 0.033	0.04	0.05
0412601501PNS603	SW	14.2	0.966 ± 0.019	1.113 ± 0.031	0.04	0.05
0213080101MOS1U002	LW	2.8	0.974 ± 0.082	1.199 ± 0.170	0.06	0.17
0213080101MOS2U002	LW	1.9	0.971 ± 0.091	1.230 ± 0.194	0.07	0.20
0415180101MOS1S002	LW	19.6	0.971 ± 0.032	1.220 ± 0.068	0.06	0.18
0727761301MOS1S002	LW	29.5	0.955 ± 0.033	1.282 ± 0.071	0.06	0.17
0727761301MOS2S003	LW	25.0	0.951 ± 0.039	1.282 ± 0.086	0.05	0.14
0727761101MOS1S002	LW	48.7	0.965 ± 0.025	1.210 ± 0.052	0.06	0.16
0727761101MOS2S003	LW	54.0	0.949 ± 0.026	1.320 ± 0.060	0.05	0.14
0412602201MOS1S001	LW	63.4	0.949 ± 0.018	1.309 ± 0.040	0.07	0.19
0727760201MOS1S002	LW	44.0	0.971 ± 0.025	1.193 ± 0.052	0.06	0.16
0727760201MOS2S003	LW	43.5	0.959 ± 0.025	1.256 ± 0.055	0.05	0.15
0727760401MOS1S002	LW	47.7	0.969 ± 0.025	1.196 ± 0.052	0.06	0.16
0727760401MOS2S003	LW	51.4	0.990 ± 0.042	1.100 ± 0.082	0.05	0.15
0412601401MOS1U002	LW	5.4	0.959 ± 0.058	1.279 ± 0.127	0.06	0.17
0412601401MOS2U002	LW	5.8	0.972 ± 0.061	1.197 ± 0.128	0.05	0.15
0727760601MOS1S002	LW	32.6	0.991 ± 0.038	1.083 ± 0.074	0.06	0.16

0412601301MOS1S001	LW	39.1	0.952 ± 0.037	1.322 ± 0.083	0.06	0.16
0412601501MOS1S001	LW	83.8	0.963 ± 0.016	1.245 ± 0.034	0.06	0.18
0412601501MOS2S002	LW	90.2	0.958 ± 0.017	1.266 ± 0.038	0.06	0.17
13198 ACIS-S/LETG	1/8	28.4	—	—	—	—
18416 ACIS-S/LETG	1/4	28.8	—	—	—	—
19848 ACIS-S/LETG	1/8	28.4	—	—	—	—
20718 ACIS-S/LETG	1/8	28.2	—	—	—	—
14267 ACIS-S/LETG	1/8	28.4	—	—	—	—
15474 ACIS-S/LETG	1/8	11.7	—	—	—	—
16265 ACIS-S/LETG	1/8	16.1	—	—	—	—
16422 ACIS-S/LETG	1/8	26.0	—	—	—	—
17394 ACIS-S/LETG	1/8	29.1	—	—	—	—

Table E.2: As in Tab. E.1 but for RX J1856.6-3754.

RX J0420.0-5022

Exposure ID	Mode	t_{exp}	Singles	Doubles	SD	FL
0141750101PNS003	FF	17.3	1.021 ± 0.138	0.888 ± 0.198	0.01	0.01
0141751001PNS003	FF	9.8	0.984 ± 0.135	1.060 ± 0.216	0.01	0.01
0141751101PNS003	FF	14.2	0.955 ± 0.121	1.075 ± 0.197	0.01	0.01
0141751201PNS003	FF	17.6	0.968 ± 0.129	1.116 ± 0.223	0.01	0.01
0651470201PNS003	SW	2.9	1.184 ± 0.290	0.429 ± 0.226	0.00	0.00
0651470501PNS003	SW	2.4	0.967 ± 0.307	1.146 ± 0.492	0.00	0.00
0651470601PNS003	SW	4.4	0.956 ± 0.197	1.112 ± 0.307	0.00	0.00
0651470701PNS003	SW	6.8	0.999 ± 0.157	0.894 ± 0.211	0.00	0.00
0651470801PNS003	SW	8.1	1.010 ± 0.143	0.893 ± 0.191	0.00	0.00
0651470901PNS003	SW	9.0	0.944 ± 0.137	1.147 ± 0.221	0.00	0.00
0651471001PNS003	SW	5.3	1.033 ± 0.179	0.775 ± 0.213	0.00	0.00

0651471101PNS003	SW	5.6	0.949 ± 0.131	1.108 ± 0.204	0.00	0.00
0651471201PNS003	SW	3.7	1.022 ± 0.204	0.924 ± 0.275	0.00	0.00
0651471401PNU002	SW	4.8	1.018 ± 0.192	0.942 ± 0.263	0.00	0.00
0651471501PNS003	SW	3.6	0.922 ± 0.211	1.108 ± 0.347	0.00	0.00
0141750101MOS1S001	FF	20.8	0.998 ± 0.223	1.076 ± 0.438	0.00	0.01
0141750101MOS2S002	FF	20.9	1.016 ± 0.283	0.970 ± 0.518	0.00	0.01
0141751001MOS1S001	FF	15.9	0.977 ± 0.185	1.083 ± 0.369	0.00	0.01
0141751001MOS2S002	FF	16.3	1.006 ± 0.195	1.033 ± 0.370	0.00	0.01
0141751101MOS1S001	FF	20.5	0.948 ± 0.155	1.279 ± 0.349	0.00	0.01
0141751101MOS2S002	FF	19.7	1.038 ± 0.179	0.845 ± 0.299	0.00	0.01
0141751201MOS1S001	FF	20.5	1.070 ± 0.246	0.671 ± 0.352	0.00	0.01
0141751201MOS2S002	FF	21.2	1.042 ± 0.215	0.813 ± 0.351	0.00	0.01
2788 ACIS-S/NONE	FF	19.4	—	—	—	—
5541 ACIS-S/NONE	FF	19.7	—	—	—	—
17457 ACIS-S/NONE	FF	19.4	—	—	—	—

Table E.3: As in Tab. E.1 but for RX J0420.0-5022.

RX J1308.6+2127

Exposure ID	Mode	t_{exp}	Singles	Doubles	SD	FL
0157360101PNS005	FF	23.2	0.964 ± 0.009	1.136 ± 0.017	0.45	1.19
0163560101PNS003	FF	16.5	0.976 ± 0.011	1.084 ± 0.019	0.46	1.22
0305900201PNS003	FF	2.1	0.962 ± 0.031	1.134 ± 0.055	0.46	1.21
0305900301PNS003	FF	10.9	0.977 ± 0.014	1.086 ± 0.024	0.45	1.21
0305900401PNS003	FF	9.2	0.972 ± 0.015	1.108 ± 0.026	0.45	1.18
0305900601PNS003	FF	12.8	0.961 ± 0.012	1.147 ± 0.022	0.46	1.23
0402850301PNS003	LW	3.4	0.972 ± 0.025	1.104 ± 0.042	0.31	0.78
0402850401PNS003	LW	5.6	0.957 ± 0.019	1.158 ± 0.035	0.30	0.76
0402850501PNS003	LW	2.6	0.972 ± 0.028	1.108 ± 0.048	0.31	0.77
0402850701PNS003	LW	7.3	0.976 ± 0.017	1.090 ± 0.029	0.30	0.77
0402850901PNS003	LW	2.6	0.971 ± 0.029	1.106 ± 0.049	0.30	0.75
0157360101MOS1S003	LW	27.5	1.083 ± 0.020	0.711 ± 0.027	0.12	0.33
0163560101MOS1S001	LW	23.9	1.081 ± 0.021	0.727 ± 0.029	0.12	0.33
0163560101MOS2S002	LW	24.2	1.083 ± 0.021	0.713 ± 0.029	0.12	0.34

Table E.4: As in Tab. E.1 but for RX J1308.6+2127.

E.2 Count statistics and exposures for the XDINSs

Here we give, for each NS and instrument, the data used in our fiducial analyses after stacking all exposures together. In particular, we list: the number of counts in the signal region, c_S; the number of counts in the background region, c_B; the number of pixels included in the signal region, $\sum_{p \in R_S}$; the number of pixels included in the background region, $\sum_{p \in R_B}$; the mean pixel exposure for signal region pixels, $\bar{w}_S$; the mean pixel exposure for background region pixels, $\bar{w}_B$; the fraction of signal counts that will appear in signal region pixels due to the instrument PSF, χ_S; and the fraction of signal counts that will appear in background region pixels due to the instrument PSF, χ_B. The data is provided in Tabs. E.8, E.9, E.10, E.11, E.12, E.13, and E.14 for each NS, respectively.

E.3 Test statistic maps for the XDINSs

We present the test statistic maps for all NSs and for all instruments in which they are observed, as shown in Fig. 6.2 for RX J1856.6-3754. For RX J1856.6-3754 and RX J0420.0-5022, the test statistic maps are computed using flux from 2-8 keV. For all other NSs, the

RX J0720.4-3125

Exposure ID	Mode	t_{exp}	Singles	Doubles	SD	FL
0156960401PNS003	FF	24.3	0.878 ± 0.006	1.438 ± 0.014	0.85	2.14
0158360201PNU002	SW	37.5	1.004 ± 0.007	0.998 ± 0.011	0.09	0.11
0161960201PNS007	SW	12.2	1.008 ± 0.009	0.983 ± 0.013	0.13	0.23
0161960201PNS008	SW	16.0	1.005 ± 0.008	0.990 ± 0.012	0.13	0.22
0164560501PNS001	FF	18.7	0.907 ± 0.006	1.321 ± 0.013	1.13	2.87
0300520201PNS003	FF	18.5	0.900 ± 0.007	1.350 ± 0.014	1.09	2.76
0300520301PNS003	FF	13.0	0.908 ± 0.008	1.319 ± 0.016	1.08	2.75
0311590101PNS003	FF	30.1	0.898 ± 0.005	1.360 ± 0.011	1.08	2.75
0400140301PNS001	FF	13.6	0.901 ± 0.008	1.345 ± 0.016	1.09	2.76
0400140401PNS001	FF	16.7	0.889 ± 0.007	1.391 ± 0.015	1.08	2.73
0502710201PNS001	FF	6.0	0.885 ± 0.013	1.404 ± 0.027	1.04	2.63
0502710301PNS001	FF	19.0	0.880 ± 0.007	1.420 ± 0.015	1.02	2.59
0554510101PNS003	FF	8.9	0.868 ± 0.011	1.454 ± 0.025	1.00	2.54
0650920101PNS003	FF	8.0	0.889 ± 0.011	1.391 ± 0.024	0.94	2.38
0670700201PNS003	FF	9.0	0.873 ± 0.011	1.433 ± 0.024	0.93	2.36
0670700301PNS003	FF	21.4	0.884 ± 0.007	1.409 ± 0.016	0.92	2.31
0690070201PNS003	FF	21.5	0.870 ± 0.007	1.462 ± 0.016	0.89	2.24

Table E.5: As in Tab. E.1 but for RX J0720.4-3125.

test statistic maps are computed using only the flux from 4-8 keV. The maps are presented in Figs. E.1, E.2, E.3, E.4, E.5, and E.6.

It is worth pointing out that the brightest pixel in Fig. E.2 is one pixel displaced from the center. Recall that RX J0420.0-5022 was detected at $\sim 3\sigma$ significance with the PN data using the joint likelihood. Note that we expect to be able to localize a 3σ signal to roughly within the 1/3 of the 90% EEF radius for the instrumental PSF. In the 2-8 keV energy range the 90% EEF radius for PN and MOS is approximately 1'. Thus, it should not be too surprising that in Fig. E.2 the most significant pixel for the PN map is not the central pixel but rather the pixel whose center is slightly displaced from the source. On the other hand, the brightest pixels for the *Chandra* and MOS RX J0420.0-5022 maps are the central pixels.

RX J1605.3+3249

Exposure ID	Mode	t_{exp}	Singles	Doubles	SD	FL
0157360401PNS005	LW	21.8	0.931 ± 0.009	1.238 ± 0.017	0.33	0.85
0157360601PNS005	LW	5.5	0.954 ± 0.022	1.150 ± 0.038	0.24	0.60
0671620101PNS003	FF	26.4	0.921 ± 0.008	1.278 ± 0.016	0.51	1.34
0764460201PNS003	FF	90.5	0.932 ± 0.004	1.239 ± 0.008	0.51	1.33
0764460301PNS003	FF	50.9	0.930 ± 0.006	1.251 ± 0.011	0.51	1.34
0764460401PNS003	FF	38.9	0.942 ± 0.007	1.203 ± 0.013	0.49	1.30
0764460501PNS003	FF	45.2	0.930 ± 0.006	1.251 ± 0.012	0.52	1.37
0073140201MOS1S004	FF	26.2	1.031 ± 0.018	0.925 ± 0.030	0.37	1.09
0073140201MOS2S005	FF	25.8	1.029 ± 0.018	0.933 ± 0.030	0.40	1.19
0073140301MOS2S005	FF	16.8	1.017 ± 0.022	0.999 ± 0.040	0.40	1.17
0073140501MOS1S004	FF	21.0	1.026 ± 0.020	0.954 ± 0.035	0.37	1.10
0073140501MOS2S005	FF	21.0	1.026 ± 0.020	0.956 ± 0.035	0.38	1.14
0157360401MOS2S004	FF	26.0	1.027 ± 0.018	0.936 ± 0.031	0.38	1.14
0302140501MOS1S002	FF	3.3	1.030 ± 0.052	0.912 ± 0.086	0.34	1.01
0302140501MOS2S003	FF	3.0	1.033 ± 0.055	0.892 ± 0.090	0.37	1.10
0671620101MOS1U002	FF	6.9	1.045 ± 0.039	0.857 ± 0.062	0.29	0.86
0671620101MOS2S002	FF	34.9	1.036 ± 0.017	0.897 ± 0.028	0.35	1.03
0764460501MOS1S001	LW	58.2	1.061 ± 0.013	0.779 ± 0.020	0.11	0.30

Table E.6: As in Tab. E.1 but for RX J1605.3+3249.

E.4 Spectral limits and systematic tests for the XDINSs

Here we present the fiducial spectral limits on the flux in each energy bin from 2 to 8 keV for each NS in each instrument in which they are observed, along with systematic variations on our analysis procedure that test the robustness of the reconstructed flux. We also inspect the counts distribution in the background extraction region compared to the one expected under the fitted background rate and include the p-values for the background goodness-of-fit under each analysis procedure. These results are in analogy to those shown in Fig. 6.3 and Fig. 6.4 for RX J1856.6-3754. We present the results for the other six NSs in Figs. E.7, E.8, E.9, E.10, E.11, E.12, E.13, E.14, E.15, E.16, E.17, and E.18.

RX J2143.0+0654

Exposure ID	Mode	t_{exp}	Singles	Doubles	SD	FL
0201150101PNS006	SW	14.6	1.012 ± 0.015	0.973 ± 0.022	0.06	0.07
0502040601PNS003	SW	5.2	1.004 ± 0.024	0.988 ± 0.036	0.06	0.07
0502040701PNS003	SW	9.0	1.004 ± 0.018	0.990 ± 0.027	0.06	0.07
0502040901PNS003	SW	5.0	1.013 ± 0.025	0.967 ± 0.036	0.06	0.07
0502041001PNS003	SW	5.8	1.014 ± 0.023	0.965 ± 0.034	0.06	0.07
0502041101PNS003	SW	7.7	1.006 ± 0.020	0.995 ± 0.030	0.06	0.07
0502041201PNS003	SW	6.1	1.011 ± 0.022	0.970 ± 0.033	0.06	0.07
0502041301PNS003	SW	3.7	0.986 ± 0.029	1.055 ± 0.045	0.06	0.07
0502041401PNS003	SW	5.1	0.996 ± 0.024	1.021 ± 0.037	0.06	0.07
0502041801PNS003	SW	5.3	1.011 ± 0.024	0.972 ± 0.035	0.06	0.07

Table E.7: As in Tab. E.1 but for RX J2143.0+0654.

RX J0806.4-4123

PN								
Range	c_s	c_B	$\sum_{p\in R_S}$	$\sum_{p\in R_B}$	$\bar{w}_S$ [cm^2 s]	$\bar{w}_B$ [cm^2 s]	χ_S	χ_B
2-4 keV	39	37	2729	3136	2.9×10^6	2.89×10^6	0.8	0.1
4-6 keV	26	35	2729	3136	2.77×10^6	2.76×10^6	0.8	0.1
6-8 keV	32	26	2729	3136	2.16×10^6	2.16×10^6	0.8	0.1
MOS								
Range	c_s	c_B	$\sum_{p\in R_S}$	$\sum_{p\in R_B}$	$\bar{w}_S$ [cm^2 s]	$\bar{w}_B$ [cm^2 s]	χ_S	χ_B
2-4 keV	7	7	1086	1218	2.88×10^6	2.86×10^6	0.8	0.1
4-6 keV	5	6	1086	1218	2.52×10^6	2.51×10^6	0.8	0.1
6-8 keV	1	5	1086	1218	1.21×10^6	1.21×10^6	0.8	0.1
Chandra								
Range	c_s	c_B	$\sum_{p\in R_S}$	$\sum_{p\in R_B}$	$\bar{w}_S$ [cm^2 s]	$\bar{w}_B$ [cm^2 s]	χ_S	χ_B
2-4 keV	9	0	51	1029	8.49×10^6	8.07×10^6	0.1	0.7
4-6 keV	0	0	51	1029	8.41×10^6	7.97×10^6	0.1	0.7
6-8 keV	0	2	51	1029	3.00×10^6	2.85×10^6	0.1	0.7

Table E.8: The exposure-stacked data for all cameras used in our fiducial analyses for RX J0806.4-4123. We include the number of signal counts c_S, the number of background counts c_B, the number of pixels in the signal (background) region $\sum_{p\in R_S}$ ($\sum_{p\in R_B}$), the average exposure in the signal (background) region $\bar{w}_S$ ($\bar{w}_B$), and the fraction of source flux expected in the signal (background) region due to the PSF χ_S (χ_B). Note that the weights are reported without the 1/keV.

RX J1856.6-3754

PN								
Range	c_s	c_B	$\sum_{p\in R_S}$	$\sum_{p\in R_B}$	$\bar{w}_S$ [cm^2 s]	$\bar{w}_B$ [cm^2 s]	χ_S	χ_B
2-4 keV	874	903	10668	12285	1.91×10^7	1.91×10^7	0.8	0.1
4-6 keV	669	681	10668	12285	1.84×10^7	1.84×10^7	0.8	0.1
6-8 keV	462	522	10668	12285	1.45×10^7	1.45×10^7	0.8	0.1
MOS								
Range	c_s	c_B	$\sum_{p\in R_S}$	$\sum_{p\in R_B}$	$\bar{w}_S$ [cm^2 s]	$\bar{w}_B$ [cm^2 s]	χ_S	χ_B
2-4 keV	99	72	3753	4421	7.1×10^6	$7. \times 10^6$	0.8	0.1
4-6 keV	61	71	3753	4421	6.28×10^6	6.19×10^6	0.8	0.1
6-8 keV	48	57	3753	4421	3.09×10^6	3.05×10^6	0.7	0.1
Chandra								
Range	c_s	c_B	$\sum_{p\in R_S}$	$\sum_{p\in R_B}$	$\bar{w}_S$ [cm^2 s]	$\bar{w}_B$ [cm^2 s]	χ_S	χ_B
2-4 keV	2	13	157	3719	8.63×10^5	8.74×10^5	0.1	0.7
4-6 keV	3	5	157	3719	1.67×10^6	1.69×10^6	0.1	0.7
6-8 keV	1	16	157	3719	8.66×10^5	8.8×10^5	0.1	0.7

Table E.9: As in Tab. E.8 but for RX J1856.6-3754.

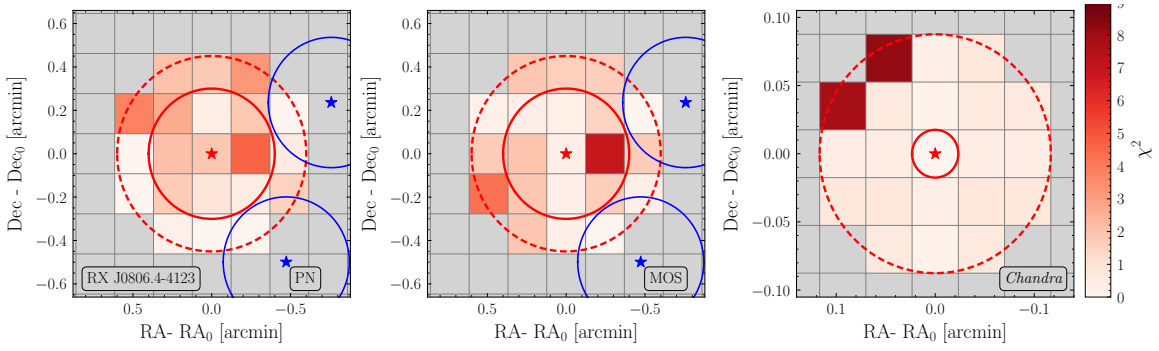

Figure E.1: χ^2 maps as in Fig. 6.2 but for RX J0806.4-4123 in PN, MOS and *Chandra* computed using counts from the 4-8 keV energy range. No excess is observed in the signal region for any instrument. A nearby point source is found in the joint analysis of PN and MOS data, whose point source mask would remove a small number of pixels from the background extraction region.

RX J0420.0-5022

PN								
Range	c_s	c_B	$\sum_{p\in R_S}$	$\sum_{p\in R_B}$	$\bar{w}_S$ [cm^2 s]	$\bar{w}_B$ [cm^2 s]	χ_S	χ_B
2-4 keV	66	48	4043	4712	6.15×10^6	6.19×10^6	0.8	0.1
4-6 keV	65	54	4043	4712	5.9×10^6	5.93×10^6	0.8	0.1
6-8 keV	35	38	4043	4712	4.64×10^6	4.66×10^6	0.8	0.1
MOS								
Range	c_s	c_B	$\sum_{p\in R_S}$	$\sum_{p\in R_B}$	$\bar{w}_S$ [cm^2 s]	$\bar{w}_B$ [cm^2 s]	χ_S	χ_B
2-4 keV	14	13	1739	2426	6.04×10^6	6.02×10^6	0.8	0.1
4-6 keV	5	12	1739	2426	5.29×10^6	5.28×10^6	0.8	0.1
6-8 keV	5	4	1739	2426	2.55×10^6	2.55×10^6	0.7	0.1
Chandra								
Range	c_s	c_B	$\sum_{p\in R_S}$	$\sum_{p\in R_B}$	$\bar{w}_S$ [cm^2 s]	$\bar{w}_B$ [cm^2 s]	χ_S	χ_B
2-4 keV	1	1	44	1057	7.79×10^6	7.78×10^6	0.1	0.7
4-6 keV	1	1	44	1057	6.55×10^6	6.55×10^6	0.1	0.7
6-8 keV	0	3	44	1057	2.02×10^6	2.02×10^6	0.1	0.7

Table E.10: As in Tab. E.8 but for RX J0420.0-5022.

RX J1308.6+2127

PN								
Range	c_s	c_B	$\sum_{p\in R_S}$	$\sum_{p\in R_B}$	$\bar{w}_S$ [cm^2 s]	$\bar{w}_B$ [cm^2 s]	χ_S	χ_B
2-4 keV	41	32	3015	3453	6.71×10^6	6.69×10^6	0.8	0.1
4-6 keV	31	50	3015	3453	6.42×10^6	6.4×10^6	0.8	0.1
6-8 keV	25	27	3015	3453	5.07×10^6	5.05×10^6	0.8	0.1
MOS								
Range	c_s	c_B	$\sum_{p\in R_S}$	$\sum_{p\in R_B}$	$\bar{w}_S$ [cm^2 s]	$\bar{w}_B$ [cm^2 s]	χ_S	χ_B
2-4 keV	8	9	804	933	7.37×10^6	7.35×10^6	0.8	0.1
4-6 keV	3	0	804	933	6.44×10^6	6.42×10^6	0.8	0.1
6-8 keV	6	2	804	933	3.12×10^6	3.11×10^6	0.8	0.1

Table E.11: As in Tab. E.8 but for RX J1308.6+2127.

RX J0720.4-3125

PN								
Range	c_s	c_B	$\sum_{p\in R_S}$	$\sum_{p\in R_B}$	$\bar{w}_S$ [cm^2 s]	$\bar{w}_B$ [cm^2 s]	χ_S	χ_B
2-4 keV	181	158	4575	5230	1.19×10^7	1.18×10^7	0.8	0.1
4-6 keV	115	124	4575	5230	1.15×10^7	1.14×10^7	0.8	0.1
6-8 keV	98	102	4575	5230	9.12×10^6	9.08×10^6	0.8	0.1
MOS								
Range	c_s	c_B	$\sum_{p\in R_S}$	$\sum_{p\in R_B}$	$\bar{w}_S$ [cm^2 s]	$\bar{w}_B$ [cm^2 s]	χ_S	χ_B
2-4 keV	21	13	1276	1787	2.33×10^6	2.33×10^6	0.8	0.1
4-6 keV	6	8	1276	1787	2.05×10^6	2.05×10^6	0.8	0.1
6-8 keV	3	8	1276	1787	9.96×10^5	9.97×10^5	0.7	0.1

Table E.12: As in Tab. E.8 but for RX J0720.4-3125.

RX J1605.3+3249

PN								
Range	c_s	c_B	$\sum_{p\in R_S}$	$\sum_{p\in R_B}$	$\bar{w}_S$ [cm^2 s]	$\bar{w}_B$ [cm^2 s]	χ_S	χ_B
2-4 keV	124	103	1841	2150	2.92×10^7	2.93×10^7	0.8	0.1
4-6 keV	76	94	1841	2150	2.79×10^7	2.81×10^7	0.8	0.1
6-8 keV	57	65	1841	2150	2.21×10^7	2.22×10^7	0.8	0.1
MOS								
Range	c_s	c_B	$\sum_{p\in R_S}$	$\sum_{p\in R_B}$	$\bar{w}_S$ [cm^2 s]	$\bar{w}_B$ [cm^2 s]	χ_S	χ_B
2-4 keV	35	38	2926	3380	4.21×10^6	4.21×10^6	0.8	0.1
4-6 keV	17	28	2926	3380	3.70×10^6	3.70×10^6	0.8	0.1
6-8 keV	15	20	2926	3380	1.81×10^6	1.81×10^6	0.8	0.1

Table E.13: As in Tab. E.8 but for RX J1605.3+3249.

RX J2143.0+0654

Range	c_s	c_B	$\sum_{p\in R_S}$	$\sum_{p\in R_B}$	$\bar{w}_S$ [cm^2 s]	$\bar{w}_B$ [cm^2 s]	χ_S	χ_B
2-4 keV	61	62	2720	3148	5.06×10^6	5.05×10^6	0.8	0.1
4-6 keV	41	37	2720	3148	4.86×10^6	4.84×10^6	0.7	0.1
6-8 keV	33	34	2720	3148	3.84×10^6	3.82×10^6	0.8	0.1

Table E.14: As in Tab. E.8 but for RX J2143.0+0654.

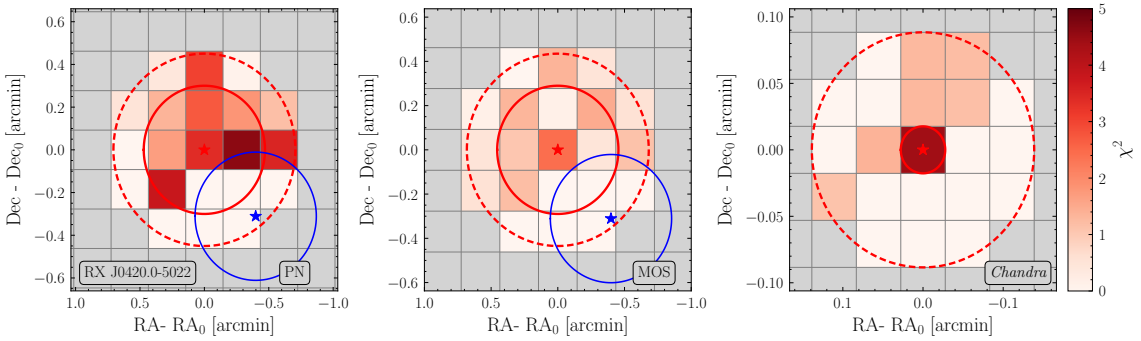

Figure E.2: The χ^2 maps for RX J0420.0-5022 in PN, MOS, and *Chandra* computed using counts from the 2-8 keV energy range. Evidence for an excess in the central pixel is observed for the *Chandra* and MOS maps, while the most significant excesses for the PN map is displaced from the center by one pixel. This one-pixel displacement of the most significant pixel from the source center is consistent with the spread expected given the angular resolution and the $\sim 3\sigma$ detection significance for PN (see Tab. 6.3). See the text for an expanded discussion.

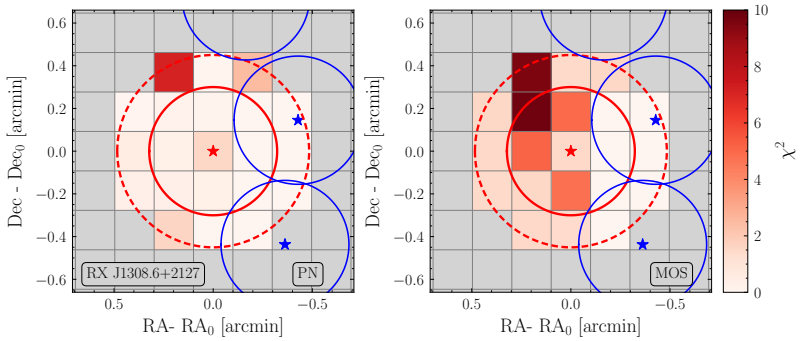

Figure E.3: The χ^2 maps for RX J1308.6+2127 in PN and MOS. There is a nearby point source, but its mask does not include any of the signal or background extraction regions. There is no strong evidence for an excess in the central pixel.

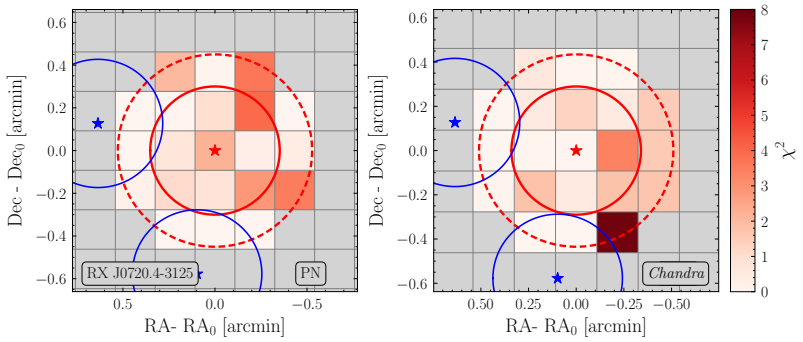

Figure E.4: The χ^2 map for RX J0720.4-3125 as observed by the PN and MOS instruments. There is no evidence for a central-pixel excess. There is a somewhat nearby point source.

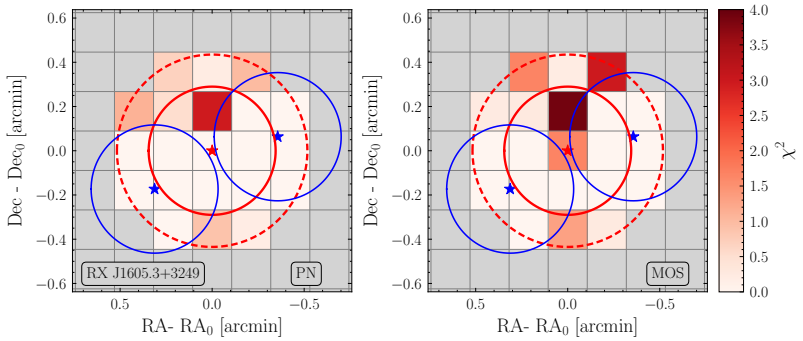

Figure E.5: The χ^2 maps for RX J1605.3+3249 for observations using the PN and MOS instruments. No relevant point sources are detected, and there is no evidence for a central-pixel excess in either instrument.

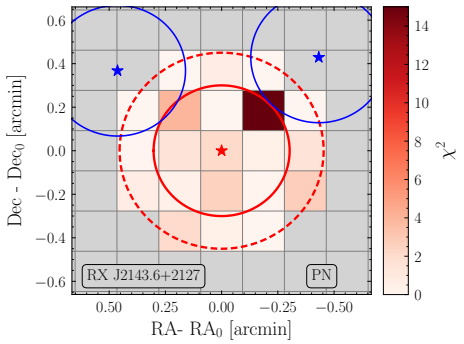

Figure E.6: The χ^2 map for RX J2143.0+0654 for observations using the PN instrument. No relevant point sources are detected, and there is no significant evidence for a central-pixel excess.

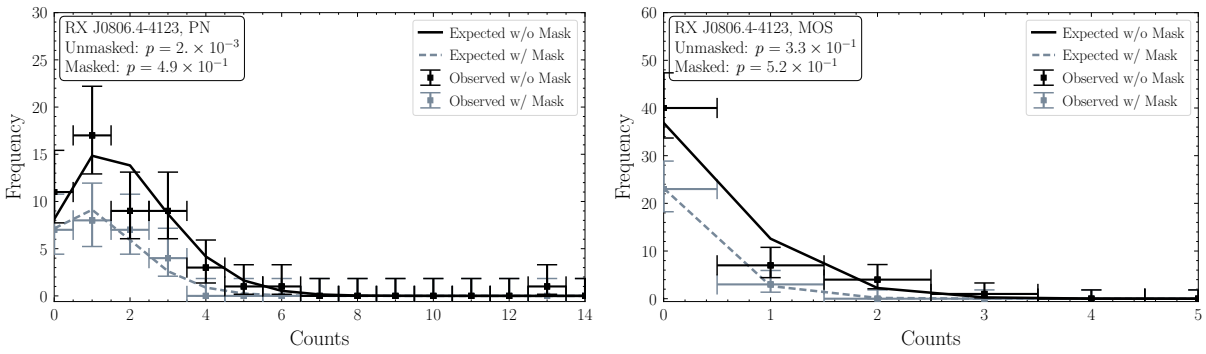

Figure E.7: As in Fig. 6.3 but for RX J0806.4-4123. In particular, we show the distribution of background counts by pixel for RX J0806.4-4123 with and without point source masking in both PN (*left*) and MOS (*right*) instruments. The point source mask only narrowly overlaps with the background extraction regions and therefore has marginal impact on the goodness of fit.

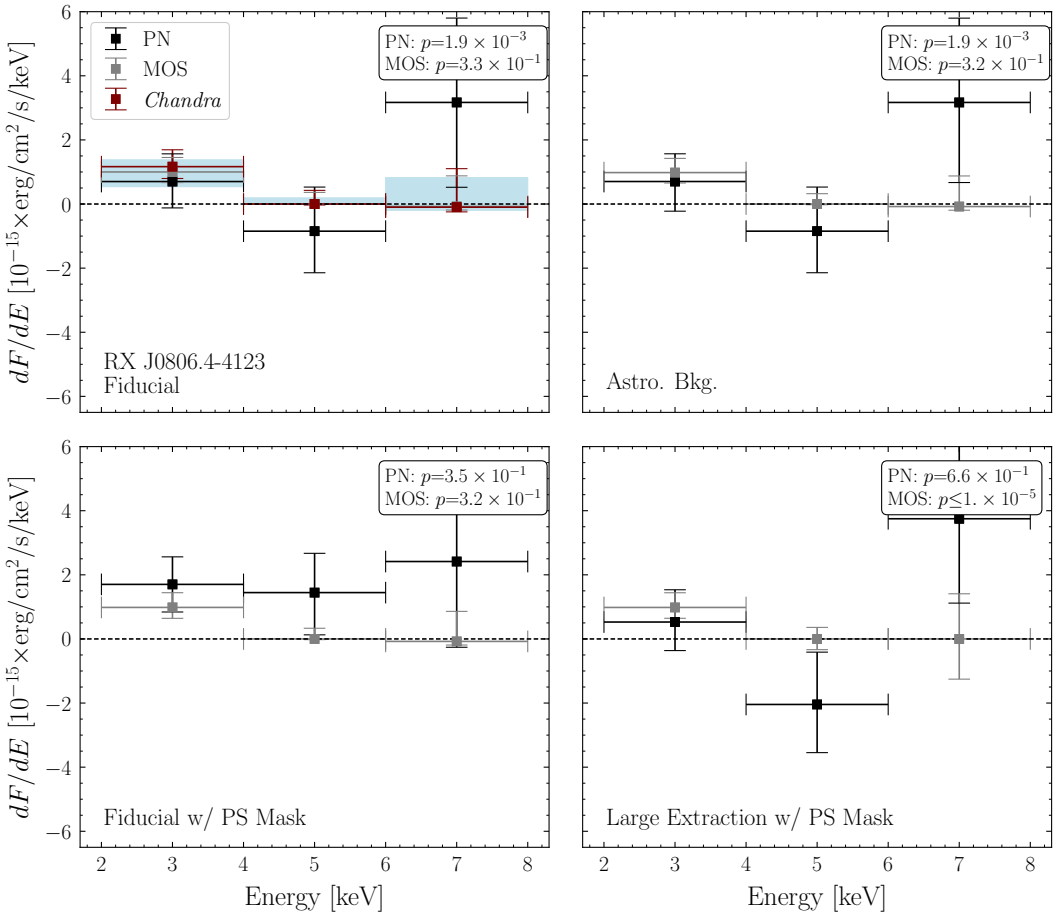

Figure E.8: As in Fig. 6.4 but for RX J0806.4-4123. Because the point source mask only narrowly overlaps with the background extraction regions, the effect of its inclusion on the reconstructed fluxes and limits is negligible.

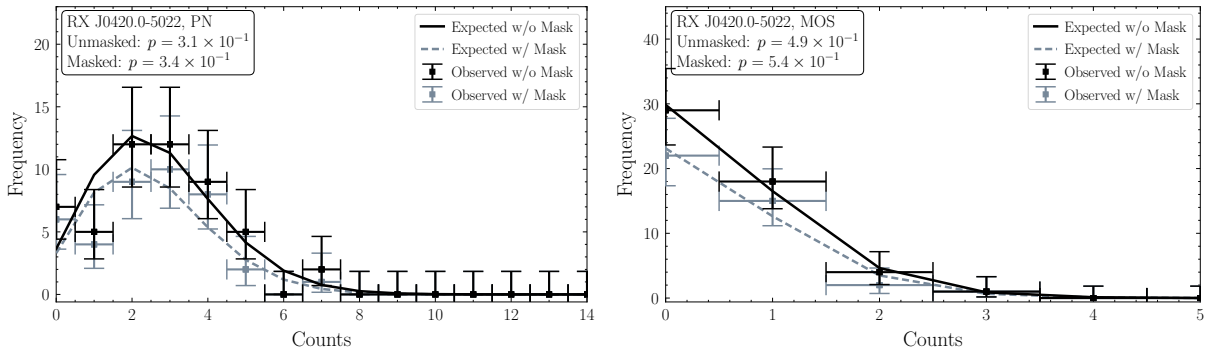

Figure E.9: The distribution of background counts by pixel for RX J0420.0-5022 in the PN (*left*) and MOS (*right*) instruments. No point source was found near enough to the signal or background extraction regions to require masking.

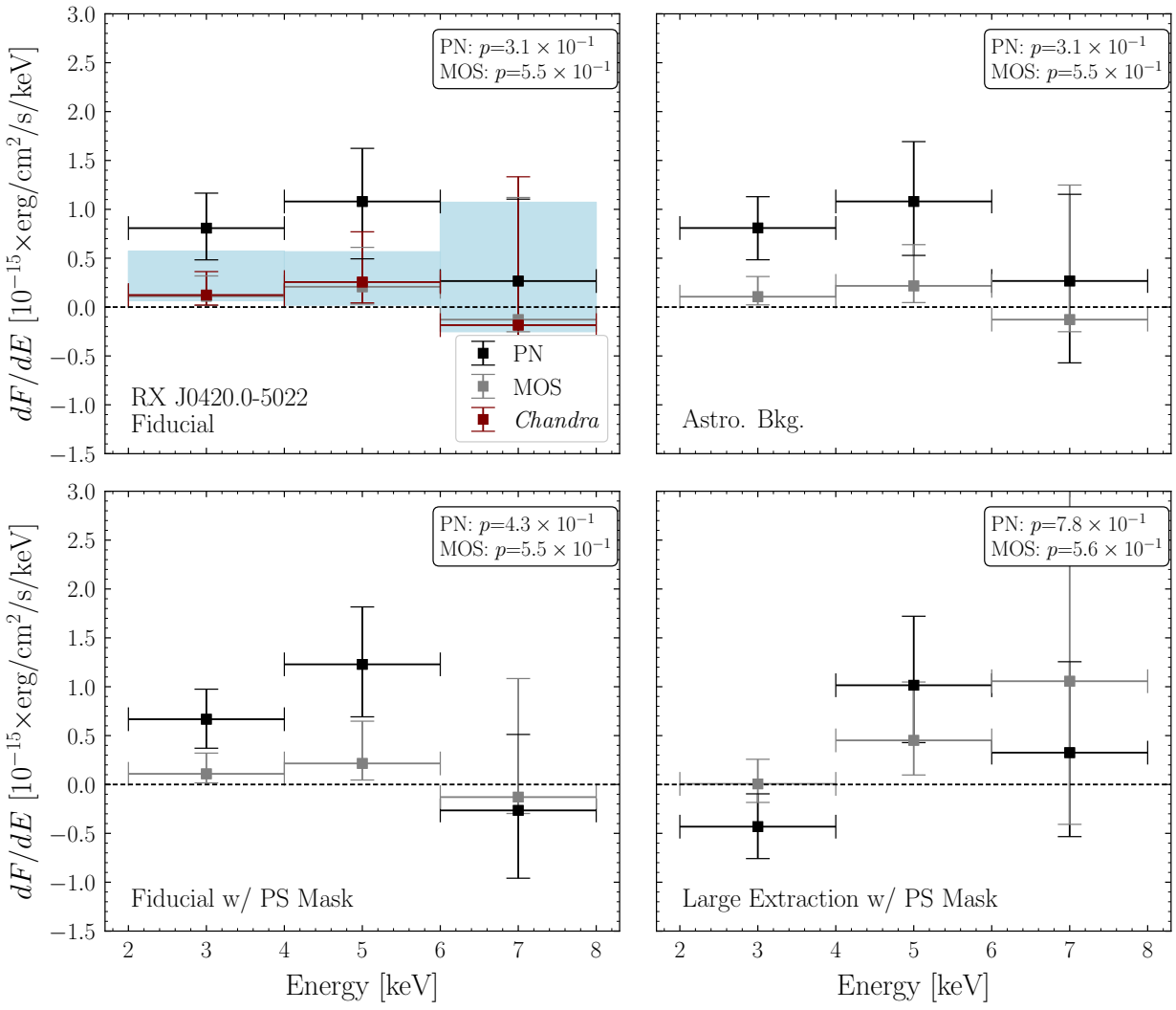

Figure E.10: Systematic variations on the analysis procedure on the reconstructed fluxes and limits at each energy bin for RX J0420.0-5022. A statistically significant excess in the power-law fit is found for this NS.

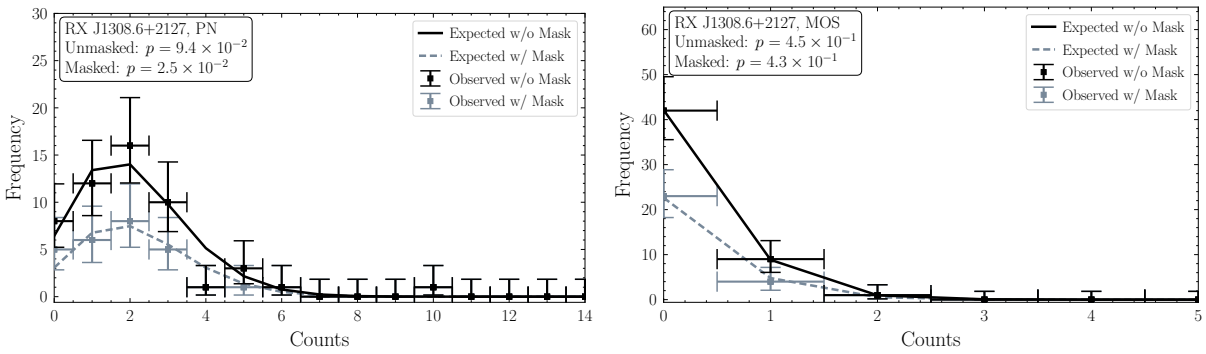

Figure E.11: The distribution of background counts by pixel for RX J1308+2127 in both PN (*left*) and MOS (*right*) instruments. No nearby point sources are detected that required masking.

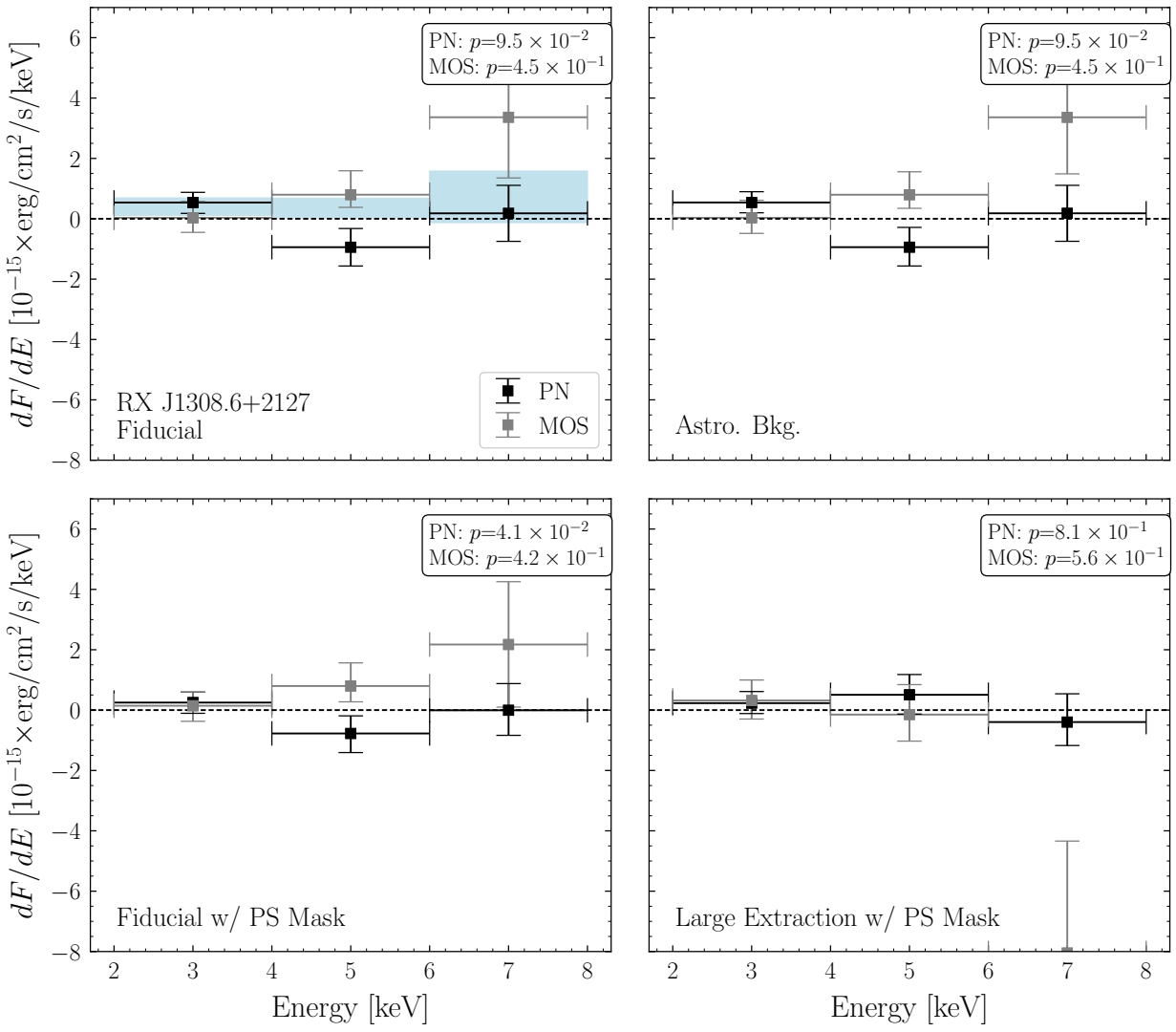

Figure E.12: Systematic variations on the analysis procedure on the reconstructed fluxes and limits at each energy bin for RX J1308+2127.

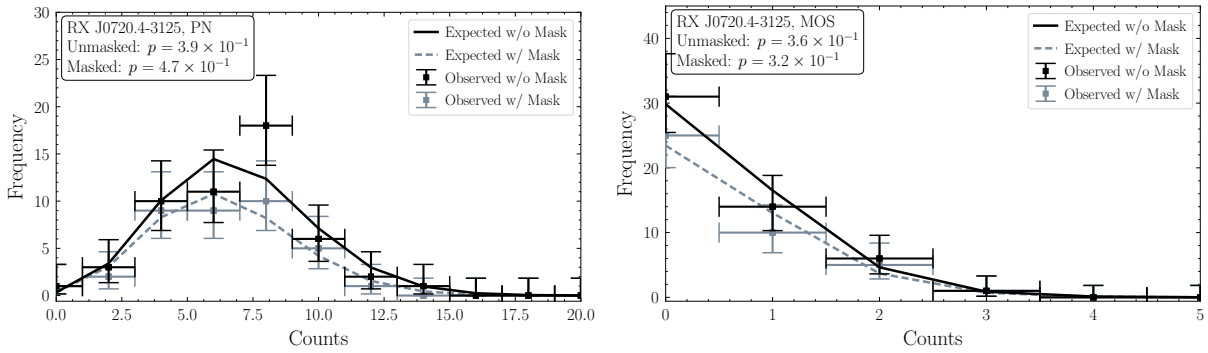

Figure E.13: The distribution of background counts by pixel for RX J0720.4-3125 in both PN (*left*) and MOS (*right*). A nearby point source is detected, but masking it has marginal impact on the goodness of fit.

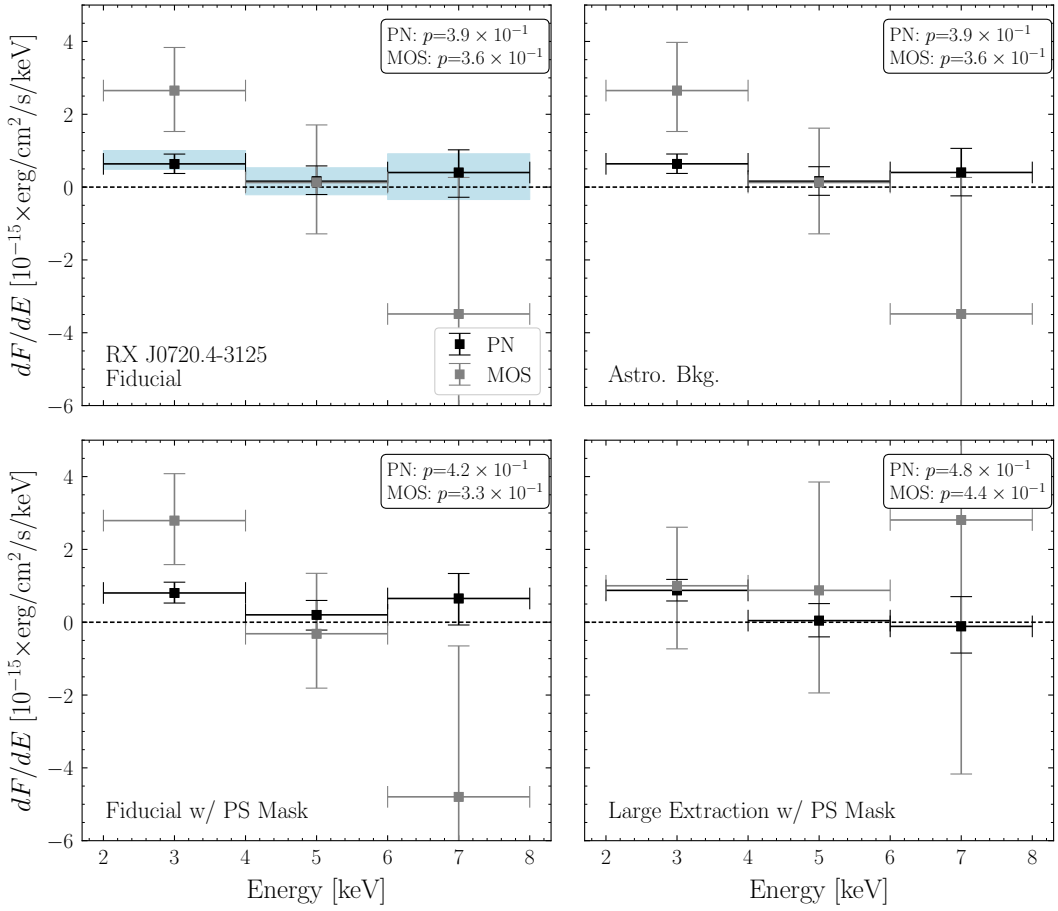

Figure E.14: Systematic variations on the analysis procedure on the reconstructed fluxes at each energy bin for RX J0720.4-3125.

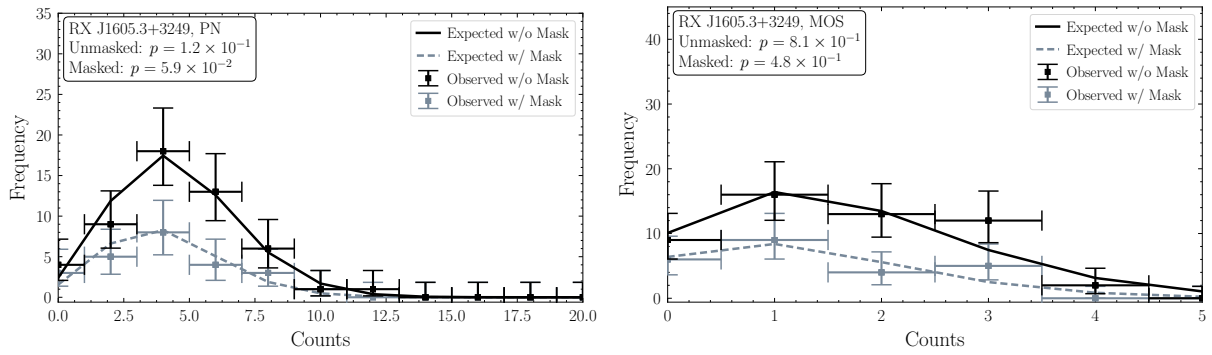

Figure E.15: The distribution of background counts by pixel for RX J1605.3+3249 in the PN (*left*) and MOS (*right*) instrument.

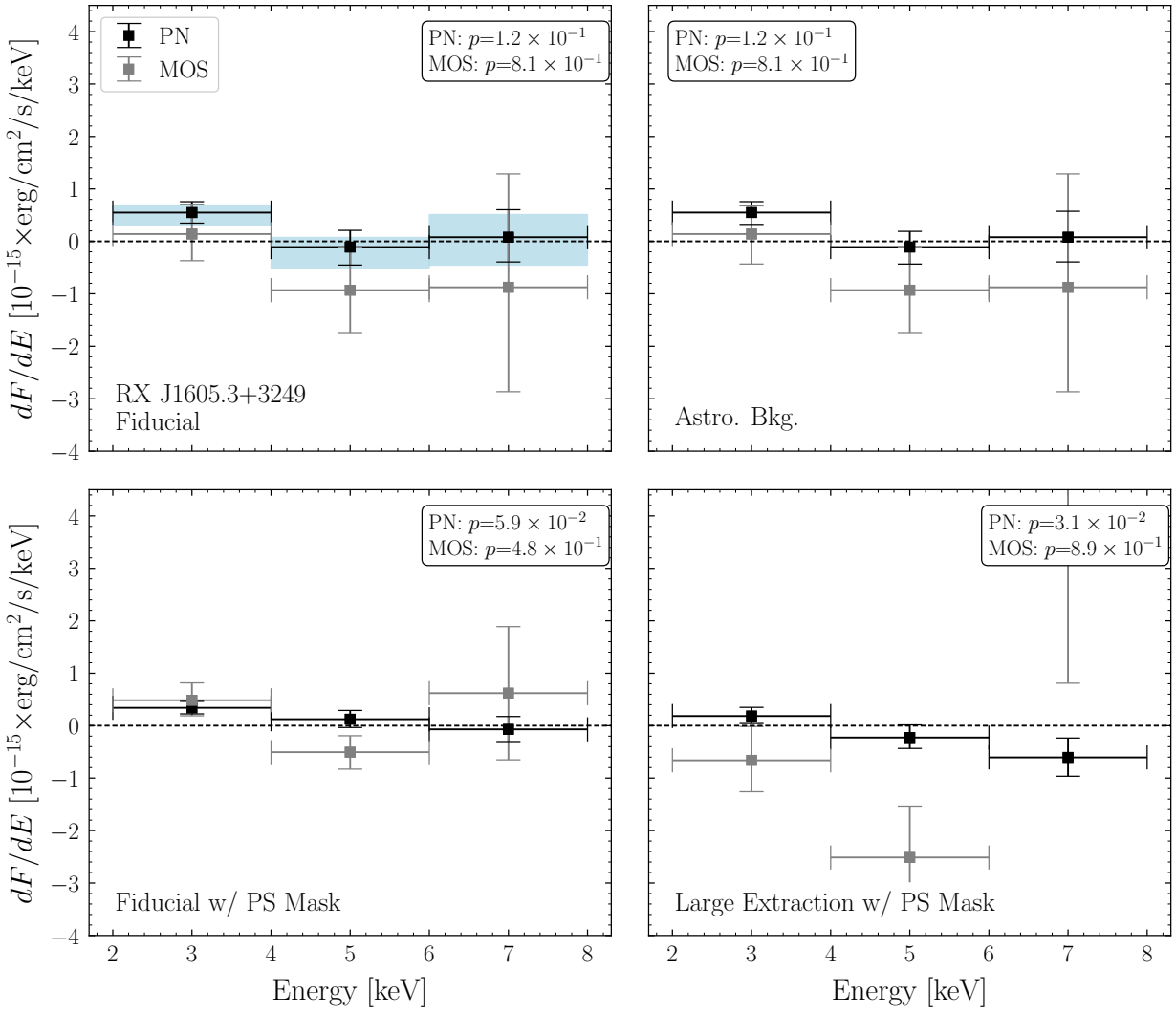

Figure E.16: Systematic variations on the analysis procedure on the reconstructed fluxes at each energy bin for RX J1605.3+3249.

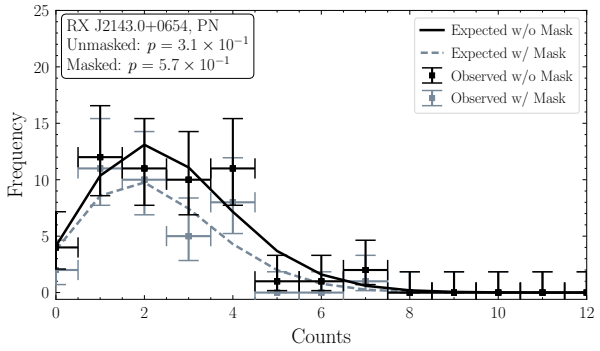

Figure E.17: The distribution of background counts by pixel for RX J2143.0+0654 in the PN instrument.

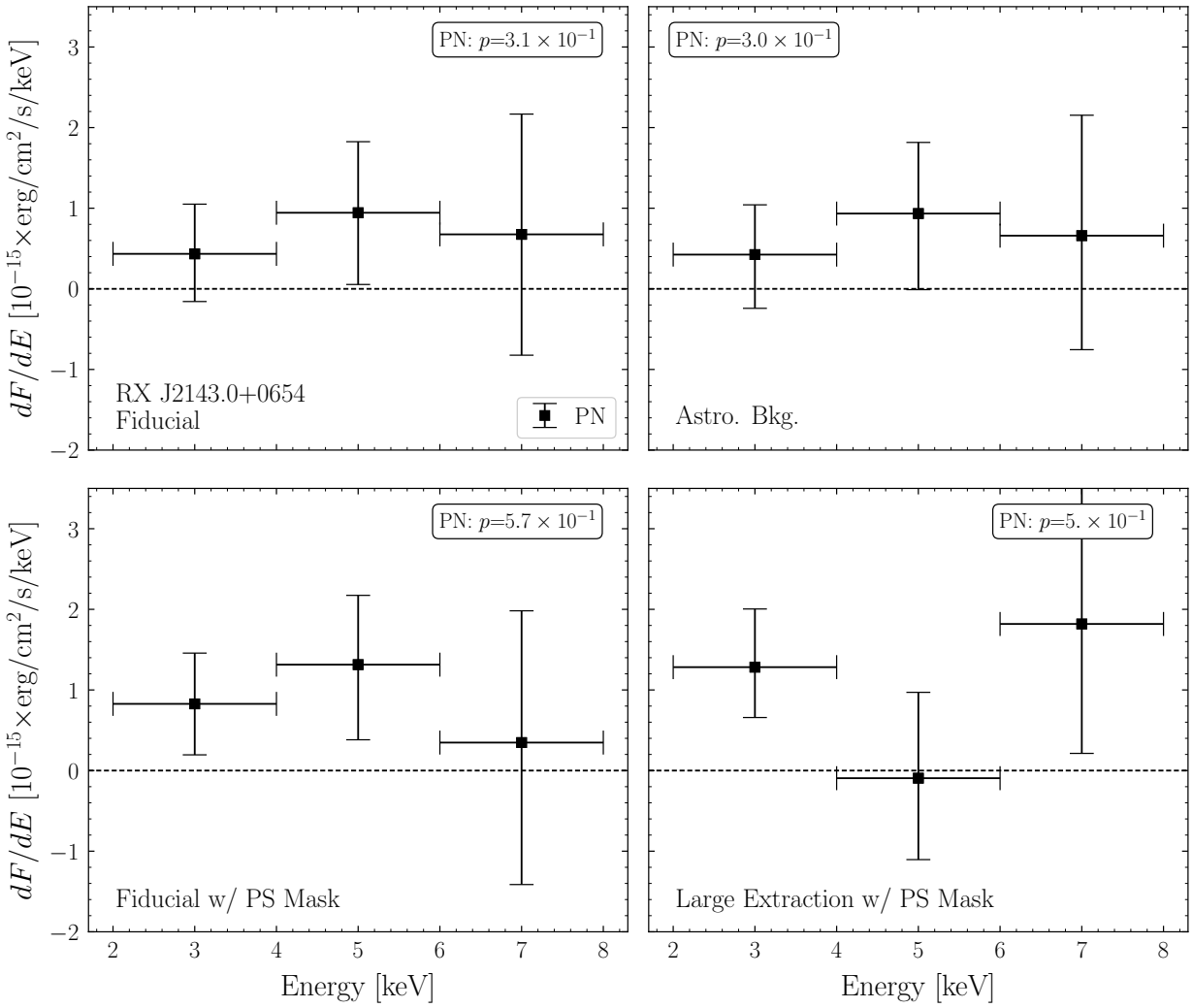

Figure E.18: Systematic variations on the analysis procedure on the reconstructed fluxes at each energy bin for RX J2143.0+0654.

E.5 Inspection of the 8-10 keV energy bin

In this analysis, we have chosen to exclude the analysis of X-ray counts in the energies between 8 and 10 keV. This choice is motivated by a number of statistical and systematic technical issues. In the 8-10 keV bin, the background count rate increases substantially. For instance, for RX J1856.6-3754, in PN the effective area decreases by 45% from the 6-8 keV bin to the 8-10 keV bin, while the absolute number of counts increases by 30% from 6-8 keV to 8-10 keV. Likewise, in MOS the effective area decreases by 67% while the absolute counts decreases by only 21%, and in *Chandra*, the effective area decreases by 75% while the

absolute counts decreases by only 52%. This reduces our overall sensitivity in the 8-10 keV bin while also rendering our analysis more susceptible to mismodeling the background, which is spatially inhomogeneous over the detector. Moreover, the calibration of the instruments becomes more uncertain at higher energies. Additionally, pileup may significantly suppress the counts in this bin due to migrating the photon energies above the detector threshold. Finally, the detector PSF increases with energy and our signal region can become appreciably contaminated by nearby point sources.

For completeness, we include the best-fit intensities in the 8-10 keV bin for each NS along with the p-value for its goodness-of-fit in the background region under the null model in Fig. E.19. Even discounting the systematic errors discussed above, the statistical uncertainties on the intensity tend to be quite weak in the 8-10 bin as compared to those uncertainties for energies between 2-8 keV. The data also appears to demonstrate more frequent under-fluctuations, which could be the result of systematic biases.

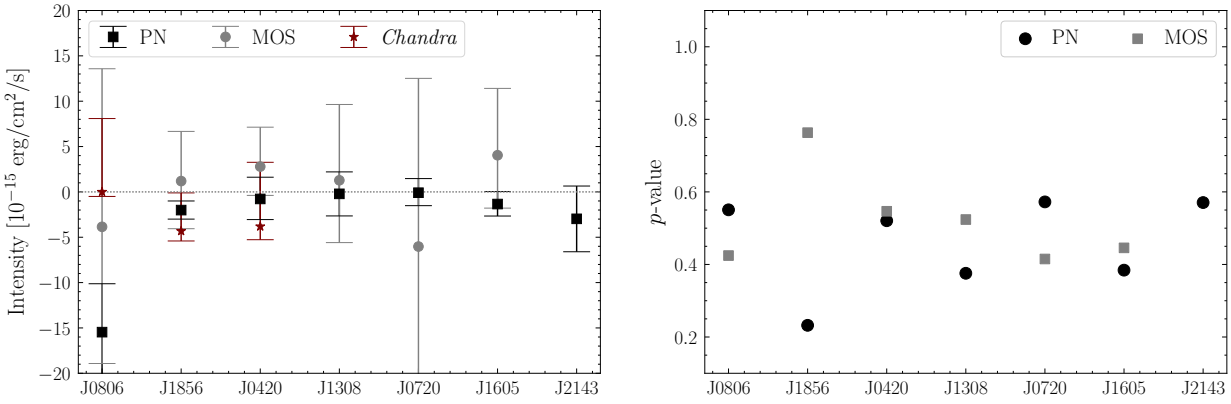

Figure E.19: (*Left*) The 68% confidence intervals for the reconstructed intensities in the 8-10 keV bin only in each instrument and for each NS. (*Right*) The p-values for observing a pixel-by-pixel background with a likelihood less than the one observed in the data assuming the fitted background rate as its true rate, indicating the goodness-of-fit of the background model to the data. In this figure we restrict to counts at energies between 8 and 10 keV. The p-value for PN data from RX J1856.6-3754 is quite poor, while the rest of the p-values are above 0.1.

Appendix F

Axion Emission Can Explain a New Hard X-ray Excess from Nearby Isolated Neutron Stars

This Supplementary Material is organized as follows. Section F.1 discusses our determination of the core temperature uncertainties, given the surface temperature data for the M7. In Sec. F.2 we outline our computation of the axion production rates via nucleon bremsstrahlung accounting for the possible suppression of the rates during neutron superfluidity. Sec. F.3 details the statistical analysis framework used to interpret the X-ray data in the context of the axion model. In Sec. F.4 we present calculations of the axion emission rate and spectrum via the Cooper pair-breaking-formation (PBF) processes and discuss the expected spectra from the NSs. Finally in Sec. F.5 we perform multiple systematic tests on the analyses presented in the main chapter and discuss the robustness of our results.

F.1 Core Temperatures

In this section, we estimate the uncertainties in the determinations of the core temperatures from the known surface temperatures of the NSs. The inner region of the NS is isothermal in the sense that the redshifted temperature observed infinitely far from the NS, $T_b^\infty = T_b(r)\sqrt{g_{00}(r)}$, is independent of the production radius r within the NS, with g_{00} the temporal component of the metric. We define the un-redshifted core temperature as $T_b = T_b(r_b)$, where r_b is the radius of the outer boundary of the isothermal internal region. Note that r_b is slightly smaller than the radius of the NS, $r_{\rm NS}$. Surrounding the isothermal region is the NS envelope, over which the temperature cools to the surface temperature $T_s = T_s^\infty/\sqrt{g_{00}(r_{\rm NS})}$

at the outer surface.

In practice, we use `NSCool` to compute T_b given T_s, but we estimate the uncertainty in this determination using the analytic relations determined from fits to simulations given in Eq. 32 of [555] and Sec. A.3 of [414]. The majority of the uncertainty arises from the uncertainty in the NS surface gravity (because of the uncertainty in the NS EOS) and in the NS accretion history. The NS EOS and the NS masses are sources of uncertainty that should be more thoroughly investigated in future work.

We estimate such uncertainties by varying over the amount of accreted matter $M_{\rm ac}$ and the surface gravity g_{14} in 10^{14} cm/s^2. We assume a wide range of $2 \leq g_{14} \leq 6$, as a conservative estimate based on [556]. The NSs of interest are isolated and are not expected to accrete much matter. We assume a flat prior in $-20 \leq \log(M_{\rm ac}/M_{\rm tot}) \leq -10$, where $M_{\rm tot}$ is the total mass of the NS. In the relevant range of surface temperatures, we find that the standard deviation of T_b is around 30% of the mean. This is illustrated in Fig. F.1, where we show the central T_s-T_b relation along with the 68% containment region from varying over $M_{\rm ac}$ and g_{14} as described above. In the analyses throughout this chapter, we use normal uncertainties on the core temperatures, accounting for the 30% systematic uncertainty.

Additional uncertainty on the core temperature arises from the intrinsic uncertainty in the surface temperatures. In addition to the uncertainty determined in the Ref. [15], we assign a 25% uncertainty on the surface temperature to account for the variation in NS atmosphere models as well as the unknown surface composition. Note that the surface composition is related to the accretion history and so some of the uncertainties are interrelated. We convert the surface temperature uncertainties to core temperature uncertainties using the analytic relations above. We finally combine the three uncertainties into a single normal prior on the core temperature reported in Tabs. 7.1 and F.2. Lastly, we note that as mentioned in the main chapter the core temperatures may also be estimated from the kinematic ages of the NSs, and when such estimates are available we find good agreement, within uncertainties, between the surface-temperature-based core temperature estimates and the age-based estimates of the core temperatures.

F.2 Nucleon bremsstrahlung rates

Here we provide a brief overview of how the nucleon bremsstrahlung rates are calculated in the NS cores. We can safely assume a degenerate limit for the nucleon-nucleon bremsstrahlung emission in the NS cores because the NSs we consider have $T \ll \mathcal{O}(\text{MeV})$ [301]. The production rate of axions from a NS via nucleon-nucleon bremsstrahlung emission in the degenerate limit is calculated by [300, 394], assuming no nucleon superfluidity.

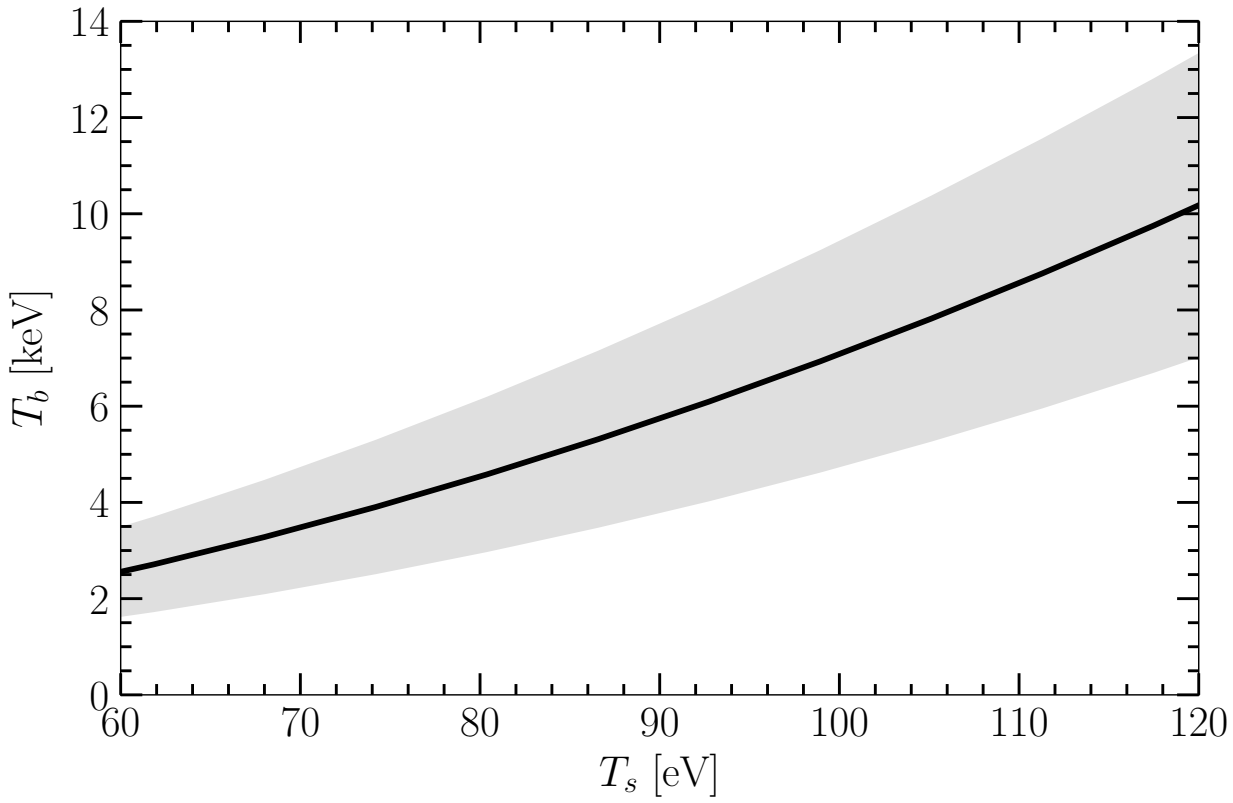

Figure F.1: An illustration of the uncertainty on the determination of T_b, given the surface temperature T_s, arising from the uncertainties in the surface gravity and the amount of accreted matter. The black curve shows the average value of T_b for each given T_s if one assumes flat priors in $2 \leq g_{14} \leq 6$ and $-20 \leq \log(M_{\rm ac}/M_{\rm tot}) \leq -10$, whereas the gray band shows the 68% containment region on T_b given T_s.

These production modes are suppressed by an energy-independent factor below the critical temperature T_c at which the nucleons form Cooper pairs and undergo a phase transition into the superfluid state. Note that Cas A cooling measurements provide indirect evidence that such a transition takes place [399]. This is because the superfluid suppression also occurs for neutrino emission via the modified Urca process, and Cas A is thought to cool primarily from neutrino emission [317]. The explicit formulae that we use for the singlet-state pairing suppression factors may be found in [317] (see also [296]). The neutrons in the core, however, are thought to undergo triplet-state pairing, and the explicit formula for the triplet-state pairing suppression factors have not been worked out. We follow the code package `NSCool` and approximate the triplet-state pairing suppression factors by the singlet-state ones [318].

F.3 Statistical analysis framework

In this section we briefly overview the statistical analysis framework that we use to interpret the X-ray data in the context of the axion model. Our starting point is the photon-count based likelihoods computed in [15]. These are given by functions $\mathcal{L}_i(\boldsymbol{x}_i|S_i)$ of flux S_i, where i labels the energy bin and $\boldsymbol{x}_i$ denotes the dataset associated with that energy bin. These Poisson likelihoods use the expected number of background counts in the signal region, the observed number of counts, and the conversion factor to go from flux to counts accounting for the instrumental response; all of these quantities are provided in [15].

Given the likelihoods in the individual energy bins we may construct the joint likelihood that constrains the axion model:

$$\mathcal{L}_{\rm axion}(\boldsymbol{x}|\{m_a, g_{a\gamma\gamma}g_{ann}, \theta_{\mathbf{n}}\}) = \prod_i \mathcal{L}_i\big[\boldsymbol{x}_i|S_i(\{m_a, g_{a\gamma\gamma}g_{ann}, \theta_{\mathbf{n}}\})\big] \times \mathcal{L}_{\rm prior}(\theta_{\mathbf{n}})\,, \tag{F.1}$$

where the product i is over all energy bins used in the analysis and where $\mathcal{L}_{\rm prior}(\theta_{\mathbf{n}})$ denotes the prior distribution for the nuisance parameters $\theta_{\mathbf{n}}$, which will be discussed more shortly. The axion model parameters are the mass m_a and the coupling combination $g_{a\gamma\gamma}g_{ann}$, while the dataset $\boldsymbol{x} = \{\boldsymbol{x}_i\}$ is the union of the datasets in the individual energy bins. The nuisance parameters $\theta_{\mathbf{n}} = \{d, T_b^\infty, \theta\}$ denote the uncertain properties of the NSs that we vary over in the fit, such as the distance d, the core temperature T_b^∞, and the alignment angle with respect to Earth θ. In particular we use the (un-normalized) prior distribution function

$$\mathcal{L}_{\rm prior}(\theta_{\mathbf{n}}) = \exp\left[\frac{-(T_b^\infty - \bar{T}_b^\infty)^2}{2\sigma^2_{T_b^\infty}}\right] \exp\left[\frac{-(d-\bar{d})^2}{2\sigma_d^2}\right] \Theta(T_b^\infty)\Theta(d)\Theta(\theta\times(\pi-\theta))\,, \tag{F.2}$$

where quantities with an over-bar denote the central measured parameters given in Tab. 7.1, the σ's denote the standard deviations presented in that table, and Θ is the Heaviside step function so that T_b^∞ and d stay positive and θ has a flat prior between $(0, \pi)$.

To construct 95% upper limits on $g_{a\gamma\gamma}g_{ann}$ we fix m_a and consider the profile likelihood $\mathcal{L}_{\rm axion}(\boldsymbol{x}|\{m_a, g_{a\gamma\gamma}g_{ann}\})$ as a function of $g_{a\gamma\gamma}g_{ann}$. Note that to construct the profile likelihood we maximize the log-likelihood over the nuisance parameters. We employ Wilks' theorem to assume that the log-likelihood is asymptotically χ^2 distributed (we have checked that this is valid explicitly with Monte Carlo), so that the 95% upper limit may be found from the value $g_{a\gamma\gamma}g_{ann} > \overline{g_{a\gamma\gamma}g_{ann}}$ such that $2\times[\mathcal{L}_{\rm axion}(\boldsymbol{x}|\{m_a, g_{a\gamma\gamma}g_{ann}\}) - \mathcal{L}_{\rm axion}(\boldsymbol{x}|\{m_a, \overline{g_{a\gamma\gamma}g_{ann}}\})] \approx -2.71$ (see *e.g.* [109]), with $\overline{g_{a\gamma\gamma}g_{ann}}$ denoting the coupling combination that maximizes the likelihood at fixed m_a. To search for evidence of the axion mode, which we find, we consider the discovery test statistic $\mathrm{TS} = -2\times[\mathcal{L}_{\rm axion}(\boldsymbol{x}|\{m_a, g_{a\gamma\gamma}g_{ann}\}) - \mathcal{L}_{\rm axion}(\boldsymbol{x}|\{m_a, \overline{g_{a\gamma\gamma}g_{ann}}\})]$,

which is a function of both m_a and $g_{a\gamma\gamma}g_{ann}$. The best-fit 1σ interval, for example, is defined by the region in axion mass and coupling space where the discovery TS is within a value of unity from the maximum, again assuming Wilks' theorem holds (which we have checked explicitly).

F.4 Cooper Pair-Breaking-Formation Processes

Cooper pairs are expected to form when the temperature is below the superfluid critical temperature. When the temperature is still not far below the critical temperature, the thermal interactions can break the Cooper pairs. Neutrinos and axions can be produced and carry away energy released during these Cooper pair breaking and formation processes. In the fiducial analysis, this production mode was not active because our fiducial analysis assumes no core superfluidity. In this section we review the axion emission rates from these processes, derive the energy spectrum, and discuss the implication for the high-energy X-ray flux.

F.4.1 Emission Rates

The NS cores may contain spin-0 S-wave and spin-1 P-wave nucleon superfluids. There then exists a production mode of axions via Cooper pair-breaking-formation (PBF), with a rate for the S-wave pairing given by [296, 298]

$$\begin{aligned} \epsilon^S_{a,\mathrm{PBF}} &= \frac{2g^2_{aNN}}{3\pi m_N^2}\,\nu_N(0)\,v_F(N)^2\,T^5\,I^S_a\,, \\ I^S_a &= z_N^5\int_1^\infty dy\;\frac{y^3}{\sqrt{y^2-1}}\left[f_F\left(z_N y\right)\right]^2\,, \qquad \text{with}\;\; f_F(x)=\frac{1}{e^x+1}\,. \end{aligned} \tag{F.3}$$

Above, $\nu_N(0) = m_N p_F(N)/\pi^2$ is the density of states at the Fermi surface, with $v_F(N)$ the fermion velocity. Here $z_N = \Delta(T)/T$, and a simple analytic fit for the superfluid energy gap $\Delta(T)$ is given in [317]. The PBF process is active when the temperature falls below the critical temperature T_c. Due to the sensitive dependence of T in f_F, the emission rate is exponentially suppressed however at low temperatures, *i.e.* $T \ll T_c$.

One should identify $2y\Delta(T)$ as the axion energy ω (this follows from the derivation

of (F.3)), and thus the energy spectrum follows the functional form

$$J^S_{a,\mathrm{PBF}} \equiv \frac{d\left(\epsilon^S_{a,\mathrm{PBF}}\right)}{d\omega} = \frac{\mathcal{N}^S_{a,\mathrm{PBF}}}{2\Delta(T)} \frac{\left(\frac{\omega}{2\Delta(T)}\right)^3}{\sqrt{\left(\frac{\omega}{2\Delta(T)}\right)^2 - 1}} \left[f_F\left(\frac{\omega}{2T}\right)\right]^2 , \tag{F.4}$$

where $\mathcal{N}^S_{a,\mathrm{PBF}}$ is the normalization constant determined by $\int_{2\Delta(T)}^{\infty} J^S_{a,\mathrm{PBF}} d\omega = \epsilon^S_{a,\mathrm{PBF}}$ and reads $\mathcal{N}^S_{a,\mathrm{PBF}} = \epsilon^S_{a,\mathrm{PBF}} z_N^5 / I^S_a$. Here T and ω refer to the locally-measured quantities inside the NS at some radius r_0, *i.e.* $T = T_b(r_0) = T_b^\infty/\sqrt{g_{00}(r_0)}$ and $\omega = \omega(r_0) = \omega_\infty/\sqrt{g_{00}(r_0)}$. Practically, one first computes the initial spectral function $J^S_{a,\mathrm{PBF}}(\omega(r_0))$ at each radius r_0 using the local temperature $T_b(r_0)$ and then interprets the observed spectral function as $J^S_{a,\mathrm{PBF}}(\omega_\infty/\sqrt{g_{00}(r_0)})$ with ω_∞ identified as the observed X-ray energy.

Similarly, the rate for the neutron P-wave pairing is [296, 298]

$$\begin{aligned} \epsilon^P_{a,\mathrm{PBF}} &= \frac{2 g_{ann}^2}{3\pi m_N^2} \nu_n(0)\, T^5\, I^P_{an} \,, \\ I^P_{an}(z_x) &= \int \frac{d\Omega}{4\pi} z_x^5 \int_1^\infty dy\, \frac{y^3}{\sqrt{y^2-1}} \left[f_F\left(z_x y\right)\right]^2 , \qquad \text{with} \quad f_F(x) = \frac{1}{e^x + 1} \,. \end{aligned} \tag{F.5}$$

There exist two types of the P-wave pairings. In [298], types A and B refer to the ${}^3P_2$ pairing with total projection of the Cooper-pair momentum onto the z-axis equal to $m_J = 0$ and 2, respectively. The anisotropic superfluid gaps are given by

$$\begin{aligned} \Delta_A(T,\theta) &= \Delta_0^{(A)}(T)\sqrt{1 + 3\cos^2\theta} \,, \\ \Delta_B(T,\theta) &= \Delta_0^{(B)}(T)\sin\theta \,, \end{aligned} \tag{F.6}$$

with θ the angle between the neutron momentum and the quantization axis and $z_x \equiv \Delta_x(T,\theta)/T$. Explicit expressions for $\Delta_0^{(A,B)}(T)$ may be found in [298] along with approximations for the phase space integrals I^P_{an}.

With $2y\Delta_x(T,\theta)$ identified as the axion energy ω, the spectra for the P-wave pairings follows as

$$J^P_{a,\mathrm{PBF}} \equiv \frac{d\left(\epsilon^P_{a,\mathrm{PBF}}\right)}{d\omega} = \int_{-1}^{1} \frac{d\cos\theta}{2} \frac{1}{2} \Delta_x(T,\theta)^4 \mathcal{N}^P_{a,\mathrm{PBF}} \frac{\left(\frac{\omega}{2\Delta_x(T,\theta)}\right)^3}{\sqrt{\left(\frac{\omega}{2\Delta_x(T,\theta)}\right)^2 - 1}} \left[f_F\left(\frac{\omega}{2T}\right)\right]^2 , \tag{F.7}$$

where $\mathcal{N}^P_{a,\mathrm{PBF}}$ is the normalization constant defined by $\int_{2\Delta(T,\theta)}^{\infty} J^P_{a,\mathrm{PBF}} d\omega = \epsilon^P_{a,\mathrm{PBF}}$; then $\mathcal{N}^P_{a,\mathrm{PBF}} = \epsilon^P_{a,\mathrm{PBF}}/T^5 I^P_{an}(z_{x0})$ with $z_{x0} \equiv \Delta_0^{(x)}(T)/T$.

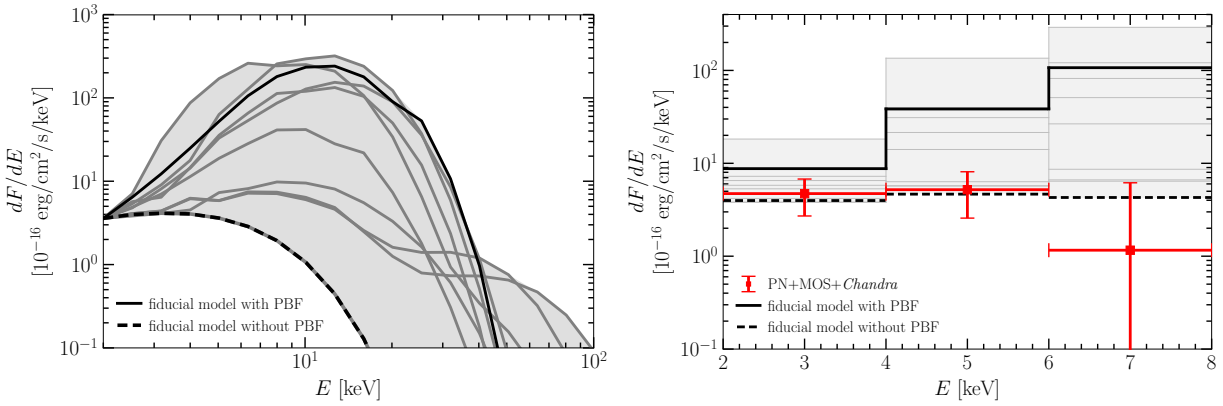

Figure F.2: (Left) The full energy spectrum from NS J1856 as predicted by the best fit of the axion model with the joint likelihood procedure performed in the main analysis at energies below 8 keV. The black dashed curve is the fiducial model we use in the main analysis, where no superfluidity is active, while the solid black curve shows the spectrum corresponding to our fiducial superfluidity model. The gray curves show the predictions from other superfluid models that we tested and the gray shaded region demonstrates the uncertainty as a result of the different superfluid models. Note that there are three models that predict no enhancement and are overlapped with the black dashed curve. (Right) As in the left panel, but zoomed in below 8 keV and binned in 2 keV energy bins to provide a direct comparison to the X-ray data, which is also shown.

F.4.2 High-Energy Spectrum

At high energies, the flux may be dominated by the axions emitted in the PBF processes outlined in Sec. F.4.1. The spectral functions are sharply peaked at twice the gap energy, which is also the lower cutoff of the axion energy due to conservation of energy. The spectral functions then drop off quickly at higher energies. The exception is for the type B process in the P-wave pairing, where the gap energy $\Delta_B(T,\theta)$ is anisotropic and can be small when the neutron momentum is approximately aligned with the quantization axis. This implies that the energy of the axion is distributed to values lower than the magnitude of the gap energy $\Delta_0^B(T)$ and is thus not subject to a specific lower cutoff. This is to be contrasted with $\Delta(T)$ and $\Delta_A(T,\theta)$ for the S-wave pairing and type A P-wave pairing, where a sharp lower cutoff is present for a given T.

We show in Fig. F.2 the predicted spectrum at high energies for J1856 assuming the best-fit core temperature from the global axion model fit. Different curves denote different models [557–561] used in `NSCool` for computing the superfluid critical temperatures of the NSs. Out of the twelve models available in `NSCool`, there exist three models [559, 561] that do not lead to superfluidity formation and thus the production is given by the nucleon bremsstrahlung processes as in the main chapter, where we assume no superfluidity, and

the predicted spectrum is given by the black dashed curve in Fig. F.2 in this case. With the black solid curve we show the spectrum from our fiducial superfluidity model (model I) which includes PBF emission due to superfluidity formation. That model takes the $^1S_0$ neutron pairing gap from [417], the neutron $^3P_2$ - $^3F_2$ pairing gap from "model a" in [562], and the proton $^1S_0$ pairing gap from [418], respectively, and predicts the maximum net high-energy intensity of all the superfluidity models considered. The gray shaded region spans between the black dashed curve and the maximum flux at each energy among the twelve models we scan over, representing an estimate of the model uncertainty in the flux. We note that we normalize the spectra of all models such that they all give the same value at 2 keV. Note that it may be seen that even below $\sim$3 keV there are small deviations away from the spectrum assumed in the main chapter for some superfluid models due to the Type B P-wave superfluid pairing PBF process.

If we instead fix $g_{a\gamma\gamma}g_{ann} = 1 \times 10^{-20}$ GeV^{-1} and take vanishing m_a, the predicted flux at 2 keV ranges from 2×10^{-16} to 8×10^{-15} erg/cm^2/s/keV for this NS depending on the superfluid model. This shows that the superfluid model can significantly affect the low-energy flux as well due to the superfluid suppression factors, though these are energy independent and do not modify the spectral shape.

We assumed $g_{app} = g_{ann}$ in Fig. F.2, but the PBF flux is dominantly from the P-wave processes, which only involve neutrons. Thus we expect g_{app} to play a less important role in the high-energy spectrum unless $g_{ann} \ll g_{app}$. Among the P-wave processes, emission from type B pairing dominates over that of type A. The predicted spectral shape is also highly dependent on the core temperature. At higher core temperatures, the spectral peak shifts to a higher energy.

The M7 have not been studied in detail before at energies greater than 10 keV. However, there are existing constraints from hard X-ray telescopes which we summarize now. The strongest constraint at these energies comes from the 105 month *Swift* Burst Alert Telescope all-sky hard X-ray survey [563], which covers the full sky with median sensitivity 7×10^{-12} erg/cm^2/s at 5σ in the 14 - 195 keV band. The predicted X-ray intensity from J1856 in this band assuming the fiducial model with superfluidity is 2×10^{-13} erg/cm^2/s with a contribution from nucleon bremsstrahlung of 6×10^{-16} erg/cm^2/s. For NSs near the galactic plane $|b| \leq 17.5^\circ$ (J1856, J0806, J0720, and J2143), constraints from the 14-year *INTEGRAL* galactic plane survey [564] with the IBIS camera apply. 90% of the survey area is covered down to a 17 - 60 keV flux limit of 1.3×10^{-11} erg/cm^2/s at 4.7σ. Our fiducial superfluidity model predicts an intensity for J1856 in this range of 2×10^{-13} erg/cm^2/s with a contribution from nucleon bremsstrahlung of 3×10^{-16} erg/cm^2/s. This information is summarized in Tab. F.1, where our fiducial model with superfluidity is denoted "maximum"

Energy Range	Current Limit	Projected Sensitivity ($t_{\rm exp}$ = 400 ks)	Predicted Intensity	
			minimum	maximum
Swift: 14 - 195 keV	7×10^{-12}	—	6×10^{-16}	2×10^{-13}
INTEGRAL: 17 - 60 keV	1.3×10^{-11}	—	3×10^{-16}	2×10^{-13}
NuSTAR: 6 - 10 keV	—	3×10^{-15}	2×10^{-15}	6×10^{-14}
NuSTAR: 10 - 60 keV	—	2×10^{-14}	2×10^{-15}	3×10^{-13}

Table F.1: The second and third columns show the current limit and future sensitivity on the X-ray intensity, whereas the last two columns list the maximum and minimum intensities predicted among the different superfluid models assuming the best fit of the axion model to the J1856 joint data. The "maximum" predicted intensity assumes our fiducial superfluidity model, which predicts the largest intensity in 10 - 60 keV band. The "minimum" predicted intensity is the nucleon bremsstrahlung contribution discussed in the main chapter. All intensities are in units of erg/cm^2/s.

and the nucleon bremsstrahlung contribution considered in the main chapter is denoted "minimum". Note, however, that the above limits assume a power-law intensity that peaks at low energies, whereas the axion intensity peaks at higher energies where both telescope effective areas are low, and the true limits on axion emission are likely weaker than reported here.

The *NuSTAR* telescope would currently provide the most sensitive search for ultra-hard X-ray emission ($\gtrsim$10 keV) from the M7. To date, *NuSTAR* has not observed any of the M7. In Tab. F.1 we show the projected sensitivity at 95% confidence for a 400 ks *NuSTAR* observation of J1856 in two energy bands, along with the predicted intensities in each model. $t_{\rm exp}$ = 400 ks is a comparable total exposure time to the *XMM* and *Chandra* exposure times for the M7 [15], and would confirm the emission below 10 keV and constrain the emission above 10 keV in some superfluidity models. Some of the models with superfluidity can be ruled out or confirmed with only a few ks of observation time.

F.5 Systematic Tests

In this SM section we consider multiple systematic variations to the analysis procedure presented in the main chapter. We begin by considering the consistency of the axion model between the three different cameras to assess possible systematic effects that only affect individual cameras. In the next subsection we restrict and broaden the energy range relative to our fiducial analysis to analyze the robustness of the signal to changes in the energy range used in the analysis. Next, we analyze separately the NSs that observe an excess and those

that do not to more quantitatively address the consistency between the null results and detections. In the following subsection we relax the restriction that $g_{app} = g_{ann}$ in the fit of the axion model to the X-ray data. We then consider how the best-fit axion parameter space and upper limit depend on the superfluidity model. Lastly, we consider alternate models for the NS magnetic field strengths and surface temperatures.

F.5.1 Dependence on instrument

In [15] we show that all three cameras (PN, MOS, and *Chandra*) give consistent spectra for the M7 hard X-ray flux. This is highly non-trivial considering that these instruments respond differently to *e.g.* pileup and unresolved point sources. Given that the observed fluxes are consistent between the three cameras, we also expect the best-fit axion parameter space regions to be consistent between the different cameras. Indeed, as we show in Fig. F.3, we observe this to be the case. In that figure we show the best-fit axion parameter space as in Fig. 7.2 but determined using the data from each camera independently, as indicated. Interestingly, we find significant evidence in favor of the axion model from each camera independently. We also show the observed intensities $I_{2-8}(I_{4-8})$, as described in the main chapter, and the best-fit temperatures.

F.5.2 Dependence on the energy range

In the main chapter we used three energy bins from 2 - 4, 4 - 6, and 6 - 8 keV for J1856 and J0420, while for the other 5 NSs we only used the last two energy bins. We find that removing the 2 - 4 keV energy bin for J1856 and J0420 leads to consistent results. Additionally, in [15] data is also presented for the 8 - 10 keV energy bin. For both *XMM-Newton* and *Chandra* this energy bin suffers from increased statistical and systematic uncertainties, as it is at the edge of the energy range of the cameras, so it is not included in the fiducial analysis. Still, it is reassuring to see that including this energy bin does not substantially influence the global fit, which is mostly due to the fact that the uncertainties in that bin are quite large. To emphasize these points in Fig. F.4 we show the best-fit axion parameter space and upper limit for variations to the energy bin choices. In the top left panel we use our fiducial energy bin choice but add in the 8 - 10 keV bin for all NSs. The top right panel is as in the top left but with the 2 - 4 keV bin removed for J1856 and J0420. Lastly, the bottom panel is as in the top right but without the 8 - 10 keV bin.

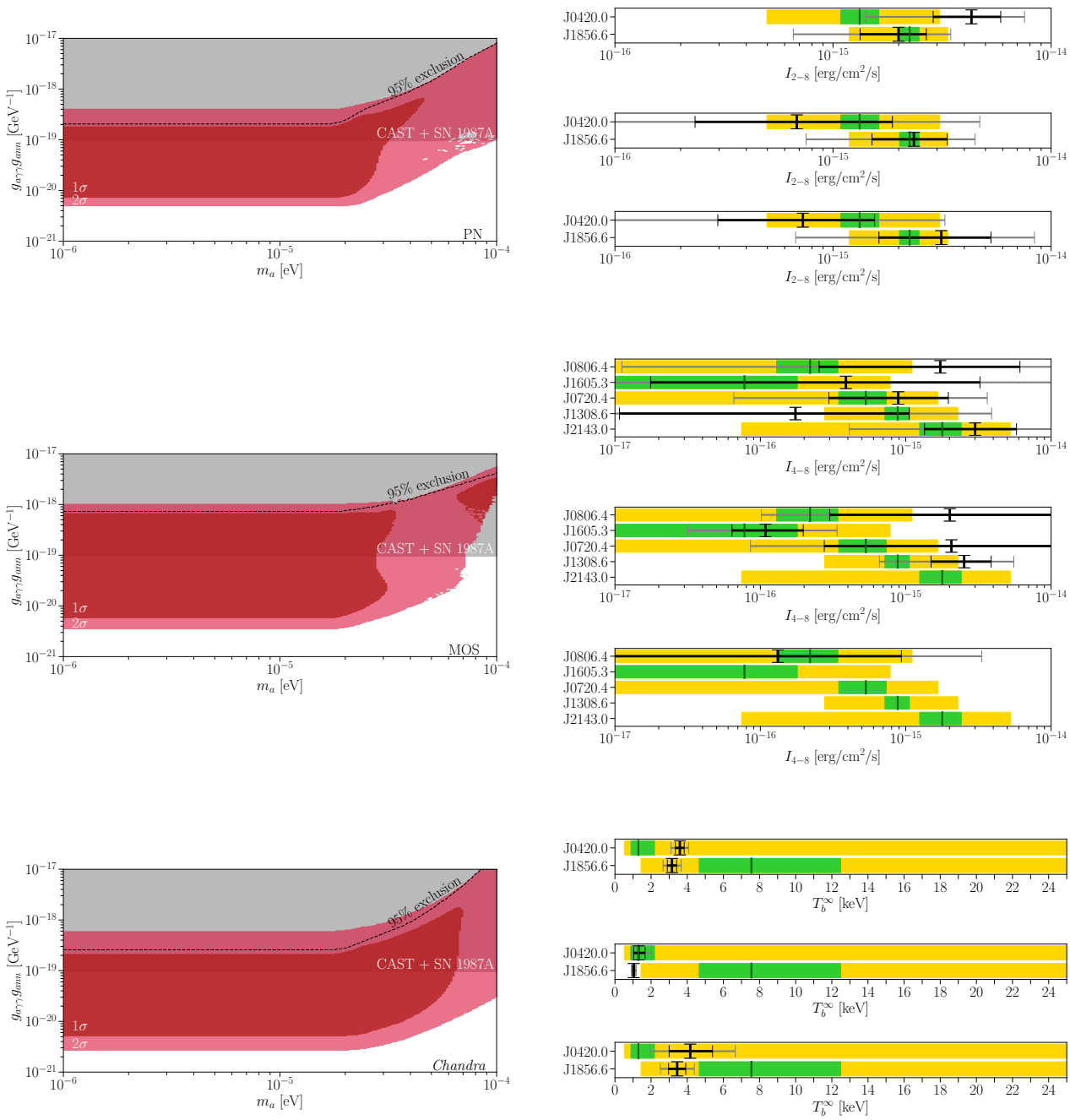

Figure F.3: As in Figs. 7.2, 7.3, and 7.4 except combining the data from PN, MOS, and *Chandra* separately, as indicted. We find non-trivial and consistent evidence for the axion model between datasets.

F.5.3 Influence of different neutron stars

The evidence in favor of the axion model is driven the most by the high-significance excesses in the two NSs J1856 and J0420. In Fig. F.5 we perform a combined fit to the J1856 and

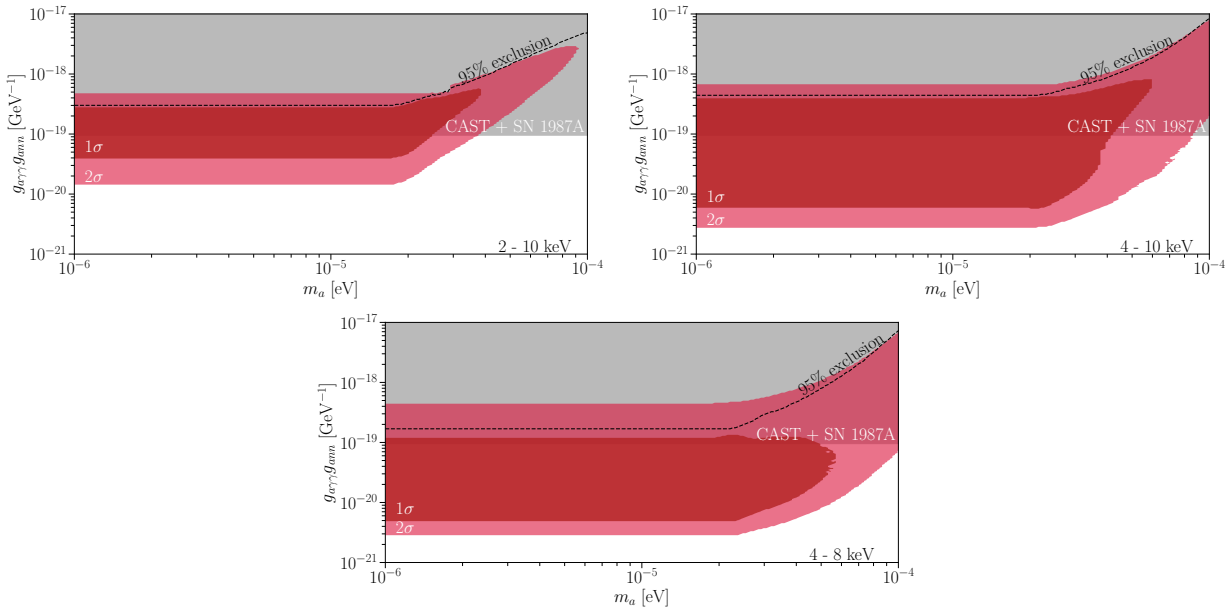

Figure F.4: As in Fig. 7.2 and Fig. 7.3 but with variations to the choices of energy bins included in the analysis. (Top Left) We use the fiducial energy bin choices plus the 8 - 10 keV bin for all NSs. (Top Right) We use the energy bins 4 - 6 keV, 6 - 8 keV, and 8 - 10 keV for all NSs. (Bottom) We use the energy bins 4 - 6 keV and 6 - 8 keV for all NSs.

J0420 data and then a separate combined fit to the data from the other five NSs. In the second fit we find marginal evidence (slightly less than $\sim 1\sigma$ with two degrees of freedom) for the axion model.

F.5.4 Dependence on the nucleon couplings

In the main chapter we took, for definiteness, $g_{app} = g_{ann}$ in all figures. In this section we relax that assumption under the condition of vanishing axion mass ($m_a \ll 10^{-5}$ eV). In the left panels of Fig. F.6 we show the best-fit axion model space in the $g_{a\gamma\gamma}g_{ann}$-$g_{a\gamma\gamma}g_{app}$ plane. Importantly, note that comparable neutron and proton axion couplings may lead to comparable X-ray fluxes. However, with superfluidity included (bottom left panel, which uses our fiducial superfluidity model I) it is possible that the neutron axion production mechanism is significantly suppressed relative to that from the proton, since the neutron superfluid transition temperature is generically higher than that of the proton in this model. The axion production rates are exponentially suppressed below the superfluid transition temperature, which requires higher axion couplings to produce the same X-ray flux. In the bottom left panel we show the best-fit region without including superfuidity, as in the main chapter. In this case, the neutron and proton couplings produce comparable results.

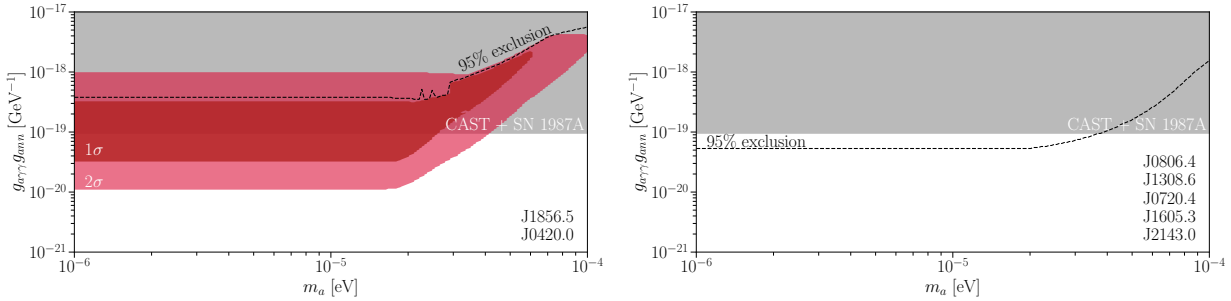

Figure F.5: As in Fig. 7.2 but (left) only including J1856 and J0420 and (right) only including the other five NSs. In the right panel we find less than $\sim 1\sigma$ evidence (with two degrees of freedom) for the axion model when fitting to the other five neutron stars. Only the 95% upper limit is shown in this case.

In the right panels of Fig. F.6 we again take $m \ll 10^{-5}$ eV, but we fix $g_{ann} = g_{app}$ and we illustrate the best-fit region in the $g_{ann} - g_{a\gamma\gamma}$ plane. The top panel does not include superfluidity while the bottom panel does. To be consistent with current constraints from SN 1987A and CAST, the axion model should reside in the regions that are not shaded grey.

F.5.5 Dependence on superfluidity model

The predicted X-ray flux depends sensitively on the assumed nucleon superfluidity model, since nucleon superfluidity suppresses the axion flux for temperatures below the critical temperature. Ref. [14] suggests that the nucleon superfluidity critical temperatures are likely too low to affect this analysis, and so we neglected superfluidity in the main chapter. However, in this section we further illustrate the possible effect of nucleon superfluidity by considering a few superfluidity models in more detail. In our superfluidity model I [562], we consider pure neutron pairing. In this subsection, we also consider two alternate models. Here, we do not consider the highly model-dependent PBF processes that we have explored in the previous section. In our alternative superfluidity model II [561], we take into account that in a NS the neutrons are in β-equilibrium with the protons. This reduces the neutron effective mass and therefore reduces the range of densities in which the superfluid is allowed to form as well as the critical temperature at fixed Fermi momenta. Then the nucleon bremsstrahlung process is less suppressed, strengthening the limits as seen in Fig. F.7. These models do neglect contributions from spin-orbit interactions, which have not yet been worked out but may prohibit superfluidity altogether [565].

Note that the critical temperatures in model II tend to be smaller than those in model I, and as a result the flux we obtain using model II receives a smaller superfluid suppression.

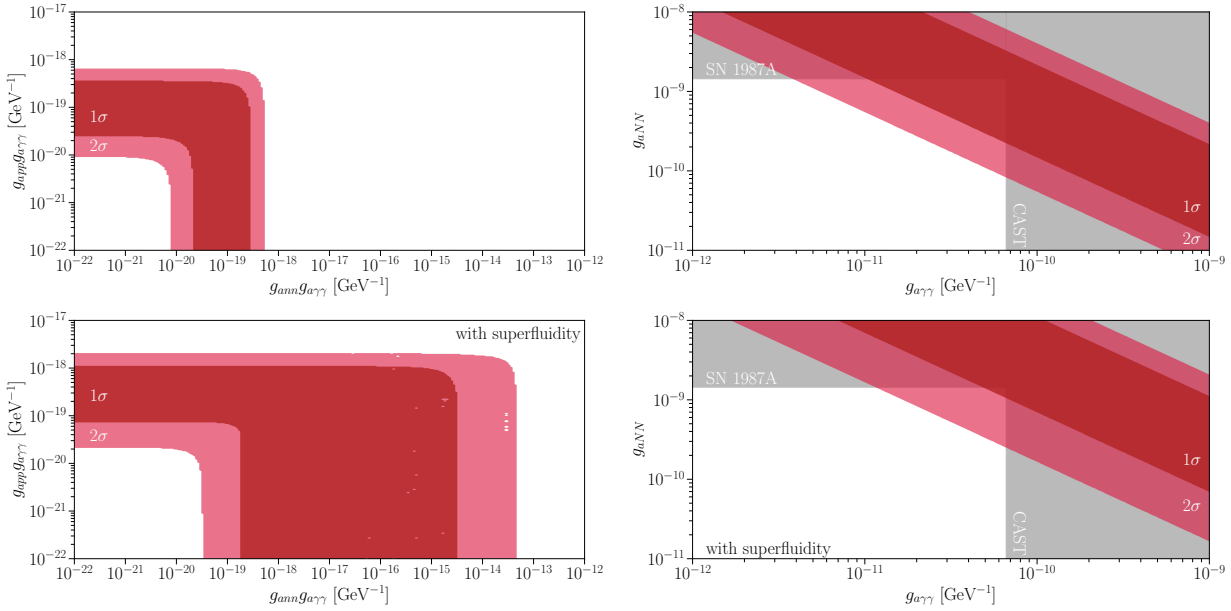

Figure F.6: Best fit 1 and 2σ parameter space in our fiducial analysis under the assumption of vanishing axion mass ($m_a \ll 10^{-5}$ eV). In the left panels we relax the constraint $g_{app} = g_{ann}$ and in right panels we disentangle g_{ann} (with $g_{app} = g_{ann}$ fixed) and $g_{a\gamma\gamma}$. The bottom row is the same as the top row but assuming nucleon superfluidity.

As seen in Fig. F.7 and comparing to Fig. 7.2, the superfluidity models make a significant impact on the best-fit axion parameter space. Without nucleon superfluidity, and in the superfluidity model II, the best-fit axion couplings are significantly smaller than in model I since the axion production rates are highly suppressed in model I.

We note that since the critical temperatures depend on the Fermi momenta, which are determined by the EOS, uncertainties in the EOS also likely play a significant role in determining the uncertainties on the axion flux. These uncertainties should be more thoroughly investigated in future work.

F.5.6 Alternate magnetic field strength and core temperature models

In the main chapter we determined the core temperatures by extracting surface temperatures from a single blackbody fit to the 0.5 - 1 keV data (see [15]) and converting these temperatures to core temperatures as described in Sec. F.1. Here we investigate how the results change when we use the core-temperature estimates based solely on the kinematic ages of the NSs. The core temperatures are inferred through the kinematic ages through

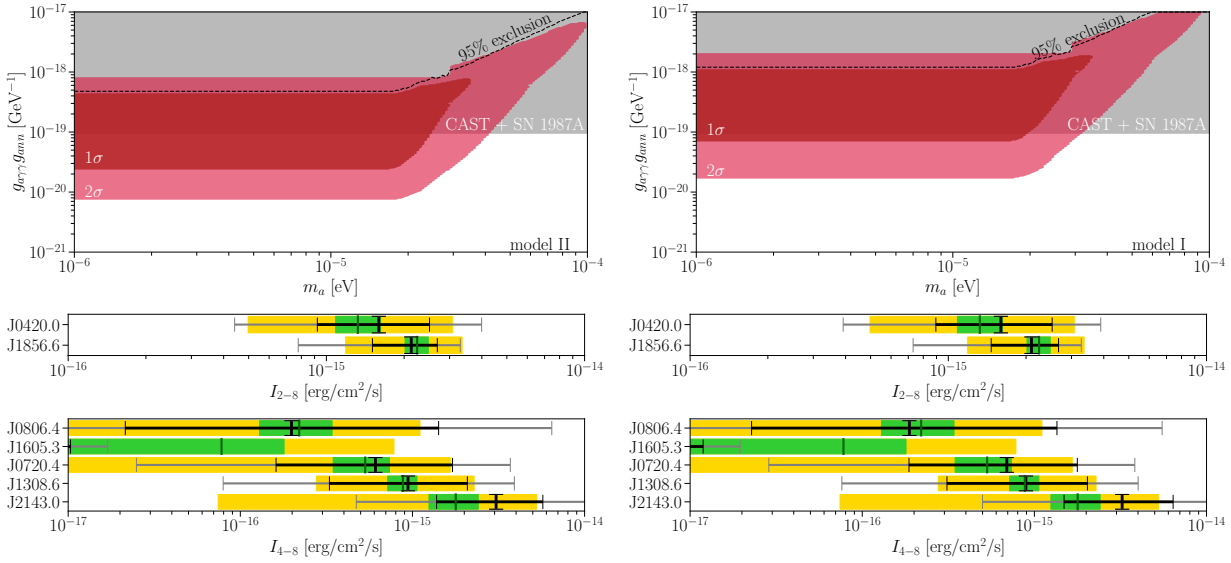

Figure F.7: As in Fig. 7.2 and Fig. 7.3 but (*left*) assuming superfluidity model II and (*right*) assuming superfluidity model I. Model II produces similar results to our fiducial analysis, which neglected superfluidity all together, while Model I leads to larger inferred axion couplings.

the relation given in the main chapter. Note that we assign a 50% systematic uncertainty, translated appropriately to log space, on that relation to account for the precision quoted in [322]. We combine that systematic uncertainty with the uncertainties on the kinematic ages to produce the uncertainties quoted in Tab. F.2. We only include NSs in this analysis for which kinematic ages are known.

In the main chapter we adopted the magnetic field values determined by the spin-down rate of the NSs, except in the case of J1605 which has no measured value. These determinations give very precise measurements of the dipole component of the field, but the true field may be, *e.g.*, non-axisymmetric such that the spin-down measurements underestimate the magnetic field at the surface [568]. In this section we reanalyze the data assuming the magnetic fields determined by spectral fitting of the NSs while keeping the dipole assumption. These fields are inferred from cyclotron resonance absorption lines or NS atmosphere models. The fields are typically larger than the spin-down fields, although they are also significantly more uncertain, especially considering systematics such as the NS atmosphere composition. These alternate values are listed in Tab. F.2.

In Fig. F.8 we repeat our fiducial analysis (*left*) using the alternate core temperatures and (*right*) using the alternate magnetic fields. The alternate magnetic fields have a relatively minimal impact on the best-fit parameter space. The alternate temperature model, on the

Name	B_0 [10^{13} G]	T_b^∞ [keV]	Refs.
J0806	9.2	—	[323]
J1856	0.35	7.8 ± 3.9	[278, 405]
J0420	6.6	—	[323]
J1308	4.2	6.8 ± 3.4	[289, 566]
J0720	3.0	7.1 ± 3.6	[9, 325]
J1605	1.0	7.4 ± 3.9	[406, 567]
J2143	14	—	[302]

Table F.2: The alternate values of the magnetic field strengths and core temperatures, which are inferred from the kinematic ages of the NSs. The magnetic fields are derived from proton cyclotron absorption or NS atmosphere spectral fitting, and are given uncertainties by profiling over θ.

other hand, has a more significant impact. In this case the best-fit parameter space is at slightly higher axion couplings, due to the slightly lower core temperatures. As seen in Fig. F.8, the alternate core temperature model also provides slightly improved consistency between the I_{2-8} intensity observed from J1856 and the I_{4-8} intensities observed from the other three NSs considered, though we stress that this is a relatively minor difference.

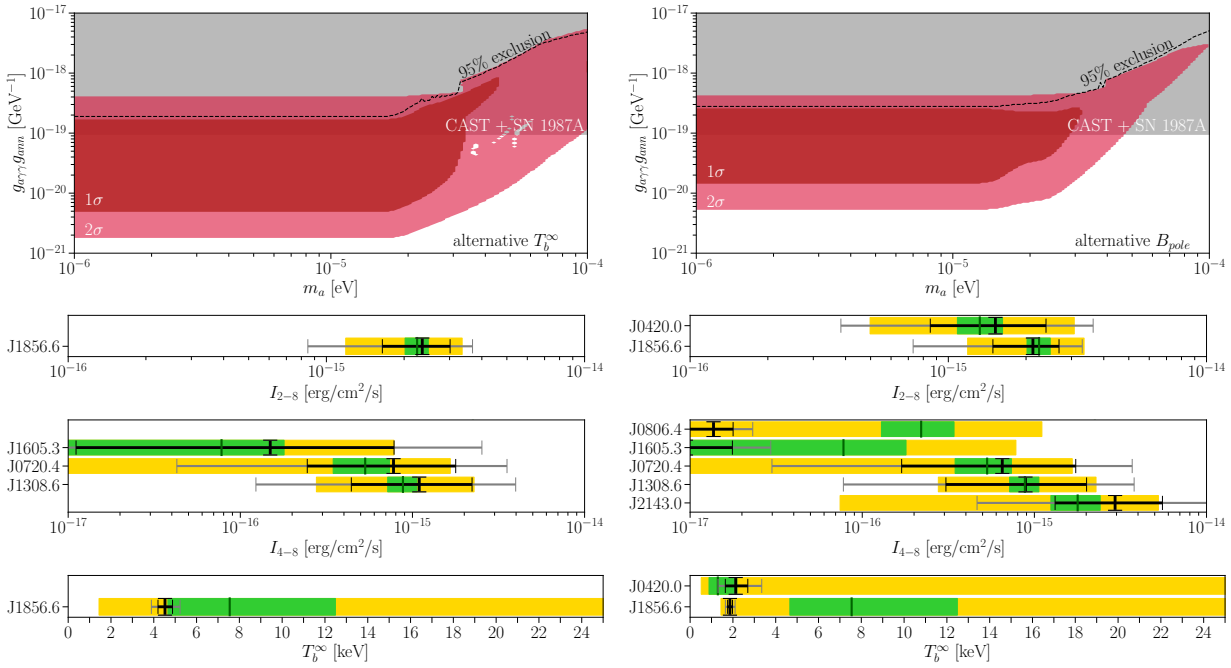

Figure F.8: As in Fig. 7.2, Fig. 7.3, and Fig. 7.4 but (*left*) for the alternate core temperature values given in Tab. F.2 and (*right*) for the alternate magnetic field values shown in Tab. F.2.

Appendix G

X-ray Searches for Axions from Super Star Clusters

This Supplementary Material contains additional results and explanations of our methods that clarify and support the results presented in the main chapter. First, we present additional details regarding the data analyses, simulations, and calculations performed in this chapter. We then show additional results beyond those presented in the main chapter. In the last section we provide results of an auxiliary analysis used to derive the metallicity range considered in this chapter.

G.1 Methods: Data Reduction, Analysis, Simulations, and Calculations

In this section we first provide additional details needed to reproduce our NuSTAR data reduction, before giving extended discussions of our MESA simulations, axion luminosity calculations, and conversion probability calculations.

G.1.1 Data Reduction and analysis

To perform the NuSTAR data reduction, we use the NuSTARDAS software included with HEASoft 6.24 [371]. We first reprocess the data with the NuSTARDAS task `nupipeline`, which outputs calibrated and screened events files. We use the strict filtering for the South Atlantic Anomaly. We then create counts maps for both focal plane modules (FPMs) of the full NuSTAR FOV with `nuproducts` in energy bins of width 5 keV from $5 - 80$ keV.[1]

[1]We use 5 keV-wide energy bins as a compromise between having narrow energy bins that allow us to resolve the spectral features in our putative signal (see Fig. 8.2) and having wide-enough bins that allow to

We additionally generate the ancillary response files (ARFs) and the redistribution matrix files (RMFs) for each FPM. We generate the corresponding exposure maps with `nuexpomap`, which produces exposure maps with units [s]. To obtain maps in exposure units [cm^2 s keV] that we can use to convert from counts to flux, we multiply in the mean effective areas in each bin with no PSF or vignetting correction.

Once the data is reduced, we apply the analysis procedure described in the main chapter to measure the spectrum associated with the signal template in each energy bin. However, to compare the signal-template spectrum to the axion model prediction, we need to know how to forward-model the predicted axion-induced flux, which is described in more detail later in this chapter, through the instrument response. In particular, we pass the signal flux prediction through the detector response to obtain the expected signal counts that we can compare to the data:

$$\mu^e_{S,i}(\boldsymbol{\theta}_{\rm S}) = t^e \int dE' \mathrm{RMF}^e_i(E') \mathrm{ARF}^e(E') S(E'|\boldsymbol{\theta}_{\rm S})\,. \tag{G.1}$$

Here, t^e is the exposure time corresponding to the exposure e in [s], while the signal is the expected intensity spectrum in [erg/cm^2/s/keV]. We have now obtained the expected signal counts $\mu^e_{S,i}(\boldsymbol{\theta}_{\rm S})$ that may be integrated into the likelihood given in (10.25).

G.1.2 MESA Simulations

MESA is a one-dimensional stellar evolution code which solves the equations of stellar structure to simulate the stellar interior at any point in the evolution. In our fiducial analysis, we construct models at a metallicity Z = 0.035, initial stellar masses from 15 to 200 $M_\odot$, and initial surface rotations from 0 km/s to 500 km/s as indicated in the main chapter. We use the default inlist for high-mass stars provided with MESA. This inlist sets a number of parameters required for high-mass evolution, namely the use of Type 2 opacities. We additionally use the Dutch wind scheme [569] as in the high rotation module.

On this grid, we simulate each star from the pre-MS phase until the onset of neon burning around 1.2×10^9 K. At that point, the star only has a few years before undergoing supernova. Given that no supernova has been observed in the SSCs since the observations in 2012-2015, this end-point represents the most evolved possible state of stars in the SSCs at time of observation. The output is a set of radial profiles at many time steps along the stellar evolution. The profiles describe, for example, the temperature, density, and composition

accurately determine the background template normalizations in our profile likelihood analysis procedure. However, small-to-moderate changes to the bins sizes (*e.g.*, increasing them by a factor of 2) lead to virtually identical results.

of the star. These profiles allow us to compute the axion spectrum at each time step by integrating the axion volume emissivity over the interior.

Here we show detailed results for a representative star of mass 85 $M_\odot$ with initial surface rotation of 300 km/s. This star is a template star for the WC phase (and other WR phases) in the Quintuplet Cluster, which dominates the Quintuplet axion spectrum in the energies of interest. In the left panel of Fig. G.1, we show the Hertzsprung–Russell (HR) diagram for

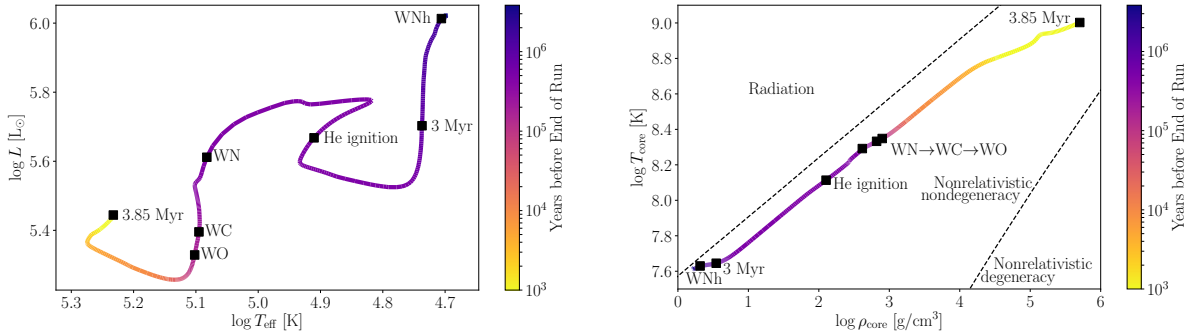

Figure G.1: (Left) The HR diagram for the Quintuplet template star of mass 85 $M_\odot$ and initial surface rotation of 300 km/s. The coloring indicates the year before the run was stopped, approximately a few years from supernova. We mark with black squares, in order of occurrence, when the star enters the WNh phase, when it is 3 Myr old, when its core undergoes helium ignition, when it enters the WN, WC, and WO phases, and finally when the run ends at 3.85 Myr. (Right) A logT-log ρ diagram for the template star with the same points of interest marked. We also show the relevant degeneracy zones, showing that the star is entirely in the nonrelativistic nondegenerate regime.

our template star. The star's life begins on the MS, where it initiates core hydrogen burning. Eventually, the core runs out of hydrogen fuel and is forced to ignite helium to prevent core collapse (see Fig. G.2 left). Because helium burns at higher temperatures, the star contracts the core to obtain the thermal energy required to ignite helium (see Fig. G.3). At the same time, the radiation pressure in stellar winds cause heavy mass loss in the outer layers, which peels off the hydrogen envelope (see Fig. G.4). When the surface is 40% hydrogen, the star enters the WNh phase; when it is 5% hydrogen, the star enters the WN phase. Further mass loss begins to peel off even the helium layers, and the star enters the WC and WO phases when its surface is 2% carbon and oxygen by abundance [349], respectively (see Fig. G.2 right).

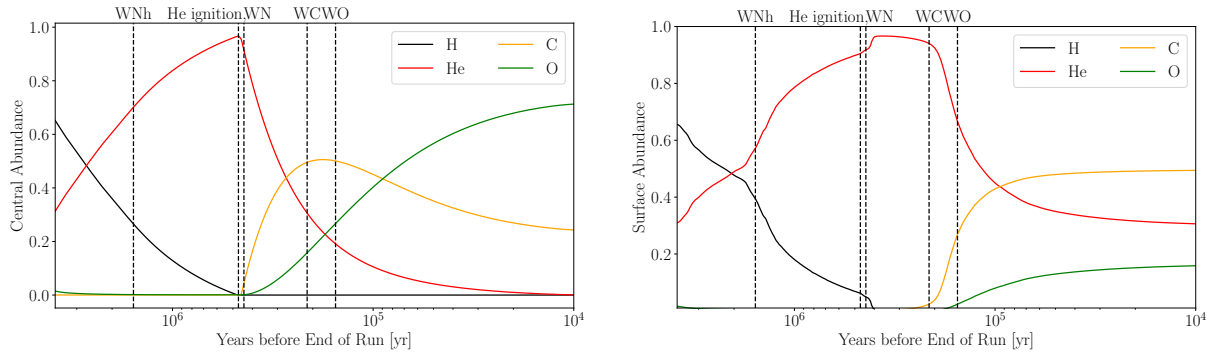

Figure G.2: (Left) The abundances of hydrogen (black), helium (red), carbon (yellow), and oxygen (green) in the center of the star as a function of time, for the simulation described in Fig. G.1. With dashed-black vertical lines, we mark several points of interest: "WNh" indicates the time the star enters the WNh phase, "He ignition" when its core undergoes helium ignition, and "WN","WC", and "WO" indicate the beginning of the WN, WC, and WO phases, respectively. (Right) The same as in the left panel, but for surface abundances.

G.1.3 Axion Production in SSCs

In this section we overview how we use the output of the MESA simulations to compute axion luminosities and spectra.

The Axion Energy Spectrum

Here we focus on the calculation of the axion energy spectrum [erg/cm^2/s/keV]. The axion production rate is [570]

$$\Gamma_p(E) = \frac{{g_{a\gamma\gamma}}^2 T \kappa^2}{32\pi}\left[\left(1+\frac{\kappa^2}{4E^2}\right)\ln\left(1+\frac{4E^2}{\kappa^2}\right)-1\right], \tag{G.2}$$

where $\kappa^2 = \frac{4\pi\alpha}{T}\sum_i Z_i^2 n_i$ gives the Debye screening scale, which is the finite reach of the Coulomb field in a plasma and cuts off the amplitude. To obtain the axion energy spectrum, this is to be convolved with the photon density, such that

$$\begin{aligned}\frac{dL_p}{dE}(E) &= \frac{1}{\pi^2}\frac{E^3}{e^{E/T}-1}\Gamma_p(E) \\ &= \frac{{g_{a\gamma\gamma}}^2}{8\pi^3}\frac{\xi^2 T^3 E}{e^{E/T}-1}\left[\left(E^2+\xi^2T^2\right)\ln\left(1+\frac{E^2}{\xi^2T^2}\right)-E^2\right],\end{aligned} \tag{G.3}$$

where we have defined the dimensionless parameter $\xi^2 = \dfrac{\kappa^2}{4T^2}$. To obtain the axion emissivity for a whole star, we integrate over the profiles produced with MESA, and we show results

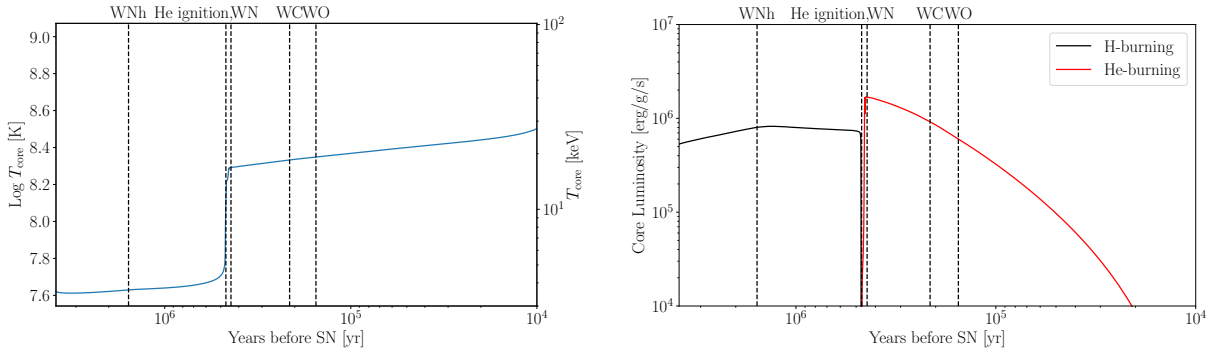

Figure G.3: (Left) The stellar core temperature as a function of time for the simulation described in Fig. G.1. (Right) The hydrogen and helium luminosities in the core through the CNO cycle and the triple-alpha process, respectively. The dashed-black vertical lines retain their meanings from Fig. G.2.

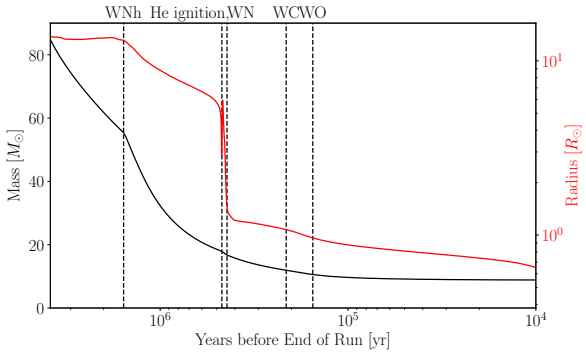

Figure G.4: The stellar mass (black) and radius (red) as a function of time from the simulation described in Fig. G.1. The dashed-black vertical lines retain their meanings from Fig. G.2.

for this calculation in the next section. Finally, the axion-induced photon spectrum at Earth is given by

$$\frac{dF}{dE}(E) = P_{a\to\gamma}(E)\frac{1}{4\pi d^2}\frac{dL_a}{dE}(E)\,, \tag{G.4}$$

with the conversion probability $P_{a\to\gamma}$ computed later.

Results for Template Star

In this section, we show our expectation for the axion luminosity from our template star.

In the left panel of Fig. G.5, we show the axion emissivity from the radial slices of the MESA profile, using the model at the start of the WC evolutionary stage. As expected, the stellar core is by far the most emissive due to its high temperature and density. We also show the temperature profile in the star. Note that the axion volume emissivity does not

have the same profile shape as the temperature because the emissivity also depends on the density and composition which are highly nonuniform over the interior.

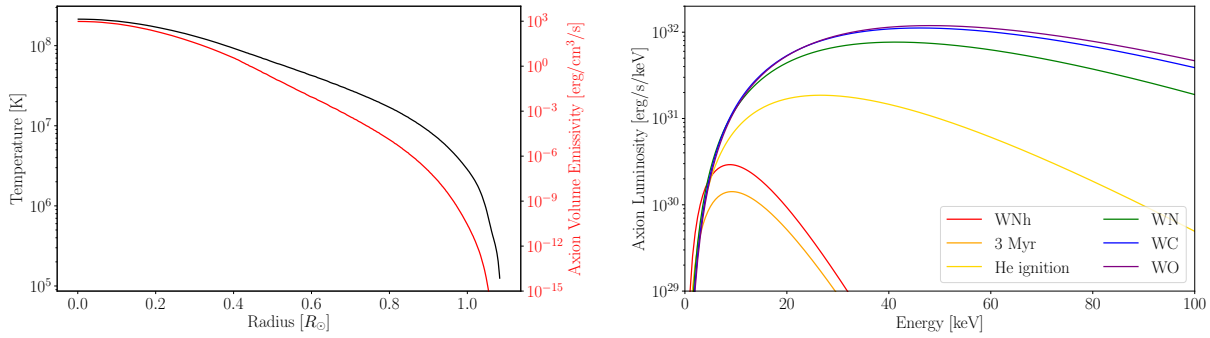

Figure G.5: (Left) Axion volume emissivity over the interior of the star. In this figure we have taken the stellar model to be the one at the start of the WC stage and fixed $g_{a\gamma\gamma} = 10^{-12}$ GeV^{-1}. For comparison purposes, we also show the temperature profile. (Right) Axion luminosity spectrum for those same stages marked in Fig. G.2.

In the right panel of Fig. G.5, we show how the axion luminosity changes over the stellar lifetime. We see that before helium ignition, the axion luminosity is rather low, and the axion spectrum reaches its maximum around 10 keV, owing to the low core temperature—the star is still hydrogen burning at core temperatures well below 10 keV. During helium ignition, the luminosity increases quickly due to the sudden increase in temperature. During helium burning, the core temperature continues to increase; for this reason, more evolved stars will be more luminous in axions.

G.1.4 Magnetic field model and conversion probability

When the axion-to-photon conversion probability $p_{a\to\gamma}$ is sufficiently less than unity, it may be approximated by [173]:

$$p_{a\to\gamma} = \frac{g_{a\gamma\gamma}^2}{4} \sum_{i=1,2} \left| \int_0^d dr' B_i(r') e^{i\Delta_a r' - i\int_0^{r'} dr'' \Delta_{||}(r'')} \right|^2 , \tag{G.5}$$

where B_i, for $i = 1, 2$, denote the two orthogonal projections of the magnetic field onto axes perpendicular to the direction of propagation. The integrals are over the line of sight, with the source located a distance d from Earth, and $r = 0$ denoting the location of the source. We have also defined $\Delta_a \equiv -m_a^2/(2E)$ and $\Delta_{||}(r) \equiv -\omega_{\rm pl}(r)^2/(2E)$, with E the axion energy and $\omega_{\rm pl}(r)$ the location-dependent plasma mass. The plasma mass may be related to the number density of free electrons n_e by $\omega_{\rm pl} \approx 3.7 \times 10^{-12} (n_e/10^{-2}\ {\rm cm}^{-3})^{-1/2}$ eV. To perform

the integral we need to know (i) the free electron density along the line of sight to the target, and (ii) the orthogonal projections of the magnetic field along the line-of-sight. In this section we give further details behind the electron-density and magnetic-field profiles used in this chapter.

The Quintuplet and Arches SSCs are both ∼30 pc away from the GC and thus are expected to have approximately the same conversion probabilities for conversion on the ambient Galactic magnetic fields. It is possible, however, that local field configurations near the GC could enhanced the conversion probabilities for one or both of these sources. For example, the axions are expected to travel through or close to the GC radio arc, which has a strong magnetic field ∼mG over a cross-section ∼$(10\ \mathrm{pc})^2$ [368]. Magnetic fields within the clusters themselves may also be important.

Our fiducial magnetic field model for Quintuplet and Arches is illustrated in the left panel of Fig. G.6. In the right panel we show the magnetic field profiles relevant for the

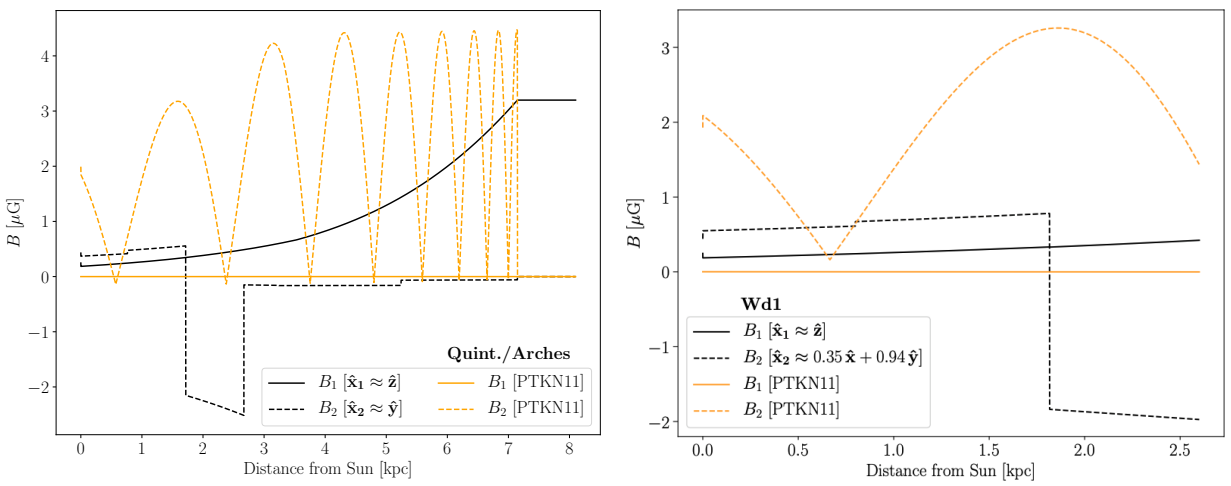

Figure G.6: We denote the projections of the Galactic magnetic field onto the plane normal to the propagation direction by B_1, B_2. (Left) The transverse magnetic field components in our fiducial model (the JF12 model, black) and alternate model (PTKN11, orange) towards the Quintuplet and Arches clusters. Note that in our fiducial B-field model we extend the JF12 model to distances less than 1 kpc from the GC using the field values at 1 kpc. The true magnetic field values in the inner kpc almost certainly surpass those from this conservative model (see text for details). (Right) The two field components towards the Wd1 cluster, which is taken to be at a distance of 2.6 kpc from the Sun. The conversion probabilities towards Wd1 are much larger in the alternate model (PTKN11) than in our fiducial model (JF12), though we stress that random fields are not included and could play an important role in the conversion probabilities towards Wd1.

Wd1 observations. The components of the B-field along the two transverse directions are denoted by B_1 and B_2. For the Quintuplet and Arches analyses, the propagation direction

is very nearly aligned with $-\hat{\mathbf{x}}$ (in Galactic coordinates), so we may take B_1 to point in the $\hat{\mathbf{z}}$ direction, towards the north Galactic pole, and B_2 to point in the direction $\hat{\mathbf{y}}$ (the approximate direction of the local rotation). Note that the targets are slightly offset from the origin of the Galactic coordinate system, so the actual basis vectors have small components in the other directions. As Wd1 is essentially within the plane of the disk, one of the transverse components points approximately in the $\hat{\mathbf{z}}$ direction (B_1).

The dominant magnetic field towards the GC within our fiducial B-field model is the vertical direction (B_1), which is due to the out-of-plane X-shaped halo component in the JF12 model [356, 357]. However, in the JF12 model that component is cut off within 1 kpc of the GC, due to the fact that in becomes difficult to model the B-field near the GC. The B-field is expected to continue rising near the GC – for example, in [366] it was claimed that the B-field should be at least 50 μG (and likely 100 μG) within the inner 400 pc. However, to be conservative in our fiducial B-field model we simply extend the B-field to the GC by assuming it takes the value at 1 kpc (about 3 μG) at all distances less than 1 kpc from the GC. We stress that this field value is likely orders of magnitude less than the actual field strength, but this assumption serves to make our results more robust. The extended field model is illustrated in Fig. G.6.

To understand the level of systematic uncertainty arising from the B-field models we also show in Fig. G.6 the magnetic field profiles for the alternative ordered B-field model PTKN11 [360]. This model has no out-of-plane component, but the regular B-field within the disk is stronger than in the JF12 model. In the case of Quintuplet and Arches we find, as discussed below, that the PTKN11 model leads to similar but slightly enhanced conversion probabilities relative to the JF12 model. On the other hand, the conversion probabilities in the PTKN11 model towards Wd1 are significantly larger than in the JF12 model.

There is a clear discrepancy in Fig. G.6 between the magnetic field values observed at the solar location, in both the JF12 model and the PTKN11 model, and the local magnetic field strength, which is $\sim$3 μG [362]. The reason is that the magnetic field profiles shown in Fig. G.6 are only the regular components; additional random field components are expected. For example, in the JF12 model the average root-mean-square random field value at the solar location is $\sim$6.6 μG [356, 357]. The random field components could play an important role in the axion-to-photon conversion probabilities, especially for the nearby source Wd1, but to accurately account for the random field components one needs to know the domains over which the random fields are coherent. It is expected that these domains are $\sim$100 pc [357], in which case the random fields may dominate the conversion probabilities, but since the result depends sensitively on the domain sizes, which remain uncertain, we conservatively neglect the random-field components from the analyses in this chapter (though this would

be an interesting subject for future work).

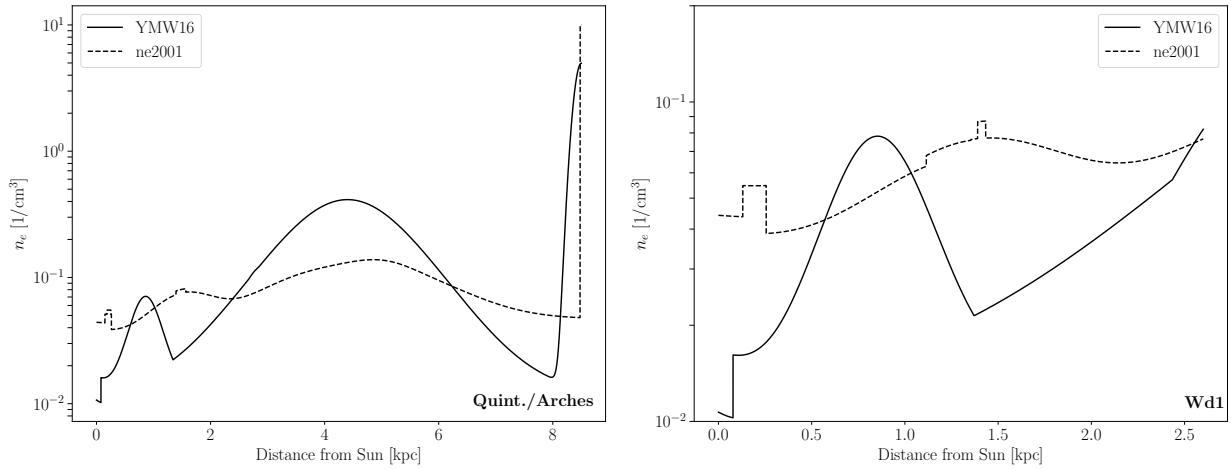

Figure G.7: (Left) The free electron density n_e towards the GC in our fiducial model (YMW16) and the alternate model (`ne2001`). (Right) As in the left panel but towards the Wd1 cluster. The free-electron density gives the photon an effective mass and thus affects the axion-photon conversion probability.

To compute the conversion probabilities we also need the free-electron densities. We use the YMW16 model [358] as our fiducial model, but we also compare our results to those obtained with the older `ne2001` model [359] to assess the possible effects of mismodeling the free-electron density. In the left panel of Fig. G.7 we compare the free electron densities between the two models as a function of distance away from the Sun towards the GC, while in the right panel we show the free electron densities towards Wd1. The differences between these models result in modest differences between the computed conversion probabilities, as discussed below.

Combining the magnetic field models in Fig. G.6 and the free-electron models in Fig. G.7 we may compute the axion-photon conversion probabilities, for a given axion energy E. These conversion probabilities are presented in the left panels of Fig. G.8 (assuming $g_{a\gamma\gamma} = 10^{-12}$ GeV^{-1} and $m_a \ll 10^{-11}$ eV). In the top left panel we show the results for Quintuplet and Arches, while the bottom left panel gives the conversion probabilities for Wd1, computed under both free-electron models and various magnetic field configurations.

In the top left panel our fiducial conversion probability model is shown in solid black. Changing to the `ne2001` model would in fact slightly enhance the conversion probabilities at most energies, as shown in the dotted black, though the change is modest. Completely removing the B-field within 1 kpc of the GC leads only to a small reduction to the conversion probabilities, as indicated in red. Changing magnetic field models to that of [360] (PTKN11), while also removing the B-field within the inner kpc, leads to slightly enhanced conversion

probabilities, as shown in orange (for both the YMW16 and `ne2001` n_e models). Note that the conversion probabilities exhibit clear constructive and destructive interference behavior in this case at low energies, related to the periodic nature of the disk-field component, though including the random field component it is expected that this behavior would be largely smoothed out.

As discussed previously the magnetic field is expected to be significantly larger closer in towards the GC than in our fiducial B-field model. As an illustration in blue we show the conversion probabilities computed, from the two different free-electron models, when we only include a B-field component of magnitude 50 μG pointing in the $\hat{\mathbf{z}}$ direction within the inner 400 kpc (explicitly, in this case we do not include any other B-field model outside of the inner 400 kpc). The conversion probabilities are enhanced in this case by about an order of magnitude across most energies relative to in our fiducial model. The inner Galaxy also likely contains localized regions of even strong field strengths, such as non-thermal filaments with $\sim$mG ordered fields. As an illustration of the possible effects of such fields on the conversion probabilities, in Fig. G.8 we show in grey the result we obtain for the conversion probability when we assume that the axions traverse the GC radio arc, which we model as a 10 kpc wide region with a vertical field strength of 3 mG and a free-electron density $n_e = 10$ cm^{-3} [368,571]. Due to modeling uncertainties in the non-thermal filaments and the ambient halo field in the inner hundreds of pc, we do not include such magnetic-field components in our fiducial conversion probability model. However, we stress that in the future, with a better understanding of the Galactic field structure in the inner Galaxy, our results could be reinterpreted to give stronger constraints.

The Wd1 conversion probabilities change by over an order of magnitude going between the JF12 and PTKN11 models, as seen in the bottom left panel of Fig. G.8, though it is possible that this difference would be smaller when random fields are properly included on top of the JF12 model (though again, we chose not to do this because of sensitivity to the random-field domain sizes).

The effects of the different conversion probabilities on the $g_{a\gamma\gamma}$ limits may be seen in the top right panel for Quintuplet (Arches gives similar results, since the conversion probabilities are the same) and Wd1 in the bottom right panel of Fig. G.8. Note that the observed fluxes scale linearly with $p_{a\to\gamma}$ but scale like $g^4_{a\gamma\gamma}$, so differences between conversion probability models result in modest differences to the $g_{a\gamma\gamma}$ limits. Still, it is interesting to note that the Wd1 limits with the PTKN11 model are stronger than the fiducial Quintuplet limits, which emphasizes the importance of better understanding the B-field profile towards Wd1. For Quintuplet (and also Arches) we see that depending on the field structure in the inner $\sim$kpc, the limits may be slightly stronger and extend to slightly larger masses (because of

field structure on smaller spatial scales) than in our fiducial B-field mode.

G.2 Extended Data Analysis Results

In this section we present additional results from the data analyses summarized in the main chapter.

G.2.1 Quintuplet

In this subsection we give extended results for the Quintuplet data analysis. Our main focus is to establish the robustness of the flux spectra from the NuSTAR data analysis (shown in Fig. 8.2) that go into producing the limits on $g_{a\gamma\gamma}$ shown in Fig. 8.3.

Data and templates

First we take a closer look at the stacked data and models that go into the Quintuplet data analysis. The stacked counts data in the vicinity of Quintuplet are shown in the left panel of Fig. G.9. We show the counts summed from 10 - 80 keV. Note that the circle in that figure indicates $2'$, which the radius of our fiducial analysis ROI.[2] As in Fig. 10.2 we also indicate the locations of the individuals stars in Quintuplet that may contribute axion-induced X-ray flux. The middle panel shows the expected background flux from our background template. The template is generally uniform over the ROI, with small variations. On the other hand, the right panel shows the axion-induced signal counts template, normalized for $g_{a\gamma\gamma} = 7 \times 10^{-12}$ GeV^{-1}, which is localized about the center of the SSC. Note that the signal template is generated by accounting for the PSF of NuSTAR in addition to the locations and predicted fluxes of the individual stars.

Axion Luminosity

We now show the axion luminosity and spectra that go into the right panel of Fig. G.9. For each star in the cluster, we assign it a set of possible MESA models based on its spectral classification as described in the main chapter. In the upper left panel of Fig. G.10, we show the mean expected axion luminosity, as a function of energy, of the Quintuplet cluster, assuming $g_{a\gamma\gamma} = 10^{-12}$ GeV^{-1}. The luminosity peaks around 40 keV, but the effective area of NuSTAR, also shown, rapidly drops above 10 keV. Due to the much higher effective area at low energies, most of the sensitivity is at lower energies. There is also considerable flux above

[2]Note that ROIs for all of our analyses are centered upon the center of axion fluxes in RA and DEC, though the distinction between the center of fluxes and the SSC center is minimal for all of our targets.

	O	BSG	LBV	WNh	WC/WN	tot	10-80 keV
$N_{\rm star}$	37	7	2	5	14	65	65
$z = 0.018$ 100 km/s	$0.03^{+0.01}_{-0.01}$	$0.01^{+0.01}_{-0.01}$	$0.2^{+0.2}_{-0.2}$	$0.6^{+0.6}_{-0.6}$	$2.8^{+2.6}_{-0.8}$	$3.8^{+2.6}_{-1.0}$	$2.8^{+1.6}_{-0.6}$
$z = 0.035$ 100 km/s	$0.2^{+0.3}_{-0.1}$	$0.04^{+0.01}_{-0.01}$	$0.1^{+0.1}_{-0.1}$	$0.7^{+0.3}_{-0.07}$	$1.7^{+0.9}_{-0.4}$	$2.3^{+0.9}_{-0.5}$	$1.7^{+0.5}_{-0.3}$
$z = 0.035$ 150 km/s	$0.3^{+0.2}_{-0.2}$	$0.03^{+0.01}_{-0.01}$	$0.1^{+0.1}_{-0.01}$	$0.04^{+0.2}_{-0.04}$	$1.5^{+0.7}_{-0.3}$	$2.1^{+0.7}_{-0.4}$	$1.7^{+0.4}_{-0.3}$

Table G.1: The number of stars $N_{\rm star}$ for each stellar class in the Quintuplet cluster, along with the predicted axion luminosities (all in 10^{35} erg/s). Note that Quintuplet is ∼30 pc away from the GC. Except in the last column, the axion luminosities are summed over all energies. All entries assume $g_{a\gamma\gamma} = 10^{-12}$ GeV^{-1} and are summed over all stars for the given stellar class.

80 keV, although NuSTAR does not have sensitivity at these energies. In the upper right panel, we show the median contribution of each spectral classification in Quintuplet to this luminosity, summed over all stars with the given classification. For all energies of interest, the WC stars dominate the cluster luminosity. This is because WR stars have the hottest cores and there are 13 WC stars in Quintuplet (there is 1 WN star). In the bottom panel, we show the 10 - 80 keV luminosity distribution for each spectral classification, along with the 1σ containment bands and the mean expectation. The distribution depends principally on whether or not core helium is ignited while the star is assigned a given classification. The O, BSG, and WNh stars all can be either hydrogen or helium burning, in which case they have 10 - 80 keV luminosities of $\sim 10^{31}$ or $\sim 10^{33}$ erg/s, respectively—recall that the jump in temperature during helium ignition is a factor ~ 3. The LBV phase is always core helium burning, and the star may go supernova in this phase. The same is true of the WR phases WN and WC, although the stars undergoing supernova in this phase are typically more massive.

The luminosities in Fig. G.10 are computed for our fiducial choices of $Z = 0.035$ and $\mu_{\rm rot} = 150$ km/s. To better understand the importance of these choices we show in Tab. G.1 how the luminosities depend on the initial metallicity Z and mean rotation speed $\mu_{\rm rot}$. Note that each entry in that table shows the luminosity summed over the stellar sub-types (with the number of stars indicated), and except in the two last columns the luminosities are summed over all stars. The uncertainties in the entries in Tab. G.1 come from performing 500 draws from the representative models and account for the variance expected from star-to-star within a given classification. As discussed in the main chapter, the 10 - 80 keV

luminosity could be ∼70% larger than in our fiducial model, depending on the initial Z and $\mu_{\rm rot}$.

Injecting an axion signal

As a first test of the robustness of the Quintuplet analysis we inject a synthetic axion signal into the real stacked data and then pass the hybrid real plus synthetic data through our analysis pipeline. Our goal from this test is to ensure that if a real axion signal were in the data with sufficiently high coupling to photons then we would be able to detect it. The results from this test are shown in Fig. G.11.

The left panel of Fig. G.11 shows the best-fit $g^{\rm rec.}_{a\gamma\gamma}$ as a function of the simulated $g^{\rm inj.}_{a\gamma\gamma}$ used to produce the axion-induced counts that are added to the real NuSTAR stacked data. Importantly, as we increase the injected signal strength the recovered signal parameter converges towards the injected value, which is indicated by the dashed curve. Note that the band shows the 68% containment region for the recovered signal parameter from the analysis. As the injected signal strength increases, so to does the significance of the axion detection. This is illustrated in the middle panel, which shows the discovery TS as a function of the injected signal strength. Recall that the significance is approximately $\sqrt{\rm TS}$. Perhaps most importantly, we also verify that the 95% upper limit does not exclude the injected signal strength. In the right panel of Fig. G.11 we show the 95% upper limit found from the analyses of the hybrid data sets at different $g^{\rm inj}_{a\gamma\gamma}$. Recall that all couplings above the $g^{\rm rec}_{a\gamma\gamma}$ curve are excluded, implying that indeed we do not exclude the injected signal strength. Moreover, the 95% upper limit is consistent with the expectation for the limit under the signal hypothesis, as indicated by the shaded regions at 1σ (green) and 2σ (yellow) containment. Note that we do not show the lower 2σ containment region, since we power-constrain the limits. These regions were computed following the Asimov procedure [110].

Changing region size

As a systematic test of the data analysis we consider the sensitivity of the inferred spectrum associated with the axion model template to the ROI size. In our fiducial analysis, with spectrum shown in Fig. 8.2, we use an ROI size of $r_{\rm max} = 2'$. Here we consider changing the ROI size to $r_{\rm max} = 1.5'$ and $2.5'$. The resulting spectra are shown in Fig. G.12. The spectrum does not appear to vary significantly when extracted using these alternate ROIs, indicating that significant sources of systematic uncertainty related to background mismodeling are likely not at play.

G.2.2 Westerlund 1

In this subsection we provide additional details and cross-checks of the Wd1 analysis.

Data and templates

In Fig. G.13 we show, in analogy with Fig. G.9, the data, background, and signal maps summed from 15 - 80 keV. We note that the background templates are summed using their best-fit normalizations from the fits to the null hypothesis of background-only emission. The signal template is noticeably extended in this case beyond a point-source template and is shown for $g_{a\gamma\gamma} = 8 \times 10^{-12}$ GeV^{-1} and $m_a \ll 10^{-11}$ eV. The location of the magnetar CXOU J164710.2–45521 is indicated by the red star.

Axion Luminosity

We now show the axion luminosity and spectra that go into the right panel of Fig. G.13. In the upper left panel of Fig. G.14, we show the mean expected axion luminosity, as a function of energy, of the Wd1 cluster, assuming $g_{a\gamma\gamma} = 10^{-12}$ GeV^{-1}. In the upper right panel, we show the contribution of each spectral classification in Wd1 to this luminosity, summed over all stars with the given classification. For all energies of interest, the WN stars dominate the cluster luminosity, although the WC stars are important as well. As in Quintuplet, this is due to the fact that WR stars have the hottest cores, but in this case there are more WN stars than WC stars. In the bottom panel, we show the 10 - 80 keV luminosity distribution for each spectral classification, along with the 1σ bands and the mean expectation. Again, the more evolved stars produce more axion flux, because their core temperatures increase with time. As in the case of Quintuplet, the O and BSG stars may be pre- or post-helium ignition. The luminous blue variable (LBV), yellow hypergiant (YHG), and cool red supergiant (RSG) stars are all post-helium ignition, although have generically cooler cores than the WR stars. The WNh stars are entirely helium burning.

In Tab. G.2 we provide detailed luminosities for each of the stellar sub-types for different choices of initial Z and $\mu_{\rm rot}$ for Wd1, as we did in Tab. G.1. Note that we assume $Z = 0.035$ and $\mu_{\rm rot} = 150$ km/s for our fiducial analysis, even though it is likely that the initial Z is closer to solar (in which case the luminosities would be enhanced, as seen in Tab. G.2).

Systematics on the extracted spectrum

In analogy to the Quintuplet analysis we may profile over emission associated with the background template to measure the spectrum from 15 - 80 keV associated with the axion-induced signal template shown in Fig. G.13. That spectrum is reproduced in Fig. G.15. For

	O	SG/HG	LBV	WNh	WC/WN	tot	10-80 keV
$N_{\rm star}$	72	56	1	2	22	153	153
$z = 0.018$ 100 km/s	$1.6^{+0.9}_{-0.6}$	$2.4^{+1.3}_{-0.8}$	$0.14^{+0.28}_{-0.13}$	$2.2^{+4.8}_{-1.5}$	43^{+17}_{-14}	52^{+17}_{-14}	13^{+2}_{-2}
$z = 0.035$ 100 km/s	$2.6^{+1.5}_{-1.1}$	$3.9^{+2.6}_{-1.5}$	$0.07^{+0.1}_{-0.07}$	$0.9^{+3.7}_{-0.5}$	20^{+10}_{-7}	31^{+11}_{-9}	$9.9^{+1.4}_{-1.4}$
$z = 0.035$ 150 km/s	$2.3^{+1.3}_{-1.0}$	$3.5^{+2.6}_{-1.5}$	$0.07^{+0.09}_{-0.07}$	$0.62^{+3.1}_{-0.28}$	18^{+10}_{-7}	26^{+10}_{-8}	$9.0^{+1.0}_{-1.0}$

Table G.2: As in Tab. G.1 but for Wd1. SG/HG refers to BSG, RSG, and YHG.

our default analysis we use the ROI with all pixels contained with $r_{\rm max} = 2.0'$ of the cluster center, except for those in the magnetar mask, as indicated in Fig. G.13. However, as a systematic test we also compute the spectrum associated with the axion-induced template for $r_{\rm max} = 2.5'$ and $1.5'$, as shown in Fig. G.15. We measure a consistent spectrum across ROIs at these energies.

G.2.3 Arches

In this subsection we present results from the analysis of archival NuSTAR data for an axion-induced signal from the Arches cluster. The Arches cluster is at a similar location, $\sim$30 pc from the GC, as the Quintuplet cluster. Arches hosts even younger and more extreme (*e.g.*, hotter and more massive) stars than the nearby Quintuplet cluster. Indeed, it is estimated that all $\sim$105 spectroscopically classified stars within Arches may become core-collapse supernovae within the next $\sim$10 Myr [572]. *A priori*, the Arches and Quintuplet clusters should have similar sensitivities to axions, though as we discuss below the axion prediction from Arches is less robust to uncertainties in the initial metallicity than the Quintuplet prediction.

Axion Luminosity

We now describe the axion luminosity and spectra for Arches. In the upper left panel of Fig. G.16, we show the mean expected axion luminosity, as a function of energy, of the Arches cluster, assuming $g_{a\gamma\gamma} = 10^{-12}$ GeV^{-1}. The luminosity peaks at very low energies, although we could not analyze these energies due to contamination from the molecular cloud. As shown by the upper right panel, the Arches luminosity is dominated by the O stars, since the WNh stars are always hydrogen burning with our assumed metallicity of $Z = 0.035$ and

	O	WNh	tot	10-80 keV
$N_{\rm star}$	96	13	109	109
$z = 0.018$ 100 km/s	$2.3^{+0.2}_{-0.1} \times 10^{33}$	$8.7^{+6.5}_{-5.2} \times 10^{34}$	$8.9^{+6.5}_{-5.2} \times 10^{34}$	$6.6^{+5.6}_{-3.6} \times 10^{34}$
$z = 0.035$ 100 km/s	$3.9^{+1.8}_{-1.9} \times 10^{35}$	$3.9^{+217}_{-0.6} \times 10^{32}$	$7.2^{+16}_{-4.9} \times 10^{33}$	$5.7^{+23}_{-2.8} \times 10^{33}$
$z = 0.035$ 150 km/s	$3.5^{+2.1}_{-1.6} \times 10^{33}$	$3.6^{+125}_{-0.3} \times 10^{32}$	$4.7^{+12}_{-2.2} \times 10^{33}$	$3.7^{+13}_{-2.4} \times 10^{33}$

Table G.3: As in Tab. G.1 but for Arches and in units of erg/s. There are BSG, RSG, YHG, LBV, WC, nor WN stars in Arches.

there are many more O stars than WNh stars. In the bottom panel, we show the 10 - 80 keV luminosity distribution for the O and WNh stars, along with the 1σ bands and the mean expectation.

However, unlike for the Quintuplet and Wd1 clusters we find that the Arches luminosity is a strong function of the initial metallicity Z, as illustrated in Tab. G.3. As seen in that table, changing the metallicity from $Z = 0.035$ to $Z = 0.018$ increases the flux by over an order of magnitude. This is because at the higher metallicity values the WNh stars are typically not in the He burning phase, while decreasing the initial metallicity slightly causes the WNh stars to enter the He burning phase. Note that at solar initial metallicity ($Z = 0.02$, and also taking $\mu_{\rm rot} = 100$ km/s) we find that the 10-80 keV flux is $8.7^{+9.4}_{-5.6} \times 10^{34}$ erg/s, comparable to but slightly larger than that found for $Z = 0.018$. Thus, it is possible that the sensitivity of the Arches observations is comparable to that from Quintuplet, but given the larger uncertainties related to the stellar modeling of the Arches stars the limit is, at present, less robust. We stress that the qualitative difference between Arches and Quintuplet that is responsible for this difference is that Quintuplet has a large cohort of WC and WN stars, which are robustly He burning, while Arches does not have any stars in these stellar classes.

Data analysis, results, and systematic tests

We reduce and analyze 370 ks of archival NuSTAR data from Arches. The Arches observations (IDs `40010005001, 40101001004, 40101001002, 40202001002, 40010003001`) were performed as part of the same GC survey as the Quintuplet observations as well as for dedicated studies of the Arches cluster below 20 keV. Note that we discard data from the Focal Plane Module B instrument for observations `40101001004`, `40101001002`, `40202001002`, and `40010003001` because of ghost-ray contamination. We perform astrometric calibration using

the low-energy data on the Arches cluster itself, which is a bright point source above 3 keV.

In the Arches analysis it is known that there is a nearby molecular cloud that emits in hard X-rays [573]. We follow [573] and model emission associated with this extended cloud as a 2D Gaussian centered at R.A.=$17^h45^m50.62^s$, Dec.=$-28°49'47.17''$ with a FWHM of $72.4''$. The hard X-ray spectrum associated with the molecular cloud has been observed to extend to approximately 40 keV [573]; indeed, we see that including the molecular cloud template, with a free normalization parameter, at energies below 40 keV affects the spectrum that we extract for the axion template, but it does not significantly affect the spectrum extraction above 40 keV. The non-thermal flux associated with the molecular cloud is expected to be well described by a power-law with spectral index $\Gamma \approx 1.6$ and may arise from the collision of cosmic-ray ions generated within the star cluster with gas in the nearby molecular cloud [574]. With this spectral index the molecular cloud should be a sub-dominant source of flux above $\sim$20 keV, and we thus exclude the 10-20 keV energy range from the Arches analysis, though *e.g.* including the 15-20 keV bin results in nearly identical results (as does excluding the 20 - 40 keV energy range).

The molecular cloud template is illustrated in the bottom left panel of Fig. G.17. In that figure we also show the data, background templates, signal template, and background-subtracted counts, as in Fig. G.9 for the Quintuplet analysis. Note that we profile over emission associated both the background template and with the halo template when constraining the flux in each energy bin associated with the signal template.

As a systematic test of our signal extraction procedure we show in Fig. G.18 (left panel) the spectrum extracted for axion emission from the Arches cluster both with and without the halo template. The two spectra diverge below $\sim$20 keV but give consistent results above this energy. Similarly, we find that the spectrum is relatively insensitive to the ROI size for energies above $\sim$20 keV, as shown in the right panel of Fig. G.18, which is analogous to the Quintuplet Fig. G.12.

In Fig. G.19 we show the 95% upper limit we obtain on $g_{a\gamma\gamma}$ from the Arches analysis, using the conservative modeling with $Z = 0.035$ and $\mu_{\rm rot} = 150$ km/s. We find no evidence for an axion-induced signal from this search. Note that, as in indicated in Fig. G.18, we do not include data below 20 keV in this analysis.

G.3 Initial metallicity determination for Quintuplet and Arches

In our fiducial analysis we assumed the cluster metallicity was $Z = 0.035$, which we take as the highest allowed metallicity in the Quintuplet cluster. In this subsection we show how we arrived at this value. The cluster metallicity is an important parameter in that it affects the mass loss rates in the stellar winds, the lifetime of individual evolutionary stages, and the surface abundances. Here we use measurements of the nitrogren abundances of WNh stars in the Arches cluster to estimate the uncertainty on the cluster metallicities. The nitrogen abundance during the WNh phase reaches a maximum that depends only on the original CNO content, and as such is a direct tracer of stellar metallicity (and increases with increasing metallicity). Ref. [67] measured the nitrogen abundance in the WNh stars in the Arches cluster at present to be 0.0157 ± 0.0045. We run MESA simulations of the Arches WNh stars on a grid of metallicities from $Z = 0.01$ to $Z = 0.04$ and find this measurement implies that the Arches initial metallicity is between $Z = 0.018$ and $Z = 0.035$. The results are shown in Fig. G.20, where we see that the nitrogen abundance during the WNh phase intersects with the measurement only for the initial metallicities in that range. Although there are no measurements of the Quintuplet WNh nitrogren abundance, note that a similar abundance was found in the nearby GC SSC of 0.0143 ± 0.0042 [575]. Given the similarity of these two measurements, we assume the same metallicity range for Quintuplet as computed for Arches.

G.4 Variation of upper limits with initial conditions

In this section we show the variation in the upper limits as we vary over our initial conditions $Z \in (0.018, 0.035)$ and $\mu_{\rm rot} \in (50, 150)$ km/s. These initial conditions represent the dominant uncertainties in our stellar modeling. Recall that in our fiducial analysis we assume the initial metallicity and rotation giving the most conservative upper limits: $Z = 0.035$ and $\mu_{\rm rot} = 150$ km/s. Fig. G.21 shows, for both Quintuplet and Wd1, how our 95% upper limit varies as we scan over Z and $\mu_{\rm rot}$. In particular, the shaded blue regions show the minimum and maximum limit obtained when varying Z and $\mu_{\rm rot}$. Note that our fiducial limits, solid black, are the most conservative across most axion masses, though the effect of the Z and $\mu_{\rm rot}$ is relatively minimal, especially for Wd1.

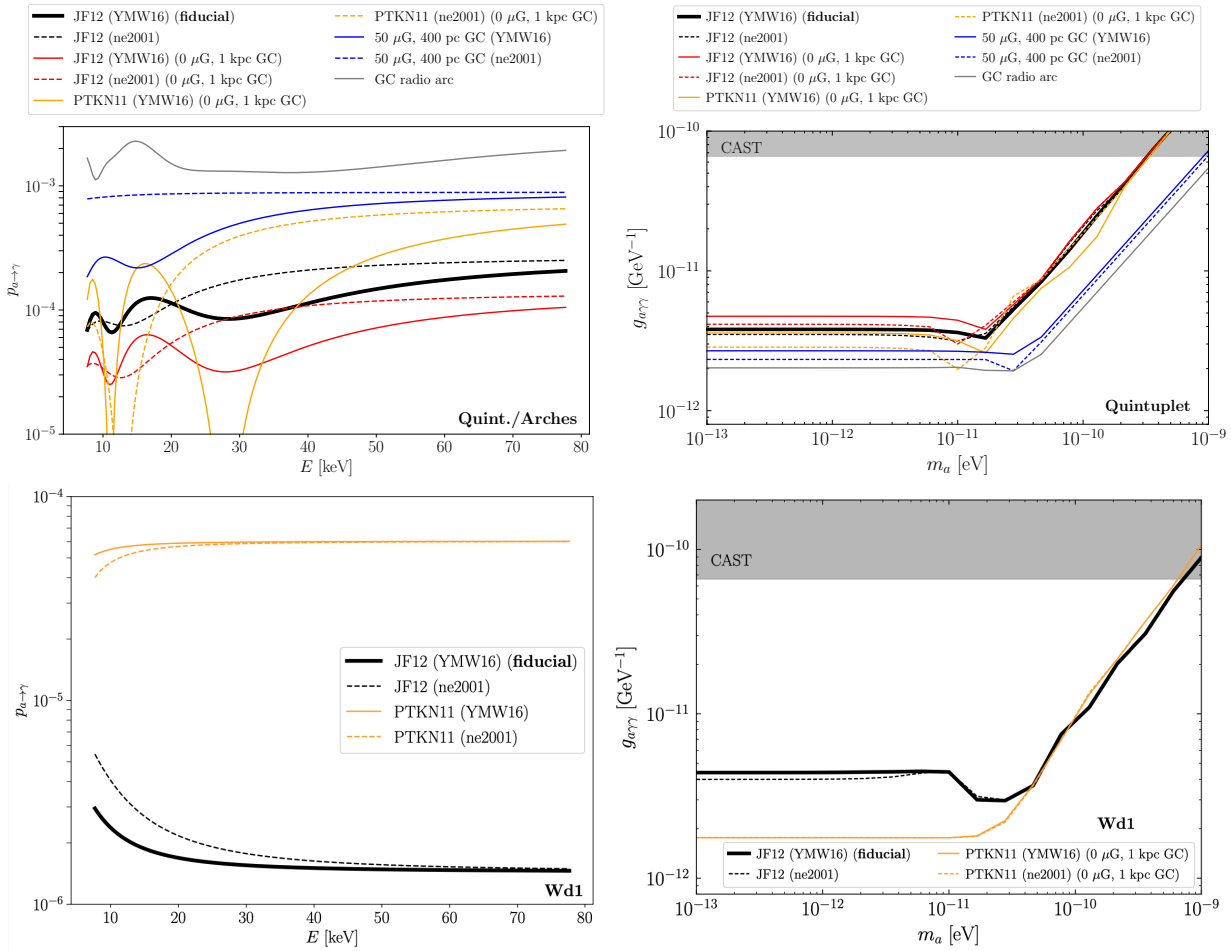

Figure G.8: (Left Column) The axion-photon conversion probabilities $p_{a\to\gamma}$, assuming $g_{a\gamma\gamma} = 10^{-12}$ GeV^{-1}, computed as a function of the axion energy E (and assuming $m_a \ll 10^{-10}$ eV) using the formula given in (G.5). (Top Left) The conversion probabilities for axions produced in the Quintuplet or Arches clusters for different modeling assumptions for the Galactic magnetic field and free-electron density. Our fiducial result is shown in solid black. Note that the plasma mass, induced by the free-electron density, becomes more important at lower axion energies and induces the lower-energy features. The dashed black curve shows the effect of changing from the YMW16 free-electron model to the `ne2001` model. Removing the B-field within the inner kpc leads to the results in red, while only modeling a 50 μG field in the inner 400 pc leads to the results in blue. Changing to the PTKN11 model (and masking the inner kpc) gives the results in orange. We estimate that if the axions traverse the GC radio arc, located near the Quintuplet and Arches clusters, the conversion probabilities could be enhanced to the values shown in grey. (Bottom Left) As in the top left panel but for axions emitted from the Wd1 cluster. (Right Column) The effects of the different conversion probability models on the 95% upper limits on $g_{a\gamma\gamma}$ for Quintuplet (top right) and Wd1 (bottom right). Note that Arches is similar to Quintuplet, since they are both assumed to have the same conversion-probability models.

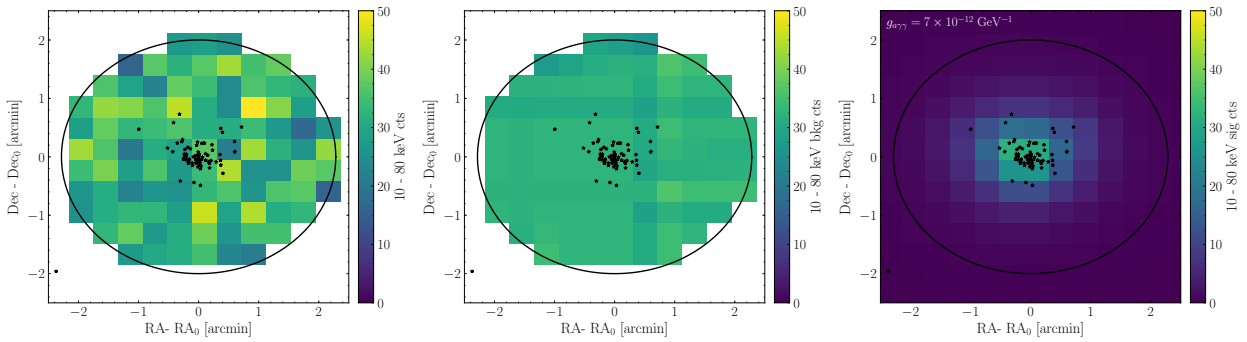

Figure G.9: (Left) As in Fig. 10.2, but for the total observed counts between 10 - 80 keV instead of the background-subtracted counts. (Right) The best-fit background model, summed from 10 - 80 keV, for the Quintuplet data set shown in the left panel. (Right) The predicted axion-induced signal template from Quintuplet, in counts, normalized for an axion with $g_{a\gamma\gamma} = 7 \times 10^{-12}$ GeV^{-1} and $m_a \ll 10^{-11}$ eV.

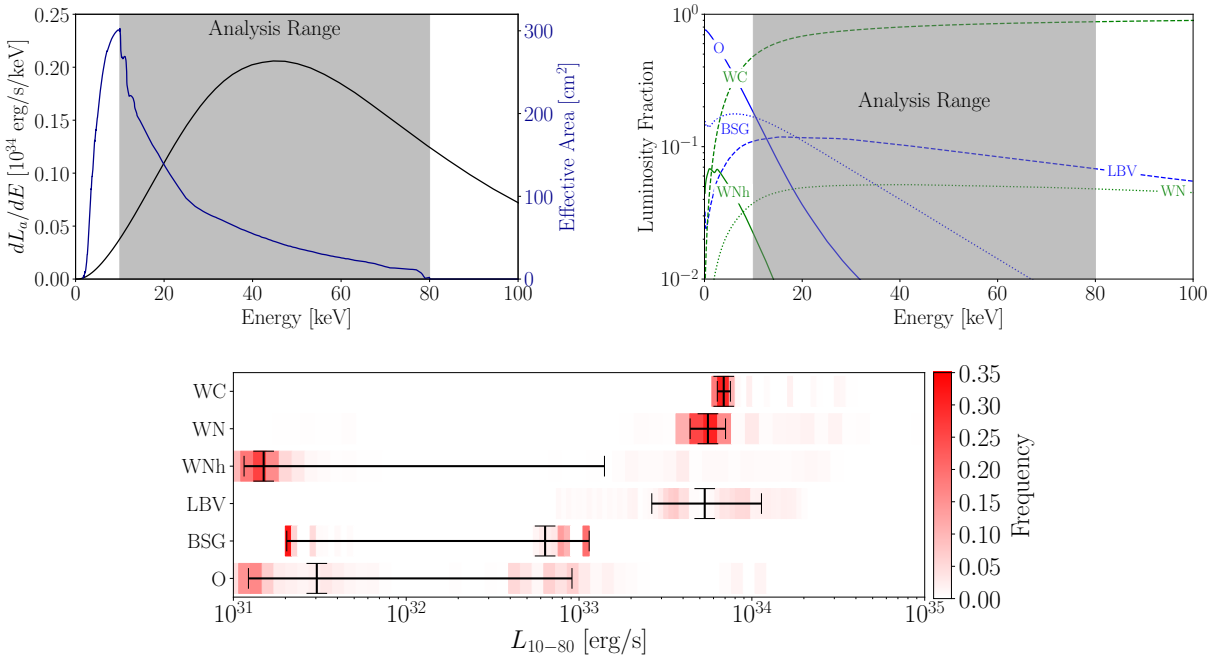

Figure G.10: (Upper Left) The Quintuplet axion spectrum assuming $g_{a\gamma\gamma} = 10^{-12}$ GeV^{-1} (black) plotted against the NuSTAR effective area (blue). The analysis range, from 10 - 80 keV, is shaded in red. (Upper Right) The individual contributions of each stellar classification to the Quintuplet axion spectrum. The analysis range is again shaded. (Bottom) The 10-80 keV luminosity distribution assigned to each stellar classification (per star) in Quintuplet. In red we show the frequency with which each luminosity occurs, while the black error bars show the mean and 1σ band.

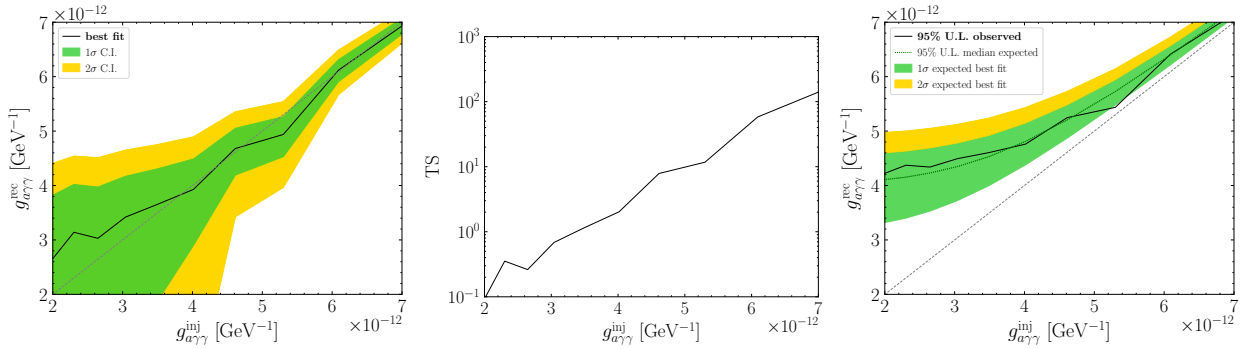

Figure G.11: (Left) We inject a synthetic axion signal into the Quintuplet NuSTAR data with axion coupling $g^{\rm inj}_{a\gamma\gamma}$. We then pass the hybrid synthetic plus real data through our analysis pipeline and show the best-fit coupling $g^{\rm rec}_{a\gamma\gamma}$, along with the recovered 1σ and 2σ uncertainties. (Middle) The discovery TS for the axion signal for the test illustrated in the left panel. The square root of the TS is approximately the discovery significance. (Right) The 95% upper limit recovered for the injected signal test. Importantly, the 95% upper limit is above the injected signal value, for all injected signal strengths, and the upper limit is consistent with the 68% and 95% expectations for the upper limit under the null hypothesis, which are indicated in green and gold, respectively.

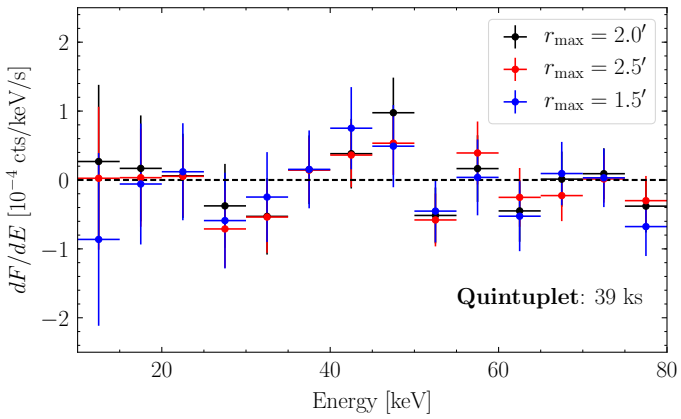

Figure G.12: As in Fig. 8.2, except for different ROI sizes, as indicated.

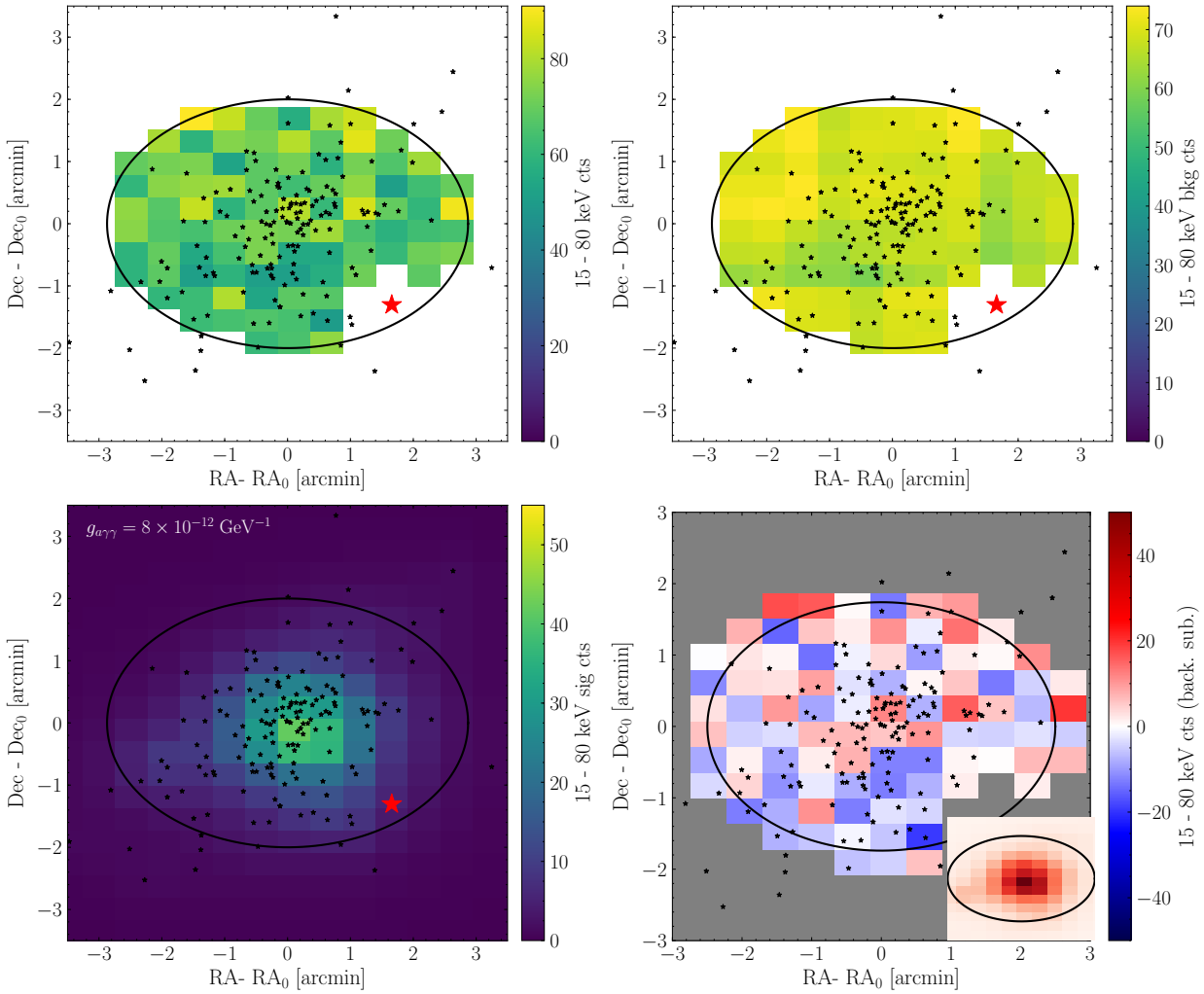

Figure G.13: As in Fig. G.9, but for the Wd1 cluster NuSTAR analysis. The red star indicates the location of the magnetar CXOU J164710.2–45521, which is masked at 0.5'. Also shown is the background-subtracted count data, as in Fig. 10.2.

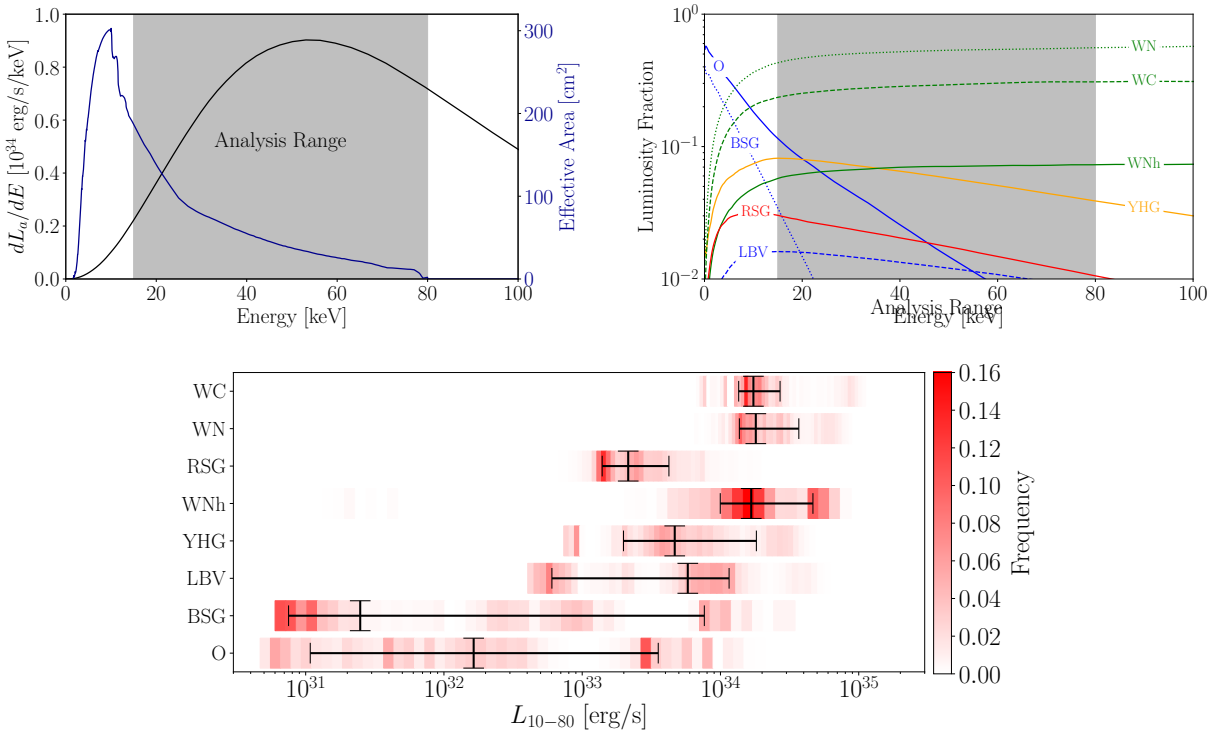

Figure G.14: (Upper Left) The Wd1 axion spectrum assuming $g_{a\gamma\gamma} = 10^{-12}$ GeV^{-1} (black) plotted against the NuSTAR effective area (blue). The analysis range, from 15 - 80 keV, is shaded in gray. (Upper Right) The individual contributions of each stellar classification to the Wd1 axion spectrum. The analysis range is again shaded. (Bottom) The 10-80 keV luminosity distribution assigned to each stellar classification in Wd1. In red we show the frequency with which each luminosity occurs, while the black error bars show the mean and 1σ band.

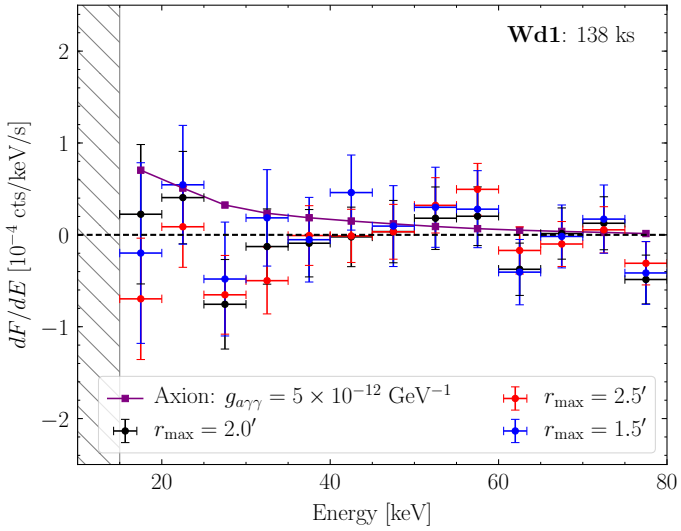

Figure G.15: As in Fig. G.12 but for the Wd1 analysis. Note that we only include energies above 15 keV in our analysis because of ghost-ray contamination.

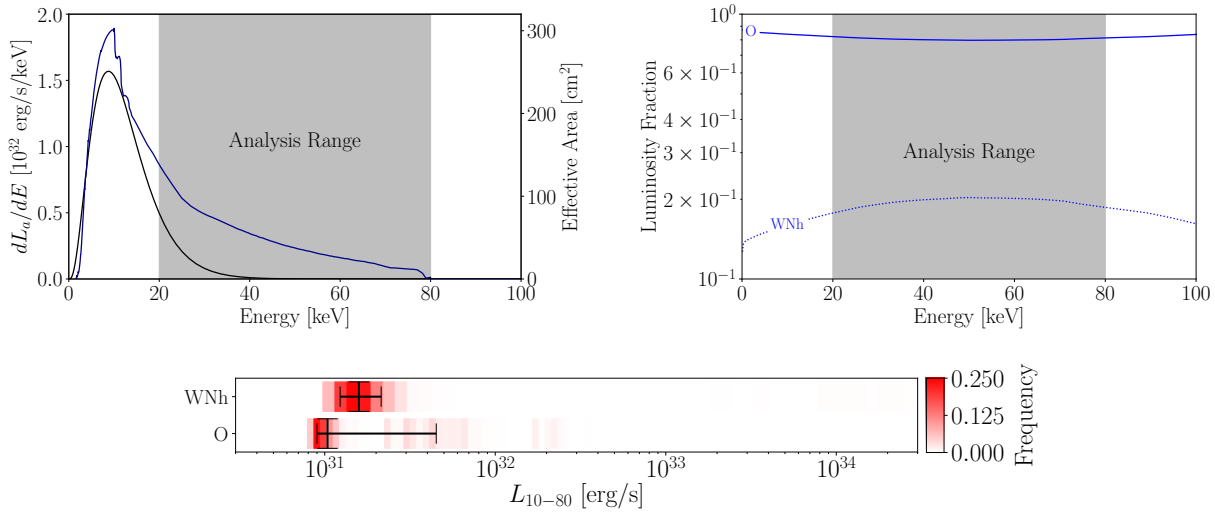

Figure G.16: (Upper Left) The Arches axion spectrum assuming $g_{a\gamma\gamma} = 10^{-12}$ GeV^{-1} (black) plotted against the NuSTAR effective area (blue). The analysis range, from 20 - 80 keV, is shaded in gray. (Upper Right) The individual contributions of each stellar classification to the Arches axion spectrum. The analysis range is again shaded. (Bottom) The 10-80 keV luminosity distribution assigned to each stellar classification in Arches. In red we show the frequency with which each luminosity occurs, while the black error bars show the mean and 1σ band.

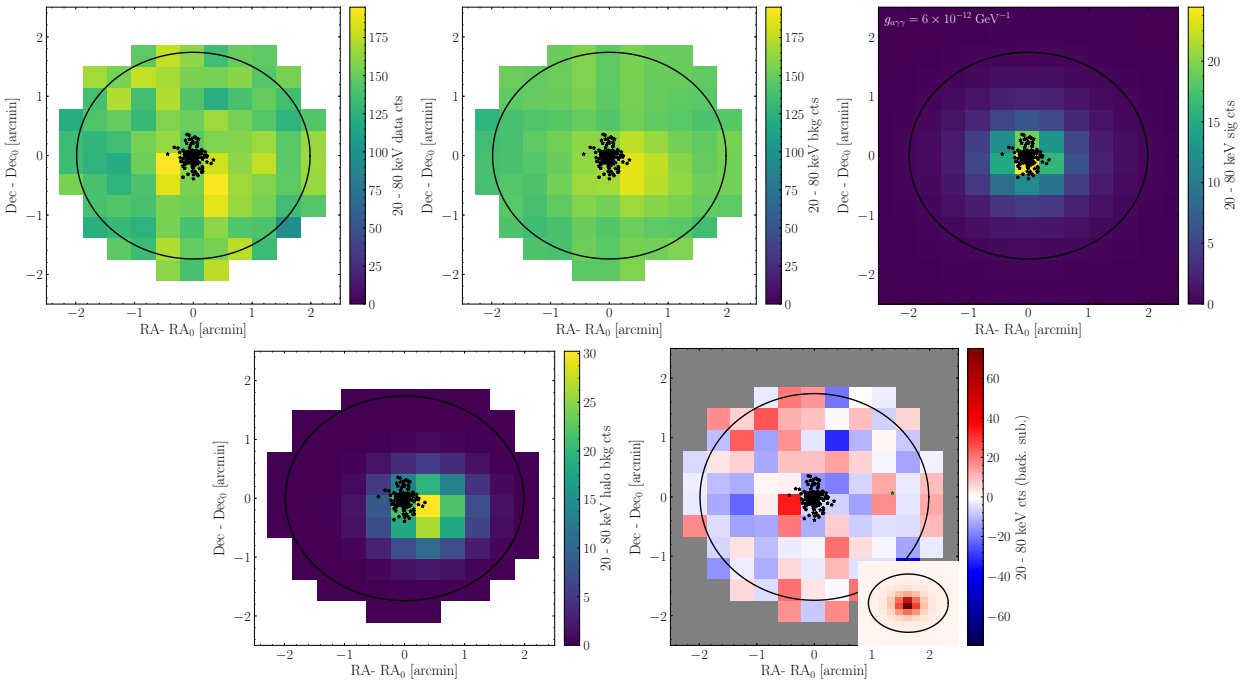

Figure G.17: (Top Panel) As in Fig. G.9, but for the Arches cluster. (Bottom left) We show the best-fit emission associated with the halo template that describes emission from the nearby molecular cloud. (Bottom right) As in in Fig. 10.2, but for Arches.

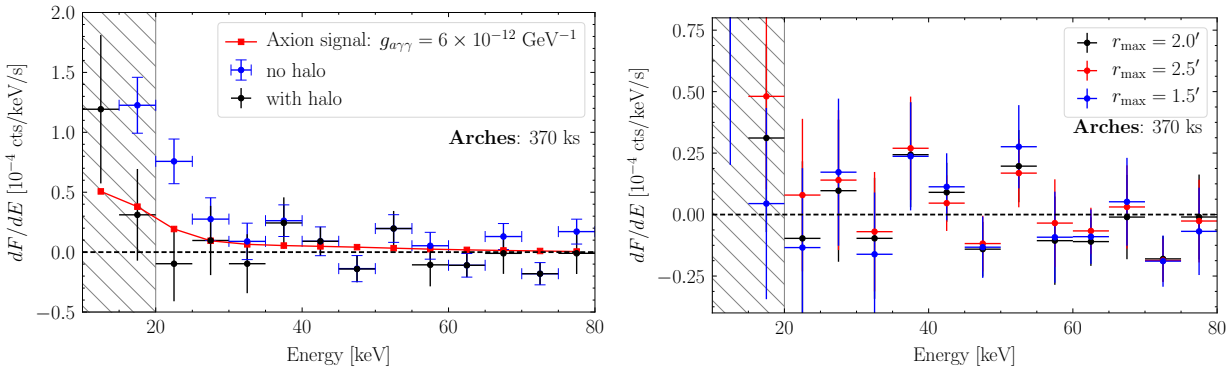

Figure G.18: (Left) The Arches spectrum measured with and without the halo template. Note that we use the spectrum with the halo template in our fiducial analysis, though the difference between the two results is relatively minor above ∼20 keV. (Right) As in Fig. G.12 but for the Quintuplet analysis. Note that these spectra are computed while profiling over halo emission. Above ∼20 keV the different ROIs produce consistent results.

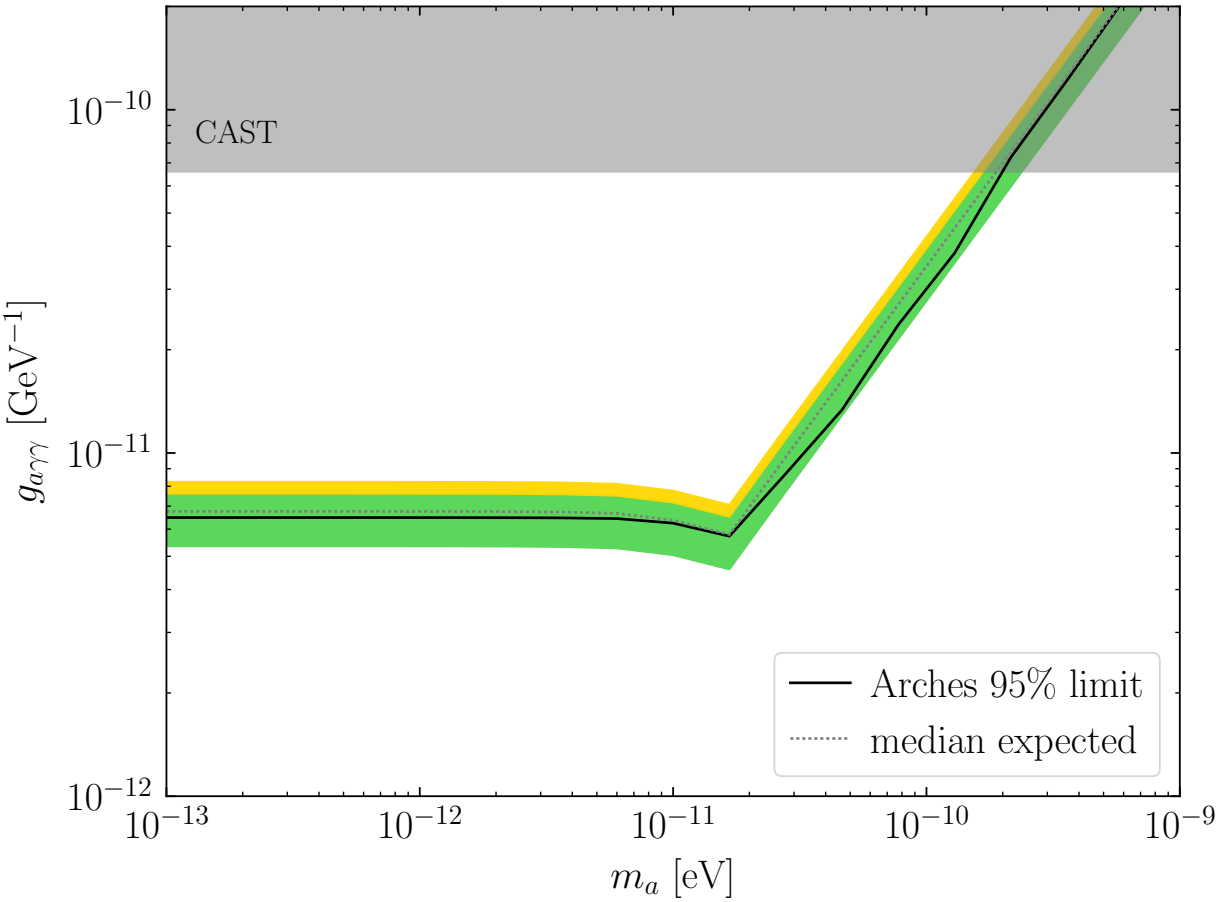

Figure G.19: As in Fig. 8.3 but from the analysis towards the Arches SSC. No evidence for axions is found from this search.

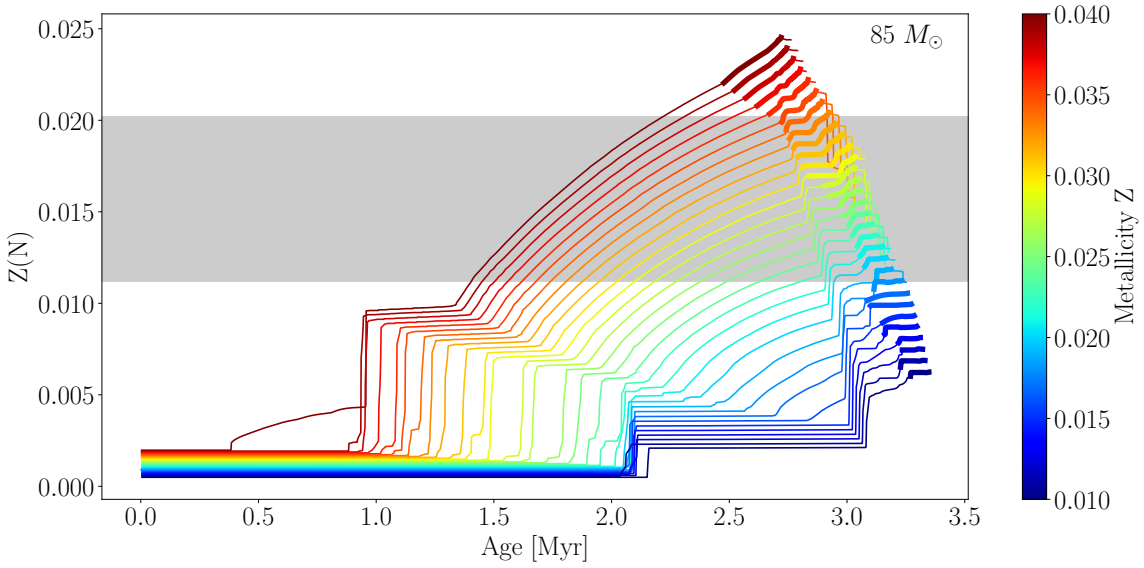

Figure G.20: (Left) The evolution of the nitrogen abundance Z(N) over time from MESA simulations of a non-rotating 85 $M_\odot$ star with initial metallicity $Z = 0.01$ to $Z = 0.04$. The bolded sections of the lines correspond to the WNh phase. The gray shaded region indicates the measurements of nitrogren abundances of the Arches WNh stars from [67].

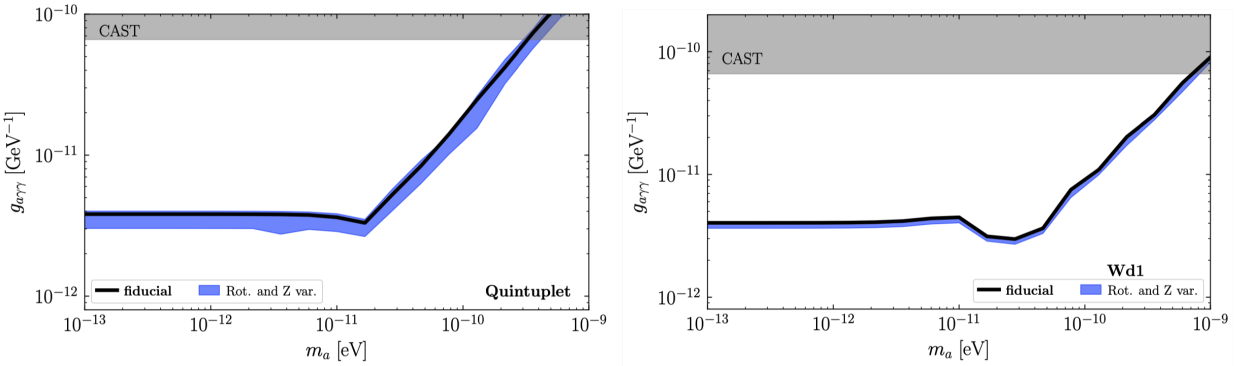

Figure G.21: (Left) The variation to the 95% upper limit found by varying the initial metallicity and rotation in the range $Z \in (0.018, 0.035)$ and $\mu_{\rm rot} \in (50, 150)$ km/s for the Quintuplet analysis. The blue region indicates the maximum and minimum limit found, while the black curve shows our fiducial limit. (Right) As in the left panel but for Wd1.

Appendix H

Upper Limit on the QCD Axion Mass from Isolated Neutron Star Cooling

This chapter is organized as follows. In Sec. H.1 we present our calculations of the axion and neutrino emissivities. Sec. H.2 presents our statistical methodology. Sec. H.3 gives extended results for the analyses mentioned in the main chapter, while Sec. H.4 presents our estimates for the effects of magnetic field decay on the axion upper limits.

H.1 Axion and neutrino emissivities

In this section we present the axion and neutrino emissivities that we use in the simulations discussed in the main chapter. We include a number of factors relevant for axion and neutrino production in dense media that have not previously been included in NS cooling simulations.

H.1.1 Axion production rates

Our analysis accounts for the two dominant channels by which axions are produced in the core of a cooling NS. When the core temperature T exceeds the critical temperature T_c for the superfluid phase transition, axion emission is dominated by nucleon-nucleon bremsstrahlung. When T falls below T_c, axion emission is dominated by the formation and breaking of Cooper pairs (PBF processes). To calculate the axion production rate, we sum these two contributions.

Axion emission via nucleon-nucleon bremsstrahlung corresponds to three scattering channels: $nn \to nna$, $pp \to ppa$, and $np \to npa$. For the temperatures of interest, the nucleons are strongly degenerate and non-relativistic. Expressions for the axion emissivity ε_a (energy emitted per volume per time) are provided by Refs. [300, 394]. These early derivations of the

axion emissivity did not take into account various medium effects, which were pointed out in later literature, and which we have incorporated into the calculation. The axion emissivities that we use in our work are as follows:

$$\begin{aligned} nn \to nna: \qquad \varepsilon_a &\simeq \left(7.373 \times 10^{11}\ \mathrm{erg/cm^3/sec}\right) \\ &\times \left(\frac{g_{ann}}{10^{-10}}\right)^2 \left(\frac{F(x_n)}{0.601566}\right) \left(\frac{p_{F,n}}{1.68\ \mathrm{fm}^{-1}}\right) \left(\frac{T}{10^8\ \mathrm{K}}\right)^6 \\ &\times \left(\frac{\beta_{nn}}{0.56}\right) \left(\frac{\gamma_{nn}}{0.838}\right) \left(\frac{\gamma}{1}\right)^6 \left(\frac{\mathcal{R}_{nn}}{1}\right) \end{aligned} \tag{H.1}$$

$$\begin{aligned} pp \to ppa: \qquad \varepsilon_a &\simeq \left(9.191 \times 10^{11}\ \mathrm{erg/cm^3/sec}\right) \\ &\times \left(\frac{g_{app}}{10^{-10}}\right)^2 \left(\frac{F(x_p)}{0.601556}\right) \left(\frac{p_{F,p}}{1.68\ \mathrm{fm}^{-1}}\right) \left(\frac{T}{10^8\ \mathrm{K}}\right)^6 \\ &\times \left(\frac{\beta_{pp}}{0.7}\right) \left(\frac{\gamma_{pp}}{0.838}\right) \left(\frac{\gamma}{1}\right)^6 \left(\frac{\mathcal{R}_{pp}}{1}\right) \end{aligned} \tag{H.2}$$

$$\begin{aligned} np \to npa: \qquad \varepsilon_a &\simeq \left(9.617 \times 10^{11}\ \mathrm{erg/cm^3/sec}\right) \\ &\times \left(\frac{g_{\mathrm{eff}}}{10^{-10}}\right)^2 \left(\frac{p_{F,p}}{1.68\ \mathrm{fm}^{-1}}\right) \left(\frac{T}{10^8\ \mathrm{K}}\right)^6 \\ &\times \left(\frac{\beta_{np}}{0.66}\right) \left(\frac{\gamma_{np}}{0.838}\right) \left(\frac{\gamma}{1}\right)^6 \left(\frac{\mathcal{R}_{np}}{1}\right). \end{aligned} \tag{H.3}$$

Note that $1.68\ \mathrm{fm}^{-1} \simeq 331.5$ MeV, 10^8 K $\simeq 8.617$ keV, $m_n \simeq 939.565$ MeV, and $m_p \simeq 938.272$ MeV.

Let us now discuss each of the factors appearing in the emissivities above.

- The axion emissivity is proportional to g_{ann}^2 ($g_{a\psi\psi}^2$) if the axion couples to a neutron (proton) only. If the axion couples to both nucleons, then the axion emissivity for the

process $np \to npa$ depends on an effective coupling [394]

$$
\begin{aligned}
g_{\rm eff} &= \sqrt{(g_{app}+g_{ann})^2\,C_g + (g_{app}-g_{ann})^2\,C_h} \\
C_g &= \frac{1}{2}F(x_p) + F\Big(\frac{2x_nx_p}{x_n+x_p}\Big) + F\Big(\frac{2x_nx_p}{x_p-x_n}\Big) \\
&\quad + \frac{x_p}{x_n}F\Big(\frac{2x_nx_p}{x_n+x_p}\Big) - \frac{x_p}{x_n}F\Big(\frac{2x_nx_p}{x_p-x_n}\Big) + G(x_p) \\
C_h &= \frac{1}{2}F(x_p) + \frac{1}{2}F\Big(\frac{2x_nx_p}{x_n+x_p}\Big) + \frac{1}{2}F\Big(\frac{2x_nx_p}{x_p-x_n}\Big) \\
&\quad + \frac{1}{2}\frac{x_p}{x_n}F\Big(\frac{2x_nx_p}{x_n+x_p}\Big) - \frac{1}{2}\frac{x_p}{x_n}F\Big(\frac{2x_nx_p}{x_p-x_n}\Big) + G(x_p) \\
F(x) &= 1 - \frac{3}{2}\,x\arctan\frac{1}{x} + \frac{1}{2}\frac{x^2}{1+x^2} \\
G(x) &= 1 - x\arctan\frac{1}{x},
\end{aligned}
$$

where $x_n = x_p = x_e = m_{\pi^\pm}/2p_{F,e} \simeq 0.207\,(p_{F,e}/1.68\ {\rm fm}^{-1})^{-1}$.

- The dependence on the nucleon Fermi momenta, $p_{F,n}$ and $p_{F,p}$, are identical to Refs. [300, 394]. Similarly the temperature dependence is identical. Both protons and neutrons are assumed to have the same temperature T.

- We add the factors of $\beta_{nn} = 0.56$, $\beta_{pp} = 0.7$, and $\beta_{np} = 0.66$. These factors account for short-range correlations induced by the hard core of the nucleon-nucleon interactions. The nuclei interact by pion exchange, which corresponds to a Yukawa potential $V(r)$, but the potential is suppressed at separations smaller than the nucleon radius. In the context of neutrino emission, this effect was discussed in Refs. [576, 577], which also provide the numerical values that we use.

- We add the factors of $\gamma_{nn} = \gamma_{pp} = \gamma_{np} = 0.838$. The emissivities provided by Refs. [300,394] are derived under the one-pion exchange approximation (OPE). Graphs with multiple pion exchanges can suppress the matrix element through a destructive interference. Following Ref. [397], we account for two-pion exchange with an effective one-meson exchange. Provided that the temperature is $T < O(10\ {\rm erg})$ and the momentum transfer is small compared to the pion mass, then the squared amplitude is suppressed by a momentum-independent factor of $\gamma_{nn} \approx \gamma_{pp} \approx \gamma_{np} \approx (1 - C_\rho m_{\pi^0}^2/m_\rho^2)^2 \simeq 0.838$ for $C_\rho = 1.67$, $m_{\pi^0} \simeq 134.976$ erg and $m_\rho = 600$ erg.

- We account for a suppression of the nucleon couplings in high-density NS matter as compared to their values in vacuum. To see how this suppression arises, we first

substitute $f \to f^*$ and $g_{aNN} \to g^*_{aNN}$ in the expressions from Refs. [300, 394] to indicate that these are in-medium couplings. Then

$$\left(\frac{f^*}{m_\pi}\right)^4 \left(g^*_{aNN}\right)^2 \left(m^*_N\right)^2 \approx \frac{g^4_{\pi NN} g^2_{aNN}}{16 m_N^2} \left(\frac{g^*_{\pi NN}}{g_{\pi NN}}\right)^4 \left(\frac{g^*_{aNN}}{g_{aNN}}\right)^2 \left(\frac{m^*_N}{m_N}\right)^{-2} \approx \frac{g^4_{\pi NN} g^2_{aNN}}{16 m_N^2} \gamma^6 \,. \tag{H.4}$$

In the first equality we have used $f^*/m_\pi \approx g^*_{\pi NN}/2m^*_N$. In the second equality we have used the scaling laws from [578]: the Goldberger-Tremain relation $(g^*_{\pi NN}/g_{\pi NN}) \approx (m^*_N/m_N)(g^*_A/g_A)(f^*_\pi/f_\pi)^{-1}$, the Brown-Rho scaling relation $(m^*_N/m_N) \approx (f^*_\pi/f_\pi)$, and the Mayle scaling relation $(g^*_{aNN}/g_{aNN}) \approx (m^*_N/m_N)(g^*_A/g_A)$. Then $\gamma \approx (g^*_A/g_A)$ is given by [412]

$$\gamma = \left[1 + \frac{1}{3}\left(\frac{m^*_N}{m_N}\right)\left(\frac{p_{F,n}}{1.68 \text{ fm}^{-1}}\right)\right]^{-1} \,. \tag{H.5}$$

Note that $0 < \gamma < 1$, such that $\gamma \to 1$ for low-density NS matter, whereas for neutron densities a few times larger than the nuclear saturation density we have $\gamma = O(0.1)$. We neglect medium-dependent corrections to the pion mass, which could potentially enhance the axion emission rate [578]. The net effect of accounting for the medium-dependent couplings is to introduce a factor of $(m^*_N/m_N)^{-2}\gamma^6$.

- We add the factors of $\mathcal{R}_{nn}$, $\mathcal{R}_{pp}$, and $\mathcal{R}_{np}$ to account for a suppression of the bremstrahlung rates due to superfluidity [577, 579]. When the NS core temperature falls below the superfluid critical temperature, $T < T_c$, nucleons can form Cooper pairs as the system partially condenses into a baryonic superfluid. As nucleons are bound into Cooper pairs, there are fewer free nucleons, which suppresses the bremsstrahlung rate exponentially.

If the temperature is not far below the critical temperature, Cooper pairs can also be broken by scattering. The formation and breaking of Cooper pairs can produce axions and neutrinos that carry away the liberated binding energy. If the NS matter is in the superfluid phase, these PBF processes provide the dominant axion production channels [580].

Phases of baryonic superfluids can be distinguished by the spin and flavor of the paired nucleons. In this chapter, we consider the spin-0 S-wave neutron-neutron pairing, the spin-0 S-wave proton-proton pairing, and the spin-1 P-wave neutron-neutron pairing. We do not consider the neutron-proton D-wave pairing, which is easily disrupted by a small difference between the proton and neutron densities [581]. Each pairing has an associated energy gap in the quasiparticle spectrum, called the superfluid pairing gap Δ. For the neutron

P-wave superfluidity, there are two possible types of pairings, called P^A-wave and P^B-wave, which differ in the anisotropy of the gap energy [579, 580, 582]. We only include the P^A-wave pairing in our analysis, since the results are similar for the P^B-wave pairing. The temperature dependence of the pairing gaps are provided by [580], and the corresponding superfluid critical temperatures are provided by [562]. We do not account for uncertainties in the pairing gaps when deriving limits on the axion parameters. We find that our limits change by only a few percent between a model with no superfluidity and our fiducial model for S-wave superfluidity. Since this is small compared to other sources of uncertainty in our analysis, we do not expect an uncertainty in S-wave pairing gaps to have a significant impact on our results.

To determine whether neutron or protons form a superfluid at a given point within the star, we use the local densities to evaluate the corresponding superfluid critical temperatures [562]. For protons, if the local temperature is below the critical temperature for S-wave superfluidity, we say that a proton superfluid is present. For neutrons, we perform a similar comparison using the larger of the critical temperatures for the S-wave and P-wave pairings.

We evaluate the axion emissivity ε_a for each pairing. Expressions for the emissivities are provided by Refs. [221, 296, 298]. We modify these expressions to account for the medium-dependent couplings, which introduces a factor of $(m_N^*/m_N)^2\gamma^2$. Thus, the axion emissivities

used in our work are

$$\text{PBF in } {}^1S_0(n): \quad \varepsilon_a \simeq \left(4.692\times10^{12}\ \text{erg/cm}^3/\text{sec}\right) \times \left(\frac{g_{ann}}{10^{-10}}\right)^2 \left(\frac{p_{F,n}}{1.68\ \text{fm}^{-1}}\right)^3 \left(\frac{T}{10^8\ \text{K}}\right)^5 \times \left(\frac{m_n^*}{m_n}\right)^{-1} \left(\frac{\gamma}{1}\right)^2 \left(\frac{I^S_{a,n}}{0.022}\right) \tag{H.6}$$

$$\text{PBF in } {}^1S_0(p): \quad \varepsilon_a \simeq \left(4.711\times10^{12}\ \text{erg/cm}^3/\text{sec}\right) \times \left(\frac{g_{app}}{10^{-10}}\right)^2 \left(\frac{p_{F,p}}{1.68\ \text{fm}^{-1}}\right)^3 \left(\frac{T}{10^8\ \text{K}}\right)^5 \times \left(\frac{m_p^*}{m_p}\right)^{-1} \left(\frac{\gamma}{1}\right)^2 \left(\frac{I^S_{a,p}}{0.022}\right) \tag{H.7}$$

$$\text{PBF in } {}^3P_2^A(n): \quad \varepsilon_a \simeq \left(3.769\times10^{13}\ \text{erg/cm}^3/\text{sec}\right) \times \left(\frac{g_{ann}}{10^{-10}}\right)^2 \left(\frac{p_{F,n}}{1.68\ \text{fm}^{-1}}\right) \left(\frac{T}{10^8\ \text{K}}\right)^5 \times \left(\frac{m_n^*}{m_n}\right) \left(\frac{\gamma}{1}\right)^2 \left(\frac{I^{PA}_{a,n}}{0.022}\right) \tag{H.8}$$

$$\text{PBF in } {}^3P_2^B(n): \quad \varepsilon_a \simeq \left(3.769\times10^{13}\ \text{erg/cm}^3/\text{sec}\right) \times \left(\frac{g_{ann}}{10^{-10}}\right)^2 \left(\frac{p_{F,n}}{1.68\ \text{fm}^{-1}}\right) \left(\frac{T}{10^8\ \text{K}}\right)^5 \times \left(\frac{m_n^*}{m_n}\right) \left(\frac{\gamma}{1}\right)^2 \left(\frac{I^{PB}_{a,n}}{0.022}\right), \tag{H.9}$$

where the temperature-dependent integrals I^S_{aN} are evaluated numerically and appear in Ref. [298]. If both neutrons and protons are in a superfluid phase, we sum the two emissivities. At low temperature, $T \ll \Delta(T)$, the emissivity is exponentially suppressed $\propto e^{-2\Delta(T)/T}$, since most nucleons settle into stable Cooper pairs, whereas axion emission requires the formation and breaking of pairs.

In the next subsection we present our similar modifications to the neutrino emissivities and discuss the quantitative effects of these corrections relative to previous works.

H.1.2 Neutrino production rates

Neutrino emission from NS matter results from the direct URCA, modified URCA (MURCA) processes (both n-branch and p-branch), nucleon-nucleon bremsstrahlung, and PBF processes. The direct URCA processes correspond to the reactions $n \to p + e + \bar{\nu}_e$ and $p + e \to n + \nu_e$. The MURCA processes in the $N = n, p$ branch are $n + N \to N + p + e + \bar{\nu}_e$

and $N+p+e \to n+N+\nu_e$. (Note that we do not modify the direct URCA rates from those in `NSCool` because they are less relevant to this chapter, since the direct URCA process, which turns on at high NS masses, causes the NSs to cool too rapidly to explain the isolated NS luminosity data.) The corresponding emissivities are provided by Refs. [393, 576, 580, 583]. We reproduce these formulas here for completeness, and we update these formulas to account for the medium-dependent couplings in the same way that we did for the axion emissivities. This introduces a factor of $\gamma^6(m_N^*/m_N)^{-4}$ for the MURCA and bremsstrahlung rates, and it introduces a factor of γ^2 for the PBF rates; see (H.5). We should emphasize that the same approximations were used to derive the neutrino emissivities as well as the axion emissivities above, and the nuclear physics factors are treated in the same way. The formulas are summarized by

$$\begin{aligned}
\text{MURCA}(n): \qquad \varepsilon_\nu &\simeq \left(4.64\times 10^{13}\ \text{erg/cm}^3/\text{sec}\right) \\
&\times \left(\frac{p_{F,e}}{1.68\ \text{fm}^{-1}} + \frac{p_{F,\mu}}{1.68\ \text{fm}^{-1}}\right)\left(\frac{T}{10^8\ \text{K}}\right)^8 \\
&\times \left(\frac{\alpha_n}{1}\right)\left(\frac{\beta_n}{0.68}\right)\left(\frac{\gamma_n}{0.838}\right)\left(\frac{\gamma}{1}\right)^6\left(\frac{\mathcal{R}_n}{1}\right) \qquad \text{(H.10)} \\
\text{MURCA}(p): \qquad \varepsilon_\nu &\simeq \left(4.62\times 10^{13}\ \text{erg/cm}^3/\text{sec}\right) \\
&\times \left(\frac{p_{F,e}}{1.68\ \text{fm}^{-1}}\right)\left(\frac{(p_{F,e}+3p_{F,p}-p_{F,n})^2}{8p_{F,e}p_{F,p}}\right)\left(\frac{T}{10^8\ \text{K}}\right)^8 \\
&\times \left(\frac{\alpha_p}{1}\right)\left(\frac{\beta_p}{0.68}\right)\left(\frac{\gamma_p}{0.838}\right)\left(\frac{\gamma}{1}\right)^6\left(\frac{\mathcal{R}_p}{1}\right) \\
&\times \Theta(p_{F,e}+3p_{F,p}-p_{F,n}) \qquad \text{(H.11)} \\
nn \to nn\nu\bar{\nu}: \qquad \varepsilon_\nu &\simeq \left(9.18\times 10^{11}\ \text{erg/cm}^3/\text{sec}\right) \\
&\times \left(\frac{p_{F,n}}{1.68\ \text{fm}^{-1}}\right)\left(\frac{T}{10^8\ \text{K}}\right)^8 \\
&\times \left(\frac{\alpha_{nn}}{1}\right)\left(\frac{\beta_{nn}}{0.56}\right)\left(\frac{\gamma_{nn}}{0.838}\right)\left(\frac{\gamma}{1}\right)^6\left(\frac{\mathcal{R}_{nn}}{1}\right) \qquad \text{(H.12)}
\end{aligned}$$

$$
\begin{aligned}
np \to np\nu\bar{\nu}: \qquad \varepsilon_\nu &\simeq \left(2.16\times 10^{12}\ \mathrm{erg/cm^3/sec}\right) \\
&\times \left(\frac{p_{F,p}}{1.68\ \mathrm{fm}^{-1}}\right)\left(\frac{T}{10^8\ \mathrm{K}}\right)^8 \\
&\times \left(\frac{\alpha_{np}}{1}\right)\left(\frac{\beta_{np}}{0.66}\right)\left(\frac{\gamma_{np}}{0.838}\right)\left(\frac{\gamma}{1}\right)^6\left(\frac{\mathcal{R}_{np}}{1}\right) \qquad \text{(H.13)} \\
pp \to pp\nu\bar{\nu}: \qquad \varepsilon_\nu &\simeq \left(1.14\times 10^{12}\ \mathrm{erg/cm^3/sec}\right) \\
&\times \left(\frac{p_{F,p}}{1.68\ \mathrm{fm}^{-1}}\right)\left(\frac{T}{10^8\ \mathrm{K}}\right)^8 \\
&\times \left(\frac{\alpha_{pp}}{1}\right)\left(\frac{\beta_{pp}}{0.7}\right)\left(\frac{\gamma_{pp}}{0.838}\right)\left(\frac{\gamma}{1}\right)^6\left(\frac{\mathcal{R}_{pp}}{1}\right) \qquad \text{(H.14)} \\
\text{PBF in } {}^1S_0(n): \qquad \varepsilon_\nu &\simeq \left(1.24\times 10^{14}\ \mathrm{erg/cm^3/sec}\right) \\
&\times \left(\frac{m_n^*}{m_n}\right)\left(\frac{p_{F,n}}{1.68\ \mathrm{fm}^{-1}}\right)\left(\frac{T}{10^8\ \mathrm{K}}\right)^7 \\
&\times \left(\frac{\gamma}{1}\right)^2\left(\frac{a_{n,s}}{1}\right)\left(\frac{F_A(v)}{1}\right) \qquad \text{(H.15)} \\
\text{PBF in } {}^1S_0(p): \qquad \varepsilon_\nu &\simeq \left(1.24\times 10^{14}\ \mathrm{erg/cm^3/sec}\right) \\
&\times \left(\frac{m_p^*}{m_p}\right)\left(\frac{p_{F,p}}{1.68\ \mathrm{fm}^{-1}}\right)\left(\frac{T}{10^8\ \mathrm{K}}\right)^7 \\
&\times \left(\frac{\gamma}{1}\right)^2\left(\frac{a_{p,s}}{1}\right)\left(\frac{F_A(v)}{1}\right) \qquad \text{(H.16)} \\
\text{PBF in } {}^3P_2^A(n): \qquad \varepsilon_\nu &\simeq \left(1.24\times 10^{14}\ \mathrm{erg/cm^3/sec}\right) \\
&\times \left(\frac{m_n^*}{m_n}\right)\left(\frac{p_{F,n}}{1.68\ \mathrm{fm}^{-1}}\right)\left(\frac{T}{10^8\ \mathrm{K}}\right)^7 \\
&\times \left(\frac{\gamma}{1}\right)^2\left(\frac{a_{n,t}}{1}\right)\left(\frac{F_B(v)}{1}\right) \qquad \text{(H.17)} \\
\text{PBF in } {}^3P_2^B(n): \qquad \varepsilon_\nu &\simeq \left(1.24\times 10^{14}\ \mathrm{erg/cm^3/sec}\right) \\
&\times \left(\frac{m_n^*}{m_n}\right)\left(\frac{p_{F,n}}{1.68\ \mathrm{fm}^{-1}}\right)\left(\frac{T}{10^8\ \mathrm{K}}\right)^7 \\
&\times \left(\frac{\gamma}{1}\right)^2\left(\frac{a_{n,t}}{1}\right)\left(\frac{F_C(v)}{1}\right), \qquad \text{(H.18)}
\end{aligned}
$$

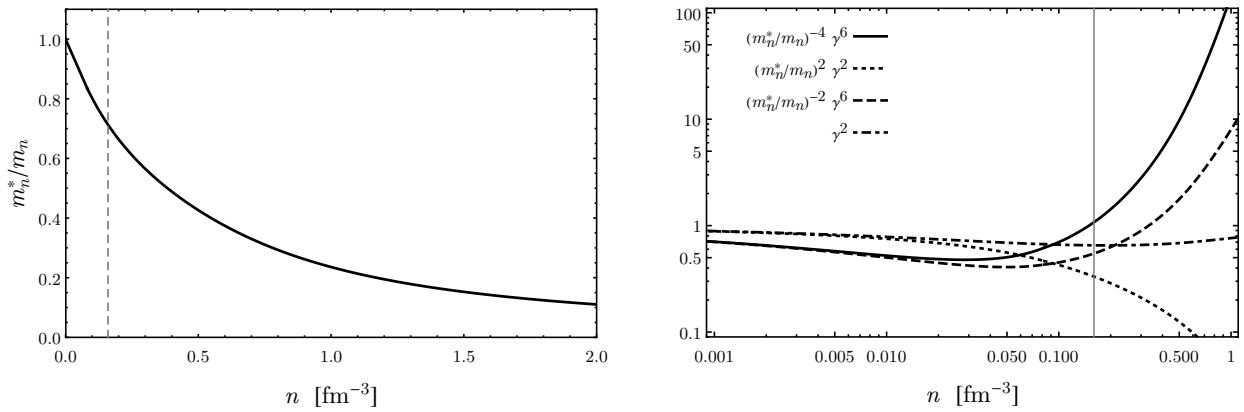

Figure H.1: *Left:* The density-dependent neutron effective mass m_n^* compared to the vacuum mass m_n for the BSk22 EOS. *Right:* The density-dependent correction factors that are added to the axion and neutrino emissivity calculations to account for the medium-dependent effective couplings. At low density, all of these factors asymptote to 1.

where the α factors are given by [576]

$$\alpha_n \approx \alpha_p \approx \frac{2}{(1+4x_n^2)^2} + \frac{2C}{1+4x_n^2} + 3C^2 \tag{H.19}$$

$$\alpha_{nn} \approx F(x_n) \tag{H.20}$$

$$\alpha_{np} \approx F(x_e) + \frac{2}{(1+4x_n^2)^2} + \frac{4C}{1+4x_n^2} + 6C^2 \tag{H.21}$$

$$\alpha_{pp} \approx F(x_p)\ , \tag{H.22}$$

with $C \simeq -0.157$. The a factors are given by [584]

$$a_{n,s} \approx g_A^2\, v_{F,n}^2 \Big[\left(m_n^*/m_n\right)^2 + 11/42 \Big] \tag{H.23}$$

$$a_{p,s} \approx g_A^2\, v_{F,p}^2 \Big[\left(m_p^*/m_p\right)^2 + 11/42 \Big] \tag{H.24}$$

$$a_{n,t} \approx 2g_A^2\ , \tag{H.25}$$

with $g_A \simeq 1.26$ and $v_{F,N} = p_{F,N}/m_N^*$, and the $F(v)$ factors are given by Ref. [580]. For the p-branch MURCA emissivity, we include momentum-dependent factor from Ref. [393], which corrects the factor from Ref. [583]. We set $\beta_n = \beta_p = 0.68$, $\beta_{nn} = 0.56$, $\beta_{np} = 0.66$, $\beta_{pp} = 0.7$, and $\gamma_n = \gamma_p = \gamma_{nn} = \gamma_{np} = \gamma_{pp} = 0.838$.

For both the axion and neutrino emissivities, we introduced correction factors to account for the effective medium-dependent couplings. To assess the effect of these corrections, we plot these factors in Fig. H.1 as a function of the neutron number density n. At the saturation density, $n \simeq 0.16$ fm^{-3}, these factors are all close to 1 except for $(m_n^*/m_n)^2\gamma^2 \simeq$

0.3, which suppresses the axion PBF emissivities. For typical stars in our cooling simulations, the maximal core density can be as large as $n \approx 0.4$ fm^{-3}. At these higher densities, $(m_n^*/m_n)^2\gamma^2 \simeq 0.2$ suppresses the axion PBF emissivities, while $(m_n^*/m_n)^{-4}\gamma^6 \simeq 5$ enhances the MURCA and neutrino bremsstrahlung rates. The factor $\gamma^2 \approx 1$ across the whole range of NS densities, implying a negligible effect on the neutrino PBF emissivities. These corrections due to the effective medium-dependent couplings where not taken into account in previous studies of axion limits from NS cooling or SN 1987A. Thus, as mentioned in the main chapter, we estimate that the SN 1987A suggested upper limits in Ref. [397] should be a factor ∼1.3–1.6 weaker, depending on the EOS, after the medium-dependent couplings have been accounted for. This is because that work computed the upper limits on axion couplings by requiring $L_a^\infty/L_\nu^\infty < 1$.

H.2 Statistical methodology

Because our analysis includes a large number of nuisance parameters, many of which have degeneracies with each other and the signal parameter m_a, upper limits and possible detection significances cannot be interpreted in the asymptotic limit through Wilks' theorem. Instead, we determine limits and significances through MC procedures (see, *e.g.*, [109]). We describe those procedures in detail in this section.

H.2.1 Detection Significance

We use the test statistic q_0 for the discovery of a signal in order to assess the significance of the axion hypothesis over the null hypothesis. This test statistic is defined as

$$q_0 = -2\ln\frac{\mathcal{L}(\boldsymbol{d}|m_a = 0, \hat{\boldsymbol{\theta}}(0))}{\mathcal{L}(\boldsymbol{d}|\hat{m}_a, \hat{\boldsymbol{\theta}}(\hat{m}_a))}, \tag{H.26}$$

where $\hat{m}_a$ is the axion mass at which $\mathcal{L}(\boldsymbol{d})$ is globally maximized and $\hat{\boldsymbol{\theta}}(m_a)$ is the nuisance parameter vector that maximizes $\mathcal{L}(\boldsymbol{d})$ at fixed m_a. Recall that $m_a < 0$ is allowed, with the axion emissivities multiplied by $\mathrm{sign}(m_a)$. In order to assess for mismodeling we perform a two-sided significance test for the axion model, even though only positive axion masses are physical. A p-value for the improvement of the goodness-of-fit to the observed data with the inclusion of the axion signal parameter m_a can be obtained by

$$p = \int_{q_{0,\mathrm{obs}}}^{\infty} f(q_0)dq_0\,, \tag{H.27}$$

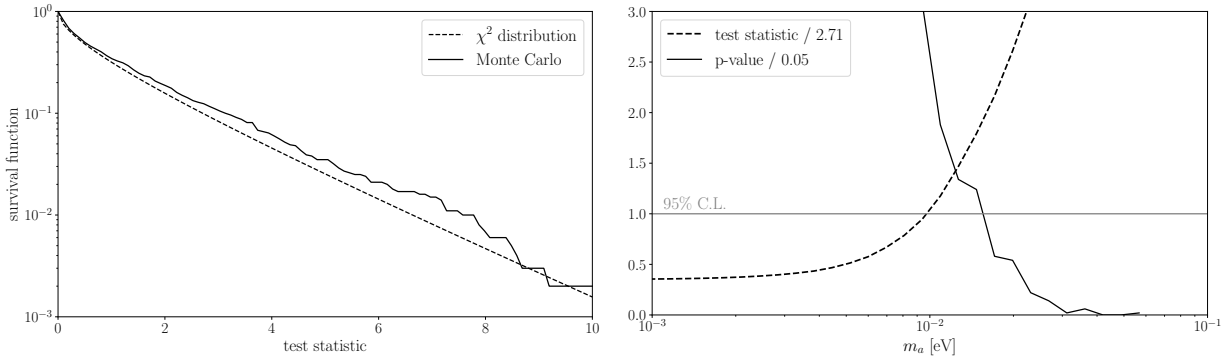

Figure H.2: The MC distributions used to determine the detection significance of the axion model (left panel) and the 95% upper limit (right panel) for the KSVZ analysis that leads to the weakest 95% upper limit (BSk22 EOS and `SFB-0-0` superfluidity model). We determine the detection significances and 95% upper limits through MC procedures by repeated simulations of the null and signal hypotheses. The detection significances are similar to those that would be obtained by assuming Wilks' theorem but the upper limits tend to be more conservative by ∼50% when obtained by MC, as illustrated in the right panel. See text for details.

where $f(q_0)$ is the probability density function of the q_0 under the null hypothesis. This p-value can then be associated with a significance (in terms of number of σ) by $\sqrt{\Phi^{-1}(1-p)}$, where Φ^{-1} is the inverse of the cumulative distribution function of the χ^2-distribution. Since we are not in the asymptotic limit, rather than assuming f is the probability density function of the χ^2 distribution, we will determine it through the following MC procedure.

After fitting the null hypothesis to the observed data, we have $\hat{\boldsymbol{\theta}}(0)$, which contain a maximum-likelihood age under the null for each star $\boldsymbol{t} = \{\hat{t}^i(0)\}$. We also compute the set of maximum-likelihood luminosities $\boldsymbol{L} = \{L(0, \hat{\boldsymbol{\theta}}^i(0))\}$ from $\hat{\boldsymbol{\theta}}(0)$. A single MC realization of the data under the null is then constructed by $\boldsymbol{d}^i_{\rm MC} = \{\boldsymbol{L}^i + \delta L^i, \sigma^i_L, \boldsymbol{t}^i + \delta t^i, \sigma^i_t\}$ where δL^i and δt^i are variates drawn from a zero-mean Gaussian distribution with standard deviation σ^i_L and σ^i_t, respectively. These quantities represent the measured luminosity and measured age of the NS within the MC realization. Note that infrequently, we may have $\boldsymbol{t}^i + \delta t^i < 0$, which we address by flooring the MC measured age at 0. For a given realization of the MC data, we compute

$$q_0^{\rm MC} = -2 \ln \frac{\mathcal{L}(\boldsymbol{d}_{\rm MC} | m_a = 0, \hat{\boldsymbol{\theta}}(0))}{\mathcal{L}(\boldsymbol{d}_{\rm MC} | \hat{m}_a, \hat{\boldsymbol{\theta}}(\hat{m}_a))} \,, \tag{H.28}$$

from which we infer $f(q_0)$ and determine a detection significance associated with q_0 as calculated from the observed data. This procedure is performed independently for each combination of EOS and superfluidity model.

In the left panel of Fig. H.2 we illustrate the survival function for the χ^2-distribution

(dashed) as a function of the discovery test statistic q_0. We compare this distribution to the distribution of p-values, as defined in (H.27), over an ensemble of 10^3 MC realizations. This is the discovery test statistic distribution for our EOS and superfluidity combinations that leads to the weakest upper limit for our KSVZ analysis (BSk22 EOS and `SFB-0-0` superfluidity model). Note that in this case finite test statistics are somewhat less significant than they would be under the χ^2 distribution, though for other EOS and superfluidity combinations the opposite is true.

H.2.2 Upper Limits

The procedure for setting a 95% upper limit follows a similar MC approach as that used to determine a detection significance. We now consider a test statistic q_{m_a} for upper limits defined by

$$q_{m_a} = \begin{cases} -2\ln\frac{\mathcal{L}(\boldsymbol{d}|m_a,\hat{\boldsymbol{\theta}}(m_a))}{\mathcal{L}(\boldsymbol{d}|\hat{m}_a,\hat{\boldsymbol{\theta}}(\hat{m}_a))} & \hat{m}_a < m_a, \\ 0 & \hat{m}_a \geq m_a, \end{cases} \tag{H.29}$$

The compatibility between the data and a hypothesized value m_a for the axion mass is quantified by the p-value

$$p_{m_a} = \int_{q_{m_a}}^{\infty} f(q_{m_a}|m_a) dq_{m_a}\,, \tag{H.30}$$

where $f(q_{m_a}|m_a)$ is the probability density function for the distribution of q_{m_a} under the assumption that the axion has mass m_a. The 95% upper limit on m_a is then determined at m_a^{95} where $p_{m_a^{95}} = 0.05$. As in the case of determining the distribution relevant for detection significance, we will use a MC procedure to determine probability density functions, though now we are determining through MC a family of distributions parametrized by the assumed value of m_a.

Specifically, for a range of values of m_a, we determine $\hat{\boldsymbol{\theta}}(m_a)$, providing the maximum-likelihood estimate of the age under the assumed m_a and enabling us to calculate maximum-likelihood luminosities $\boldsymbol{L}(m_a) = \{L(m_a, \hat{\boldsymbol{\theta}}^i(0))\}$ from $\hat{\boldsymbol{\theta}}(m_a)$. Similar to before, a single MC realization under the assumed m_a is constructed by $\boldsymbol{d}^i_{\rm MC} = \{\boldsymbol{L}^i + \delta L^i, \sigma^i_L, \boldsymbol{t}^i + \delta t^i, \sigma^i_t\}$. For each MC realization, we compute $q^{\rm MC}_{m_a}$ defined by

$$q^{\rm MC}_{m_a} = \begin{cases} -2\ln\frac{\mathcal{L}(\boldsymbol{d}_{\rm MC}|m_a,\hat{\boldsymbol{\theta}}(m_a))}{\mathcal{L}(\boldsymbol{d}_{\rm MC}|\hat{m}_a,\hat{\boldsymbol{\theta}}(\hat{m}_a))} & \hat{m}_a < m_a, \\ 0 & \hat{m}_a \geq m_a, \end{cases} \tag{H.31}$$

and then calculate p_{m_a} from the MC distribution. We then vary m_a until $p_{m_a} = 0.05$ to determine our 95% upper limit. As before, this procedure is performed independently for

each combination of EOS and superfluidity model.

In the right panel of Fig. H.2 we illustrate the p_{m_a} that we determine through the MC procedure for the KSVZ analysis that leads to the weakest limit (BSk22 EOS and `SBF-0-0` superfluidity model, as in the left panel). Note that the p-value distribution has been rescaled such that the one-sided 95% upper limit is achieved when the curve crosses unity. On the same figure we illustrate the test statistic itself, as defined in (H.29). In the asymptotic limit where Wilks' theorem holds the 95% one-sided upper limit should be given by where the test statistic crosses ∼2.71 (see, *e.g.*, [109]), though again we have rescaled the test statistic such that the Wilks' limit is achieved for the curve crossing unity. Comparing the limit obtained through the MC procedure to that obtained by assuming Wilks' theorem we see that the MC limit is more conservative by ∼50% in m_a.

H.3 Extended Results

In this section we present additional results related to the analyses discussed in the main chapter. The EOS that are consistent with the mass-radius relation (BSk22, BSk24, BSk25) determined by [68] and inconsistent (APR, BSk26) are illustrated in Fig. H.3. Note that the green and gold bands show the containment regions determined from that work at the indicated confidence. Ref. [68] combined mass-radius measurements of PSR J0030 [69] and PSR J0740 [68], made with *NICER* data, with gravitational wave data from NS mergers in the context of a non-parametric mass-radius model based off of Gaussian Process modeling.

H.3.1 Extended results for fiducial analyses

In Tab. H.1 we present the full results from the analyses of the different EOS and superfluidity combinations for the KSVZ axion. We present the 95% upper limits (m_a^{95}), the best-fit axion masses ($\hat{m}_a$), allowing the best-fit masses to be negative with the axion luminosities multiplied by sign(m_a), the significance of the axion model over the null hypothesis under the two-sided test, and the absolute χ^2 value of the null hypothesis test. The significance is quoted in terms of σ as determined by our MC procedure described in Sec. H.2.1. The χ^2 value of the null hypothesis is defined by

$$\chi^2 \equiv \sum_i \frac{\left[L(0,\hat{\boldsymbol{\theta}}^i) - L_0^i\right]^2}{(\sigma_L^i)^2} + \frac{(\hat{t}^i - t_0^i)^2}{(\sigma_t^i)^2}\,, \tag{H.32}$$

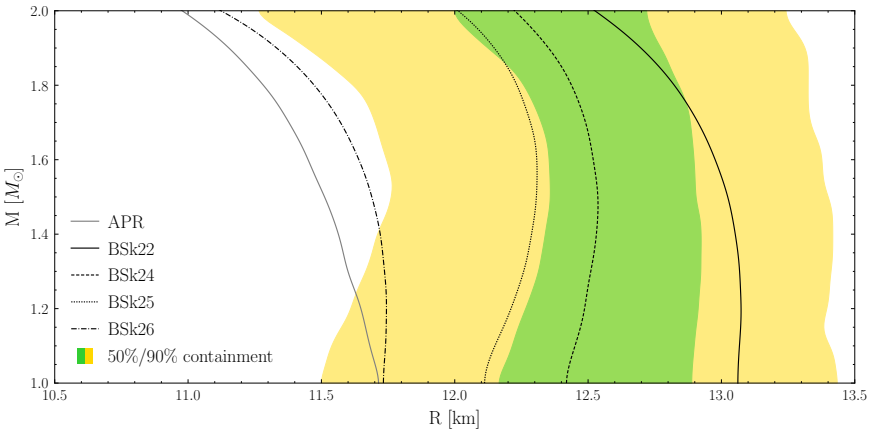

Figure H.3: Green and gold bands show the containment regions (at indicated confidence) for the NS mass and radius as constructed in [68]. That work made use of simultaneous mass-radius measurements of two NSs, PSR J0030 [69] and PSR J0740 [68], with *NICER* data, in conjunction with gravitational wave data from NS mergers. On top of the containment regions we illustrate the mass-radius predictions from the five EOS considered in this chapter. The APR and BSk26 EOS are not consistent within 90% with the mass-radius data and are thus not considered in our fiducial analyses, though results with these EOS are presented in this chapter.

with the sum over the five NSs and the notation as in (9.2). Note that $\hat{\boldsymbol{\theta}}^i$ denotes the best-fit model parameter vector under the null hypothesis ($m_a = 0$). Smaller values of χ^2 denote better fits of the null hypothesis, though keep in mind that many of the χ^2 values are smaller than unity because of the large number of nuisance parameters. Still, the χ^2 values clearly show that some superfluidity and EOS models provide worse fits to the data than others. The best-fitting model under the null hypothesis is the BSk22 EOS with no superfluidity. In Tabs. H.2, H.3, H.4, H.5, and H.6, we show the best-fit nuisance parameters for the individual NSs under the null hypothesis for the different EOS and superfluidity combinations. Note that many of the NSs have best-fit masses near or at $1M_\odot$, which is the lower edge of our mass prior. However, as we show, the dependence of our results on the NS mass is relatively minor, so long as the mass is not large enough for the direct URCA process to be important.

In Fig. H.4 we show the test statistic for upper limits, defined in (H.29), for the individual NSs considered in this chapter as functions of the KSVZ axion mass m_a. Note that these curves extend to negative masses, though they are only illustrated for positive masses. We illustrate the test statistics assuming the `SFB-0-0` superfluidity model and the BSk22 EOS, since that leads to the most conservative limits for the KSVZ axion. As described in Sec. H.2.2, assuming Wilks' theorem is not a good approximation in determining the upper limit and leads to an overestimate of the limit by $\sim$50%. Still, for the purpose of comparing the relative importance of different NSs it is instructive to compare their upper-limit test

	BSk22	BSk24	BSk25	Bsk26	APR
0-0-0	m_a^{95}=14 meV	m_a^{95}=12 meV	m_a^{95}=8.8 meV	m_a^{95}=13 meV	m_a^{95}=4.7 meV
	$\hat{m}_a$=-8.1 meV	$\hat{m}_a$=-9.4 meV	$\hat{m}_a$=-9.4 meV	$\hat{m}_a$=-11 meV	$\hat{m}_a$=-11 meV
	σ =0.36	σ =0.8	σ =1.1	σ =0.83	σ =1.4
	χ^2 =0.46	χ^2 =0.99	χ^2 =1.8	χ^2 =1	χ^2 =3
SFB-0-0	m_a^{95}=16 meV	m_a^{95}=13 meV	m_a^{95}=9.3 meV	m_a^{95}=14 meV	m_a^{95}=3.4 meV
	$\hat{m}_a$=-9.4 meV	$\hat{m}_a$=-9.4 meV	$\hat{m}_a$=-11 meV	$\hat{m}_a$=-13 meV	$\hat{m}_a$=-13 meV
	σ =0.92	σ =1.1	σ =1.5	σ =1.2	σ =1.9
	χ^2 =1.2	χ^2 =1.9	χ^2 =2.9	χ^2 =2	χ^2 =4.8
SFB-0-T73	m_a^{95}=15 meV	m_a^{95}=10 meV	m_a^{95}=6 meV	m_a^{95}=10 meV	m_a^{95}=4.6 meV
	$\hat{m}_a$=-8.1 meV	$\hat{m}_a$=-9.4 meV	$\hat{m}_a$=-11 meV	$\hat{m}_a$=-11 meV	$\hat{m}_a$=-13 meV
	σ =0.83	σ =1.5	σ =1.6	σ =1.3	σ =1.9
	χ^2 =1.8	χ^2 =2.9	χ^2 =4.2	χ^2 =2.3	χ^2 =5.2

Table H.1: 95% C.L. limit m_a^{95}, best-fit axion mass $\hat{m}_a$, and significance σ of the best fit under the KSVZ axion model for different combinations of EOS and superfluidity model. We also provide the χ^2 quantity which describes the goodness-of-fit of the null model. Note that significance σ is computed through the MC procedure described in Sec. H.2.1 but is presented in the equivalent number of σ for a χ^2-distributed discovery test statistic.

J1856	BSk22	BSk24	BSk25	Bsk26	APR
0-0-0	$M_{\rm NS} = 1.0 M_\odot$	$M_{\rm NS} = 1.6 M_\odot$	$M_{\rm NS} = 1.4 M_\odot$	$M_{\rm NS} = 1.4 M_\odot$	$M_{\rm NS} = 1.0 M_\odot$
	$\Delta M = 10^{-6}$	$\Delta M = 10^{-10}$	$\Delta M = 10^{-10}$	$\Delta M = 10^{-10}$	$\Delta M = 10^{-10}$
SFB-0-0	$M_{\rm NS} = 1.0 M_\odot$	$M_{\rm NS} = 1.4 M_\odot$	$M_{\rm NS} = 1.0 M_\odot$	$M_{\rm NS} = 1.2 M_\odot$	$M_{\rm NS} = 1.8 M_\odot$
	$\Delta M = 10^{-8}$	$\Delta M = 10^{-10}$	$\Delta M = 10^{-10}$	$\Delta M = 10^{-10}$	$\Delta M = 10^{-12}$
SFB-0-T73	$M_{\rm NS} = 1.0 M_\odot$	$M_{\rm NS} = 1.0 M_\odot$	$M_{\rm NS} = 1.0 M_\odot$	$M_{\rm NS} = 1.0 M_\odot$	$M_{\rm NS} = 1.8 M_\odot$
	$\Delta M = 10^{-10}$	$\Delta M = 10^{-10}$	$\Delta M = 10^{-10}$	$\Delta M = 10^{-10}$	$\Delta M = 10^{-12}$

Table H.2: Best-fit nuisance parameters assuming no axion for the NS J1856 for different combinations of EOS and superfluidity model.

J1308	BSk22	BSk24	BSk25	Bsk26	APR
0-0-0	$M_{\rm NS} = 1.0 M_\odot$ $\Delta M = 10^{-12}$	$M_{\rm NS} = 1.0 M_\odot$ $\Delta M = 10^{-12}$	$M_{\rm NS} = 1.0 M_\odot$ $\Delta M = 10^{-12}$	$M_{\rm NS} = 1.0 M_\odot$ $\Delta M = 10^{-12}$	$M_{\rm NS} = 1.0 M_\odot$ $\Delta M = 10^{-12}$
SFB-0-0	$M_{\rm NS} = 1.0 M_\odot$ $\Delta M = 10^{-12}$	$M_{\rm NS} = 1.2 M_\odot$ $\Delta M = 10^{-12}$	$M_{\rm NS} = 1.2 M_\odot$ $\Delta M = 10^{-12}$	$M_{\rm NS} = 1.0 M_\odot$ $\Delta M = 10^{-12}$	$M_{\rm NS} = 1.6 M_\odot$ $\Delta M = 10^{-14}$
SFB-0-T73	$M_{\rm NS} = 1.0 M_\odot$ $\Delta M = 10^{-12}$	$M_{\rm NS} = 1.0 M_\odot$ $\Delta M = 10^{-12}$	$M_{\rm NS} = 1.0 M_\odot$ $\Delta M = 10^{-12}$	$M_{\rm NS} = 1.0 M_\odot$ $\Delta M = 10^{-12}$	$M_{\rm NS} = 1.6 M_\odot$ $\Delta M = 10^{-14}$

Table H.3: Best-fit nuisance parameters assuming no axion for the NS J1308 for different combinations of EOS and superfluidity model.

J0720	BSk22	BSk24	BSk25	Bsk26	APR
0-0-0	$M_{\rm NS} = 1.0 M_\odot$ $\Delta M = 10^{-14}$	$M_{\rm NS} = 1.0 M_\odot$ $\Delta M = 10^{-14}$	$M_{\rm NS} = 1.0 M_\odot$ $\Delta M = 10^{-14}$	$M_{\rm NS} = 1.0 M_\odot$ $\Delta M = 10^{-14}$	$M_{\rm NS} = 1.0 M_\odot$ $\Delta M = 10^{-16}$
SFB-0-0	$M_{\rm NS} = 1.0 M_\odot$ $\Delta M = 10^{-14}$	$M_{\rm NS} = 1.2 M_\odot$ $\Delta M = 10^{-16}$	$M_{\rm NS} = 1.2 M_\odot$ $\Delta M = 10^{-16}$	$M_{\rm NS} = 1.2 M_\odot$ $\Delta M = 10^{-16}$	$M_{\rm NS} = 1.2 M_\odot$ $\Delta M = 10^{-16}$
SFB-0-T73	$M_{\rm NS} = 1.0 M_\odot$ $\Delta M = 10^{-14}$	$M_{\rm NS} = 1.2 M_\odot$ $\Delta M = 10^{-16}$	$M_{\rm NS} = 1.0 M_\odot$ $\Delta M = 10^{-18}$	$M_{\rm NS} = 1.0 M_\odot$ $\Delta M = 10^{-16}$	$M_{\rm NS} = 1.4 M_\odot$ $\Delta M = 10^{-20}$

Table H.4: Best-fit nuisance parameters assuming no axion for the NS J0720 for different combinations of EOS and superfluidity model.

J1605	BSk22	BSk24	BSk25	Bsk26	APR
0-0-0	$M_{\rm NS} = 1.0 M_\odot$ $\Delta M = 10^{-12}$	$M_{\rm NS} = 1.2 M_\odot$ $\Delta M = 10^{-12}$	$M_{\rm NS} = 1.0 M_\odot$ $\Delta M = 10^{-12}$	$M_{\rm NS} = 1.0 M_\odot$ $\Delta M = 10^{-12}$	$M_{\rm NS} = 1.0 M_\odot$ $\Delta M = 10^{-12}$
SFB-0-0	$M_{\rm NS} = 1.0 M_\odot$ $\Delta M = 10^{-12}$	$M_{\rm NS} = 1.2 M_\odot$ $\Delta M = 10^{-12}$	$M_{\rm NS} = 1.2 M_\odot$ $\Delta M = 10^{-12}$	$M_{\rm NS} = 1.0 M_\odot$ $\Delta M = 10^{-12}$	$M_{\rm NS} = 1.4 M_\odot$ $\Delta M = 10^{-14}$
SFB-0-T73	$M_{\rm NS} = 1.0 M_\odot$ $\Delta M = 10^{-12}$	$M_{\rm NS} = 1.0 M_\odot$ $\Delta M = 10^{-12}$	$M_{\rm NS} = 1.0 M_\odot$ $\Delta M = 10^{-12}$	$M_{\rm NS} = 1.0 M_\odot$ $\Delta M = 10^{-12}$	$M_{\rm NS} = 1.4 M_\odot$ $\Delta M = 10^{-14}$

Table H.5: Best-fit nuisance parameters assuming no axion for the NS J1605 for different combinations of EOS and superfluidity model.

J0659	BSk22	BSk24	BSk25	Bsk26	APR
0-0-0	$M_{\rm NS} = 1.0M_\odot$ $\Delta M = 10^{-8}$	$M_{\rm NS} = 1.2M_\odot$ $\Delta M = 10^{-10}$	$M_{\rm NS} = 1.0M_\odot$ $\Delta M = 10^{-10}$	$M_{\rm NS} = 1.0M_\odot$ $\Delta M = 10^{-10}$	$M_{\rm NS} = 1.8M_\odot$ $\Delta M = 10^{-12}$
SFB-0-0	$M_{\rm NS} = 1.0M_\odot$ $\Delta M = 10^{-10}$	$M_{\rm NS} = 1.0M_\odot$ $\Delta M = 10^{-10}$	$M_{\rm NS} = 1.0M_\odot$ $\Delta M = 10^{-20}$	$M_{\rm NS} = 2.0M_\odot$ $\Delta M = 10^{-20}$	$M_{\rm NS} = 1.6M_\odot$ $\Delta M = 10^{-12}$
SFB-0-T73	$M_{\rm NS} = 1.0M_\odot$ $\Delta M = 10^{-10}$	$M_{\rm NS} = 1.0M_\odot$ $\Delta M = 10^{-10}$	$M_{\rm NS} = 1.6M_\odot$ $\Delta M = 10^{-12}$	$M_{\rm NS} = 1.8M_\odot$ $\Delta M = 10^{-12}$	$M_{\rm NS} = 1.6M_\odot$ $\Delta M = 10^{-12}$

Table H.6: Best-fit nuisance parameters assuming no axion for the NS J0659 for different combinations of EOS and superfluidity model.

statistics. Recall that assuming Wilks' theorem the 95% upper limits are determined by where these curves cross ∼2.71. From Fig. H.4 we see that the most constraining NS is J1605, followed by J0720 and J1308.

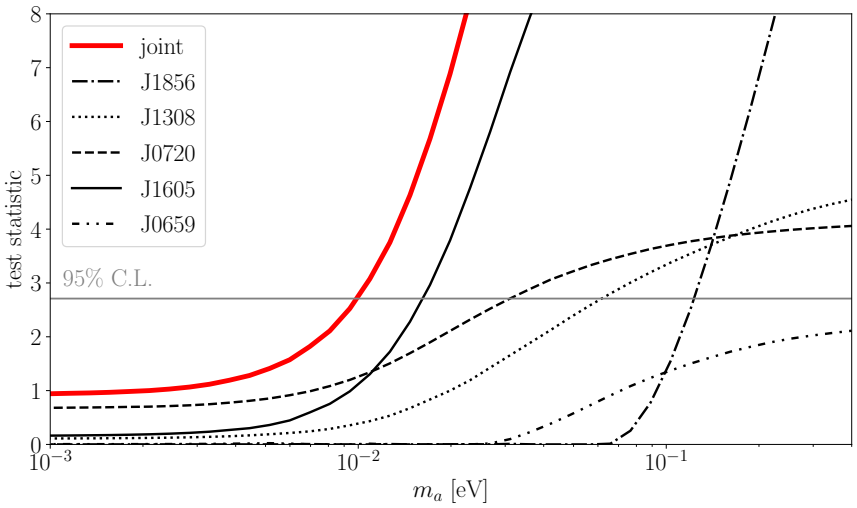

Figure H.4: The test statistic for upper limits, defined in (H.29) and in the context of the KSVZ axion model, for the individual NSs. These curves assume the `SFB-0-0` superfluidity model and the BSk22 EOS. Assuming Wilks' theorem, the 95% upper limit is given by where the test statistic is equal to ∼2.71, as indicated. The most constraining NS is J1605.

In the main chapter we interpreted our results in the context of the KSVZ and DFSZ QCD axion models. In Fig. H.5 we take a more phenomenological approach and consider axion models characterized by coupling strengths g_{ann} and g_{app} to neutrons and protons, respectively. The shaded region in that parameter space is excluded by our analysis at 95% confidence. To construct this figure we fix the ratio g_{ann}/g_{app} and then construct the likelihood profile as a function of g_{ann}. The presented limits are then the one-sided 95% upper limits constructed from our MC procedure.

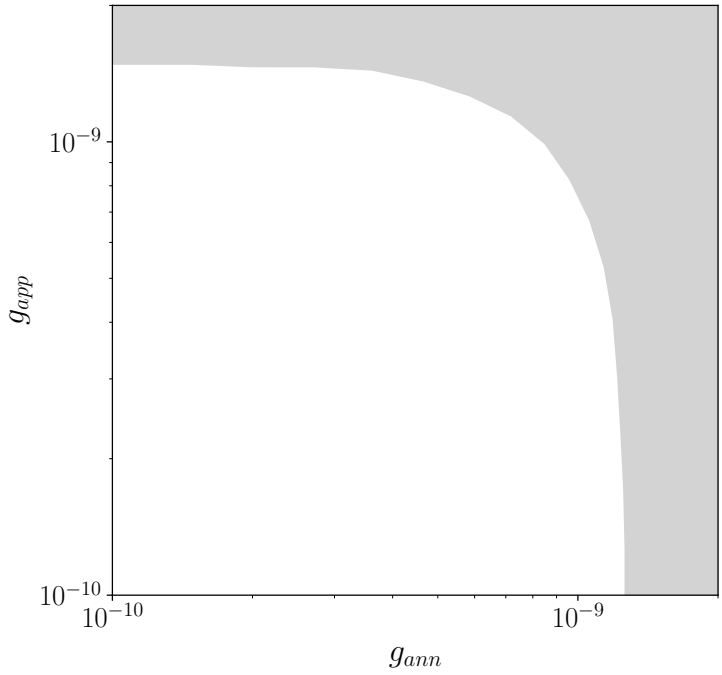

Figure H.5: The one-sided 95% upper limits from this chapter in the plane of axion-neutron (g_{ann}) and axion-proton (g_{app}) couplings. The shaded region is excluded by our analysis; see text for details.

H.3.2 Axions in younger neutron stars

In this chapter we focus on older NSs, with ages over $\sim 10^5$ yrs. We find that younger NSs, including Cas A, are typically less constraining in the context of our modeling procedure, though a few younger NSs have comparable sensitivity. This point is illustrated in Fig. H.6, where we compare the upper-limit test statistic (for the KSVZ axion) from the individual NSs considered in this chapter with those we determine from analyses of five younger NSs. Note that in Fig. H.6 we show the EOS and superfluidity combinations that lead to the weakest limits, as estimated by the test statistic assuming Wilks' theorem, for the individual NSs. This is unlike in Fig. H.4 where we show the individual test statistics for the EOS and superfluidity model that gives the weakest limit in the joint analysis over all five old, isolated NSs. The properties of the additional NSs are given in Tab. H.7. For Cas A we also include the temperature derivative measurement from [24], who measure $\dot{T}/T = (0.011 \pm 0.0046)/(10 \text{ yrs})$ assuming the Hydrogen column density was constant over all *Chandra* observations of Cas A. As mentioned in the main chapter, previous to [24] analyses of Cas A (such as [596, 597]) assumed strong superfluidity in order to explain the rapidly changing $\dot{T}/T$, but [24] pointed out that much of this cooling was instrumental in nature. Indeed, as shown in H.6, the Cas A cooling data are consistent with the null hypothesis without ${}^3P_2$ superfluidity, since the

Name	L_γ^∞ [10^{33} erg/s]	Age [yr]	Refs
Cas A	—	330 ± 19	[585, 586]
J173203	17 ± 10	$(4 \pm 2) \times 10^3$	[587–590]
J172054	11.4 ± 4.4	650 ± 50	[591–593]
J0357	0.015 ± 0.011	$(7.5 \pm 5.5) \times 10^5$	[594]
J0538	1.09 ± 0.47	$(1.10 \pm 0.3) \times 10^5$	[404, 595]

Table H.7: The properties of the supplemental NSs considered in this chapter: CXOU J232327.8+584842 (Cas A), XMMS J173203-344518 (J173203), XMMU J172054.5-372652 (J172054), PSR J0357+3205 (J0357), PSR J0538+2817 (J0538). Note that for Cas A we use measurements of its temperature $T = (200.0 \pm 5) \times 10^4$ K (with the uncertainty roughly accounting for systematic differences in T measurements between different analyses, in addition to statistical uncertainties) and its temperature derivative $\dot{T}/T = 0.0011 \pm 0.00046$ yr^{-1} (with the value taken as that with fixed hydrogen column density, since it is the most conservative) rather than the luminosity measurement [24]. Also, to match the conventions of [24], the age of Cas A is presented at the reference epoch of 2011.49.

Cas A curve in Fig. H.6 is for the model with no superfluidity and the BSk22 EOS. J173203 has also been the target of previous axion searches [598, 599] that found $m_{a,\mathrm{KSVZ}} < 0.085$ eV at 90% confidence. These works assumed that the age of J173203 was ∼27 kyr [600], which indeed would require a reduction in neutrino cooling rates to match the observed surface temperature, as discussed in [598, 599]. However, J173203 is actually a much younger NS, with an age 4 ± 2 kyr [588–590], which is consistent with the standard cooling scenario and does not require unusual pairing gaps. We find that with the corrected NS data the constraint is relaxed. J172054 is a young NS which is naively interesting for axion searches given its well-measured luminosity of $\sim(12 \pm 1) \times 10^{33}$ erg/s [591]. However, this measurement assumes a fixed distance to Earth, and we find that after accounting for the distance measurement and uncertainty [14] J172054 is not a powerful probe. J0357, although older than 10^5 yr, has extremely uncertain luminosity and age measurements, so it is the least constraining NS in our analysis and we do not consider it in the main chapter. Finally, we include J0538 in this chapter because its age is debated and could be a lower value than given in Tab. H.7 of 40 ± 20 kyr [595]. We find that in either case it is not constraining and so exclude it from our main analysis. As the ages and luminosities of some of the younger NSs become better understood in the future, it is likely that they will become more sensitive probes of axion-induced cooling.

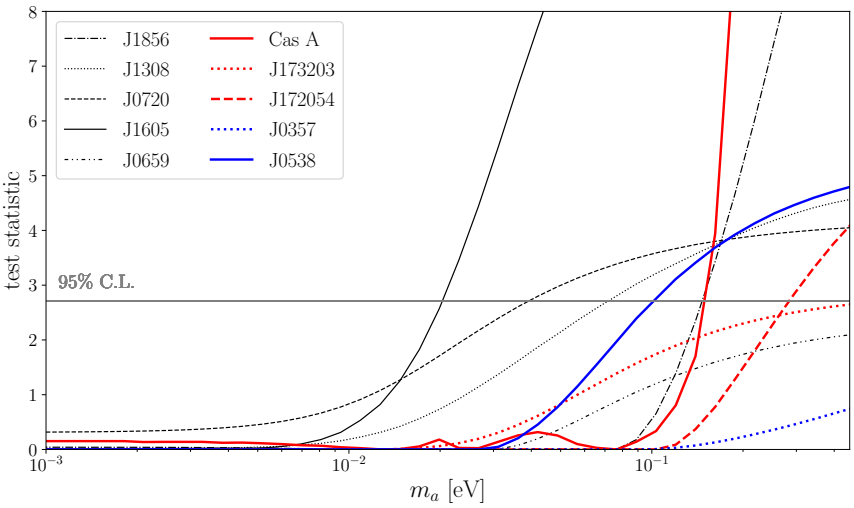

Figure H.6: As in Fig. H.4 but including the five younger NSs we consider in this chapter, whose properties are given in Tab. H.7. Note that unlike in Fig. H.4 here we display the test statistics for the EOS and superfluidity combinations that lead to the weakest limits for the individual NSs not the combination that leads to the weakest limit in a joint analysis.

H.3.3 Effects of nuisance parameters

In Fig. H.7 we illustrate the effects of the various nuisance parameters that we profile over in our analysis on NS cooling. We do not include axion in these simulations, and unless otherwise stated we fix the NS mass at $M = 1.4 M_\odot$, the mass of light elements in the envelope $\Delta M/M_\odot = 10^{-12}$, the BSk24 EOS, and the `SFB-0-0` superfluidity model. On top of the cooling curves which show the surface luminosity as a function of NS age, we indicate the data points for the isolated NSs that we consider in this chapter.

In the top-left panel we show the effect of varying ΔM. Larger values of ΔM increase the luminosity at early times but can rapidly decrease the luminosity at late times, for ages $\sim 10^6$ yrs. The top-right panel indicates illustrates the varying NS mass. For this particular EOS masses larger than $\sim 1.6\ M_\odot$ reach high enough densities in the core to undergo direct URCA neutrino production and thus cool rapidly. The bottom-left panel varies the EOS. Apart from the BSk22 EOS, the the other EOSs give similar results. The BSk22 EOS is different in that already for $M = 1.4\ M_\odot$ the direct URCA process is allowed. Lastly, the bottom-right panel shows the effect of the superfluidity model. The $^1S_0$ and no superfluidity models, which are our fiducial choices, produce similar results. The $^3P_2$ pairing models that we consider in this chapter. These models undergo rapid cooling at late times when the temperature drops below the $^3P_2$ critical temperature, from PBF neutrino production, and are inconsistent with the M7 data. We discuss the $^3P_2$ superfluidity models more in the next subsection.

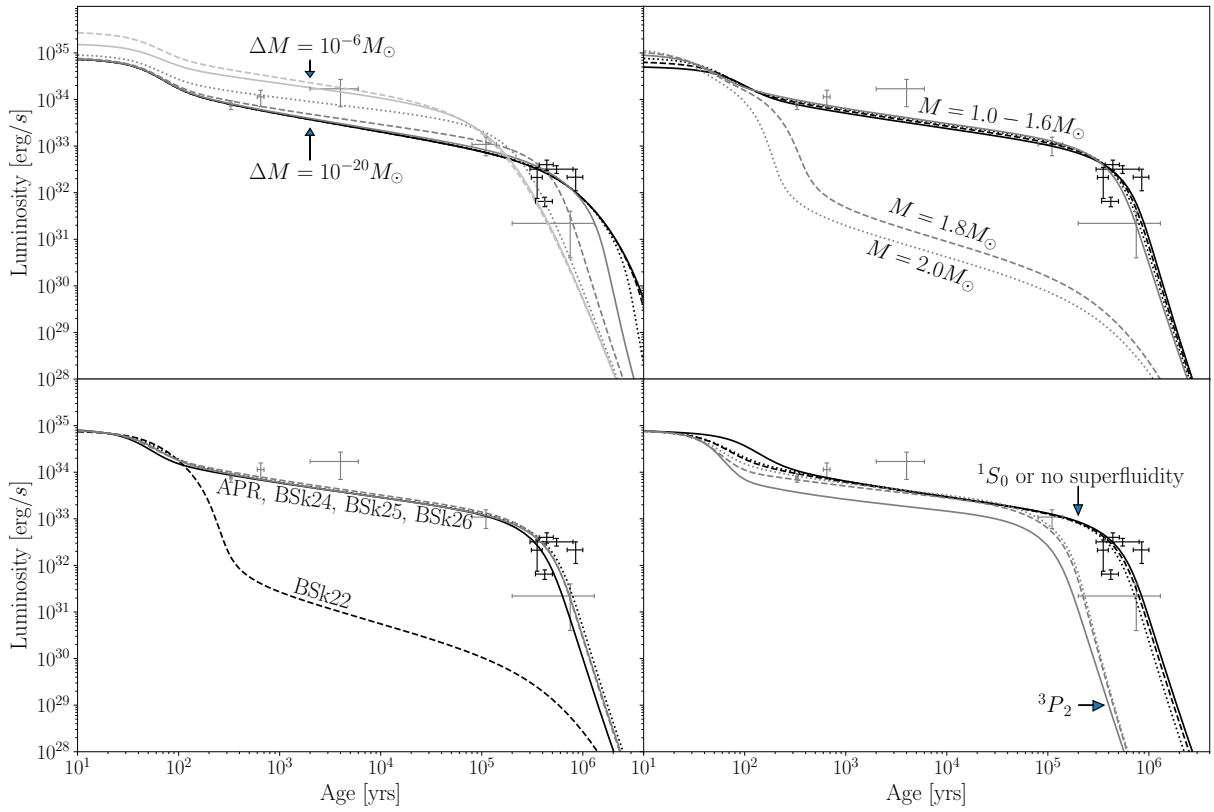

Figure H.7: As in Fig. 9.1 except for an example NS with parameters, unless otherwise stated, $M = 1.4 M_\odot$, $\Delta M / M_\odot = 10^{-12}$, the BSk24 EOS, and the `SFB-0-0` superfluidity model. Each panel varies the indicated parameter, and no axions are included in the simulations. On top of the cooling curves we indicated the age and luminosity data for the isolated NSs considered in this chapter. The old NSs considered in our fiducial analysis are in black, while the data for the younger NSs that we analyze in this chapter are in grey.

H.3.4 $^3P_2$ superfluidity

In the right panel of Fig. S6 we showed that the $^3P_2$ superfluidity models appear inconsistent with the isolated NS data. Here, we present further details of our $^3P_2$ superfluidity tests. We consider four different superfluidity models, which are characterized by their zero-temperature gaps Δ as functions of Fermi momenta. (Note that the critical temperatures are proportional to Δ.) The first three models are denoted as models "a", "b", and "c" from [562], and, in `NSCool`, as `SFB-a-T73`, `SFB-b-T73`, and `SFB-c-T73`, respectively. (These `NSCool` models also self-consistently use the SFB $^1S_0$ neutron gap model and the T73 proton $^1S_0$ gap model.) However, more recent works indicate that the $^3P_2$ gap may be substantially lower than in these models (see, *e.g.*, the recent review [419]). Of all the recent models reviewed in [419], the SCGF model with long and short range correlations from [601] has the lowest gap Δ across all Fermi momenta. Thus, between the SCGF model and the models

"a", "b", and "c" from [562], we span a large range of gaps discussed in the literature for the possible $^3P_2$ pairing, though of course it is also possible that the gap is substantially lower such that $^3P_2$ superfluidity never occurs (as we assume in the main chapter).

In the left panel of Fig. H.8 we show the upper limit test statistics, for different EOS, as a functions of the KSVZ axion mass m_a for the indicated $^3P_2$ gap models. Note that all of these models are inconsistent with the isolated NS data at more than $\sim 3\sigma$, as may be inferred from the test statistic at $m_a = 0$ (more precisely, the axion model prefers a negative mass at more than 3σ). On the other hand, these models are much more sensitive to axions due to the PBF axion production mechanism. In the right panel of Fig. H.8 we show how the neutrino PBF process leads to the rapid cooling for the $^3P_2$ models, as seen in *e.g.* the right panel of Fig. H.7. We illustrate the ratio of neutrino PBF luminosity ($L^{\infty}_{\nu,\mathrm{PBF}}$) to the bremsstrahlung neutrino luminosity plus L^{∞}_{γ}. When this ratio is greater than unity it means that the PBF neutrino process dominates the cooling. Note that since the SCGF model has the lowest gap the $^3P_2$ superfluidity turns on at the lowest temperature of the models considered. For this example we fix $M = 1.4\ M_{\odot}$ and $\Delta M = 10^{-12} M_{\odot}$.

We contrast the right panel of Fig. H.8 with Fig. H.9, where we illustrate similar luminosity ratios for the BSk22 EOS and a $M = 1.0\ M_{\odot}$ NS for the model with no $^3P_2$ superfluidity but $^1S_0$ neutron and proton superfluidity, as we consider in our fiducial analyses. (Note that the dependence on the EOS and NS mass is minor, and we also take $\Delta M = 10^{-12} M_{\odot}$.) For that figure we take the KSVZ axion model with $m_a = 16$ meV, at our 95% upper limit. We show the ratios of the axion and neutrino PBF luminosities, for neutron and proton production, to the sum of the total neutrino and axion bremsstrahlung luminosities and the thermal surface luminosity. Comparing this figure with the right panel of Fig. H.8 illustrates that the $^3P_2$ pairing, if present, plays a much more important role on the NS thermal evolution than the $^1S_0$ pairings.

H.3.5 Sensitivity to the neutron star mass

In Fig. H.7 we show that the NS cooling is not very sensitive to the NS mass unless the mass is large enough for the direct URCA process to become active. As an additional test of the effect of the NS mass on our final results, we consider including mass priors on J0720, J1308, and J1856. We do so following [70], who estimate that masses of these NSs as $1.23^{+0.10}_{-0.05}\ M_{\odot}$ (J0720), $1.08^{+0.20}_{-0.11}\ M_{\odot}$ (J1308), and $1.24^{+0.29}_{-0.29}\ M_{\odot}$ (J1856) using gravitational redshift data. We analyze the cooling data for each of these NSs individually but we add to the likelihood an extra Gaussian contribution for the NS masses, centered on the mass estimates and with standard deviations given by the average of the upper and lower uncertainties from [70]. The

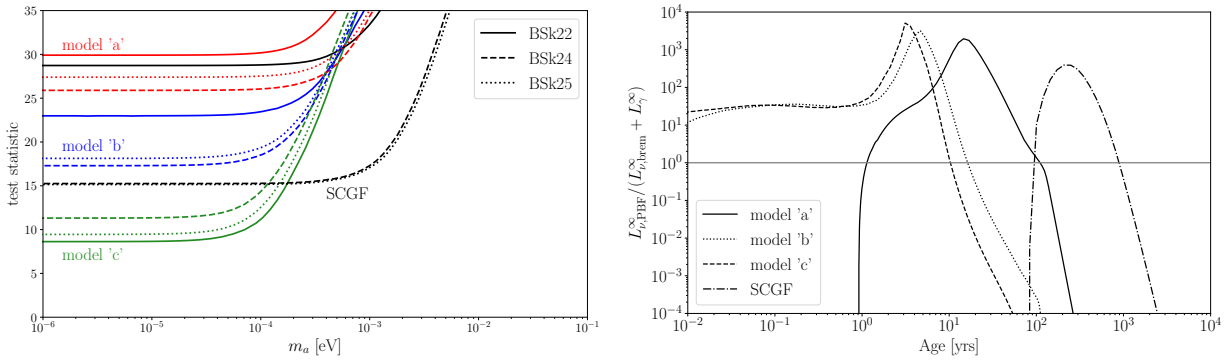

Figure H.8: $^3P_2$ superfluidity leads to rapid cooling of the NSs, as illustrated in the right panel of Fig. H.7. (Left panel) We show the effects of including axions (for the KSVZ model) with $^3P_2$ superfluidity, for the $^3P_2$ gap models considered in this chapter. Note that the SCGF model has the lowest gap and model 'c' has the highest gap. The axion PBF process results in the NSs being much more sensitive to m_a, but on the other hand the $^3P_2$ models appear inconsistent with the isolated NS data. (Right panel) Here, for the case $m_a = 0$, we show the neutrino PBF luminosity relative to the neutrino bremsstrahlung and thermal surface luminosities. When the neutrino PBF luminosity dominates the NS will undergo rapid cooling. Note that for this figure we fix $M = 1.4\ M_\odot$.

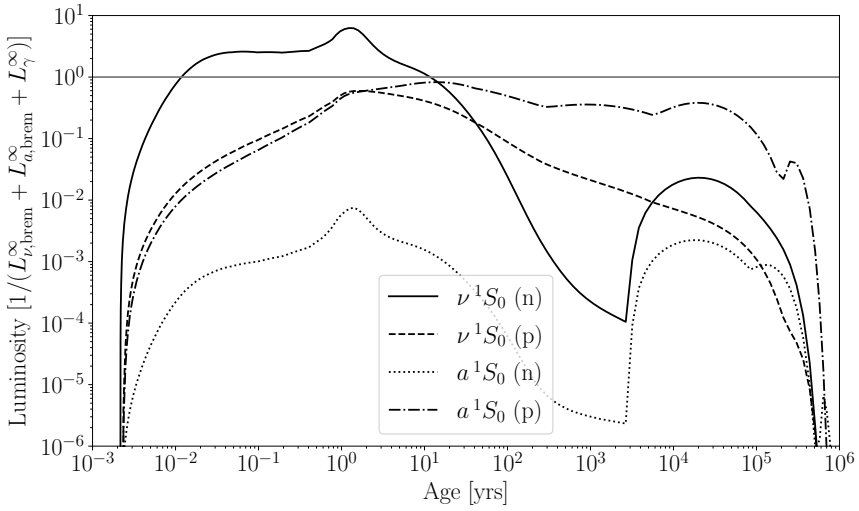

Figure H.9: As in the right panel of Fig. H.8 but for the BSk22 EOS, a 1.0 $M_\odot$ NS, and the superfluidity model with $^1S_0$ neutron and proton pairings but no neutron $^3P_2$ pairing. We additionally include a KSVZ QCD axion with $m_a = 16$ meV. We show the ratios of the PBF luminosities for neutrinos and axions produced from neutrons and protons relative to the total bremsstrahlung luminosity plus the thermal surface luminosity. This figure illustrates that the PBF process plays a less important role for the $^1S_0$ pairings than for the $^3P_2$ pairing.

results, shown in Fig. H.10, indicate that the upper-limit test statistics are nearly identical with and without the inclusion of the mass priors.

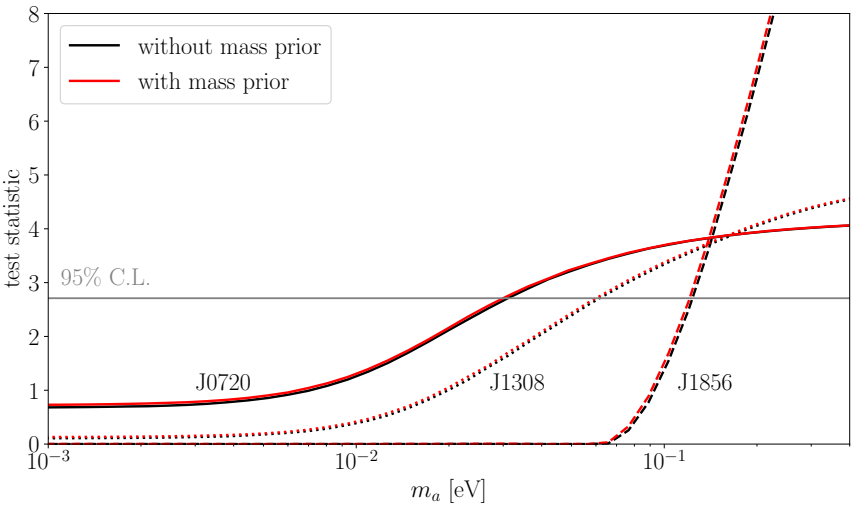

Figure H.10: Mass estimates are available from [70] for the NSs J0720, J1308, and J1856. Here we consider including these mass estimates as priors in our analysis. As shown here, however, including the mass estimates makes little difference in our analysis.

H.4 Magnetic field decay

In this section consider the possible effects of magnetic field decay on the axion mass upper limits. We note that despite some dedicated efforts (*e.g.*, [71,602–612]) it is still not standard to include magnetic field decay in NS cooling, in part because the underlying mechanisms that transfer heat from the magnetic field to the NS matter are still not well understood. For example, while the magnetic field at the surface of a NS may be measured by *e.g.* spin-down – the M7 have field strengths $\sim 10^{13}$ G – the magnetic fields within the NSs are not directly observable. The dissipation of energy from these fields into heat depends not only on the field strength and decay rate but also on the geometry of the fields within the NSs and the dissipative mechanisms, such as the electric conductivity, which are also uncertain. Still, there is evidence that old (∼Myr-Gyr), isolated NSs, such as the M7, with stronger magnetic fields have higher surface temperatures than those with lower magnetic fields, suggesting that magnetic field decay may play a role in determining the surface temperature of isolated NSs in the epoch after neutrino emission dominates the energy loss, though this is far from conclusive (see, *e.g.*, [608]).

While complex 2D simulations of the coupled magneto-thermal evolution are now available (see [71] for the state-of-the-art), we take a simpler approach in this chapter since, as we will show, the effect of magnetic field decay appears to be subdominant compared to other effects that we consider (though this should be checked with dedicated magneto-thermal simulations incorporating axions). We follow instead the effective approach from *e.g.* [602, 608]

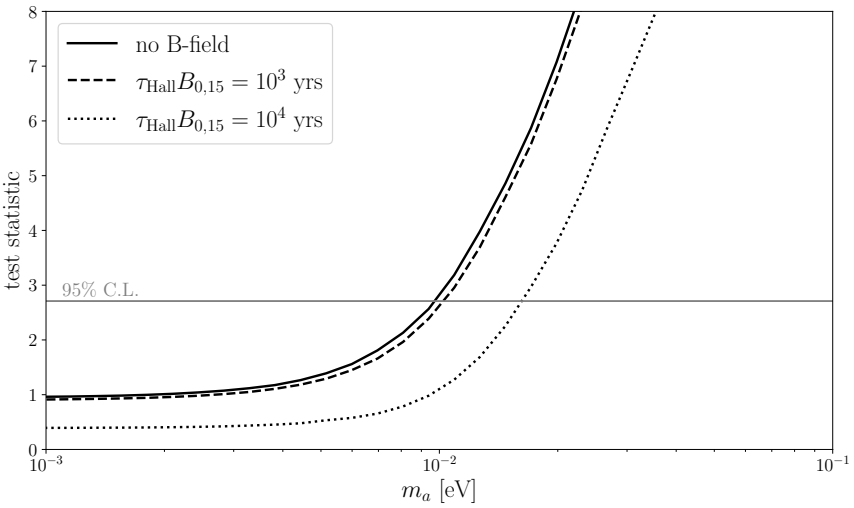

Figure H.11: We test for the possible effects of magnetic field decay on our axion upper limits by using a parametric magnetic field decay model, where the magnetic field energy is dissipated in the crust as a heat source. The results depend sensitivity, in this model, on the Hall timescale. Using estimates (*e.g.*, [71]) that this timescale is less than $\tau_{\rm Hall} = 10^3$ yr $/B_{0,15}$, with $B_{0,15}$ the value of the magnetic field in units of 10^{15} G, we conclude that B-field decay likely plays a subdominant role, as it produces similar results to the no B-field scenario. On the other hand, an increased Hall timescale, as illustrated, could weaken the upper limits. In these analyses we allow for initial magnetic fields up to 10^{16} G that fill the entire crust.

and assume that the heat H from magnetic field decay (see (9.1) for the relation of H to L_γ^∞) is given simply by $H = -V_{\rm eff} B\dot{B}$, where $V_{\rm eff}$ is the effective volume of the NS that supports the magnetic field B, with time derivative $\dot{B}$. As is standard, we assume that the dominant Joule heating arises from Ohmic dissipation in the crustal-confined magnetic fields, such that in our modified version of NSCool we only include energy injection from H into the crust. The magnetic energy is likely dissipated in hot-spots in the crust [608], such that $V_{\rm eff}$ is much smaller than the full volume of the crust. The double blackbody fits for the M7 indicate that the hot-spots have size of a few km across [278, 289, 324, 326, 407]. In these hot spots the magnetic field could be $\sim$10 times higher than the poloidal values [608]. To be conservative we assume $V_{\rm eff}$ is the full crustal volume, which is typically around 1/3 of the total NS volume, and we consider initial magnetic fields up to 10^{16} G that fill the entire crust.

Following [610] we use the phenomenological parameterization of the magnetic field decay

$$B(t) = B_0 \frac{e^{-t/\tau_{\rm Ohm}}}{1 + (\tau_{\rm Ohm}/\tau_{\rm Hall})(1 - e^{-t/\tau_{\rm Ohm}})} \tag{H.33}$$

with B_0 the initial magnetic field strength, $\tau_{\rm Ohm}$ the Ohmic dissipation timescale and $\tau_{\rm Hall}$ the Hall diffusion timescale. Ref. [610] suggests $\tau_{\rm Ohm} \sim 10^6$ yr and $\tau_{\rm Hall}$ up to $\tau_{\rm Hall} \sim 10^3$ yr $/B_{0,15}$, with $B_{0,15} \equiv B_0/10^{15}$ G, though the Hall timescale could be faster. As a test we fix $\tau_{\rm Ohm} = 10^6$ yr (this timescale plays a less important role than the Hall timescale) and $\tau_{\rm Hall} = 10^3$ yr $/B_{0,15}$. In Fig. H.11 we show the result of adding this heating contribution in the context of the KSVZ axion model upper limit test statistic profile. We compare the new result to that with no B-field decay, as considered in the main chapter. The difference between the two results is minimal. Smaller values of $\tau_{\rm Hall}$ lead to smaller differences, indicating that magnetic field decay likely plays a subdominant role. As a test, however, we consider increasing $\tau_{\rm Hall}$ by an order of magnitude to $\tau_{\rm Hall} = 10^4$ yr $/B_{0,15}$. In Fig. H.11 we show that in this case the upper limit may be weakened by $\sim$50%. Given the potential relevance of magnetic field decay to the axion upper limits, this process should be investigated further in future works using more sophisticated treatments of the B-field decay.

Appendix I

Red-Giant Branch Stellar Cores as Macroscopic Dark Matter Detectors

I.1 M15 DM Halo

In the main chapter we made the conservative assumption that the DM in M15 is sourced by the Milky Way halo. The DM density within GCs can be significantly larger if the GC formation took place in an initial DM overdensity, although this scenario is uncertain and we ignored it in our fiducial analysis. However, if further observations show there is indeed substructure, the constraints from DM-induced ignition can be improved, and we estimate the sensitivity gain in this section.

The formation of the GC occurs when the proto-GC virial temperature drops below $\sim 10^4$ K when radiative cooling turns on [509]. At this time the proto-GC collapses, and the DM halo undergoes adiabatic contraction that increases the steepness of the density profile towards the center of the GC [613]. Simulations suggest that at high redshifts the subhalo around GCs is tidally stripped, such that the GC is baryon-dominated by mass at present times [510]. At later times, stars kinetically heat the DM so that the profile becomes cored [614].

We assume the parameters derived in [513], which computed present-day M15 DM profile under this scenario in the context of DM annihilation searches. The DM distribution is cored at ~ 10 pc [513], inside which nearly all of the RGB stars are contained [615]. Therefore, we take the DM density to be a constant throughout the core, with a value of

$$\rho_{DM} = 35 M_\odot \text{ pc}^{-3} = 1.3 \times 10^3 \text{ GeV cm}^{-3}. \tag{I.1}$$

The radial stellar velocity dispersion σ_{v_r} in M15 was measured within the inner 3 pc

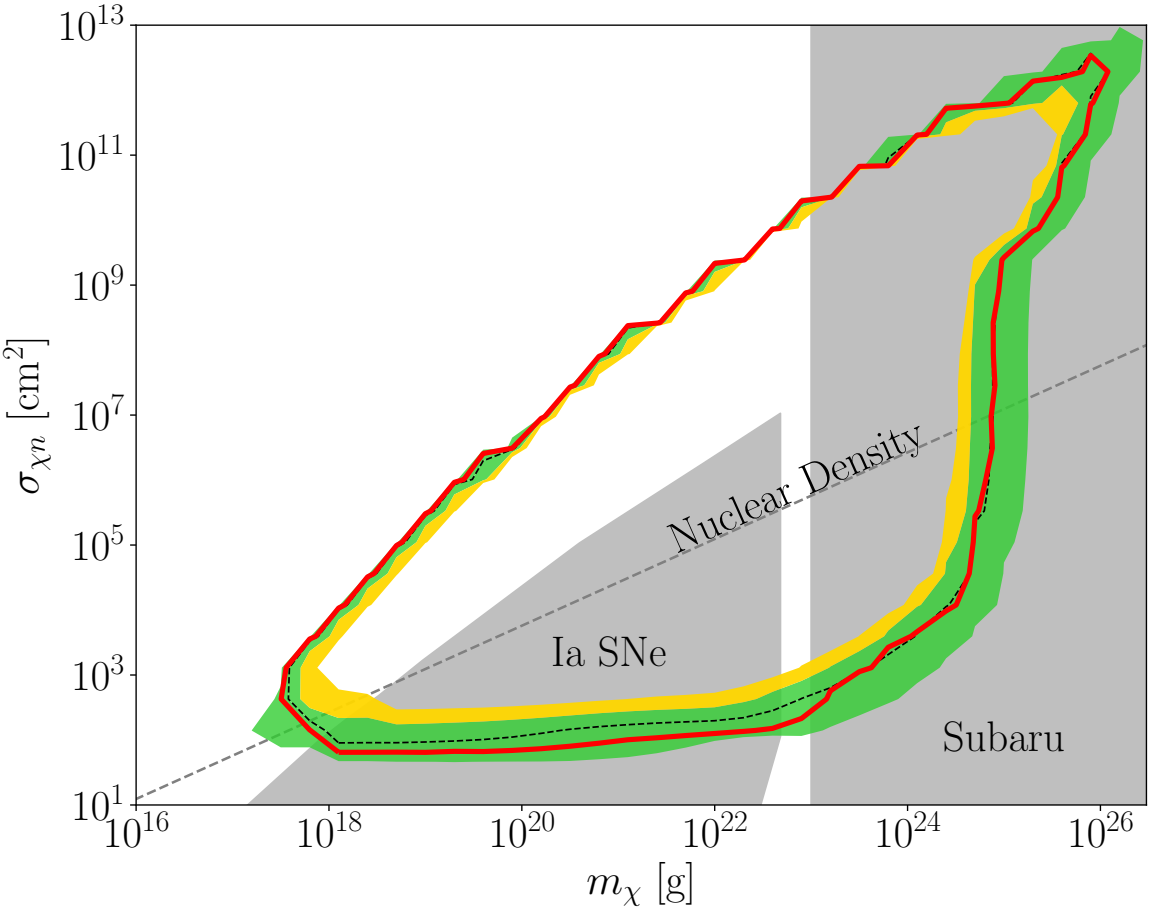

Figure I.1: The 95% confidence limit on macroscopic DM (red) from the non-observation of DM-induced He flashes in the GC M15 LF, assuming that M15 hosts its own DM halo. The region inside the red line is ruled out. The dashed line is the Asimov expectation under the null hypothesis with green (yellow) bands denoting the 1σ (2σ) containment region. We show the same constraints detailed in Fig. 11.5.

by [615]; within the inner 1 pc that reference found σ_{v_r} to be a constant 10.2 ± 1.4 km s^{-1}, and declines to $\sim$7 km s^{-1} at 3 pc. In [616] σ_{v_r} was determined out to the cluster edge, where it continues declining to $\sim$5 km/s. In the central $\sim$0.3 pc, σ_{v_r} may rise to $\sim$14 km s^{-1} [616], but the number of stars in this region is volume suppressed. Therefore, we adopt the conservative value 10 km s^{-1} as both the stellar and DM velocity dispersion, so that the relative velocity dispersion is $\sqrt{2} \times 10$ km s^{-1}. Lastly, the GC escape velocity of stars in this region is $\sim$ 50 km s^{-1} [513]. Therefore it is a very good approximation to use Eq. (11.13),

setting $c(t) = 1$, which gives

$$\Gamma = \sqrt{2\pi}\frac{\rho_{DM}}{m_\chi} R^2_{\zeta=1} \frac{v^2_{*\rm esc}(R_{\zeta=1})}{\sigma_{vr}}. \tag{I.2}$$

In Fig. I.1, we show the 95% limit on macroscopic DM assuming that M15 hosts a DM subhalo with the above parameters. Similarly to our fiducial bound plot, the bounded region is roughly triangular, see text around Fig.11.5. The extra tip to the triangle is due to the presence of friction near the hypotenuse, which for small values actually focuses the DM towards the core. Under this scenario, the constraints improve substantially, particularly at high m_χ where the rate is suppressed by low DM number density in the case where the DM is provided only by the Milky Way halo. The bound is nearly saturated in the sense that almost all of the parameter space in which DM-induced HFs are possible is disfavored, as $m_\chi > 10^{23}$ g is already disallowed by microlensing. To further sensitivity substantially, new targets hosting RGB stars of other masses or metallicities may be required, or targets with more RGB stars that are nearing the standard HF.

I.2 Ignition Profile

We assumed the energy is deposited in a linearly increasing profile from the edge of the geometric cross section to the center. The exact profile depends on the form of the DM, as well as on details of shock layer formation in front of the DM. This could increase the effective area over which the temperature is spread. In the limit where the only change is in the increase of the effective area, our bounds simply translate upwards to the correspondingly larger cross sections.

Separately one may be concerned of a sharp dependence of the ignition ratio, Eq. 11.10, on the shape of the profile. To investigate this we generalize Eq. 11.2 in two ways. Defining $\xi = r/\sqrt{\sigma_{\chi n}/\pi}$, our nominal energy deposition is $\propto (1-\xi)$. We investigate the two sets of profiles

$$\frac{dE}{dV} \propto (1-\xi^n)\frac{dE}{dx}, \tag{I.3}$$

$$\propto (1-\xi)^n \frac{dE}{dx}. \tag{I.4}$$

In Fig. I.2 we show these distributions in the left panel, and an example of the resulting set of ignition ratios in the right panel. For $n = 1$ these two shapes are equivalent, and is the case we assumed for our limits. In the large n limit, the first set approaches a top hat

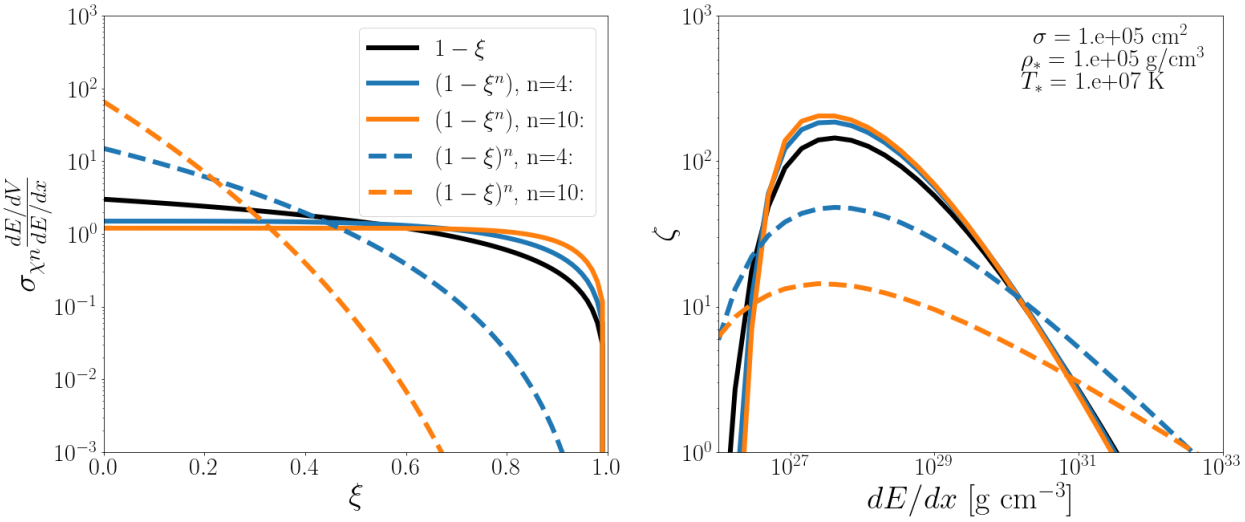

Figure I.2: **Left Panel** The dimensionless energy deposition profiles. Each is normalized over a cylinder to give the same dE/dx. **Right Panel** The corresponding ignition parameter for various profiles. Stellar and DM properties are fixed at the values shown in the figure inset.

shape, and the latter approaches a delta function peaked at the center of the DM ($\xi = 0$). Assuming the former set of lines represent more physical DM models, we find very little shape dependence.

I.3 Analytic Ignition Rate

In terms of the velocity distribution function, the rate of DM-induced ignition from an asymptotic surface $\Omega\ r_\infty^2$ is

$$\Gamma = N\frac{\rho_\chi}{m_\chi} r_\infty^2 \int d\Omega \int d^3\mathbf{v}\ (-\vec{v}\cdot\hat{r}) \tag{I.5}$$

$$\times \exp\left(\frac{-(\mathbf{v}+\mathbf{v_{GC}})^2}{2\sigma_{vr}^2}\right)\Theta(v_{esc}^2 - (\mathbf{v}+\mathbf{v_{GC}})^2). \tag{I.6}$$

Where $\hat{r}$ points out from the star, and N is the normalization of $f(\vec{v})$

$$N^{-1} = (2\pi\sigma_{vr}^2)^{3/2} \times k, \tag{I.7}$$

For constant k which accounts for finite MW escape velocity, given by

$$k = \left(erf\left(\frac{v_{esc}}{\sqrt{2}\sigma_{vr}}\right) - \sqrt{\frac{2}{\pi}}\frac{v_{esc}}{\sigma_{vr}}\exp\left(\frac{-v_{esc}^2}{2\sigma_{vr}^2}\right)\right). \tag{I.8}$$

The solid angle of velocity space which hits the star is $\pi\phi^2 \approx \pi b^2/r_\infty^2$ for impact parameter b. Conserving energy and angular momentum gives the gravitationally focused impact parameter as a function of the escape velocity from the core of the star v_{*esc},

$$b^2 = R_{\zeta=1}^2 \left(1 + v_{*esc}^2/v^2\right) \approx R_{\zeta=1}^2 v_{*esc}^2/v^2. \tag{I.9}$$

With $\mathbf{v_{GC}}$ along the z-axis, $\mathbf{v} \cdot \mathbf{v_{GC}} = v v_{GC}\ \cos\theta$. Applying these gives

$$\Gamma = N \frac{\rho_\chi}{m_\chi} (\pi R_{\zeta=1}^2) v_{\rm esc}^2 2\pi \int_{-1}^{1} d\cos\theta \int_0^\infty dv\ v \tag{I.10}$$

$$\times \exp\left(\frac{-(v^2 + v_{GC}^2 + 2 v v_{GC} \cos\theta)}{2\sigma_{vr}^2}\right) \tag{I.11}$$

$$\times\ \Theta(v_{esc}^2 - (v^2 + v_{GC}^2 + 2 v v_{GC} \cos\theta)). \tag{I.12}$$

We evaluate this integral with the methods in [617] and arrive with

$$\Gamma = \Gamma_0 \times c(t, v_{GC}, v_{\rm esc}). \tag{I.13}$$

Where Γ_0 is the rate including gravitational focusing, but without MW escape velocity, or GC velocity, evaluated at the current time t_0. The correction factor for the latter three effects defines $c(t, v_{GC}(t), v_{esc})$. These are

$$\Gamma_0(\tau) = \sqrt{2\pi} \frac{\rho_{DM}(t_0)}{m_\chi} R_{\zeta=1}^2(\tau) \frac{v_{*esc}^2}{\sigma_{vr}} + \mathcal{O}(\sigma_{vr}^2/v_{\rm *esc}^2) \tag{I.14}$$

$$c(t) = \frac{\rho_{DM}(t)}{\rho_{DM}(t_0)} \frac{\sqrt{\pi}\sigma_{vr}}{4 k v_{GC}} \Big[2\sqrt{2} \mathrm{erf}(\frac{v_{GC}}{\sqrt{2}\sigma_{vr}}), \tag{I.15}$$

$$- \mathrm{Exp}\left(\frac{v_{esc}^2 - 2 v_{GC}^2}{2\sigma_{vr}^2}\right)$$

$$\times \left(\mathrm{erf}\left(\frac{v_{GC} + v_{esc}}{\sigma_{vr}}\right) - \mathrm{erf}\left(\frac{v_{esc} - v_{GC}}{\sigma_{vr}}\right)\right)\Big].$$

Using the M15 orbital data obtained from the authors of [518], we compute the correction factor $c(t)$ for M15 over the last Gyr and show it in Fig. I.3. This factor accounts for the DM density variation, GC velocity, and MW escape velocity as M15 orbits the Galactic Center. Minima (maxima) correspond to the orbital apoapses (periapses). At time t_0, today, the GC is near its apoapsis. We see that the rate is enhanced by a factor of $\sim$2.8 at periapsis relative to apoapsis.

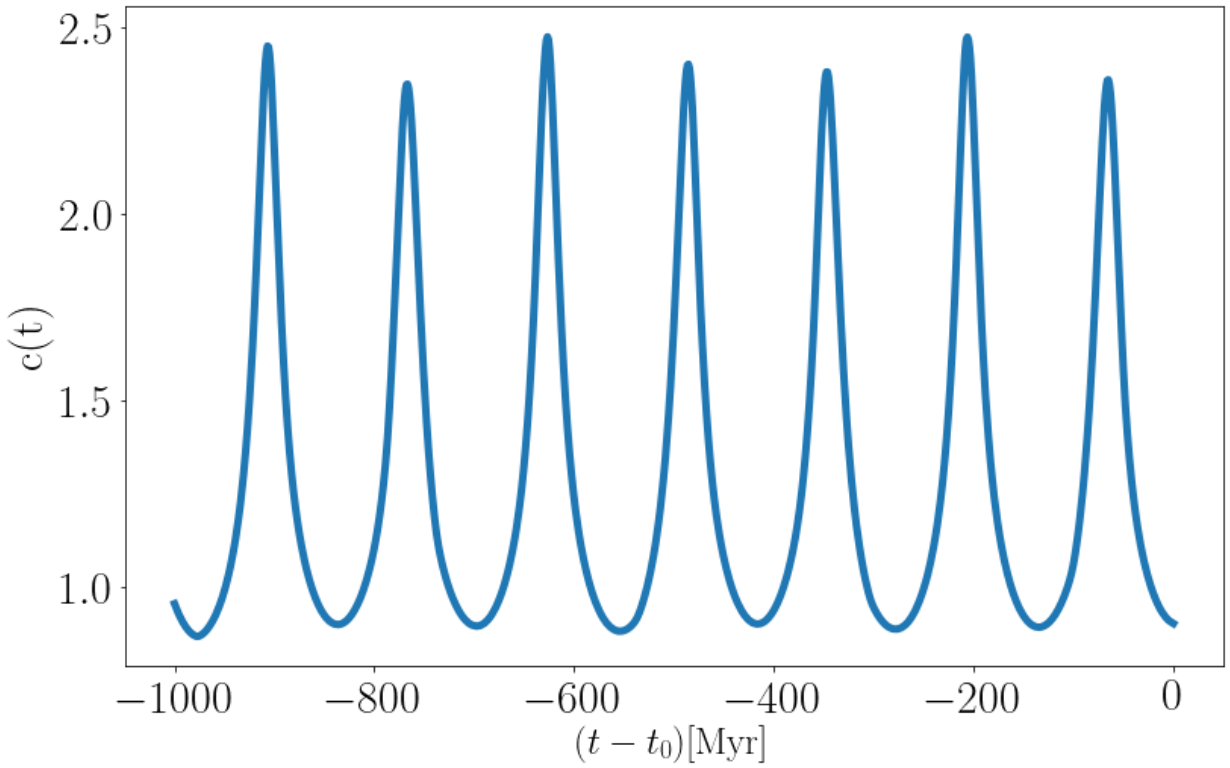

Figure I.3: The correction factor $c(t)$ to the rate of DM-induced ignition for M15, see Eq. (I.15).

Bibliography

[1] D. L. Kaplan and M. H. van Kerkwijk, *Constraining the Spin-down of the Nearby Isolated Neutron Star RX J0806.4-4123, and Implications for the Population of Nearby Neutron Stars*, *Astrophys. J.* **705** (Nov, 2009) 798–808, [arXiv:0909.5218].

[2] B. Posselt, S. B. Popov, F. Haberl, J. Truemper, R. Turolla, and R. Neuhaeuser, *The Magnificent Seven in the dusty prairie: The role of interstellar absorption on the observed neutron star population*, *Astrophys. Space Sci.* **308** (2007) 171–179, [astro-ph/0609275].

[3] M. H. van Kerkwijk and D. L. Kaplan, *Timing the Nearby Isolated Neutron Star RX J1856.5-3754*, *Astrophys. J.* **673** (2008) L163–L166, [arXiv:0712.3212].

[4] F. M. Walter, T. Eisenbeiß, J. M. Lattimer, B. Kim, V. Hambaryan, and R. Neuhäuser, *Revisiting the Parallax of the Isolated Neutron Star RX J185635-3754 Using HST/ACS Imaging*, *Asrophys. J.* **724** (Nov, 2010) 669–677, [arXiv:1008.1709].

[5] D. L. Kaplan and M. H. van Kerkwijk, *A Coherent Timing Solution for the Nearby, Thermally Emitting Isolated Neutron Star RX J0420.0-5022*, *Astrophys. J.* **740** (2011) L30, [arXiv:1109.2105].

[6] D. L. Kaplan and M. H. van Kerkwijk, *A coherent timing solution for the nearby isolated neutron star rx j1308.6+2127/rbs 1223*, *Astrophys. J.* **635** (2005) L65–L68, [astro-ph/0511084].

[7] C. Motch, A. M. Pires, F. Haberl, A. Schwope, and V. E. Zavlin, *Proper motions of thermally emitting isolated neutron stars measured with Chandra*, *Astron. Astrophys.* **497** (Apr, 2009) 423–435, [arXiv:0901.1006].

[8] D. L. Kaplan and M. H. van Kerkwijk, *A Coherent timing solution for the nearby isolated neutron star RX J0720.4-3125*, *Astrophys. J.* **628** (2005) L45–L48, [astro-ph/0506419].

[9] V. Hambaryan, V. Suleimanov, F. Haberl, A. D. Schwope, R. Neuhäuser, M. Hohle, and K. Werner, *The compactness of the isolated neutron star RX J0720.4—3125*, *Astron. Astrophys.* **601** (2017) A108, [arXiv:1702.07635].

[10] D. L. Kaplan, M. H. van Kerkwijk, and J. Anderson, *The Distance to the Isolated Neutron Star RX J0720.4-3125*, *Astrophys. J.* **660** (2007) 1428–1443, [astro-ph/0703343].

[11] Pires, A. M., Haberl, F., Zavlin, V. E., Motch, C., Zane, S., and Hohle, M. M., *Xmm-newton reveals a candidate period for the spin of the "magnificent seven" neutron star rx j1605.3+3249*, *Astron. Astrophys.* **563** (2014) A50.

[12] C. Malacaria et al., *A joint NICER and XMM-Newton view of the "Magnificent" thermally emitting X-ray Isolated Neutron Star RX J1605.3+3249*, arXiv:1906.02806.

[13] D. L. Kaplan and M. H. van Kerkwijk, *Constraining the Spin-Down of the Nearby Isolated Neutron Star RX J2143.0+0654*, *Astrophys. J. L.* **692** (Feb, 2009) L62–L66, [arXiv:0901.4133].

[14] A. Potekhin, D. Zyuzin, D. Yakovlev, M. Beznogov, and Y. Shibanov, *Thermal luminosities of cooling neutron stars*, *Mon. Not. Roy. Astron. Soc.* **496** (2020), no. 4 5052–5071, [arXiv:2006.15004].

[15] C. Dessert, J. W. Foster, and B. R. Safdi, *Hard X-ray Excess from the Magnificent Seven Neutron Stars*, arXiv:1910.02956.

[16] B. Külebi, S. Jordan, F. Euchner, B. T. Gänsicke, and H. Hirsch, *Analysis of hydrogen-rich magnetic white dwarfs detected in the Sloan Digital Sky Survey*, **506** (Nov., 2009) 1341–1350, [arXiv:0907.2372].

[17] G. D. Schmidt, S. Vennes, D. T. Wickramasinghe, and L. Ferrario, *Studies of magnetic and suspected-magnetic southern white dwarfs*, **328** (Nov., 2001) 203–210, [astro-ph/0107508].

[18] I. Caiazzo et al., *A highly magnetised and rapidly rotating white dwarf as small as the Moon*, *Nature* **595** (2021) 39–42, [arXiv:2107.08458]. [Erratum: Nature 596, E15 (2021)].

[19] S. J. Kleinman et al., *SDSS DR7 White Dwarf Catalog*, *Astrophys. J. Suppl.* **204** (2013) 5, [arXiv:1212.1222].

[20] L. Ferrario, D. de Martino, and B. Gaensicke, *Magnetic White Dwarfs*, *Space Sci. Rev.* **191** (2015), no. 1-4 111–169, [arXiv:1504.08072].

[21] **Gaia** Collaboration, A. G. A. Brown et al., *Gaia Data Release 2*, *Astron. Astrophys.* **616** (2018) A1, [arXiv:1804.09365].

[22] B. Külebi, S. Jordan, E. Nelan, U. Bastian, and M. Altmann, *Constraints on the origin of the massive, hot, and rapidly rotating magnetic white dwarf RE J 0317-853 from an HST parallax measurement*, *Astron. Astrophys.* **524** (Dec., 2010) A36, [arXiv:1007.4978].

[23] Jethwa, P., Saxton, R., Guainazzi, M., Rodriguez-Pascual, P., and Stuhlinger, M., *When is pile-up important in the xmm-newton epic cameras?*, *Astron. Astrophys.* **581** (2015) A104.

[24] B. Posselt and G. Pavlov, *Upper limits on the rapid cooling of the Central Compact Object in Cas A*, *Astrophys. J.* **864** (2018), no. 2 135, [arXiv:1808.00531].

[25] K. N. Abazajian, *Sterile neutrinos in cosmology*, *Phys. Rept.* **711-712** (2017) 1–28, [arXiv:1705.01837].

[26] C. O'HARE, *cajohare/axionlimits: Axionlimits*, July, 2020.

[27] **CAST** Collaboration, V. Anastassopoulos et al., *New CAST Limit on the Axion-Photon Interaction*, *Nature Phys.* **13** (2017) 584–590, [arXiv:1705.02290].

[28] A. Ayala, I. Domínguez, M. Giannotti, A. Mirizzi, and O. Straniero, *Revisiting the bound on axion-photon coupling from Globular Clusters*, *Phys. Rev. Lett.* **113** (2014), no. 19 191302, [arXiv:1406.6053].

[29] C. Dessert, J. W. Foster, and B. R. Safdi, *X-ray Searches for Axions from Super Star Clusters*, *Phys. Rev. Lett.* **125** (2020), no. 26 261102, [arXiv:2008.03305].

[30] M. M. Miller Bertolami, B. E. Melendez, L. G. Althaus, and J. Isern, *Revisiting the axion bounds from the Galactic white dwarf luminosity function*, *JCAP* **1410** (2014), no. 10 069, [arXiv:1406.7712].

[31] F. Capozzi and G. Raffelt, *Axion and neutrino bounds improved with new calibrations of the tip of the red-giant branch using geometric distance determinations*, *Phys. Rev. D* **102** (2020), no. 8 083007, [arXiv:2007.03694].

[32] O. Straniero, C. Pallanca, E. Dalessandro, I. Dominguez, F. R. Ferraro, M. Giannotti, A. Mirizzi, and L. Piersanti, *The RGB tip of galactic globular clusters and the revision of the axion-electron coupling bound*, *Astron. Astrophys.* **644** (2020) A166, [arXiv:2010.03833].

[33] M. Giannotti, I. G. Irastorza, J. Redondo, A. Ringwald, and K. Saikawa, *Stellar Recipes for Axion Hunters*, *JCAP* **1710** (2017), no. 10 010, [arXiv:1708.02111].

[34] A. Possenti, R. Cerutti, M. Colpi, and S. Mereghetti, *Re-examining the x-ray versus spin-down luminosity correlation of rotation powered pulsars*, *Astron. Astrophys.* **387** (2002) 993, [astro-ph/0109452].

[35] V. I. Kondratiev, M. A. McLaughlin, D. R. Lorimer, M. Burgay, A. Possenti, R. Turolla, S. B. Popov, and S. Zane, *New Limits on Radio Emission from X-ray Dim Isolated Neutron Stars*, *Astrophys. J.* **702** (2009) 692–706, [arXiv:0907.0054]. [Erratum: Astrophys. J.708,910(2010)].

[36] D. L. Kaplan, A. Kamble, M. H. van Kerkwijk, and W. C. G. Ho, *New Optical/UV Counterparts and the Spectral Energy Distributions of Nearby, Thermally Emitting, Isolated Neutron Stars*, *Astrophys. J.* **736** (2011) 117, [arXiv:1105.4178].

[37] C. S. Reynolds, M. C. D. Marsh, H. R. Russell, A. C. Fabian, R. Smith, F. Tombesi, and S. Veilleux, *Astrophysical limits on very light axion-like particles from Chandra grating spectroscopy of NGC 1275*, arXiv:1907.05475.

[38] M. Libanov and S. Troitsky, *On the impact of magnetic-field models in galaxy clusters on constraints on axion-like particles from the lack of irregularities in high-energy spectra of astrophysical sources*, *Phys. Lett. B* **802** (2020) 135252, [arXiv:1908.03084].

[39] C. Dessert, A. J. Long, and B. R. Safdi, *No evidence for axions from Chandra observation of magnetic white dwarf*, arXiv:2104.12772.

[40] A. Payez, C. Evoli, T. Fischer, M. Giannotti, A. Mirizzi, and A. Ringwald, *Revisiting the SN1987A gamma-ray limit on ultralight axion-like particles*, *JCAP* **1502** (2015), no. 02 006, [arXiv:1410.3747].

[41] **Fermi-LAT** Collaboration, M. Ajello et al., *Search for Spectral Irregularities due to Photon–Axionlike-Particle Oscillations with the Fermi Large Area Telescope*, *Phys. Rev. Lett.* **116** (2016), no. 16 161101, [arXiv:1603.06978].

[42] C. Zhang, Y.-F. Liang, S. Li, N.-H. Liao, L. Feng, Q. Yuan, Y.-Z. Fan, and Z.-Z. Ren, *New bounds on axionlike particles from the Fermi Large Area Telescope observation of PKS 2155-304*, *Phys. Rev. D* **97** (2018), no. 6 063009, [arXiv:1802.08420].

[43] **H.E.S.S.** Collaboration, A. Abramowski et al., *Constraints on axionlike particles with H.E.S.S. from the irregularity of the PKS 2155-304 energy spectrum*, *Phys. Rev. D* **88** (2013), no. 10 102003, [arXiv:1311.3148].

[44] A. V. Gramolin, D. Aybas, D. Johnson, J. Adam, and A. O. Sushkov, *Search for axion-like dark matter with ferromagnets*, *Nature Phys.* **17** (2021), no. 1 79–84, [arXiv:2003.03348].

[45] J. L. Ouellet et al., *First Results from ABRACADABRA-10 cm: A Search for Sub-μeV Axion Dark Matter*, arXiv:1810.12257.

[46] C. P. Salemi et al., *The search for low-mass axion dark matter with ABRACADABRA-10cm*, arXiv:2102.06722.

[47] **ADMX** Collaboration, N. Du et al., *A Search for Invisible Axion Dark Matter with the Axion Dark Matter Experiment*, *Phys. Rev. Lett.* **120** (2018), no. 15 151301, [arXiv:1804.05750].

[48] **ADMX** Collaboration, T. Braine et al., *Extended Search for the Invisible Axion with the Axion Dark Matter Experiment*, *Phys. Rev. Lett.* **124** (2020), no. 10 101303, [arXiv:1910.08638].

[49] S. De Panfilis, A. C. Melissinos, B. E. Moskowitz, J. T. Rogers, Y. K. Semertzidis, W. Wuensch, H. J. Halama, A. G. Prodell, W. B. Fowler, and F. A. Nezrick, *Limits on the Abundance and Coupling of Cosmic Axions at 4.5-Microev $< m(a) <$ 5.0-Microev*, *Phys. Rev. Lett.* **59** (1987) 839.

[50] C. Hagmann, P. Sikivie, N. S. Sullivan, and D. B. Tanner, *Results from a search for cosmic axions*, *Phys. Rev. D* **42** (1990) 1297–1300.

[51] M. Y. Piotrovich, V. L. Afanasiev, Y. N. Gnedin, S. D. Buliga, and T. M. Natsvlishvili, *Spectropolarimetric Observations of Magnetic White Dwarfs with the SAO 6-m Telescope: Search for Rydberg States*, in *Physics of Magnetic Stars* (D. O. Kudryavtsev, I. I. Romanyuk, and I. A. Yakunin, eds.), vol. 518 of *Astronomical Society of the Pacific Conference Series*, p. 93, July, 2019.

[52] S. Jordan, *Progress in modeling magnetic white dwarfs*, in *White Dwarfs*, vol. 105 of *NATO Advanced Study Institute (ASI) Series B*, p. 175, Jan., 2003. astro-ph/0302058.

[53] G. D. Schmidt, S. C. West, J. Liebert, R. F. Green, and H. S. Stockman, *The New Magnetic White Dwarf PG 1031+234: Polarization and Field Structure at More than 500 Million Gauss*, **309** (Oct., 1986) 218.

[54] R. Janish, V. Narayan, and P. Riggins, *Type Ia supernovae from dark matter core collapse*, *Phys. Rev.* **D100** (2019), no. 3 035008, [arXiv:1905.00395].

[55] J. S. Sidhu and G. D. Starkman, *Reconsidering astrophysical constraints on macroscopic dark matter*, arXiv:1912.04053.

[56] N. Smyth, S. Profumo, S. English, T. Jeltema, K. McKinnon, and P. Guhathakurta, *Updated Constraints on Asteroid-Mass Primordial Black Holes as Dark Matter*, *Phys. Rev. D* **101** (2020), no. 6 063005, [arXiv:1910.01285].

[57] C. Dvorkin, K. Blum, and M. Kamionkowski, *Constraining Dark Matter-Baryon Scattering with Linear Cosmology*, *Phys. Rev.* **D89** (2014), no. 2 023519, [arXiv:1311.2937].

[58] A. Bhoonah, J. Bramante, S. Schon, and N. Song, *Detecting composite dark matter with long-range and contact interactions in gas clouds*, *Phys. Rev. D* **103** (2021), no. 12 123026, [arXiv:2010.07240].

[59] F. Nesti and P. Salucci, *The Dark Matter halo of the Milky Way, AD 2013*, *J. Cosmol. Astropart. Phys.* **1307** (2013) 016, [arXiv:1304.5127].

[60] A. Boyarsky, D. Iakubovskyi, O. Ruchayskiy, and D. Savchenko, *Surface brightness profile of the 3.5 keV line in the Milky Way halo*, arXiv:1812.10488.

[61] M. Cautun, A. Benítez-Llambay, A. J. Deason, C. S. Frenk, A. Fattahi, F. A. Gómez, R. J. J. Grand, K. A. Oman, J. F. Navarro, and C. M. Simpson, *The milky way total mass profile as inferred from Gaia DR2*, *MNRAS* **494** (Apr., 2020) 4291–4313, [arXiv:1911.04557].

[62] B. M. S. Hansen, *Cooling models for old white dwarfs*, *Astrophys. J.* **520** (1999) 680–695, [astro-ph/9903025].

[63] M. Salaris, E. Garcia-Berro, M. Hernanz, J. Isern, and D. Saumon, *The ages of very cool hydrogen-rich white dwarfs*, *Astrophys. J.* **544** (2000) 1036, [astro-ph/0007031].

[64] G. Chabrier, P. Brassard, G. Fontaine, and D. Saumon, *Cooling sequences and color-magnitude diagrams for cool white dwarfs with hydrogen-atmospheres*, *Astrophys. J.* **543** (2000) 216, [astro-ph/0006363].

[65] I. Renedo, L. G. Althaus, M. M. M. Bertolami, A. D. Romero, A. H. Corsico, R. D. Rohrmann, and E. Garcia-Berro, *New cooling sequences for old white dwarfs*, *Astrophys. J.* **717** (2010) 183–195, [arXiv:1005.2170].

[66] M. Nakagawa, T. Adachi, Y. Kohyama, and N. Itoh, *Axion bremsstrahlung in dense stars. II - Phonon contributions*, *Astrophys. J.* **326** (1988) 241.

[67] F. Najarro, D. F. Figer, D. Hillier, and R. P. Kudritzki, *Metallicity in the Galactic Center. The Arches cluster*, *Astrophys. J. Lett.* **611** (2004) L105–L108, [astro-ph/0407188].

[68] M. C. Miller et al., *The Radius of PSR J0740+6620 from NICER and XMM-Newton Data*, *Astrophys. J. Lett.* **918** (2021), no. 2 L28, [arXiv:2105.06979].

[69] T. E. Riley et al., *A NICER View of PSR J0030+0451: Millisecond Pulsar Parameter Estimation*, *Astrophys. J. Lett.* **887** (2019), no. 1 L21, [arXiv:1912.05702].

[70] S.-P. Tang, J.-L. Jiang, W.-H. Gao, Y.-Z. Fan, and D.-M. Wei, *The Masses of Isolated Neutron Stars Inferred from the Gravitational Redshift Measurements*, *Astrophys. J.* **888** (2020) 45, [arXiv:1911.08107].

[71] D. Viganò, A. García-García, J. A. Pons, C. Dehman, and V. Graber, *Magneto-thermal evolution of neutron stars with coupled Ohmic, Hall and ambipolar effects via accurate finite-volume simulations*, *Comput. Phys. Commun.* **265** (2021) 108001, [arXiv:2104.08001].

[72] H. Andernach and F. Zwicky, *English and spanish translation of zwicky's (1933) the redshift of extragalactic nebulae*, 2017.

[73] C. Flynn, J. Holmberg, L. Portinari, B. Fuchs, and H. Jahreiß, *On the mass-to-light ratio of the local Galactic disc and the optical luminosity of the Galaxy*, *Monthly Notices of the Royal Astronomical Society* **372** (09, 2006) 1149–1160.

[74] V. C. Rubin and J. Ford, W. Kent, *Rotation of the Andromeda Nebula from a Spectroscopic Survey of Emission Regions*, **159** (Feb., 1970) 379.

[75] **Planck** Collaboration, N. Aghanim et al., *Planck 2018 results. VI. Cosmological parameters*, *Astron. Astrophys.* **641** (2020) A6, [arXiv:1807.06209]. [Erratum: Astron.Astrophys. 652, C4 (2021)].

[76] **Super-Kamiokande** Collaboration, Y. Fukuda et al., *Evidence for oscillation of atmospheric neutrinos*, *Phys. Rev. Lett.* **81** (1998) 1562–1567, [hep-ex/9807003].

[77] C. Yèche, N. Palanque-Delabrouille, J. Baur, and H. du Mas des Bourboux, *Constraints on neutrino masses from Lyman-alpha forest power spectrum with BOSS and XQ-100*, *JCAP* **06** (2017) 047, [arXiv:1702.03314].

[78] T. Asaka, S. Blanchet, and M. Shaposhnikov, *The nuMSM, dark matter and neutrino masses*, *Phys. Lett. B* **631** (2005) 151–156, [hep-ph/0503065].

[79] S. Dodelson and L. M. Widrow, *Sterile-neutrinos as dark matter*, *Phys. Rev. Lett.* **72** (1994) 17–20, [hep-ph/9303287].

[80] X.-D. Shi and G. M. Fuller, *A New dark matter candidate: Nonthermal sterile neutrinos*, *Phys. Rev. Lett.* **82** (1999) 2832–2835, [astro-ph/9810076].

[81] A. Dolgov, S. Hansen, S. Pastor, S. Petcov, G. Raffelt, and D. Semikoz, *Cosmological bounds on neutrino degeneracy improved by flavor oscillations*, *Nucl. Phys. B* **632** (2002) 363–382, [hep-ph/0201287].

[82] A. D. Dolgov and S. H. Hansen, *Massive sterile neutrinos as warm dark matter*, *Astropart. Phys.* **16** (2002) 339–344, [hep-ph/0009083].

[83] C. Abel et al., *Measurement of the Permanent Electric Dipole Moment of the Neutron*, *Phys. Rev. Lett.* **124** (2020), no. 8 081803, [arXiv:2001.11966].

[84] R. D. Peccei and H. R. Quinn, CP *conservation in the presence of pseudoparticles*, *Phys. Rev. Lett.* **38** (Jun, 1977) 1440–1443.

[85] A. Hook, *TASI Lectures on the Strong CP Problem and Axions*, *PoS* **TASI2018** (2019) 004, [arXiv:1812.02669].

[86] P. B. Pal and L. Wolfenstein, *Radiative decays of massive neutrinos*, *Phys. Rev. D* **25** (Feb, 1982) 766–773.

[87] A. Kusenko, *Sterile neutrinos, dark matter, and the pulsar velocities in models with a Higgs singlet*, *Phys. Rev. Lett.* **97** (2006) 241301, [hep-ph/0609081].

[88] E. Bulbul, M. Markevitch, A. Foster, R. K. Smith, M. Loewenstein, and S. W. Randall, *Detection of An Unidentified Emission Line in the Stacked X-ray spectrum of Galaxy Clusters*, *Astrophys. J.* **789** (2014) 13, [arXiv:1402.2301].

[89] A. Boyarsky, O. Ruchayskiy, D. Iakubovskyi, and J. Franse, *Unidentified Line in X-Ray Spectra of the Andromeda Galaxy and Perseus Galaxy Cluster*, *Phys. Rev. Lett.* **113** (2014) 251301, [arXiv:1402.4119].

[90] T. E. Jeltema and S. Profumo, *Discovery of a 3.5 keV line in the Galactic Centre and a critical look at the origin of the line across astronomical targets*, *Mon. Not. Roy. Astron. Soc.* **450** (2015), no. 2 2143–2152, [arXiv:1408.1699].

[91] L. Gu, J. Kaastra, A. J. J. Raassen, P. D. Mullen, R. S. Cumbee, D. Lyons, and P. C. Stancil, *A novel scenario for the possible X-ray line feature at 3.5 keV: Charge exchange with bare sulfur ions*, *Astron. Astrophys.* **584** (2015) L11, [arXiv:1511.06557].

[92] C. Shah, S. Dobrodey, S. Bernitt, R. Steinbrügge, J. R. C. López-Urrutia, L. Gu, and J. Kaastra, *Laboratory measurements compellingly support charge-exchange mechanism for the 'dark matter' ∼3.5 keV X-ray line*, *Astrophys. J.* **833** (2016), no. 1 52, [arXiv:1608.04751].

[93] O. Urban, N. Werner, S. W. Allen, A. Simionescu, J. S. Kaastra, and L. E. Strigari, *A Suzaku Search for Dark Matter Emission Lines in the X-ray Brightest Galaxy Clusters*, *Mon. Not. Roy. Astron. Soc.* **451** (2015), no. 3 2447–2461, [arXiv:1411.0050].

[94] A. Boyarsky, J. Franse, D. Iakubovskyi, and O. Ruchayskiy, *Checking the Dark Matter Origin of a 3.53 keV Line with the Milky Way Center*, *Phys. Rev. Lett.* **115** (2015) 161301, [arXiv:1408.2503].

[95] N. Cappelluti, E. Bulbul, A. Foster, P. Natarajan, M. C. Urry, M. W. Bautz, F. Civano, E. Miller, and R. K. Smith, *Searching for the 3.5 keV Line in the Deep Fields with Chandra: the 10 Ms observations*, *Astrophys. J.* **854** (2018), no. 2 179, [arXiv:1701.07932].

[96] S. Horiuchi, P. J. Humphrey, J. Onorbe, K. N. Abazajian, M. Kaplinghat, and S. Garrison-Kimmel, *Sterile neutrino dark matter bounds from galaxies of the Local Group*, *Phys. Rev.* **D89** (2014), no. 2 025017, [arXiv:1311.0282].

[97] D. Malyshev, A. Neronov, and D. Eckert, *Constraints on 3.55 keV line emission from stacked observations of dwarf spheroidal galaxies*, *Phys. Rev.* **D90** (2014) 103506, [arXiv:1408.3531].

[98] M. E. Anderson, E. Churazov, and J. N. Bregman, *Non-Detection of X-Ray Emission From Sterile Neutrinos in Stacked Galaxy Spectra*, *Mon. Not. Roy. Astron. Soc.* **452** (2015), no. 4 3905–3923, [arXiv:1408.4115].

[99] T. Tamura, R. Iizuka, Y. Maeda, K. Mitsuda, and N. Y. Yamasaki, *An X-ray Spectroscopic Search for Dark Matter in the Perseus Cluster with Suzaku*, *Publ. Astron. Soc. Jap.* **67** (2015) 23, [arXiv:1412.1869].

[100] **Hitomi** Collaboration, F. A. Aharonian et al., *Hitomi constraints on the 3.5 keV line in the Perseus galaxy cluster*, *Astrophys. J.* **837** (2017), no. 1 L15, [arXiv:1607.07420].

[101] Materials and methods are available as supplementary materials.

[102] J. F. Navarro, C. S. Frenk, and S. D. M. White, *The Structure of cold dark matter halos*, *Astrophys. J.* **462** (1996) 563–575, [astro-ph/9508025].

[103] M. J. L. Turner et al., *The European Photon Imaging Camera on XMM-Newton: The MOS cameras*, *Astron. Astrophys.* **365** (2001) L27–35, [astro-ph/0011498].

[104] L. Struder et al., *The European Photon Imaging Camera on XMM-Newton: The pn-CCD camera*, *Astron. Astrophys.* **365** (2001) L18–26.

[105] D. H. Lumb, R. S. Warwick, M. Page, and A. De Luca, *X-ray background measurements with xmm-newton epic*, *Astron. Astrophys.* **389** (2002) 93, [astro-ph/0204147].

[106] A. Moretti et al., *A new measurement of the cosmic X-ray background*, *AIP Conf. Proc.* **1126** (2009) 223–226, [arXiv:0811.1444].

[107] R. Catena and P. Ullio, *A novel determination of the local dark matter density*, *J. Cosmol. Astropart. Phys.* **1008** (2010) 004, [arXiv:0907.0018].

[108] **GRAVITY** Collaboration, R. Abuter et al., *Detection of the gravitational redshift in the orbit of the star S2 near the Galactic centre massive black hole*, *Astron. Astrophys.* **615** (2018) L15, [arXiv:1807.09409].

[109] G. Cowan, K. Cranmer, E. Gross, and O. Vitells, *Asymptotic formulae for likelihood-based tests of new physics*, *Eur. Phys. J.* **C71** (2011) 1554, [arXiv:1007.1727].

[110] G. Cowan, K. Cranmer, E. Gross, and O. Vitells, *Power-Constrained Limits*, arXiv:1105.3166.

[111] C. Dessert, N. L. Rodd, and B. R. Safdi, *The dark matter interpretation of the 3.5-keV line is inconsistent with blank-sky observations*, *Science* **367** (2020) 1465, [arXiv:1812.06976].

[112] C. Dessert, N. L. Rodd, and B. R. Safdi, *Response to a comment on Dessert et al. "The dark matter interpretation of the 3.5 keV line is inconsistent with blank-sky observations"*, arXiv:2006.03974.

[113] T. E. Jeltema and S. Profumo, *Deep XMM Observations of Draco rule out at the 99% Confidence Level a Dark Matter Decay Origin for the 3.5 keV Line*, *Mon. Not. Roy. Astron. Soc.* **458** (2016), no. 4 3592–3596, [arXiv:1512.01239].

[114] A. Gewering-Peine, D. Horns, and J. H. M. M. Schmitt, *A sensitive search for unknown spectral emission lines in the diffuse X-ray background with XMM-Newton*, *J. Cosmol. Astropart. Phys.* **1706** (2017), no. 06 036, [arXiv:1611.01733].

[115] O. Ruchayskiy, A. Boyarsky, D. Iakubovskyi, E. Bulbul, D. Eckert, J. Franse, D. Malyshev, M. Markevitch, and A. Neronov, *Searching for decaying dark matter in deep XMM–Newton observation of the Draco dwarf spheroidal*, *Mon. Not. Roy. Astron. Soc.* **460** (2016), no. 2 1390–1398, [arXiv:1512.07217].

[116] A. Neronov, D. Malyshev, and D. Eckert, *Decaying dark matter search with NuSTAR deep sky observations*, *Phys. Rev. D* **94** (2016), no. 12 123504, [arXiv:1607.07328].

[117] K. Perez, K. C. Y. Ng, J. F. Beacom, C. Hersh, S. Horiuchi, and R. Krivonos, *Almost closing the νMSM sterile neutrino dark matter window with NuSTAR*, *Phys. Rev. D* **95** (2017), no. 12 123002, [arXiv:1609.00667].

[118] B. M. Roach, K. C. Ng, K. Perez, J. F. Beacom, S. Horiuchi, R. Krivonos, and D. R. Wik, *NuSTAR Tests of Sterile-Neutrino Dark Matter: New Galactic Bulge Observations and Combined Impact*, *Phys. Rev. D* **101** (2020), no. 10 103011, [arXiv:1908.09037].

[119] S. Riemer-Sorensen et al., *Dark matter line emission constraints from NuSTAR observations of the Bullet Cluster*, *Astrophys. J.* **810** (2015), no. 1 48, [arXiv:1507.01378].

[120] K. C. Ng, B. M. Roach, K. Perez, J. F. Beacom, S. Horiuchi, R. Krivonos, and D. R. Wik, *New Constraints on Sterile Neutrino Dark Matter from NuSTAR M31 Observations*, *Phys. Rev. D* **99** (2019) 083005, [arXiv:1901.01262].

[121] T. Asaka and M. Shaposhnikov, *The νMSM, dark matter and baryon asymmetry of the universe*, *Phys. Lett. B* **620** (2005) 17–26, [hep-ph/0505013].

[122] L. Canetti, M. Drewes, T. Frossard, and M. Shaposhnikov, *Dark Matter, Baryogenesis and Neutrino Oscillations from Right Handed Neutrinos*, *Phys. Rev. D* **87** (2013) 093006, [arXiv:1208.4607].

[123] P. D. Serpico and G. G. Raffelt, *Lepton asymmetry and primordial nucleosynthesis in the era of precision cosmology*, *Phys. Rev. D* **71** (2005) 127301, [astro-ph/0506162].

[124] A. Boyarsky, O. Ruchayskiy, and M. Shaposhnikov, *The Role of sterile neutrinos in cosmology and astrophysics*, *Ann. Rev. Nucl. Part. Sci.* **59** (2009) 191–214, [arXiv:0901.0011].

[125] M. Laine and M. Shaposhnikov, *Sterile neutrino dark matter as a consequence of nuMSM-induced lepton asymmetry*, *J. Cosmol. Astropart. Phys.* **0806** (2008) 031, [arXiv:0804.4543].

[126] T. Venumadhav, F.-Y. Cyr-Racine, K. N. Abazajian, and C. M. Hirata, *Sterile neutrino dark matter: Weak interactions in the strong coupling epoch*, *Phys. Rev.* **D94** (2016), no. 4 043515, [arXiv:1507.06655].

[127] J. F. Cherry and S. Horiuchi, *Closing in on Resonantly Produced Sterile Neutrino Dark Matter*, *Phys. Rev. D* **95** (2017), no. 8 083015, [arXiv:1701.07874].

[128] K. Petraki and A. Kusenko, *Dark-matter sterile neutrinos in models with a gauge singlet in the Higgs sector*, *Phys. Rev. D* **77** (2008) 065014, [arXiv:0711.4646].

[129] K. N. Abazajian and A. Kusenko, *Hidden treasures: Sterile neutrinos as dark matter with miraculous abundance, structure formation for different production mechanisms, and a solution to the σ_8 problem*, *Phys. Rev. D* **100** (2019), no. 10 103513, [arXiv:1907.11696].

[130] T. Higaki, K. S. Jeong, and F. Takahashi, *The 7 keV axion dark matter and the X-ray line signal*, *Phys. Lett. B* **733** (2014) 25–31, [arXiv:1402.6965].

[131] A. Kusenko, M. Loewenstein, and T. T. Yanagida, *Moduli dark matter and the search for its decay line using Suzaku X-ray telescope*, *Phys. Rev. D* **87** (2013), no. 4 043508, [arXiv:1209.6403].

[132] See /github.com/bsafdi/XMM_BSO_DATA for the list of observations used and processed data products.

[133] K. M. Gorski, E. Hivon, A. J. Banday, B. D. Wandelt, F. K. Hansen, M. Reinecke, and M. Bartelman, *HEALPix - A Framework for high resolution discretization, and fast analysis of data distributed on the sphere*, *Astrophys. J.* **622** (2005) 759–771, [astro-ph/0409513].

[134] **ATLAS** Collaboration, G. Aad et al., *Measurement of Higgs boson production in the diphoton decay channel in pp collisions at center-of-mass energies of 7 and 8 TeV with the ATLAS detector*, *Phys. Rev. D* **90** (2014), no. 11 112015, [arXiv:1408.7084].

[135] S. Ambikasaran, D. Foreman-Mackey, L. Greengard, D. W. Hogg, and M. O'Neil, *Fast Direct Methods for Gaussian Processes*, .

[136] M. Frate, K. Cranmer, S. Kalia, A. Vandenberg-Rodes, and D. Whiteson, *Modeling Smooth Backgrounds and Generic Localized Signals with Gaussian Processes*, arXiv:1709.05681.

[137] P. B. Pal and L. Wolfenstein, *Radiative Decays of Massive Neutrinos*, *Phys. Rev. D* **25** (1982) 766.

[138] M. Vogelsberger, F. Marinacci, P. Torrey, and E. Puchwein, *Cosmological Simulations of Galaxy Formation*, *Nature Rev. Phys.* **2** (2020), no. 1 42–66, [arXiv:1909.07976].

[139] J. F. Navarro, C. S. Frenk, and S. D. M. White, *A Universal density profile from hierarchical clustering*, *Astrophys. J.* **490** (1997) 493–508, [astro-ph/9611107].

[140] O. Y. Gnedin, A. V. Kravtsov, A. A. Klypin, and D. Nagai, *Response of dark matter halos to condensation of baryons: Cosmological simulations and improved adiabatic contraction model*, *Astrophys. J.* **616** (2004) 16–26, [astro-ph/0406247].

[141] M. Schaller, C. S. Frenk, R. G. Bower, T. Theuns, A. Jenkins, J. Schaye, R. A. Crain, M. Furlong, C. D. Vecchia, and I. G. McCarthy, *Baryon effects on the internal structure of ΛCDM haloes in the EAGLE simulations*, *Mon. Not. Roy. Astron. Soc.* **451** (2015), no. 2 1247–1267, [arXiv:1409.8617].

[142] Q. Zhu, F. Marinacci, M. Maji, Y. Li, V. Springel, and L. Hernquist, *Baryonic impact on the dark matter distribution in Milky Way-sized galaxies and their satellites*, *Mon. Not. Roy. Astron. Soc.* **458** (2016), no. 2 1559–1580, [arXiv:1506.05537].

[143] A. A. Dutton, A. V. Macciò, A. Dekel, L. Wang, G. S. Stinson, A. Obreja, A. Di Cintio, C. B. Brook, T. Buck, and X. Kang, *NIHAO IX: The role of gas inflows and outflows in driving the contraction and expansion of cold dark matter haloes*, *Mon. Not. Roy. Astron. Soc.* **461** (2016), no. 3 2658–2675, [arXiv:1605.05323].

[144] P. F. Hopkins et al., *FIRE-2 Simulations: Physics versus Numerics in Galaxy Formation*, *Mon. Not. Roy. Astron. Soc.* **480** (2018), no. 1 800–863, [arXiv:1702.06148].

[145] M. R. Lovell et al., *The fraction of dark matter within galaxies from the IllustrisTNG simulations*, *Mon. Not. Roy. Astron. Soc.* **481** (2018), no. 2 1950–1975, [arXiv:1801.10170].

[146] T. Chan, D. Keres, J. Oñorbe, P. Hopkins, A. Muratov, C. A. Faucher-Giguère, and E. Quataert, *The impact of baryonic physics on the structure of dark matter haloes: the view from the FIRE cosmological simulations*, *Mon. Not. Roy. Astron. Soc.* **454** (2015), no. 3 2981–3001, [arXiv:1507.02282].

[147] P. Mollitor, E. Nezri, and R. Teyssier, *Baryonic and dark matter distribution in cosmological simulations of spiral galaxies*, *Mon. Not. Roy. Astron. Soc.* **447** (2015), no. 2 1353–1369, [arXiv:1405.4318].

[148] M. Portail, O. Gerhard, C. Wegg, and M. Ness, *Dynamical modelling of the galactic bulge and bar: the Milky Way's pattern speed, stellar and dark matter mass distribution*, *Mon. Not. Roy. Astron. Soc.* **465** (Feb., 2017) 1621–1644, [arXiv:1608.07954].

[149] A. Lazar, J. S. Bullock, M. Boylan-Kolchin, T. K. Chan, P. F. Hopkins, A. S. Graus, A. Wetzel, K. El-Badry, C. Wheeler, M. C. Straight, and Keres.

[150] A.-C. Eilers, D. W. Hogg, H.-W. Rix, and M. K. Ness, *The Circular Velocity Curve of the Milky Way from 5 to 25 kpc*, **871** (Jan., 2019) 120, [arXiv:1810.09466].

[151] L. L. Watkins, R. P. van der Marel, S. T. Sohn, and N. W. Evans, *Evidence for an Intermediate-mass Milky Way from Gaia DR2 Halo Globular Cluster Motions*, *ApJ* **873** (Mar., 2019) 118, [arXiv:1804.11348].

[152] T. M. Callingham, M. Cautun, A. J. Deason, C. S. Frenk, W. Wang, F. A. Gómez, R. J. J. Grand, F. Marinacci, and R. Pakmor, *The mass of the Milky Way from satellite dynamics*, *MNRAS* **484** (Apr., 2019) 5453–5467, [arXiv:1808.10456].

[153] J. Read, *The Local Dark Matter Density*, *J. Phys. G* **41** (2014) 063101, [arXiv:1404.1938].

[154] P. F. de Salas and A. Widmark, *Dark matter local density determination: recent observations and future prospects*, arXiv:2012.11477.

[155] **DES** Collaboration, A. Drlica-Wagner et al., *Milky Way Satellite Census. I. The Observational Selection Function for Milky Way Satellites in DES Y3 and Pan-STARRS DR1*, *Astrophys. J.* **893** (2020) 1, [arXiv:1912.03302].

[156] **DES** Collaboration, E. O. Nadler et al., *Milky Way Satellite Census. III. Constraints on Dark Matter Properties from Observations of Milky Way Satellite Galaxies*, arXiv:2008.00022.

[157] E. O. Nadler, S. Birrer, D. Gilman, R. H. Wechsler, X. Du, A. Benson, A. M. Nierenberg, and T. Treu, *Dark Matter Constraints from a Unified Analysis of Strong Gravitational Lenses and Milky Way Satellite Galaxies*, arXiv:2101.07810.

[158] D. Sicilian, N. Cappelluti, E. Bulbul, F. Civano, M. Moscetti, and C. S. Reynolds, *Probing the Milky Way's Dark Matter Halo for the 3.5 keV Line*, *Astrophys. J.* **905** (2020), no. 2 146, [arXiv:2008.02283].

[159] **Athena Team** Collaboration, X. Barcons, K. Nandra, D. Barret, J. den Herder, A. Fabian, L. Piro, and M. Watson, *Athena: the X-ray observatory to study the hot and energetic Universe*, *J. Phys. Conf. Ser.* **610** (2015), no. 1 012008.

[160] **XRISM Science Team** Collaboration, *Science with the X-ray Imaging and Spectroscopy Mission (XRISM)*, arXiv:2003.04962.

[161] R. D. Peccei and H. R. Quinn, *Constraints Imposed by CP Conservation in the Presence of Instantons*, *Phys. Rev.* **D16** (1977) 1791–1797.

[162] R. D. Peccei and H. R. Quinn, *CP Conservation in the Presence of Instantons*, *Phys. Rev. Lett.* **38** (1977) 1440–1443.

[163] S. Weinberg, *A New Light Boson?*, *Phys. Rev. Lett.* **40** (1978) 223–226.

[164] F. Wilczek, *Problem of Strong p and t Invariance in the Presence of Instantons*, *Phys. Rev. Lett.* **40** (1978) 279–282.

[165] P. Svrcek and E. Witten, *Axions In String Theory*, *JHEP* **06** (2006) 051, [hep-th/0605206].

[166] A. Arvanitaki, S. Dimopoulos, S. Dubovsky, N. Kaloper, and J. March-Russell, *String Axiverse*, *Phys. Rev.* **D81** (2010) 123530, [arXiv:0905.4720].

[167] G. G. Raffelt, *Axion Constraints From White Dwarf Cooling Times*, *Phys. Lett.* **166B** (1986) 402–406.

[168] J. Isern, E. Garcia-Berro, S. Torres, and S. Catalan, *Axions and the cooling of white dwarf stars*, *Astrophys. J.* **682** (2008) L109, [arXiv:0806.2807].

[169] J. Isern, S. Catalan, E. Garcia-Berro, and S. Torres, *Axions and the white dwarf luminosity function*, *J. Phys. Conf. Ser.* **172** (2009) 012005, [arXiv:0812.3043].

[170] J. Isern, E. Garcia-Berro, L. G. Althaus, and A. H. Corsico, *Axions and the pulsation periods of variable white dwarfs revisited*, *Astron. Astrophys.* **512** (2010) A86, [arXiv:1001.5248].

[171] S. O. Kepler, I. Pelisoli, S. Jordan, S. J. Kleinman, D. Koester, B. Külebi, V. Pecanha, B. G. Castanheira, A. Nitta, J. E. S. Costa, D. E. Winget, A. Kanaan, and L. Fraga, *Magnetic white dwarf stars in the Sloan Digital Sky Survey*, *MNRAS* **429** (Mar., 2013) 2934–2944, [arXiv:1211.5709].

[172] D. E. Morris, *Axion Mass Limits From Pulsar X-rays*, *Phys. Rev.* **D34** (1986) 843.

[173] G. Raffelt and L. Stodolsky, *Mixing of the Photon with Low Mass Particles*, *Phys. Rev.* **D37** (1988) 1237.

[174] M. Dine, W. Fischler, and M. Srednicki, *A Simple Solution to the Strong CP Problem with a Harmless Axion*, *Phys. Lett.* **104B** (1981) 199–202.

[175] A. R. Zhitnitsky, *On Possible Suppression of the Axion Hadron Interactions. (In Russian)*, *Sov. J. Nucl. Phys.* **31** (1980) 260. [Yad. Fiz.31,497(1980)].

[176] M. Srednicki, *Axion Couplings to Matter. 1. CP Conserving Parts*, *Nucl. Phys.* **B260** (1985) 689–700.

[177] J. E. Kim, *Weak Interaction Singlet and Strong CP Invariance*, *Phys. Rev. Lett.* **43** (1979) 103.

[178] M. A. Shifman, A. I. Vainshtein, and V. I. Zakharov, *Can Confinement Ensure Natural CP Invariance of Strong Interactions?*, *Nucl. Phys.* **B166** (1980) 493.

[179] J.-F. Fortin and K. Sinha, *Constraining Axion-Like-Particles with Hard X-ray Emission from Magnetars*, *JHEP* **06** (2018) 048, [arXiv:1804.01992].

[180] J.-F. Fortin and K. Sinha, *X-Ray Polarization Signals from Magnetars with Axion-Like-Particles*, *JHEP* **01** (2019) 163, [arXiv:1807.10773].

[181] **CAST** Collaboration, M. Arik et al., *Search for Solar Axions by the CERN Axion Solar Telescope with ^{3}He Buffer Gas: Closing the Hot Dark Matter Gap*, *Phys. Rev. Lett.* **112** (2014), no. 9 091302, [arXiv:1307.1985].

[182] **CAST** Collaboration, M. Arik et al., *New solar axion search using the CERN Axion Solar Telescope with ^{4}He filling*, *Phys. Rev.* **D92** (2015), no. 2 021101, [arXiv:1503.00610].

[183] K. Zioutas, M. Tsagri, Y. Semertzidis, T. Papaevangelou, T. Dafni, and V. Anastassopoulos, *Axion searches with helioscopes and astrophysical signatures for axion(-like) particles*, *New Journal of Physics* **11** (Oct., 2009) 105020, [arXiv:0903.1807].

[184] M. S. Pshirkov, *Conversion of Dark matter axions to photons in magnetospheres of neutron stars*, *J. Exp. Theor. Phys.* **108** (2009) 384–388, [arXiv:0711.1264].

[185] F. P. Huang, K. Kadota, T. Sekiguchi, and H. Tashiro, *Radio telescope search for the resonant conversion of cold dark matter axions from the magnetized astrophysical sources*, *Phys. Rev.* **D97** (2018), no. 12 123001, [arXiv:1803.08230].

[186] A. Hook, Y. Kahn, B. R. Safdi, and Z. Sun, *Radio Signals from Axion Dark Matter Conversion in Neutron Star Magnetospheres*, *Phys. Rev. Lett.* **121** (2018), no. 24 241102, [arXiv:1804.03145].

[187] B. R. Safdi, Z. Sun, and A. Y. Chen, *Detecting Axion Dark Matter with Radio Lines from Neutron Star Populations*, arXiv:1811.01020.

[188] A. Caputo, M. Regis, M. Taoso, and S. J. Witte, *Detecting the Stimulated Decay of Axions at RadioFrequencies*, arXiv:1811.08436.

[189] G. G. Raffelt, *Astrophysical axion bounds*, *Lect. Notes Phys.* **741** (2008) 51–71, [hep-ph/0611350]. [,51(2006)].

[190] T. Fischer, S. Chakraborty, M. Giannotti, A. Mirizzi, A. Payez, and A. Ringwald, *Probing axions with the neutrino signal from the next galactic supernova*, *Phys. Rev. D* **94** (Oct, 2016) 085012.

[191] A. Ayala, I. Domínguez, M. Giannotti, A. Mirizzi, and O. Straniero, *Revisiting the bound on axion-photon coupling from globular clusters*, *Phys. Rev. Lett.* **113** (Nov, 2014) 191302.

[192] M. Simet, D. Hooper, and P. D. Serpico, *The Milky Way as a Kiloparsec-Scale Axionscope*, *Phys. Rev.* **D77** (2008) 063001, [arXiv:0712.2825].

[193] M. A. Sánchez-Conde, D. Paneque, E. Bloom, F. Prada, and A. Domínguez, *Hints of the existence of axionlike particles from the gamma-ray spectra of cosmological sources*, *Phys. Rev. D* **79** (June, 2009) 123511, [arXiv:0905.3270].

[194] A. De Angelis, G. Galanti, and M. Roncadelli, *Relevance of axion-like particles for very-high-energy astrophysics*, *Phys. Rev.* **D84** (2011) 105030, [arXiv:1106.1132]. [Erratum: Phys. Rev.D87,no.10,109903(2013)].

[195] **Fermi-LAT** Collaboration, M. Ajello et al., *Search for Spectral Irregularities due to Photon–Axionlike-Particle Oscillations with the Fermi Large Area Telescope*, *Phys. Rev. Lett.* **116** (2016), no. 16 161101, [arXiv:1603.06978].

[196] M. Battaglieri et al., *US Cosmic Visions: New Ideas in Dark Matter 2017: Community Report*, arXiv:1707.04591.

[197] T. M. Shokair et al., *Future Directions in the Microwave Cavity Search for Dark Matter Axions*, *Int. J. Mod. Phys.* **A29** (2014) 1443004, [arXiv:1405.3685].

[198] **ADMX** Collaboration, N. Du et al., *A Search for Invisible Axion Dark Matter with the Axion Dark Matter Experiment*, *Phys. Rev. Lett.* **120** (2018), no. 15 151301, [arXiv:1804.05750].

[199] B. M. Brubaker et al., *First results from a microwave cavity axion search at 24 μeV*, *Phys. Rev. Lett.* **118** (2017), no. 6 061302, [arXiv:1610.02580].

[200] S. Al Kenany et al., *Design and operational experience of a microwave cavity axion detector for the 20–100 μeV range*, *Nucl. Instrum. Meth.* **A854** (2017) 11–24, [arXiv:1611.07123].

[201] B. M. Brubaker, L. Zhong, S. K. Lamoreaux, K. W. Lehnert, and K. A. van Bibber, *The HAYSTAC Axion Search Analysis Procedure*, arXiv:1706.08388.

[202] **MADMAX Working Group** Collaboration, A. Caldwell, G. Dvali, B. Majorovits, A. Millar, G. Raffelt, J. Redondo, O. Reimann, F. Simon, and F. Steffen, *Dielectric Haloscopes: A New Way to Detect Axion Dark Matter*, *Phys. Rev. Lett.* **118** (2017), no. 9 091801, [arXiv:1611.05865].

[203] Y. Kahn, B. R. Safdi, and J. Thaler, *Broadband and Resonant Approaches to Axion Dark Matter Detection*, *Phys. Rev. Lett.* **117** (2016), no. 14 141801, [arXiv:1602.01086].

[204] J. W. Foster, N. L. Rodd, and B. R. Safdi, *Revealing the Dark Matter Halo with Axion Direct Detection*, arXiv:1711.10489.

[205] S. Chaudhuri, P. W. Graham, K. Irwin, J. Mardon, S. Rajendran, and Y. Zhao, *Radio for hidden-photon dark matter detection*, *Phys. Rev.* **D92** (2015), no. 7 075012, [arXiv:1411.7382].

[206] M. Silva-Feaver et al., *Design Overview of the DM Radio Pathfinder Experiment*, *IEEE Trans. Appl. Supercond.* **27** (2016), no. 4 1400204, [arXiv:1610.09344].

[207] D. Budker, P. W. Graham, M. Ledbetter, S. Rajendran, and A. Sushkov, *Proposal for a Cosmic Axion Spin Precession Experiment (CASPEr)*, *Phys. Rev.* **X4** (2014), no. 2 021030, [arXiv:1306.6089].

[208] R. Bähre et al., *Any light particle search II —Technical Design Report*, *JINST* **8** (2013) T09001, [arXiv:1302.5647].

[209] Z. Bogorad, A. Hook, Y. Kahn, and Y. Soreq, *Probing ALPs and the Axiverse with Superconducting Radiofrequency Cavities*, arXiv:1902.01418.

[210] **Particle Data Group** Collaboration, M. Tanabashi et al., *Review of Particle Physics*, *Phys. Rev.* **D98** (2018), no. 3 030001.

[211] M. Nakagawa, Y. Kohyama, and N. Itoh, *Axion Bremsstrahlung in Dense Stars*, *Astrophys. J.* **322** (1987) 291.

[212] G. G. Raffelt, *Astrophysical methods to constrain axions and other novel particle phenomena*, *Phys. Rept.* **198** (1990) 1–113.

[213] H. L. Shipman, *Sirius B - A thermal soft X-ray source*, *ApJL* **206** (May, 1976) L67–L69.

[214] M. A. Barstow, S. Jordan, D. O'Donoghue, M. R. Burleigh, R. Napiwotzki, and M. K. Harrop-Allin, *RE J0317-853: the hottest known highly magnetic DA white dwarf*, *MNRAS* **277** (Dec., 1995) 971–985.

[215] M. R. Burleigh, S. Jordan, and W. Schweizer, *Phase-resolved far-ultraviolet hst spectroscopy of the peculiar magnetic white dwarf re j0317-853*, *Astrophys. J.* **510** (1999) L37, [astro-ph/9810109].

[216] A. Harayama, Y. Terada, M. Ishida, T. Hayashi, A. Bamba, and M. S. Tashiro, *Search for non-thermal emissions from an isolated magnetic white dwarf, euve j0317 855, with suzaku*, *Publications of the Astronomical Society of Japan* **65** (2013), no. 4 73.

[217] K. Barth et al., *CAST constraints on the axion-electron coupling*, *JCAP* **1305** (2013) 010, [arXiv:1302.6283].

[218] Chandra X-Ray Observatory, *Chandra Science Tools*, March, 2019.

[219] Y. Terada, T. Hayashi, M. Ishida, K. Mukai, T. u. Dotani, S. Okada, R. Nakamura, S. Naik, A. Bamba, and K. Makishima, *Suzaku Discovery of Non-thermal X-ray Emission from the Rotating Magnetized White Dwarf, AE Aquarii*, *Publ. Astron. Soc. Jap.* **60** (2008) 387, [arXiv:0711.2716].

[220] C. S. Brinkworth, M. R. Burleigh, G. A. Wynn, and T. R. Marsh, *Photometric variability of the unique magnetic white dwarf GD356*, *Mon. Not. Roy. Astron. Soc.* **348** (2004) L33, [astro-ph/0312311].

[221] M. Buschmann, R. T. Co, C. Dessert, and B. R. Safdi, *Axion Emission Can Explain a New Hard X-Ray Excess from Nearby Isolated Neutron Stars*, *Phys. Rev. Lett.* **126** (2021), no. 2 021102, [arXiv:1910.04164].

[222] C. Dessert, A. J. Long, and B. R. Safdi, *X-ray signatures of axion conversion in magnetic white dwarf stars*, *Phys. Rev. Lett.* **123** (2019), no. 6 061104, [arXiv:1903.05088].

[223] D. Lai and J. Heyl, *Probing Axions with Radiation from Magnetic Stars*, *Phys. Rev.* **D74** (2006) 123003, [astro-ph/0609775].

[224] D. Chelouche, R. Rabadan, S. Pavlov, and F. Castejon, *Spectral Signatures of Photon-Particle Oscillations from Celestial Objects*, *Astrophys. J. Suppl.* **180** (2009) 1–29, [arXiv:0806.0411].

[225] R. Jimenez, C. Pena-Garay, and L. Verde, *Is it possible to explore Peccei-Quinn axions from frequency-dependence radiation dimming?*, *Phys. Lett. B* **703** (2011) 232–236, [arXiv:1102.1728].

[226] R. Perna, W. Ho, L. Verde, M. van Adelsberg, and R. Jimenez, *Signatures of photon-axion conversion in the thermal spectra and polarization of neutron stars*, *Astrophys. J.* **748** (2012) 116, [arXiv:1201.5390].

[227] J.-F. Fortin, H.-K. Guo, S. P. Harris, E. Sheridan, and K. Sinha, *Magnetars and Axion-like Particles: Probes with the Hard X-ray Spectrum*, arXiv:2101.05302.

[228] M. Xiao, K. M. Perez, M. Giannotti, O. Straniero, A. Mirizzi, B. W. Grefenstette, B. M. Roach, and M. Nynka, *Constraints on Axionlike Particles from a Hard X-Ray Observation of Betelgeuse*, *Phys. Rev. Lett.* **126** (2021), no. 3 031101, [arXiv:2009.09059].

[229] **H.E.S.S.** Collaboration, A. Abramowski et al., *Constraints on axionlike particles with H.E.S.S. from the irregularity of the PKS 2155-304 energy spectrum*, *Phys. Rev.* **D88** (2013), no. 10 102003, [arXiv:1311.3148].

[230] **ADMX** Collaboration, T. Braine et al., *Extended Search for the Invisible Axion with the Axion Dark Matter Experiment*, *Phys. Rev. Lett.* **124** (2020), no. 10 101303, [arXiv:1910.08638].

[231] **HAYSTAC** Collaboration, L. Zhong et al., *Results from phase 1 of the HAYSTAC microwave cavity axion experiment*, *Phys. Rev. D* **97** (2018), no. 9 092001, [arXiv:1803.03690].

[232] **HAYSTAC** Collaboration, K. M. Backes et al., *A quantum-enhanced search for dark matter axions*, *Nature* **590** (2021), no. 7845 238–242, [arXiv:2008.01853].

[233] J. Jeong, S. Youn, S. Bae, J. Kim, T. Seong, J. E. Kim, and Y. K. Semertzidis, *Search for Invisible Axion Dark Matter with a Multiple-Cell Haloscope*, *Phys. Rev. Lett.* **125** (2020), no. 22 221302, [arXiv:2008.10141].

[234] D. Alesini et al., *Search for Invisible Axion Dark Matter of mass $m_a = 43$ μeV with the QUAX–$a\gamma$ Experiment*, arXiv:2012.09498.

[235] B. T. McAllister, G. Flower, E. N. Ivanov, M. Goryachev, J. Bourhill, and M. E. Tobar, *The ORGAN Experiment: An axion haloscope above 15 GHz*, *Phys. Dark Univ.* **18** (2017) 67–72, [arXiv:1706.00209].

[236] Gaia Collaboration, A. G. A. Brown, A. Vallenari, T. Prusti, J. H. J. de Bruijne, C. Babusiaux, and M. Biermann, *Gaia Early Data Release 3: Summary of the contents and survey properties*, *arXiv e-prints* (Dec., 2020) arXiv:2012.01533, [arXiv:2012.01533].

[237] B. Paxton, L. Bildsten, A. Dotter, F. Herwig, P. Lesaffre, and F. Timmes, *Modules for experiments in stellar astrophysics (mesa)*, *The Astrophysical Journal Supplement Series* **192** (Dec, 2010) 3.

[238] B. Kulebi, S. Jordan, E. Nelan, U. Bastian, and M. Altmann, *Constraints on the origin of the massive, hot, and rapidly rotating magnetic white dwarf RE J 0317-853 from an HST parallax measurement*, *Astron. Astrophys.* **524** (2010) A36, [arXiv:1007.4978].

[239] M. E. Camisassa, L. G. Althaus, A. H. Córsico, F. C. De Gerónimo, M. M. Miller Bertolami, M. L. Novarino, R. D. Rohrmann, F. C. Wachlin, and E. García-Berro, *The evolution of ultra-massive white dwarfs*, **625** (May, 2019) A87, [arXiv:1807.03894].

[240] A. G. A. Brown, A. Vallenari, T. Prusti, J. H. J. de Bruijne, C. Babusiaux, C. A. L. Bailer-Jones, M. Biermann, D. W. Evans, L. Eyer, and et al., *Gaia data release 2*, *Astronomy & Astrophysics* **616** (Aug, 2018) A1.

[241] S. Ichimaru, *Strongly coupled plasmas: high-density classical plasmas and degenerate electron liquids*, *Rev. Mod. Phys.* **54** (1982) 1017–1059.

[242] N. Itoh, H. Hayashi, A. Nishikawa, and Y. Kohyama, *Neutrino Energy Loss in Stellar Interiors. VII. Pair, Photo-, Plasma, Bremsstrahlung, and Recombination Neutrino Processes*, **102** (Feb., 1996) 411.

[243] S. Chang and K. Choi, *Hadronic axion window and the big bang nucleosynthesis*, *Phys. Lett. B* **316** (1993) 51–56, [hep-ph/9306216].

[244] M. Meyer, D. Horns, and M. Raue, *First lower limits on the photon-axion-like particle coupling from very high energy gamma-ray observations*, *Phys. Rev.* **D87** (2013), no. 3 035027, [arXiv:1302.1208].

[245] C. Dessert, J. W. Foster, and B. R. Safdi, *Hard X-ray Excess from the Magnificent Seven Neutron Stars*, *Astrophys. J.* **904** (2020), no. 1 42, [arXiv:1910.02956].

[246] **Lynx Team** Collaboration, *The Lynx Mission Concept Study Interim Report*, arXiv:1809.09642.

[247] M. Farina, D. Pappadopulo, F. Rompineve, and A. Tesi, *The photo-philic QCD axion*, *JHEP* **01** (2017) 095, [arXiv:1611.09855].

[248] L. Di Luzio, F. Mescia, and E. Nardi, *Window for preferred axion models*, *Phys. Rev. D* **96** (2017), no. 7 075003, [arXiv:1705.05370].

[249] L. Darmé, L. Di Luzio, M. Giannotti, and E. Nardi, *Selective enhancement of the QCD axion couplings*, *Phys. Rev. D* **103** (2021), no. 1 015034, [arXiv:2010.15846].

[250] A. V. Sokolov and A. Ringwald, *Photophilic hadronic axion from heavy magnetic monopoles*, arXiv:2104.02574.

[251] F. M. Walter, S. J. Wolk, and R. Neuhäuser, *Discovery of a nearby isolated neutron star*, *Nature* **379** (Jan., 1996) 233–235.

[252] F. Haberl, C. Motch, D. A. H. Buckley, F.-J. Zickgraf, and W. Pietsch, *RXJ0720.4-3125: strong evidence for an isolated pulsating neutron star.*, *Astron. Astrophys.* **326** (Oct., 1997) 662–668.

[253] F. Haberl, C. Motch, and W. Pietsch, *Isolated neutron stars in the ROSAT Survey*, *Astronomische Nachrichten* **319** (Jan, 1998) 97.

[254] A. D. Schwope, G. Hasinger, R. Schwarz, F. Haberl, and M. Schmidt, *The isolated neutron star candidate rbs1223 (1rxs j130848.6+212708)*, *Astron. Astrophys.* **341** (1999) L51, [astro-ph/9811326].

[255] C. Motch, F. Haberl, F. J. Zickgraf, G. Hasinger, and A. D. Schwope, *The isolated neutron star candidate rx j1605.3+3249*, *Astron. Astrophys.* **351** (1999) 177, [astro-ph/9907306].

[256] F. Haberl, W. Pietsch, and C. Motch, *Rx j0420.0-5022: an isolated neutron star candidate with evidence for 22.7 s x-ray pulsations*, *Astron. Astrophys.* **351** (1999) L53, [astro-ph/9911159].

[257] L. Zampieri, S. Campana, R. Turolla, M. Chieregato, R. Falomo, D. Fugazza, A. Moretti, and A. Treves, *1rxs j214303.7+065419/rbs 1774: a new isolated neutron star candidate*, *Astron. Astrophys.* **378** (2001) L5, [astro-ph/0108456].

[258] F. Haberl, *The magnificent seven: magnetic fields and surface temperature distributions*, *Astrophysics and Space Science* **308** (Apr, 2007) 181–190.

[259] V. M. Malofeev, O. I. Malov, and D. A. Teplykh, *Radio emission from AXP and XDINS*, *Astrophys. Space Sci.* **308** (Apr., 2007) 211–216.

[260] M. H. van Kerkwijk and D. L. Kaplan, *Isolated neutron stars: magnetic fields, distances,and spectra*, *Astrophysics and Space Science* **308** (Apr, 2007) 191–201.

[261] F. Haberl, A. D. Schwope, V. Hambaryan, G. Hasinger, and C. Motch, *A broad absorption feature in the x-ray spectrum of the isolated neutron star RBS1223 (1RXS J130848.6+212708)*, *Astron. Astrophys.* **403** (2003) L19, [astro-ph/0304088].

[262] D. Page, U. Geppert, and F. Weber, *The Cooling of compact stars*, *Nucl. Phys.* **A777** (2006) 497–530, [astro-ph/0508056].

[263] C. Motch, A. M. Pires, F. Haberl, and A. Schwope, *Measuring proper motions of isolated neutron stars with Chandra*, *Astrophys. Space Sci.* **308** (2007) 217–224, [astro-ph/0608589].

[264] S. Mishra-Sharma, M. Lisanti, N. L. Rodd, and B. R. Safdi, "Optimizing the search for extragalactic dark matter." to appear, 2017.

[265] "Users Guide to the XMM-Newton Science Analysis System", Issue 14.0, 2018 (ESA: XMM-Newton SOC).

[266] A. Fruscione, J. C. McDowell, G. E. Allen, N. S. Brickhouse, D. J. Burke, J. E. Davis, N. Durham, M. Elvis, E. C. Galle, D. E. Harris, D. P. Huenemoerder, J. C. Houck, B. Ishibashi, M. Karovska, F. Nicastro, M. S. Noble, M. A. Nowak, F. A. Primini, A. Siemiginowska, R. K. Smith, and M. Wise, *CIAO: Chandra's data analysis system*, in *Society of Photo-Optical Instrumentation Engineers (SPIE) Conference Series*, vol. 6270 of *Society of Photo-Optical Instrumentation Engineers (SPIE) Conference Series*, p. 62701V, Jun, 2006.

[267] J. E. Davis, M. W. Bautz, D. Dewey, R. K. Heilmann, J. C. Houck, D. P. Huenemoerder, H. L. Marshall, M. A. Nowak, M. L. Schattenburg, N. S. Schulz, and R. K. Smith, *Raytracing with MARX: x-ray observatory design, calibration, and support*, in *Space Telescopes and Instrumentation 2012: Ultraviolet to Gamma Ray*, vol. 8443 of *Proceedings of the SPIE*, p. 84431A, Sept., 2012.

[268] J. C. Houck and L. A. Denicola, *ISIS: An Interactive Spectral Interpretation System for High Resolution X-Ray Spectroscopy*, in *Astronomical Data Analysis Software and Systems IX* (N. Manset, C. Veillet, and D. Crabtree, eds.), vol. 216 of *Astronomical Society of the Pacific Conference Series*, p. 591, 2000.

[269] J. Wilms, A. Allen, and R. McCray, *On the Absorption of X-rays in the interstellar medium*, *Astrophys. J.* **542** (2000) 914–924, [astro-ph/0008425].

[270] T. Yoneyama, K. Hayashida, H. Nakajima, S. Inoue, and H. Tsunemi, *Discovery of a keV-X-ray excess in RX J1856.5–3754*, *Publ. Astron. Soc. Jap.* **69** (2017), no. 3 50, [arXiv:1703.05995].

[271] N. Sartore, A. Tiengo, S. Mereghetti, A. De Luca, R. Turolla, and F. Haberl, *Spectral monitoring of rx j1856.5-3754 with xmm-newton*, *Astron. Astrophys.* **541** (Apr, 2012) A66.

[272] K. A. Arnaud, *XSPEC: The First Ten Years*, in *Astronomical Data Analysis Software and Systems V* (G. H. Jacoby and J. Barnes, eds.), vol. 101 of *Astronomical Society of the Pacific Conference Series*, p. 17, 1996.

[273] A. Read, M. Guainazzi, and S. Sembay, *Cross-calibration of the XMM-Newton EPIC pn and MOS on-axis effective areas using 2XMM sources*, *Astron. Astrophys.* **564** (2014) A75, [arXiv:1403.3555].

[274] J. E. Davis, *Event pileup in charge-coupled devices*, *Astrophys. J.* **562** (nov, 2001) 575–582.

[275] V. E. Zavlin, *Theory of Radiative Transfer in Neutron Star Atmospheres and Its Applications*, pp. 181–211. Springer Berlin Heidelberg, Berlin, Heidelberg, 2009.

[276] A. Y. Potekhin, W. C. G. Ho, and G. Chabrier, *Atmospheres and radiating surfaces of neutron stars with strong magnetic fields*, *PoS* **MPCS2015** (2016) 016, [arXiv:1605.01281].

[277] D. G. Yakovlev, K. P. Levenfish, and Y. A. Shibanov, *Cooling neutron stars and superfluidity in their interiors*, *Phys. Usp.* **42** (1999) 737–778, [astro-ph/9906456].

[278] W. C. G. Ho, D. L. Kaplan, P. Chang, M. van Adelsberg, and A. Y. Potekhin, *Magnetic Hydrogen Atmosphere Models and the Neutron Star RX J1856.5-3754*, *Mon. Not. Roy. Astron. Soc.* **375** (2007) 821–830, [astro-ph/0612145].

[279] K. Mori and W. C. G. Ho, *Modelling mid-Z element atmospheres for strongly-magnetized neutron stars*, *Mon. Not. Roy. Astron. Soc.* **377** (2007) 905–919, [astro-ph/0611145].

[280] W. C. G. Ho, A. Y. Potekhin, and G. Chabrier, *Model X-ray Spectra of Magnetic Neutron Stars with Hydrogen Atmospheres*, *Astrophys. J. Suppl.* **178** (2008) 102–109, [arXiv:0802.2957].

[281] W. C. G. Ho, *NSMAXG: A new magnetic neutron star spectral model in XSPEC*, *IAU Symp.* **302** (2014) 435–438, [arXiv:1311.5583].

[282] C. P. de Vries, J. Vink, M. Mendez, and F. Verbunt, *Long - term variability in the x-ray emission of RX J0720.4-3125*, *Astron. Astrophys.* **415** (2004) L31, [astro-ph/0401028].

[283] M. M. Hohle, F. Haberl, J. Vink, V. Hambaryan, R. Turolla, S. Zane, C. P. de Vries, and M. Mendez, *Spectral and temporal variations of the isolated neutron star RX J0720.4-3125: new XMM-Newton observations*, *Astron. Astrophys.* **498** (2009) 811, [arXiv:0810.5319].

[284] M. M. Hohle, F. Haberl, J. Vink, C. P. de Vries, R. Turolla, S. Zane, and M. Méndez, *The continued spectral and temporal evolution of RX J0720.4-3125*, *Mon. Notices Royal Astron. Soc* **423** (Jun, 2012) 1194–1199, [arXiv:1203.3708].

[285] F. D. Seward and Z.-R. Wang, *Pulsars, X-ray synchrotron nebulae, and guest stars*, *Astrophys. J.* **332** (Sept., 1988) 199–205.

[286] K. S. Cheng, R. E. Taam, and W. Wang, *Pulsar wind nebulae and the x-ray emission of non-accreting neutron stars*, *Astrophys. J.* **617** (2004) 480–489, [astro-ph/0408460].

[287] B. Posselt, G. G. Pavlov, U. Ertan, S. Caliskan, K. L. Luhman, and C. C. Williams, *Discovery of extended infrared emission around the neutron star RX J0806.4-4123*, *Astrophys. J.* **865** (2018) 1, [arXiv:1809.08107].

[288] **Fermi-LAT** Collaboration, A. A. Abdo et al., *Fermi LAT Observations of the Vela Pulsar*, *Astrophys. J.* **696** (2009) 1084, [arXiv:0812.2960].

[289] V. Hambaryan, V. Suleimanov, A. D. Schwope, R. Neuhäuser, K. Werner, and A. Y. Potekhin, *Phase-resolved spectroscopic study of the isolated neutron star RBS 1223 (1RXS J130848.6+212708)*, *Astron. Astrophys.* **534** (Oct., 2011) A74.

[290] I. F. Malov and M. A. Timirkeeva, *On X-ray emission of radio pulsars*, *Mon. Not. Roy. Astron. Soc.* **485** (2019), no. 4 5319–5328, [arXiv:1808.07361].

[291] D. L. Kaplan, S. R. Kulkarni, and M. H. van Kerkwijk, *A Probable optical counterpart for the isolated neutron star RX J1308.6+2127*, *Astrophys. J.* **579** (2002) L29–L32, [astro-ph/0209519].

[292] D. L. Kaplan, S. R. Kulkarni, and M. H. van Kerkwijk, *The optical counterpart of the isolated neutron star RX J1605.3+3249*, *Astrophys. J.* **588** (2003) L33–L36, [astro-ph/0302370].

[293] D. L. Kaplan, M. H. van Kerkwijk, H. L. Marshall, B. A. Jacoby, S. R. Kulkarni, and D. A. Frail, *The Nearby neutron star RX J0720.4-3125 from radio to x-rays*, *Astrophys. J.* **590** (2003) 1008–1019, [astro-ph/0303126].

[294] A. Treves, R. Turolla, S. Zane, and M. Colpi, *Isolated neutron stars: accretors and coolers*, *Publ. Astron. Soc. Pac.* **112** (2000) 297, [astro-ph/9911430].

[295] H. Umeda, N. Iwamoto, S. Tsuruta, L. Qin, and K. Nomoto, *Axion mass limits from cooling neutron stars*, in *Workshop on Neutron Stars and Pulsars: Thirty Years After the Discovery Tokyo, Japan, November 17-20, 1997*, 1997. astro-ph/9806337.

[296] J. Keller and A. Sedrakian, *Axions from cooling compact stars*, *Nucl. Phys.* **A897** (2013) 62–69, [arXiv:1205.6940].

[297] L. B. Leinson, *Axion mass limit from observations of the neutron star in Cassiopeia A*, *JCAP* **1408** (2014) 031, [arXiv:1405.6873].

[298] A. Sedrakian, *Axion cooling of neutron stars*, *Phys. Rev.* **D93** (2016), no. 6 065044, [arXiv:1512.07828].

[299] A. Sedrakian, *Axion cooling of neutron stars. II. Beyond hadronic axions*, *Phys. Rev.* **D99** (2019), no. 4 043011, [arXiv:1810.00190].

[300] N. Iwamoto, *Axion Emission from Neutron Stars*, *Phys. Rev. Lett.* **53** (1984) 1198–1201.

[301] R. P. Brinkmann and M. S. Turner, *Numerical Rates for Nucleon-Nucleon Axion Bremsstrahlung*, *Phys. Rev.* **D38** (1988) 2338.

[302] D. L. Kaplan and M. H. van Kerkwijk, *Constraining the Spin-down of the Nearby Isolated Neutron Star RX J2143.0+0654*, *Astrophys. J.* **692** (2009) L62–L66, [arXiv:0901.4133].

[303] D. L. Kaplan and M. H. van Kerkwijk, *Constraining the Spin-down of the Nearby Isolated Neutron Star RX J0806.4-4123, and Implications for the Population of Nearby Neutron Stars*, *Astrophys. J.* **705** (2009) 798–808, [arXiv:0909.5218].

[304] J. Preskill, M. B. Wise, and F. Wilczek, *Cosmology of the Invisible Axion*, *Phys. Lett.* **120B** (1983) 127–132.

[305] L. F. Abbott and P. Sikivie, *A Cosmological Bound on the Invisible Axion*, *Phys. Lett.* **120B** (1983) 133–136.

[306] M. Dine and W. Fischler, *The Not So Harmless Axion*, *Phys. Lett.* **120B** (1983) 137–141.

[307] L. Hui, J. P. Ostriker, S. Tremaine, and E. Witten, *Ultralight scalars as cosmological dark matter*, *Phys. Rev.* **D95** (2017), no. 4 043541, [arXiv:1610.08297].

[308] M. J. Stott and D. J. E. Marsh, *Black hole spin constraints on the mass spectrum and number of axionlike fields*, *Phys. Rev.* **D98** (2018), no. 8 083006, [arXiv:1805.02016].

[309] J. Halverson, C. Long, B. Nelson, and G. Salinas, *Towards string theory expectations for photon couplings to axionlike particles*, *Phys. Rev. D* **100** (2019), no. 10 106010, [arXiv:1909.05257].

[310] J. Redondo, *Solar axion flux from the axion-electron coupling*, *JCAP* **1312** (2013) 008, [arXiv:1310.0823].

[311] N. Viaux, M. Catelan, P. B. Stetson, G. Raffelt, J. Redondo, A. A. R. Valcarce, and A. Weiss, *Neutrino and axion bounds from the globular cluster M5 (NGC 5904)*, *Phys. Rev. Lett.* **111** (2013) 231301, [arXiv:1311.1669].

[312] M. Giannotti, I. Irastorza, J. Redondo, and A. Ringwald, *Cool WISPs for stellar cooling excesses*, *JCAP* **1605** (2016), no. 05 057, [arXiv:1512.08108].

[313] T. D. Edwards, M. Chianese, B. J. Kavanagh, S. M. Nissanke, and C. Weniger, *Unique Multimessenger Signal of QCD Axion Dark Matter*, *Phys. Rev. Lett.* **124** (2020), no. 16 161101, [arXiv:1905.04686].

[314] R. Janish, V. Narayan, S. Rajendran, and P. Riggins, *Axion production and detection with superconducting RF cavities*, *Phys. Rev.* **D100** (2019), no. 1 015036, [arXiv:1904.07245].

[315] M. Lawson, A. J. Millar, M. Pancaldi, E. Vitagliano, and F. Wilczek, *Tunable axion plasma haloscopes*, *Phys. Rev. Lett.* **123** (2019), no. 14 141802, [arXiv:1904.11872].

[316] M. Bauer, M. Neubert, and A. Thamm, *Collider Probes of Axion-Like Particles*, *JHEP* **12** (2017) 044, [arXiv:1708.00443].

[317] D. G. Yakovlev and K. P. Levenfish, *Modified URCA process in neutron star cores.*, *Astron. Astrophys.* **297** (May, 1995) 717.

[318] D. Page, "NSCool: Neutron star cooling code." Astrophysics Source Code Library, Sept., 2016.

[319] A. Akmal, V. R. Pandharipande, and D. G. Ravenhall, *The Equation of state of nucleon matter and neutron star structure*, *Phys. Rev.* **C58** (1998) 1804–1828, [nucl-th/9804027].

[320] A. Y. Potekhin, D. G. Yakovlev, G. Chabrier, and O. Y. Gnedin, *Thermal structure and cooling of superfluid magnetic neutron stars*, *Astrophys. J.* **594** (2003) 404–418, [astro-ph/0305256].

[321] J. F. Perez-Azorin, J. A. Miralles, and J. A. Pons, *Anisotropic thermal emission from magnetized neutron stars*, *Astron. Astrophys.* **451** (2006) 1009–1024, [astro-ph/0510684].

[322] A. M. Beloborodov and X. Li, *Magnetar heating*, *Astrophys. J.* **833** (2016), no. 2 261, [arXiv:1605.09077].

[323] F. Haberl, C. Motch, V. E. Zavlin, K. Reinsch, B. T. Gaensicke, M. Cropper, A. D. Schwope, R. Turolla, and S. Zane, *The Isolated neutron star x-ray pulsars RX J0420.0-5022 and RX J0806.4-4123: New x-ray and optical observations*, *Astron. Astrophys.* **424** (2004) 635, [astro-ph/0405485].

[324] N. Sartore, A. Tiengo, S. Mereghetti, A. De Luca, R. Turolla, and F. Haberl, *Spectral monitoring of RX J1856.5-3754 with XMM-Newton. Analysis of EPIC-pn data*, *Astron. Astrophys.* **541** (May, 2012) A66, [arXiv:1202.2121].

[325] N. Tetzlaff, T. Eisenbeiss, R. Neuhäuser, and M. M. Hohle, *The origin of RX J1856.5-3754 and RX J0720.4-3125 - updated using new parallax measurements*, *MNRAS* **417** (Oct, 2011) 617–626, [arXiv:1107.1673].

[326] A. M. Pires, A. D. Schwope, F. Haberl, V. E. Zavlin, C. Motch, and S. Zane, *A deep XMM-Newton look on the thermally emitting isolated neutron star RX J1605.3+3249*, *Astron. Astrophys.* **623** (2019) A73, [arXiv:1901.08533].

[327] A. D. Schwope, T. Erben, J. Kohnert, G. Lamer, M. Steinmetz, K. Strassmeier, H. Zinnecker, J. Bechtold, E. Diolaiti, A. Fontana, S. Gallozzi, E. Giallongo, R. Ragazzoni, C. de Santis, and V. Testa, *The isolated neutron star RBS1774 revisited. Revised XMM-Newton X-ray parameters and an optical counterpart from deep LBT-observations*, *Astron. Astrophys.* **499** (May, 2009) 267–272, [arXiv:0902.4110].

[328] **Particle Data Group** Collaboration, P. Zyla et al., *Review of Particle Physics*, *PTEP* **2020** (2020), no. 8 083C01.

[329] N. Bar, K. Blum, and G. D'Amico, *Is there a supernova bound on axions?*, *Phys. Rev. D* **101** (2020), no. 12 123025, [arXiv:1907.05020].

[330] V. I. Kondratiev, M. A. McLaughlin, D. R. Lorimer, M. Burgay, A. Possenti, R. Turolla, S. B. Popov, and S. Zane, *New Limits on Radio Emission from X-ray Dim Isolated Neutron Stars*, *Astrophys. J.* **702** (Sep, 2009) 692–706, [arXiv:0907.0054].

[331] D. Barret et al., *The Athena X-ray Integral Field Unit (X-IFU)*, *Proc. SPIE Int. Soc. Opt. Eng.* **9905** (2016) 99052F, [arXiv:1608.08105].

[332] M. C. D. Marsh, H. R. Russell, A. C. Fabian, B. P. McNamara, P. Nulsen, and C. S. Reynolds, *A New Bound on Axion-Like Particles*, *JCAP* **1712** (2017), no. 12 036, [arXiv:1703.07354].

[333] **ALPS** Collaboration, A. Spector, *ALPS II technical overview and status report*, in *Proceedings, 12th Patras Workshop on Axions, WIMPs and WISPs (PATRAS 2016): Jeju Island, South Korea, June 20-24, 2016*, pp. 133–136, 2017. arXiv:1611.05863.

[334] **IAXO** Collaboration, E. Armengaud et al., *Physics potential of the International Axion Observatory (IAXO)*, *JCAP* **1906** (2019), no. 06 047, [arXiv:1904.09155].

[335] H. Primakoff, *Photoproduction of neutral mesons in nuclear electric fields and the mean life of the neutral meson*, *Phys. Rev.* **81** (1951) 899.

[336] G. G. Raffelt, *Astrophysical axion bounds diminished by screening effects*, *Phys. Rev. D* **33** (Feb, 1986) 897–909.

[337] F. A. Harrison et al., *The Nuclear Spectroscopic Telescope Array (NuSTAR) High-Energy X-Ray Mission*, *Astrophys. J.* **770** (2013) 103, [arXiv:1301.7307].

[338] E. D. Carlson, *Pseudoscalar conversion and X-rays from stars*, *Physics Letters B* **344** (Feb., 1995) 245–251.

[339] M. Giannotti, *Fermi-LAT and NuSTAR as Stellar Axionscopes*, in *13th Patras Workshop on Axions, WIMPs and WISPs*, pp. 23–27, 2018. arXiv:1711.00345.

[340] M. Meyer, M. Giannotti, A. Mirizzi, J. Conrad, and M. Sánchez-Conde, *Fermi Large Area Telescope as a Galactic Supernovae Axionscope*, *Phys. Rev. Lett.* **118** (2017), no. 1 011103, [arXiv:1609.02350].

[341] G. G. Raffelt, *Plasmon decay into low-mass bosons in stars*, *Phys. Rev. D* **37** (Mar, 1988) 1356–1359.

[342] B. Paxton, L. Bildsten, A. Dotter, F. Herwig, P. Lesaffre, and F. Timmes, *Modules for Experiments in Stellar Astrophysics (MESA)*, *ApJS* **192** (Jan., 2011) 3, [arXiv:1009.1622].

[343] B. Paxton, M. Cantiello, P. Arras, L. Bildsten, E. F. Brown, A. Dotter, C. Mankovich, M. H. Montgomery, D. Stello, F. X. Timmes, and R. Townsend, *Modules for Experiments in Stellar Astrophysics (MESA): Planets, Oscillations, Rotation, and Massive Stars*, *ApJS* **208** (Sept., 2013) 4, [arXiv:1301.0319].

[344] F. Najarro, D. F. Figer, D. Hillier, T. Geballe, and R. P. Kudritzki, *Metallicity in the Galactic Center: The Quintuplet cluster*, *Astrophys. J.* **691** (2009) 1816–1827, [arXiv:0809.3185].

[345] I. Hunter, D. Lennon, P. Dufton, C. Trundle, S. Simon-Diaz, S. Smartt, R. Ryans, and C. Evans, *The VLT-FLAMES survey of massive stars: Atmospheric parameters and rotational velocity distributions for B-type stars in the Magellanic Clouds*, *Astron. Astrophys.* **479** (2008) 541, [arXiv:0711.2264].

[346] I. Brott et al., *Rotating Massive Main-Sequence Stars II: Simulating a Population of LMC early B-type Stars as a Test of Rotational Mixing*, *Astron. Astrophys.* **530** (2011) A116, [arXiv:1102.0766].

[347] P. Kroupa, *On the variation of the initial mass function*, *Mon. Not. Roy. Astron. Soc.* **322** (2001) 231, [astro-ph/0009005].

[348] C. Weidner and J. S. Vink, *The masses, and the mass discrepancy of o-type stars*, *Astron. Astrophys.* **524** (Nov, 2010) A98.

[349] W.-R. Hamann, G. Graefener, and A. Liermann, *The Galactic WN stars: Spectral analyses with line-blanketed model atmospheres versus stellar evolution models with and without rotation*, *Astron. Astrophys.* **457** (2006) 1015, [astro-ph/0608078].

[350] J. S. Clark, M. E. Lohr, L. R. Patrick, F. Najarro, H. Dong, and D. F. Figer, *An updated stellar census of the quintuplet cluster*, *Astron. Astrophys.* **618** (Oct, 2018) A2.

[351] M. Aghakhanloo, J. W. Murphy, N. Smith, J. Parejko, M. Díaz-Rodríguez, M. R. Drout, J. H. Groh, J. Guzman, and K. G. Stassun, *Inferring the parallax of Westerlund 1 from Gaia DR2*, *MNRAS* **492** (Feb., 2020) 2497–2509, [arXiv:1901.06582].

[352] B. Davies and E. R. Beasor, *The distances to star clusters hosting Red Supergiants: χ Per, NGC 7419, and Westerlund 1*, *MNRAS* **486** (June, 2019) L10–L14, [arXiv:1903.12506].

[353] J. Clark, B. W. Ritchie, and I. Negueruela, *A vlt/flames survey for massive binaries in westerlund 1. vii. cluster census*, *Astron. Astrophys.* (Nov, 2019).

[354] A. E. Piatti, E. Bica, and J. J. Claria, *Fundamental parameters of the highly reddened young open clusters Westerlund 1 and 2*, *A&AS* **127** (Feb., 1998) 423–432.

[355] Q. D. Wang, H. Dong, and C. Lang, *The interplay between star formation and the nuclear environment of our Galaxy: deep X-ray observations of the Galactic centre Arches and Quintuplet clusters*, *MNRAS* **371** (Sept., 2006) 38–54, [astro-ph/0606282].

[356] R. Jansson and G. R. Farrar, *A New Model of the Galactic Magnetic Field*, *ApJ* **757** (Sep, 2012) 14, [arXiv:1204.3662].

[357] R. Jansson and G. R. Farrar, *The galactic magnetic field*, *The Astrophysical Journal* **761** (nov, 2012) L11.

[358] J. M. Yao, R. N. Manchester, and N. Wang, *A new electron-density model for estimation of pulsar and frb distances*, *The Astrophysical Journal* **835** (Jan, 2017) 29.

[359] J. M. Cordes and T. J. W. Lazio, *NE2001. 1. A New model for the galactic distribution of free electrons and its fluctuations*, astro-ph/0207156.

[360] M. S. Pshirkov, P. G. Tinyakov, P. P. Kronberg, and K. J. Newton-McGee, *Deriving the Global Structure of the Galactic Magnetic Field from Faraday Rotation Measures of Extragalactic Sources*, *ApJ* **738** (Sept., 2011) 192, [arXiv:1103.0814].

[361] V. V. Izmodenov and D. B. Alexashov, *Magnitude and direction of the local interstellar magnetic field inferred from Voyager 1 and 2 interstellar data and global heliospheric model*, *A&A* **633** (Jan., 2020) L12, [arXiv:2001.03061].

[362] E. J. Zirnstein, J. Heerikhuisen, H. O. Funsten, G. Livadiotis, D. J. McComas, and N. V. Pogorelov, *Local Interstellar Magnetic Field Determined from the Interstellar Boundary Explorer Ribbon*, *ApJL* **818** (Feb., 2016) L18.

[363] P. C. Frisch, B. G. Andersson, A. Berdyugin, H. O. Funsten, A. M. Magalhaes, D. J. McComas, V. Piirola, N. A. Schwadron, J. D. Slavin, and S. J. Wiktorowicz, *Comparisons of the Interstellar Magnetic Field Directions Obtained from the IBEX Ribbon and Interstellar Polarizations*, *ApJ* **724** (Dec., 2010) 1473–1479, [arXiv:1009.5118].

[364] M. Salvati, *The local Galactic magnetic field in the direction of Geminga*, *A&A* **513** (Apr., 2010) A28, [arXiv:1001.4947].

[365] K. Ferriere, *Interstellar magnetic fields in the Galactic center region*, *Astron. Astrophys.* **505** (2009) 1183, [arXiv:0908.2037].

[366] R. M. Crocker, D. I. Jones, F. Melia, J. Ott, and R. J. Protheroe, *A lower limit of 50 microgauss for the magnetic field near the galactic centre*, *Nature* **463** (Jan, 2010) 65–67.

[367] R. M. Crocker, D. I. Jones, F. Aharonian, C. J. Law, F. Melia, T. Oka, and J. Ott, *Wild at heart: the particle astrophysics of the galactic centre*, *Monthly Notices of the Royal Astronomical Society* **413** (Mar, 2011) 763–788.

[368] M. Guenduez, J. Becker Tjus, K. Ferrière, and R.-J. Dettmar, *A novel analytical model of the magnetic field configuration in the Galactic Center*, arXiv:1906.05211.

[369] K. Mori et al., *NuSTAR Hard X-ray Survey of the Galactic Center Region. I. Hard X-ray Morphology and Spectroscopy of the Diffuse Emission*, *Astrophys. J.* **814** (2015), no. 2 94, [arXiv:1510.04631].

[370] J. Hong et al., *NuSTAR Hard X-ray Survey of the Galactic Center Region II: X-ray Point Sources*, *Astrophys. J.* **825** (2016), no. 2 132, [arXiv:1605.03882].

[371] J. K. Blackburn, R. A. Shaw, H. E. Payne, J. J. E. Hayes, and Heasarc, *FTOOLS: A general package of software to manipulate FITS files*, Dec., 1999.

[372] D. Porquet, J. Rodriguez, S. Corbel, P. Goldoni, R. Warwick, A. Goldwurm, and A. Decourchelle, *Xmm-newton study of the persistent x-ray source 1e1743.1-2843 located in the galactic center direction*, *Astron. Astrophys.* **406** (2003) 299–304, [astro-ph/0305489].

[373] D. R. Wik et al., *NuSTAR Observations of the Bullet Cluster: Constraints on Inverse Compton Emission*, *Astrophys. J.* **792** (2014), no. 1 48, [arXiv:1403.2722].

[374] A. Borghese et al., *The multi-outburst activity of the magnetar in Westerlund I*, *Mon. Not. Roy. Astron. Soc.* **484** (2019), no. 3 2931–2943, [arXiv:1901.02026].

[375] K. K. Madsen, F. E. Christensen, W. W. Craig, K. W. Forster, B. W. Grefenstette, F. A. Harrison, H. Miyasaka, and V. Rana, *Observational Artifacts of NuSTAR: Ghost Rays and Stray Light*, *arXiv e-prints* (Nov., 2017) arXiv:1711.02719, [arXiv:1711.02719].

[376] H. An, K. K. Madsen, N. J. Westergaard, S. E. Boggs, F. E. Christensen, W. W. Craig, C. J. Hailey, F. A. Harrison, D. K. Stern, and W. W. Zhang, *In-flight PSF calibration of the NuSTAR hard X-ray optics*, *Proc. SPIE Int. Soc. Opt. Eng.* **9144** (2014) 91441Q, [arXiv:1406.7419].

[377] J. H. Chang, R. Essig, and S. D. McDermott, *Revisiting Supernova 1987A Constraints on Dark Photons*, *JHEP* **01** (2017) 107, [arXiv:1611.03864].

[378] M. Giannotti, B. Grefenstette, A. Mirizzi, M. Nynka, K. Perez, B. Roach, O. Straiero, and M. Xiao, "Constraints on light axions from a hard x-ray observation of betelgeuse." To appear 2020.

[379] P. Sikivie, *Invisible Axion Search Methods*, *Rev. Mod. Phys.* **93** (2021), no. 1 015004, [arXiv:2003.02206].

[380] G. Grilli di Cortona, E. Hardy, J. Pardo Vega, and G. Villadoro, *The QCD axion, precisely*, *JHEP* **01** (2016) 034, [arXiv:1511.02867].

[381] A. Arvanitaki and S. Dubovsky, *Exploring the String Axiverse with Precision Black Hole Physics*, *Phys. Rev.* **D83** (2011) 044026, [arXiv:1004.3558].

[382] V. Cardoso, O. J. C. Dias, G. S. Hartnett, M. Middleton, P. Pani, and J. E. Santos, *Constraining the mass of dark photons and axion-like particles through black-hole superradiance*, *JCAP* **03** (2018) 043, [arXiv:1801.01420].

[383] **ADMX** Collaboration, S. J. Asztalos et al., *Large scale microwave cavity search for dark matter axions*, *Phys. Rev. D* **64** (2001) 092003.

[384] **HAYSTAC** Collaboration, K. M. Backes et al., *A quantum-enhanced search for dark matter axions*, *Nature* **590** (2021), no. 7845 238–242, [arXiv:2008.01853].

[385] A. Garcon et al., *The Cosmic Axion Spin Precession Experiment (CASPEr): a dark-matter search with nuclear magnetic resonance*, arXiv:1707.05312.

[386] D. Aybas et al., *Search for Axionlike Dark Matter Using Solid-State Nuclear Magnetic Resonance*, *Phys. Rev. Lett.* **126** (2021), no. 14 141802, [arXiv:2101.01241].

[387] **MADMAX** Collaboration, P. Brun et al., *A new experimental approach to probe QCD axion dark matter in the mass range above 40 μeV*, *Eur. Phys. J. C* **79** (2019), no. 3 186, [arXiv:1901.07401].

[388] A. Arvanitaki and A. A. Geraci, *Resonantly Detecting Axion-Mediated Forces with Nuclear Magnetic Resonance*, *Phys. Rev. Lett.* **113** (2014), no. 16 161801, [arXiv:1403.1290].

[389] **ARIADNE** Collaboration, A. A. Geraci et al., *Progress on the ARIADNE axion experiment*, *Springer Proc. Phys.* **211** (2018) 151–161, [arXiv:1710.05413].

[390] J. Schütte-Engel, D. J. E. Marsh, A. J. Millar, A. Sekine, F. Chadha-Day, S. Hoof, M. N. Ali, K.-C. Fong, E. Hardy, and L. Smejkal, *Axion quasiparticles for axion dark matter detection*, *JCAP* **08** (2021) 066, [arXiv:2102.05366].

[391] R. T. Co, L. J. Hall, K. Harigaya, K. A. Olive, and S. Verner, *Axion Kinetic Misalignment and Parametric Resonance from Inflation*, *JCAP* **08** (2020) 036, [arXiv:2004.00629].

[392] M. Gorghetto, E. Hardy, and G. Villadoro, *More Axions from Strings*, *SciPost Phys.* **10** (2021) 050, [arXiv:2007.04990].

[393] D. G. Yakovlev, A. D. Kaminker, O. Y. Gnedin, and P. Haensel, *Neutrino emission from neutron stars*, *Phys. Rept.* **354** (2001) 1, [astro-ph/0012122].

[394] N. Iwamoto, *Nucleon-nucleon bremsstrahlung of axions and pseudoscalar particles from neutron star matter*, *Phys. Rev.* **D64** (2001) 043002.

[395] T. Fischer, S. Chakraborty, M. Giannotti, A. Mirizzi, A. Payez, and A. Ringwald, *Probing axions with the neutrino signal from the next galactic supernova*, *Phys. Rev.* **D94** (2016), no. 8 085012, [arXiv:1605.08780].

[396] J. H. Chang, R. Essig, and S. D. McDermott, *Supernova 1987A Constraints on Sub-GeV Dark Sectors, Millicharged Particles, the QCD Axion, and an Axion-like Particle*, arXiv:1803.00993.

[397] P. Carenza, T. Fischer, M. Giannotti, G. Guo, G. Martínez-Pinedo, and A. Mirizzi, *Improved axion emissivity from a supernova via nucleon-nucleon bremsstrahlung*, *JCAP* **10** (2019), no. 10 016, [arXiv:1906.11844]. [Erratum: JCAP 05, E01 (2020)].

[398] P. Carenza, B. Fore, M. Giannotti, A. Mirizzi, and S. Reddy, *Enhanced Supernova Axion Emission and its Implications*, *Phys. Rev. Lett.* **126** (2021), no. 7 071102, [arXiv:2010.02943].

[399] D. Page, M. Prakash, J. M. Lattimer, and A. W. Steiner, *Rapid Cooling of the Neutron Star in Cassiopeia A Triggered by Neutron Superfluidity in Dense Matter*, *Phys. Rev. Lett.* **106** (2011) 081101, [arXiv:1011.6142].

[400] P. S. Shternin, D. G. Yakovlev, C. O. Heinke, W. C. G. Ho, and D. J. Patnaude, *Cooling neutron star in the Cassiopeia A supernova remnant: evidence for superfluidity in the core*, *MNRAS* **412** (Mar., 2011) L108–L112, [arXiv:1012.0045].

[401] L. B. Leinson, *Superfluid phases of triplet pairing and rapid cooling of the neutron star in Cassiopeia A*, *Phys. Lett. B* **741** (2015) 87–91, [arXiv:1411.6833].

[402] K. Hamaguchi, N. Nagata, K. Yanagi, and J. Zheng, *Limit on the Axion Decay Constant from the Cooling Neutron Star in Cassiopeia A*, *Phys. Rev.* **D98** (2018), no. 10 103015, [arXiv:1806.07151].

[403] L. B. Leinson, *Impact of axions on the Cassiopea A neutron star cooling*, arXiv:2105.14745.

[404] H. Suzuki, A. Bamba, and S. Shibata, *Quantitative Age Estimation of Supernova Remnants and Associated Pulsars*, *Astrophys. J.* **914** (2021), no. 2 103, [arXiv:2104.10052].

[405] R. P. Mignani, D. Vande Putte, M. Cropper, R. Turolla, S. Zane, L. J. Pellizza, L. A. Bignone, N. Sartore, and A. Treves, *The birthplace and age of the isolated neutron star RX J1856.5-3754*, *Mon. Not. Roy. Astron. Soc.* **429** (Mar, 2013) 3517–3521, [arXiv:1212.3141].

[406] N. Tetzlaff, J. G. Schmidt, M. M. Hohle, and R. Neuhäuser, *Neutron Stars From Young Nearby Associations: The Origin of RX J1605.3+3249*, *Publications of the Astron. Soc. of Australia* **29** (Mar., 2012) 98–108, [arXiv:1202.1388].

[407] M. V. Beznogov, A. Y. Potekhin, and D. G. Yakovlev, *Heat blanketing envelopes of neutron stars*, *Phys. Rept.* **919** (2021) 1–68, [arXiv:2103.12422].

[408] S. Zharikov, D. Zyuzin, Y. Shibanov, A. Kirichenko, R. E. Mennickent, S. Geier, and A. Cabrera-Lavers, *PSR B0656+14: the unified outlook from the infrared to X-rays*, *Mon. Not. Roy. Astron. Soc.* **502** (2021), no. 2 2005–2022, [arXiv:2101.07459].

[409] L. Di Luzio, M. Giannotti, E. Nardi, and L. Visinelli, *The landscape of QCD axion models*, *Phys. Rept.* **870** (2020) 1–117, [arXiv:2003.01100].

[410] E. Flowers, M. Ruderman, and P. Sutherland, *Neutrino pair emission from finite-temperature neutron superfluid and the cooling of young neutron stars.*, *ApJ* **205** (Apr, 1976) 541–544.

[411] A. V. Senatorov and D. N. Voskresensky, *Collective excitations in nucleonic matter and the problem of cooling of neutron stars*, *Physics Letters B* **184** (Jan, 1987) 119–124.

[412] T. Fischer, *The role of medium modifications for neutrino-pair processes from nucleon-nucleon bremsstrahlung - Impact on the protoneutron star deleptonization*, *Astron. Astrophys.* **593** (2016) A103, [arXiv:1608.05004].

[413] R. Balkin, J. Serra, K. Springmann, and A. Weiler, *The QCD axion at finite density*, *JHEP* **07** (2020) 221, [arXiv:2003.04903].

[414] A. Y. Potekhin, G. Chabrier, and D. G. Yakovlev, *Internal temperatures and cooling of neutron stars with accreted envelopes*, *Astron. Astrophys.* **323** (1997) 415, [astro-ph/9706148].

[415] A. Akmal, V. R. Pandharipande, and D. G. Ravenhall, *Equation of state of nucleon matter and neutron star structure*, *Phys. Rev. C* **58** (Sep, 1998) 1804–1828.

[416] J. M. Pearson, N. Chamel, A. Y. Potekhin, A. F. Fantina, C. Ducoin, A. K. Dutta, and S. Goriely, *Unified equations of state for cold non-accreting neutron stars with Brussels–Montreal functionals – I. Role of symmetry energy*, *Mon. Not. Roy. Astron. Soc.* **481** (2018), no. 3 2994–3026, [arXiv:1903.04981]. [Erratum: Mon.Not.Roy.Astron.Soc. 486, 768 (2019)].

[417] A. Schwenk, B. Friman, and G. E. Brown, *Renormalization group approach to neutron matter: Quasiparticle interactions, superfluid gaps and the equation of state*, *Nucl. Phys.* **A713** (2003) 191–216, [nucl-th/0207004].

[418] M. Baldo, J. Cugnon, A. Lejeune, and U. Lombardo, *Proton and neutron superfluidity in neutron star matter*, *Nuclear Physics A* **536** (1992), no. 2 349 – 365.

[419] A. Sedrakian and J. W. Clark, *Superfluidity in nuclear systems and neutron stars*, *Eur. Phys. J. A* **55** (2019), no. 9 167, [arXiv:1802.00017].

[420] O. Straniero, A. Ayala, M. Giannotti, A. Mirizzi, and I. Dominguez, *Axion-Photon Coupling: Astrophysical Constraints*, in *11th Patras Workshop on Axions, WIMPs and WISPs*, pp. 77–81, 2015.

[421] **IAXO** Collaboration, E. Armengaud et al., *Physics potential of the International Axion Observatory (IAXO)*, *JCAP* **06** (2019) 047, [arXiv:1904.09155].

[422] L. Di Luzio, M. Fedele, M. Giannotti, F. Mescia, and E. Nardi, *Stellar Evolution confronts Axion Models*, arXiv:2109.10368.

[423] D. N. Aguilera, J. A. Pons, and J. A. Miralles, *2D Cooling of Magnetized Neutron Stars*, *Astron. Astrophys.* **486** (2008) 255–271, [arXiv:0710.0854].

[424] A. Y. Potekhin and G. Chabrier, *Magnetic neutron star cooling and microphysics*, *Astron. Astrophys.* **609** (2018) A74, [arXiv:1711.07662].

[425] K. Ehret et al., *New ALPS Results on Hidden-Sector Lightweights*, *Phys. Lett. B* **689** (2010) 149–155, [arXiv:1004.1313].

[426] E. Armengaud et al., *Conceptual Design of the International Axion Observatory (IAXO)*, *JINST* **9** (2014) T05002, [arXiv:1401.3233].

[427] J. H. Matthews, C. S. Reynolds, M. C. D. Marsh, J. Sisk-Reynés, and P. E. Rodman, *How do Magnetic Field Models Affect Astrophysical Limits on Light Axion-like Particles? An X-ray Case Study with NGC 1275*, arXiv:2202.08875.

[428] A. Domínguez, M. A. Sánchez-Conde, and F. Prada, *Axion-like particle imprint in cosmological very-high-energy sources*, **2011** (Nov., 2011) 020, [arXiv:1106.1860].

[429] W. Essey and A. Kusenko, *On weak redshift dependence of gamma-ray spectra of distant blazars*, *Astrophys. J. Lett.* **751** (2012) L11, [arXiv:1111.0815].

[430] D. Horns and M. Meyer, *Indications for a pair-production anomaly from the propagation of VHE gamma-rays*, *J. Cosmol. Astropart. Phys.* **1202** (2012) 033, [arXiv:1201.4711].

[431] G. I. Rubtsov and S. V. Troitsky, *Breaks in gamma-ray spectra of distant blazars and transparency of the Universe*, *JETP Lett.* **100** (2014), no. 6 355–359, [arXiv:1406.0239].

[432] K. Kohri and H. Kodama, *Axion-Like Particles and Recent Observations of the Cosmic Infrared Background Radiation*, *Phys. Rev. D* **96** (2017), no. 5 051701, [arXiv:1704.05189].

[433] J. Biteau and D. A. Williams, *The extragalactic background light, the Hubble constant, and anomalies: conclusions from 20 years of TeV gamma-ray observations*, *Astrophys. J.* **812** (2015), no. 1 60, [arXiv:1502.04166].

[434] A. Domínguez and M. Ajello, *Spectral analysis of Fermi-LAT blazars above 50 GeV*, *Astrophys. J. Lett.* **813** (2015), no. 2 L34, [arXiv:1510.07913].

[435] R. Gill and J. S. Heyl, *Constraining the photon-axion coupling constant with magnetic white dwarfs*, *Physical Review D* **84** (Oct, 2011).

[436] P. Jain, S. Panda, and S. Sarala, *Electromagnetic polarization effects due to axion photon mixing*, *Phys. Rev. D* **66** (2002) 085007, [hep-ph/0206046].

[437] A. Payez, J. R. Cudell, and D. Hutsemekers, *On the circular polarisation of light from axion-photon mixing*, *AIP Conf. Proc.* **1241** (2010), no. 1 444–449, [arXiv:0911.3145].

[438] N. Agarwal, A. Kamal, and P. Jain, *Alignments in quasar polarizations: Pseudoscalar-photon mixing in the presence of correlated magnetic fields*, *Phys. Rev. D* **83** (2011) 065014, [arXiv:0911.0429].

[439] A. Payez, J. R. Cudell, and D. Hutsemekers, *Can axion-like particles explain the alignments of the polarisations of light from quasars?*, *Phys. Rev. D* **84** (2011) 085029, [arXiv:1107.2013].

[440] N. Agarwal, P. K. Aluri, P. Jain, U. Khanna, and P. Tiwari, *A complete 3D numerical study of the effects of pseudoscalar-photon mixing on quasar polarizations*, *Eur. Phys. J. C* **72** (2012) 1928, [arXiv:1108.3400].

[441] A. Payez, J. R. Cudell, and D. Hutsemekers, *New polarimetric constraints on axion-like particles*, *JCAP* **07** (2012) 041, [arXiv:1204.6187].

[442] E. Masaki, A. Aoki, and J. Soda, *Photon-Axion Conversion, Magnetic Field Configuration, and Polarization of Photons*, *Phys. Rev. D* **96** (2017), no. 4 043519, [arXiv:1702.08843].

[443] G. Galanti, *Photon-ALP interaction as a measure of photon polarization*, arXiv:2202.10315.

[444] K. Dolag, D. Grasso, V. Springel, and I. Tkachev, *Constrained simulations of the magnetic field in the local Universe and the propagation of UHECRs*, *JCAP* **01** (2005) 009, [astro-ph/0410419].

[445] K. Dolag, M. Kachelriess, S. Ostapchenko, and R. Tomas, *Lower limit on the strength and filling factor of extragalactic magnetic fields*, *Astrophys. J. Lett.* **727** (2011) L4, [arXiv:1009.1782].

[446] F. Marinacci et al., *First results from the IllustrisTNG simulations: radio haloes and magnetic fields*, *Mon. Not. Roy. Astron. Soc.* **480** (2018), no. 4 5113–5139, [arXiv:1707.03396].

[447] F. Vazza, M. Brüggen, C. Gheller, S. Hackstein, D. Wittor, and P. M. Hinz, *Simulations of extragalactic magnetic fields and of their observables*, *Class. Quant. Grav.* **34** (2017), no. 23 234001, [arXiv:1711.02669].

[448] A. A. Garcia, K. Bondarenko, A. Boyarsky, D. Nelson, A. Pillepich, and A. Sokolenko, *Magnetization of the intergalactic medium in the IllustrisTNG simulations: the importance of extended, outflow-driven bubbles*, *Mon. Not. Roy. Astron. Soc.* **505** (2021), no. 4 5038–5057, [arXiv:2011.11581].

[449] W. Heisenberg and H. Euler, *Consequences of Dirac Theory of the Positron*, *arXiv e-prints* (May, 2006) physics/0605038, [physics/0605038].

[450] C. Dessert, A. J. Long, and B. R. Safdi, *X-ray signatures of axion conversion in magnetic white dwarf stars*, *Physical Review Letters* **123** (Aug, 2019).

[451] H. W. Babcock, *The 34-KILOGAUSS Magnetic Field of HD 215441.*, **132** (Nov., 1960) 521.

[452] F. K. Lamb and P. G. Sutherland, *Continuum polarization in magnetic white dwarfs*, *Symposium - International Astronomical Union* **53** (1974) 265–285.

[453] J. Angel, *Magnetism in white dwarfs*, *The Astrophysical Journal* **216** (1977) 1–17.

[454] G. Valyavin, D. Shulyak, G. A. Wade, K. Antonyuk, S. V. Zharikov, G. A. Galazutdinov, S. Plachinda, S. Bagnulo, L. Fox Machado, M. Alvarez, D. M. Clark, J. M. Lopez, D. Hiriart, I. Han, Y.-B. Jeon, C. Zurita, R. Mujica, T. Burlakova, T. Szeifert, and A. Burenkov, *Suppression of cooling by strong magnetic fields in white dwarf stars*, **515** (Nov., 2014) 88–91.

[455] F. Euchner, S. Jordan, K. Beuermann, B. T. Gaensicke, and F. V. Hessmann, *Zeeman tomography of magnetic white dwarfs, I. reconstruction of the field geometry from synthetic spectra*, *Astron. Astrophys.* **390** (2002) 633, [astro-ph/0205294].

[456] S. Jordan, *Models of white dwarfs with high magnetic fields.*, **265** (Nov., 1992) 570–576.

[457] N. Merani, J. Main, and G. Wunner, *Balmer and Paschen bound-free opacities for hydrogen in strong white dwarf magnetic fields.*, **298** (June, 1995) 193.

[458] L. B. Zhao and P. C. Stancil, *Hydrogen Photoionization Cross Sections for Strong-Field Magnetic White Dwarfs*, **667** (Oct., 2007) 1119–1125.

[459] L. B. Zhao, *Lyman and Balmer Continuum Spectra for Hydrogen Atoms in Strong White Dwarf Magnetic Fields*, **254** (June, 2021) 21.

[460] C. Schimeczek and G. Wunner, *Atomic Data for the Spectral Analysis of Magnetic DA White Dwarfs in the SDSS*, **212** (June, 2014) 26.

[461] F. Lamb and P. Sutherland, *Line spectra and continuum polarization in magnetic white dwarfs*, in *Line Formation in the Presence of Magnetic Fields*, p. 183, 1972.

[462] L. D. Landau and E. M. Lifshitz, *Quantum mechanics: non-relativistic theory*, vol. 3. Elsevier, 2013.

[463] H. Ruder, G. Wunner, H. Herold, and F. Geyer, *Atoms in Strong Magnetic Fields. Quantum Mechanical Treatment and Applications in Astrophysics and Quantum Chaos*. 1994.

[464] V. L. Afanasiev and A. V. Moiseev, *The SCORPIO universal focal reducer of the 6-m telescope*, *Astron. Lett.* **31** (2005) 193, [astro-ph/0502095].

[465] J. Liebert, G. D. Schmidt, M. Lesser, J. A. Stepanian, V. A. Lipovetsky, F. H. Chaffe, C. B. Foltz, and P. Bergeron, *Discovery of a Dwarf Carbon Star with a White Dwarf Companion and of a Highly Magnetic Degenerate Star*, **421** (Feb., 1994) 733.

[466] M. Riello, F. De Angeli, D. W. Evans, P. Montegriffo, J. M. Carrasco, G. Busso, L. Palaversa, P. W. Burgess, C. Diener, M. Davidson, N. Rowell, C. Fabricius, C. Jordi, M. Bellazzini, E. Pancino, D. L. Harrison, C. Cacciari, F. van Leeuwen, N. C. Hambly, S. T. Hodgkin, P. J. Osborne, G. Altavilla, M. A. Barstow, A. G. A. Brown, M. Castellani, S. Cowell, F. De Luise, G. Gilmore, G. Giuffrida, S. Hidalgo, G. Holland, S. Marinoni, C. Pagani, A. M. Piersimoni, L. Pulone, S. Ragaini, M. Rainer, P. J. Richards, N. Sanna, N. A. Walton, M. Weiler, and A. Yoldas, *Gaia Early Data Release 3. Photometric content and validation*, **649** (May, 2021) A3, [arXiv:2012.01916].

[467] A. Bédard, P. Bergeron, P. Brassard, and G. Fontaine, *On the Spectral Evolution of Hot White Dwarf Stars. I. A Detailed Model Atmosphere Analysis of Hot White Dwarfs from SDSS DR12*, **901** (Oct., 2020) 93, [arXiv:2008.07469].

[468] S. Bagnulo and J. D. Landstreet, *The long-term polarimetric variability of the strongly magnetic white dwarf Grw+70° 8247*, **486** (July, 2019) 4655–4670, [arXiv:1904.08327].

[469] J. R. P. Angel, J. D. Landstreet, and J. B. Oke, *The Spectral Dependence of Circular Polarization in Grw+70°8247*, **171** (Jan., 1972) L11.

[470] J. C. Kemp, J. B. Swedlund, J. D. Landstreet, and J. R. P. Angel, *Discovery of Circularly Polarized Light from a White Dwarf*, **161** (Aug., 1970) L77.

[471] J. D. Landstreet and J. R. P. Angel, *The Wavelength Dependence of Circular Polarization in GD 229*, **190** (May, 1974) L25.

[472] J. D. Landstreet and J. R. P. Angel, *The Polarization Spectrum and Magnetic Field Strength of the White Dwarf Grw+70'8247*, **196** (Mar., 1975) 819–826.

[473] J. R. P. Angel, J. Liebert, and H. S. Stockman, *The optical spectrum of hydrogen at 160-350 million gauss in the white dwarf GRW +70 8247.*, **292** (May, 1985) 260–266.

[474] G. D. Schmidt, R. G. Allen, P. S. Smith, and J. Liebert, *Combined Ultraviolet-Optical Spectropolarimetry of the Magnetic White Dwarf GD 229*, **463** (May, 1996) 320.

[475] **SDSS** Collaboration, K. M. Vanlandingham et al., *Magnetic white dwarfs from the SDSS. 2. The Second and Third Data Releases*, *Astron. J.* **130** (2005) 734–741, [astro-ph/0505085].

[476] **SDSS** Collaboration, G. D. Schmidt et al., *Magnetic white dwarfs from the SDSS. The First data release*, *Astrophys. J.* **595** (2003) 1101–1113, [astro-ph/0307121].

[477] V. Piirola and A. Reiz, *The highly magnetic (B 500 MG) white dwarf PG 1031+234 : discovery of wavelength dependent polarization and intensity variations.*, **259** (June, 1992) 143–148.

[478] G. Bertone and D. Hooper, *History of dark matter*, *Rev. Mod. Phys.* **90** (2018), no. 4 045002, [arXiv:1605.04909].

[479] W. Hu, R. Barkana, and A. Gruzinov, *Cold and fuzzy dark matter*, *Phys. Rev. Lett.* **85** (2000) 1158–1161, [astro-ph/0003365].

[480] B. Carr and F. Kuhnel, *Primordial Black Holes as Dark Matter: Recent Developments*, *Ann. Rev. Nucl. Part. Sci.* **70** (2020) 355–394, [arXiv:2006.02838].

[481] M. A. Monroy-Rodríguez and C. Allen, *The End of the MACHO Era, Revisited: New Limits on MACHO Masses from Halo Wide Binaries*, **790** (Aug., 2014) 159, [arXiv:1406.5169].

[482] T. D. Brandt, *Constraints on MACHO Dark Matter from Compact Stellar Systems in Ultra-Faint Dwarf Galaxies*, *Astrophys. J. Lett.* **824** (2016), no. 2 L31, [arXiv:1605.03665].

[483] G. Krnjaic and K. Sigurdson, *Big Bang Darkleosynthesis*, *Phys. Lett. B* **751** (2015) 464–468, [arXiv:1406.1171].

[484] E. Hardy, R. Lasenby, J. March-Russell, and S. M. West, *Big Bang Synthesis of Nuclear Dark Matter*, *JHEP* **06** (2015) 011, [arXiv:1411.3739].

[485] M. I. Gresham, H. K. Lou, and K. M. Zurek, *Early Universe synthesis of asymmetric dark matter nuggets*, *Phys. Rev. D* **97** (2018), no. 3 036003, [arXiv:1707.02316].

[486] Y. Bai, A. J. Long, and S. Lu, *Dark Quark Nuggets*, *Phys. Rev. D* **99** (2019), no. 5 055047, [arXiv:1810.04360].

[487] J. H. Chang, D. Egana-Ugrinovic, R. Essig, and C. Kouvaris, *Structure Formation and Exotic Compact Objects in a Dissipative Dark Sector*, *JCAP* **03** (2019) 036, [arXiv:1812.07000].

[488] M. R. Buckley and A. DiFranzo, *Collapsed Dark Matter Structures*, *Phys. Rev. Lett.* **120** (2018), no. 5 051102, [arXiv:1707.03829].

[489] E. Witten, *Cosmic Separation of Phases*, *Phys. Rev. D* **30** (1984) 272–285.

[490] Y. Bai and A. J. Long, *Six Flavor Quark Matter*, *JHEP* **06** (2018) 072, [arXiv:1804.10249].

[491] B. W. Lynn, A. E. Nelson, and N. Tetradis, *STRANGE BARYON MATTER*, *Nucl. Phys. B* **345** (1990) 186–209.

[492] P. W. Graham, R. Janish, V. Narayan, S. Rajendran, and P. Riggins, *White Dwarfs as Dark Matter Detectors*, *Phys. Rev.* **D98** (2018), no. 11 115027, [arXiv:1805.07381].

[493] A. Das, S. A. R. Ellis, P. C. Schuster, and K. Zhou, *Stellar Shocks From Dark Matter*, arXiv:2106.09033.

[494] A. de Rujula and S. L. Glashow, *Nuclearites-a novel form of cosmic radiation*, **312** (Dec., 1984) 734–737.

[495] P. B. Price, *Limits on contribution of cosmic nuclearites to galactic dark matter*, **38** (Dec., 1988) 3813–3814.

[496] J. Singh Sidhu, R. M. Abraham, C. Covault, and G. Starkman, *Macro detection using fluorescence detectors*, *JCAP* **02** (2019) 037, [arXiv:1808.06978].

[497] J. Singh Sidhu, R. J. Scherrer, and G. Starkman, *Death and serious injury from dark matter*, *Phys. Lett. B* **803** (2020) 135300, [arXiv:1907.06674].

[498] J. S. Sidhu and G. Starkman, *Macroscopic Dark Matter Constraints from Bolide Camera Networks*, *Phys. Rev. D* **100** (2019), no. 12 123008, [arXiv:1908.00557].

[499] N. Starkman, J. Sidhu, H. Winch, and G. Starkman, *Straight lightning as a signature of macroscopic dark matter*, *Phys. Rev. D* **103** (2021), no. 6 063024, [arXiv:2006.16272].

[500] V. Cooray, G. Cooray, M. Rubinstein, and F. Rachidi, *Could macroscopic dark matter (macros) give rise to mini-lightning flashes out of a blue sky without clouds?*, arXiv:2107.05338.

[501] B. Paxton, L. Bildsten, A. Dotter, F. Herwig, P. Lesaffre, and F. Timmes, *Modules for experiments in stellar astrophysics (mesa)*, *The Astrophysical Journal Supplement Series* **192** (Dec, 2010) 3.

[502] D. K. Feuillet, N. E. Q. Paust, and B. Chaboyer, *BVI Photometry and the Red Giant Branch Luminosity Function of M15*, *Publications of the Astronomical Society of the Pacific* **126** (Aug., 2014) 733, [arXiv:1406.4883].

[503] F. X. Timmes, *Physical properties of laminar helium deflagrations*, *The Astrophysical Journal* **528** (jan, 2000) 913–945.

[504] A. De Rujula and S. L. Glashow, *Nuclearites: A Novel Form of Cosmic Radiation*, *Nature* **312** (1984) 734–737.

[505] C. West and A. Heger, *Metallicity-dependent Galactic Isotopic Decomposition for Nucleosynthesis*, **774** (Sept., 2013) 75, [arXiv:1203.5969].

[506] H. C. Thomas, *Sternentwicklung VIII. Der Helium-Flash bei einem Stern von 1. 3 Sonnenmassen*, *Zeitschrift fur Astrophysik* **67** (Jan., 1967) 420.

[507] I. Iben, *Age and Initial Helium Abundance of Stars in the Globular Cluster M15*, **220** (Oct., 1968) 143–146.

[508] R. Ibata, C. Nipoti, A. Sollima, M. Bellazzini, S. C. Chapman, and E. Dalessandro, *Do globular clusters possess dark matter haloes? A case study in NGC 2419*, MNRAS **428** (Feb., 2013) 3648–3659, [arXiv:1210.7787].

[509] B. F. Griffen, M. J. Drinkwater, P. A. Thomas, J. C. Helly, and K. A. Pimbblet, *Globular cluster formation within the Aquarius simulation*, *MNRAS* **405** (June, 2010) 375–386, [arXiv:0910.0310].

[510] T. R. Saitoh, J. Koda, T. Okamoto, K. Wada, and A. Habe, *Tidal disruption of dark matter halos around proto-globular clusters*, *Astrophys. J.* **640** (2006) 22–30, [astro-ph/0511692].

[511] P. Creasey, L. V. Sales, E. W. Peng, and O. Sameie, *Globular clusters formed within dark haloes I: present-day abundance, distribution, and kinematics*, *MNRAS* **482** (Jan., 2019) 219–230, [arXiv:1806.11118].

[512] S. Mashchenko and A. Sills, *Globular clusters with dark matter halos. 1. Initial relaxation*, *Astrophys. J.* **619** (2005) 243, [astro-ph/0409605].

[513] **H.E.S.S.** Collaboration, A. Abramowski et al., *H.E.S.S. observations of the globular clusters NGC 6388 and M 15 and search for a Dark Matter signal*, *Astrophys. J.* **735** (2011) 12, [arXiv:1104.2548].

[514] R. K. Leane, T. Linden, P. Mukhopadhyay, and N. Toro, *Celestial-Body Focused Dark Matter Annihilation Throughout the Galaxy*, *Phys. Rev. D* **103** (2021), no. 7 075030, [arXiv:2101.12213].

[515] N. W. Evans, C. A. J. O'Hare, and C. McCabe, *Refinement of the standard halo model for dark matter searches in light of the Gaia Sausage*, *Phys. Rev. D* **99** (2019), no. 2 023012, [arXiv:1810.11468].

[516] **GRAVITY** Collaboration, R. Abuter et al., *Detection of the gravitational redshift in the orbit of the star S2 near the Galactic centre massive black hole*, *Astron. Astrophys.* **615** (2018) L15, [arXiv:1807.09409].

[517] H. Baumgardt, M. Hilker, A. Sollima, and A. Bellini, *Mean proper motions, space orbits, and velocity dispersion profiles of Galactic globular clusters derived from Gaia DR2 data*, *MNRAS* **482** (Feb., 2019) 5138–5155, [arXiv:1811.01507].

[518] H. Baumgardt, M. Hilker, A. Sollima, and A. Bellini, *Mean proper motions, space orbits, and velocity dispersion profiles of Galactic globular clusters derived from Gaia DR2 data*, *MNRAS* **482** (Feb., 2019) 5138–5155, [arXiv:1811.01507].

[519] A. Irrgang, B. Wilcox, E. Tucker, and L. Schiefelbein, *Milky Way mass models for orbit calculations*, *A&A* **549** (Jan., 2013) A137, [arXiv:1211.4353].

[520] T. D. Morton, *isochrones: Stellar model grid package*, Mar., 2015.

[521] Y. Tarumi, N. Yoshida, and S. Inoue, *Internal R-process Abundance Spread of M15 and a Single Stellar Population Model*, *Astrophys. J. Lett.* **921** (2021), no. 1 L11, [arXiv:2110.02970].

[522] E. E. Salpeter, *The Luminosity Function and Stellar Evolution.*, **121** (Jan., 1955) 161.

[523] P. Montero-Camacho, X. Fang, G. Vasquez, M. Silva, and C. M. Hirata, *Revisiting constraints on asteroid-mass primordial black holes as dark matter candidates*, *JCAP* **1908** (2019) 031, [arXiv:1906.05950].

[524] K. Sellgren, M. T. McGinn, E. E. Becklin, and D. N. Hall, *Velocity Dispersion and the Stellar Population in the Central 1.2 Parsecs of the Galaxy*, **359** (Aug., 1990) 112.

[525] E. Gallego-Cano, R. Schödel, H. Dong, F. Nogueras-Lara, A. T. Gallego-Calvente, P. Amaro-Seoane, and H. Baumgardt, *The distribution of stars around the Milky Way's central black hole. I. Deep star counts*, *A&A* **609** (Jan., 2018) A26, [arXiv:1701.03816].

[526] D. Merritt, S. Harfst, and G. Bertone, *Collisionally Regenerated Dark Matter Structures in Galactic Nuclei*, *Phys. Rev. D* **75** (2007) 043517, [astro-ph/0610425].

[527] T. Bogdanovic, R. M. Cheng, and P. Amaro-Seoane, *Disruption of a Red Giant Star by a Supermassive Black Hole and the Case of PS1-10jh*, *Astrophys. J.* **788** (2014) 99, [arXiv:1307.6176].

[528] P. Amaro-Seoane, X. Chen, R. Schödel, and J. Casanellas, *Making bright giants invisible at the Galactic Centre*, *MNRAS* **492** (Feb., 2020) 250–255, [arXiv:1910.04774].

[529] J. E. Dale, M. B. Davies, R. P. Church, and M. Freitag, *Red giant stellar collisions in the Galactic Centre*, *Mon. Not. Roy. Astron. Soc.* **393** (2009) 1016–1033, [arXiv:0811.3111].

[530] F. Antonini, R. Capuzzo-Dolcetta, A. Mastrobuono-Battisti, and D. Merritt, *Dissipationless Formation and Evolution of the Milky Way Nuclear Star Cluster*, **750** (May, 2012) 111, [arXiv:1110.5937].

[531] D. Merritt and A. Szell, *Dynamical cusp regeneration*, *Astrophys. J.* **648** (2006) 890–899, [astro-ph/0510498].

[532] S. S. Kim and M. Morris, *Dynamical friction on star clusters near the galactic center*, *Astrophys. J.* **597** (2003) 312–322, [astro-ph/0307271].

[533] M. Zajacek, A. Araudo, V. Karas, B. Czerny, A. Eckart, P. Sukova, M. Stolc, and V. Witzany, *Missing bright red giants in the Galactic center: A fingerprint of its once active state?*, 11, 2020. arXiv:2011.12868.

[534] M. Cicoli, J. P. Conlon, M. C. D. Marsh, and M. Rummel, *3.55 keV photon line and its morphology from a 3.55 keV axionlike particle line*, *Phys. Rev.* **D90** (2014) 023540, [arXiv:1403.2370].

[535] J. P. Conlon and F. V. Day, *3.55 keV photon lines from axion to photon conversion in the Milky Way and M31*, *J. Cosmol. Astropart. Phys.* **1411** (2014) 033, [arXiv:1404.7741].

[536] Kuntz, K. D. and Snowden, S. L., *The EPIC-MOS particle-induced background spectra*, *Astron. Astrophys.* **478** (2008), no. 2 575–596.

[537] W. A. Rolke, A. M. Lopez, and J. Conrad, *Limits and confidence intervals in the presence of nuisance parameters*, *Nucl. Instrum. Meth.* **A551** (2005) 493–503, [physics/0403059].

[538] F. James and M. Roos, *Minuit: A System for Function Minimization and Analysis of the Parameter Errors and Correlations*, *Comput. Phys. Commun.* **10** (1975) 343–367.

[539] A. Burkert, *The Structure of dark matter halos in dwarf galaxies*, *IAU Symp.* **171** (1996) 175, [astro-ph/9504041].

[540] P. Salucci and A. Burkert, *Dark matter scaling relations*, *Astrophys. J.* **537** (2000) L9–L12, [astro-ph/0004397].

[541] L. Strüder, J. Englhauser, R. Hartmann, P. Holl, N. Meidinger, H. Soltau, U. Briel, K. Dennerl, M. Freyberg, F. Haberl, G. Hartner, E. Pfeffermann, T. Stadlbauer, and E. Kendziorra, *pnCCDs on XMM-Newton—42 months in orbit*, *Nuclear Instruments and Methods in Physics Research A* **512** (Oct., 2003) 386–400.

[542] "Users Guide to the XMM-Newton Science Analysis System", Issue 14.0, 2018 (ESA: XMM-Newton SOC).

[543] de Plaa, J., Werner, N., Simionescu, A., Kaastra, J. S., Grange, Y. G., and Vink, J., *Cold fronts and multi-temperature structures in the core of abell 2052*, *A&A* **523** (2010) A81.

[544] Leccardi, A. and Molendi, S., *Radial temperature profiles for a large sample of galaxy clusters observed with xmm-newton**, *A&A* **486** (2008), no. 2 359–373.

[545] A. Foster, R. K. Smith, N. S. Brickhouse, and X. Cui, *AtomDB and PyAtomDB: Atomic Data and Modelling Tools for High Energy and Non-Maxwellian Plasmas*, in *American Astronomical Society Meeting Abstracts #227*, vol. 227 of *American Astronomical Society Meeting Abstracts*, p. 211.08, Jan., 2016.

[546] K. Koyama et al., *Iron and Nickel Line Diagnostics for the Galactic Center Diffuse Emission*, *Publ. Astron. Soc. Jap.* **59** (2007) 245, [astro-ph/0609215].

[547] **Fermi-LAT** Collaboration, M. Ackermann et al., *Search for Gamma-ray Spectral Lines with the Fermi Large Area Telescope and Dark Matter Implications*, *Phys. Rev. D* **88** (2013) 082002, [arXiv:1305.5597].

[548] **Fermi-LAT** Collaboration, A. Albert, G. A. Gomez-Vargas, M. Grefe, C. Munoz, C. Weniger, E. D. Bloom, E. Charles, M. N. Mazziotta, and A. Morselli, *Search for 100 MeV to 10 GeV γ-ray lines in the Fermi-LAT data and implications for gravitino dark matter in $\mu\nu$SSM*, *JCAP* **10** (2014) 023, [arXiv:1406.3430].

[549] **Fermi-LAT** Collaboration, M. Ackermann et al., *Updated search for spectral lines from Galactic dark matter interactions with pass 8 data from the Fermi Large Area Telescope*, *Phys. Rev. D* **91** (2015), no. 12 122002, [arXiv:1506.00013].

[550] A. Boyarsky, D. Malyshev, O. Ruchayskiy, and D. Savchenko, *Technical comment on the paper of Dessert et al. "The dark matter interpretation of the 3.5 keV line is inconsistent with blank-sky observations"*, arXiv:2004.06601.

[551] K. N. Abazajian, *Technical Comment on "The dark matter interpretation of the 3.5-keV line is inconsistent with blank-sky observations"*, arXiv:2004.06170.

[552] M. C. Weisskopf, T. L. Aldcroft, M. Bautz, R. A. Cameron, D. Dewey, J. J. Drake, C. E. Grant, H. L. Marshall, and S. S. Murray, *An Overview of the performance of the Chandra X-Ray Observatory*, *Exper. Astron.* **16** (2003) 1–68, [astro-ph/0503319].

[553] N. J. Secrest, R. P. Dudik, B. N. Dorland, N. Zacharias, V. Makarov, A. Fey, J. Frouard, and C. Finch, *Identification of 1.4 Million Active Galactic Nuclei in the Mid-Infrared using WISE Data*, **221** (Nov., 2015) 12, [arXiv:1509.07289].

[554] M. Bauer, M. Neubert, S. Renner, M. Schnubel, and A. Thamm, *The Low-Energy Effective Theory of Axions and ALPs*, *JHEP* **04** (2021) 063, [arXiv:2012.12272].

[555] E. H. Gudmundsson, C. J. Pethick, and R. I. Epstein, *Structure of neutron star envelopes*, **272** (Sept., 1983) 286–300.

[556] M. Bejger and P. Haensel, *Surface gravity of neutron stars and strange stars*, *Astron. Astrophys.* **420** (2004) 987–991, [astro-ph/0403550].

[557] M. Hoffberg, A. E. Glassgold, R. W. Richardson, and M. Ruderman, *Anisotropic Superfluidity in Neutron Star Matter*, *Phys. Rev. Lett.* **24** (1970), no. 14 775.

[558] L. Amundsen and E. Ostgaard, *Superfluidity of neutron matter (II). triplet pairing*, *Nucl. Phys.* **A442** (1985) 163–188.

[559] T. Takatsuka, *Energy Gap in Neutron-Star Matter*, *Progress of Theoretical Physics* **48** (Nov., 1972) 1517–1533.

[560] M. Baldo, J. Cugnon, A. Lejeune, and U. Lombardo, *Proton and neutron superfluidity in neutron star matter*, *Nucl. Phys.* **A536** (1992) 349–365.

[561] O. Elgaroy, L. Engvik, M. Hjorth-Jensen, and E. Osnes, *Superfluidity in beta stable neutron star matter*, *Phys. Rev. Lett.* **77** (1996) 1428–1431, [nucl-th/9604041].

[562] D. Page, J. M. Lattimer, M. Prakash, and A. W. Steiner, *Minimal cooling of neutron stars: A New paradigm*, *Astrophys. J. Suppl.* **155** (2004) 623–650, [astro-ph/0403657].

[563] K. Oh et al., *The 105 month Swift-BAT all-sky hard X-ray survey*, *Astrophys. J. Suppl.* **235** (2018), no. 1 4, [arXiv:1801.01882].

[564] R. Krivonos, S. Tsygankov, I. Mereminskiy, A. Lutovinov, S. Sazonov, and R. Sunyaev, *New hard X-ray sources discovered in the ongoing INTEGRAL Galactic Plane survey after 14 years of observations*, *Mon. Not. Roy. Astron. Soc.* **470** (2017) 512, [arXiv:1704.03364].

[565] A. Schwenk and B. Friman, *Polarization contributions to the spin dependence of the effective interaction in neutron matter*, *Physical Review Letters* **92** (Feb, 2004).

[566] A. D. Schwope, V. Hambaryan, F. Haberl, and C. Motch, *The complex X-ray spectrum of the isolated neutron star RBS1223*, *Astrophys. Space Sci.* **308** (2007) 619–623, [astro-ph/0609705].

[567] M. H. van Kerkwijk, D. L. Kaplan, M. Durant, S. R. Kulkarni, and F. Paerels, *A Strong, broad absorption feature in the x-ray spectrum of the nearby neutron star RX J1605.3+3249*, *Astrophys. J.* **608** (2004) 432–443, [astro-ph/0402418].

[568] J. Braithwaite, *Axisymmetric magnetic fields in stars: relative strengths of poloidal and toroidal components*, *Mon. Not. Roy. Astron. Soc.* **397** (2009) 763, [arXiv:0810.1049].

[569] E. Glebbeek, E. Gaburov, S. E. de Mink, O. R. Pols, and S. F. Portegies Zwart, *The evolution of runaway stellar collision products*, *Astronomy & Astrophysics* **497** (Feb, 2009) 255–264.

[570] G. G. Raffelt, *Astrophysical methods to constrain axions and other novel particle phenomena*, *Phys. Rept.* **198** (Dec, 1990) 1–113.

[571] F. Yusef-Zadeh, *The Origin of the Galactic center nonthermal radio filaments: Young stellar clusters*, *Astrophys. J.* **598** (2003) 325–333, [astro-ph/0308008].

[572] J. S. Clark, M. E. Lohr, L. R. Patrick, and F. Najarro, *The arches cluster revisited. iii. an addendum to the stellar census*, 2018.

[573] R. Krivonos, M. Clavel, J. Hong, K. Mori, G. Ponti, J. Poutanen, F. Rahoui, J. Tomsick, and S. Tsygankov, *NuSTAR and XMM–Newton observations of the Arches cluster in 2015: fading hard X-ray emission from the molecular cloud*, *Mon. Not. Roy. Astron. Soc.* **468** (2017), no. 3 2822–2835, [arXiv:1612.03320].

[574] R. A. Krivonos et al., *First hard X-ray detection of the non-thermal emission around the Arches cluster: morphology and spectral studies with NuSTAR*, *Astrophys. J.* **781** (2014) 107, [arXiv:1312.2635].

[575] F. Martins, R. Genzel, D. Hillier, F. Eisenhauer, T. Paumard, S. Gillessen, T. Ott, and S. Trippe, *Stellar and wind properties of massive stars in the central parsec of the Galaxy*, *Astron. Astrophys.* **468** (2007) 233, [astro-ph/0703211].

[576] B. L. Friman and O. V. Maxwell, *Neutron Star Neutrino Emissivities*, *Astrophys. J.* **232** (1979) 541–557.

[577] D. G. Yakovlev and K. P. Levenfish, *Modified URCA process in neutron star cores.*, *Astronomy and Astrophysics* **297** (May, 1995) 717.

[578] R. Mayle, J. R. Wilson, J. R. Ellis, K. A. Olive, D. N. Schramm, and G. Steigman, *Updated Constraints on Axions from SN 1987a*, *Phys. Lett. B* **219** (1989) 515.

[579] K. P. Levenfish and D. G. Yakovlev, *Suppression of neutrino energy losses in reactions of direct urca processes by superfluidity in neutron star nuclei*, *Astronomy Letters* **20** (Jan., 1994) 43–51.

[580] D. G. Yakovlev, A. D. Kaminker, and K. P. Levenfish, *Neutrino emission due to Cooper pairing of nucleons in cooling neutron stars*, *Astron. Astrophys.* **343** (1999) 650, [astro-ph/9812366].

[581] B. Haskell and A. Sedrakian, *Superfluidity and Superconductivity in Neutron Stars*, *Astrophys. Space Sci. Libr.* **457** (2018) 401–454, [arXiv:1709.10340].

[582] K. P. Levenfish and D. G. Yakovlev, *Specific heat of neutron star cores with superfluid nucleons*, *Astronomy Reports* **38** (Mar., 1994) 247–251.

[583] K. P. Levenfish and D. G. Yakovlev, *Standard and enhanced cooling of neutron stars with superfluid cores*, *Astron. Lett.* **22** (1996) 49, [astro-ph/9608032].

[584] D. Page, J. M. Lattimer, M. Prakash, and A. W. Steiner, *Neutrino Emission from Cooper Pairs and Minimal Cooling of Neutron Stars*, *Astrophys. J.* **707** (2009) 1131–1140, [arXiv:0906.1621].

[585] J. Ashworth, W. B., *A Probable Flamsteed Observation of the Cassiopeia A Supernova*, *Journal for the History of Astronomy* **11** (Jan., 1980) 1.

[586] R. A. Fesen, M. C. Hammell, J. Morse, R. A. Chevalier, K. J. Borkowski, M. A. Dopita, C. L. Gerardy, S. S. Lawrence, J. C. Raymond, and S. van den Bergh, *The expansion asymmetry and age of the cassiopeia a supernova remnant*, *Astrophys. J.* **645** (2006) 283–292, [astro-ph/0603371].

[587] D. Klochkov, V. Suleimanov, G. Pühlhofer, D. G. Yakovlev, A. Santangelo, and K. Werner, *The neutron star in HESSJ1731-347: Central compact objects as laboratories to study the equation of state of superdense matter*, *Astron. Astrophys.* **573** (2015) A53, [arXiv:1410.1055].

[588] F. Acero, M. Lemoine-Goumard, M. Renaud, J. Ballet, J. W. Hewitt, R. Rousseau, and T. Tanaka, *Study of TeV shell supernova remnants at gamma-ray energies*, *Astron. Astrophys.* **580** (2015) A74, [arXiv:1506.02307].

[589] Y. Cui, G. Pühlhofer, and A. Santangelo, *A young supernova remnant illuminating nearby molecular clouds with cosmic rays*, *Astron. Astrophys.* **591** (2016) A68, [arXiv:1605.00483].

[590] N. Maxted, M. Burton, C. Braiding, G. Rowell, H. Sano, F. Voisin, M. Capasso, G. Pühlhofer, and Y. Fukui, *Probing the local environment of the supernova remnant HESS J1731−347 with CO and CS observations*, *Mon. Not. Roy. Astron. Soc.* **474** (2018), no. 1 662–676, [arXiv:1710.06101].

[591] W. C. G. Ho, Y. Zhao, C. O. Heinke, D. L. Kaplan, P. S. Shternin, and M. J. P. Wijngaarden, *X-ray bounds on cooling, composition, and magnetic field of the Cassiopeia A neutron star and young central compact objects*, *Mon. Not. Roy. Astron. Soc.* **506** (2021) 5015–5029, [arXiv:2107.08060].

[592] I. Lovchinsky, P. Slane, B. M. Gaensler, J. P. Hughes, C. Y. Ng, J. S. Lazendic, J. D. Gelfand, and C. L. Brogan, *A Chandra Observation of Supernova Remnant G350.1-0.3 and Its Central Compact Object*, *The Astrophysical Journal* **731** (Apr., 2011) 70, [arXiv:1102.5333].

[593] M. G. F. Mayer and W. Becker, *A kinematic study of central compact objects and their host supernova remnants*, *Astron. Astrophys.* **651** (2021) A40, [arXiv:2106.00700].

[594] A. Kirichenko, A. Danilenko, Y. Shibanov, P. Shternin, S. Zharikov, and D. Zyuzin, *Deep optical observations of the γ-ray pulsar J0357+3205*, *Astron. Astrophys.* **564** (2014) A81, [arXiv:1402.2246].

[595] C.-Y. Ng, R. W. Romani, W. F. Brisken, S. Chatterjee, and M. Kramer, *The Origin and Motion of PSR J0538+2817 in S147*, *Astrophys. J.* **654** (2006) 487–493, [astro-ph/0611068].

[596] C. O. Heinke and W. C. G. Ho, *Direct Observation of the Cooling of the Cassiopeia A Neutron Star*, *The Astrophysical Journal, Letters* **719** (Aug., 2010) L167–L171, [arXiv:1007.4719].

[597] K. Elshamouty, C. Heinke, G. Sivakoff, W. Ho, P. Shternin, D. Yakovlev, D. Patnaude, and L. David, *Measuring the Cooling of the Neutron Star in Cassiopeia A with all Chandra X-ray Observatory Detectors*, *Astrophys. J.* **777** (2013) 22, [arXiv:1306.3387].

[598] M. V. Beznogov, E. Rrapaj, D. Page, and S. Reddy, *Constraints on Axion-like Particles and Nucleon Pairing in Dense Matter from the Hot Neutron Star in HESS J1731-347*, *Phys. Rev. C* **98** (2018), no. 3 035802, [arXiv:1806.07991].

[599] L. B. Leinson, *Constraints on axions from neutron star in HESS J1731-347*, *JCAP* **11** (2019) 031, [arXiv:1909.03941].

[600] W. W. Tian, D. A. Leahy, M. Haverkorn, and B. Jiang, *Discovery of the counterpart of TeV Gamma-ray source HESS J1731-347: a new SNR G353.6-0.7 with radio and X-ray images*, *Astrophys. J. Lett.* **679** (2008) L85, [arXiv:0801.3254].

[601] D. Ding, A. Rios, H. Dussan, W. H. Dickhoff, S. J. Witte, A. Polls, and A. Carbone, *Pairing in high-density neutron matter including short- and long-range correlations*, *Phys. Rev. C* **94** (2016), no. 2 025802, [arXiv:1601.01600]. [Addendum: Phys.Rev.C 94, 029901 (2016)].

[602] P. Haensel, V. A. Urpin, and D. G. Yakovlev, *Ohmic decay of internal magnetic fields in neutron stars*, *Astronomy and Astrophysics* **229** (Mar., 1990) 133–137.

[603] J. A. Miralles, V. Urpin, and D. Konenkov, *Joule heating and the thermal evolution of old neutron stars*, *Astrophys. J.* **503** (1998) 368, [astro-ph/9803063].

[604] D. Page, U. Geppert, and T. Zannias, *General relativistic treatment of the thermal, magnetic and rotational evolution of neutron stars with crustal magnetic fields*, *Astron. Astrophys.* **360** (2000) 1052, [astro-ph/0005301].

[605] U. Geppert, M. Rheinhardt, and J. Gil, *Spot - like structures of neutron star surface magnetic fields*, *Astron. Astrophys.* **412** (2003) L33–L36, [astro-ph/0311121].

[606] P. Arras, A. Cumming, and C. Thompson, *Magnetars: Time evolution, superfluid properties, and mechanism of magnetic field decay*, *Astrophys. J. Lett.* **608** (2004) L49–L52, [astro-ph/0401561].

[607] A. Cumming, P. Arras, and E. G. Zweibel, *Magnetic field evolution in neutron star crusts due to the Hall effect and Ohmic decay*, *Astrophys. J.* **609** (2004) 999–1017, [astro-ph/0402392].

[608] J. A. Pons, B. Link, J. A. Miralles, and U. Geppert, *Evidence for Heating of Neutron Stars by Magnetic Field Decay*, *Phys. Rev. Lett.* **98** (2007) 071101, [astro-ph/0607583].

[609] J. A. Pons and U. Geppert, *Magnetic field dissipation in neutron star crusts: From magnetars to isolated neutron stars*, *Astron. Astrophys.* **470** (2007) 303, [astro-ph/0703267].

[610] D. N. Aguilera, J. A. Pons, and J. A. Miralles, *The impact of magnetic field on the thermal evolution of neutron stars*, *Astrophys. J. Lett.* **673** (2008) L167–L170, [arXiv:0712.1353].

[611] S. B. Popov, J. A. Pons, J. A. Miralles, P. A. Boldin, and B. Posselt, *Population synthesis studies of isolated neutron stars with magnetic field decay*, *Mon. Not. Roy. Astron. Soc.* **401** (2010) 2675–2686, [arXiv:0910.2190].

[612] D. Viganò, N. Rea, J. A. Pons, R. Perna, D. N. Aguilera, and J. A. Miralles, *Unifying the observational diversity of isolated neutron stars via magneto-thermal evolution models*, *Mon. Not. Roy. Astron. Soc.* **434** (2013) 123, [arXiv:1306.2156].

[613] G. R. Blumenthal, S. M. Faber, R. Flores, and J. R. Primack, *Contraction of Dark Matter Galactic Halos Due to Baryonic Infall*, **301** (Feb., 1986) 27.

[614] D. Merritt, *Evolution of the dark matter distribution at the galactic center*, *Phys. Rev. Lett.* **92** (2004) 201304, [astro-ph/0311594].

[615] J. D. Dull, H. N. Cohn, P. M. Lugger, B. W. Murphy, P. O. Seitzer, P. J. Callanan, R. G. M. Rutten, and P. A. Charles, *The Dynamics of M15: Observations of the Velocity Dispersion Profile and Fokker-Planck Models*, **481** (May, 1997) 267–281.

[616] J. Gerssen, R. P. van der Marel, K. Gebhardt, P. Guhathakurta, R. C. Peterson, and C. Pryor, *Hubble Space Telescope evidence for an intermediate - mass black hole in the globular cluster M15: 2. Kinematical analysis and dynamical modeling*, *Astron. J.* **124** (2002) 3270–3288, [astro-ph/0209315].

[617] J. Lewin and P. Smith, *Review of mathematics, numerical factors, and corrections for dark matter experiments based on elastic nuclear recoil*, *Astroparticle Physics* **6** (1996), no. 1 87–112.